POWER QUALITY – MONITORING, ANALYSIS AND ENHANCEMENT

Edited by **Ahmed Faheem Zobaa,**
Mario Mañana Canteli and **Ramesh Bansal**

Power Quality – Monitoring, Analysis and Enhancement
Edited by Ahmed Faheem Zobaa, Mario Mañana Canteli and Ramesh Bansal

Contents

Preface

Power quality has become an important issue in recent times when many utilities around the world find very difficult to meet energy demands which leads to load shedding and power quality problems. This book on power quality written by experts in their fields will be of great benefit to professionals, engineers and researchers. This book comprises of 16 chapters which are arranged in two sections. Section one covers power quality monitoring, classification, and analysis aspects. Power quality enhancement, reactive power compensation and voltage sag mitigation of disturbances in transmission and distribution system are presented in the second section. Brief discussion of each chapter is as follows.

Chapter 1 presents the monitoring of voltage sags to find its origin and detect types of sags. The calculations of various types of faults which may cause voltage sags have been discussed. Optimal placement of voltage sag monitors has also been discussed in the chapter.

Chapter 2 proposes the applications of discrete wavelet transform (DWT), principal component analysis (PCA) and artificial neural networks (ANN) in order to classify power quality disturbances. The method proposes to analyse seven classes of signals, namely Sinusoidal Waveform, Capacitor Switching Transient, Flicker, Harmonics, Interruption, Notching and Sag, which is composed of four main stages: (1) signal analysis using the DWT; (2) feature extraction; (3) data reduction using PCA; (4) classification using a radial basis function network (RBF). The MRA (Multiresolution Analysis) technique of DWT is employed to extract the discriminating features of distorted signals at different resolution levels. Subsequently, the PCA is used to condense information of a correlated set of variables into a few variables, and a RBF network is employed to classify the disturbance types.

Chapter 3 presents a critical review of apparent power, reactive power and power factor definitions. These definitions are reviewed for single phase and three phase systems and are evaluated under different conditions such as sinusoidal, non sinusoidal, one phase, and balanced and unbalanced three phase systems. Then, a methodology to measure power and power quality indexes based on the instant power theory under non sinusoidal conditions is presented.

Chapter 4 deals with the application of power quality monitoring in power system network comprising of distributed energy sources (DER). The importance to integrate power quality analysis functions into protection relay has been described. The voltage and current transducers for measurement of line voltage and current signals have been discussed.

Chapter 5 discusses the applications of signal processing techniques for power quality monitoring. This chapter also presents various classification techniques which are very useful for power system disturbances, e.g. ANN, support vector machines (SVM), pattern recognition, etc. Filter and Wrapper based methods used for removal of irreverent and redundant data and feature selection are discussed.

Chapter 6 presents different methods for the power quality analysis. A comparative analysis of Discrete Fourier Transform (DFT), Short-Time Fourier Transform (STFT), Discrete Wavelet Transform (DWT) and Discrete Stockwell Transform (DST) is presented for power quality analysis.

Chapter 7 presents a review of various preprocessing (DWT, Shannon entropy, signal energy, and fractal dimension) and intelligent techniques (ANN, adaptive Neural-Fuzzy Interface Systems (ANFIS), and Neural-Genetic) used for power quality analysis. This chapter also demonstrates the application of ATP (alternative transients program) software preprocessing and disturbance analysis of real distribution system.

Chapter 8 presents the selection of the voltage referential (reference point) which can influence the total harmonic distortion, unbalance factors, voltage sags and swells in three-phase system. The definition of apparent power is reviewed using voltage referential. A methodology based on Blakesley's theorem is presented in order to allow the association of the most common voltage measurement approaches in such a way that the power quality and power components definitions are not be improperly influenced.

Chapter 9 deals with problems of location of the disturbance source based on the measurements made at a single point of a network (PCC). Methodologies are presented for high harmonics, voltage fluctuations, voltage dips and unbalance that allow the determination of location of the disturbance source at the supplier side (upstream) or at the customer side (downstream) viewed from PCC.

Chapter 10 discusses the theoretical background on STFT, wave transform (WT) and S-transform. The indices which are most frequently used in international standards and four new power quality indices for transient disturbances based on S-transform are defined. The performance of the new power quality indices is evaluated using mathematical and PSCAD/EMTDC simulated disturbance signals.

Chapter 11 presents detailed analysis of active load balancing in a three phase system using reactive power compensation. This chapter develops a mathematical model associated to the circuit proposed by Steinmetz which is commonly used in major

industrial applications. Sizing the compensator elements on the criterion of reactive power demand from network is discussed.

Chapter 12 presents a novel and optimized switching strategy and control approach for a three level two-quadrant chopper in a three-level neutral point clamped (NPC) voltage source inverter (VSI) superconducting magnetic energy storage(SMES). Using the proposed switching strategy, the voltage of the inverter capacitors in SMES can be independently controlled and minimum power and switching losses can be achieved using this same strategy. In addition, this chapter proposes a new algorithm for SMES to compensate the voltage sag in the power networks. Simulation results show that the VSI SMES, when combined with the proposed algorithm, is able to compensate the voltage sag and phase voltage in less than one cycle, which is five times better than other voltage sag compensators.

Chapter 13 presents optimal placement and control of FACTS devices and discusses a methodology that coordinates the expertise of power system engineer formulated in flexible fuzzy rules to dynamically adjust the reactive power compensation based on three phase model of shunt FACTS controller (SVC) installed at critical buses. The main target of the proposed technique is to reduce the asymmetrical voltage and to enhance the system loadability with consideration of unbalanced electrical network.

Chapter 14 presents a novel topology of the dynamic voltage restorer (DVR) with split capacitors and new installation of the capacitors filtering scheme using a three phase four wire, three phase inverter with six Insulated Gate Bipolar Transistor (IGBTs). Experimental and simulation results show the advantages of proposed DVR over traditional DVRs.

Chapter 15 presents an overview on utility efforts in voltage sag mitigation employing the network reconfiguration strategy. The theoretical background of the proposed method is first introduced and then the analysis and simulation tests on a practical system are described to highlight the suitability of network reconfiguration as a method for voltage sag mitigation. The analyses of simulation results suggest significant findings which can assist utility engineers to take the right decision in network reconfiguration.

Chapter 16 presents the applications of artificial intelligence techniques for power quality enhancement in distribution system. The proposed approach is tested on a 75 bus practical system using fuzzy adaptive evolutionary computing.

Editors are grateful to many people who have contributed to this book. In particular Editors would like to thank all authors for their contributions. Editors are indebted to all the reviewers for reviewing the book chapters which has improved the quality of the book. Editors would like to thank the authorities and staff members of and The University of Queensland, University of Cantabria and Brunel University who have

been very generous and helpful in maintaining a cordial atmosphere and extending all the facilities required for the book. Thanks are due to InTech - Open Access Publisher, especially to Ms. Sandra Bakic Publishing Process Manager for making sincere efforts in timely bringing out the book. Editors would like to express thanks and sincere regards to their family members who have provided great support for completion of this book.

Ahmed Faheem Zobaa
Brunel University, Uxbridge,
U.K.

Mario Mañana Canteli
University of Cantabria (UC), Santander,
Spain

Ramesh Bansal
The University of Queensland,
Australia

Part 1

Power Quality Monitoring, Classification, Measurements, and Analysis

Power Quality Monitoring

Kazem Mazlumi
Zanjan University, Zanjan
Iran

1. Introduction

Power quality is the measure, analysis, and improvement of a load bus voltage, to maintain that voltage to be a sinusoid at rated voltage and frequency. The phenomena related to power quality are generally physical stochastic events in the sense that in many cases are appearing and disappearing arbitrarily. Therefore, power quality measure is more than a simple measurement of an electrical parameter; i.e. it is necessary to record them over an enough long time interval. In order to reduce the huge amount of data by recording and analyzing several electrical parameters over a long period of time, some recording limits are set. If these limits are exceeded, the monitoring instruments evaluate the raw data and record only the essential data of the important events.

There are several reasons for monitoring power quality. The most important reason is the economic damage produced by electromagnetic phenomena in critical process loads. Effects on equipment and process operations can include malfunctions, damage, process disruption, and other anomalies.

It is noted that monitoring, alone, is not the solution for power quality problems. In order to solve the power quality problems, some other remedies more than the installation of power quality monitors are needed. In fact, monitoring provides the essential data which are needed for the improvement of power quality. In many projects related to finding a solution for power quality problems, monitoring plays a decisive role, and, therefore, managing monitoring properly helps to minimize the cost of solving problems.

The recorded power quality data depends on the way the instruments record the disturbance levels and how the signals are interpreted. In order to have a correct interpretation of the recorded data, users need to know the specifications of the monitoring instruments such as sampling rate, accuracy, resolution, anti-aliasing filter. The mis-interpretation may result in non-existent errors and recording disturbances which in turn may lead to incorrect conclusions and costly decisions.

Effective monitoring programs are important for power reliability assurance for both utilities and customers. It is worth pointing out that most customer power quality problems originate within the customer facility. Monitoring power quality ensures optimal power system performance and effective energy management. Voltage sags, harmonics, interruptions, high-frequency noise, etc., are the most important power quality problems which are seen in industrial and commercial installations. Troubleshooting these problems requires measuring and analyzing power quality and that leads to the importance of monitoring instruments in order to localize the problems and find solutions. Although the

power quality monitoring relies on measuring various parameters, only voltage sags and locating their origins are studied in this chapter for brevity.

2. Voltage sag

Voltage sags are short duration reductions in rms voltage. According to the standards, voltage sag is "a decrease in voltage at the power frequency for durations of half a cycle to 1 minute". The voltage sag is a multi-dimensional disturbance; i.e. the voltage sag is mainly characterized by duration and retained voltage. The duration of a voltage sag is the amount of time during which the voltage magnitude is below the sag threshold. The retained voltage of the voltage sag is the lowest rms voltage in any of the three phases.

Voltage sags are mainly caused by short circuits, starting (or re-accelerating) of large motors, and transformer energizing. It is noted that when an induction motor starts, it can draw very high currents until the rotor comes up to speed. Many disturbances are due to normal operations such as switching loads and capacitors or faults and the opening of circuit breakers to clear faults. Faults are usually caused by natural or accidental events outside the utility's control such as lightning, birds flying close to power lines and getting electrocuted, and trees or equipment contacting power lines.

Several random factors are involved in the analysis of voltage sags. Some of them are listed as follows:

- Fault type: Three-phase faults are more severe than single-phase faults, but the latter happen more frequently.
- Fault location: Faults originated in transmission systems cause sags which can be seen tens of kilometers away.
- Fault impedance: Solid faults cause more severe sags than impedance faults.
- Fault duration: Self-cleared faults cause sags whose duration depends on the fault itself, not on the protection setting.
- Power system modifications: The impedance between the point of observation and the fault point affects the magnitude of the fault caused sag.

As mentioned before, the drop in voltage during a sag may be due to a short circuit being present in the system. The moment the short circuit fault is cleared by the protection system, the voltage starts to return to its original value. Thus, the duration of a sag is determined by the fault clearing time. However, the actual duration of a sag is normally longer than the fault clearing time.

The commonly used definition of sag duration is the number of cycles during which the rms voltage is below a given threshold. This threshold is somewhat different for each monitor but typical values are around 90% of the nominal voltage. A power quality monitor typically calculates the rms value once every cycle. The main problem is that the so-called post-fault sag affects the sag duration. When the fault is cleared, the voltage does not recover immediately. This is mainly due to the re-energizing and re-acceleration of induction motor load. This post-fault sag may last several seconds, much longer than the actual sag. Therefore, the sag duration as defined before, is no longer equal to the fault clearing time. More seriously, different power quality monitors give different values for the sag duration. As the rms voltage recovers slowly, a small difference in threshold setting may already lead to a serious difference in recorded sag duration. Faults in transmission systems are usually cleared faster than faults in distribution systems. In transmission systems, the critical fault clearing time is rather small.

Thus, fast protection and fast circuit breakers are essential. Also, transmission and sub-transmission systems are normally operated as a grid, requiring distance protection or differential protection, both of which allow for fast clearing of the fault. The principal form of protection in distribution systems is over-current protection. This requires a certain amount of time-grading, which increases the fault clearing time. An exception is formed by systems in which current-limiting fuses are used. These have the ability to clear a fault within one half-cycle. In overhead distribution systems, the instantaneous trip of the re-closer leads to a short sag duration, but the clearing of a permanent fault gives a sag with much longer duration.

One of the interests in voltage sags is due to the problems they cause on several types of equipments. Some of the equipments trip when the rms voltage drops below 90% for longer than one or two cycles. Such the equipments trip tens of times a year. A voltage sag is not as damaging to industry as a interruption, but as there are far more voltage sags than interruptions, the total damage due to sags is still larger. Another important aspect of voltage sags is that they are hard to mitigate. Short and long interruptions can be prevented via simple measures in the local distribution network. Voltage sags at equipment terminals usually is due to short-circuit faults hundreds of kilometers away in the transmission system. It is clear that there is no simple method to prevent the sags. In this chapter we consider all of the sags originate with the faults.

The magnitude of voltage sag is determined from the rms voltage. There are various ways of obtaining the sag magnitude from the rms voltages. Most power quality monitors take the lowest value obtained during the event. As sags normally have a constant rms value during the deep part of the sag, using the lowest value is an acceptable approximation. The sag is characterized through the remaining voltage during the event. This is then given as a percentage of the nominal voltage. Thus, a 90% sag in a 400 kV system means that the voltage dropped to 360 kV.

Fault location also affects the level of the voltage sags on different parts of the network. For example, consider the distribution network shown in Fig. 1, where F1 through F4 indicate fault positions and B1 through B4 indicate the loads. A fault in fault position F1 causes serious sag for the substation bordering the faulted line. This sag is transferred down to all customers fed from the substation A1. As there is normally no generation connected at lower voltage levels, there is nothing to keep up the voltage. The result is that all customers (B2, B3, and B4) experience serious sag. A fault at position F2 does not cause much voltage drop for customer B1. The impedance of the transformers between substation A1 and substation A2 is large enough to considerably limit the voltage drop at high-voltage side of the transformer. The fault at position F2, however, causes a deep sag at substations A3 and A4 and thus for all customers fed from here (B3 and B4). A fault at position F3 causes an interruption for customer B4 when the protection clears the fault. Only customer B3 experiences serious sag whereas customer B1 does not probably sense anything from this fault.

To calculate sag magnitude in radial systems, shown in Fig. 2, a method (the voltage divider method) is introduced now. Where Z_S is the source impedance at the Point of Common Coupling (PCC), and Z_L is the impedance between the PCC and the fault point. The PCC is the point from which both the fault and the load are fed. In the voltage divider method, the voltage at the PCC is found as follows:

$$V_{PCC} = \frac{Z_L}{Z_S + Z_L} \qquad (1)$$
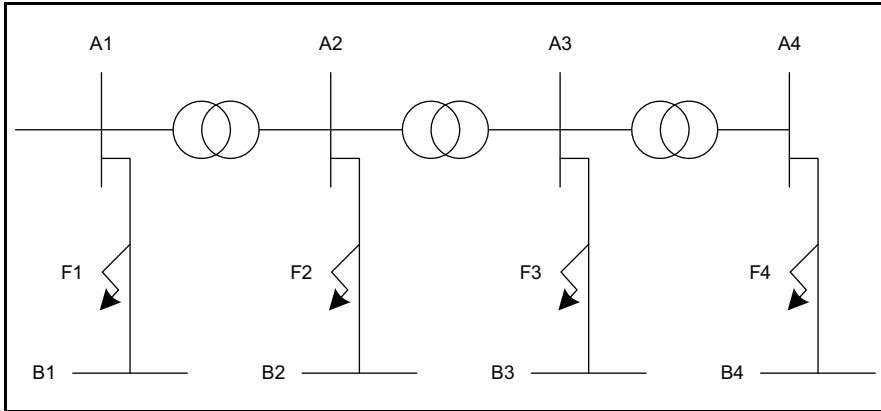
Fig. 1. Sample network for the effects of fault location on voltage sag level
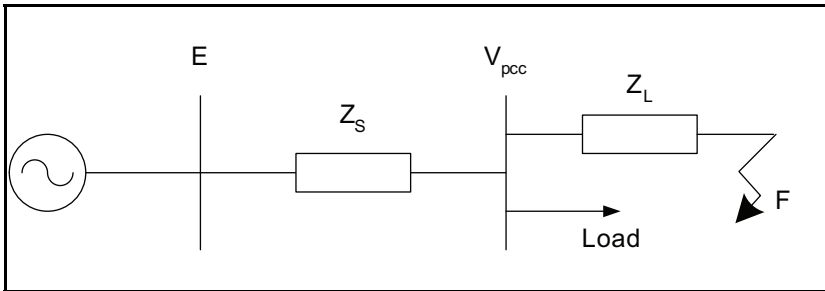
Fig. 2. Voltage sag in a radial network

In Equation (1), the load currents are neglected and it is assumed that the pre-fault voltage is exactly 1 p.u. (e.g., E = 1). Equation (1) shows that the sag becomes more dangerous for faults electrically closer to the customer (i.e., Z_L is smaller), and for weaker systems (i.e., Z_S is larger). It is noted that Equation (1) is suitable for the calculation of the voltage sag in radial networks. For more complicated systems like interconnected transmission systems, matrix calculation is more appropriate. For these cases, the admittance or impedance matrices are used to represent the system.

The voltage sag magnitude is also calculated directly from the fault levels at the PCC and at the fault position. If S_{FL} and S_{PCC} are the fault level at the fault position and the PCC, respectively, the sag voltage at the PCC is written as follows:

$$V_{PCC} = 1 - \frac{S_{FL}}{S_{PCC}} \qquad (2)$$

The faults in power systems may be symmetrical or unsymmetrical leading to balanced or unbalanced sags, respectively. For the symmetrical faults, only the positive sequence network is required to analyze the during-fault voltage. However the majority of the faults are Single Line to Ground (SLG) faults. The symmetrical components are used to analyze the SLG faults.

3. Power quality monitoring

The process of the power quality analysis consists of four steps, namely, detection, classification, characterization, and location. Power quality monitoring is used to detect the power quality problems. The monitoring solutions depend on the power quality problems being studied. For example, monitoring of the voltage sags caused by remote faults requires a long-time monitoring. To monitor the power quality problems, the instruments such as multi-meters, oscilloscope, disturbance analyzers, flicker meters, and energy monitors may be used. Some other measuring devices are used for monitoring power quality problems. Although the main purpose of these devices is not the monitoring of the power quality problems, they can be used for this reason. Digital Fault Recorders (DFRs), power meters, and etc. are in this category.

DFR is a monitoring device usually used for monitoring the faults related to the power system disturbances. The DFR is used for metering the bus voltages, line currents, and etc. The high sampling rates (between 6 and 10 kHz) of the DFRs make them possible to record almost all of the events as the transient faults. The DFRs have huge memories for recording and storing the events for a long time.

Monitoring may be used for locating the origins of the power quality disturbances such as voltage sags, harmonics, flickers, and etc. Since the origins of the most voltage sags are the short-circuit faults, the fault locating method and the optimum placement of the monitoring devices are discussed in the rest of this chapter.

4. Voltage sag measurement

Once the fault is cleared, the normal service is restored as soon as possible. The permanent short-circuit faults need to repair the causes of the faults. Therefore, finding the fault location of a permanent fault is necessary to remove the fault cause and to re-energize the network. The fault location problem is usually related to the transmission line for which terminal measurements are available. In this case, the objective of the metering is to find the exact fault location.

The retained voltage during the fault gives the magnitude of a voltage sag. Depending on the type of fault that causes the sag, the voltage during the event may be equal or different in the three phases. According to the symmetrical component classification, two types of symmetrical and unsymmetrical voltage sags are recognized.

Three-phase fault causes balanced voltage sag meaning that the phase voltages during the fault are equal in the three phases. For this kind of voltage sags, only one phase voltage is needed to characterize the magnitude and phase angle of the sag. An unsymmetrical fault may cause the sags with the main drop in one phase or two phases. The equations for voltages during the fault are derived for symmetrical and unsymmetrical faults.

5. Balanced voltage sag

As mentioned above, a three-phase fault causes balanced voltage sag. Consider a network with n buses and its impedance matrix $\mathbf{Z}$. According to the superposition theorem, the voltage during the fault equals the pre-fault voltage at the bus plus the change in the voltage due to the fault. Therefore, the voltage at bus k (= 1, 2, …, n) during a three-phase fault at bus f (= 1, 2, …, n) is given as follows

$$v_{kf} = v_{\mathrm{pref},k} + \Delta v_{kf} \tag{3}$$

where $v_{\mathrm{pref},k}$ is the pre-fault voltage at bus k and Δv_{kf} is the voltage-change at bus k due to the fault at bus f. The n^2 equations of Equation (3) can be shown in the matrix form as follows

$$\mathbf{V}_{\mathrm{dfv}} = \mathbf{V}_{\mathrm{pref}} + \Delta\mathbf{V} \tag{4}$$

The sag matrix $\mathbf{V}_{\mathrm{dfv}}$ contains the during fault voltages (v_{kf}). For example, the row k of $\mathbf{V}_{\mathrm{dfv}}$ contains the retained voltages at bus k when faults occur at buses 1, 2, …, f, …, n. Also, the column f of $\mathbf{V}_{\mathrm{dfv}}$ contains the retained voltage at buses 1, 2, …, k, …, n for a fault at bus f. $\mathbf{V}_{\mathrm{pref}}$ is the pre-fault voltage matrix. Since the pre-fault voltage at bus k is the same for a fault at any bus, the pre-fault voltage matrix is conformed by n equal columns. $\Delta\mathbf{V}$ is a matrix containing the changes in voltage due to faults everywhere. This matrix-based approach is useful for computational implementation of the stochastic assessment.

The voltage changes Δv_{kf} are calculated by using the impedance matrix. During a three-phase fault at bus f, the current injected to the bus f, i_f, is calculated by

$$i_f = -\frac{v_{\mathrm{pref},f}}{Z_{ff}} \tag{5}$$

where $v_{\mathrm{pref},f}$ is the pre-fault voltage at the faulted bus f and Z_{ff} is the impedance seen looking into the network at the faulted bus f. It is noted that only the positive sequence is needed to calculate the fault currents.

By obtaining the injected current due to the fault at bus f, the change in voltage at bus k is calculated using the transfer impedance Z_{kf} as follows

$$\Delta v_{kf} = -Z_{kf}\frac{v_{\mathrm{pref},f}}{Z_{ff}} \tag{6}$$

The transfer impedance is the voltage that exists on bus k when bus f is driven by an injection current of unity. Replacing Δv_{kf} from Equation (6) in Equation (3) results in

$$v_{kf} = v_{\mathrm{pref},k} - Z_{kf}\frac{v_{\mathrm{pref},f}}{Z_{ff}} \tag{7}$$

Equation (7) is simplified by neglecting the load, which allows taking the pre-fault voltages equal to 1p.u. This equation shows that the voltage change at a bus k due to a three-phase fault at bus f is given by the quotient between the transfer impedance and the driven point impedance at the faulted bus. The positive sequence impedance matrix Z is a diagonal dominant full matrix for a connected network. This means that every bus is exposed to sag due to fault everywhere in the network. However, the magnitude of the voltage drop depends on the transfer impedance between the observation bus and the faulted point. Therefore, the load buses are not seriously affected by faults located far away in the system. The voltage change also depends on the driving impedance at the faulted bus. The driving impedance determines the weakness of the bus.

6. Unbalanced voltage sag

Unbalanced voltage sags are caused by unsymmetrical faults. To analyze the unsymmetrical faults the use of symmetrical components is required. Since the sequences in symmetrical systems are independent, Equation (3) can be written for each sequence network and determine the during-fault voltage for each of the sequence components. Before the occurrence of the fault, bus voltages only contain a positive-sequence component, thus pre-fault voltage matrices of zero and negative sequences are null.

$$
\begin{aligned}
V_{\text{dfv}}^0 &= 0 + \Delta V^0 \\
V_{\text{dfv}}^1 &= V_{\text{pref}}^1 + \Delta V^1 \\
V_{\text{dfv}}^2 &= 0 + \Delta V^2
\end{aligned}
\tag{8}
$$

Once the sequence during-fault voltages are determined the phase voltages are calculated applying the symmetrical components transformation. The superscripts 0, 1, and 2 indicate the zero, positive and negative sequences, respectively. Therefore Equation (9) gives the phase voltages considering phase A as the symmetrical phase.

$$
\begin{aligned}
V_{\text{dfv}}^A &= V_{\text{dfv}}^0 + V_{\text{dfv}}^1 + V_{\text{dfv}}^2 \\
V_{\text{dfv}}^B &= V_{\text{dfv}}^0 + a^2 V_{\text{dfv}}^1 + a V_{\text{dfv}}^2 \\
V_{\text{dfv}}^C &= V_{\text{dfv}}^0 + a V_{\text{dfv}}^1 + a^2 V_{\text{dfv}}^2
\end{aligned}
\tag{9}
$$

Where the superscripts A, B, and C indicate the three phase voltages. By replacing Equation (8) in Equation (9), Equation (10) is written as follows

$$
\begin{aligned}
V_{\text{dfv}}^A &= V_{\text{pref}}^1 + \Delta V^0 + \Delta V^1 + \Delta V^2 \\
V_{\text{dfv}}^B &= a^2 V_{\text{pref}}^1 + \Delta V^0 + a^2 \Delta V^1 + a \Delta V^2 \\
V_{\text{dfv}}^C &= a V_{\text{pref}}^1 + \Delta V^0 + a \Delta V^1 + a^2 \Delta V^2
\end{aligned}
\tag{10}
$$

Equation (10) gives the retained phase voltages during the fault and is independent of the fault type. The only missing part is the change in the voltage during the fault ΔV for each sequence. The following sub-sections derive these expressions. Equations are derived for a general element (k, f) but matrix expressions are derived from them. All the analysis is for phase A as the symmetrical phase.

6.1 Voltage changes in Single Line to Ground (SLG) fault

SLG faults cause one of the types of the unsymmetrical voltage sags. The short circuit current is found by connecting the sequence networks in series. So the current flowing through the three sequence networks is the same. Thus Equation (11) gives the injected currents in the positive, negative and zero sequence networks.

$$
i_f^0 = i_f^1 = i_f^2 = \frac{-v_{\text{pref},f}^A}{Z_{ff}^0 + Z_{ff}^1 + Z_{ff}^2}
\tag{11}
$$

The sequence voltage changes at bus k due to the SLG fault at bus f are given by Equation (12).

$$\Delta v_{kf}^{1} = -Z_{kf}^{1} \frac{v_{\mathrm{pref},f}^{A}}{Z_{ff}^{0} + Z_{ff}^{1} + Z_{ff}^{2}}$$

$$\Delta v_{kf}^{2} = -Z_{kf}^{2} \frac{v_{\mathrm{pref},f}^{A}}{Z_{ff}^{0} + Z_{ff}^{1} + Z_{ff}^{2}} \qquad (12)$$

$$\Delta v_{kf}^{0} = -Z_{kf}^{0} \frac{v_{\mathrm{pref},f}^{A}}{Z_{ff}^{0} + Z_{ff}^{1} + Z_{ff}^{2}}$$

The pre-fault voltage at the load bus k, $v_{\mathrm{pref},k}$, only contains the positive-sequence component and is equal to the pre-fault voltage in phase A. The during-fault sequence voltages at bus k are given by Equation (13).

$$v_{kf}^{1} = v_{\mathrm{pref},k}^{A} - Z_{kf}^{1} \frac{v_{\mathrm{pref},f}^{A}}{Z_{ff}^{0} + Z_{ff}^{1} + Z_{ff}^{2}}$$

$$v_{kf}^{2} = -Z_{kf}^{2} \frac{v_{\mathrm{pref},f}^{A}}{Z_{ff}^{0} + Z_{ff}^{1} + Z_{ff}^{2}} \qquad (13)$$

$$v_{kf}^{0} = -Z_{kf}^{0} \frac{v_{\mathrm{pref},f}^{A}}{Z_{ff}^{0} + Z_{ff}^{1} + Z_{ff}^{2}}$$

After transforming the equations into the phase components, Equation (14) is derived.

$$v_{kf}^{A} = v_{\mathrm{pref},k}^{A} - \left(Z_{kf}^{1} + Z_{kf}^{2} + Z_{kf}^{0}\right) \frac{v_{\mathrm{pref},f}^{A}}{Z_{ff}^{0} + Z_{ff}^{1} + Z_{ff}^{2}}$$

$$v_{kf}^{B} = a^{2} v_{\mathrm{pref},k}^{A} - \left(a^{2} Z_{kf}^{1} + a Z_{kf}^{2} + Z_{kf}^{0}\right) \frac{v_{pref,f}^{A}}{Z_{ff}^{0} + Z_{ff}^{1} + Z_{ff}^{2}} \qquad (14)$$

$$v_{kf}^{C} = a v_{\mathrm{pref},k}^{A} - \left(a Z_{kf}^{1} + a^{2} Z_{kf}^{2} + Z_{kf}^{0}\right) \frac{v_{\mathrm{pref},f}^{A}}{Z_{ff}^{0} + Z_{ff}^{1} + Z_{ff}^{2}}$$

From Equation (13), it is clear that the phase voltages at bus k do not contain a zero sequence component if the zero sequence of the transfer impedance Z_{kf} is null. The zero sequence of the transfer impedance is null when the load and the fault buses are at different sides of a transformer with delta winding. Equation (14) gives the retained phase voltage for a general case. The negative sequence impedance matrix is usually equals to the positive sequence impedance matrix. If the zero sequence voltage can be neglected, Equation (14) is simplified as Equation (15).

$$v_{kf}^{A} = v_{\mathrm{pref},k}^{A} - \left(Z_{kf}^{1}\right) \frac{v_{\mathrm{pref},f}^{A}}{\dfrac{Z_{ff}^{0}}{2} + Z_{ff}^{1}}$$

$$v_{kf}^{B} = a^{2} v_{\mathrm{pref},k}^{A} + \left(\frac{1}{2} Z_{kf}^{1}\right) \frac{v_{\mathrm{pref},f}^{A}}{\dfrac{Z_{ff}^{0}}{2} + Z_{ff}^{1}} \qquad (15)$$

$$v_{kf}^{C} = a v_{\mathrm{pref},k}^{A} + \left(\frac{1}{2} Z_{kf}^{1}\right) \frac{v_{\mathrm{pref},f}^{A}}{\dfrac{Z_{ff}^{0}}{2} + Z_{ff}^{1}}$$

Equation (15) shows that the retained phase voltages at the observation bus is calculated using a balanced short circuit algorithm by adding a fault impedance equal to half of the value of the zero sequence driving point impedance at the faulted bus. This means that a SLG fault is less severe than a three phase fault in regard to the depression in the voltage seen at the load bus. Due to the zero-sequence impedance, the faulted phase shows a smaller drop compared to a sag originated by a three-phase fault.

6.2 Voltage changes in Line to Line (LL) fault

For a LL fault, only the positive and the negative sequence networks are considered to analyze the fault. There is no zero sequence current and voltage. In this type of fault, the positive sequence current at the fault location is equal in magnitude to the negative sequence current, but in opposite direction. Equation (16) gives the injected currents in the sequence networks.

$$i_f^1 = -\frac{v_{\text{pref},f}^A}{Z_{ff}^1 + Z_{ff}^2} = -i_f^2 \tag{16}$$

The change in positive and negative sequence voltages are given by Equation (17). There is no zero sequence voltage change.

$$\Delta v_{kf}^1 = -Z_{kf}^1 \frac{v_{pref,f}^A}{Z_{ff}^1 + Z_{ff}^2}$$
$$\Delta v_{kf}^2 = Z_{kf}^2 \frac{v_{pref,f}^A}{Z_{ff}^1 + Z_{ff}^2} \tag{17}$$

The retained phase voltages are obtained by adding the pre-fault voltage to Equation (17). Equation (18) shows transforming the sequence components into the phase components.

$$v_{kf}^A = v_{\text{pref},k}^A + \left(Z_{kf}^2 - Z_{kf}^1\right) \frac{v_{\text{pref},f}^A}{Z_{ff}^1 + Z_{ff}^2}$$

$$v_{kf}^B = a^2 v_{\text{pref},k}^A + \left(a Z_{kf}^2 - a^2 Z_{kf}^1\right) \frac{v_{\text{pref},f}^A}{Z_{ff}^1 + Z_{ff}^2} \tag{18}$$

$$v_{kf}^C = a.v_{pref,k}^A + \left(a^2 . Z_{kf}^2 - a . Z_{kf}^1\right) \frac{v_{pref,f}^A}{Z_{ff}^1 + Z_{ff}^2}$$

If the positive sequence impedance matrix is equal to the negative sequence impedance matrix, Equation (18) is simplified as indicated in Equation (19).

$$v_{kf}^A = v_{\text{pref},k}^A$$

$$v_{kf}^B = a^2 v_{\text{pref},k}^A + \left(j\sqrt{3}Z_{kf}^1\right) \frac{v_{\text{pref},f}^A}{2Z_{ff}^1} \tag{19}$$

$$v_{kf}^C = a v_{\text{pref},k}^A - \left(j\sqrt{3}Z_{kf}^1\right) \frac{v_{\text{pref},f}^A}{2Z_{ff}^1}$$

6.3 Voltage changes in Double Line to Ground (DLG) fault

In DLG faults, the sequence networks are connected in parallel to derive the fault current. Equation (20) gives the injected currents in each one of the sequence networks.

$$i_f^1 = -\frac{v_{\text{pref},f}^A}{Z_{ff}^1 + \dfrac{Z_{ff}^0 . Z_{ff}^2}{Z_{ff}^0 + Z_{ff}^2}}$$

$$i_f^2 = -\frac{Z_{ff}^0}{Z_{ff}^0 + Z_{ff}^2} i_f^1 \tag{20}$$

$$i_f^0 = -\frac{Z_{ff}^2}{Z_{ff}^0 + Z_{ff}^2} i_f^1$$

Equation (21) gives the retained sequence voltages in a DLG fault.

$$v_{kf}^1 = v_{\text{pref},k}^A + Z_{kf}^1 . i_f^1$$

$$v_{kf}^2 = Z_{kf}^2 \left(-\frac{Z_{ff}^0}{Z_{ff}^2 + Z_{ff}^0} i_f^1 \right) \tag{21}$$

$$v_{kf}^0 = Z_{kf}^0 \left(-\frac{Z_{ff}^2}{Z_{ff}^2 + Z_{ff}^0} i_f^1 \right)$$

Finally, the retained phase voltages are found by applying the symmetrical component transformation. The transforming equations are shown in Equation (22).

$$v_{kf}^A = v_{\text{pref},k}^A + \frac{\left(Z_{kf}^2 - Z_{kf}^1\right)Z_{ff}^0 + \left(Z_{kf}^0 - Z_{kf}^1\right)Z_{ff}^2}{Z_{ff}^1 . Z_{ff}^0 + Z_{ff}^2 . Z_{ff}^1 + Z_{ff}^2 . Z_{ff}^0} v_{\text{pref},f}^A$$

$$v_{kf}^B = a^2 . v_{\text{pref},k}^A + \frac{\left(a.Z_{kf}^2 - a^2 . Z_{kf}^1\right)Z_{ff}^0 + \left(Z_{kf}^0 - a^2 . Z_{kf}^1\right)Z_{ff}^2}{Z_{ff}^1 . Z_{ff}^0 + Z_{ff}^2 . Z_{ff}^1 + Z_{ff}^2 . Z_{ff}^0} v_{\text{pref},f}^A \tag{22}$$

$$v_{kf}^C = a . v_{\text{pref},k}^A + \frac{\left(a^2 . Z_{kf}^2 - a.Z_{kf}^1\right)Z_{ff}^0 + \left(Z_{kf}^0 - a.Z_{kf}^1\right)Z_{ff}^2}{Z_{ff}^1 . Z_{ff}^0 + Z_{ff}^2 . Z_{ff}^1 + Z_{ff}^2 . Z_{ff}^0} v_{\text{pref},f}^A$$

7. Prediction of voltage sags

Voltage sags originated by faults have many predictable characteristics. For a three-phase fault the voltage sag matrix is given by

$$\mathbf{V}_{\text{dfv}} = \mathbf{V}_{\text{pref}} - \mathbf{Z}(\text{diag}\mathbf{Z})^{-1} \mathbf{V}_{\text{pref}}^T \tag{23}$$

where $\mathbf{Z}$ is the impedance matrix, $\mathbf{V}_{\text{pref}}$ is the pre-fault voltage matrix, and $(\text{diag}\mathbf{Z})^{-1}$ is the matrix formed by the inverse of the diagonal elements of the impedance matrix. If the pre-fault loads are neglected, then voltages before the fault are considered 1 pu. Under this assumption, Equation (23) is written as follows

$$\mathbf{V}_{dfv} = \mathbf{1} - \mathbf{Z}\left(\text{diag}\mathbf{Z}\right)^{-1}\mathbf{1} \tag{24}$$

where $\mathbf{1}$ is a matrix full of ones and such that its dimension is equal to the dimension of $\mathbf{Z}$.
The square $n \times n$ matrix $\mathbf{V}_{dfv}$ contains the sags at each bus of the network due to faults at each one of the buses. The during fault voltage at a general bus j when a fault occurs at that bus is contained in the diagonal of $\mathbf{V}_{dfv}$ and is zero for a solid three phase fault. Off-diagonal elements of $\mathbf{V}_{dfv}$ are the sags at a general bus k due to a fault at a general position f. Hence, column f contains the during-fault voltages at buses 1, 2, …, f,…, n during the fault at bus f. This means that the effect, in terms of sags, of a fault at a given bus of the system is contained in columns of the voltage sag matrix. This information is usually presented on the single line diagram of the power system and it is called affected area. A sample $n \times n$ sag matrix is shown as follows

$$V_{dfv} = \begin{bmatrix} 0 & 1 - \dfrac{z_{12}}{z_{22}} & \cdots & 1 - \dfrac{z_{1n}}{z_{nn}} \\ 1 - \dfrac{z_{21}}{z_{11}} & 0 & \cdots & 1 - \dfrac{z_{2n}}{z_{nn}} \\ \vdots & \vdots & \ddots & \vdots \\ 1 - \dfrac{z_{n1}}{z_{11}} & 1 - \dfrac{z_{n2}}{z_{22}} & \cdots & 0 \end{bmatrix} \tag{25}$$

In this chapter, a real sample network is used for description of the voltage sag matrix. Fig. 3 shows a 41-bus 230-kV of Tehran Regional Electric Company in Iran.
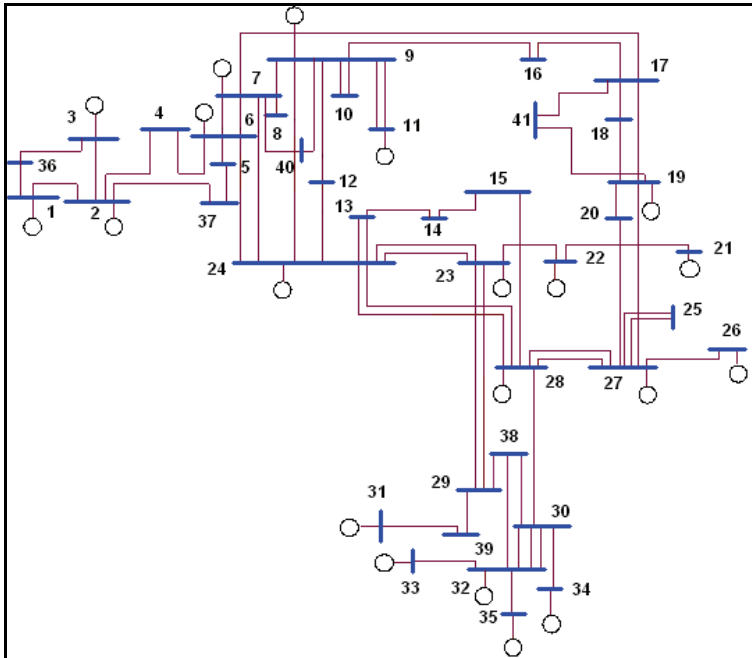
Fig. 3. Single line diagram of a 230 kV real case study

Applying Equation (23), it is found the during fault voltages for the 41 buses due to the faults on each one of the 41 buses. Equation (26) shows the resulting voltage sag matrix. It is seen that column 34 of the sag matrix contains the during fault voltages at each one of the 41 buses when a three-phase fault occurs at bus 34. Column 34 of the sag matrix contains the information to draw the affected area of the system due to a fault at bus 34.

$$
V_{dfv} = \begin{bmatrix}
0 & 1-\dfrac{z_{1,2}}{z_{2,2}} & \cdots & 1-\dfrac{z_{1,34}}{z_{34,34}} & \cdots & 1-\dfrac{z_{1,41}}{z_{41,41}} \\[2ex]
1-\dfrac{z_{2,1}}{z_{1,1}} & 0 & \cdots & 1-\dfrac{z_{2,34}}{z_{34,34}} & \cdots & 1-\dfrac{z_{2,41}}{z_{41,41}} \\[2ex]
\vdots & \vdots & \vdots & \vdots & \vdots & \vdots \\[1ex]
1-\dfrac{z_{34,1}}{z_{1,1}} & 1-\dfrac{z_{34,2}}{z_{2,2}} & \cdots & 0 & \cdots & 1-\dfrac{z_{34,41}}{z_{41,41}} \\[2ex]
\vdots & \vdots & \vdots & \vdots & \vdots & \vdots \\[1ex]
1-\dfrac{z_{41,1}}{z_{1,1}} & 1-\dfrac{z_{41,2}}{z_{2,2}} & \cdots & 1-\dfrac{z_{41,34}}{z_{34,34}} & \cdots & 0
\end{bmatrix} \tag{26}
$$
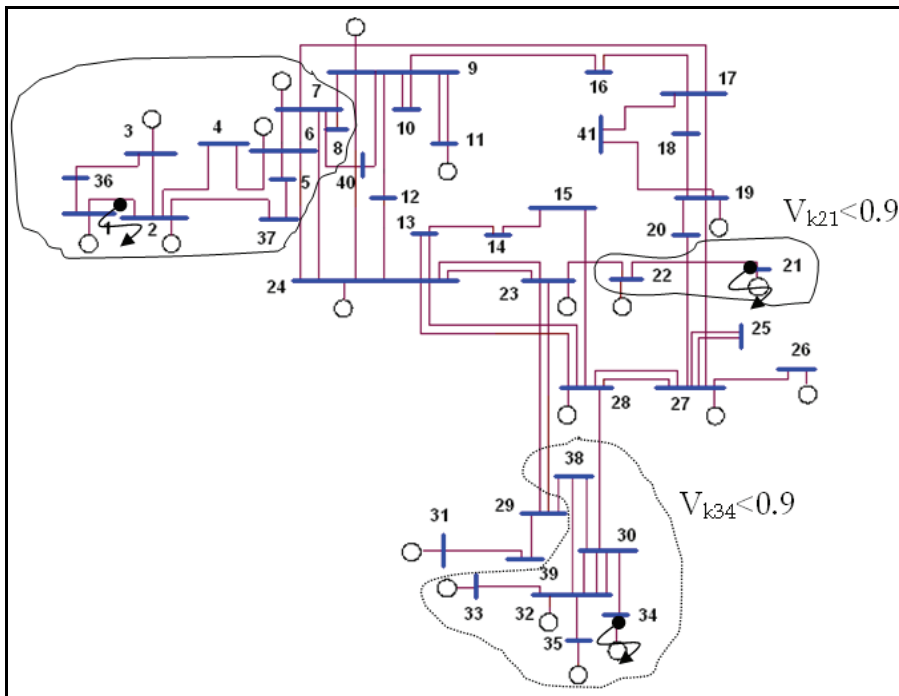
Fig. 4. Affected areas for three-phase fault at buses 34 and 21

The affected area contains the load buses that present a during fault voltage lower than a given value due to a fault at a given bus. In Fig. 4, three affected areas are presented for

three-phase faults on the middle of the line 1-2 and the buses 21 and 34. The areas enclose the load buses presenting a sag more severe than a retained voltage of 0.9 p.u. If the threshold is less than 0.9, the areas are smaller than the areas shown in Fig. 4. Only the original impedance matrix of positive sequence of the system is used to build the exposed areas. Faults on lines are more frequent than fault on buses of the system, however faults on buses cause more severe sags in terms of magnitude and therefore are considered for building the affected areas. In the rest of this chapter, only faults on the buses are to be considered.

The exposed area (area of vulnerability) is contained in rows of the voltage sag matrix and as in the case of the affected area can be graphically presented on the single line diagram. Fig. 5 presents the exposed area of bus 32. The exposed area encloses the buses and line segments where faults cause a sag more severe than a given value. In Fig. 5, the 0.5 p.u. exposed area of bus 32 contains buses 30 and 32. Similarly, the 0.8 pu exposed area for bus 32 contains all the buses where faults cause a retained voltage lower than 0.8 pu. Fig. 5 suggests that the exposed area is a closed set containing buses.
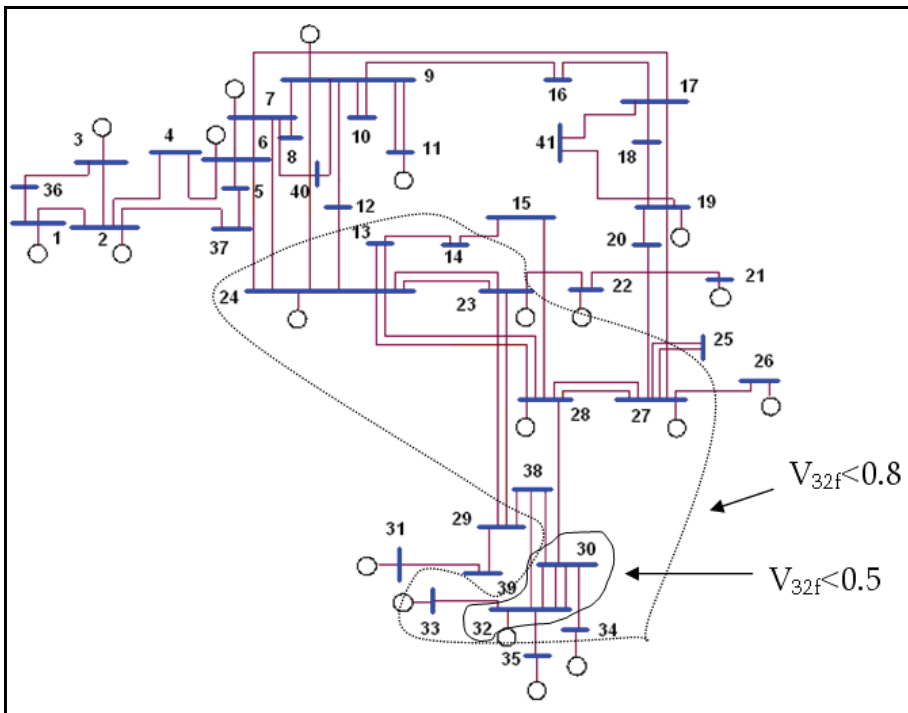
Fig. 5. Exposed area of bus 32 for three-phase faults

Unsymmetrical faults can also be considered to define the exposed area of a sensitive load. Positive, negative, and zero sequence impedance matrices are needed to perform the calculations.

To show the exposed areas for symmetrical and unsymmetrical faults, the exposed areas of a three phase fault and a SLG fault at bus 35 are illustrated in Fig. 6. In this figure, the 0.8 pu

SLG fault exposed area of bus 35 contains buses 30 and 32. Also, the 0.8 pu three phase fault exposed area contains buses 30, 32, and 38. The SLG fault exposed area is almost coincident with the three phase fault exposed area, however, a bit smaller.
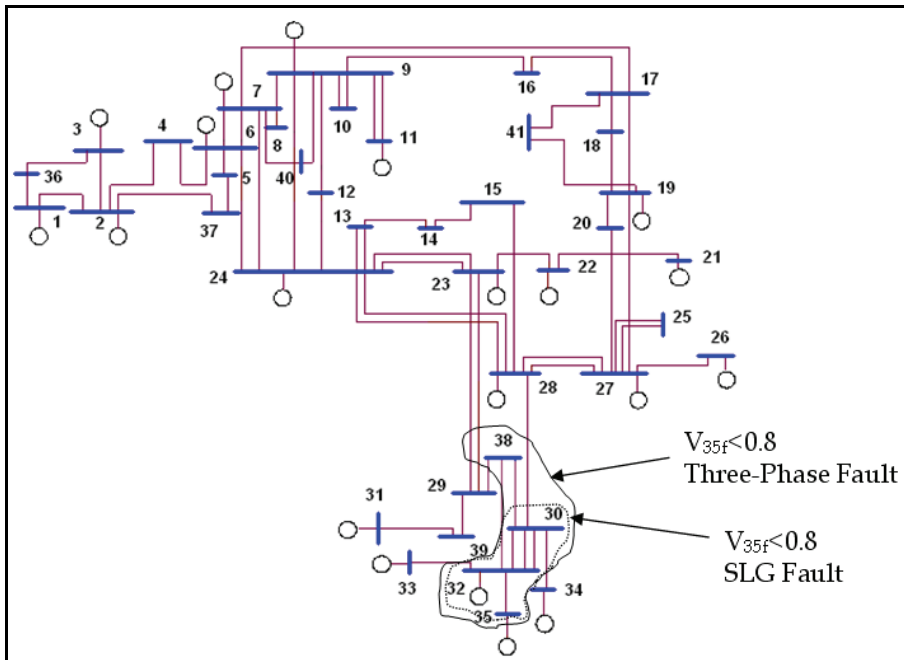
Fig. 6. Exposed area of bus 35 for SLG and three-phase faults

It is noted that the exposed area is also the area for which a monitor, installed at a particular bus k, is able to detect faults. For example, if a monitor is installed at bus 30 and the boundary for sag recording is adjusted to 0.8 pu, then the monitor is be able to see the faults in the 0.8 pu exposed area of bus 30. When referring to power quality monitors the exposed area is called Monitor Reach Area (MRA). In the next section, the way of optimal locating of the monitors is described to monitor all of the faults in the system.

8. Optimal placement of voltage sag monitors

In order to find optimal monitor locations for a monitoring program, the following two premises are considered:
• A minimum number of monitors should be used.
• No essential data concerning the performance of load buses in terms of sags should be missed.

The number of voltage sags recorded at a substation during a given monitoring time depends upon the critical threshold setting of the power quality monitor. It is considered the threshold level as the voltage p in pu at which the monitor starts recording. If the threshold is set too low (e.g., 0.5 pu), then the monitor do not capture an important number of disturbances. On the other extreme, if the threshold (p) is set high (e.g., 0.9 pu or higher)

then the number of voltage sags recorded are excessive and even exceed the storage capability of the monitor. This increase or decrease in the number of events captured can be explained from the growth of the exposed area with increasing sensitivity of the monitor.

The MRA is defined as the area of the network that is observed from a given monitor position. The exposed area of a bus k is exactly the monitor reach area of a monitor installed at that bus. The ability of the monitor to sense the remote faults is determined by the voltage threshold setting p. The MRA is greater for small voltage changes than for big ones. In other words, one monitor is theoretically able to capture all faults in the network for p equal to 1 pu. Similarly, only solid faults occurring at the monitor position is seen for a threshold p equal to 0 pu.

8.1 Monitor Reach Area (MRA)

The part of the network that is observed by a monitor installed at bus k is thought as an area containing bus k and its electrical neighbourhood. The size of this area depends mainly upon the value of the voltage threshold of the monitor (p). This area is called $\mathbf{MRA}_p$ for bus k. $\mathbf{MRA}_p$ is the area of the transmission network, surrounding the monitor position k, for which the monitor is able to capture voltage drops that result in a retained voltage less than or equal to p pu.

The $\mathbf{MRA}_p$ of bus k is shown as a set of buses. The $\mathbf{MRA}_{k,p}$ is the set containing the indices of the buses within the $\mathbf{MRA}_p$ of bus k. Using the voltage sag matrix $\mathbf{V}_{\text{dfv}}$, $\mathbf{MRA}_{k,p}$ is determined as follows:

$$\mathbf{MRA}_{k,p} = \{k,i\} \quad i = 1,\ldots,k,\ldots,n$$

$$\text{subject to} \tag{27}$$

$$v_{ki} \leq p \qquad \forall k$$

The $\mathbf{MRA}$ is easily determined from the rows of the voltage sag matrix. A given bus i is part of the $\mathbf{MRA}$ of bus k if the voltage at bus k during a fault at bus i is lower than or equal to p pu. Equation (27) allows describing all the monitor reach areas and for any voltage threshold setting of the monitor.

An alternative method to describe the MRAs is by using a binary matrix. For a given voltage threshold setting p, the MRAs are described through an $n \times n$ binary matrix in which a 1 in entry (i, j) indicates that bus j belongs to the MRA of bus i. Equation (28) shows this matrix, where v_{ij} is the (i, j) entry of the voltage sag matrix.

$$\mathbf{MRA}_p = \left[mra_{ij} \right] = \begin{cases} 1 & if \ v_{ij} \leq p \\ 0 & if \ v_{ij} > p \end{cases} \quad \forall i, j \tag{28}$$

Once the MRAs for all possible locations are determined the optimization problem is formulated to locate the optimum number of the monitors.

8.2 Optimization problem

Consider a binary variable row vector $\mathbf{X}$ of length n indicating if a monitor is needed at bus i. Each element of $\mathbf{X}$, x_i, is indicated as follows

$$x_i = \begin{cases} 1 & \text{if monitor at bus } i \\ 0 & \text{otherwise} \end{cases} \quad \forall i \qquad (29)$$

The vector **X** is called Monitor Position Vector (MPV). A given combination of ones and zeros indicates where to install the monitors as expressed in Equation (29).
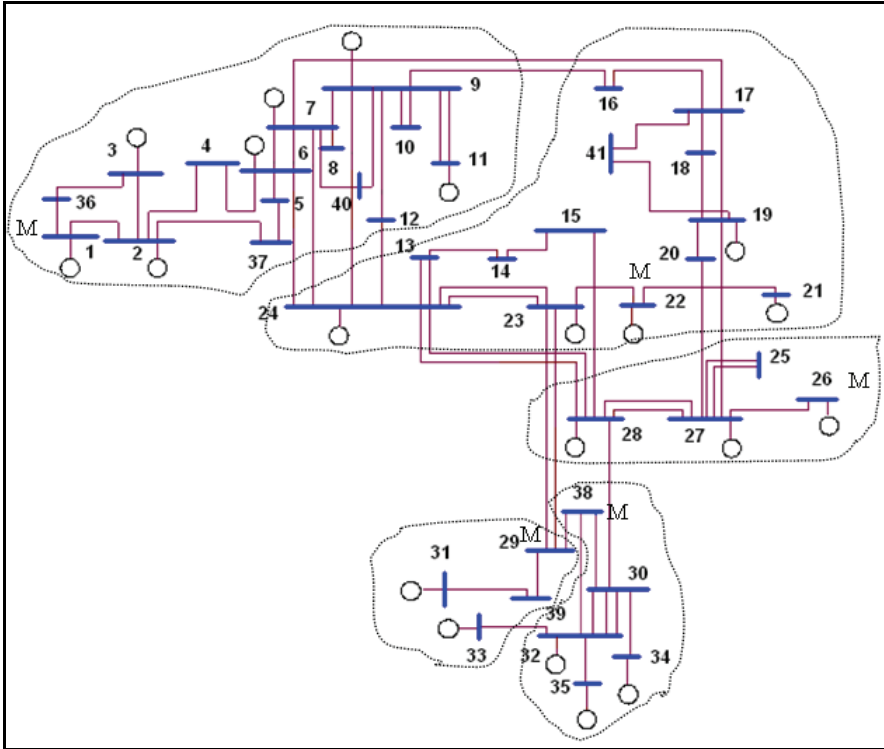
Fig. 7. Optimal Monitors Emplacements

It is noted that for a given value of the MPV the product of **X** by the **MRA**$_p$ matrix indicates the number of MRAs that contain each one of the buses i. In order to satisfy the second premise, this product should be greater than or equal to 1 for each bus; meaning that each bus should be in at least one monitor reach area. Let b be a row vector containing ones. The Objective Function (OF) of the optimization problem is formulated as follows

$$\min OF = \sum_{i=1}^{n} x_i$$

subject to   (30)

$$\sum_{i=1}^{n} x_i mra_{ij} \geq b_i, \quad j = 1, 2, \ldots, n$$

Where x_i is the binary decision variable indicating the need for a monitor at bus i; n is the number of potential monitor positions. The right hand side, vector b, defines the level of

redundancy of the monitoring program. A particular value of b_i indicates that a fault at the fault position i trigger at least b_i monitors. The level of redundancy of the monitoring program is the minimum number of monitors that is guaranteed to trigger on the occurrence of a fault. The letter T over **MRA**$_p$ indicates transposition of the **MRA** matrix for voltage threshold p.

The voltage sag matrix can be used instead of the **MRA**$_p$ matrix to formulate the optimization problem. This option allows modelling different voltage threshold setting for the monitors. The problem described by Equation (30) is an integer programming optimization problem. A number of algorithms, e.g. Branch and bound Algorithm (BBA) and Genetic Algorithm (GA), have been proposed for solving this type of problem.

As an example, the optimization method is applied to the sample network of Fig. 3. The BBA algorithm is used to solve the optimization problem. Let the voltage threshold p of the monitors equals to 0.9pu. If all of the faults are considered to be three phase faults, the results of the optimization show that the monitors should be installed at the buses 1, 22, 26, 29, and 38. It is clear that the number of monitors needed to cover the whole system increases with the decrease of the monitor threshold. Fig. 7 shows the optimal monitors emplacements and their reach area.

In Fig. 7, letter M shows the monitor places. The dashed lines also show the reach area of each of the monitors.

9. Conclusion

Power quality monitoring is necessary to characterize electromagnetic phenomena at a particular location on an electric power circuit. In this chapter, the monitoring of voltage sag which is one of the most important power quality phenomena has been discussed. The voltage sag magnitude has been monitored to find the origin of the voltage sag and detect all of the sags in the system.

Voltage sags are determined by fault types, fault impedances, and etc. With respect to the fault type, the shape of the rms voltage evolution shows different behavior. The calculations of all types of faults which may cause the sags have also been discussed in this chapter.

Ideally, a full monitoring program can be used to characterize the performance of entire system, i.e. every load bus should be monitored. Such a monitoring program is not economically justifiable and only a limited set of buses can be chosen for a monitoring program. This has led to the optimal monitoring program which has been proposed in this chapter.

10. References

Baggini, A. (2008). *Handbook of Power Quality,* Wiley-IEEE Press, ISBN 978-0-470-06561-7, John Wiley & Sons Ltd, West Sussex, England

Bollen, M.H.J. (1999). *Understating Power Quality Problems: Voltage Sags and Interruptions,* Wiley-IEEE Press, ISBN 978-0-7803-4713-7, New-York, USA

Casarotto, C. & Gomez, J.C. (2009). Calculation of Voltage Sags Originated in Transmission Systems Using Symmetrical Components, *Proceedings of the 20th International Conference on Electricity Distribution (CIRED)*, Parague, June 8-11, 2009

Gerivani, Y. ; Askarian Abyaneh, H. & Mazlumi, K. (2007). An Efficient Determination of Voltage Sags from Optimal Monitoring, *Proceedings of the 19th International Conference on Electricity Distribution (CIRED)*, Vienna, Austria, May 21-24, 2007

Grigsby, L.L. (2001). *The Electric Power Engineering Handbook,* CRC Press, ISBN 978-1-4200-3677-0, Florida, USA

Mazlumi, K.; Askarian Abyaneh, H. ; Gerivani, Y. & Pordanjani, I.R. (2007). A New Optimal Meter Placement Method for Obtaining a Transmission System Indices, *Proceedings of Power Tech 2007 conference*, pp. 1165-1169, Lausanne, Switzerland, July 1-5, 2007

Milanovic, J.V.; Aung, M.T. & Gupta, C.P. (2005). The Influence of Fault Distribution on Stochastic Prediction of Voltage Sags. *IEEE Transactions on Power Delivery,* Vol.20, No.1, (January 2005), pp. 278-285

Moschakis, M.N. & Hatziargyriou, N.D. (2006). Analytical Calculation and Stochastic Assessment of Voltage Sags. *IEEE Transactions on Power Delivery,* Vol.21, No.3, (July 2006), pp. 1727-1734

Olguin, G. & Bollen, M.H.J. (2002). Stochastic Prediction of Voltage Sags: an Overview, *Proceedings of Probabilistic Methods Applied to Power Systems Conference*, Naples, Italy, September 22-26, 2002

Olguin, G. (2005). *Voltage Dip (Sag) Estimation in Power Systems based on Stochastic Assessment and Optimal Monitoring,* Ph.D. Thesis, Chalmers University of Technology, Göteborg, Sweden

Olguin, G.; Bollen, M.H.J. (2002). The Method of Fault Position for Stochastic Prediction of Voltage Sags: A Case Study, *Proceedings of Probabilistic Methods Applied to Power Systems Conference*, Naples, Italy, september 22-26, 2002

Salim, F. & Nor, K.M. (2008). Optimal voltage sag monitor locations, *Proceedings of the Australasian Universities Power Engineering Conference (AUPEC '08)*, Sydney, Australia, December 14-17, 2008

Wavelet and PCA to Power Quality Disturbance Classification Applying a RBF Network

Giovani G. Pozzebon[1], Ricardo Q. Machado[1], Natanael R. Gomes[2],
Luciane N. Canha[2] and Alexandre Barin[2]
*[1]São Carlos School of Engineering, Department of Electrical Engineering,
University of São Paulo*
[2]Federal University of Santa Maria
Brazil

1. Introduction

The quality of electric power became an important issue for the electric utility companies and their customers. It is often synonymous with voltage quality since electrical equipments are designed to operate within a certain range of supply specifications. For instance, current microelectronic devices are very sensitive to subtle changes in power quality, which can be represented as a disturbance-induced variation of voltage amplitude, frequency and phase (Dugan et al., 2003).

Poor power quality (PQ) is usually caused by power line disturbances such as transients, notches, voltage sags and swells, flicker, interruptions, and harmonic distortions (IEEE Std. 1159, 2009). In order to improve electric power quality, the sources and causes of such disturbances must be known. Therefore, the monitoring equipment needs to firstly and accurately detect and identify the disturbance types (Santoso et al., 1996). Thus, the use of new and powerful tools of signal analysis have enabled the development of additional methods to accurately characterize and identify several kinds of power quality disturbances (Karimi et al., 2000; Mokhtary et al., 2002).

Santoso et al. proposed a recognition scheme that is carried out in the wavelet domain using a set of multiple neural networks. The network outcomes are then integrated by using decision-making schemes such as a simple voting scheme or the Dempster-Shafer theory. The proposed classifier is capable of providing a degree of belief for the identified disturbance waveform (Santoso et al., 2000a, 2000b). A novel classification method using a rule-based method and wavelet packet-based hidden Markov models (HMM) was proposed bay Chung et al. The rule-based method is used to classify the time-characterized-feature disturbance and the wavelet packet-based on HMM is used for frequency-characterized-feature power disturbances (Chung et al., 2002). Gaing presented a prototype of wavelet-based network classifier for recognizing power quality disturbances. The multiresolution-analysis technique of discrete wavelet transforms (DWT) and Parseval's theorem are used to extract the energy distribution features of distorted signals at different resolution levels. Then, the probabilistic neural network classifies these extracted features of disturbance type identification according to the transient duration and energy features (Gaing, 2004). Zhu et

al. proposed an extended wavelet-based fuzzy reasoning approach for power quality disturbance recognition and classification. The energy distribution of the wavelet part in each decomposition level is calculated. Based on this idea, basic rules are generated for the extended fuzzy reasoning. Then, the disturbance waveforms are classified (Zhu et al., 2004). Further on, Chen and Zhu presented a review of the wavelet transform approach used in power quality processing. Moreover, a new approach to combine the wavelet transform and a rank correlation is introduced as an alternative method to identify capacitor-switching transients (Chen & Zhu, 2007).

Taking into account these ideas, this chapter proposes the application of a different method of power quality disturbance classification by combining discrete wavelet transform (DWT), principal component analysis (PCA) and an artificial neural network in order to classify power quality disturbances. The method proposes to analyze seven classes of signals, namely Sinusoidal Waveform, Capacitor Switching Transient, Flicker, Harmonics, Interruption, Notching and Sag, which is composed by four main stages: (1) signal analysis using the DWT; (2) feature extraction; (3) data reduction using PCA; (4) classification using a radial basis function network (RBF). The MRA technique of DWT is employed to extract the discriminating features of distorted signals at different resolution levels. Subsequently, the PCA is used to condense information of a correlated set of variables into a few variables, and a RBF network is employed to classify the disturbance types.
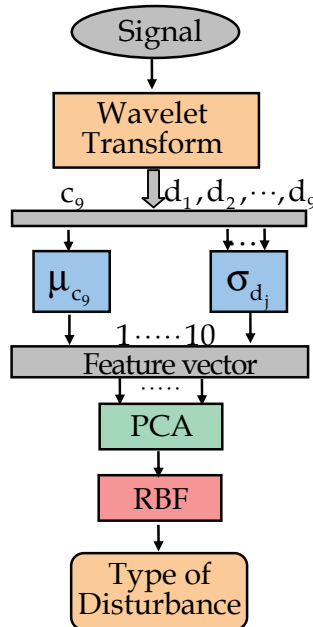
2. Proposed classification scheme

Fig. 1. Diagram of the proposed classification scheme

This section presents the mainframe of the scheme proposed in this paper using the wavelet transform, principal components and neural networks to classify PQ disturbances. The

proposed scheme diagram is shown in Fig. 1. Initially, the input signals are analyzed using the discrete wavelet transform tool, which employs two sets of functions called scaling functions and wavelet functions associated with low pass and high pass filters, respectively. Then, the signal is decomposed into different resolution levels aiming to discriminate the signal disturbances. The output of the DWT stage is used as the input to the feature extraction stage, on which the featuring signal vectors are built. In order to reduce the amount of data, the PCA technique is applied to the feature vector in order to concentrate the information from the disturbance signal and to reduce the amount of the training data used, consequently minimizing the number of input RBF neurons while maintaining the recognition accuracy. Finally, an RBF network is employed to perform the disturbance type classification.

As aforementioned, in the introduction, this work proposes to analyze seven classes of different types of PQ disturbances as follows: Pure sine (C_1); Capacitor switching (C_2); Flicker (C_3); Harmonics (C_4); Interruption (C_5); Notching (C_6); Sag (C_7). The databases used for training and evaluation of the proposed system and classification algorithms were performed in Matlab®. The tools used in this approach are presented in sequence.

2.1 The wavelet transform and multiresolution analysis

The DWT is a versatile signal processing tool that has many engineering and scientific applications (Barmada et al., 2003). One area in which the DWT has been particularly successful is transient analysis in power systems (Santoso et al., 2000a, 2000b; Yilmaz et al., 2007), used to capture the transient features and to accurately localize them in both time and frequency contexts. The wavelet transform is particularly effective in representing various aspects of non-stationary signals such as trends, discontinuities and repeated patterns, in which other signal processing approaches fail or are not as effective. Through wavelet decomposition, transient features are accurately captured and localized in both time and frequency contexts.

A wavelet is an effective time–frequency analysis tool to detect transient signals. Its features of extraction and representation properties can be used to identify various transient events in power signals. The discrete wavelet transform analyzes the signal at different frequency bands with different resolutions by decomposing the signal into a coarse approximation and detail information (Chen & Zhu, 2007). This capability to expand function or signal with different resolutions is termed as Multiresolution Analysis (MRA) (Mallat, 1989). The DWT employs two sets of functions called scaling functions, $\phi_{j,n}[t]$, and wavelet functions, $\psi_{j,n}[t]$, which are associated with low-pass and high-pass filters, respectively. The decomposition of the signal into the different frequency bands is simply obtained by successive high-pass and low-pass filtering of the time domain signal. The discrete forms of scale and wavelet functions are, respectively, defined as follows.

$$\phi_{j,n}[t] = 2^{\frac{j}{2}} \sum_n c_{j,n} \phi[2^j t - n] \tag{1}$$

$$\psi_{j,n}[t] = 2^{\frac{j}{2}} \sum_n d_{j,n} \psi[2^j t - n] \tag{2}$$

Where c_j and d_j are the scaling and wavelet coefficients indexed by j, and both functions must be orthonormal.

The wavelet and scaling functions are used to perform simultaneously a multiresolution analysis decomposition and reconstruction of the signal. The former can decompose the original signal in several other signals at different resolution levels. From these decomposed signals, the original signal can be recovered without losing any information. Therefore, in power quality disturbance signals, the MRA technique discriminates the disturbances from original signals, and then they can be analyzed separately (Debnath, 2002). The recursive mathematical representation of MRA is as follows:

$$V_j = W_{j+1} \oplus V_{j+1} = W_{j+1} \oplus W_{j+2} \oplus \cdots \oplus W_{j+n} \oplus V_n \qquad (3)$$

Where: V_{j+1} is the approximate version of a given signal at scale j+1; W_{j+1} is the detailed version displaying all transient phenomena of the given signal at scale j+1; symbol $\oplus$ denotes an orthogonal summation; and n represents the decomposition level.

Since $\psi_{j,n} \in W_j$ it follows immediately that $\psi_{j,n}$ is orthonormal to $\phi_{j,n}$ because all $\phi_{j,n} \in V_j$ are $V_j \perp W_j$. Also, because all V_j are mutually orthogonal, it follows that the wavelets are orthonormal across scaling. A detailed approach about this theory can be found in (Mallat, 1989; Strang & Nguyen, 1997; Debnath, 2002).

From the engineering point of view, DWT is a digital filtering process in the time domain, by discrete convolution, using the analyses Finite-Impulse-Response (FIR) filters h and g, followed by a down sampling of two. The filter g(k) can generate a detailed version of the signal, while h(k) produces an approximate version of the signal. In the DWT, the resulting coefficients from the low-pass filtering process can be processed again as entrance data for a subsequent bank of filters, generating another group of approximation and detail coefficients.

The schematic diagram in Fig. 2 shows two decomposed levels of DWT. The input signal f(t) is split into the approximation $c_{j,k}$ and the detail $d_{j,k}$ by a low-pass and a high-pass filters named h(k) and g(k), respectively. Both, output approximation and detail are decimated by 2. In a practical approach, a DWT depends on:

- the original signal, f(t);
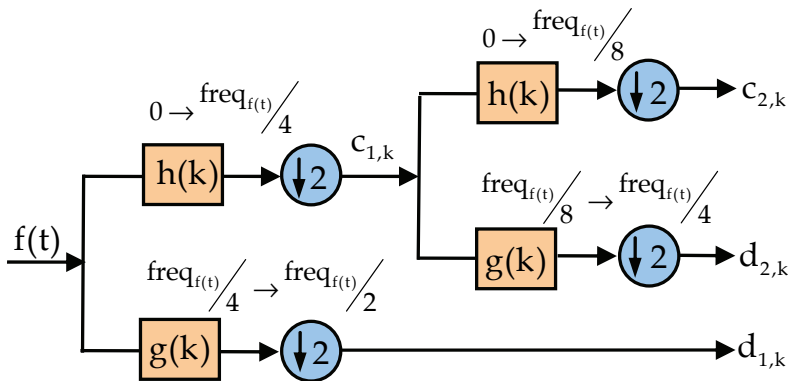- the low-pass filter, h(k), used;
- the high-pass filter, g(k), used.

Fig. 2. Decomposition of f(t) into 2 scales

There are several families of wavelet functions which contain filters of several supports (filter size). However, in this application, as in (Zhu et al., 2004; Chen & Zhu, 2007), the Daubechie "db4" wavelet was adopted to perform the DWT. As can be seen in (Daubechies, 1992), the "db4" is a wavelet of support four, i.e., each filter has four coefficients, $h = \begin{bmatrix} h_0 & h_1 & h_2 & h_3 \end{bmatrix}$. The analysis filter h is always the QMF (quadrature mirror filter) pair of g. Therefore, from the high-pass filter g the low-pass filter h is obtained, inverting the order and putting the negative sign alternately as follows, $g = \begin{bmatrix} h_3 & -h_2 & h_1 & -h_0 \end{bmatrix}$. The coefficients of the "db4" wavelet filters, h and g are presented as follows (Daubechies, 1992).

$$h = \begin{bmatrix} \dfrac{1+\sqrt{3}}{4\sqrt{2}} & \dfrac{3+\sqrt{3}}{4\sqrt{2}} & \dfrac{3-\sqrt{3}}{4\sqrt{2}} & \dfrac{1-\sqrt{3}}{4\sqrt{2}} \end{bmatrix} \tag{4}$$

$$g = \begin{bmatrix} \dfrac{1-\sqrt{3}}{4\sqrt{2}} & \dfrac{-3+\sqrt{3}}{4\sqrt{2}} & \dfrac{3+\sqrt{3}}{4\sqrt{2}} & \dfrac{-1-\sqrt{3}}{4\sqrt{2}} \end{bmatrix} \tag{5}$$

In practice, the previous filters are the only elements required to calculate the DWT of any signal. As previously mentioned, it is a digital filtering process in the time domain by discrete convolution. In (6) and (7) the relations from the level c_j to the next level, c_{j+1} and d_{j+1} are given. This relation involves the filters h and g. For specific filter, these equations allow to find the wavelet coefficients using samples of the signal f(t), once the samples are the initial coefficients c_j (Mix & Olejniczak, 2003).

$$c_{j+1}(k) = \sum_n h(n-2k)c_j(n) \tag{6}$$

$$d_{j+1}(k) = \sum_n g(n-2k)c_j(n) \tag{7}$$

Approximation and detail coefficients are down-sampled by 2 in each decomposition level. According to the Nyquist theorem cited in (Mallat, 1989), the maximum frequency of an original signal f(t) sampled at $freq_{f(t)}$ Hz is ($freq_{f(t)}/2$) Hz. Therefore, the maximum frequencies $freq_{Level}$ of signals c_j and d_j at each resolution level, are given by (8), where $freq_s$ is the sampling frequency.

$$freq_{Level} = \frac{freq_s}{2^{Level}} \tag{8}$$

The sampling frequency and amplitude for all types of disturbances considered in this approach are 15.36 kHz (256 samples per period – fundamental frequency of 60 Hz) and 1 p.u., respectively. The wavelet transform is applied to perform a 9-level decomposition of each discrete disturbance signal to obtain the detailed version coefficients ($d_1 - d_9$), and the approximated version coefficient (c_9). In this experiment, the adopted frequency bandwidths at each decomposition level are shown in Table 1.

Following, it is presented an example of a simple algorithm in MatLab® to demonstrate how the DWT is applied in practice (Mix & Olejniczak, 2003).

% with f as the original signal; N the length of f; and **g** *and* **h** *the wavelet filters*:
% for one decomposition level, the following is done:

```
f0=conv(g,f);              % convolution of g with f.
f1=conv(h,f);              % convolution of h with f.
f0=f0(1,2:N+1);            % eliminate first value.
f1=f1(1,2:N+1);
f0=reshape(f0,2,N/2);      % down sampling.
f1=reshape(f1,2,N/2);
c1=f0(1,:);                % the output c of length N/2.
d1=f1(1,:);                % the output d of length N/2.
```

This example code produces decomposed signals (c_1 and d_1) at level 1, which are the approximated and detailed version of the original signal f, respectively. In this example the signal f contains N samples, but the two derived signals c_1 and d_1 contain N/2 samples due to down-sampling.

Level	Parameter	Frequency band (Hz)	Harmonics included
9	$c_{9,k}$	0 – 15	-
9	$d_{9,k}$	15 – 30	-
8	$d_{8,k}$	30 – 60	1st
7	$d_{7,k}$	60 – 120	1st – 2nd
6	$d_{6,k}$	120 – 240	2nd – 4th
5	$d_{5,k}$	240 – 480	4th – 8th
4	$d_{4,k}$	480 – 960	8th – 16th
3	$d_{3,k}$	960 – 1920	16th – 32th
2	$d_{2,k}$	1920 – 3840	32th – 64th
1	$d_{1,k}$	3840 – 7680	64th – 128th

Table 1. Scale to Frequency Range Conversion Based on 60 Hz Power Frequency

Fig. 3. The voltage interruption signal and detail coefficients: first decomposed level (d1), third decomposed level (d3), and fifth decomposed level (d5)

Figures 3, 4 and 5 show the decomposition plots of the signals using the "db4" wavelet. An example of interruption disturbance and the detail coefficients d1, d3 and d5 are shown in Fig. 3. Fig. 4 shows an oscillatory transient disturbance due to a capacitor switching transient, and detail coefficients d1, d2 and d3, respectively. Fig. 5 depicts a sag disturbance and detail coefficients d1, d3 and d5, respectively.
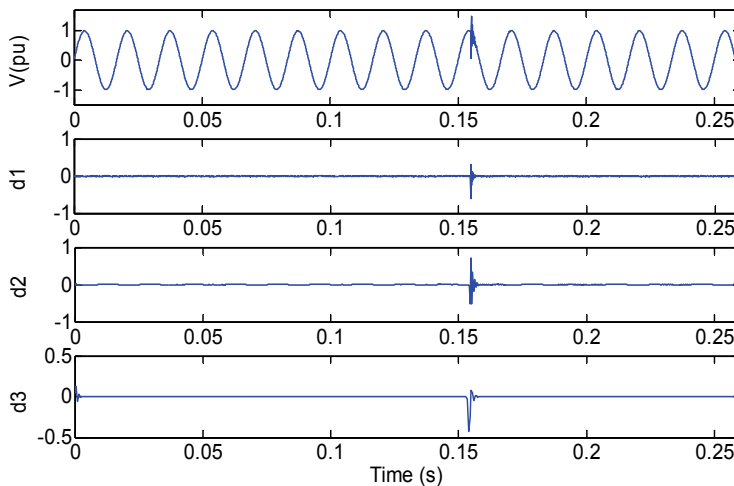
Fig. 4. The capacitor switching signal and detail coefficients: first decomposed level (d1), second decomposed level (d2), and third decomposed level (d3)
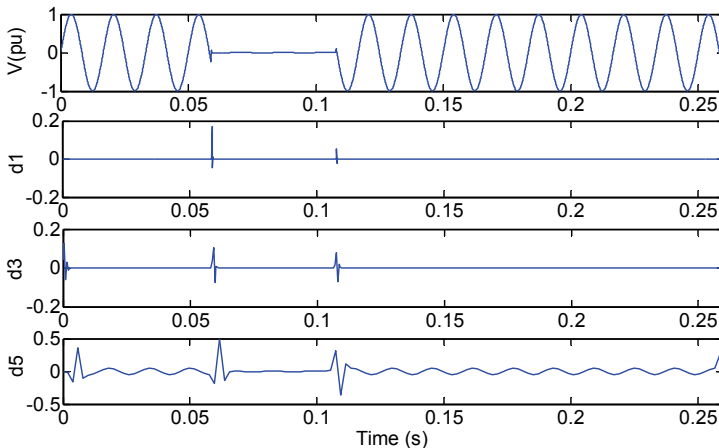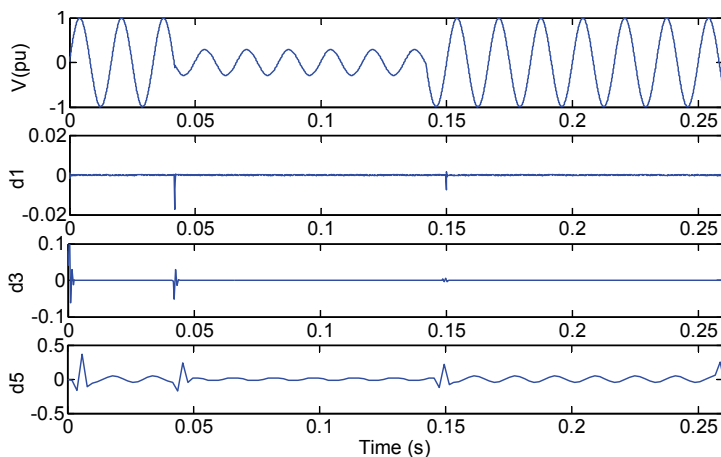

Fig. 5. The voltage sag and detail coefficients: first decomposed level (d1), third decomposed level (d3), and fifth decomposed level (d5)

2.2 Feature extraction

Using the DWT technique to analyze a signal through the level of MRA will generate severe variation in coefficients d_j. Therefore, applying the standard deviation at different resolution

levels one can quantify the variation magnitude of the signals (Oleskovicz et al., 2006; Kanitpanyacharoean & Premrudeepreechacharn, 2004). The standard deviation is defined as in (9).

$$\sigma_X = \sqrt{\frac{\sum_{i=1}^{n}(X_i - \overline{X})^2}{n-1}} \tag{9}$$

where X_i represents the detail coefficient data; $\overline{X}$ is the data average; and n is the amount of data.

Figure 6 shows a comparison of the two standard deviation curves along the 9 decomposition levels. One of these curves is from the analysis of a signal containing a sag disturbance, and the other curve is from a sinusoidal waveform analysis. By observing Fig. 6 one can notice there was a decrease in the coefficients of the 8th decomposition level, which concentrates most of the fundamental frequency components. While Fig. 7 shows the standard deviation curve of the detail coefficients from MRA analysis of an oscillatory transient signal caused by capacitor switching compared with a pure sinusoidal analysis. Differently from Fig. 6, which presents variations at the 8 level, Fig. 7 displays variations at the 3 and 4 levels, which concentrate high frequencies.
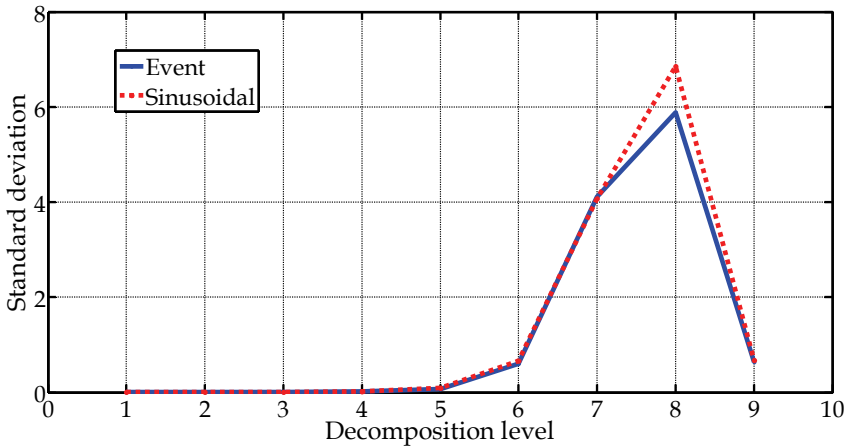
Fig. 6. Standard deviation curves – sag disturbance analysis compared with a sinusoidal waveform analysis

Several simulation tests were performed in order to determine the number of levels, hence reaching better results with 9 decomposition levels. With a lower number of levels some important features can be suppressed at lower frequencies. On the other hand, a higher number of levels can generate non-representative features since there is not sufficient information at the last levels due to the number of signal data considered in this paper. Additionally, in order to take into account these features that originated from the low frequency components (smaller than 60 Hz), this paper includes the approximated version, c_9, of the original disturbance signal f(t). Experimentally, better results were obtained when using the mean of c_9 rather then the standard deviation. The average of data is defined by (10).

$$\mu_X = \frac{1}{n}\sum_{i=1}^{n} X_i \tag{10}$$

where X_i represents the approximate coefficients and n is the total of data.

The features extracted from the standard deviation and the average value will compound the feature vector, $\mathbf{x} = \begin{bmatrix} \sigma_{d1} & \sigma_{d2} & \cdots & \sigma_{dL} & \mu_{cL} \end{bmatrix}^T$, of each signal, where L is the number of MRA levels.
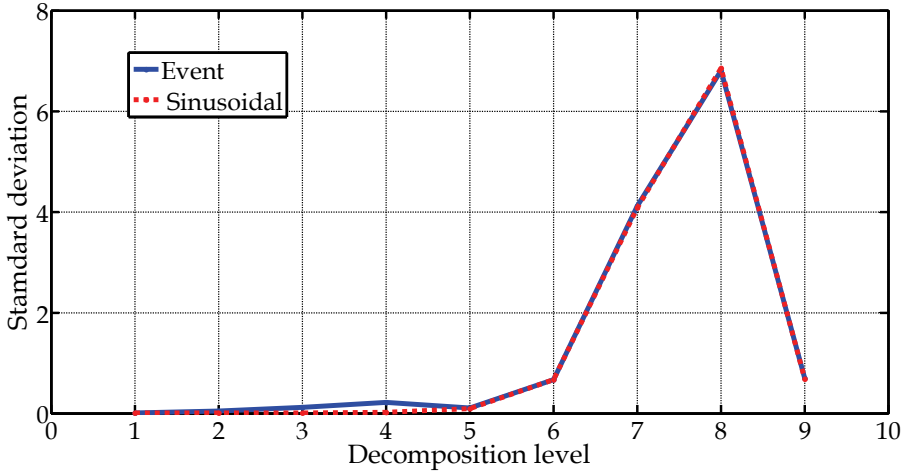
Fig. 7. Standard deviation curves – oscillatory transient disturbance analysis compared with a sinusoidal waveform analysis

2.3 Principal component analysis

The principal component analysis is a statistical technique whose purpose is to condense information from a large set of correlated variables into fewer variables ("principal components"), while preserving the variability that is in the data set (Jolliffe, 2002). Each component contains new information about the data set, and it is ordered in such a way that the first few components account for most of the variability.

The PCA transforms a random vector $\mathbf{x} \in \mathbb{R}^m$ into another vector $\mathbf{y} \in \mathbb{R}^n$ (for $n \leq m$), projecting $\mathbf{x}$ into n orthogonal directions with more variance. Generally, most of the data variance is explained by a reduced number of components, so it is possible to reject other components without losing relevant information.

Let $\mathbf{X} = \begin{bmatrix} \mathbf{x}_1 & \mathbf{x}_2 & \cdots & \mathbf{x}_M \end{bmatrix}_{N \times M}$ be a matrix formed by M feature vectors $\mathbf{x}$, previously defined, where $\mathbf{x}_1$, $\mathbf{x}_2$, $\cdots, \mathbf{x}_M$ are the M observation disturbance signals, and N=10 is the dimension of each feature vector. As in (Jolliffe, 2002; Castells et al., 2007), derivation of the principal components is based on the assumption that $\mathbf{x}$ is a random process characterized by the correlation matrix $\mathbf{R}_x = E[\mathbf{xx}^T]$. Then, the principal components of $\mathbf{x}$ are obtained from the application of an orthonormal linear transformation $\mathbf{\Phi} = [\varphi_1 \varphi_2 \cdots \varphi_N]$ to $\mathbf{x}$,

$$\mathbf{w} = \mathbf{\Phi}^T \mathbf{x}, \tag{11}$$

so that, the elements of the principal component vector $\mathbf{w} = \begin{bmatrix} w_1 & w_2 & \cdots & w_N \end{bmatrix}^T$ become mutually uncorrelated. The first principal component is obtained as a scalar product $w_1 = \varphi_1^T \mathbf{x}$, where vector φ_1 is chosen so that the variance of w_1, is

$$E[w_1^2] = E[\varphi_1^T \mathbf{x}\mathbf{x}^T \varphi_1] = \varphi_1^T \mathbf{R_x} \varphi_1 ,\tag{12}$$

maximally subject to the constraint $\varphi_1^T \varphi_1 = 1$. The maximal variance is obtained when φ_1 is the normalized eigenvector corresponding to the largest eigenvalue of $\mathbf{R_x}$, denoted by λ_1. The resulting variance is:

$$E[w_1^2] = \varphi_1^T \mathbf{R_x} \varphi_1 = \lambda_1 \varphi_1^T \varphi_1 = \lambda_1 ,\tag{13}$$

The second principal component w_2 is obtained by choosing φ_2 as the eigenvector corresponding to the second largest eigenvalue of $\mathbf{R_x}$, and so on until the variance of $\mathbf{x}$ is completely represented by $\mathbf{w}$. Hence, to obtain the whole set of N different principal components, the eigenvector equation for $\mathbf{R_x}$ needs to be solved, according to (14).

$$\mathbf{R_x}\boldsymbol{\Phi} = \boldsymbol{\Phi}\boldsymbol{\Lambda} ,\tag{14}$$

where $\boldsymbol{\Lambda}$ denotes a diagonal matrix with the eigenvalues $\lambda_1,\ldots,\lambda_N$. Since $\mathbf{R_x}$ is rarely known in practice, the $N \times N$ sample correlation matrix, is defined by

$$\hat{\mathbf{R}}_x = \frac{1}{M} \mathbf{X}\mathbf{X}^T ,\tag{15}$$

replacing $\mathbf{R_x}$ when the eigenvectors are calculated in (13).
As previously mentioned, to obtain the principal components, it is necessary to calculate the eigenvalues and eigenvectors of $\hat{\mathbf{R}}_x$, which is the covariance matrix of the $N \times M$ data matrix $\mathbf{X}$. Therefore, once matrix $\boldsymbol{\Phi}$ is known it is possible to calculate the principal components. In this experiment, the 4 first principal components were adopted, which are w_1, w_2, w_3 and w_4, since their contributions correspond to more than 90% of the data variability, i.e., $\beta_P > 90\%$, defined according to (16) as

$$\beta_P = \frac{\sum_{k=1}^{P} \lambda_k}{\sum_{k=1}^{N} \lambda_k} 100\% ,\tag{16}$$

where λ_k are the eigenvalues of $\hat{\mathbf{R}}_x$, $N = 10$ and $P = 4$.
Note that the PCA result is a set of independent elements that could be used as an orthonormal basis to approximate the original feature set extracted from the analyzed signals. It is possible, through a linear combination of such components, to generate those features used to characterize the analyzed signals. In this paper, the contributions of the first 4 principal components, resulting from the PCA technique, is 97.72% as the canonical weights to feature vectors in the training data set. Fig. 8 shows the principal components and their respective percentage of variances.
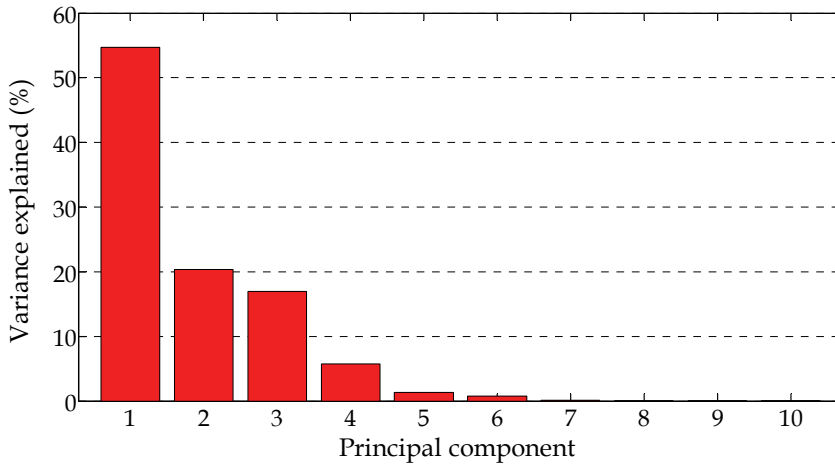
Fig. 8. Variance explained by principal components

The $\mathbf{W}$ matrix containing the principal components is applied to perform a new data set to represent each disturbance signal. These new set is calculated as in (17).

$$\mathbf{Y} = \mathbf{W}_{N \times P}{}^{T} \mathbf{X}_{N \times M} \ , \tag{17}$$

where $\mathbf{X}_{N \times M}$ is the original data matrix, and $\mathbf{W}_{N \times P}$ is a matrix containing the P first components. Hence, $\mathbf{Y}$ is a $P \times N$ matrix representing a new uncorrelated data set.

2.4 The radial basis function network

The PQ disturbances classification is the last stage of the algorithm. In order to execute such classifications this paper proposes a radial-basis function (RBF) network. The classifications are performed by the RBF into two ways: one by not applying PCA algorithm and the other applying PCA algorithm so as to validate this proposed method.
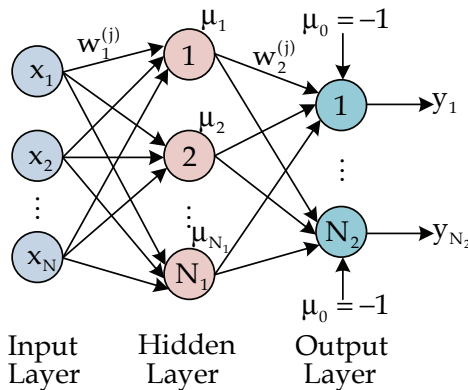
Fig. 9. A typical radial basis function network

Construction of a RBF network, in its most basic form, involves three layers with entirely different roles. The input layer is made up of source nodes connecting the network to its environment. The second layer, the only hidden layer in the network, applies a nonlinear transformation from the input layer space to the hidden layer space; in most applications the hidden space is of high dimensionality. The output layer is linear, supplying the network response to the activation pattern (signal) applied to the input layer (Fyfe, 1996). In other words, the hidden neuronal function forms a basis for the input vectors and output neurons merely by calculating a linear combination of the hidden neuron's output. A typical RBF network is shown in Fig. 9.

In pattern classification problems, the separation of classes in the RBF is accomplished with radial-basis functions. The maximum distance criteria are specified so as to obtain the classification. An often-used set of basis functions is the Gaussian functions whose mean and variance may be determined to a certain degree by the input data (Haykin, 1998).

2.4.1 The RBF training process

The RBF training consists of two stages, i.e., the hidden layer training process followed by the output layer training process. The RBF configuration for both classification procedures is as follows.

- Neurons at the input layer: feature vector lengths (4 or 10).
- Neurons at the hidden layer: 45.
- Neurons at the output layer: 7.
- Output learning rate: 10^{-4}.
- Output accuracy: 10^{-8}.

For the hidden layer training a non-supervised method was used, i.e., a typical grouping algorithm. The objective is to adjust the center of each Gaussian function in areas of input vectors tending to form groups. This procedure can be done by means of vector quantization using the "K-means" algorithm (Tou & Gonzalez, 1974; Haykin, 1998).

Training the output layer was only executed after of the function base parameters executed in the previous stage were determined. The training group of the output layer is formed by input/output pairs $\{\mu(k), d(k)\}$, whose vectors are specified after training the first layer. The output layer was trained using the "generalized delta rule" algorithm, which adjusts the network weights minimizing the quadratic error between $\mu(k)$ and $d(k)$ (Haykin, 1998). The Gaussian function usually used as an activation function for neurons of the hidden layer has the following form:

$$\mu_j = \exp\left(-\frac{\left(x(k) - w_1^{(j)}\right)^{\mathrm{T}}\left(x(k) - w_1^{(j)}\right)}{2\sigma_j^2}\right),\tag{18}$$

where $j = 1 \cdots N_1$ are the inputs, $w_1^{(j)}$ are the synaptic weights connecting the input layer to the hidden layer, and σ_j^2 are the variances between $x(k)$ and $w_1^{(j)}$ calculated during the training of the hidden layer. Then, the maximum answer of each neuron should happen when $x(k)$ is very close to $w_1^{(j)}$. The answer decreases as $x(k)$ moves away from $w_1^{(j)}$, making the Gaussian cone narrower, as the variance σ_j^2 becomes smaller. Additionally, these cones have an identical output for inputs that are at a fixed distance of the Gaussian

function center. Finally, the outputs y_j of the exit layer neurons were obtained in the following way:

$$y_j = g\left(\sum_{i=0}^{N_1} w_{2ji}\mu_i\right) = \sum_{i=0}^{N_1} w_{2ji}\mu_i \ , \tag{19}$$

where $j = 1\cdots N_1$, y_j is the output of the jth neuron of the output layer, w_{2ji} is the synaptic weights matrix of the second layer, $g(\cdot)$ is the linear function activation, and μ_i is the output value of the ith neuron of the first neural layer (added by the threshold), being $\mu_0 = -1$.

3. Computational results

The classification results are presented in this section and the proposed method using the PCA algorithm is evaluated by considering two situations. Firstly, the RBF training and the PQ disturbance classification was performed without using the PCA algorithm. Then, in the second situation, the PCA algorithm was applied to perform the RBF training and classification. The processing time was obtained, as well as the number of training epochs, the mean squared error (MSE) and the classification accuracies in both situations so as to compare the proposed classification performance. Table 2 shows an overview of the RBF's computational performance obtained in the training and classification procedures. Table 3 shows the classification results of the first situation when the classification process was performed without using the PCA. The classification results with the PCA are shown in Table 4. In this situation the feature vector dimension was reduced, preserving those features with more variability, as presented in section II. In both tables each row represents a disturbance to be classified and each column shows which category that disturbance was classified in.

	PCA	Without PCA
Neurons at the input layer	4	10
Training epochs	48385	49065
Mean squared error	0.1223	0.1276
Training time	243.3 s	203.5 s
Classification time	44.9 ms	45.0 ms

Table 2. RBF classification performances

	C_1	C_2	C_3	C_4	C_5	C_6	C_7	(%)
Sinusoidal	25	0	0	0	0	0	0	100
Transient	0	25	0	0	0	0	0	100
Flicker	5	0	18	0	0	1	1	72
Harmonics	0	0	0	25	0	0	0	100
Interruption	0	0	0	0	23	0	2	92
Notching	2	0	0	0	0	23	0	92
Sag	1	0	0	0	1	0	23	92
Overall accuracy: 92.57 %								

Table 3. Classification results using PCA algorithm

	C_1	C_2	C_3	C_4	C_5	C_6	C_7	(%)
Sinusoidal	25	0	0	0	0	0	0	100
Transient	2	23	0	0	0	0	0	92
Flicker	6	1	16	0	0	1	1	64
Harmonics	0	0	0	25	0	0	0	100
Interruption	0	0	0	0	23	0	2	92
Notching	2	0	0	0	0	23	0	92
Sag	1	0	0	0	1	0	23	92
Overall accuracy: 90.29 %								

Table 4. Classification results without using PCA algorithm

4. Final comments

The main goal of this approach is to accomplish classifications of PQ disturbances, which are responsible for degrading the quality of electric power systems, by applying a RBF network. To best adapt the PQ disturbance signals, several stages of preprocessing were necessary. For instance, by applying the wavelet transform it was possible to analyze signals at different ranges of frequencies and to maintain the time resolution. This makes wavelet transformation a highly applicable tool in PQ analysis as broached in this paper. This is so because several disturbances happen with different characteristics in time and frequency, which are difficult to analyze with simple Fourier transform.

Among the several forms of analysis for the DWT coefficients, this paper proposes the calculation of the standard deviation curve of details and the average of approximation coefficients as a complement to this analysis. By observing Figs. 6 and 7, variations of the decomposition levels are clearly observable according to the disturbance contained in the signals.

The PCA tool has shown to be an effective and very interesting tool when it is applied to the pre-processing classification. By applying the PCA it was possible to reduce the amounts of data inserted into the RBF network, and it was also possible to choose which data were more significant and best representative of the disturbances. Although with a reduction of 60% in the feature vectors, the principal components could represent 97.72% of the information that characterized the disturbances. In addition, the method using PCA to perform a disturbance classification did not increase the processing time of the RBF network, as shown in Table 2.

Finally, taking into account the amount of disturbance classes considered in this paper, the classification results applying the proposed PCA method were better than those obtained when PCA was not applied. Using the same RBF configuration, the classification using PCA obtained 92.57% of success, while the classification not using PCA obtained only 90.29%.

As shown in Table 3, three disturbance classes were classified with 100% of success. The sinusoidal signals (without any type of disturbance), were inserted in the classification to discriminate those signals containing disturbances from those without any disturbances. Therefore, the signals containing some disturbance type were classified as not containing disturbance. This can be due to a very low disturbance intensity, which might have characterized the signals as pure sinusoidal signals.

5. Conclusion

In this work, wavelet and neural network methodology was employed to extract features and classify disturbance signals, respectively. Different from other works, which adopted similar approaches; this paper is concerned in eliminating redundant information from the feature space, therefore, reducing the number of input data and maintaining the processing time. The PCA technique was used to reduce feature space dimension, allowing the implementation of a neural network with a lower number of neurons, hence performing a better classification process.

By comparing the classification results and processing time from two systems discussed in this work, it was possible to demonstrate the validity of the PCA technique, which was able to classify the disturbances with an average accuracy of 92.57%.

6. Acknowledgment

7. References

Barmada, S., Landi, A., Papi, M. & Sani, L. (2003). Wavelet multiresolution analysis for monitoring the occurrence of arcing on overhead electrified railways, *Journal Proceedings of the Institution of Mechanical Engineers, Part F: Journal of Rail and Rapid Transit*, Vol.217, No.3, (2003), pp.(177-187), ISSN 2041-3017.

Castells, F., Laguna, P., Bollmann, A. & Roig, J. M. (2007). Principal component analysis in ECG signal processing, *EURASIP Journal on Advances in Signal Processing,* Vol.2007, No.1, (January 2007), pp. (98-98), ISSN 1110-8657.

Chen, S. & Zhu, H. Y. (2007). Wavelet transform for processing power quality disturbances, *EURASIP Journal on Advances in Signal Processing,* Vol.2007, No.1, (January 2007), pp. (176-176), ISSN 1110-8657.

Chung, J., Powers, E. J., Grady, W. M. & Bhatt, S. C. (2002). Power disturbance classifier using a rule-based method and wavelet packet-based hidden markov model, *IEEE Transaction on Power Delivery,* Vol.17, No.1, (January 2002), pp. (233–241), ISSN 0885-8977.

Daubechies, I. (1992). *Ten Lectures on wavelet*, Society for Industrial and Applied Mathematics (SIAM), ISBN 0-89871-274-2, Philadelphia, PA, USA.

Daubechies, I. (1996). Where Wavelets Come From? – A Personal Point of View, *Proceedings of the IEEE*, Vol.84, No.4, (April 1996), pp. (510-513), ISSN 0018-9219.

Debnath, L. (2002). *Wavelet Transforms and Their Applications*. (1st Edition), Birkhäuser: Boston, ISBN 0-8176-4204-8, Boston, USA.

Dugan, Roger C., McGranaghan, Mark F., Santoso, Surya & Beaty, H. Wayne (2003). *Electrical Power Systems Quality* (2nd Edition), McGraw-Hill, ISBN 978-0-07-138622-7.

Fyfe, C. (1996). *Artificial Neural Networks,* (Edition 1.1), Department of Computing and Information Systems, The University of Paisley, pp. 113-126.

Gaing, Z.-L. (2004). Wavelet-based neural network for power disturbance recognition and classification, *IEEE Transaction on Power Delivery,* Vol. 9, No.4, (October 2004), pp. (1560-568), ISSN 0885-8977.

Haykin, S. (1998). *Neural Networks: A Comprehensive Foundation,* (2nd Edition), Prentice Hall, ISBN 0132733501, Saddle River, NJ, USA.

IEEE Standard 1159-2009 (2009). *IEEE Recommended Practice for Monitoring Electric Power Quality*, *(Revision of IEEE Std 1159-1995)* pp. (c1-81), June 26 2009, doi: 10.1109/IEEESTD.2009.5154067.

Jolliffe, I. T. (2002). *Principal Component Analysis,* (2nd Edition), Springer, ISBN 0-387-95422-2, New York, NY, USA.

Kanitpanyacharoean, W. and Premrudeepreechacharn, S. (2004). Power Quality Problem Classification Using Wavelet Transformation and Artificial Neural Networks, *Power Systems Conference and Exposition, 2004. IEEE PES*, ISBN 0-7803-8718-X, Vol.3, pp. (1496-1501), October 2004.

Karimi, M., Mokhtari, H. & Iravani, M.R. (2000). Wavelet Based On-Line Disturbance Detection for Power Quality Applications, *IEEE Transactions on Power Delivery*, Vol. 15, No.4, (October 2000), pp. (1212– 220), ISSN 0885-8977.

Mallat, S. G. (1989). A theory for multiresolution signal decomposition: the wavelet representation, *IEEE Transaction on Pattern Analysis and Machine intelligence,* Vol.11, No.7, (July 1989), pp. (674–693), ISSN 0162-8828.

Mix, D. F & Olejniczak, K. J. (2003). *Elements of wavelets for engineers and scientists*. (1stEdition), John Wiley & Sons, Inc., ISBN 0-471-46617-4, Hoboken, New Jersey,USA.

Oleskovicz, M., Coury, D. V., Carneiro, A. M. F, Arruda, E., Filho, O. D. &. Souza, S. A (2006). Estudo comparativo de ferramentas modernas de análise aplicadas à qualidade da energia elétrica, *Revista Controle & Automação,* Vol.17, No.3, (September 2006), pp. (331–341), ISSN 0103-1759.

Santoso, S., Powers, E. J., Grady, W. M. & Hofmann, P. (1996). Power quality assessment via wavelet transformation analysis, *IEEE Transaction on Power Delivery,* Vol.11, No.2, (April 1996), pp. (924–930), ISSN 0885-8977.

Santoso, S., Powers, E. J., Grady, W. M. & Parsons, A. C. (2000a). Power quality disturbance waveform recognition using wavelet-based neural classifier—Part 1: Theoretical foundation, *IEEE Transaction on Power Delivery,* Vol. 15, No.1, (January 2000), pp. (222–228), ISSN 0885-8977.

Santoso, S., Powers, E. J., Grady, W. M. & Parsons, A. C. (2000b). Power quality disturbance waveform recognition using wavelet-based neural classifier—Part 2: Application, *IEEE Transaction on Power Delivery,* Vol. 15, No.1, (January 2000), pp. (229–235), ISSN 0885-8977.

Strang, G. & Nguyen, T. (1997). *Wavelets and Filter Banks.* (2nd Edition), Wellesley-Cambridge Press, ISBN 0-9614088-7-1, Wellesley, USA.

Tou, J. T. & Gonzalez, R. C. (1974). *Pattern Recognition Principles*, Addison-Wesley, Reading, MA, USA.

Yilmaz, A. S., Subasi, A., Bayrak, M., Karsli, V.M. & Ercelebi, E. (2007). Application of lifting based wavelet transforms to characterize power quality events, *Energy Conversion and Management*, Vol.48, No.1, (January 2007),pp. (112-123), ISSN 0196-8904.

Zhu, T. X., Tso, S. K., & Lo, K. L. (2004). Wavelet-based fuzzy approach to power-quality disturbance recognition, *IEEE Transaction on Power Delivery,* Vol.19, No.4, (October 2004), pp. (1928–935), ISSN 0885-8977.

3

Power Quality Measurement Under Non-Sinusoidal Condition

Magnago Fernando, Reineri Claudio and Lovera Santiago
Universidad Nacional de Río Cuarto
Argentina

1. Introduction

The interest on problems related to non linear devices and their influence on the systems increased considerably since 1980. This is due to the development of new power semiconductor devices and, as a consequence, the development of new converters that increment the non linearity in electric power signals substantially (Arrillaga et al., 1995).

Several research institutions have estimated that seventy percent of all electrical power usage passes through a semiconductor device at least once in the process of being used by consumers. The increase on the utilization of electronic equipment modified the sinusoidal nature of electrical signals. These equipments increase the current waveform distortion and, as a consequence, increment the voltage waveform distortion which causes over voltage, resonance problems in the system, the increase of losses and the decrease in devices efficiency (Dugan et al., 1996).

In general, quantities used in electrical power systems are defined for sinusoidal conditions. Under non sinusoidal conditions, some quantities can conduct to wrong interpretations, and others can have no meaning at all. Apparent power (S) and reactive power (Q) are two of the most affected quantities (Svensson, 1999). Conventional power definitions are well known and implemented extensively. However, only the active power has a clear physical meaning even for non sinusoidal conditions. It represents the average value of the instantaneous power over a fix period. On the other hand, the mathematical formulation of reactive power may cause incorrect interpretation, aggravated when the analysis is extended to three phase systems (Filipski, 1984; Emanuel, 1999).

Although definitions of apparent, active, and reactive power for sinusoidal systems are universally accepted, since IXX century researchers pointed out that the angle difference between voltage and current produces power oscillation between the source and the load. All these research effort remark the importance of the power factor and the reactive power on the optimal economic dispatch. One of the initial proposals consists on dividing the power term into active, reactive and distortion power, and was the most accepted one. In the 80´s the discussion about the definitions mentioned above increased because the use of non linear loads incremented considerably. Although many researchers remark the important implications of non sinusoidal conditions, up today it is very difficult to define a unique power definition for electric networks under distorted conditions. The lack of a unique definition makes that commercial measurement systems utilize different definitions,

producing different results, and as a consequence, generates significant economic effects (Ghosh & Durante, 1999; Cataliotti, 2008). Therefore, measurement systems, may present different results, not only because of different principle of operation, but because of the adoption of different quantities definitions as well.

This chapter presents a critical review of apparent power, reactive power and power factor definitions. First, the most commonly used definitions for apparent power are presented, after that, reactive power and the power factor definitions are studied. These definitions are reviewed for single phase and three phase systems and are evaluated under different conditions such as sinusoidal, non sinusoidal, one phase, and balanced and unbalanced three phase systems. Then, a methodology to measure power and power quality indexes based on the instant power theory under non sinusoidal conditions is presented. Finally, the most remarkable conclusions are discussed.

2. Electrical power definition under sinusoidal conditions

The classical definition of instant power for pure sinusoidal conditions is:

$$p(t) = v(t) * i(t) \tag{1}$$

Where $p_{(t)}$, $v_{(t)}$ e $i_{(t)}$ are the instant power, instant voltage and instant current respectively. Considering sinusoidal voltage and current signals represented by the equations $v_{(t)} = \sqrt{2} * V * \sin(\omega t)$ and $i(t) = \sqrt{2} * I * \sin(\omega t - \phi)$ respectively, then Eq. (1) takes the following form:

$$\begin{aligned} p(t) = V * I * \cos(\phi) - V * I * \cos(\phi) * \cos(2 * \omega t) + \\ + V * I * \sin(\phi) * \sin(2 * \omega t) \end{aligned} \tag{2}$$

$$p(t) = P * (1 - \cos(2 * \omega t)) + Q * \sin(2 * \omega t) \tag{3}$$

The mean value of $p_{(t)}$ is known as active power P and can be represented by:

$$P = V * I * \cos\phi \tag{4}$$

Where V and I are the root means square (r.m.s.) value of the voltage and current signals respectively and ϕ is the phase shift between $v_{(t)}$ and $i_{(t)}$

In a similar manner, the reactive power Q is defined as:

$$Q = V * I * \sin\phi \tag{5}$$

The geometric sum of P and Q is know as apparent power S and can be calculated as follow:

$$S = V * I = \sqrt{P^2 + Q^2} \tag{6}$$

Another important term related to the power definition is the relationship between the active power with respect to the apparent power, it isknown as the system power factor FP and gives an indication of the system utilization efficiency:

$$FP = \frac{P}{S} = \cos\phi \tag{7}$$

Analyzing Eq. (1) to (7), the following important properties related to the reactive power can be summarized (Svensson, 1999; Filipski, & Labaj, 1992): a) Q can be represented as a function of $V * I * \sin(\omega t)$, b) Q is a real number, c) For a given Bus, the algebraic sum of all reactive power is zero, d) Q is the bidirectional component of the instant power $p_{(t)}$, e) $Q = 0$ means that the power factor FP is one, f) Q can be compensated by inductive or capacitive devices, g)The geometric sum of P and Q is the apparent power S, h) The voltage drop through transmission lines is produced mostly by the reactive power Q.

These properties apply exclusively to pure sinusoidal signals; therefore in the case of non sinusoidal conditions not all of these properties are fulfilled. Next section presents different power definitions proposed for that purpose, and discusses for which conditions they meet the above properties.

2.1 Electrical power definitions under non-sinusoidal conditions

In order to represent a non-sinusoidal condition, let's consider voltage and current signals with harmonic components, then the apparent power can be represented by the following equation:

$$S^2 = \sum_{n=0}^{\infty} V_n^2 * \sum_{n=0}^{\infty} I_n^2 = V^2 * I^2 \tag{8}$$

For simplicity, let's assume the case where only harmonic signals are present within the current signals and a voltage signal with only a fundamental component, then:

$$S^2 = V_1^2 * \sum_{n=0}^{\infty} I_n^2 = V_1^2 * I_1^2 + V_1^2 * \sum_{n \neq 1}^{\infty} I_n^2 \tag{9}$$

By definition, the active power is:

$$P = \frac{1}{T} * \int_0^T v(t) * i(t) * dt = V_1 * I_1 * \cos(\phi_1) \tag{10}$$

And the reactive power Q :

$$Q = \sum_{n=1}^{\infty} V_n * I_n * \sin(\phi_n) = V_1 * I_1 * \sin(\phi_1) \tag{11}$$

Examining the expressions given by Eq. (9) to (11) and comparing them with Eq. (6), can be concluded that if the signals have components in addition to the fundamental sinusoidal component (60Hz or 50 Hz) , the following expression obeys:

$$P^2 + Q^2 = V_1^2 * I_1^2 \neq S^2 \tag{12}$$

From the inequality represented by Eq. (12) it is observed that the sum of the quadratic terms of P and Q involves only the first term of Eq. (9), therefore property g) does not comply. Hence, definitions of apparent and reactive power useful for sinusoidal conditions may produce wrong results, thus, new definitions for non-sinusoidal conditions are needed. There are proposals to extend apparent power and reactive power formulations for non-sinusoidal situations; the most used ones are described next.

2.2 Reactive power and distortion power definitions

One of the first power definitions that include the presence of harmonics was given by Budenau in 1927 (Budeneau, 1927, as cited in Yildirim & Fuchs 1999), where the active and reactive powers are defined by the following expressions:

$$P = \sum_h V_h * I_h * \cos\phi_h \tag{13}$$

$$Q_B = \sum_h V_h * I_h * \sin\phi_h \tag{14}$$

Where h is the harmonic number. Representing the active and reactive power by Eq. (13) and Eq. (14), the power triangle does not comply, therefore Budenau defined a new term know as distortion power:

$$D = \sqrt{S^2 - P^2 - Q_B{}^2} \tag{15}$$

Based on the distortion power, a complementary or fictitious power is also defined:

$$F = \sqrt{S^2 - P^2} = Q_B^2 + D^2 \tag{16}$$

The physical meaning of Eq. (16) is a power oscillation between the source and the sink, however this only stand when all elements are purely linear and reactive (i.e. capacitors and inductors), which means that Eq. (16) can not be used for reactive compensation design.

Based on this initial definition of distortion power, several other authors proposed different definitions of D as a function of r.m.s. voltage and current harmonic signals and their phase shift. Reference (Emanuel, 1990) proposes the following definition:

$$D^2 = \sum_{\substack{m,n=1 \\ m \neq n}} V_m^2 * I_n^2 + V_n^2 * I_m^2 - 2 * V_m * V_n * I_m * I_n * \cos(\phi_m - \phi_n) \tag{17}$$

where V_m, I_m, V_n y I_n are the r.m.s. harmonic components. The harmonic angles are $\varphi_m = \alpha_m - \beta_m$, $\varphi_n = \alpha_n - \beta_n$, with $\propto_m$, $\propto_n$, β_m y β_n the angle shift between the voltage and current harmonic components.

Another different definition was proposed by reference (Filipski, 1984):

$$D = \sqrt{\sum_m \sum_n \left[V_m^2 * I_n^2 - V_m * V_n * I_m * I_n * \cos\left(\phi_m - \phi_n\right) \right]} \tag{18}$$

After that, Czarnecki (Czarnecki, 1993) recommended the following formulae for D:

$$D = \sqrt{\frac{1}{2} \sum_m \sum_n \left[V_m^2 * I_n^2 - 2 * V_m * V_n * I_m * I_n * \cos\left(\phi_m - \phi_n\right) \right]} \tag{19}$$

Similar definition than the one described by Eq. (18) was proposed by the IEEE Std. 100-1996 (Institute of Electrical and Electronic Engineering [IEEE], 1996). Recently, different authors compared them and discussed their advantages and applicability. Yildirim and Fuchs (Yildirim & Fuchs, 1999) compared Eq. (17) to (19) and performed experimental

measurements using different type of voltage and current distortions, recommending the following distortion definition:

$$D^2 = \sum_{m=0}^{h-1} \sum_{m \neq 1}^{h} \left[V_m^2 * I_n^2 + V_n^2 * I_m^2 - 2 * V_m * V_n * I_m * I_n * \cos\left(\phi_m - \phi_n\right) \right] \tag{20}$$

The most important conclusions from their studies are that Eq. (17) presents important difference with respect to practical results; results calculated using Eq. (18) to (20) are identical and consistent with experimental results. Eq. (18) and (19) have all terms that multiply variables with the same harmonic order, while in Eq. (20) all terms multiply variables of different harmonic order.

2.3 Reactive power definition proposed by Fryze

The reactive power definition proposed by Fryze is based on the division of the current into two terms; the active current term and the reactive current term (Fryze, 1932, as cited in Svensson 1999):

$$i = i_a + i_r \tag{21}$$

Considering that these terms are orthogonal, the following property applies:

$$\frac{1}{T} \int_0^T i_a * i_b * dt = 0 \quad \text{(orthogonal)} \tag{22}$$

i_a can be calculated from the active power:

$$i_a(t) = \frac{P}{V^2} * v(t) \tag{23}$$

Then, from Eq. (21), the reactive power i_r is:

$$i_r(t) = i(t) - i_a(t) \tag{24}$$

Based on these definitions and considering Eq. (16), the reactive power representation proposed by Fryze is:

$$Q_F = V * I_r = \sqrt{\left(V * I\right)^2 - \left(V * I_a\right)^2} = \sqrt{S^2 - P^2} = \sqrt{Q_B^2 + D^2} \tag{25}$$

Eq. (25) shows that Q_F is a function of S and P, therefore, the advantage of this representation is that there is no need to measure the reactive power. However, Q_F is always a positive magnitude, then, property b) does not apply, hence, it can not be used for power flow analysis. On the other hand, since it is always positive, it can be compensated by injecting a negative current $-i_r$ which makes it suitable for active filter design.

2.4 Reactive power definition proposed by Emanuel

Emanuel observed that in most cases, the principal contribution to the reactive power is due to the fundamental component of the voltage signal, then, he proposed the following definition for the reactive power term (Emanuel, 1990):

$$Q_1 = V_1 * I_1 * \sin\phi_1 \tag{26}$$

Based on this definition, an additional term named complementary power can be formulated:

$$P_C^2 = S^2 - P^2 - Q_1^2 \tag{27}$$

Finally, both active and reactive terms can be represented by two terms; the fundamental and the harmonic component:

$$S^2 = \left(P_1 + P_h\right)^2 + Q_F^2 \tag{28}$$

Where Q_F is the reactive power defined by Fryze.
Expressing Q_F as a function of the fundamental and harmonic term:

$$Q_F^2 = Q_1^2 + Q_h^2 \tag{29}$$

And replacing Eq. (29) into Eq. (28), the apparent power is:

$$S^2 = \left(P_1 + P_h\right)^2 + Q_1^2 + Q_h^2 \tag{30}$$

Since Q_F is defined adding two different terms, the fundamental reactive power Q_1 and the harmonic reactive power Q_H, this definition became an effective tool for active filters control and monitoring and power factor shift compensation design.

2.5 Definition proposed by Czarnecki

Based on previous definitions, Czarnecki proposed new definitions based on a orthogonal current decomposition that allows to identify different phenomena that cause the efficiency decrease of the electrical energy transmission (Czarnecki, 1993).
The total current is decomposed in active, reactive, harmonic and disperses terms:

$$I^2 = I_A^2 + I_R^2 + I_S^2 + I_H^2 \tag{31}$$

The latest three terms are the ones responsible of the efficiency transmission decrease. Where the reactive term is given by:

$$I_R = \sqrt{\sum_{n=N} B_n^2 * V_n^2} \tag{32}$$

Index k is the harmonic component that is not present in the N voltage terms, the harmonic term is calculated as:

$$I_H = \sqrt{\sum_{n=K} I_n^2} \tag{33}$$

And the disperse current can be represented as follow:

$$I_R = \sqrt{\sum_{n=N} \left(G_n - G\right)^2 * V_n^2} \tag{34}$$

Where the equivalent load conductance is:

$$G = \frac{P}{V^2} \tag{35}$$

And the n-order harmonic component of the load is:

$$Y_n = G_n + jB_n \tag{36}$$

Using this decomposition, the apparent power can be expressed as:

$$S^2 = P^2 + D_S^2 + Q_R^2 + D_H^2 \tag{37}$$

Where the reactive power, the distortion power and the harmonic power are respectivelly:

$$Q_R = V * I_R \tag{38}$$

$$D_S = V * I_S \tag{39}$$

$$D_H = V * I_H \tag{40}$$

One of the main feature of this definition is that is based on suceptances instead of voltages, currents and powers. For systems that contain currents with large harmonic values and voltage with small harmonic values, will present the problem of phase shift uncertainty and, as a concequence, large uncertainty of parameter B_N. This issue may produce errors in the reactive current determination.

2.6 Definition proposed by the IEEE Std 1459-2000

This standard proposes the decomposition of both current and voltage signals into fundamental and harmonic terms (Institute of Electrical and Electronic Engineering [IEEE], 2000):

$$I^2 = I_1^2 + I_H^2 \tag{41}$$

$$V^2 = V_1^2 + V_H^2 \tag{42}$$

Where the harmonic components V_H, I_H include all harmonic terms and the direct current component as well:

$$V_H^2 = \sum_{h \neq 1}^{\infty} V_h^2 \tag{43}$$

$$I_H^2 = \sum_{h \neq 1}^{\infty} I_h^2 \tag{44}$$

Based on these terms, the active power can be represented as the sum of the fundamental and harmonic components:

$$P = P_1 + P_H \tag{45}$$

Where the fundamental and harmonic components are respectivelly:

$$P_1 = \sum_{h \neq 1}^{\infty} V_1 I_1 \cos \phi_1 \tag{46}$$

$$P_H = \sum_{h \neq 1}^{\infty} V_h I_h \cos \phi_h \tag{47}$$

Similarly, the reactive power can be represented:

$$Q = Q_1 + Q_H \tag{48}$$

Where the fundamental and harmonic components are:

$$Q_1 = \sum_{h \neq 1}^{\infty} V_1 I_1 \sin \phi_1 \tag{49}$$

$$Q_H = \sum_{h \neq 1}^{\infty} V_h I_h \sin \phi_h \tag{50}$$

Considering that the square of the apparent power can be represented as a function of the voltage and current terms:

$$S^2 = (VI)^2 = (V_1 I_1)^2 + (V_1 I_H)^2 + (V_H I_1)^2 + (V_H I_H)^2 \tag{51}$$

And representing the apparent power S as the sum of a fundamental and non fundamental term:

$$S^2 = S_1^2 + S_N^2 \tag{52}$$

It is possible to conclude by comparing Eq. (51) with Eq. (52), that the first term of the square of the apparent power, which is a function of the fundamental components, can be also represented as a function of the fundamental active and reactive components. These terms are:

$$S_1^2 = (V_1 I_1)^2 = P_1^2 + Q_1^2 \tag{53}$$

And term S_N is composed by the rest of the terms present in Eq. (51):

$$S_N^2 = (V_1 I_H)^2 + (V_H I_1)^2 + (V_H I_H)^2 = D_I^2 + D_V^2 + S_H^2 \tag{54}$$

Where the distortion power due to the harmonic current is:

$$D_I = V_1 I_H \tag{55}$$

And due to the harmonic voltage:

$$D_V = V_H I_1 \tag{56}$$

Finally the last term is known as the harmonic apparent power:

$$S_H = V_H I_H \tag{57}$$

Defining the relationship between the harmonic current and the fundamental current components as the total harmonic current distortion $I_H/I_1 = THDi$ and similarly for the voltage $V_H/V_1 = THDv$ then the equations can be represented as a function of the distortion:

$$D_I = S_1 * THD_I \tag{58}$$

$$D_V = S_1 * THD_V \tag{59}$$

$$S_H = S_1 * THD_I * THD_V \tag{60}$$

Finally, the apparent power can be decomposed into the active power P and the non-active power N:

$$S^2 = (V\,I)^2 = P^2 + N^2 \tag{61}$$

Since the harmonic power term is the only one that can have an active component, it can be formulated as follow:

$$S_H^2 = (V_H I_H)^2 = P_H^2 + N_H^2 \tag{62}$$

From all these equations, several important observations can be made: $(P_1 + P_H)$ is the active power, The harmonic power S_H has *(n-1)* terms as a function of $V_h * I_h * \cos \varphi_h$, these terms can have the following values: Null, if V_h or I_h are null, or the phase shift is *90º*. Positive, if V_h and I_h are not null and the phase shift verifies the following inequalities$-90º < \varphi_h < 90º$. Negative, if V_h and I_h are not null and the phase shift verifies the following inequalities$90º < \varphi_h < 270º$. Some harmonic component can produce and others can consume power, and in general P_H is negative. Relationship S_N/S_1 is a good indicator of harmonic distortion. The following inequality stand:

$$S_N \geq S_H \geq P_H \tag{63}$$

The power factor due to the fundamental component, also known as shift power factor is:

$$PF_1 = \cos\phi_1 = \frac{P_1}{S_1} \tag{64}$$

The total power factor is given by the following expression:

$$PF = \frac{P}{S} = \frac{(P_1 + P_H)}{S} = \frac{\left(P_1/S_1\right) * \left[1 + \left(P_H/P_1\right)\right]}{\sqrt{1 + \left(S_N/S_1\right)^2}} = \frac{\left[1 + \left(P_H/P_1\right)\right] * PF_1}{\sqrt{1 + THD_I^2 + THD_V^2 + \left(THD_I * THD_V\right)^2}} \tag{65}$$

In summary, the discussion related to the different definitions is focused on which of the property is complied and which one is not (Filipski & Labaj, 1992). Nevertheless, it is also

important to undertand the meaning of the different expressions and to select the correct index for the specific application such as compensation, voltaje control, identify the source of the harmonic perturbation, or to evaluate the power losses determinado (Balci & Hocaoglu, 2004). The same type of analysis can be extended for multiphase systems, the apparent power definitions for three phase systems is described next.

3. Electric power definitions for three phase systems

Similarly to a single phase system, the definition of apparent power for a three phase system under non sinusoidal conditions has no physical meaning, therefore may drives to wrong interpretations. The measurement, analysis and definition of the different terms of three phase power signal, where voltages and currents are unbalanced and distorted, have been studied in order to standardize the correct indexes that quantify the level of harmonic and distortion (Emanuel, 1999, 2004). An incorrect interpretation or error measurements may produce the wrong operation of the system and as a consequence, a high economic impact.

The normal indicators such as apparent power and nominal voltage that are very important for equipment selection (i.e. transformers, machines) are set for balanced, symmetric and sinusoidal signals. Moreover, they are used by utilities to design the tariff scenario. The power factor index quantifies the energy utilization efficiency (Catallioti et al., 2008, 2009a). As a consequence, nowadays, to have an accurate and consensual definition of apparent, reactive power and power factor for non-sinusoidal three phase systems becomes relevant. In the next section the most used definitions are discussed.

3.1 Apparent power definition for three phase systems

There are several definitions related to the calculation of apparent power for unbalanced three phase systems. In this section the most relevant ones are reviewed (Pajic & Emanuel, 2008; Eguiluz & Arrillaga, 1995; Deustcher Industrie Normen [DIN], 2002; Institute of Electrical and Electronic Engineering [IEEE], 2000).

Based on the single phase definitions, in a multiphase system, the apparent power vector is:

$$S_V = \sqrt{\left(\sum_{k=a}^{c} P_k\right)^2 + \left(\sum_{k=a}^{c} Q_{bk}\right)^2 + \left(\sum_{k=a}^{c} D_k\right)^2}$$

(66)

The arithmetic apparent power can be represented as de sum of all phase's apparent power:

$$S_A = \sum_{k=a}^{c} \sqrt{P_k^2 + Q_{bk}^2 + D_k^2}$$

(67)

For a phase k, P_k is the active power, and Q_{bk} and D_k are de reactive and distortion power defined by Budeanu, respectively. The definitions described by Eq. (66) and Eq (67) are identical and produce correct results for balanced load and sinusoidal voltage and current signals. However, for general unbalanced and/or distorted signals, it can be proved that:

$$S_V \leq S_A$$

(68)

In addition, the power factor index will also produce different results depending on which definition is used:

$$FP_V = \frac{P}{S_V} \geq FP_A = \frac{P}{S_A} \qquad (69)$$

Where FP_V and FP_A are the power factor using the apparent power vector and the arithmetic definition respectively.

The following expression to calculate the apparent power is proposed in (Goodhue, 1933 cited in Depenbrock, 1992; Emanuel, 1998):

$$S = \sqrt{\frac{V_{ab}^2 + V_{bc}^2 + V_{ac}^2}{3}} \sqrt{I_a^2 + I_b^2 + I_c^2} \qquad (70)$$

Conceptually, Eq (70) illustrates that for a given three phase system it is possible to define an equivalent apparent power known as the effective apparent power that is defined as follow:

$$S_e = 3 * V_e * I_e \qquad (71)$$

Where V_e y I_e are the r.m.s. effective voltage and current values respectively.

Recently, several authors proposed different mathematical representation based on Eq. (71). The most important ones are the one described by the standard DIN40110-2 (Deustcher Industrie Normen [DIN], 2002) and the one developed by the IEEE Working Group (Institute of Electrical and Electronic Engineering [IEEE], 1996) that was the origin of the IEEE Standard 1459-2000 (Institute of Electrical and Electronic Engineering [IEEE], 2000). These two formulations are described next.

3.2 Definition described in the standard DIN40110-2

This method, known as FBD method (from the original authors Fryze, Buchholz, Depenbrock) was developed based on Eq. (71) (Depenbrok, 1992, 1998; Deustcher Industrie Normen [DIN], 2002). It defines the effective values of currents and voltages based on the representation of an equivalent system that shares the same power consumption than the original system.

Then, the effective current can be calculated by the following expression:

$$I_{eT} = \sqrt{\frac{1}{3}\left(I_r^2 + I_s^2 + I_t^2 + I_n^2\right)} = \sqrt{(I_+)^2 + (I_-)^2 + 4*(I_0)^2} \qquad (72)$$

Where i_r, i_s, i_t are the line currents and i_n the neutral current.

Similarly, the effective voltage is:

$$V_e = \sqrt{\frac{(V_r^2 + V_s^2 + V_t^2) + (V_{rs}^2 + V_{rt}^2 + V_{ts}^2)}{12}} =$$
$$= \sqrt{(V_+)^2 + (V_-)^2 + \frac{1}{4}*(V_0)^2} \qquad (73)$$

This method allows decomposing both currents and voltages into active and non active components. Moreover, it allows distinguishing each component of the total non active term, becoming a suitable method for compensation studies.

3.3 Definition proposed by the IEEE Standard 1459-2000

This standard assumes a virtual balanced system that has the same power losses than the unbalanced system that it represents. This equivalent system defines an effective line current I_e and an effective phase to neutral voltage V_e.

$$I_e = \sqrt{\frac{1}{3}\left(I_r^2 + I_s^2 + I_t^2 + \rho * I_n^2\right)} \tag{74}$$

Where the factor $\rho = r_n/r$ can vary from 0.2 to 4.

Similar procedure can be followed in order to obtain a representation for the effective voltage V_e. In this case, the load is represented by three equal resistances conected in a star configuration, and three equal resistances connected in a delta configuration, the power relationship is defined by factor $\varepsilon = P_\Delta/P_Y$.

Considering that the power losses are the same for both systems, the effective phase to neutral voltage for the equivalent system is:

$$V_e = \sqrt{\frac{3*(V_r^2 + V_s^2 + V_t^2) + \varepsilon*(V_{rs}^2 + V_{rt}^2 + V_{ts}^2)}{9*(1+\varepsilon)}} \tag{75}$$

In order to simplify the formulations, the standard assumes unitary value of ρ and ε, then Eq. (74) and (75) can be represented as:

$$I_e = \sqrt{\frac{1}{3}\left(I_r^2 + I_s^2 + I_t^2 + I_n^2\right)} \tag{76}$$

$$V_e = \sqrt{\frac{3*(V_r^2 + V_s^2 + V_t^2) + (V_{rs}^2 + V_{rt}^2 + V_{ts}^2)}{18}} \tag{77}$$

These effective current and voltage can also be represented as a function of sequence components:

$$I_e = \sqrt{(I_+)^2 + (I_-)^2 + 4*(I_0)^2} \tag{78}$$

$$V_e = \sqrt{(V_+)^2 + (V_-)^2 + \frac{1}{2}*(V_0)^2} \tag{79}$$

Since one of the objectives of these formulations is to separate the funtamental term from the distortion terms, the effective values can be further decomposed into fundamental and harmonic terms:

$$V_e^2 = V_{e1}^2 + V_{eH}^2 \tag{80}$$

$$I_e^2 = I_{e1}^2 + I_{eH}^2 \tag{81}$$

Where the fundamental terms are:

$$V_{e1} = \sqrt{\frac{3*(V_{r1}^2 + V_{s1}^2 + V_{t1}^2) + (V_{rs1}^2 + V_{rt1}^2 + V_{ts1}^2)}{18}} \quad (\varepsilon = 1) \tag{82}$$

$$I_{e1} = \sqrt{\frac{1}{3}\left(I_{r1}^2 + I_{s1}^2 + I_{t1}^2 + I_{n1}^2\right)} \quad (\rho=1) \tag{83}$$

And the harmonic terms:

$$V_{eH}^2 = V_e^2 - V_{e1}^2 \tag{84}$$

$$I_{eH}^2 = I_e^2 - I_{e1}^2 \tag{85}$$

Considering these definitions, the effective apparent power can be calculated as follow:

$$S_e^2 = (3*V_{e1}*I_{e1})^2 + (3*V_{e1}*I_{eH})^2 + (3*V_{eH}*I_{e1})^2 + (3*V_{eH}*I_{eH})^2 \tag{86}$$

Where the fundamental term of the effective apparent power is:

$$S_{e1} = 3*V_{e1}*I_{e1} \tag{87}$$

The fundamental term can also be represented as a function of active and reactive sequence powers:

$$\left(S_1^+\right)^2 = \left(P_1^+\right)^2 + \left(Q_1^+\right)^2 \tag{88}$$

Where:

$$P_1^+ = 3*V_1^+*I_1^+*\cos\phi_1^+ \tag{89}$$

$$Q_1^+ = 3*V_1^+*I_1^+*\sin\phi_1^+ \tag{90}$$

Then, the square of the fundamental effective apparent power can be represented as the addition of two terms:

$$S_{e1}^2 = \left(S_1^+\right)^2 + \left(S_{U1}\right)^2 \tag{91}$$

Where the term S_{U1} is due to the system unbalance. Similarly, the non fundamental term S_{eN} can be represented by:

$$S_{eN}^2 = (3*V_{e1}*I_{eH})^2 + (3*V_{eH}*I_{e1})^2 + (3*V_{eH}*I_{eH})^2 \tag{92}$$

Where the three terms can be represented as a function of the total harmonic distortion, defining the distortion power due to the current as:

$$D_{eI} = 3*V_{e1}*I_{eH} = 3*S_{e1}*THD_I \tag{93}$$

The distortion power due to the voltage:

$$D_{eV} = 3*V_{eH}*I_{e1} = 3*S_{e1}*THD_V \tag{94}$$

And the effective harmonic apparent power:

$$S_{eH} = 3 * V_{eH} * I_{eH} = 3 * S_{e1} * THD_V * THD_I \tag{95}$$

Finally, the harmonic active power can be calculated:

$$P_H = \sum_{\substack{h \neq 1 \\ i = r,s,t}} V_{ih} * I_{ih} * \cos\phi_{ih} = P - P_1 \tag{96}$$

The main features of the formulations proposed by this standard are: P_1^+ can be separated from the rest of the active power component. In general P_H , P_1^- y P_1^0 can be neglected since are small with respect to P_1^+ , therefore results obtained by measuring only this term is accurate enough. Identify Q_1^+ from the rest of the reactive power componets, it allows to design the appropriate capacitor bank in order to compensate the power factor shift $\cos\phi_1^+$. The non fundamental apparent power S_{eN} allows evaluating the distortion severity and becomes a usefull parameter to estimate the harmonic filter size to compensate the distortion.

Analyzing the apparent power definitions for three phase systems can be observed that the apparent power may have different values depending on the system conditions and the selected definition, being (Eguiluz & Arrillaga, 1995; Emanuel, 1999):

$$S_v \leq S_a \leq S_e \tag{97}$$

Similarly observation stands for the power factor values:

$$FP_V = \frac{P}{S_{VEC}} \geq FP_A = \frac{P}{S_{AVA}} \geq FP_e = \frac{P}{S_e} \tag{98}$$

Method FBD is replaced by the one proposed by the IEEE because it is simpler and is more related to the network parameters

4. Power measurement under non-sinusoidal conditions

The determination of the different power terms such as active power, reactive power, distortion, fundamental component of the positive sequence, and other important parameters ($i.e. FP, DFP, THDv, THDi$) are becoming relevant. The power measurement algorithms included in the electronic devices are based on these definitions. Therefore, it is always a concern to implement the most accurate methodology, since errors in power measurement may translate into huge economic losses (Filipsky & Labaj, 1992; Cook & Williams, 1990). In general, these errors are negligible if the system is sinusoidal and balanced; however, this is not the scenario when the system has harmonic or/and unbalanced signals (Cataliotti et al., 2009a, 2009b; Gunther & McGranaghan, 2010).

New technology allows the use of accurate, fast, and low cost measurement systems, however the lack of a unique apparent power definition for unbalanced and distorted systems makes the results of the measurements if not wrong, at least a controversial issue (Morsi & El-Hawary, 2007; Cataliotti et al., 2009a).

In this section, based on the power definitions explained in previous sections and the instantaneous power theory, a methodology to measure power under unbalanced conditions is proposed.

The algorithm is based on the standard IEEE 1459 – 2000 (Institute of Electrical and Electronic Engineering [IEEE], 2000), the instant power theory, currently used for active filter design, is used for the signal processing phase (Akagi et al, 1983; Herrera & Salmerón, 2007; Watanabe et al., 1993; Akagi et al., 2007; Czarneky, 2006, 2004; Seong-Jeub, 2008) . The Fundamentals of this theory is explained next.

4.1 Instant power theory

A three phase system can be represented by three conductors where the voltage are v_r, v_s, v_t and the line currents are i_r, i_s, i_t then, this system can be represented by an equivalent two phase system with the following voltages and currents:

$$\begin{bmatrix} v_\alpha \\ v_\beta \end{bmatrix} = T * \begin{bmatrix} v_r \\ v_s \\ v_t \end{bmatrix} \quad \text{and} \quad \begin{bmatrix} i_\alpha \\ i_\beta \end{bmatrix} = T * \begin{bmatrix} v_r \\ v_s \\ v_t \end{bmatrix} \tag{99}$$

Where T is known as the Park transformation matrix:

$$T = \sqrt{\frac{2}{3}} \begin{bmatrix} 1 & -1/2 & -1/2 \\ 0 & \sqrt{3}/2 & -\sqrt{3}/2 \end{bmatrix} \tag{100}$$

Then, the active and reactive power can be calculated as follow:

$$p = v_\alpha * i_\alpha + v_\beta * i_\beta \tag{101}$$

$$q = v_\alpha * i_\beta - v_\beta * i_\alpha \tag{102}$$

where: v_α: instant voltage, direction α, v_β : instant voltage, direction β, i_α : instant current direction α, i_β : instant current, direction β, p: instant active power [W], q: instant reactive power [VA].
Using matrix notation, the power equation can be represented as:

$$\begin{bmatrix} p \\ q \end{bmatrix} = \begin{bmatrix} v_\alpha & v_\beta \\ -v_\beta & v_\alpha \end{bmatrix} \begin{bmatrix} i_\alpha \\ i_\beta \end{bmatrix} \tag{103}$$

And the following expression stands:

$$P_{3\varphi} = v_r * i_r + v_s * i_s + v_t * i_t = v_\alpha * i_\alpha + v_\beta * i_\beta \tag{104}$$

Where $P_{3\varphi}$ is the three phase instant power.
These expressions can be extended for a four conductor system; in this case a zero sequence term is needed:

$$\begin{bmatrix} v_0 \\ v_\alpha \\ v_\beta \end{bmatrix} = \sqrt{\frac{2}{3}} \begin{bmatrix} 1/\sqrt{2} & 1/\sqrt{2} & 1/\sqrt{2} \\ 1 & -1/2 & -1/2 \\ 0 & \sqrt{3}/2 & -\sqrt{3}/2 \end{bmatrix} \begin{bmatrix} v_r \\ v_s \\ v_t \end{bmatrix} \tag{105}$$

Where: v_0: Instant zero sequence voltage, i_0: Instant zero sequence current. Similar expressin can be obtained for the currents. Defining the instant zero sequence power p_0 as:

$$p_0 = v_0 * i_0 \tag{106}$$

Then, the power vector can be calculated as follow:

$$\begin{bmatrix} p_0 \\ p \\ q \end{bmatrix} = \begin{bmatrix} v_0 & 0 & 0 \\ 0 & v_\alpha & v_\beta \\ 0 & -v_\beta & v_\alpha \end{bmatrix} \begin{bmatrix} i_0 \\ i_\alpha \\ i_\beta \end{bmatrix} \tag{107}$$

And the three phase power can be represented by:

$$\begin{aligned} P_{3\varphi} &= v_r * i_r + v_s * i_s + v_t * i_t = \\ &= v_\alpha * i_\alpha + v_\beta * i_\beta + v_0 * i_0 \end{aligned} \tag{108}$$

From Eq. (106) and (108) the three phase power can be calculated:

$$P_{3\varphi} = p + p_0 \tag{109}$$

Power terms p, q y p_0 can be decomposed using Fourier series and rearranged as a constant power and an harmonic power with a zero mean value:

$$\begin{aligned} p &= \bar{p} + \tilde{p}; \\ q &= \bar{q} + \tilde{q}; \\ p_0 &= \bar{p_0} + \tilde{p_0} \end{aligned} \tag{110}$$

Where: $\bar{p}$: $p$mean value, $\tilde{p}$: Oscillatory component of p, $\bar{q}$: $q$mean value, $\tilde{q}$: Oscillatory component of q, $\bar{p_0}$: mean value of p_0 and $\tilde{p_0}$: Oscillatory component of p_0. Assuming a three phase system distorted, the line current can be represented as a function of the symmetrical components:

$$\begin{aligned} i_r(t) &= \sum_{n=1}^{\infty} \sqrt{2} * I_{0n} * \sin(\omega_n t + \phi_{0n}) + \\ &+ \sum_{n=1}^{\infty} \sqrt{2} * I_{+n} * \sin(\omega_n t + \phi_{+n}) + \\ &+ \sum_{n=1}^{\infty} \sqrt{2} * I_{-n} * \sin(\omega_n t + \phi_{-n}) \end{aligned} \tag{111}$$

Same formulae can be obtained for i_s, i_t. Similar expressions can be formulated for the voltages. Then, the power equation described in Eq. (110) can be written as a function of symmetrical currents and voltages:

$$\bar{p} = \sum_{n=1}^{\infty} 3V_{+n} * I_{+n} * \cos(\varphi_{+n} - \delta_{+n}) + 3V_{-n} * I_{-n} * \cos(\varphi_{-n} - \delta_{-n}) \tag{112}$$

$$\tilde{p} = \sum_{\substack{m=1 \\ m \neq n}}^{\infty} \left[\sum_{n=1}^{\infty} 3V_{+m} * I_{+n} * \cos\left((\omega_m - \omega_n)t + \varphi_{+m} - \delta_{+n}\right) \right] +$$

$$+ \sum_{\substack{m=1 \\ m \neq n}}^{\infty} \left[\sum_{n=1}^{\infty} 3V_{-m} * I_{-n} * \cos\left((\omega_m - \omega_n)t + \varphi_{-m} - \delta_{-n}\right) \right] +$$

$$+ \sum_{m=1}^{\infty} \left[\sum_{n=1}^{\infty} -3V_{+m} * I_{-n} * \cos\left((\omega_m - \omega_n)t + \varphi_{+m} - \delta_{-n}\right) \right] +$$

$$+ \sum_{m=1}^{\infty} \left[\sum_{n=1}^{\infty} -3V_{-m} * I_{+n} * \cos\left((\omega_m - \omega_n)t + \varphi_{-m} - \delta_{+n}\right) \right] \tag{113}$$

$$\overline{q} = \sum_{n=1}^{\infty} -3V_{+n} * I_{+n} * \sin(\varphi_{+n} - \delta_{+n}) + 3V_{-n} * I_{-n} * \sin(\varphi_{-n} - \delta_{-n}) \tag{114}$$

$$\tilde{q} = \sum_{\substack{m=1 \\ m \neq n}}^{\infty} \left[\sum_{n=1}^{\infty} -3V_{+m} * I_{+n} * \sin\left((\omega_m - \omega_n)t + \varphi_{+m} - \delta_{+n}\right) \right] +$$

$$+ \sum_{\substack{m=1 \\ m \neq n}}^{\infty} \left[\sum_{n=1}^{\infty} 3V_{-m} * I_{-n} * \sin\left((\omega_m - \omega_n)t + \varphi_{-m} - \delta_{-n}\right) \right] +$$

$$+ \sum_{m=1}^{\infty} \left[\sum_{n=1}^{\infty} 3V_{+m} * I_{-n} * \sin\left((\omega_m - \omega_n)t + \varphi_{+m} - \delta_{-n}\right) \right] +$$

$$+ \sum_{m=1}^{\infty} \left[\sum_{n=1}^{\infty} -3V_{-m} * I_{+n} * \sin\left((\omega_m - \omega_n)t + \varphi_{-m} - \delta_{+n}\right) \right] \tag{115}$$

$$\overline{p}_0 = \sum_{n}^{\infty} 3V_{on} * I_{0n} * \cos(\varphi_{0n} - \delta_{0n}) \tag{116}$$

$$\tilde{p}_0 = \sum_{\substack{m=1 \\ m \neq n}}^{\infty} \left[\sum_{n=1}^{\infty} 3V_{om} * I_{0n} * \cos\left((\omega_m - \omega_n)t + \varphi_{0n} - \delta_{0n}\right) \right] +$$

$$+ \sum_{m=1}^{\infty} \left[\sum_{n=1}^{\infty} -3V_{om} * I_{0n} * \cos\left((\omega_m - \omega_n)t + \varphi_{0n} - \delta_{0n}\right) \right] \tag{117}$$

Finally, based on the oscillatory terms, reference (Watanabe et al, 1993) defined the distortion power terms as follow:

$$H = \sqrt{\tilde{p}^2 + \tilde{q}^2} \tag{118}$$

4.2 Measurement algorithm evaluation

These previous equations define expressions for real, imaginary and zero sequence power terms as a function of symmetrical components. Based on them, expressions that allow the apparent power calculation considering different conditions are explained next.

Case 1 - Balanced and sinusoidal system: In this case, the oscillatory, the negative sequence, and the zero sequence terms of both the real and the imaginary power components are zero, therefore the following expression can be proposed for apparent power calculation:

$$S^2 = \bar{p}^2 + \bar{q}^2 + H^2 = \bar{p}^2 + \bar{q}^2 \tag{119}$$

Then the apparent power can be calculated as follow:

$$S^2 = \left(3 * V_{+1} * I_{+1}\right)^2 = S_e^2 \tag{120}$$

Case 2 - Unbalanced load: From Eq. (119), for this case the apparent power is:

$$S^2 = \left[3 * V_{+1} * \left(I_{+1}^2 + I_{-1}^2\right)\right]^2 = \left(3 * V_{+1} * I_{+1}\right)^2 + \left(3 * V_{+1} * I_{-1}\right)^2 = S_e^2 \tag{121}$$

Case 3 - Unbalanced voltages and currents: In this case, the apparent power is:

$$S^2 = S_e^2 + 18 * \left(V_{+1} * V_{-1} * I_{+1} * I_{-1}\right) * \cos(\varphi_{+1} - \delta_{+1} + \varphi_{-1} - \delta_{-1}) \tag{122}$$

Figure 1 shows the error of **S** with respect to **S_e** as a function of the current unbalance ($I = (I_-/I_+)$). Each curve is parameterized for different values of voltage unbalance ($DV = (V_-/V)$). For simplicity, the harmonic distortion, and the phase shift between voltage and current are zero. The relative error is calculated as follow:
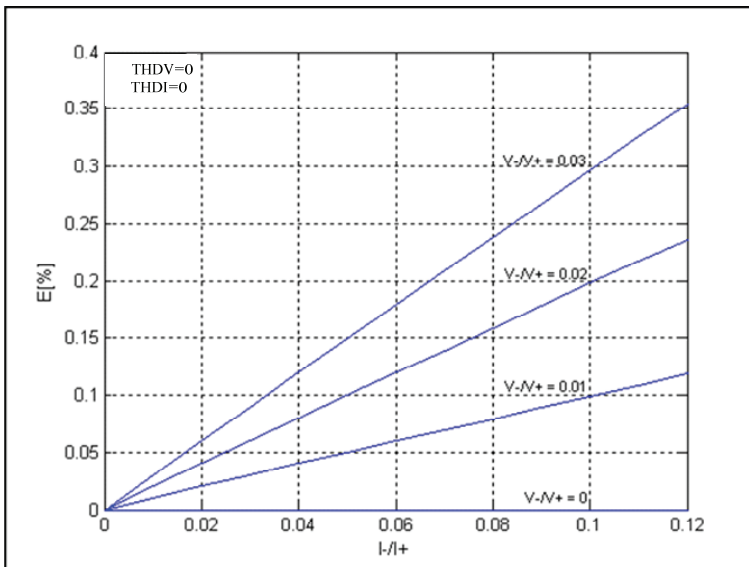
$$E[\%] = \frac{S - S_e}{S_e} \tag{123}$$

Fig. 1. Measurement error for an unbalanced system

Case 4 - Balanced and non sinusoidal system: The apparent power for this case can have different formulations depending on where the distortion is present; in the current or in the voltage signals.
a.   Distorted current

$$S^2 = 9 * V_{+1}^2 * \sum_{n=1}^{\infty} I_{+n}^2 = S_e^2 \tag{124}$$

b.   Distorted voltaje and current

$$S^2 = S_e^2 + 18 * \sum_{n=1}^{\infty} \sum_{m=n+1}^{\infty} \left(V_{+n} * V_{+m} * I_{+n} * I_{+m} * \cos(\varphi_{+n} - \varphi_{+m} - \delta_{+n} + \delta_{+m}) \right) \tag{125}$$

Case 5 - Non sinusoidal system with unbalanced and distorted load: Similar to the previous case, the formulation is different depending on where the distortion is present.
a.   Distorted current, sinusoidal voltage

$$S^2 = 9 * V_{+1}^2 * \sum_{n=1}^{\infty} \left(I_{+n}^2 + I_{-n}^2 \right) = S_e^2 \tag{126}$$

b.   Distorted voltaje

$$S^2 = S_e^2 + 18 * \sum_{n=1}^{\infty} \sum_{m=n+1}^{\infty} \left\{ V_{+n} * V_{+m} * \left[I_{+n} * I_{+m} * \cos(\varphi_{+n} - \varphi_{+m} - \delta_{+n} + \delta_{+m}) + \right. \right.$$
$$\left. \left. + I_{-n} * I_{-m} * \cos(\varphi_{+n} - \varphi_{+m} + \delta_{-n} - \delta_{-m}) \right] \right\} \tag{127}$$

Case 6 - Non sinusoidal system, with unbalanced currents and voltages: This is the most general case where the apparent power, based on Eq.(119) S is determined by the Eq. (128). Eq. (128) is the most general formulation of the apparent power and can be used to calculate the apparent power in all practical cases; all other expressions are a subset of this general one.

$$S^2 = S_e^2 + 18 * \sum_{n=1}^{\infty} \sum_{m=n+1}^{\infty} \left\{ V_{+n} * V_{+m} * \left[I_{+n} * I_{+m} * \cos(\varphi_{+n} - \varphi_{+m} - \delta_{+n} + \delta_{+m}) + \right. \right.$$
$$\left. \left. + I_{-n} * I_{-m} * \cos(\varphi_{+n} - \varphi_{+m} + \delta_{-n} - \delta_{-m}) \right] \right\} +$$
$$+ 18 * \sum_{n=1}^{\infty} \sum_{m=n+1}^{\infty} \left\{ V_{-n} * V_{-m} * \left[I_{+n} * I_{+m} * \cos(\varphi_{-n} - \varphi_{-m} + \delta_{+n} - \delta_{+m}) + \right. \right.$$
$$\left. \left. + I_{-n} * I_{-m} * \cos(\varphi_{-n} - \varphi_{-m} - \delta_{-n} + \delta_{-m}) \right] \right\} +$$
$$+ 18 * \sum_{n=1}^{\infty} \sum_{m=n+1}^{\infty} \left\{ V_{+n} * V_{-m} * \left[I_{+n} * I_{-m} * \cos(\varphi_{+n} + \varphi_{-m} - \delta_{+n} - \delta_{-m}) + \right. \right.$$
$$\left. \left. + I_{+m} * I_{-n} * \cos(\varphi_{+n} + \varphi_{-m} - \delta_{+m} - \delta_{-n}) \right] \right\} + \tag{128}$$
$$+ 18 * \sum_{n=1}^{\infty} \sum_{m=n+1}^{\infty} \left\{ V_{+m} * V_{-n} * \left[I_{+n} * I_{-m} * \cos(\varphi_{+m} + \varphi_{-n} - \delta_{+n} - \delta_{-m}) + \right. \right.$$
$$\left. \left. + I_{+m} * I_{-n} * \cos(\varphi_{+m} + \varphi_{-n} - \delta_{+m} - \delta_{-n}) \right] \right\} +$$
$$+ 18 * \sum_{n=1}^{\infty} V_{+n} * V_{-n} * I_{+n} * I_{-n} * \cos(\varphi_{+n} - \delta_{+n} + \varphi_{-n} - \delta_{-n})$$
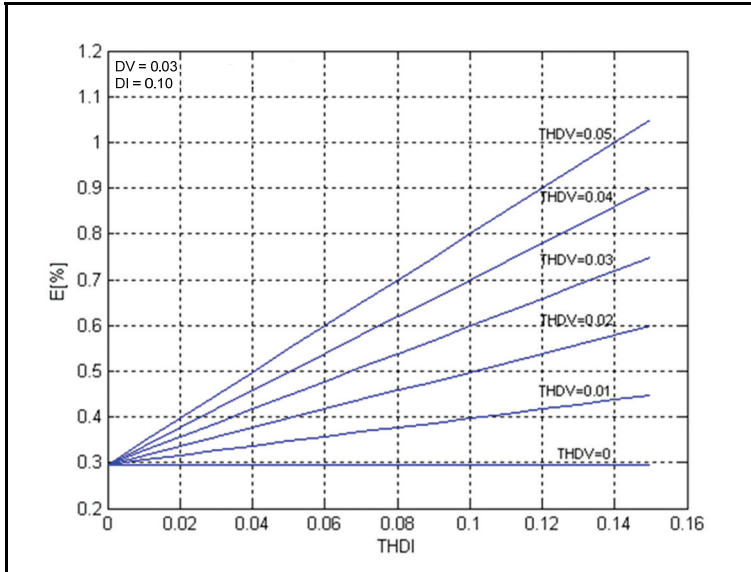
Fig. 2. Measurement error due to voltage and current distortion in an unbalanced system

As an illustrative example, in the case of a three phase system with distortion in both current and voltage signals but with unbalanced load only, the first two terms of Eq. (128) are not zero, then the equation becomes Eq. (125). Figure 2 shows the apparent power deviation with respect to S_e for different values of $THDv$ as a function of $THDi$. These curves are parameterized for a voltage distortion of 3% and a current distortion of 10%. The figure describes that if THDv is zero, the error is constant regardless of the value of THDi, moreover, the deviation is due to the current and voltage unbalance.

From these results can be seen that the apparent power value is different from the effective apparent power defined by the IEEE only if there is unbalanced or distortion in both current and voltage signals. The maximum relative error can be evaluated from Fig.1 and 2, where the error in the presence of voltage and current unbalance can be determined by the following relationship:

$$E_R\% \cong DI * DV * 100 \tag{129}$$

Similarly for the case of voltage and current distortion:

$$E_R\% \cong THDI * THDV * 100 \tag{130}$$

Therefore, in a general situation, the maximum error is:

$$E_R\% \cong (DI * DV + THDI * THDV) * 100 \tag{131}$$

These relationships mean that the máximum deviation of S can be evaluated knowing the system condition at the measurement point. In addition to the the formulation presented in this section, the signals can be further processed in order to obtain additional indexes such as the total harmonic distortion, power factor, fundamental power terms, and the active and

reactive harmonic power terms (P_1, Q_1, S_1, P_H, Q_H, S_H).by using low pass filters and matrix transformations, the proposed general methodology is described in Figure 3.
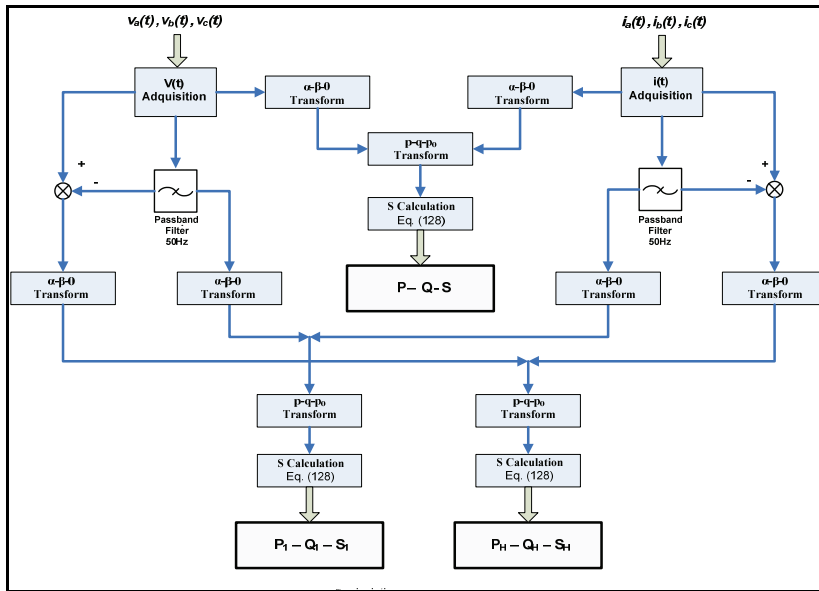

Fig. 3. Flow chart for power components calculations

The proposed methodology uses instant power value instead of r.m.s values and filters; band pass filters for fundamental components, and low pass filters for mean values. The total active, fundamental and harmonic powers can be calculated from the mean real power even for unbalanced conditions. Finally, additional indexes such as THDv, THDi, power phase shift, power factor are also calculated.

5. Conclusion

In this chapter a critical review of the most commonly used apparent power, reactive power and power factor definitions for both single phase and three phase systems were presented. The utilization of these definitions was evaluated under different conditions such as sinusoidal, non sinusoidal, one phase, and balanced and unbalanced three phase systems.
Finally a methodology to measure power and power quality indexes based on the instant power theory under non sinusoidal conditions is proposed. Results demonstrate that using this methodology, accurate values of the different power quality indexes can be obtained in a simpler manner even for the worst case scenario that may include unbalance and distortion signals.

6. References

Akagi, H., Watanabe, E., Aredes, M. (2007). Instantaneous Power Theory and Applications to Power Conditioning, Wiley, ISBN 978-0-470-10761-4, Canada.

Akagi, H., Kanazawa, Y., Nabae, A. (1983). Generalized Theory of the Instantaneous Reactive Power in Three-Phase Circuits, *IEEE – IPEC 83*, (1983), pp 1375-1386, Tokio, Japan.

Arrillaga, J., Bradley, D., Bodger, P. (1995). Power Systems Harmonics, Wiley, ISBN 0471906409, Canada.

Balci, M. & Hocaoglu, M. (2004). Comparison of power definitions for reactive power compensation in nonsinusoidal conditions. *11th International Conference on Harmonics and Quality of Power*, (2004), pp. 519-524.

Cataliotti, A., Cosentino, V., Nuccio, S. (2009). Metrological Characterization and Operating Principle Identification of Static Meters for Reactive Energy: An Experimental Approach Under Nonsinusoidal Test Conditions. *Instrumentation and Measurement, IEEE Transactions on*, vol. 58, no. 5, (2009), pp. 1427-1435, 2009, ISSN 0018-9456

Cataliotti, A,. Cosentino, V., Lipari, A., Nuccio, S. (2009). Static Meters for the Reactive Energy in the Presence of Harmonics: An Experimental Metrological Characterization, *Instrumentation and Measurement, IEEE Transactions on*, vol. 58, no. 8, (2009), pp. 2574-2579, ISSN 0018-9456.

Cataliotti, A., Cosentino, V., Nuccio, S. (2008). The Measurement of Reactive Energy in Polluted Distribution Power Systems: An Analysis of the Performance of Commercial Static Meters. *Power Delivery, IEEE Transactions on*, vol. 23, no. 3, (2008), pp. 1296-1301, ISSN 0885-8977

Czarnecki, L. (2006). Instantaneous reactive power p-q theory and power properties of three-phase systems. *Power Delivery, IEEE Transactions on*, vol. 21, no. 1, (2006), pp. 362-367, ISSN 0885-8977.

Czarnecki, L. (2004). On some misinterpretations of the instantaneous reactive power p-q theory. *Power Electronics, IEEE Transactions on,* vol. 19, no. 3, (2004), pp. 828-836, ISSN 0885-8993

Czarnecki, S. (1993). Phisical Reasons of Currents RMS Value Increase in Power Sistems with Nonsinusoidal Voltage. *IEEE Trans. On Power Delivery*, Vol. 8, No. 1, (January 1993), pp. 437-447, ISSN 0885-8977

Cox, M. & Williams, T. (1990). Induction VArhour and solid-state VArhour meters performances on nonlinear loads, *Power Delivery, IEEE Transactions on*, vol. 5, no. 4, (1990), pp. 1678-1686, ISSN 0885-8977.

Depenbrock, M. & Staudt, V., (1998). The FBD-method as tool for compensating total nonactive currents. Harmonics And Quality of Power. *Proceedings. 8th International Conference on*, vol. 1, (14-18 Oct 1998), pp. 320-324.

Depenbrock, M. (1992). The FBD-Method, A Generally Applicable Tool For Analyzing Power Relations. *Harmonics in Power Systems., ICHPS V International Conference on*, (22-25 Sep 1992), pp. 135-141.

DIN 40110-2, Quantities used in alternating current theory - Part 2: Multi-line circuits, Deutsches Institut Fur Normung E.V. (German National Standard) / 01-Nov-2002 / 8 pages.

Dugan, R., McGranahan, M., Beaty, W. (1996). Electrical Power Systems Quality, McGraw-Hill, Germany.

Eguiluz, L. & Arillaga, J. (1995). Comparison of power definitions in presence of waveform distortion. *International Journal Electronic Enging. Educ*. Vol 32, (1995), pp. 141-153, Manchester U. P. Great Britain, 1995.

Emanuel, E. (2004). Summary of IEEE standard 1459: definitions for the measurement of electric power quantities under sinusoidal, nonsinusoidal, balanced, or unbalanced conditions. *Industry Applications, IEEE Transactions on*, vol. 40, no. 3, (xxx 2004), pp. 869-876, ISSN 0093-9994.

Emanuel, A. (1999). Apparent power definitions for three-phase systems. *Power Delivery, IEEE Transactions on*, vol. 14, no. 3, (1999), pp. 767-772, ISSN 0885-8977

Emanuel, E. (1998). The Buchholz-Goodhue apparent power definition: the practical approach for nonsinusoidal and unbalanced systems. *Power Delivery, IEEE Transactions on*, vol. 13, no. 2, (1998), pp. 344-350, 1998, ISSN 0885-8977.

Emanuel, A. (1990). Powers in nonsinusoidal situations: A Review of Definitions and Physical Meaning. *IEEE Trans. On Power Delivery*, vol. 5, No. 3, (July 1990), pp. 1377- 1389, ISSN 0885-8977.

Filipski, P. & Labaj, P. (1992). Evaluation of reactive power meters in the presence of high harmonic distortion. *Power Delivery, IEEE Transactions on*, vol. 7, no. 4, pp. 1793-1799, ISSN 0885-8977.

Filipski, P. (1984). The measurement of Distortion Current and Distortion Power. *IEEE Trans. On Instr. And Meas*., Vol. IM-33, No. 1, (March 1984), pp. 36-40, ISSN 0018-9456.

Ghosh, P. & Durante, L. (1999). Measurement Performance Testing for Nonsinusoidal Enviroments. *IEEE Transactions on Power Systems*, vol. 14, n° 4, (November 1999), pp. 1526-1532, ISSN 0885-8950.

Gunther, E., McGranaghan, M. (2002). Power Measurement in Distorted and Unbalanced Condition – An Overview of IEEE Trial-Use Standard 1459-2000. *Power Engineering Society Summer Meeting, 2002 IEEE*, vol. 2, (25 July 2002), pp. 930-934.

Herrera, R. &. Salmerón, P. (2007). Instantaneous Reactive Power Theory: A Comparative Evaluation of Different Formulation. IEEE *Transactions on Power Delivery*, Vol. 22, no 14, (January 2007), pp. 595-604, ISSN 0278-0046.

IEEE Working Group on Nonsinusoidal Situations. (1996). Effects on Meter Performance and Definitions of Power, "Practical Definitions for Powers in Systems with Nonsinusoidal Waveforms and Unbalanced Loads: A Discussion". *IEEE Transactions on Power Delivery*, vol. 11, n° 1, (January 1996), pp. 79-87, ISSN 0885-8977.

IEEE Std 1459-2000, IEEE Trial-Use Standard Definitions for the Measurement of Electric Power Quantities Under Sinusoidal, Non-sinusoidal, Balanced, Or Unbalanced Conditions. IEEE 2000.

Morsi, W. & El-Hawary, M. (2007). Defining Power Components in Nonsinusoidal Unbalanced Polyphase Systems: The Issues. *Power Delivery, IEEE Transactions on*, vol. 22, no. 4, (2007), pp. 2428-2438, ISSN 0885-8977.

Pajic, S. & Emanuel, A. (2006). A comparison among apparent power definitions. *Power Engineering Society General Meeting, 2006. IEEE*, (2006), 8 pp.

Seong-Jeub, J. (2008). Unification and Evaluation of the Instantaneous Reactive Power Theories. *Power Electronics, IEEE Transactions on*, vol. 23, no. 3, (2008), pp. 1502-1510, ISSN 0885-8993.

Svensson, S. (1999). *Power Measurement Techniques for Non Sinusoidal Conditions*, Doctoral Thesis, Departament of Electric Power Engineering - Chalmers University of Technology, ISBN 91-7197-760-0, Goteborg, Sweden.

Watanabe, E., Stephan, R, Aredes, M. (1993). New Concepts of Instantaneous Active and Reactive Powers in Electrical Systems with Generic Loads. *IEEE Transactions on Power Delivery*, Vol. 8, no 2, (April 1993), pp. 697-703, ISSN 0885-8977.

Yildirim, D. & Fuchs, E. (1999). Comentary on Various Formulations of Distortion Power D. *IEEE Power Engineering Review*, vol. 19, n° 5, (May 1999), pp. 50-52, ISSN 0272-1724.

Power Quality Monitoring in a System with Distributed and Renewable Energy Sources

Andrzej Nowakowski, Aleksander Lisowiec and Zdzisław Kołodziejczyk
Tele-and Radio Research Institute
Poland

1. Introduction

The chapter deals with three issues concerning power quality monitoring in power grids with distributed energy sources. The structure of the grid has been described with pointing out the sources of voltage disturbances and the disturbance susceptibility of the grid components. Conclusions have been drawn at what nodes it is necessary to employ power quality monitoring. The technical solutions needed to integrate power quality analysis functions into protection relay have been described. New types of voltage and current transducers for use in primary circuits of power station have been presented.

The growing share of unconventional energy sources in the total energy balance of distribution companies carries with itself a necessity to provide adequate energy quality and energy safety to the final user. The importance of this issue has been underlined by many documents accepted by the governments of the individual European countries and by the European Commission itself.

The successful integration of various energy sources and consumers in the grid with the general diagram presented in Figure 1 requires meeting the demands of energy sellers who want to sell electricity and consumers who want to use electricity in an economically efficient way. The grid has to be balanced and the energy supplied to the customer has to meet quality standards. The need to supply consumers with the required electricity carries with itself the necessity to monitor the power quality.

When incorporating renewable energy sources within power distribution networks it is very important to provide power quality analysis at many nodes in the network.

The nature of renewable energy sources is such that they produce either a DC voltage – as is the case with solar panels and energy containers in the form of supercapacitors or an AC voltage of varying frequency as is the case with wind turbines and wave turbines (Ackerman T. ed. 2005), (Gilbert M. 2004). The renewable energy sources must be either synchronized or converted to alternating current before their energy can be injected into the grid. The power electronic devices that convert AC voltage to DC voltage and DC voltage to AC voltage are inverters and during the conversion process disturbances in the form of harmonics, voltage sags and overshoots are created which have to be kept under control. Also many loads that are now connected to the power networks exhibit nonlinear dependence of drawn current on supply voltage. These nonlinearities are the source of higher current harmonics that are injected into the grid. As the impedance of the power

lines is not zero, voltage harmonics appear. Particularly important is the measurement and analysis of possible adverse effects of harmonics on the equipment connected to the network. Power quality analyzers that measure the harmonic content in the supply voltage are too expensive to apply at each node where the renewable source is connected to the network.
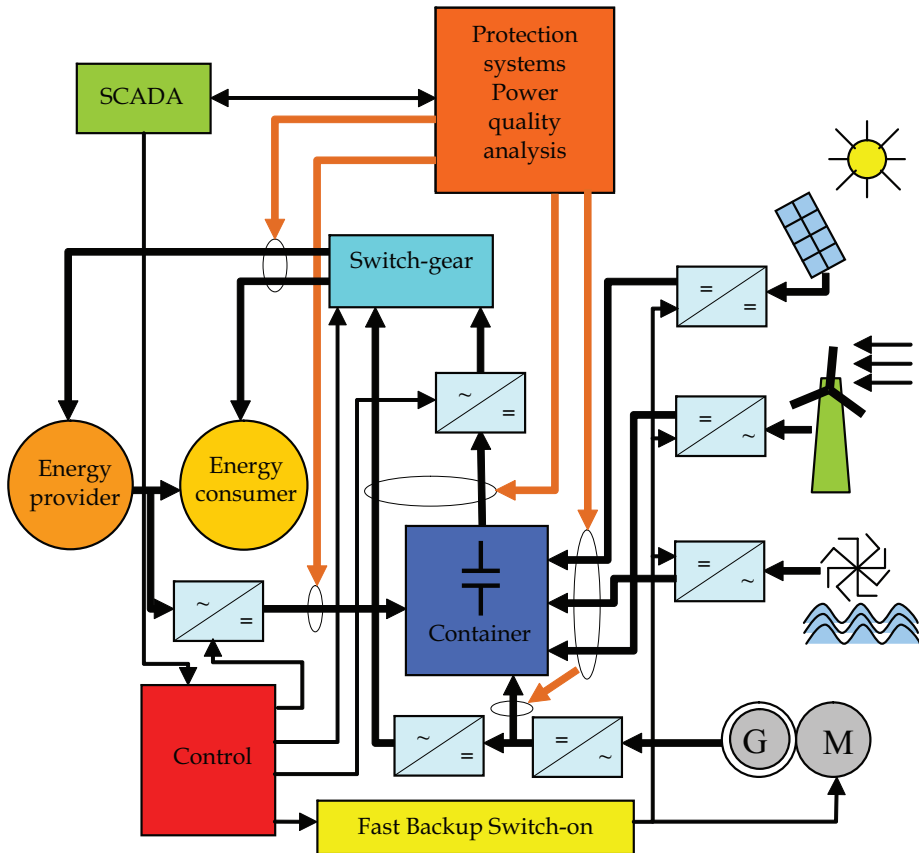

Fig. 1. A structure of protection, monitoring and control system integrating distributed renewable energy sources and energy containers

The solution to the problem of mass scale power quality monitoring and control is to equip conventional protection relays with power quality analysis functions, Figure 2. The natural nodes to place the combined devices are at the output of the inverters marked in Figure 2 by red color. The tremendous advance in the DSP microprocessor technology enables to implement the power quality analysis software, particularly harmonics and interharmonics level determination, at a very small additional cost for the end user. The advanced signal processing algorithms like signal resampling in the digital domain are the key to achieving design objectives. To keep the cost of the developed protection relay low, the developed algorithms should put minimal requirements on hardware.
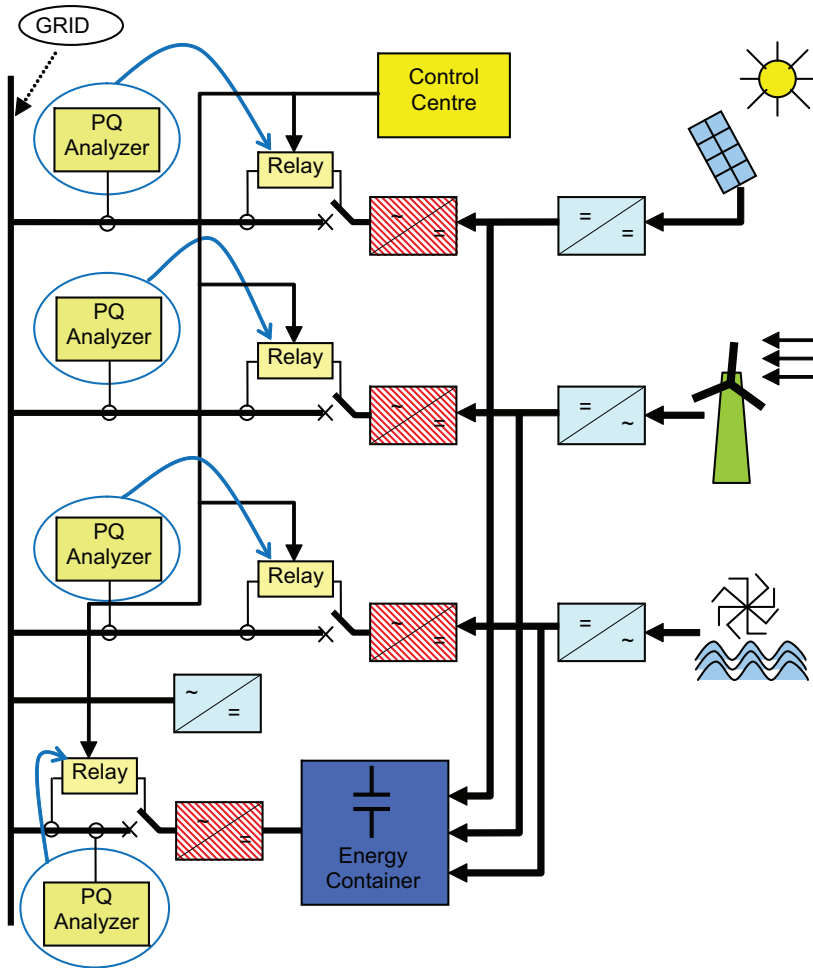
Fig. 2. Power grid with the nodes at which it is possible to combine protection functions with power quality analysis

2. Integrating power quality analysis and protection relay functions

The main issue in the development of protection relay integrated with power quality analyser is the necessity to elaborate efficient algorithms for line voltage and current signals frequency spectrum determination with harmonic and interharmonic content up to 2 kHz. The mass use of power quality monitoring, postulated in the previous paragraph, demands that incorporation of power quality analysis functions into protection relay comes at a negligible additional cost to the end user. The cost of the additional hardware has thus to be as low as possible with the burden of extra functionality placed on the software.

Modern microprocessor controlled protection relays employ sampling of analogue current and voltage signals and digital signal processing of the sample sequences to obtain signal

parameters like RMS, which are then used by protection algorithms. In this respect they are similar to stand alone power quality analysers that also carry out the calculations of signal parameters from sample sequences. The availability of fast and high resolution analogue to digital converters enables cost effective signal front end design suited equally well for protection relay and power quality analyser.
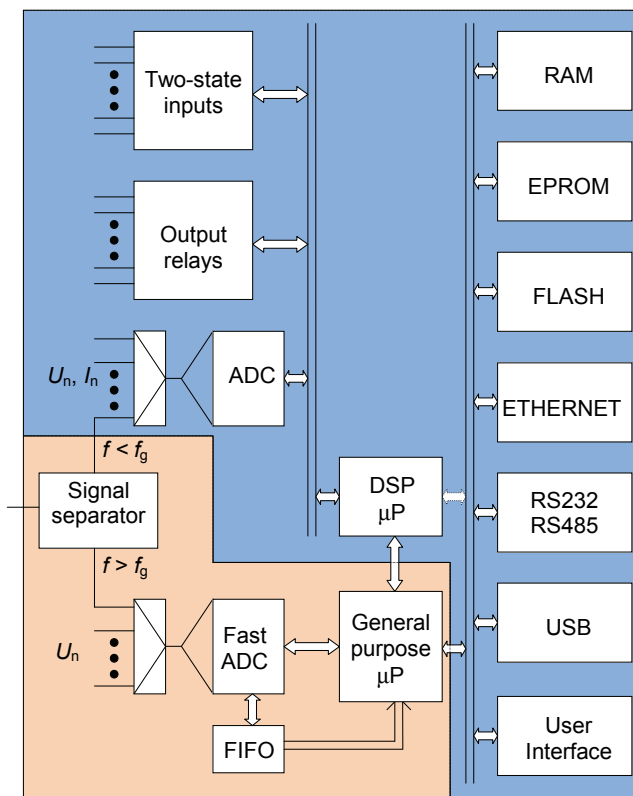

Fig. 3. Block diagram of combined protection relay and power quality analyser

The architecture of combined protection relay and power quality analyser has been shown in Figure 3. The architectures of power quality analyzer and protection relay are very similar. They differ only in the transient voltage surge measurement module, which has been marked by a different colour in Figure 3. While the basic signal parameterization software implemented in both devices uses Fourier techniques for spectrum determination, the protection relays contain additionally the protection algorithms software and power quality analyzers contain more elaborate spectrum analysis and statistical software. Power quality analyzers also have wider input bandwidth to measure accurately harmonic and interharmonic content of the signal up to 2 kHz. To merge protection relay and power quality analyser in a single device in a cost effective way it is necessary to employ advanced signal processing techniques like oversampling and changing the effective sampling rate in digital domain.

2.1 Harmonic and interharmonic content determination
2.1.1 Introduction
The international standards concerning power quality analysis (EN 50160, EN 61000-4-7:2002, EN 61000-4-30:2003) define precisely which parameters of line voltage and current signals are to be measured and the preferred methods of measurement in order to determine power quality. In compliance with these requirements, for harmonic content determination, power quality analyzers employ sampling procedures with sampling frequency precisely synchronized to the exact multiple of line frequency. This is necessary for correct spectrum determination as is known from Fourier theory (Oppenheim & Schafer, 1998). If the sampling frequency is not equal to the exact multiple of line frequency, the spectral components present in the signal are computed with error and moreover false components appear in the spectrum.

Efficient computation of signal spectrum with the use of FFT transform demands that the number of samples in the measurement interval be equal to the power of two. With sampling frequency synchronized to the multiple of line frequency, it is impossible to satisfy this requirement both in one line period measurement interval – when the measurement results are used for protection functions, and ten line periods measurement interval when interharmonic content is determined. This is the reason why some power quality analyzers available on the market offer interharmonic content measurement over 8 or 16 line periods interval. Another disadvantage of synchronizing sampling frequency to the line signal frequency is the inability to associate with each recorded signal waveform sample a precise moment in time. When the power quality meter is playing also the role of disturbance recorder, the determination of a precise time of an event is very difficult in such case. A better method to achieve the number of samples equal to the power of two both in one and ten line periods, with varying line frequency, is to use constant sampling frequency and employ digital multirate signal processing techniques.

As the digital multirate signal processing involves a change in the sample rate, the sampling frequency can be chosen with the aim of simplifying the antialiasing filters that precede the analog to digital converter. According to the EN 61000-4-7:2002 standard, the signal bandwidth that has to be accurately reproduced for power quality determination is 2 kHz. The complexity of the low-pass filter preceding the A/D converter depends significantly on the distance between the highest harmonic in the signal that has to be passed with negligible attenuation (in this case the 40-th harmonic) and the frequency equal to the half of the sampling frequency. When the sampling frequency around 16 kHz is chosen, a simple 3-pole RC active filter filters can be used.

2.1.2 Multirate digital signal processing in protection relay
In multirate digital signal processing (Oppenheim & Schafer, 1998) it is possible to change the sampling rate by a rational factor N/M using entirely digital methods. The input signal sampled with constant frequency f_s is first interpolated by a factor of N and then decimated by a factor of M – both these processes are called collectively resampling. The output sequence consists of samples representing the input signal sampled at an effective frequency f_{seff} , where

$$f_{seff}=f_s\cdot(N/M) \tag{1}$$

The first thing that has to be determined is how many samples are needed to calculate the spectral components of the signal. For protection purposes, the knowledge of harmonics up

to 11th used to be enough in the past. The increasing use of nonlinear loads (and competition) has led leading manufacturers of protection relays to develop devices with the ability to determine the signal spectrum up to 40 or even 50-th harmonic. Thus, taking into account that the number of samples, for computational reasons, must equal the power of two, 128 samples per period are needed (Oppenheim & Schafer, 1998). The ideal sampling frequency is then $f_{sid} = f_{line} \cdot 128$ Hz (= 6400 Hz at 50 Hz line frequency). For power quality analysis, the EN 61000-4-7 standard demands that the measurement interval should equal ten line periods and the harmonics up to 40th (equivalently interharmonics up to 400th) have to be calculated. This gives 1024 as the minimum number of samples over ten line periods meeting the condition of being equal to the power of two. The ideal sampling frequency f_{sid} for interharmonic content determination should be equal to $((f_{line})/10) \cdot 1024$ Hz which is 5120 Hz at $f_{line} = 50$ Hz. Knowing the needed effective sampling frequency and the actual sampling frequency f_s – which for the rest of the chapter is assumed to be equal to 16 kHz, the equation (1) can be used to determine interpolation and decimation N, M values. Tables 1 and 2 gather the values of N and M (without common factors) computed from (1) for a range of line frequencies.

f_{line}	49.5	49.55	49.6	49.65	49.7	49.75	49.8	49.85	49.9	49.95
N	99	991	248	993	497	199	249	997	499	999
M	250	2500	625	2500	1250	500	625	2500	1250	2500

Table 1. Interpolation and decimation factors protection function

50.0	50.05	50.1	50.15	50.2	50.25	50.3	50.35	50.4	50.45	50.5
2	1001	501	1003	251	201	503	1007	252	1009	101
5	2500	1250	2500	625	500	1250	2500	625	2500	250

Table 1, cont.

f_{line}	49.5	49.55	49.6	49.65	49.7	49.75	49.8	49.85	49.9	49.95
N	198	991	992	993	994	199	996	997	998	999
M	625	3125	3125	3125	3125	625	3125	3125	3125	3125

Table 2. Interpolation and decimation factors for interharmoncs determination

50.0	50.05	50.1	50.15	50.2	50.25	50.3	50.35	50.4	50.45	50.5
8	1001	1002	1003	1004	201	1006	1007	1008	1009	202
25	3125	3125	3125	3125	625	3125	3125	3125	3125	625

Table 2, cont.

For some line frequencies the values of N and M computed from (1) are very large, e.g. for $f_{line} = 49.991$ Hz, $N = 49991$ and $M = 125000$. The computational complexity of the resampling procedure depends on how large the values of N and M are.

The interpolation process consists in inserting a *N-1* number of zero samples between each original signal sample pair. The resulting sample train corresponds to a signal with the bandwidth compressed with *N* ratio and multiplied on a frequency scale *N* times (Oppenheim & Schafer, 1998). To recover the original shape of the signal, the samples have to be passed through a low pass filter with the bandwidth equal to the *B/N* bandwidth of the signal prior to interpolation. In time domain the filter interpolates the zero samples that have been inserted between the original signal samples.
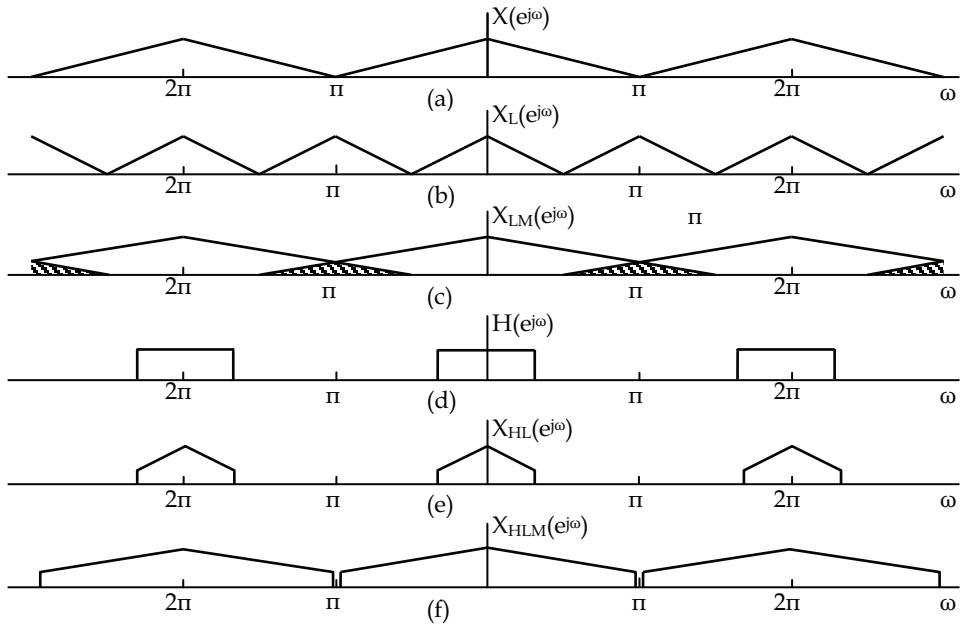
Fig. 4. The effect of interpolation and decimation on signal spectrum

The decimation process consists in deleting *M-1* samples from each consecutive group of *M* samples. The resulting sample train corresponds to a signal prior to the decimation but with the bandwidth expanded by a factor of *M*. To prevent the effect of aliasing, the sample sequence to be decimated has to be passed through a low pass filter with the bandwidth equal to $2\pi/M$ in normalized frequency. The operation of interpolation and decimation on the bandwidth of the signal has been shown in Figure 4 for *N* = 2 and *M* = 3. In this figure $X(e^{j\omega})$ is the spectrum of the original signal, $X_L(e^{j\omega})$ is the spectrum of the original signal with zero samples inserted and $X_{LM}(e^{j\omega})$ the spectrum of the original signal with zero samples inserted and then decimated with the *M* ratio. As can be seen in Figure 4 c) there is a frequency aliasing. If the signal after interpolation is passed through a low pass filter with suitable frequency characteristic $H(e^{j\omega})$ the effect of frequency aliasing is avoided as shown in Figure 4 d).

To preserve as much of the bandwidth of the original signal as possible, the low pass filter used in the resampling process has to have a steep transition between a pass and stop bands. The complexity of the filter depends heavily on the magnitude of the greater of the values of *N* and *M*. This is one of the many reasons why the values of *N* and *M* should be

chosen as low as possible but at the same time the f_{eff} computed from (1) should be as close as is necessary to the ideal sampling frequency f_{sid}.

The accuracy with which f_{eff} is to approximate f_{sid} could be determined from simulating how different values of N and M affect the accuracy of spectrum determination. However some clues about the values of N and M can be obtained from EN 61000-4-7 standard. In chapter 4.4.1 it states that the time interval between the rising edge of the first sample in the measurement interval (200 ms in 50 Hz systems) and the rising edge of the first sample in the next measurement interval should equal 10 line periods with relative accuracy not worse than 0.03%. Therefore, for each line frequency, the values of N and M should be chosen so as the relative difference E_{eff} between the ideal sampling frequency f_{sid}, and the effective sampling frequency f_{eff} meets the following condition

$$E_{eff} = \left| \frac{(f_{seff} \cdot f_{sid})}{f_{sid}} \right| \le 0.003 \tag{2}$$

The frequency characteristic of the low pass filter used in the resampling procedure depends on the values of N and M. If a different filter is used for each N, M pair it places a heavy burden on limited resources of DSP processor system in a protection relay. A solution to this problem is to fix the value of N and choose M according to the following formula

$$M = Round\left(\frac{N \cdot f_s}{\left(\frac{f_{line}}{L} \right) \cdot SN} \right) \tag{3}$$

where L is the number of periods used in the spectrum determination and SN is the number of the samples in L periods (128 samples per one period for protection functions, 1024 samples per 10 periods for power quality analysis). The $Round(x)$ function gives the integer closest to x. The low pass filter is then designed with the bandwidth equal to $2\pi/M_{min}$ where M_{min} is the value of M computed from (2) for highest line frequency f_{line}.

For power quality analysis when the interharmonics content has to be determined, N=600, the minimum value of M is 1630 at f_{line} = 57.5 Hz, the maximum value of M is 2206 at f_{line} = 42.5 Hz.   The maximum absolute value of E_{eff} is equal to 0.03% and the effective sampling frequency is within the range recommended by EN 61000-4-7 standard. As the error of spectrum determination increases with increasing E_{eff} it is sufficient to carry out the analysis of the accuracy of spectrum determination for line frequency, for which the E_{eff} is largest. The obtained accuracy should then be compared with the accuracy of spectrum determination when the sampling frequency is synchronized to the multiple of the same line frequency with the error of 0.03%. For the analysis a signal composed of the fundamental component, 399 interharmonic with 0.1 amplitude relative to the fundamental, 400 interharmonic with 0.05 amplitude relative to the fundamental and 401 interharmonic with 0.02 amplitude relative to the fundamental should be selected. This is the worst case signal because on the one hand the error is greatest at the upper limit of the frequency range, and on the other hand when close interharmonics are present, there is leakage from the strongest interharmonic to the others. Figure 5 shows the spectrum of the test signal determined when the synchronization technique is used and Figure 6 shows the spectrum when the digital resampling technique is used. In both cases the resulting sample rate is identical.
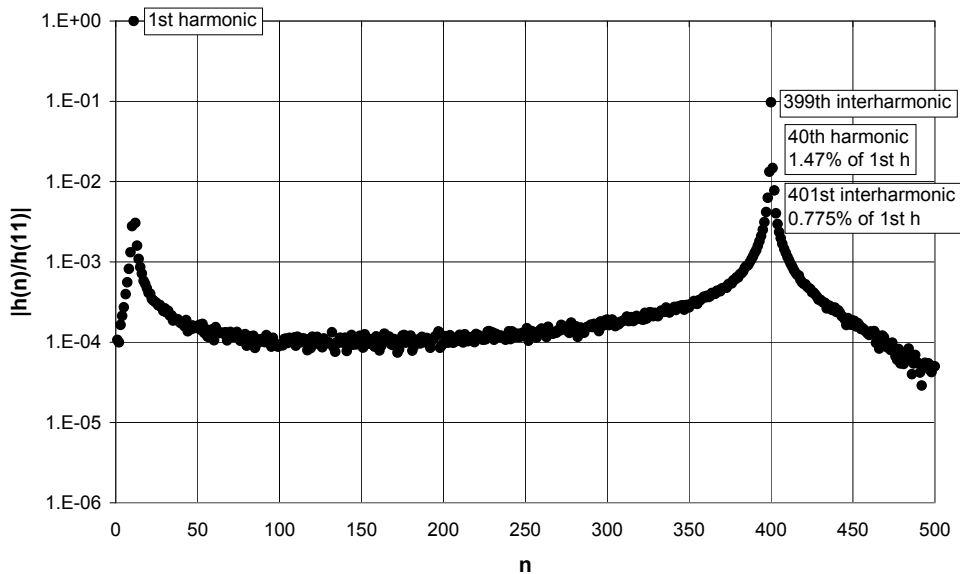
Fig. 5. Spectrum of the test signal when synchronization of the sampling frequency to the multiple of line frequency is used
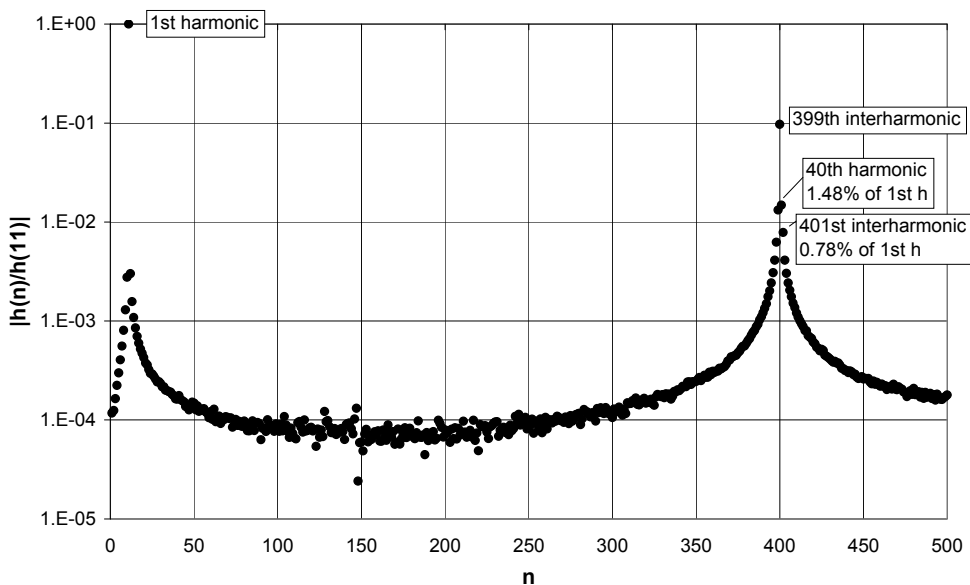

Fig. 6. Spectrum of the test signal when resampling technique is used

The two spectra are almost identical and they both give the same error in the interharmonic level determination. The level of 399th interharmonic is very close to the true value. However the level of 40th harmonic is almost three times higher than the true value and the level of 401st interharmonic is almost four times higher than the true value. The observed effect can be explained by leakage of the spectrum from 399th interharmonic of relatively large level to neighbouring interharmonics (Bollen & Gu 2006). The detailed analysis carried out for the whole range of line frequency and various signal composition shows that if the error between the ideal sample rate and actual sample rate at the input of Fourier spectrum computing procedure is the same, both methods give equally accurate results.

For the protection functions the needed frequency resolution is ten times lower than for interharmonic levels determination. It suggests, that the values of N and M can be chosen such that the maximum value of E_{eff} < 0.3%. With N=80, the minimum value of M equal to 174 at f_{line} = 57.5 Hz, and the maximum value of M equal to 235 at f_{line} = 42.5 Hz, the maximum absolute value of E_{eff} is equal to 0.284%. The detailed analysis shows that harmonics are determined with the accuracy which is better than 1%.

3. New input circuits used for parameters determination of line current and voltage signals

The measurement of line voltage and current signals for power quality analysis demands much higher accuracy than is needed for protection purposes. Traditional voltage and current transducers used in primary circuits of power stations cannot meet the requirements of increased accuracy and wide measurement bandwidth. New types of voltage and current transducers are needed with frequency measurement range equal to at least the 40-th harmonic of fundamental frequency, high dynamic range and very good linearity. For current measurements Rogowski coils may be used. They have been used for many years in applications requiring measurements of large current in wide frequency bandwidth. The traditional technologies used for making such coils were characterized by large man labour. Research work has been carried out at many laboratories to develop innovative technologies for Rogowski coil manufacture. These technologies are based on multilayer PCB.

3.1 Principle of PCB Rogowski coil construction

The principle of Rogowski coil operation is well known (http://www.axilane.com/PDF_Files/Rocoil_Pr7o.pdf). The basic design consists in winding a number of turns of a wire on a non-magnetic core, Figure 7.

The role of the core is only to support mechanically the windings. The voltage V(t) induced at the terminations is expressed by the following equation

$$V(t) = -\frac{d\Phi}{dt} = -\mu_0 \cdot n \cdot A \cdot \frac{dI}{dt}$$ (4)

where μ_0 is the magnetic permeability of the vacuum, n is the number of turns, A is the area of the single turn (referring to Figure 7, $A=\pi \cdot r^2$) and I is the current flowing in the conductor coming through the coil.
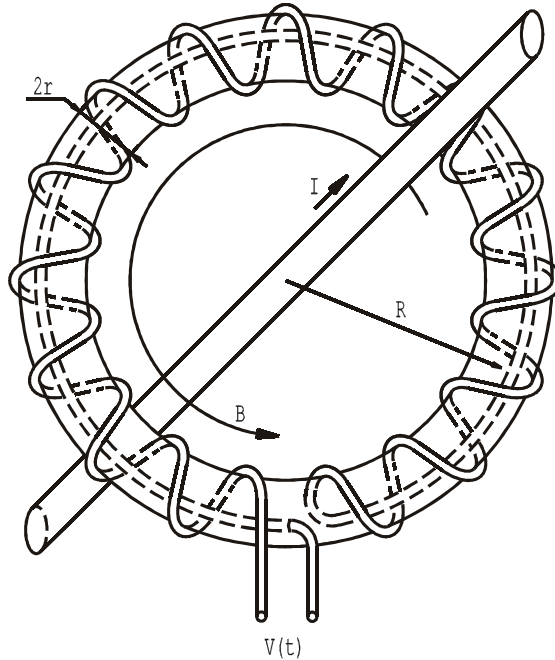
Fig. 7. A simplified construction of the Rogowski coil

The most important parameter of the Rogowski coil is its sensitivity S. It is the ratio of the RMS value of the voltage at coil terminations to the RMS value of the sine current flowing in the wire going through the centre of the coil. Because of the factor dI/dt in equation (4), the sensitivity is directly proportional to the frequency of the current signal. In applications of the Rogowski coil in the power industry sector the sensitivity is given at the fundamental line frequency 50 Hz or 60 Hz. The sensitivity of the coil which has the shape as shown in Figure 7, is given by the following formula:

$$S = \mu_0 \cdot A_{ef} \cdot \omega \cdot \frac{n}{2 \cdot \pi \cdot R} \tag{5}$$

where n is the total number of the turns, ω is the angular pulsation of the sinusoidal current I, and R is the radius of the coil. The factor A has been replaced with A_{ef} because in practice not every turn has to have the same dimensions. The last factor in the equation (5) shows that the sensitivity of the coil is directly proportional to the density l of the turns where $l=n/(2 \pi \cdot R)$. The PCB design of the Rogowski coil replaces the wire turns by induction coils printed on multilayer boards. On each layer there is a basic coil in the form of a spiral. The coils on neighboring layers are connected by vias. The vias can be buried or through. The buried vias leave more board space for the coil but are much more expensive to manufacture. A design of the first 4 layers of 16-layer board with buried vias is presented in Figure 8. Photos of the multilayer board designs with through and buried vias are presented in Figures 9 a) and 9 b) respectively.
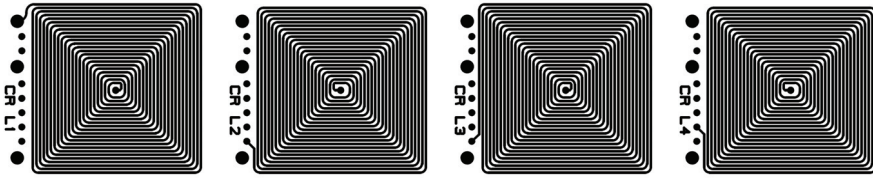
Fig. 8. Individual layers of the multilayer board with buried vias connecting the coils
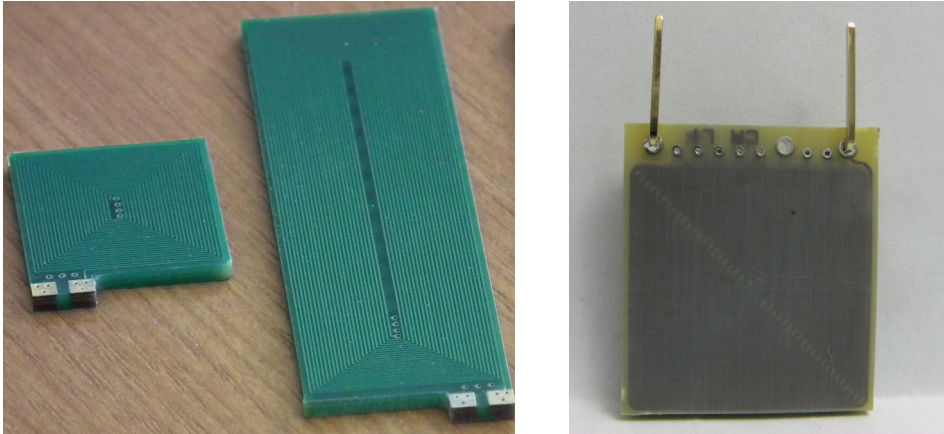

Fig. 9. a) Multilayer boards with through vias, b) multilayer boards with buried vias

The multilayered boards are attached to a base board which provides mechanical support and connects all the boards together electrically. Figure 10 presents some of the base board designs. The base boards are double sided printed circuit boards and their cost is relatively small as compared to the cost of multilayer boards with printed coils on them.
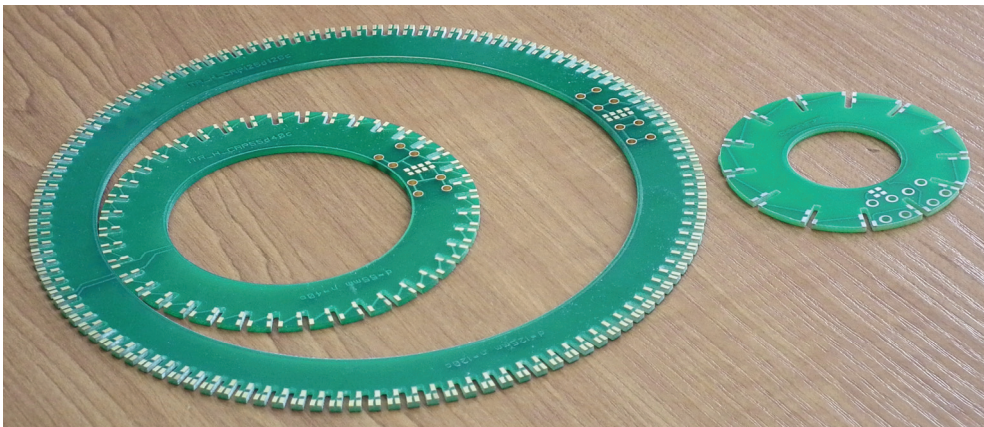

Fig. 10. Various designs of the base board

There are various methods of fastening the multilayered boards to the base board. The one that requires least labor is to squeeze the base boards into the slots milled in the base board as shown in Figure 11 b). Another method uses pins soldered on the one side to the base board and on the other to the multilayer boards, Figure 11 a).
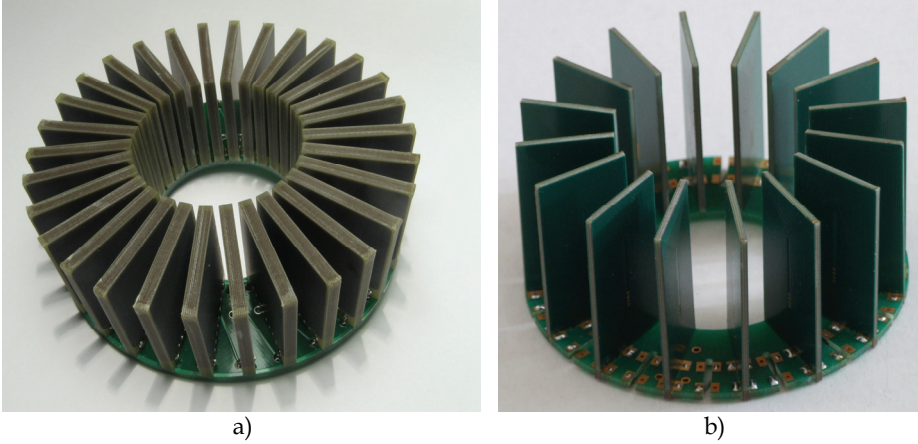

a)   b)

Fig. 11. a) Rogowski coil with pin mounted multilayer boards, b) Rogowski coil with multilayer boards squeezed into the base board

3.2 Design of the coil

The design of the coil starts with the required dimensions of the coil. They determine the dimensions of the multilayer boards and the diameter of the base board. Then it should be determined if the dimensions of the multilayer boards enable to achieve the required coil sensitivity. The minimal thickness of the single layer of the multilayer board is limited by the available technology. Therefore the maximal number of the layers per unit circumference, l_{max}, is fixed. Furthermore, the number of the layers in the multilayer boards is determined by the cost of manufacturing the board. With l bounded by the available technology, the coil sensitivity, according to the equation (5), can only be increased by increasing the A_{ef}. This in turn means thinner tracks and greater coil resistance. It should be said that the coil with higher density of the turns l and lower A_{ef} is superior to the coil with lower l and higher A_{ef}. This is because the sensitivity of the coil to external magnetic fields not connected with the measured current increases with increasing A_{ef}. If the coil dimensions are small, the external magnetic fields are more uniform across the coil. The voltage induced by these fields has equal magnitude but different sign for turns lying on the opposite sides of the coil and the cancellation takes place. The effective area of the spiral inductive coil shown in Figure 12 can be computed with the following formula

$$A_{ef} = \left(\sum_{i=0}^{i=n-1} \left(\left(a - (a1+a2) \right) - \frac{i\left(a - (a1+a2)\right)}{2(n \cdot 1)} \right) \left(\left(b - (b1+b2) \right) - \frac{i\left(b - (b1+b2)\right)}{2(n \cdot 1)} \right) \right) \qquad (6)$$

where n is the number of the turns in the spiral and a, $a1$, $a2$, b, $b1$ and $b2$ are the dimensions of the mosaic as shown in Figure 12.
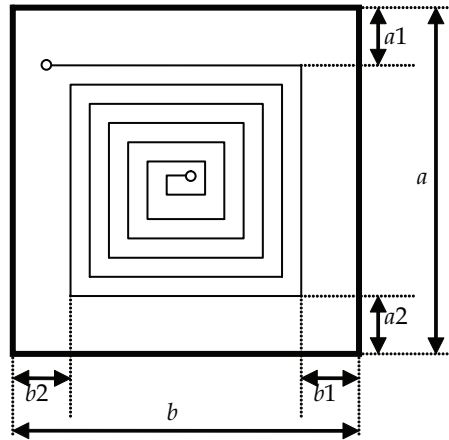
Fig. 12. A simplified printed circuit coil

The upper bound on *n* in equation (6) is determined by the minimal track thickness. Practical experience shows that the sensitivity of the coil computed using equations (5) and (6) is within 10% of the coil sensitivity obtained from the measurement. The design of the coil is therefore an iterative process. First, given *S* and *l*, the value of A_{ef} is computed using equation (5). Then the basic multilayer board is designed using equation (6) and the base board for holding the necessary number of multilayer boards. The coil is manufactured and its sensitivity measured. In the second iteration it is usually necessary to modify only the base board to accommodate slightly smaller or larger number of the multilayer boards.

The PCB technology for Rogowski coils manufacture is characterized by relatively high cost of materials – multilayer PCB are expensive to manufacture, and low cost of man labor. The main advantage of multilayer PCB technology manufacture is that the coils have very repeatable parameters. They can thus be used in applications when exact sensitivity is necessary like in power quality monitoring.

3.3 Voltage transducers

For voltage measurement in wide frequency bandwidth, reactance dividers, resistive dividers and air core transformers can be used. The reactance and resistive dividers have been known for quite a long time and commercial products are available. The resistive dividers, though most accurate of all the transducers provide a galvanic path between the measured primary high voltage and secondary low voltage equipment. The work has been carried out to develop a method to isolate galvanically the resistive divider and preserve at the same time the wide measurement bandwidth. One such solution is an air core transformer.

The voltage transducer made as air core transformer must be characterized by low main inductance which makes it impossible to connect it directly to MV line. In order to limit the current flowing through primary winding it is necessary to use additional elements connected in series with primary winding, Figure 13. These can be resistors or capacitors. The design challenge is to develop an air core transformer with output voltage equal to 200 mV at input current not larger than 1 mA. These conditions result from the necessity to achieve the necessary accuracy (min. 1%) and permissible power dissipation within the

transducer. Because Rogowski coils have no magnetic core, the mutual inductance between individual multilayer boards of the two coils forming the transformer is very low which results in low output voltage. The design objectives that are also not easy to achieve are sufficient isolation between layers and precise and durable boards connection.
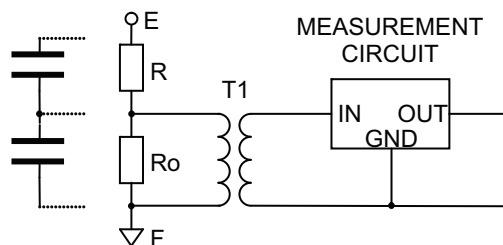

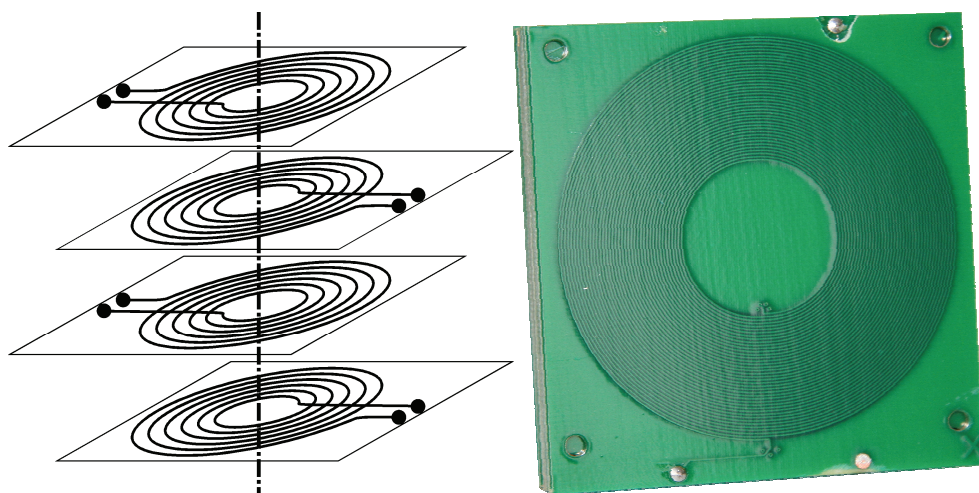Fig. 13. An air core transformer connection in a measurement circuit

Fig. 14. Principle of the air core transformer and its laboratory model

The construction that has been finaly developed at Tele-and Radio Research Institute consists of alternately placed printed circuit boards forming primary and secondary transformer windings respectively. Each board is made up of several layers containing printed coils in the form of spirals. The coils on consecutive layers are conneted in a way preserving the turns directions. The boards are placed with their centers aligned, Figure 14 and as close to each other as possible thus forming a sandwich with two secondary winding boards between every primary winding board.

4. References

Ackerman T. ed. (2005) *Wind Power in Power Systems*, ISBN 0-470-85508-8, John Wiley & Sons, England

Bollen, M. H. J. & Gu I. (2006) *Signal Processing of Power Quality Disturbances*, IEEE Press, ISBN-13 978-0-471-73168-9, USA

European Standard EN 50160: *Voltage characteristics of electricity supplied by public distribution systems*

European Standard EN 61000-4-30:2003: *Electromagnetic compatibility* (EMC) Part 4-30: Testing and measurement techniques – Power quality measurement methods

European Standard EN 61000-4-7:2002: *Electromagnetic compatibility* (EMC) Part 4-7: Testing and measurement techniques – General guide on harmonics and interharmonics measurements and instrumentation, for power supply systems and equipment connected thereto

Gilbert M. (2004) *Renewable and efficient electric power systems*, ISBN 0-471-28060-7, John Wiley & Sons, Inc., Hoboken, New Jersey

http://www.axilane.com/PDF_Files/Rocoil_Pr7o.pdf

Oppenheim A.V. & Schafer R.W. (1998) *Discrete-Time Signal Processing*, 2ed., PH, USA

Application of Signal Processing in Power Quality Monitoring

Zahra Moravej[1], Mohammad Pazoki[2] and Ali Akbar Abdoos[3]
[1][2]Electric and computer engineering faculty, Semnan University,
[3]Electric and computer engineering faculty, Babol Noshirvani University of Technology
Iran

1. Introduction

The definition of power quality according to the Institute of Electrical and Electronics Engineers (IEEE) dictionary [159, page 807] is that "power quality is the concept of powering and grounding sensitive equipment in a matter that is suitable to the operation of that equipment."

In recent years, power quality (PQ) has become a significant issue for both utilities and customers. PQ issues and the resulting problems are the consequences of the increasing use of solid-state switching devices, non-linear and power electronically switched loads, unbalanced power systems, lighting controls, computer and data processing equipment, as well as industrial plant rectifiers and inverters. These electronic-type loads cause quasi-static harmonic dynamic voltage distortions, inrush, pulse-type current phenomenon with excessive harmonics, and high distortion. A PQ problem usually involves a variation in the electric service voltage or current, such as voltage dips and fluctuations, momentary interruptions, harmonics, and oscillatory transients, causing failure or inoperability of the power service equipment. Hence, to improve PQ, a fast and reliable detection of disturbances and sources and causes of such disturbances must be known before any appropriate mitigating action can be taken.

The algorithms for detection and classification of power quality disturbances (PQDs) are generally divided into three main steps: (1) generation of PQDs, (2) feature extraction, and (3) classification of extracted vectors (Uyara et al., 2008; Gaing 2004; Moravej et al., 2010; Moravej et al., 2011a).

It will be evident that the electricity supply waveform, often thought of as composed of pure sinusoidal quantities, can suffer a wide variety of disturbances. Mathematical equations and simulation software such as MATLAB simulink (MATLAB), PSCAD/EMTDC (PSCAD/EMTDC 1997), ATP (ATPDraw for Windows 1998) are usually used for generation of PQ events. To make the study of Power Quality problems useful, the various types of disturbances need to be classified by magnitude and duration. This is especially important for manufacturers and users of equipment that may be at risk. Manufacturers need to know what is expected of their equipment, and users, through monitoring, can determine if an equipment malfunction is due to a disturbance or problems within the equipment itself. Not surprisingly, standards have been introduced to cover this field. They define the types and sizes of disturbance, and the tolerance of various types of equipment to the possible

disturbances that may be encountered. The principal standards in this field are IEC 61000, EN 50160, and IEEE 1159. Standards are essential for manufacturers and users alike, to define what is reasonable in terms of disturbances that might occur and what equipment should withstand. Broad classifications of the disturbances that may occur on a power system are described as follows.

- Voltage Dips: The major cause of voltage dips on a system is local and remote faults, inductive loading, and switch on of large loads.
- Voltage surges: The major cause of Voltage surges on a system is Capacitor switching, Switch off of large loads and Phase faults.
- Overvoltage: The major cause of overvoltage on a system is Load switching, Capacitor switching, and System voltage regulation.
- Harmonics: The major cause of Harmonics on a system is Industrial furnaces Non-linear loads Transformers/generators, and Rectifier equipment.
- Power frequency variation: The major cause of Power frequency variation on a system is Loss of generation and Extreme loading conditions.
- Voltage fluctuation: The major cause of Voltage fluctuation on a system is AC motor drives, Inter-harmonic current components, and Welding and arc furnaces.
- Rapid voltage change: The major cause of Rapid voltage change on a system is Motor starting, Transformer tap changing.
- Voltage imbalance: The major cause of Voltage imbalance on a system is unbalanced loads, and Unbalanced impedances.
- Short and long voltage interruptions: The major cause of Short and long voltage interruptions on a system are Power system faults, Equipment failures, Control malfunctions, and CB tripping.
- Undervoltage: The major cause of Undervoltage on a system are Heavy network loading, Loss of generation, Poor power factor, and Lack of var support.
- Transients: The major cause of Transients on a system are Lightning, Capacitive switching, Non –linear switching loads, System voltage regulation.

2. Feature extraction

There are several reasons for monitoring power quality. The most important reason is the economic damage produced by electromagnetic phenomena in critical process loads. Effects on equipment and process operations can include malfunctions, damage, process disruption and other anomalies (Baggini 2010; IEEE 1995).

Troubleshooting these problems requires measuring and analyzing power quality and that leads us to the importance of monitoring instruments in order to localize the problems and find solutions. The critical stage for any pattern recognition problem is the extraction of discriminative features from the raw observation data. The combination of several scalar features forms the feature vector. For the classification of power quality events, the appropriate characteristics should be extracted. These characteristics should be chosen to have low computation time and can separate disturbances with high precision. Therefore, the similarities between these characteristics should be few and the number of them must be low (Moravej et al., 2010; Moravej et al., 2011a). Digital signal processing, or signal processing in short, concerns the extraction of features and information from measured digital signals. A wide variety of signal-processing methods have been developed through

the years both from the theoretical point of view and from the application point of view for a wide range of signals. Some prevalent used signal processing techniques are as follows (Moravej et al., 2010; Moravej et al., 2011a, 2001b; Heydt et al., 1999; Aiello 2005; Mishra et al., 2008):

- Fourier transform
- Short time Fourier transform
- Wavelet transform
- Hilbert transform
- Chirp Z transform
- S transform

More frequently, features extracted from the signals are used as the input of a classification system instead of the signal waveform itself, as this usually leads to a much smaller system input. Selecting a proper set of features is thus an important step toward successful classification. It is desirable that the selected set of features may characterize and distinguish different classes of power system disturbances. This can roughly be described as selecting features with a large interclass (or between-class) mean distance and a small intraclass (or within-class) distance. Furthermore, it is desirable that the selected features are uncorrelated and that the total number of features is small. Other issues that could be taken into account include mathematical definability, numerical stability, insensitivity to noise, invariability to affine transformations, and physical interpretability (Bollen & GU 2006). The signal decomposition and various parametric models of signals, where the extraction of signal characteristics (or features, attributes) becomes easier in some analysis domain as compared with directly using signal waveforms in the time domain.

3. Classification

These features can be used as the input of a classification system. For many real-world problems we may have very little knowledge about the characteristics of events and some incomplete knowledge of the systems. Hence, learning from data is often a practical way of analyzing the power system disturbances. Among numerous methodologies of machine learning, we shall concentrate on a few methods that are commonly used or are potentially very useful for power system disturbance analysis and diagnostics. These methods include:

(a) Learning machines using linear discriminates, (b) probability distribution– based Bayesian classifiers and Neyman–Pearson hypothesis tests, (c) multilayer neural networks, (d) statistical learning theory–based support vector machines, and (e) rule-based expert systems. A typical pattern recognition system consists of the following steps: feature extraction and optimization, selection of classifier topologies (or architecture), supervised/unsupervised learning, and finally the testing. It is worth noting that for each particular system some of these steps may be combined or replaced (Bollen & GU 2006).

Mathematically, designing a classifier is equivalent to finding a mapping function between the input space and the feature space followed by applying some decision rules that map the feature space onto the decision space. There are many different ways of categorizing the classifiers. A possible distinction is between statistical-based classifiers (e.g., Bayes, Neyman–Pearson, SVMs) and non-statistical-based classifiers (e.g., syntactic pattern recognition methods, expert systems). A classifier can be linear or nonlinear. The mapping

function can be parametric (e.g., kernel functions) or nonparametric (e.g., K nearest neighbors) as well. Some frequently used classifiers are listed below:

- Linear machines
- Artificial neural networks
- Bayesian classifiers
- Kernel machines
- Support vector machines
- Rule-based expert systems
- Fuzzy classification systems

4. Signal processing techniques

4.1 Short Time Fourier Transform

The purpose of the signal processing in various applications is to extract useful information through suitable technique. The non-stationary signals, in time-frequency analysis, need a tool that transform a signal into time frequency domain (Gu et al., 2000; Rioul & Vetterli 1991).

Fourier transform of $x(t)w(t-\tau)$ is defined Short Time Fourier Transform (STFT). It relies on the assumption that the non-stationary signal $x(t)$ can be segmented into sections confined by a window boundary $w(t)$ within which it can be treated as the stationary one.

$$X_w(jw,\tau) = \int_{-\infty}^{+\infty} x(t)w(t-\tau)e^{-jwt} \tag{1}$$

where: $w(t) = \begin{cases} 0 & t < 0, t > t_w \\ w(t) & 0 < t < t_w \end{cases}$.

The STFT depicts rime evolution of the signal spectrum by shifted $w(t)$ in time: $w(t-\tau)$.

The discrete form of STFT can be expressed by following equation:

$$X_w(n,m) = \sum_{k=0}^{M-1} x(k)w(k-m)e^{-junk} \tag{2}$$

where:

υ : an angle between sample, M : number of samples within the window.

The STFT as time-frequency analysis technique depends critically on the choice of the window. When a window has been selected for the STFT, the frequency resolution is unique at all frequency (Rioul & Vetterli 1991).

In (Gu et al., 2000) the spectral content as a function of time by using discrete STFT is obtained. Discrete STFT detects and analyses transients in the voltage disturbances by suitable selection of window size. Since the STFT has a fixed resolution at all frequency the interpretation of it terms of harmonics are easier. The band-pass filter outputs from discrete STFT are well associated with harmonics and are suitable for power system analysis. Also the STFT method is compared to wavelet in (Gu et al., 2000). The Authors of (Gu et al., 2000) believes that the choice of these methods depends heavily on particular applications. Overall it appears more favorable to use discrete STFT than dyadic wavelet and Binary-Tree Wavelet Filters (BT-WF) for voltage disturbance analysis.

4.2 Discrete Wavelet Transform (DWT)

Wavelet-based techniques are powerful mathematical tools for digital signal processing, and have become more and more popular since the 1980s. It finds applications in different areas of engineering due to its ability to analyze the local discontinuities of signals. The main advantages of wavelets is that they have a varying window size, being wide for slow frequencies and narrow for the fast ones, thus leading to an optimal time–frequency resolution in all the frequency ranges (Rioul & Vetterli 1991).

The DWT of a signal x is calculated by passing it through a series of filters. First the samples are passed through a low pass filter with impulse response g resulting in a convolution of the two:

$$y[n] = (x * g)[n] = \sum_{k=-\infty}^{\infty} x[k]g[n-k]. \tag{3}$$

The signal is also decomposed simultaneously using a high-pass filter h. The outputs giving the detail coefficients (from the high-pass filter) and approximation coefficients (from the low-pass). It is important that the two filters are related to each other and they are known as a quadrature mirror filter. However, since half the frequencies of the signal have now been removed, half the samples can be discarded according to Nyquist's rule. The filter outputs are:

$$y_{low}[n] = \sum_{k=-\infty}^{\infty} x[k]g[2n-k] \tag{4}$$

$$y_{high}[n] = \sum_{k=-\infty}^{\infty} x[k]h[2n+1-k]. \tag{5}$$

This decomposition has halved the time resolution since only half of each filter output characterizes the signal. However, each output has half the frequency band of the input so the frequency resolution has been doubled. For multi level resolution the decomposition is repeated to further increase the frequency resolution and the approximation coefficients decomposed with high and low pass filters. This is represented as a binary tree with nodes representing a sub-space with different time-frequency localization. The tree is known as a filter bank (Moravej et al., 2010; Moravej et al., 2011a; Rioul & Vetterli 1991).

4.3 The Discrete S-Transform

The short term Fourier transforms (STFT) is commonly used in time-frequency signal processing (Stockwell 1991; Stockwell & Mansinha 1996). However, one of its drawbacks is the fixed width and height of the analyzing window. This causes misinterpretation of signal components with period longer than the window width; also the finite width limits time resolution of high-frequency signal components. One solution is to scale the dimensions of the analyzing window to accommodate a similar number of cycles for each spectral component, as in wavelets. This leads to the S-transform introduced by Stockwell, Mansinha and Lowe (Stockwell & Mansinha 1996). Like the STFT, it is a time-localized Fourier spectrum which maintains the absolute phase of each localized frequency component. Unlike the STFT, though, the S-transform has a window whose height and width frequency-varying (Stockwell 1991).

The S-transform was originally defined with a Gaussian window whose standard deviation is scaled to be equal to one wavelength of the complex Fourier spectrum. The original expression of S-transform as presented in (Stockwell 1991; Stockwell & Mansinha 1996) is

$$S(\tau,f) = \int_{-\infty}^{\infty} x(t) \frac{|f|}{\sqrt{2\pi}} e^{-\frac{(\tau-t)^2 f^2}{2}} e^{-i2\pi ft} dt. \tag{6}$$

The normalizing factor of $|f|/\sqrt{2\pi}$ in (1) ensures that, when integrated over all τ, $S(\tau,f)$ converges to $X(f)$, the Fourier transform of $x(t)$

$$\int_{-\infty}^{\infty} S(\tau,f) = \int_{-\infty}^{\infty} x(t) e^{-i2\pi ft} dt = X(f) \tag{7}$$

It is clear from (2) that $x(t)$ can be obtained from $S(\tau,f)$. Therefore, S-transform is invertible. Let $x[kT]$, $k = 0,1,...,N-1$ denote a discrete time series, corresponding to $x(t)$, with a time sampling interval of T. The discrete Fourier transform is given by

$$X\left[\frac{n}{NT}\right] = \frac{1}{N} \sum_{k=0}^{N-1} x[kT] e^{-\frac{i2\pi nk}{N}} \tag{8}$$

where $N = 0,1,...,N-1$. In the discrete case, the S-transform is the projection of the vector defined by the time series $x[kT]$ onto a spanning set of vectors. The spanning vectors are not orthogonal, and the elements of the S-transform are not independent. Each basis vectors (of the Fourier transform) is divided into N localized vectors by an element-by-element product with N shifted Gaussians, such that the sum of these N localized vectors is the original basis vector.

Letting $f \rightarrow n/NT$ and $\tau \rightarrow jT$, the discrete version of the S-transform is given in (Stockwell & Mansinha 1996) as follows:

$$S\left[jT,\frac{n}{NT}\right] = \sum_{m=0}^{N-1} X\left[\frac{m+n}{NT}\right] e^{-\frac{2\pi^2 m^2}{n^2}} e^{\frac{i2\pi mj}{N}} \tag{9}$$

and for the $n = 0$ voice is equal to the constant defined as

$$S[jT,0] = \frac{1}{N} \sum_{m=0}^{N-1} x\left(\frac{m}{NT}\right) \tag{10}$$

where j, m and $n = 0,1,...,N-1$. Equation (5) puts the constant average of the time series into the zero frequency voice, thus assuring the inverse is exact for the general time series.

Besides, standard ST suffers from poor energy concentration in the time-frequency domain. It gives degradation in time resolution at lower frequency and poor frequency resolution at higher frequency. In (Sahu et al., 2009) a modified Gaussian window has been proposed which scales with the frequency in an efficient manner to provide improved energy concentration of the S-transform. In this improved ST scheme the window function has been considered as the same Gaussian window but, an additional parameter δ is introduced into the Gaussian window where its width varies with frequency as follows (Sahu et al., 2009):

$$\sigma(f) = \frac{\delta}{|f|}. \tag{11}$$

Hence the generalized ST becomes

$$S(\tau, f, \delta) = \int_{-\infty}^{+\infty} x(t) \frac{|f|}{\sqrt{2\pi}\delta} e^{-\frac{(\tau-t)^2 f^2}{2\delta^2}} e^{-j2\pi ft} dt \tag{12}$$

where the Gaussian window becomes

$$g(t, f, \delta) = \frac{|f|}{\sqrt{2\pi}\delta} e^{-\frac{t^2 f^2}{2\delta^2}} \tag{13}$$

and its frequency domain representation is

$$G(\alpha, f, \delta) = e^{-\frac{2\pi^2 \alpha^2 \delta^2}{f^2}} \tag{14}$$

The adjustable parameter δ represents the number of periods of Fourier sinusoid that are contained within one standard deviation of the Gaussian window. If δ is too small the Gaussian window retains very few cycles of the sinusoid. Hence the frequency resolution degrades at higher frequencies. If δ is too high the window retains more sinusoids within it. As a result the time resolution degrades at lower frequencies. It indicates that the δ value should be varied judiciously so that it would give better energy distribution in the time-frequency plane. The trade off between the time-frequency resolutions can be reduced by optimally varying the window width with the parameter δ. At lower δ value $(\delta < 1)$ the window widens more with less sinusoids within it, thereby it catches the low frequency components effectively. At higher δ value $(\delta > 1)$ the window width decreases more with more sinusoids within it, thereby it resolves the high frequency components better. The parameter δ is varied linearly with frequency within a certain range as given by (Stockwell 1991):

$$\delta(f) = k f \tag{15}$$

where k is the slope of the linear curve. The discrete version of (6) is used to compute the discrete IST by taking the advantage of the efficiency of the Fast Fourier Transform (FFT) and the convolution theorem.

4.4 Hyperbolic S-transform

The S-transform has an advantage that it provides multi-resolution analysis while retaining the absolute phase of each frequency. But the Gaussian window has no parameter to allow its width to be adjusted in the time or frequency domain. Hence, the generalized ST which has a greater control over the window function has been introduced in (Pinnega & Mansinha 2003). Thus, at high frequencies, where the window is narrow and time resolution is good in any case, a more symmetrical window should be used. At low frequencies, where the window is wider and frequency resolution is less critical, a more asymmetrical window may be used to prevent the event from appearing too far ahead on the S-transform. This

concept led us to design the "hyperbolic" window w_{HY}. The hyperbolic window is a pseudo-Gaussian, obtained from the generalized window as follows (Pinnega & Mansinha 2003):

$$w_{HY} = \frac{2|f|}{\sqrt{2\pi}\left(\gamma_{HY}^{F} + \gamma_{HY}^{B}\right)} \times \exp\left\{\frac{-f^2\left[X\left(\tau - t, \left\{\gamma_{HY}^{F}, \gamma_{HY}^{B}, \lambda_{HY}^{2}\right\}\right)\right]^2}{2}\right\} \tag{16}$$

where

$$X\left(\tau - t, \left\{\gamma_{HY}^{F}, \gamma_{HY}^{B}, \lambda_{HY}^{2}\right\}\right) = \frac{\gamma_{HY}^{F} + \gamma_{HY}^{B}}{2\gamma_{HY}^{F}\gamma_{HY}^{B}}(\tau - t - \zeta) + \frac{\gamma_{HY}^{F} - \gamma_{HY}^{B}}{2\gamma_{HY}^{F}\gamma_{HY}^{B}}\sqrt{(\tau - t - \zeta)^2 + \lambda_{HY}^{2}} \tag{17}$$

In equation (4), X is a hyperbola in $(\tau - t)$ which depends upon a backward-taper parameter γ_{HY}^{B} a forward-taper parameter γ_{HY}^{F} (we assume $0 < \gamma_{HY}^{F} < \gamma_{HY}^{B}$), and a positive curvature parameter λ_{HY} which has units of time. The translation by ζ ensures that the peak of w_{HY} occurs at $(\tau - t) = 0$; ζ is defined by

$$\zeta = \sqrt{\frac{\left(\gamma_{HY}^{B} - \gamma_{HY}^{F}\right)^2 \lambda_{HY}^{2}}{4\gamma_{HY}^{B}\gamma_{HY}^{F}}} \tag{18}$$

The output of HST is a $N \times M$ matrix with complex values and is called the HS-Matrix whose rows pertain to frequency and whose columns pertain to time. Important information in terms of magnitude, phase and frequency can be extracted from the S-matrix.

Feature extraction is done by applying standard statistical techniques to the S-matrix. Many features such as amplitude, slope (or gradient) of amplitude, time of occurrence, mean, standard deviation and energy of the transformed signal are widely used for proper classification. Some extracted features based on S-transform are (Mishra et al., 2008; Gargoom et al., 2008).

- Standard deviation of magnitude contour.
- Energy of the magnitude contour.
- Standard deviation of the frequency contour.
- Energy of the of the frequency contour.
- Standard deviation of phase contour.

4.5 Slantlet Transform

Selesnick in (Selesnick 1999) has proposed new transform method called Slantlet Transform (SLT) in signal processing application. The SLT primarily based on an improved model of Discrete Wavelet Transform (DWT) has evolved. The DWT utilize tree structure for implementation whereas the SLT filter-bank is implemented in type of a parallel structure with shorter support of component filters.

For better comparison between DWT and SLT, let two-scale orthogonal DWT namely D_2 (which is proposed by Daubechies) and also the corresponding filter-bank actualized by SLT. It is potential to implement filters of shorter length whereas satisfying orthogonality and zero moment conditions (Selesnick 1999; Panda et al., 2002).

Recently, the SLT with improved time localization compared to DWT, is applicable in signal processing and data compression. In (Panda et al., 2002), the SLT used as a tool in making an effective method for compression of power quality disturbances. Data compression and reconstruction of impulse, sag, swell, harmonics, interruption, oscillatory transient and voltage flicker by using two-scale SLT was implemented.

Transforming of input signal by SLT, thresholding of transformed coefficients and reconstruction by inverse SLT are three main step of proposed method. Input data are generated using MATLAB code at sampling rate of 3 kHz. The obtained results, in (Panda et al., 2002), indicate SLT based compressing algorithm achieve better performance compared to Discrete Cosine Transform (DCT) and DWT.

Power quality events classification system contains SLT and fuzzy logic based classifier proposed in (Meher 2008). The decomposition level using SLT was selected as 3.five feature from SLT coefficient are selected as attributes to classification of disturbances. Six power quality events: sag, swell, interruption, transients, notch and spike are generated by MATLAB code at a sampling frequency of 5 kHz and up to 10 cycles. Under noisy conditions the proposed method is evaluated.

In (Hsieh et al., 2010), authors has implemented field programmable gate array (FPGA)-based hardware realization for identification of electrical power system disturbances. For each cycles of voltage interruption, sag, swell, harmonics and transient, 2950 points sampled and examined.

4.6 Hilbert Transform

The Hilbert Transform (HT) is a signal processing method technique which is a linear operator in the mathematics. The HT of a signal $x(t)$: $H[x(t)]$ is defined as (Kschischang 2006):

$$H[x(t)] = x(t) * \frac{1}{\pi t} = \frac{1}{\pi} \int_{-\infty}^{+\infty} \frac{x(\tau)}{t - \tau} d\tau = \frac{1}{\pi} \int_{-\infty}^{+\infty} \frac{x(t - \tau)}{\tau} d\tau \qquad (19)$$

where τ is the shifting operator. The HT can be considered as the convolution of $x(t)$ with the signal $1/\pi t$.

Clearly the HT of a signal $x(t)$ in a time domain is another time domain signal $H[x(t)]$. The output of the HT is 90 degree phase shift of the original signal (Shukla et al., 2009).

A pattern recognition system has been proposed in (Jayasree et al., 2010) based on HT. The envelope of the power quality disturbances are calculated by using HT. The type of the power quality events is detected by the shape of the envelope. Some statistical information from the coefficients of HT is used. Means, standard deviation, peak value and energy of the HT coefficient are employed as input vector of the neural network classifier. Data generation is done by MATLAB/simulink. Sag, swell, transients, harmonics and voltage fluctuation along with normal signal were considered in (Jayasree et al., 2010). 500 samples from each class which were sample at 256 point/cycle with normal frequency 50 Hz. The method of (Jayasree et al., 2010) shows the HT features less sensitive to noise level.

The combination of EMD and HT are suggested in (Shukla et al., 2009). The HT is applied to first three IMF extracted from EMD to assess instantaneous amplitude and phase which are then employed for feature vector construction. The pattern recognition system used PNN classifier for identification the various power quality events.

Nine types of power quality disturbances are generated in MATLAB with a sampling frequency 3.2 kHz. The events are as follows: sag, swell, harmonics, flicker, notch, spike, transients, sag with harmonics, and swell with harmonics. Moreover, the efficiency of the method is compared to ST.

4.7 Empirical Mode Decomposition

The Empirical Mode Decomposition (EMD) is as key part of Hilbert-hung transform. The EMD is a technique for generation Intrinsic Mode Function (IMF) from non-linear and non-stationary signals.

An IMF which is belonging to a collection of IMF must be satisfied the following conditions (Huang et al., 1998; Rilling et al., 2003; Flandrin et al., 2004):

1. In the raw signal, the number of extrema and the number of zero-crossing must be equal (or extremely one number difference)
2. At any point, the mean value of the envelope specified by the local maxima and the envelope specified by the local minima is zero.

The decomposition procedure of EMD as called "sifting process". The sifting process is used to extract IMF. The following steps to generate the IMF for signal $X(t)$, should be run:

- Determination of all extrema of raw signal $X(t)$
- Using interpolation of local maxima and minima
- Calculation m_1 as the mean of upper and lower envelop which are obtained from previous step
- Calculation of first component h_1 : $h_1 = X(t) - m_1$
- h_1 is treated as the raw date, then, by same process to obtain m_1 , m_{11} is also calculated and $h_{11} = h_1 - m_{11}$
- The sifting process is repeated k times, until h_{1k} is an IMF, that is : $h_{1(k-1)} - m_{1k} = h_{1k}$
- It is considered as the first IMF from the raw data $c_1 = h_{1k}$
- The first extracted IMF component contains the shortest period variation in the data. For the stopping of the sifting process, the residual, r , can be defined by $X(t) - c_1 = r_1$.

    The residue, r_1 treated as a new raw data and consequently same sifting procedure, as explained above, is applied. This algorithm can be repeated on r_j : $r_{n-1} - c_n = r_n$ until all

    r_j are obtained. Last r_j can be calculated when the more IMF cannot be extracted in fact

    r_n becomes a monotonic function. Finally, From the above equations it is obtained:

    $$X(t) = \sum_{i=1}^{n} c_i + r_i .$$

Therefore, a decomposition of the data into n-EMD modes is obtained (Huang et al., 1998).

In a few paper the EMD is applied for identification of different power quality events. One of the main reasons is the EMD method is relatively new. The high speed of the EMD is the most important advantage of the algorithm because all procedure is done in time domain only.

In (Lu et al., 2005) EMD proposed as a signal processing tool for power quality monitoring. The EMD has the ability to detect and localize transient features of power disturbances. In order to evaluate the proposed method, periodical notch, voltage dip, and oscillatory transient have been investigated. Three calculated IMF, c_1 , c_2 and c_3 , show the ability of the EMD to extract important features from several types of power quality disturbances. The

sampling frequency used in (Lu et al., 2005) is 5 kHz and the noisy condition, where signal to noise ratio value is about 26 dB, is considered.

5. Classification techniques

5.1 Feed Forward Neural Networks (FFNN)

Neural networks are composed of simple elements operating in parallel. These elements are inspired by biological nervous systems. As in nature, the connections between elements largely determine the network function. Neural networks can be trained to perform a particular function by adjusting the values of the connections (weights and biases) between elements. Generally, neural networks are adjusted, or trained, so that a particular input leads desired target output. The network is adjusted, based on a comparison of the output and the target, until the network output matches the target. Usually, many such input/target pairs are needed to train a network. Neural networks have been trained to perform complex functions in various fields, including pattern recognition, identification, classification, speech, vision, and control systems.

Neural networks can also be trained to solve problems that are difficult for conventional computers or human beings. Neural networks are usually applied for one of the three following goals:

- Training a neural network to fit a function
- Training a neural network to recognize patterns
- Training a neural network to cluster data

The training process requires a set of examples of proper network behavior i.e. network inputs and target outputs. During training the weights and biases of the network are iteratively adjusted to minimize the network performance function (Moravej et al., 2002).

5.2 Radial Basis Function Network (RBFN)

The RBFN model (Mao et al., 2000) consists of three layers: the inputs and hidden and output layers. The input space can either be normalized or an actual representation can be used. This is then fed to the associative cells of the hidden layer, which acts as a transfer function. The hidden layer consists of radial basis function like a sigmoidal function used in MLP network. The output layer is a linear layer. The RBF is similar to Gaussian density function, which is de.ned by the "center" position and "width" parameter. The RBF gives the maximum output when the input to the neuron is at the center and the output decreases away from the center. The width parameter determines the rate of decrease of the function as the input pattern distance increases from the center position. Each hidden neuron receives as net input the distance between its weight vector and the input vector. The output of the RBF layer is given as

$$O_k = \exp(-[X - C_k]^T [X - C_k] / 2\sigma_k^2) \qquad (20)$$

where $K = 1, 2, ..., N$, where N is the number of hidden nodes

O_k = output of the K th node of the hidden layer
X = input pattern vector
C_k = center of the RBF of K th node of the hidden layer
σ_k = spread of the K th RBF

Each neuron in the hidden layer outputs a value depending on its weight from the center of the RBF. The RBFN uses a Gaussian transfer function in the hidden layer and linear function in the output layer. The output of the j th node of the linear layer is given by

$$Y_j = W_j^T O_j \qquad\qquad (21)$$

where $j = 1, 2, ..., M$, where M is the number of output nodes

Y_j = output of the j th node

W_j = weight vector for node j

O_j = output vector from the j th hidden layer (can be augmented with bias vector)

Choosing the spread of the RBF depends on the pattern to be classified. The learning process undertaken by a RBF network may be visualized as follows. The linear weights associated with the output units of the network tend to evolve on a different "time scale" compared to the nonlinear activation functions of the hidden units. Thus, as the hidden layer's activation functions evolve slowly in accordance with some nonlinear optimization strategy, the output layer's weights adjust themselves rapidly through a linear optimization strategy. The important point to note is that the different layers of an RBF network perform different tasks, and so it is reasonable to separate the optimization of the hidden and output layers of the network by using different techniques, and perhaps operating on different time scales. There are different learning strategies that can be followed in the design of an RBF network, depending on how the centers of the radial basis functions of the network are specified. Essentially following three approaches are in use:

- Fixed centers selected at random
- Self-organized selection of centers
- Supervised selection of centers

5.3 Probabilistic neural network (PNN)

The PNN was first proposed in (Spetch 1990; Mao et al., 2000). The development of PNN relies on the Parzen window concept of multivariate probability estimates. The PNN combines the Baye's strategy for decision-making with a non-parametric estimator for obtaining the Probability Density Function (PDF) (Spetch 1990; Mao et al., 2000). The PNN architecture includes four layers; input, pattern, summation, and output layers. The input nodes are the set of measurements. The second layer consists of the Gaussian functions formed using the given set of data points as centers. The third layer performs an average operation of the outputs from the second layer for each class. The fourth layer performs a vote, selecting the largest value. The associated class label is then determined (Spetch 1990). The input layer unit does not perform any computation and simply distributes the input to the neurons. The most important advantages of PNN classifier are as below:

- Training process is very fast
- An inherent parallel structure
- It converges to an optimal classifier as the size of the representative training set increases
- There are not local minima issues
- Training patterns can be added or removed without extensive retraining

5.4 Support vector machines (SVMs)

The SVM finds an optimal separating hyperplane by maximizing the margin between the separating hyperplane and the data (Cortes et al., 1995; Vapnik 1998; Steinwart 2008, Moravej et al., 2009). Suppose a set of data $T = \{x_i, y_i\}_{i=1}^{m}$ where $x_i \in R^n$ denotes the feature vectors, $y_i \in \{+1, -1\}$ stands for two classes, and m is the sample number, if two classes are linearly separable, the hyperplane $f(x) = 0$ can be determined such that separates the given feature vectors.

$$f(x) = w.x + b = \sum_{k=1}^{m} w_k.x_k + b = 0 \tag{22}$$

where w and b denote the weight vector and the bias term, respectively. The position of the separating hyperplane is defined by setting these parameters. Thus the separating hyperplane satisfy the following constraints:

$$y_i f(x_i) = y_i(w.x_i + b) \geq 1, \quad i = 1, 2, ..., m \tag{23}$$

ξ_i are positive slack variables that measure the distance between the margin and the vectors x_i that lie on the incorrect side of the margin. Then, in order to obtain the optimal hyperplane, the following optimization problem must be solved:

$$\text{Minimize} \quad \frac{1}{2}\|w\|^2 + C\sum_{i=1}^{m}\xi_i, \quad i = 1, 2, ..., m$$
$$\text{subject to} \begin{cases} y_i(w.x_i + b) \geq 1 - \xi_i \\ \xi_i \geq 0 \end{cases} \tag{24}$$

where C is the error penalty.

By introducing the Lagrangian multipliers α_i, the above-mentioned optimization problem is transformed into the dual quadratic optimization problem, as follows:

$$\text{Maximize} \quad L(\alpha) = \sum_{i=1}^{m}\alpha_i - \frac{1}{2}\sum_{i,j=1}^{m}\alpha_i\alpha_j y_i y_j(x_i.x_j) \tag{25}$$

$$\text{Subject to} \sum_{i=1}^{m}\alpha_i y_i = 0, \alpha_i \geq 0, i = 1, 2, ..., m \tag{26}$$

Thus, the linear decision function is created by solving the dual optimization problem, which is defined as:

$$f(x) = \text{sign}\left(\sum_{ij=1}^{m}\alpha_i y_i(x_i, x_j) + b\right) \tag{27}$$

If the linear classification is not possible, the nonlinear mapping function ϕ can be used to map the original data x into a high dimensional feature space that the linear classification is possible. Then, the nonlinear decision function is:

$$f(x) = \text{sign}\left(\sum_{ij=1}^{m}\alpha_i y_i K(x_i, x_j) + b\right) \tag{28}$$

where $K(x_i, x_j)$ is called the kernel function, $K(x_i, x_j) = \phi(x_i)\phi(x_j)$. Linear, polynomial, Gaussian radial basis function and sigmoid are the most commonly used kernel functions (Cortes et al., 1995; Vapnik 1998; Steinwart 2008). To classify more than two classes, two simple approaches could be applied. The first approach uses a class by class comparison technique with several machines and combines the outputs using some decision rule. The second approach for solving the multiple class detection problem using SVMs is to compare one class against all others, therefore, the number of machines is the same number of classes. These two methods have been described in details in (Steinwart 2008).

5.5 Relevance Vector Machines

Michael E. Tipping proposed Relevance Vector Machine (RVM) in 2001 (Tipping 2000). It assumes knowledge of probability in the areas of Bayes' theorem and Gaussian distributions including marginal and conditional Gaussian distributions (Fletcher 2010). RVMs are established upon a Bayesian formulation of a linear model with an appropriate prior that cause a sparse representation. Consequently, they can generalize well and provide inferences at low computational cost (Tzikas 2006; Tipping 2000). The main formulation of RVMs is presented in (Tipping 2000).

New combination of WT and RVMs are suggested in (Moravej et al., 2011a) for automatic classification of power quality events. The Authors in (Moravej et al., 2011a) employed the WT techniques to extract the feature from details and approximation waves. The constructed feature vectors as input of RVM classifier are applied for training the machines to monitoring the power quality events. The feature extracted from various power quality signals are as follow:

1. Standard deviation of level 2 of detail.
2. Minimum value of absolute of level n of approximation. (n is desirable decomposition levels)
3. Mean of average of absolute of all level of details.
4. Mean of disturbances energy.
5. Energy of level 3 of detail.
6. RMS value of main signal.

Sag, swell, interruption, harmonics, swell with harmonics, sag with harmonics, transient, and flicker, was studied. Data is generated by parametric equation an MATLAB environment. The procedure of classification is tested in noisy conditions and the results show the efficiency of the method. The CVC method for classification of nine power quality events is proposed. First time that RVM based classifier for recognition of power quality events is applied in (Moravej et al., 2011a).

5.6 Logistic Model Tree and Decision Tree

Logistic Model Tree (LMT) is a machine for supervised learning issues. The LMT combines linear logistic regression and tree induction. The LogitBoost algorithm for building the structure of logistic regression functions at the nodes of a tree is used. Also, the renowned Classification and Regression Tree (ACRT) algorithm for pruning are employed. The LogitBoost is employed to pick the foremost relevant attributes in the data when performing logistic regression by performing a simple regression in each iteration and stopping before convergence to the maximum likelihood solution. The LMT does not require any tuning of parameters by the user (Landwehr 2005; Moravej et al., 2011b).

A LMT includes standard Decision Tree (DT) (Kohavi & Quinlan 1999) structure with logistic regression functions at the leaves. Compared to ordinary DTs, a test on one of the attributes is related to every inner node.

The new combination as pattern recognition system has been proposed in (Moravej et al., 2011b). The Authors used LMT based classifier for identification of nine power quality disturbances. Sag, swell, interruption, harmonics, transient, and flicker, was studied. Simultaneously disturbances consisting of sag and harmonics, as well as swell and harmonics, are also considered. Data is generated by parametric equation an MATLAB environment. The sampling frequency is 3.2 kHz. The feature vector composed of four features extracted by ST method. In (Moravej et al., 2011b), the features are based on the Standard Deviation (SD) and energy of the transformed signal and are extracted as follows:

Feature 1: SD of the dataset comprising the elements corresponding to the maximum magnitude of each column of the S-matrix.

Feature 2: Energy of the dataset comprising of the elements corresponding to the maximum magnitude of each column of the S-matrix.

Feature 3: SD of the dataset values corresponding to the maximum value of each row of the S-matrix.

Feature 4: Energy of the dataset values corresponding to the maximum value of each row of the S-matrix.

For classification of power quality disturbances, 100 cases of each class are generated for the training phase, and another 100 cases are generated for the testing phase (Moravej et al., 2011b). The Sensitivity of the algorithm, in (Moravej et al., 2011b), is also investigated under noisy condition.

6. Pattern recognition techniques

The functionality of an automated pattern recognition system can be divided into two basic tasks, as shown in Fig. 1: the description task generates attributes of PQ disturbances using feature extraction techniques, and the classification task assigns a group label to the PQ disturbance based on those attributes with a classifier. The description and classification tasks work together to determine the most accurate label for each unlabeled object analyzed by the pattern recognition system (Moravej et al., 2010; Moravej et al., 2011a).

Feature extraction is a critical stage because it reduces the dimension of input data to be handled by the classifier. The features which truly discriminate among groups will assist in identification, while the lack of such features can prevent the classification task from arriving at an accurate identification. The final result of the description task is a set of features, commonly called a feature vector, which constitutes a representation of the data. The classification task uses a classifier to map a feature vector to a group. Such a mapping can be specified by hand or, more commonly, a training phase is used to induce the mapping from a collection of feature vectors known to be the representative of the various groups among which discrimination is being performed (i.e., the training set). Once formulated, the mapping can be used to assign identification to each unlabeled feature vector subsequently presented to the classifier. So, it is obvious that a good feature extraction technique should be able to derive significant feature vectors in an automated way along with determining less number of relevant features to characterize the complete systems. Thus, the subsequent computational burden of the classifier can be reduced.
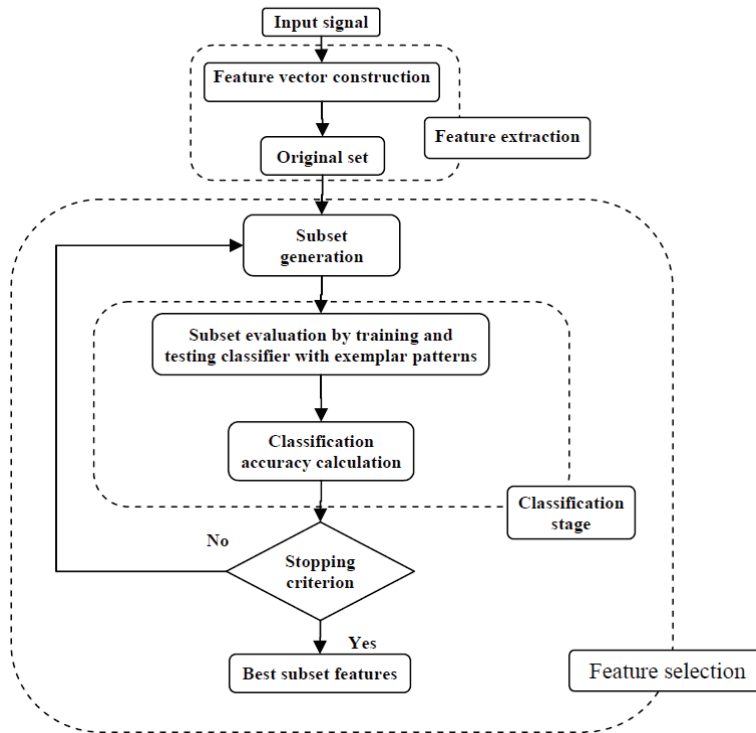
Fig. 1. General pattern recognition algorithm for PQ events classification

7. Feature selection

By removing the most irrelevant and redundant features from the data, feature selection helps to improve the performance of learning models by alleviating the effect of the curse of dimensionality, enhancing generalization capability, speeding up learning process and improving model interpretability. If the size of initial feature set is large, exhaustive search may not be feasible due to processing time considerations. In that case, a suboptimal selection algorithm is preferred. However, none of these algorithms guarantee that the best feature set is obtained. The selection methods provide useful information about superiority of selected features, superiority of feature selection strategy and the relation between the useful features and the desired feature size (Gunal et al., 2009). Generally the feature selection methods give answer to some question arises from PQ classification problem as follows.

7.1 Filter
Filter type methods are based on data processing or data filtering methods. Features are selected based on the intrinsic characteristics, which determine their relevance or discriminate powers with regard to the targeted classes. Some of these methods are described as follows (Proceedings of the Workshop on Feature Selection for Data Mining).

7.1.1 Correlation

A correlation function is the correlation between random variables at two different points in space or time, usually as a function of the spatial or temporal distance between the points. If one considers the correlation function between random variables representing the same quantity measured at two different points then this is often referred to as an autocorrelation function being made up of autocorrelations. Correlation functions of different random variables are sometimes called cross correlation functions to emphasize that different variables are being considered and because they are made up of cross correlations. Correlation functions are a useful indicator of dependencies as a function of distance in time or space, and they can be used to assess the distance required between sample points for the values to be effectively uncorrelated. In addition, they can form the basis of rules for interpolating values at points for which there are observations.

The most familiar measure of dependence between two quantities is the Pearson product-moment correlation coefficient, or "Pearson's correlation." It is obtained by dividing the covariance of the two variables by the product of their standard deviations. The population correlation coefficient $\rho_{X,Y}$ between two random variables X and Y with expected values μ_X and μ_Y and standard deviations σ_X and σ_Y is defined as (Rodgers & Nicewander 1988; Dowdy & Wearden 1983):

$$\rho_{X,Y} = \text{corr}(X,Y) = \frac{\text{cov}(X,Y)}{\sigma_X \sigma_Y} = \frac{E[(X - \mu_X)(Y - \mu_Y)]}{\sigma_X \sigma_Y} \qquad (29)$$

where E is the expected value operator, cov means covariance, and, corr a widely used alternative notation for Pearson's correlation.

The Pearson correlation is +1 in the case of a perfect positive (increasing) linear relationship (correlation), −1 in the case of a perfect decreasing (negative) linear relationship (anticorrelation), and some value between −1 and 1 in all other cases, indicating the degree of linear dependence between the variables. As it approaches zero there is less of a relationship (closer to uncorrelated). The closer the coefficient is to either −1 or 1, the stronger the correlation between the variables. Some feature can be selected from feature space based on the obtained correlation coefficient of potential features.

7.1.2 Product-Moment Correlation Coefficient (PMCC)

For each signal, a set of features may be extracted that characterize the signal. The purpose of the feature selection is to reduce the dimension of feature vector while maintaining admissible classification accuracy. In order to, select the most meaningful features Product-Moment Correlation Coefficient (PMCC or Pearson correlation) method has been applied to feature vector obtained in feature extraction step.

The Pearson correlation between two variables X and Y, giving a value between +1 and -1. A correlation of +1 means that there is a perfect positive linear relationship between variables. A correlation of -1 means that there is a perfect negative linear relationship between variables. A correlation of 0 means there is no linear relationship between the two variables.

Pearson's correlation coefficient between two variables is computed as (Son & Baek 2008):

$$r = \frac{\sum_{i=1}^{n}(X_i - \overline{X})(Y_i - \overline{Y})}{(n-1)S_X S_Y} \qquad (30)$$

where

r : correlation coefficient

$\overline{X}, \overline{Y}$: the means of X and Y respectively

S_X, S_Y : the standard deviation of X and Y respectively.

The correlation coefficient r is selected as 0.95, 0.9, and 0.85 respectively. The extracted features, those have correlation more than r will be removed automatically. The dimension reduction of the feature vector has several advantages including: low computational burden for training and testing phases of machine learning, high speed of training phase, and minimization of misclassifications.

Afterwards, feature normalization is applied to ensure that each feature in a feature vector is properly scaled. Therefore, the different features are equally weighted as an input of classifiers.

7.1.3 Minimum Redundancy Maximum Relevance (MRMR)

The MRMR method that considers the linear independency of the feature vectors as well as their relevance to the output variable so it can remove redundant information and collinear candidate inputs in addition to the irrelevant candidates. This technique is done in two steps. At first if the mutual information between a candidate variable and output feature is greater than a pre specified value then it is kept for further processing else it is discarded. This is the first step of the feature selection technique (''Maximum Relevance'' part of the MRMR principle). In the next step, the cross-correlation is performed on the retained features obtained from the first step. If the correlation coefficient between two selected features is smaller than a pre specified value both features are retained; else, only the features with largest mutual information are retained. The cross-correlation process is the second step of the feature selection technique (''Minimum Redundancy'' part of the MRMR principle) (Peng et al., 2005). So, the proposed feature selection technique is composed of a mutual information based filter to remove irrelevant candidate inputs and a correlation based filter to remove collinear and redundant candidates. Two thresholds values must be determined for two applied filters in the first and second steps. Retained variables after the two steps of the feature selection are selected as the input of the forecast engine. In order to obtain an efficient classification scheme, threshold values (adjustable parameters) must be fine tuned.

7.2 Wrapper

Wrapper based methods use a search algorithm to seek through the space of possible features and evaluate each subset by running a model on the selected subset. Wrappers usually need huge computational process and have a risk of over fitting to the model.

7.2.1 Sequential forward selection

Sequential forward selection was first proposed in (Whitney 1971). It operates in the bottom-to-top manner. The selection procedure begins with a null subset initially. Then, at each step, the feature that maximizes the criterion function is added to the current subset. This procedure continues until the requested number of features is selected. The nesting effect is present such that a feature added into the set in a step can not be removed in the subsequent steps (Gunal et al., 2009). As a consequence, SFS method can yield only the suboptimal result.

7.2.2 Sequential backward selection

Sequential backward selection method proposed in works in a top-to-bottom manner (Marill & Green 1963). It is the reverse case of SFS method. Initially, complete feature set is considered. At each step, a single feature is removed from the current set so that the criterion function is maximized for the remaining features within the set. The removal operation continues until the desired number of features is obtained. Once a feature is eliminated from the set, it can not enter into the set in the subsequent steps (Gunal et al., 2009).

7.2.3 Genetic algorithm

Genetic algorithms belong to the larger class of Evolutionary Algorithms (EA), which generate solutions to optimization problems using techniques inspired by natural evolution, such as mutation, selection, and crossover. The evolution usually starts from a population of randomly generated individuals and happens in generations. In each generation, the fitness of every individual in the population is evaluated, multiple individuals are stochastically selected from the current population based on their fitness, and modified (recombined and possibly randomly mutated) to form a new population. The new population is then used in the next iteration of the algorithm. Commonly, the algorithm terminates when either a maximum number of generations has been produced, or a satisfactory fitness level has been reached for the population (Yang & Honavar 1998). The chromosomes are encoded with {0, 1} binary alphabet. In a chromosome, ''1'' indicates the selected features while ''0'' indicates the unselected ones. For example, a chromosome defined as:

$$\{1\ 0\ 1\ 0\ 1\ 1\ 0\ 0\ 0\ 1\} \tag{31}$$

specifies that the features with index 1, 3, 5, 6, and 10 are selected while the others are unselected. The fitness value corresponding to a chromosome is usually defined as the classification accuracy obtained with the selected features.

7.2.4 Generalized sequential forward selection (GSFS)

In generalized version of SFS, instead of single feature, n features are added to the current feature set at each step (Kittler 1978). The nesting effect is still present.

7.2.5 Generalized sequential backward selection (GSBS)

In generalized form of SBS (GSBS), instead of single feature, n features are removed from the current feature set at each step. The nesting effect is present here, too (Kittler 1978).

7.2.6 Plus-l takeaway-r (PTA)

The nesting effect present in SFS and SBS can be partly avoided by moving in the reverse direction of selection for certain number of steps. With this purpose, at each step, l features are selected using SFS and then r features are removed with SBS. This method is called as PTA (Stearn 1976). Although the nesting effect is reduced with respect to SFS and SBS, PTA still provides suboptimal results.

7.2.7 Sequential forward floating selection (SFFS)

Dynamic version of PTA leads to SFFS method. Unlike the PTA method that parameters l and r are fixed, they are float in each step (Pudil et al., 1994). Thus, sub-selection searching

process, different number of features can be added to or removed from the set until a better criterion value is attained. The flexible structure of SFSS causes the feature dimension to be different in each step.

8. Review of proposed pattern recognition algorithms and conclusions

In the Table 1 some references are mentioned which use the pattern recognition schemes for detection of power quality events. These detection algorithms are composed of combination a feature extraction and a classification method.

Reference	Method	Reference	Method
(Moravej et al., 2010; Eristi & Demir 2010)	WT+SVM	(Behera et al., 2010)	ST+Fuzzy
(Moravej et al., 2011a)	WT+RVM	(Huang et al., 2010)	HST+PNN
(Moravej et al., 2011b)	ST+LMT	(Meher 2008)	SLT+Fuzzy
(RathinaPrabha 2009; Hooshmand & Enshaee 2010)	DFT+Fuzzy	(Jayasree et al., 2010)	HT+RBFN
(Mehera et al., 2004; Kaewarsa et al., 2008)	WT+ANN	(Mishra et al., 2008)	ST+PNN
(Liao & Lee 2004; Hooshmand & Enshaee 2010)	WT+Fuzzy	(Zhang et al., 2011)	DFT+DT
(Uyar et al., 2009; Hooshmand & Enshaee 2010)	ST+ANN		

Table 1. Review of proposed pattern recognition algorithms

Power Quality is a term used to broadly encompass the entire scope of interaction among electrical suppliers, the environment, the systems and products energized, and the users of those systems and products. It is more than the delivery of "clean" electric power that complies with industry standards. It involves the maintainability of that power, the design, selection, and the installation of every piece of hardware and software in the electrical energy system.

Many algorithms have been proposed for detection and classification of power quality events. Pattern recognitions schemes are very popular solution for detection of power quality events. The combinations of signal processing and classification tools have been widely applied in detection methods. The most useful features are extracted by analysis of signals and then they are discriminated by using a classifier or by definition of a proper index.

9. References

Aiello M.; Cataliotti A.; Nuccio S (2005). A Chirp-Z transform-based synchronizer for power system measurements, *IEEE Transaction on Instrument Measurement*, Vol. 54, No. 3, (2005), pp. 1025–1032.

ATPDraw for Windows 3.1x/95/NT version 1.0 User's Manual, Trondheim, Norway 15th October 1998.

Baggini A. (2008), *Handbook of Power Quality*, John Wiley & Sons Ltd, The Atrium, Southern Gate, Chichester,West Sussex PO19 8SQ, England, 2008.

Behera, H.S. Dash, P.K.; Biswal, B. Power quality time series data mining using S-transform and fuzzy expert system, (2010) *Applied Soft Computing*, Vol. 10, (2010), pp. 945–955.

Bollen, M.H.J.; GU, Y.H. (2006) Signal Processing of Power Quality Disturbances, *Institute of Electrical and Electronics Engineers*, Published by John Wiley & Sons, Inc.

Cortes, C, Vapnik, V. Support vector networks. *Machine Learning*, Vol. 20, pp. 273-297, 1995.

Dowdy, S.; Wearden, S.; Statistics for Research, Wiley, 1983. ISBN 0471086029, pp. 230.

Eristi, H.; Y. Demir, A new algorithm for automatic classification of power quality events based on wavelet transform and SVM, *Expert Systems with Applications*, Vol. 37, (2010), pp. 4094–4102.

Flandrin, P.; Rilling, G.; Gonçalvés P. (2004). Empirical mode decomposition as a filter bank, *IEEE Signal Processing Letters*, Vol.11, No.2, (February 2004), pp. 112-114.

Fletcher , T. Relevance Vector Machines Explained, 2010, www .cs .ucl. ac. uk/ sta_ /T .Fletcher/.

Gaing Z.L (2004). Wavelet-based neural network for power disturbance recognition and classification. *IEEE Transaction on Power Delivery*, Vol.19, No.4, (2004), pp. 1560–1568.

Gargoom, M.; Wen, N.E.; Soong, L. (2008). Automatic Classification and charachterization of power quality events. *IEEE Transaction on Power Delivery*, Vol. 23, No. 4, (2008), pp. .

Gu, Y.H.; M.H.J., Bollen (2000). Time-frequency and time-scale domain analysis of voltage disturbances, *IEEE Transaction on Power Delivery*, Vol. 15, No. 4, (October 2000), .

Gunal, S.; Gerek, O.N.; Ece, D.G.; Edizkan, R (2009). The search for optimal feature set in power quality event classification. *Expert Systems with Application*, Vol. 36, (2009), pp. 10266–10273.

Heydt, G.T.; Fjeld P.S.; Liu, C.C.; Pierce, D.; Tu, L.; Hensley, G. (1999) Applications of the windowed FFT to electric power quality assessment. *IEEE Transaction Power Delivery*, Vol. 14, No. 4, (1999), pp. 1411–1416.

Hooshmand, R.; Enshaee, A.; (2010) Detection and classification of single and combined power quality disturbances using fuzzy systems oriented by particle swarm optimization algorithm, *Electric Power Systems Research*, Vol. 80, (2010), pp. 1552–1561.

Hsieh, C.T.; Lin, J.M.; Huang, S.J. (2010). Slant transform applied to electric power quality detection with field programmable gate array design enhanced, *Electrical Power and Energy Systems*, Vol. 32, (2010) pp. 428–432.

Huang, N.E.; Shen, Z.; Long, S.R.; Wu, M.C.; Shih, H.H.; Yen, Q.Z.N. ; Tung, C.C.; Liu, H.H.; The empirical mode decomposition and the Hilbert spectrum for nonlinear and non-stationary time series analysis, *Proc. R. Soc. Lond. A*, Printed in Great Britain (1998), 454, pp. 903-995.

Huang, N.; Xu, D.; Liu, X. (2010), Power Quality Disturbances Recognition Based on HS-transform, *First International Conference on Pervasive Computing Signal Processing and Applications (PCSPA)*, Issue Date: 17-19 Sept. 2010.

IEEE 1159: 1995, Recommended practice for monitoring electric power quality, 1995.

Jayasree, T.; Devaraj, D.; Sukanesh, R (2010). Power quality disturbance classification using Hilbert transform and RBF networks, *Neurocomputing*, Vol. 73, (2010), pp. 1451–1456.

Kaewarsa, S.; Attakitmongcol, K.; Kulworawanichpong, T. (2008), Recognition of power quality events by using multi wavelet-based neural networks. *International journal of Electric Power Energy and System*, Vol. 30, (2008), pp. 254–260.

Kittler, J. Feature set search algorithms. In C. H. Chert (Ed.), Pattern recognition and signal processing, 1978, pp. 41–60. Mphen aan den Rijn, Netherlands:Sijthoff and Noordhoff.

Kohavi, R.; Quinlan, R.; Decision Tree Discovery, Data Mining, University of New South Wales, Sydney 2052 Australia, 1999.

Kschischang, F.R.; The Hilbert Transform, Department of Electrical and Computer Engineering University of Toronto, October 22, 2006.

Landwehr, N., Hall, M., and Frank, E., Logistic Model Tree, *Machine Learning*, Springer Science, Vol. 59, (2005) pp.161-205.

Liao, Y.; Lee, J.B.; A fuzzy-expert system for classifying power quality disturbances, *Electrical Power and Energy Systems*, (2004), Vol. 26, pp. 199–205.

Lu, Z.; Smith, J.S.; Wu, Q.H.; Fitch, J. (2005) Empirical mode decomposition for power quality monitoring, *2005 IEEE/PES Transmission and Distribution Conference & Exhibition: Asia and Pacific Dalian*, China.

Mao, K.Z.; Tan, K.C.; Ser, W. Probabilistic neural-network structure determination for pattern classification, *IEEE Transaction on Neural Networks*, Vol. 11, (2000), pp. 1009-1016.

Marill, T.; Green, D.M.; (1963), On the effectiveness of receptors in recognition systems. *IEEE Transaction on Information Theory*, Vol. 9, (1963), pp. 11–17.

MATLAB 7.4 Version Wavelet Toolbox, Math Works Company, Natick, MA. (MATLAB)

Meher, S.K. (2008), A Novel Power Quality Event Classification Using Slantlet Transform and Fuzzy Logic, (2008) *International Conference on Power System Technology India*, 2008.

Mehera, S.K.; Pradhan, A.K.; Panda, G. (2004). An integrated data compression scheme for power quality events using spline wavelet and neural network. *Electric Power Systems Research*, Vol. 69, (2004), pp. 213–220.

Mishra, S.; Bhende, C.N.; Panigrahi, B.K. (2008) Detection and classification of power quality disturbances using S-transform and probabilistic neural network, *IEEE Transaction on Power Delivery*, Vol. 23, No. 1, (January 2008), pp. 280–287.

Moravej, Z.; Vishvakarma, D.N.; Singh, S.P.; (2002) Protection and condition monitoring of power transformer using ANN. *Electric Power Components and systems*, Vol.30, No.3, (March 2002), pp. 217-231.

Moravej, Z.; Vishwakarma, D.N.; Singh, S.P. (2003) Application of radial basis function neural network for differential relaying of a power transformer, *Computers & Electrical Engineering*, Vol.29, No.3, (May 2003) pp. 421-434.

Moravej, Z. ; Banihashemi, S.A.; Velayati, M.H. (2009), Power quality events classification and recognition using a novel support vector algorithm. *Energy Conversion and Management,* Vol. 50, (2009), pp. 3071-3077.

Moravej Z.; Abdoos A.A.; Pazoki M. (2010). Detection and classification of power quality disturbances using wavelet transform and support vector machines. *Electric Power Components and Systems*, Vol.38, (2010), pp. 182–196.

Moravej Z. Pazoki M,; Abdoos A.A (2011). Wavelet transform and multi-class relevance vector machines based recognition and classification of power quality disturbances, *European Transaction on Electrical Power*, Vol.21, No.1, (January 2011), pp. .

Moravej, Z.; Abdoos, A.A.; Pazoki, M.; (2011), New Combined S-transform and Logistic Model Tree Technique for Recognition and Classification of Power Quality Disturbances, *Electric Power Components and Systems*, Vol.39, No.1, (2011), pp. 80-98.

Oleskovicz, M.; Coury, D.V.; Felho, O.D.; Usida, W.F.; Carneiro, A.F.M.; Pires, R.S.; Power quality analysis applying a hybrid methodology with wavelet transforms and neural networks. *Electrical Power and Energy Systems*, Vol. 31, (2009), pp. 206–212.

Panda, G.; Dash, P.K.; Pradhan, A.K.; & Meher S.K. (2002). Data Compression of Power Quality Events Using the Slantlet Transform, *IEEE Transaction on Power Delivery*, Vol.17, No.2, (April 2002), pp. 662-662.

Peng, H.; Long, F.; Ding C.; (2005). Feature Selection Based on Mutual Information: Criteria of Max-Dependency, Max-Relevance, and Min-Redundancy. *IEEE Transaction on Pattern Analysis and Machine Intelligence*, Vol.27, No.8, (August 2005), pp. 1226-1238.

Pinnega, C.R.; Mansinha L.; The S -transform with windows of arbitrary and varying shape. *Geophysics*, Vol. 68, (2003), pp. 381–385.

Proceedings of the Workshop on Feature Selection for Data Mining: Interfacing Machine Learning and Statistics in conjunction with the *2005 SIAM International Conference on Data Mining* April 23, 2005 Newport Beach, CA.

PSCAD/EMTDC Power systems simulation Manual, Winnipeg, MB, Canada, 1997.

Pudil, P.; Novovicova, J.; Kittler, J. (1994), Floating search methods in feature selection. *Pattern Recognition Letters*, Vol. 15, (1994), pp. 1119–1125.

Rathina Prabha, N.; Marimuthu, N.S.; Babulal, C.K. (2009). Adaptive neuro-fuzzy inference system based total demand distortion factor for power quality evaluation, *Neurocomputing*, Vol. 73, (2009), pp. 315–323.

Rilling, G.; Flandrin, P.; Gonçalvés, P. (2003).ON Empirical mode decomposition and its algorithm. (2003) *IEEE-EURA SIP Workshop on Nonlinear Signal and Image Processing* NSIP-03, Grado (I), 2003.

Rioul, O.; Vetterli, M. (1991). Wavelet and Signal Processing. *IEEE Signal Processing Magazine,* Vol. 8, No. 4, (October 1991), pp. 14 – 38.

Rodgers, J.L.; Nicewander, W.A. (1988). Thirteen ways to look at the correlation coefficient. *The American Statistician*, Vol. 42, (1988), pp. 59–66.

Sahu, S.S.; Panda G.; George, N.V. (2009). An improved S-transform for time-frequency analysis. *IEEE International Advance Computing Conference* (IACC 2009) Patiala, India, 6-7 March 2009, pp. 315-319.

Selesnick, I.W. (1999), The Slantlet Transform, *IEEE Transaction On Signal Processing*, Vol.47, No.5, (May 1999), pp. 1304-1313.

Shukla, S.; Mishra, S.; Singh, B. (2009). Empirical-mode decomposition with Hilbert transform for power-quality assessment, *IEEE Transaction on Power Delivery*, Vol. 24, No. 4, (October 2009), pp. 2159-2165.

Son, Y.S.; Baek, J.; A modified correlation coefficient based similarity measure for clustering time-course gene expression data, *Pattern Recognition Letters*, Vol. 29, (2008) pp. 232-242.

Specht, D.F.; Probabilistic neural network. *Neural networks*, Vol. 1, pp.109-118, 1990.

Stearn, S.D.; On selecting features for pattern classifiers. In *Proceedings of the third international conference on pattern recognition*, 1976, pp. 71–75, Coronado,CA.

Steinwart, A. Christmann. Support Vector Machines; New York: Springer, 2008.

Stockwell, R.G (1991). Why use the S-transform?. Northwest Research Associates, Colorado Research Associates Division, 3380 Mitchell Lane, Boulder Colorado USA 80301. American Mathematical Society 1991.

Stockwell, R.G.; Mansinha, L.; Lowe, R.P. (1996). Localization of the complex spectrum: the S-transform. *IEEE Transactions on Signal Processing*, (1996), Vol. 4, pp. 998–1001.

Tipping, M.E. (2000), the relevance vector machine. Solla SA, Leen TK, Muller KR. *Advances in Neural Information Processing Systems* 2000; 12: MIT Press, Cambridge, MA.

Tipping ME. The Relevance Vector Machine. Microsoft Research, U.K, 2000.

Tzikas, G.D.; Wei, L.; Likas, A.; Yang, Y.; Galatsanos, N.P. (2006). A tutorial on relevance vector machines for regression and classification with applications, University of Ioannina, Ioanni, GREECE, Illinois Institute of Technology, Chicago, USA, 2006.

Uyar, M.; Yildirim, S.; Gencoglu, M.T.; (2009). An expert system based on S-transform and neural network for automatic classification of power quality disturbances, *Expert Systems with Applications*, Vol. 36, (2009), pp. 5962–5975.

Uyara, M.; Yildirima, S. & Gencoglub MT (2008). An effective wavelet-based feature extraction method for classification of power quality disturbance signals. *Electric Power System Research*, Vol. 78, (2008), pp. 1747–1755.

Vapnik, V.N. Statical Learning Theory; Wiely: New York, 1998.

Whitney, A.W. (1971) A direct method of nonparametric measurement selection. *IEEE Transaction on Computers*, Vol.20, (1971), pp. 1100-1103.

Yang, J.; Honavar, V. (1998), Feature subset selection using a genetic algorithm. *IEEE Intelligent Systems and their Applications*, Vol. 2, (1998), pp. 44–49.

Zhang, M.; Li, K.; Hu, Y.; (1998) A real-time classification method of power quality disturbances, *Electric Power Systems Research*, Vol. 81, (1998), pp. 660–666, 2011.

Methodes of Power Quality Analysis

Gabriel Găspăresc
"Politehnica" University of Timişoara
Romania

1. Introduction

In the last decades electronics and telecommunications have known an unprecedented development, the number of non-linear loads (power electronics) has increased. New more energy efficient devices and equipments, controlled by microprocessors, have appeared. They are also more sensitive to electromagnetic disturbances, produced by neighborhood devices or as a result of the shared infrastructure, which can affect the power quality for many industries or even for the domestic consumers. A poor power quality can cause the malfunction of electrical and electronic devices and equipments, instability, short lifetime. In case of computers the disturbances may lead to: corrupted files, losing files and to the destruction of the hardware components. Additional costs can occur for both, suppliers and consumers (for instance, after a power interruption on a production line a certain time is needed to restart, which leads to a reduction in production) (Bollen et al., 2006), (Dungan et al., 2004), (Ignea, 1998).

Simultaneously, the expansion of the suppliers, the competition on the market, the increase of the studies in this field, the better informed customers have led nowadays to higher requirements for power quality. Both categories, the suppliers and the consumers are more concerned about the power quality. In order to satisfy consumers' requirements, suppliers have invested in more energy efficient equipments. Frequently, just these are affected by power problems, and they become in turn disturbances sources.

A power quality monitoring system provides huge volume of raw data from different locations, acquired during long periods of time and the amount of data is increasing daily (Barrera Nunez et al., 2008). The visual inspection method is laborious, time consuming and is not a solution. Features extraction of power quality disturbances using methods of power quality analysis, in order to achive automatic disturbance recognition, is important for understanding the cause-effect relation and to improve the power quality.

Features extraction of power quality disturbances using methods of power quality analysis, in order to achive automatic disturbance recognition, is important for understanding the cause-effect relation and to improve the power quality.

The classical method of power quality analysis used in power quality monitoring sytems has been the discrete Fourier transform (DFT). Nowadays new methods has been proposed in literature: short time Fourier transform (STFT) (Bollen et al., 2006), discrete wavelet transform (DWT) (Driesen et al., 2003) and discrete Stockwell transform (DST) (Gargoom, 2008). Sometimes those methodes are integrated in company with fuzzy logic (FL) (Chilukuri et al., 2004), artificial neural networks (ANN) (Dash, 2007), (Gang, 2004) or super vector machines (SVM) (Yong, 2005). A comparative study is presented as follows.

2. Discrete Fourier transform

In Fourier analysis a signal is decomposed into a sum of sinusoidal signals (harmonics). The Fourier transform is a mathematical transformation from the time domain to the frequency domain.

The Discrete Fourier Transform (DFT) provides frequency domain analysis of discrete periodic signals. For such a signal $x[n]$ with finite length N the Fourier transform is defined according to next relation

$$X(k) = \sum_{n=0}^{N-1} x[n] e^{-j\frac{2\pi}{N}kn} \tag{1}$$

where $k=0,1,\dots,N-1$.

For the input signal $x[n]$ if the number of samples N is power of 2 it can be applied FFT (Fast Fourier Transform) algorithm. The aim of the algorithm is to reduce the number of operations and implicit the calculation time.

The use of Fourier transform for signals affected by electromagnetic disturbances reveals changes of spectral components of initial signals caused by the disturbances presence. Fig. 1 shows a sinusoidal signal disturbed with harmonic distortions. From the frequency spectrum, obtained appling FFT on this signal, are calculated the odd harmonic orders: the 3rd, 5th and 7th.
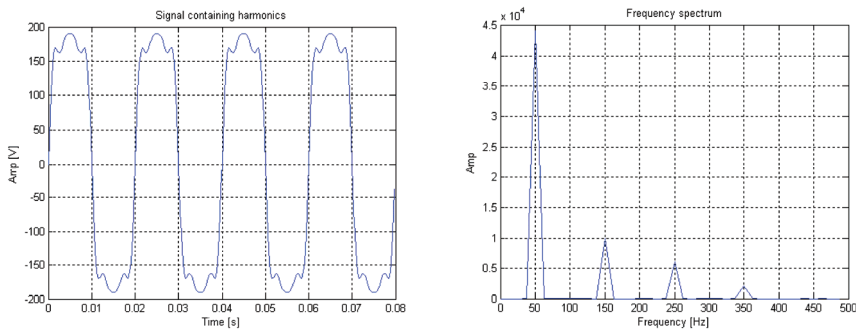
Fig. 1. Harmonic distortions
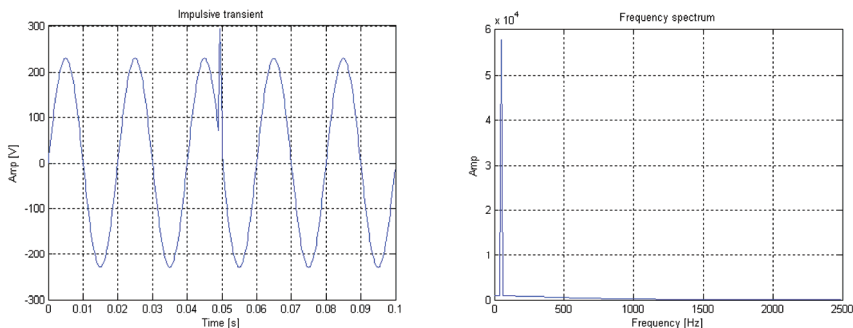
Fig. 2. Impulsive transient

In most cases the power quality disturbances are nonstationary and nonperiodic. For power quality analysis is useful to achive time localization of the disturbances (determining the start and end times of the event) which can not be done by Fourier transform. The limitation is obvious especially for transient phenomenas (quick variations), difficult to observe visually. In Fig. 2 is considered a sinusoidal signal disturbed with an impulsive transient. Like in Fig. 1 below, the frequency spectrum provides informations about frequency spectral components but no information about time localization.

3. Short time Fourier transform

The Short-Time Fourier Transform (STFT) provides informations in time domain (start time, stop time, rise time, duration) and frequency domain about disturbances. Usually signals parameters (amplitude, frequency, phase) are not constants in time and the signals are nonstationary. For a discrete signal $x[n]$ the discrete transform is defined

$$X[n,\lambda] = \sum_{m=-\infty}^{\infty} x[n+m] \, w[m] \, e^{-j\lambda m} \tag{2}$$

where $w[m]$ is a window function with size L.
Usually the number of samples N of the signal $x[n]$ is finite and the window $w[m]$ has the next expression

$$\begin{aligned} w[l] \neq 0, \text{ for } 0 \leq l \leq L-1 \\ w[l] = 0, \text{ for } l < 0 \text{ and } l \geq L \end{aligned} \tag{3}$$

where L is window size.
The window size L can be smaller or equal to N, the number of samples of signal $x[n]$

$$N \geq L \tag{4}$$

Relation (2) becomes

$$X[n,\lambda] = \sum_{l=0}^{L-1} x[n+l] \, w[l] \, e^{\frac{jl\lambda}{N}} \tag{5}$$

The square modulus of short time Fourier transform is called spectrogram and is a time-frequency representation.
Power quality disturbances cover a broad frequency spectrum, starting from a few Hz (flicker) to a few MHz (transient phenomenas). The frequency spectrum of a signal affected by a transient voltage contains high frequency components and also low frequency components. It is difficult to analyze such a signal using the STFT because the window size and implicit time-frequency resolution are fixed.

3.1 Window functions
The window functions are useful for time domain smoothing of acquired signals, reduction of spectral distortions and better resolution.
Main parameters of window function are:
-    main lobe width;

- side lobe attenuation;
- minimum stopband attenuation.

The main lobe width has influence on frequency resolution. The possibility to distinguish two signals with close frequencies increases when the lobe width decreases, but for a narrow lobe the energy of side lobes increase against main lobe energy. The results are the increase of side lobe amplitudes and attenuation. Consequently, it is necessary a compromise between time and frequency resolution. A narrow window provides a good time resolution while a large one is useful for good frequency resolution.

Figure 3 shows the time domain and frequency domain representations of the rectangular, Hanning and Hamming window.
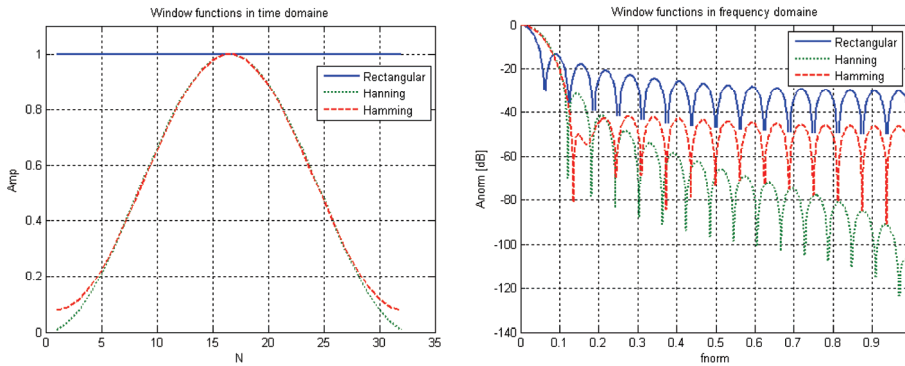
Fig. 3. Window functions

The rectangular window is defined in the next relation

$$w(n) = 1 \tag{6}$$

where *n=0,1, 2, N-1* and *N* is window size.

This function (fig. 3) provides just time truncation of signals, it does not affect the amplitudes of signals and the spectral distortions are the biggest from window functions. It is useful in analysis of transient disturbances with duration smaller like window size and close amplitudes.

The Hanning window is defined as

$$w(n) = 0,5 + 0,5 \cos\left(\frac{2n\pi}{N}\right) \tag{7}$$

where n=0,1, 2, N-1.

The window has lower side lobes like previous function (fig. 3). It is used for transient disturbances with duration bigger like window size, usually when the signals components are not knowed

The Hamming window is described in next relation

$$w(n) = 0,54 + 0,46 \cos\left(\frac{2n\pi}{N}\right) \tag{8}$$

where n=0,1, 2, N-1.

In time domain the window has a shape similar to the Hanning window (fig. 3), the differences are: the ends of window are not so close to zero, in frequency domain the side lobes are lower and main lobe width is larger. It is used specially for sinusoidal signals with close frequencies.

The table 1 shows the side lobe level of smoothing windows: the rectangular window has the lowest attenuation level and the Hamming window has the highest value.

Window function	Side lobe level [dB]
Rectangular	-13
Hanning	-31
Hamming	-42

Table 1. Side lobe level of smoothing windows

3.2 Using the STFT-transform for transient signal analysis

A sinusoidal signal with frequency of 50 Hz is disturbed by an oscillatory transient with the frequency of 1000 Hz. The obtained spectograms for rectangular, Hanning and Hamming windows, with size 16, are presented in figure 4.
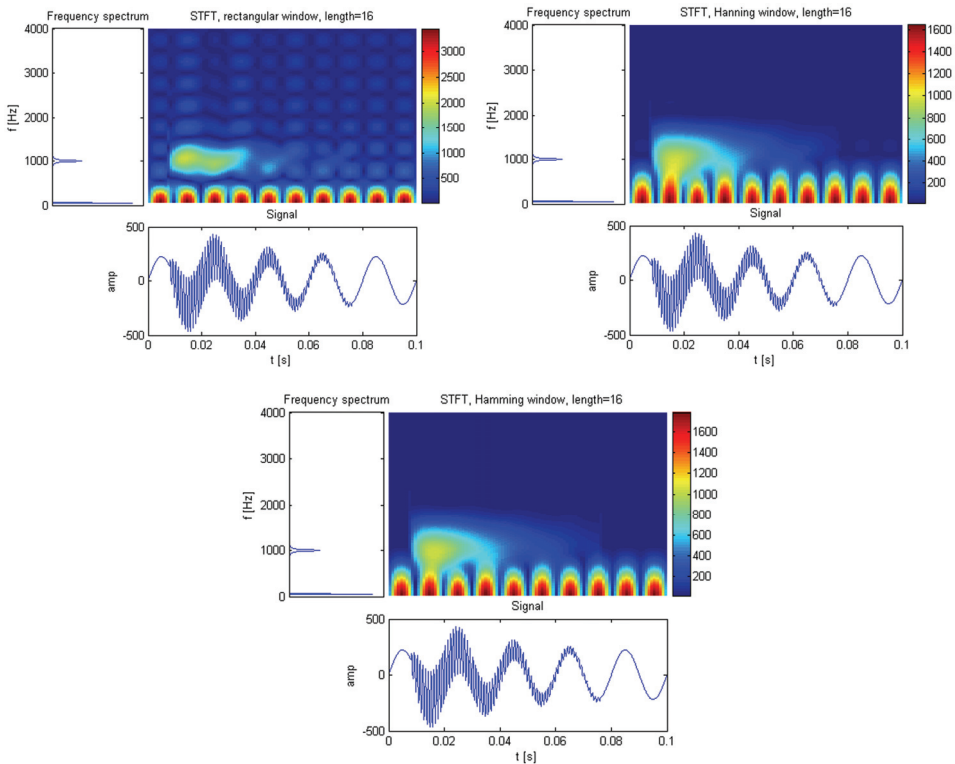
Fig. 4. STFT of an oscillatory transient

From previous figure it can be seen that for rectangular window the spectral distorsions are the biggest, it fallows Hanning window with smaller distortsions and Haming window with the smallest distortsions (according to Table 1). Suplementary, for the disturbance it can be observed the start time, stop time, duration and frequency domain.

The influence of window size is shown in figure 5. The increase of window size it has increased also the resolution in frequency domain, but has decreased the resolution in time domain. In figure 5, for the window with the largest width, it can be seen that the maximum spectral component is 1000 Hz and this value is the frequency of oscillatory transient overlapped on the sinusoidal signal. In the time domain appears a sliding to zero in comparison with the rest of spectrograms.
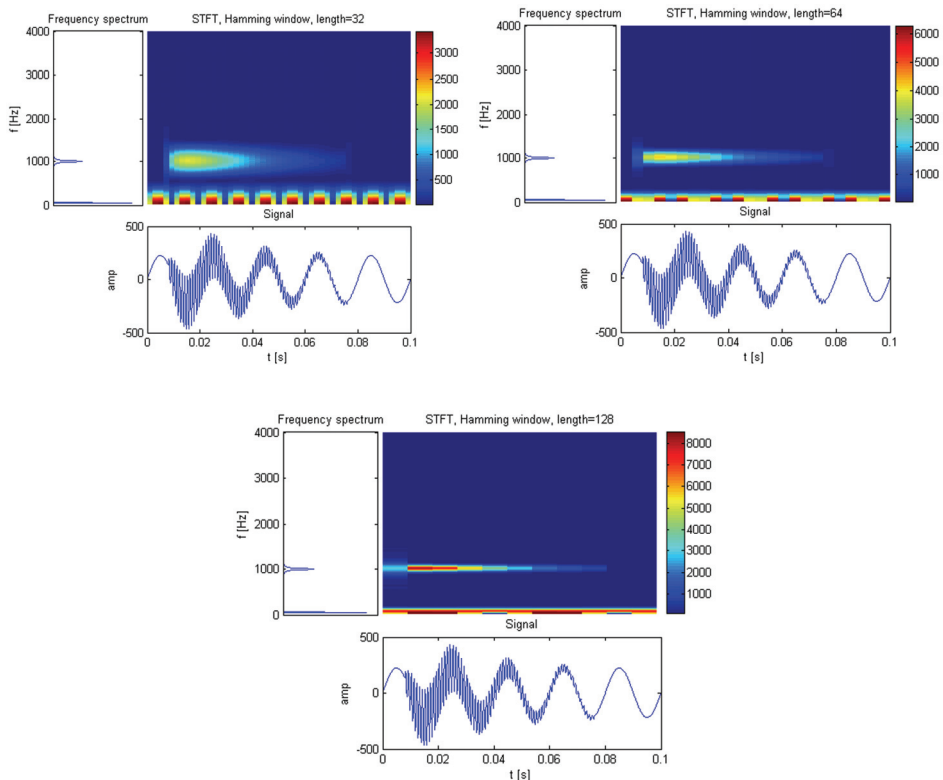
Fig. 5. Influence of window size on time and frequency resolution

A solution to obtain high resolution in the time domain and also in the frequency domain is to use two window functions with different size: a narrow window for good time resolution and a large window for good frequency resolution. Than the STFT is applied two times using both windows. But this method has a disadvantage, it increases the number of operations.

Figure 6 shows the spectrograms obtained for a sinusoidal signal with frequency of 50 Hz disturbed by an oscillatory transient with the frequency of 1500 Hz (the sampling rate is

8000 Hz). The first spectogram is obtained using a narrow window (16 samples) and is useful for time localization. For the second spectrogram is used a large window (480 samples). In this case it can be seen the frequency of the oscillatory transient.
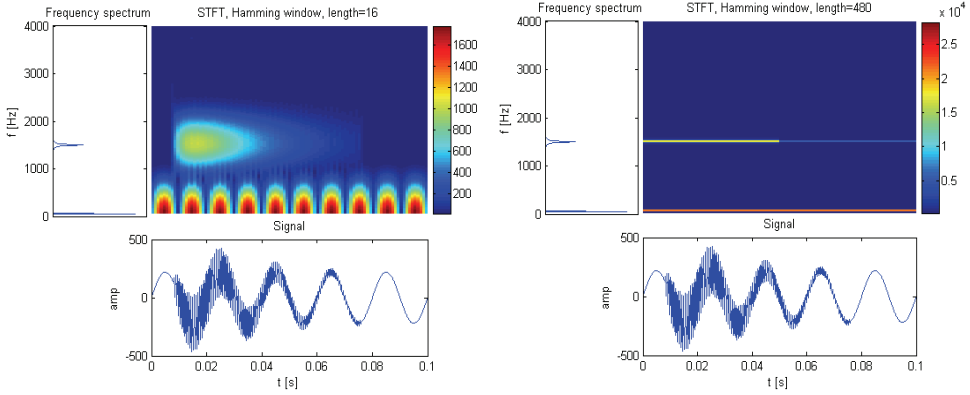
Fig. 6. Using STFT with two window functions

4. Discrete wavelet transform

The wavelet transform is an alternative solution in order to overcome the limitations of STFT. Multiresolutions signal decompositon is based on subbads decomposition using low-pass filtering and high-pass filtering. This transform ensure progressive resolution for time localization and characterization of the transient phenomenas.
The Fourier analysis decomposes a signal into a sum of harmonics and wavelet analysis into wavelets. A wavelet is a waveform of limited duration, usually irregular and asymmetric.
For a discrete signal $x[n]$ the discrete transform is defined

$$x(t) = A_{j_0}(t) + \sum_{j=0}^{j_0} D_j(t) \tag{9}$$

where

$$A_j(t) = \sum_k c_j(k)\varphi_{j,k}(t) \tag{10}$$

$$D_j(t) = \sum_k d_j(k)\Psi_{j,k}(t) \tag{11}$$

$c_j(k)$ are the scaling function coefficients and $d_j(k)$ are the wavelet function coefficients, j_0 is the scale and $\varphi(t)$ is the scaling function.
For a given signal $x(t)$ and a three level wavelet decomposition the relation (9) become

$$x(t) = A_1 + D_1 = A_2 + D_2 + D_1 = A_3 + D_3 + D_2 + D_1 \tag{12}$$

and at each decomposition level the signal is split into an approximation and a detail.

In order to classify the disturbances using disturbances patterns is necessary to calculate the deviation between the energy distributions of the disturbed signal and the clean signal (Vega, 2009), (Resende, 2001)

$$dp(j)[\%] = \left[\frac{en\_dist(j) - en\_ref(j)}{en\_ref(m)} \right] * 100 \qquad (13)$$

where
j is the wavelet transform level;
$dp(j)[\%]$ is the deviation between the energy distributions;
$en\_dist(j)$ is the energy distribution of the disturbed signal;
$en\_ref(j)$ is the energy distribution of the clean signal (or fundamental component of the disturbed signal).
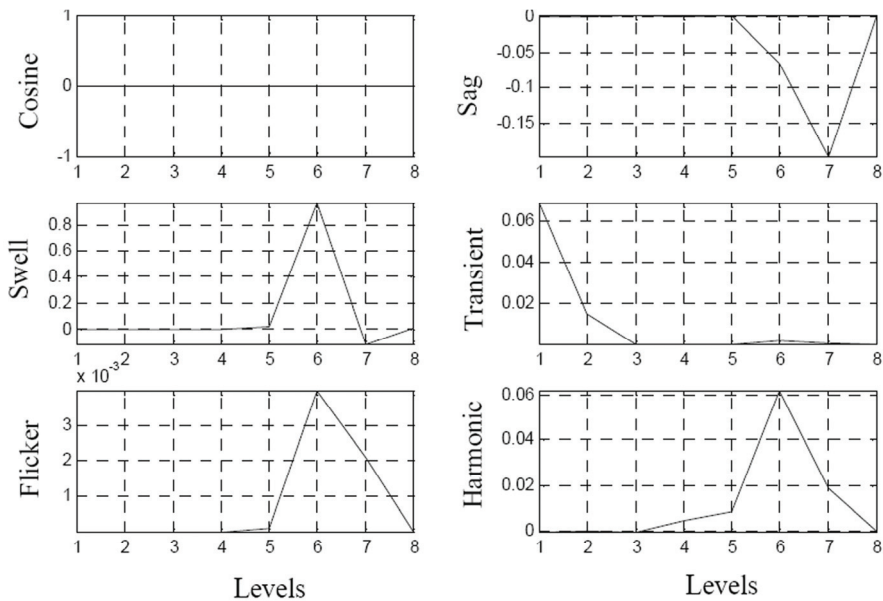
Fig. 7. Disturbances patterns

The energy distributions are calculated based on Parseval's theorem: "the energy that a time domaine function contains is equal to the sum of all energy concentrated in in the different resolution levels of the corresponding wavelet transformed signal" (Resende, 2001). According to this theorem we have (Gaouda, 1999)

$$\sum_{n=1}^{N} |f(n)|^2 = \sum_{n=1}^{N} |a_J|^2 + \sum_{j=1}^{J} \sum_{n=1}^{N} |d_j(n)|^2 \qquad (14)$$

where
$f(n)$ is the time domaine signal;

N is the number of signal samples;
the total energy of the *f(n)* signal is

$$\sum_{n=1}^{N}|f(n)|^2 \qquad (15)$$

the total energy concentrated in the level *j* of the approximation coefficient is

$$\sum_{n=1}^{N}\left|a_J\right|^2 \qquad (16)$$

the total energy concentrated in the detail coefficients (from level 1 to level *j*) is

$$\sum_{j=1}^{J}\sum_{n=1}^{N}\left|d_j(n)\right|^2 . \qquad (17)$$

In figure 7 (Duarte, 2006) are shown the disturbances patterns for the main types of power quality disturbances.

4.1 Using the discrete wavelet transform for transient signal analysis

A sinusoidal signal with frequency of 50 Hz is disturbed by an oscillatory transient with the frequency of 1000 Hz. The Daubechis "db10" function is used as mother wavelet (figure 8) and the signal is decomposed using 8 decomposition levels (figure 9). It can be seen that the coefficients D_2 and D_3 (Fig. 9) provide information on time localization of the oscillatory transient (start time, stop time, duration), magnitude and frequency spectrum.

Fig. 8. The Daubechis "db10" function

Decomposition level	Frequency Band [Hz]
1	1920-3840
2	960-1920
3	480-960
4	240-480
5	120-240
6	60-120
7	30-60
8	15-30
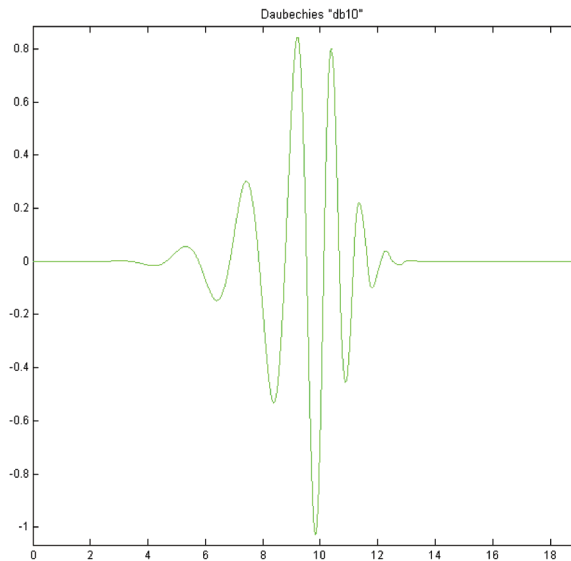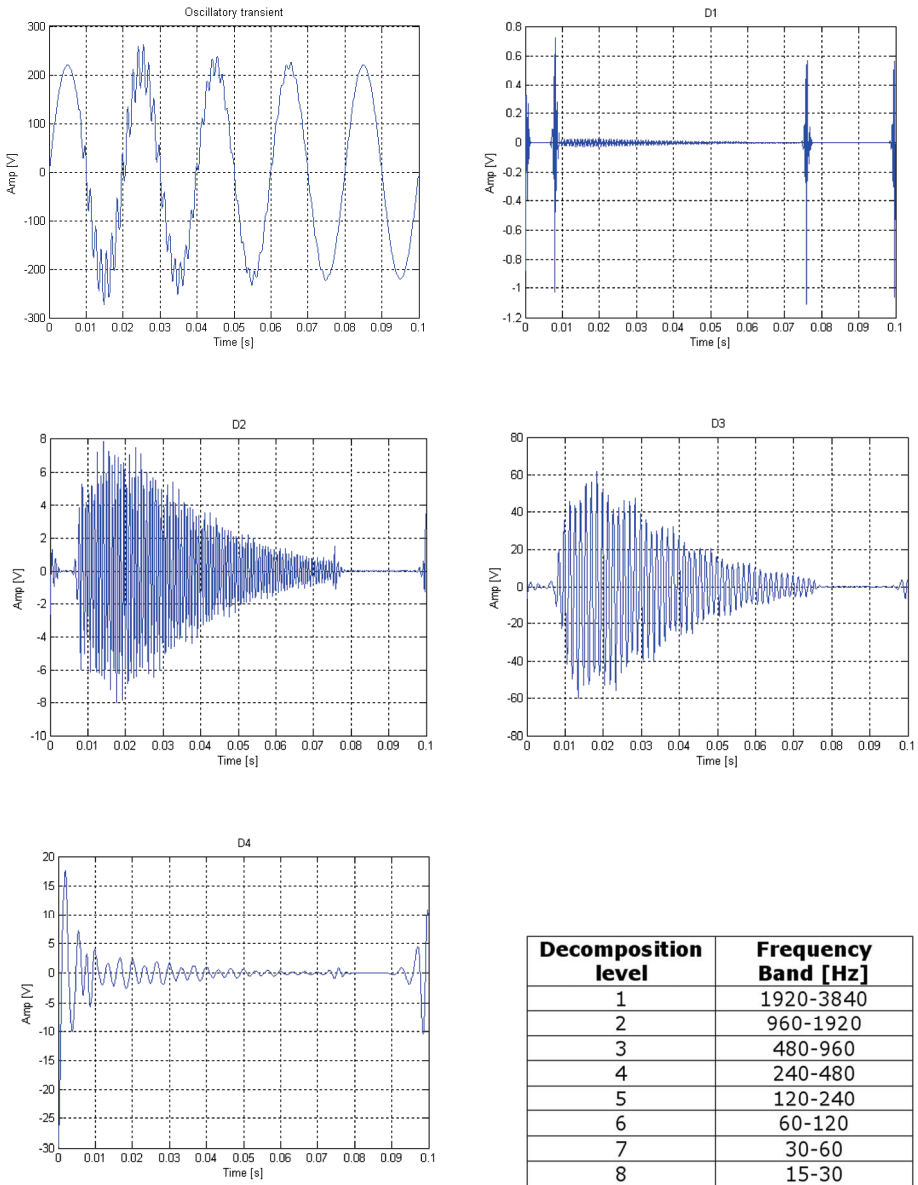
Fig. 9. Eight-level discrete wavelet decomposition

Figure 10 shows that the energy is concentrated in the frequency bands of decomposition levels two and three (240-960 Hz) and the event is classified as low-frequency transient (Resende, 2001).
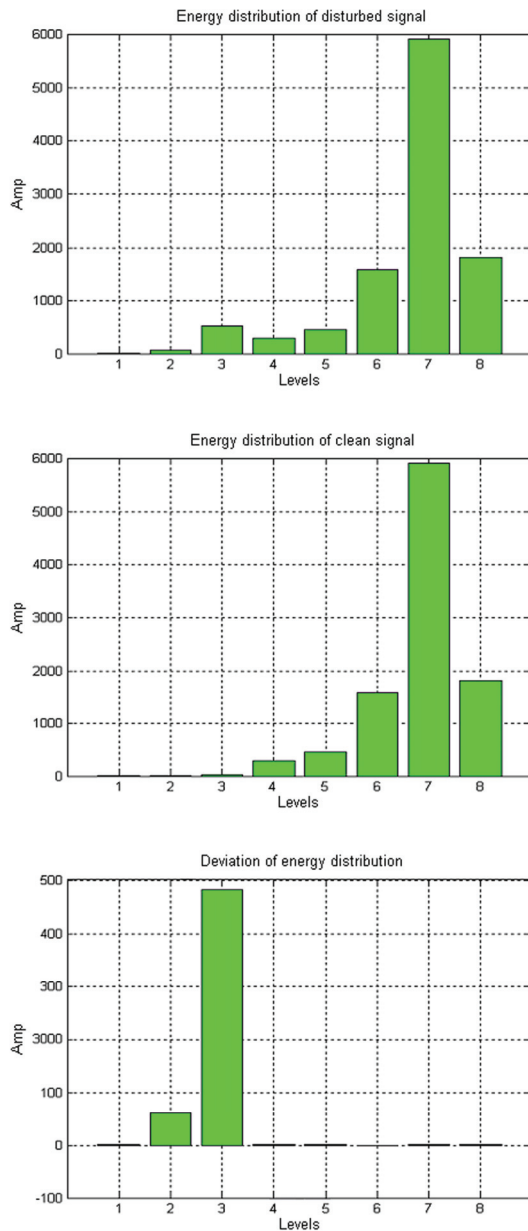
Fig. 10. Energy distribution

5. Discrete Stockwell transform

The discrete Stockwell transform (DST) of the N point time series $h[kT]$ is

$$S\left[jT,\frac{n}{NT}\right] = \sum_{m=0}^{N-1} H\left[\frac{m+n}{NT}\right] e^{-2\pi^2 m^2/n^2} \; e^{i2\pi mj/N} \tag{18}$$

where $n\neq0$ and *H[n/NT]* is the Fourier transform of time series.

The STFT transform limitation is the fixed window width, chosen *a priori*, for analysis of nonstationary signals containing low-frequency and high-frequency components. Consequently, the frequency-time resolution is fixed too and is difficult to analyze a sinusoidal signal of low frequecy (for instance the signal from power supply network) affected by a high frequency disturbance (for instance a transient phenomenon).

The wavelet transform limitations are: low resolution for low-frequency components, the decomposition frequency bands are fixed, noise sensitivity.

The S transform is an extension of the wavelet transform resulted using a phase correction which provides superior resolution.

Applying DST on a signal the result is a matrix within the rows are frequences and the columns are time values.

5.1 Using the S-transform

To ilustrate the ability of the ST to detect, localize and quantify power quality disturbances are considered two signals. First signal is afected by a voltage swell (low-frequency components) and the second by an impulsive transient (high-frequency components). Figure 11 shows the 3D ST plots for both signals. From the 3D plots can be observed the amplitude variations of the frequency spectral components in the signals.
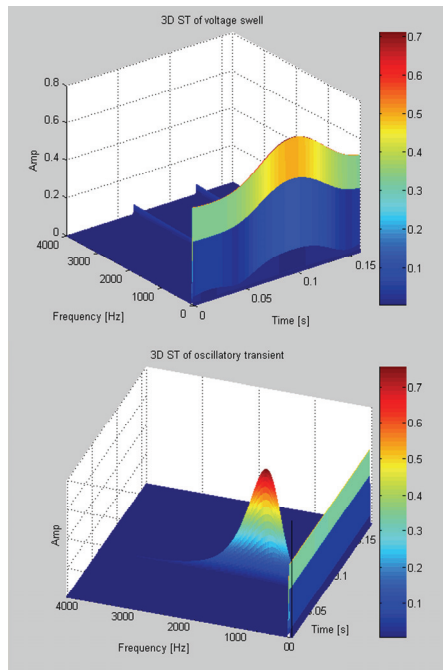
Fig. 11. S-transform 3D representation

Figure 12 presents the ST of a clean signal and six types of power quality disturbances (voltage sag, voltage swell, voltage interruption, voltage harmonics, impulsive transient and oscillatory transient): a) the signal, b) the normalized time-frequency contour of ST, c) the maximum of amplitude-time characteristic of S transform and d) the maximum of amplitude-frequency characteristic of of S transform. From visual inspection of these plots are obtained amplitude, frequency and time information in order to detect, localize and classify the disturbance.
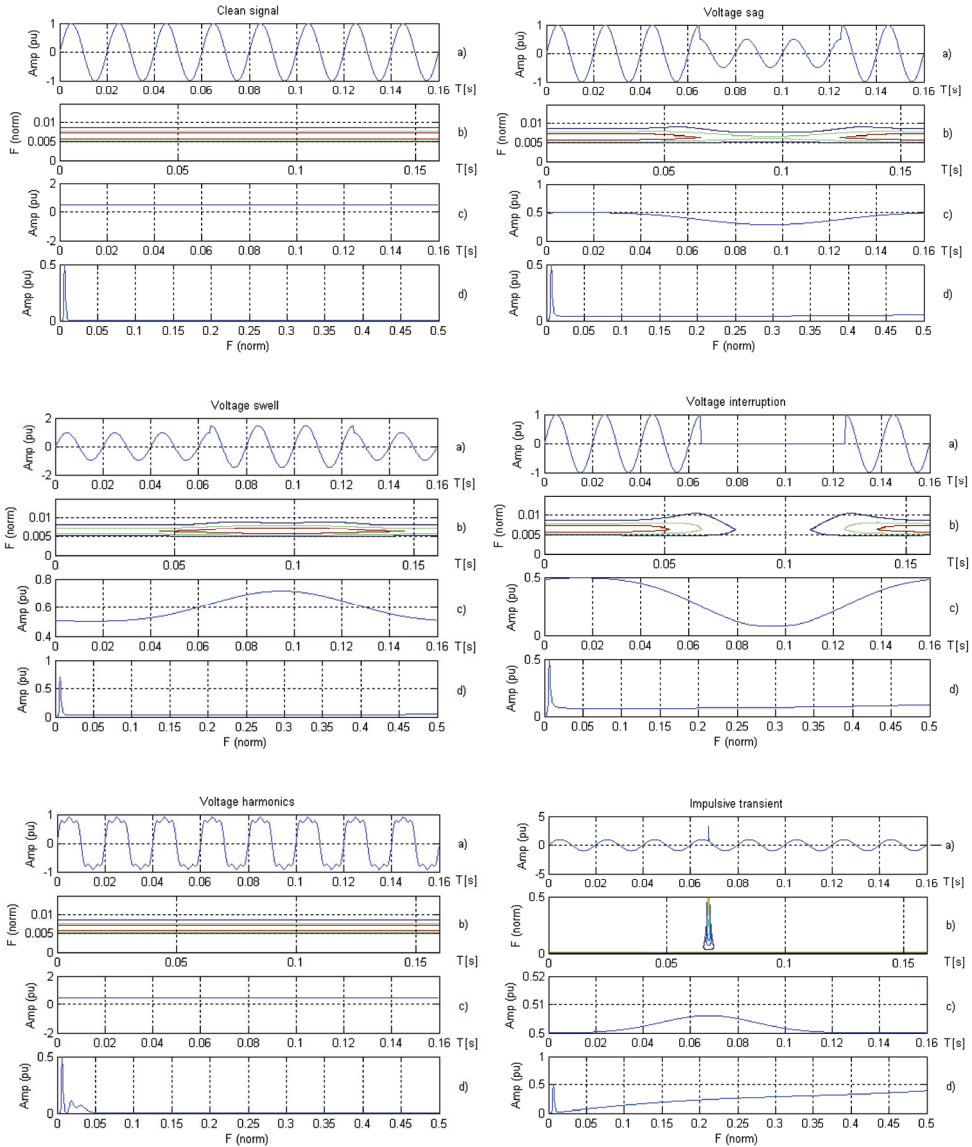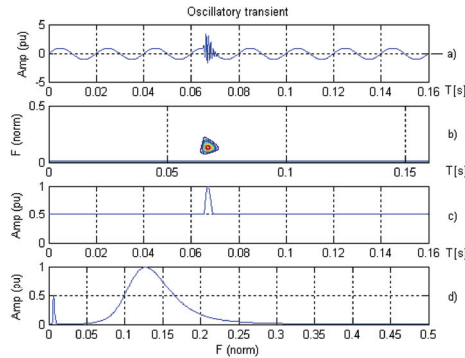
Fig. 12. S-transform

Figure 12 shows that the maximum of amplitude-time characteristic of S transform is constant for the clean signal and voltage harmonics and the maximum of amplitude-frequency characteristic of S transform reflects the changes in frequency domain due the presence of disturbances.

6. Impulsive transient characterization

The power quality disturbances that may occur in power supply networks are classified in various categories (Dungan, 2004): transient phenomenons, short duration variations, long duration variations, voltage imbalances, waveform distortions, power frequency variations and flickers.

Transient phenomenons are sudden and short-duration change in the steady-state condition of the voltage, current or both. These phenomenons are classified in two categories: impulsive and oscillatory transient. The first category has exponential rise and falling fronts and is characterized by magnitude, rise time (the time required for a signal to rise from 10% to 90% of final value), decay time (the time until a signal is greater than ½ from its magnitude) and its spectral content.

In order to calculate the rise time for an impulsive transient (biexponential impulse) is proposed a simple algorithm. First are calculated 10%, 90% and 50% of peak amplitude. Than is necessary a loop to find the sample position of the previous values in waveform. Finally the rise time and the decay time are calculated as the difference between the positions found below. In Fig. 13 *Rise time c* is calculated using the previously described method and *Rise time* is the exact value of rise time. In Fig. 14 *Decay time c* is calculated also using the previous algorithm and *Decay time* is the exact value of decay time.

The result of the rise time calculation depends on sampling frequency. Table 2 contains the informations corresponding to a biexponential impulse (Fig. 13) when the sampling frequency is increased six times: *Ve* represents the exact value of rise time, *V1* and *V2* are the values obtained at low sampling rate and respectively at increased sampling rate, *Er1* and *Er2* are the errors between *V1* and *V2* and respectively *Ve* and *Er1/Er2* is the last column of Table 2.
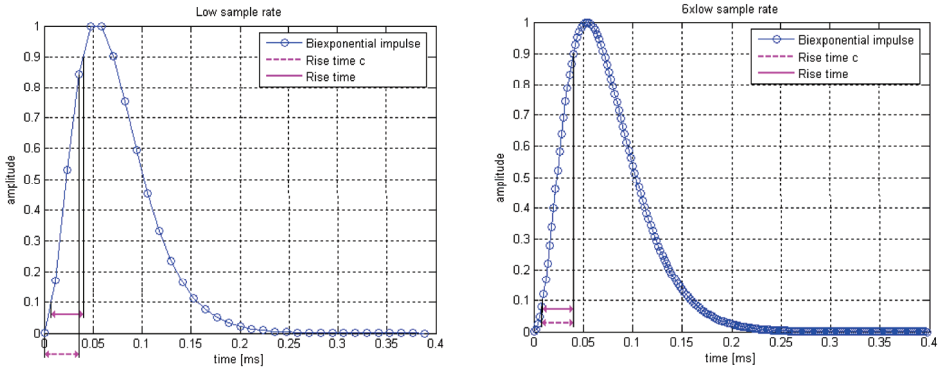
Fig. 13. Influence of sample rate on accuracy of rise time calculation

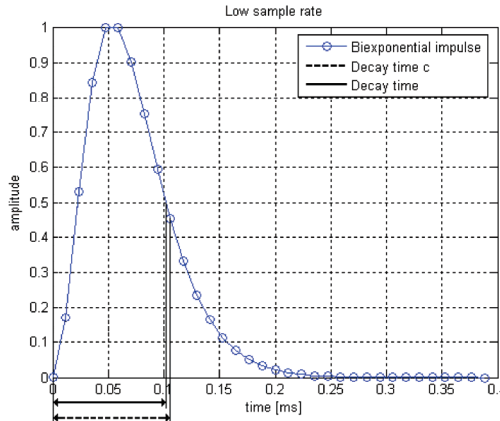|	Ve	V1	V2	Er1 [%]	Er2 [%]	Er1/Er2
Tcr [ms]	31.03	35.3	32	13.761	3.13	4.396

Table 2. Rise time calculation

Fig. 14. Influence of sample rate on accuracy of decay time calculation

7. Conclusion

Nowadays, the researchers must to choose the most appropiate method to analyse the raw data. The main objectiv is features extraction of power quality disturbances in order to achive automatic disturbance recognition. A comparative study between DFT, STFT, DWT and ST is presented accompany with applications in power quality disturbances detection. Supplementary, a solution to improve the STFT analysis is described. Impulsive transients characterization is also presented.

8. References

Amaris, H. ; Alvarez, C. ; Alonso, M. ; Florez, D. ; Lobos, T. ; Janik, P.; Rezmer, J. ; Waclawek, Z. (2009). Computation of Voltage Sag Initiation with Fourier based Algorithm, Kalman Filter and Wavelets, *Proceedings of IEEE Bucharest PowerTech*.

Azam, M. S.; Tu, F.; Pattipati, K. R.; Karanam, R. (2004). A Dependency Model Based Approach for Identifying and Evaluating Power Quality Problems, *IEEE Transactions on Power Delivery* 19(3) , pp. 1154-1166.

Barrera Nunez, V. ; Melendez Frigola, J. ; Herraiz Jaramillo, S. (2008). A Survey on Voltage Dip Events in Power Systems, *Proceedings of the Internatiional Conference on Renewable Energies and Power Quality*.

Bollen, M. H. J.; Gu, I. Y. H. (2006). *Signal Processing of Power Quality Disturbances*, John Wiley & Sons.

Castro, R.; Diaz, H. (2002). An Overview of Wavelet Transform Application in Power Systems, *Proceedings of the 14th Power Systems Computation Conference*.

Chen, S.; Zhu, Y. (2007). Wavelet Transform for Processing Power Quality Disturbances, *EURASIP Journal on Advances in Signal Processing*.

Chilukuri, M. V.; Dash, P. K. (2004). Multiresolution S-Transform-based fuzzy recognition system for power quality events, *IEEE Transaction on Power Delivery* 19(1), pp. 323-330.

Cornforth, D. ; Middleton, R. ; Tusek, J. (2000). Visualisation of Electrical Transients using the Wavelet Transform, *Proceedings of the Internatiional Conference on Advances in Intelligent Systems.*

Dash, P. K.; Nayak, M ; Senapati, M. R.; Lee, I. W. C.. (2007). Mining for similarities in time series data using wavelet-based feature vectors and neural networks, *Engineering Applications of Artificial Intelligence* 20, pp. 185-201.

Dehghani, M. D. (2009). Comparison of S-transform and Wavelet Transform in Power Quality Analysis, *World Academy of Science, Engineering and Technology* 50, pp. 395-398.

Driesen, J. ; Belmans, R. (2002). Time-Frequency Analysis in Power Measurement using Complex Wavelets, *Proceedings of the IEEE International Symposium on Circuits and Systems.*

Driesen, J.; Belmans, R. (2003). Wavelet-based Power Quantification Approaches, *IEEE Transactions on Instrumentation and Measurement* 52(4), pp. 1232-1238.

Duarte, G., Cesar; Vega, G., Valdomiro; Ordonez, P., Gabriel (2006). Automatic Power Quality Disturbances Detection and Classification Based on Discrete Wavelet Transform and Artificial Intelligence, *Proceedings of the IEEE PES Transmission and Distribution Conference and Exposition Latin America*.

Dungan, R. C.; McGranaghan M. F., Santoso S., Beaty H. W. (2004). *Electrical Power System Quality*, McGraw-Hill.

Eldin, E. S. M. T. (2006). Characterisation of power quality disturbances based on wavelet transforms, *International Journal of Energy Technology and Policy* 4(1-2), pp. 74-84.

Fernandez, R. M. C.; Rojas, H. N. D. (2002). An overview of wavelet transforms application in power systems, *Proceedings of the 14th Power System Computational Conference.*

Gang, Z. L. (2004). Wavelet-based neural network for power disturbance recognition and classification, *IEEE Transaction on Power Delivery* 19(4), pp. 1560-1568.

Gaouda, A. M. ; Sultan, M. R. ; Chikhani, A. Y. (1999). Power Quality Detection and Classification Using Wavelet-Multiresolution Signal Decomposition, *IEEE Transaction on Power Delivery* 14(4)*,* pp. 1469-1476.

Gargoom, A. M.; Ertugrul, N., Soong, W. L. (2008). Automatic Classification and Characterization of Power Quality Events, *IEEE Transactions on Power Delivery* 23(4), pp. 2417-2425.

He, H. ; Shen, X., Starzyk, J. A. (2009). Power quality disturbances analysis based on EDMRA method, *International Journal of Electrical Power and Energy Systems* 31, pp. 258-268.

Ignea, A. (1998). *Introducere în compatibilitatea electromagnetică*, Editura de Vest

Jena, G. ; Baliarsingh , R. ; Prasad, G. M. V. (2006). Application of S Transform in Digital Signal/Image, *Proceedings of the National Conference on Emerging Trends in Electronics & Communication*.

Khan, U. N. (2009). Signal Processing Techniques used in Power Quality Monitoring, *Proceedings of the International Conference on Environment and Electrical Engineering*.

Leonowicz, Z. ; Lobos, T. ; Wozniak, K. (2009). Analysis of non-stationary electric signals using the S-transform, *The International Journal for Computation and Mathematics in Electrical and Electronic Engineering* 28(2), pp. 204-2010.

Nath, S. ; Dey, A. ; Chakrabarti, A. (2009). Detection of Power Quality Disturbances using Wavelet Transform, *Journal of World Academy of Science, Engineering and Technology* 49*,* pp. 869-873.

Panigrahi, B. K. ; Hota, P. K. ; Dash, S. (2004). Power Quality Analysis Using Phase Correlated Wavelet Transform, *Iranian Journal of Electrical and Computer Engineering* 3(2)*,* pp. 151-155.

Reddy, J. B. ; Mohanta, D. K. ; Karan, B. M. (2004). Power System Disturbance Recognition Using Wavelet and S-Transform Techniques, *International Journal of Emerging Electric Power Systems* 1(2).

Resende, J. W. ; Chaves , M. L. R. ; Penna, C. (2001). Identification of power disturbances using the MATLAB wavelet transform toolbox, *Proceedings of the International Conference on Power Systems Transients*.

Samantaray, S. R. ; Dash, P. K. ; Panda, G. (2006). Power System Events Classification Using Pattern Recognition Approach, *International Journal of Emerging Electric Power Systems* 6(1).

Saxena, D. ; Verma, K. S. ; Singh, S. N. (2010). Power quality event classification: an overview and key issues, *International Journal of Engineering, Science and Technology* 2(3).

Stockwell, R. G. (2007). A basis for efficient representation of the S-transform, *Digital Signal Processing* 17(1), pp. 371-393.

Uyar, M. ; Yildirim, S. ; Gencoglu, M. T. (2004). An expert system based on S-transform and neural network for automatic classification of power quality disturbances, *Expert Systems with Applications* 36*,* pp. 5962-5975.

Vega, G. V. ; Duarte G. C. ; Ordóñez P. G. (2009). Automatic Power Quality Disturbances Detection and Classification Based on Discrete Wavelet Transform and Support Vector Machines, *Proceedings of the 20th International Conference and Exhibition Electicity Distribution*.

Vetrivel, A. M. ; Malmurugan, N. ; Jovitha, J. (2009). A Novel Method of Power Quality Disturbances Measures Using Discrete Orthogonal S Transform (DOST) with Wavelet Support Vector Machine (WSVM) Classifier, *International Journal of Electrical and Power Engineering* 3(1), pp. 59-68.

Yong, Z; Hao-Zhong C.; Yi-Feng, D.; Gan-Yun, L.; Yi-Bin, S. (2005). S-Transform-based classification of power quality disturbance signals by support vector machines, *Proceedins of the CSEE*, pp. 51-56.

Zhu, T. X. ; Tso, S. K. ; Lo, K. L. (2004). Wavelet-Based Fuzzy Reasoning Approach to Power-Quality Disturbance Recognition, *IEEE Transaction on Power Delivery* 19(4), pp. 1928-1935.

Pre-Processing Tools and Intelligent Systems Applied to Power Quality Analysis

Ricardo A. S. Fernandes[1], Ricardo A. L. Rabêlo[1], Daniel Barbosa[2],
Mário Oleskovicz[1] and Ivan Nunes da Silva[1]
[1]Engineering School of São Carlos, University of São Paulo (USP),
[2]Salvador University (UNIFACS)
Brazil

1. Introduction

In the last few years the power quality has become the target of many researches carried out either by academic or by utility companies. Moreover, a desired good power quality is essential for the Power Distribution System (PDS). The PDS can have (or impose) inherent operational conditions, that affect frequency and three-phase voltage signals. Among the main disturbances that indicate a poor power quality, the following can be highlighted: voltage sag/swell, overvoltage, undervoltage, interruption, oscillatory transient, noise, flicker and harmonic distortion (Dugan et al., 2003).

Actually, in literature, a diversity of papers can be found concerning detection and identification of power quality disturbances by applying intelligent systems, such as Artificial Neural Networks (ANN) (Janik & Lobos, 2006; Oleskovicz et. al., 2009; Jayasree, Devaraj & Sukanesh, 2010) and Fuzzy Inference Systems (Zhu, Tso & Lo, 2004; Hooshmand & Enshaee, 2010; Meher & Pradhan, 2010; Behera, Dash & Biswal, 2010). However, only some papers use data pre-processing tools before the application of intelligent systems. Among these papers, the use of Discrete Wavelet Transform (DWT) (Zhu, Tso & Lo, 2004; Uyar, Yildirim & Gencoglu, 2008; Oleskovicz et. al., 2009) and Discrete Fourier Transform (DFT) (Zhang, Li & Hu, 2011) can be highlighted in the pre-processing stage. According to the literature, it should also be mentioned that the pre-processing tools help to ensure a better detection and identification of disturbances in the power quality context.

In Hooshmand & Enshaee (2010), the authors propose a new method for detecting and classifying power quality disturbances. However, this method can be used both for the occurrence of one and multiple disturbances. This is a method that uses techniques for data pre-processing combined with intelligent systems. In this case, the authors extracted features of a time-varying voltage signal, such as:

- Fundamental component;
- Phase angle shift;
- Total harmonic distortion;
- Number of the maximums of the absolute value of wavelet coefficients;
- Calculation of energy of the wavelet coefficients;

- Number of zero-crossing of the missing voltage; and
- Number of peaks of Root Mean Square (RMS) value.

After the pre-processing step, the authors conducted the detection and classification of disturbances by means of an hybrid intelligent system where two fuzzy systems were developed (one being the detector and other the classifier of the disturbances). However, what classifies this intelligent system as hybrid is the use of Particle Swarm Optimization (PSO) to tune/adjust the membership functions. The results obtained tries to validate the proposed methodology, where it was found satisfactory correctness rate.

In the paper done by Jayasree, Devaraj & Sukanesh (2010), the authors employ the Hilbert Transform (HT) as pre-processing stage instead of the Fourier or Wavelet Transforms, which are commonly used for the same purpose (detect and/or classify power quality disturbances). So, after obtaining the coefficients from the HT, the following calculations are performed: mean, standard deviation, peak value and energy. Thus, each of these statistical calculations are submitted to the inputs of the Radial Basis Function (RBF) neural network that is responsible for classifying the disturbances contained in the measured voltage signal. Despite the good results achieved by the proposed method, tests were also performed, where was replaced the HT by DWT and S-Transform. Another test was done by replacing the RBF neural network by a Multilayer Perceptron (MLP) with Backpropagation training algorithm and by a Fuzzy ARTMAP. Thus, the proposed method, which is based on HT and RBF neural network, presents better response in terms of accuracy.

In Zhu, Tso & Lo (2004), a wavelet neural network was proposed for disturbances classification. However, a pre-processing step based on entropy calculation was accomplished. The results presented evidenced the potential of the proposed method for disturbances classification even under the influence of noise.

Among the intelligent systems used for power quality analysis, ANN and Fuzzy Inference Systems are the most applied, as mentioned before. Intelligent systems are used because they present, as inherent characteristics, the possibility of extracting the system dynamic and being able to generalize the response provided from the system. The intelligent systems are normally applied to the pattern recognition, functional approximation and processes optimization.

Taking this into account, the main purpose of this chapter is to present a collection of tools for data pre-processing including the DWT (Addison, 2002), fractal dimension calculation (Al-Akaidi, 2004), Shannon entropy (Shannon, 1948) and signal energy calculation (Hu, Zhu & Zhang, 2007). In addition to the detailed implementation of these tools, this chapter will be developed focusing on the pre-processing efficiency, considering and analyzing simulated data, when used before the intelligent system application. The results from this application show that the global performance of intelligent systems, together with the pre-processing data, was highly satisfactory concerning accuracy of response.

The performance of the methodology proposed was analyzed by simulated data via ATP software (EEUG, 1987). In this case, a lot of measures were obtained by the power distribution system simulated under power quality disturbances conditions, such as: voltage sags, voltage swells, oscillatory transients and interruptions. The next step was to submit the voltage measured in the substation to the windowing. Thus, the intelligent systems have been tested on data with and without pre-processing stage. This methodology allowed to verify the improvement in power quality analysis. The results showed the efficiency of the pre-processing tools combined with the intelligent systems.

2. Pre-processing tools

In this chapter, four main pre-processing tools will be presented, which are: Discrete Wavelet Transform, Fractal Dimension, Shannon Entropy and Signal Energy.

2.1 Discrete Wavelet Transform

The Wavelet Transform (WT) has been widely used because of its most relevant features: the possibility of examining a signal simultaneously in time and frequency (Addison, 2002). Although the WT have arisen in the mid-1980s, it started to be used only by engineering in the 1990s (Addison, 2002). It is worth mentioning that the WT calculation can be performed in a continuous or discrete manner, however, in the power quality area and, more specifically in detection and classification of disturbances, it is common to use the Discrete Wavelet Transform (DWT) (Oleskovicz et. al., 2009; Moravej, Pazoki & Abdoos, 2011). The DWT can be better understood through Figure 1.
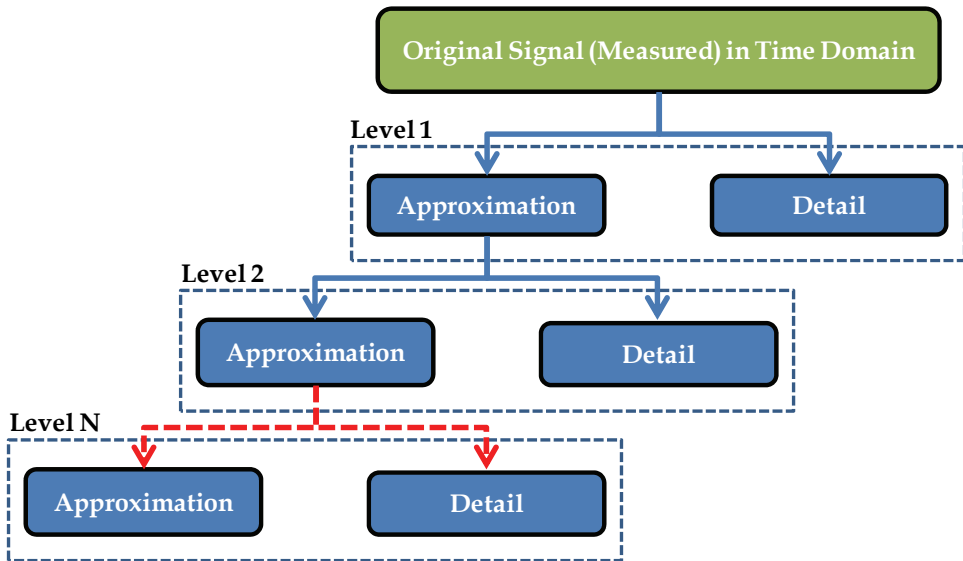
Fig. 1. Illustrative example of decomposition performed by wavelet transform

As shown in Figure 1, the WT allows the decomposition of a discrete signal in time into two levels, which are called approximation and detail. The approximations store the information concerning the low frequency components, while the details store the high frequency information. As the WT is applied to the signal, it is decomposed into other levels. Such levels are known as the leaves of the decomposition wavelet tree.

From level 1, the filtered signal is decomposed into other levels from the leaf of detail, resulting in the process of downsampling by 2 (Walker, 1999), where the number of samples is reduced to half (approximation and detail of level 2) of the parent leaf (detail of level 1), as well as the frequency. This process allows us to say that with the increment of decomposition levels, the resolution in frequency increases, but the resolution in time decreases.

Normally, in some literature, the term multi-resolution can be found linked with WT. This term refers to the time-frequency decomposition; however, in this case it is necessary to finish the wavelet decomposition in an intermediate level. This way, a good resolution both in frequency and time domain can be ensured.

In summary, the WT can also be defined as the application of an analysis filter, which is composed by two filters (low-pass and high-pass). However, the inverse process can be performed, where a synthesis filter can be applied to obtain the original signal from the decomposed/filtered signal. These process can be viewed in Figure 2.

```
┌─────────────────────────────────────────────────────┐
│     Original Signal (Measured) in Time Domain        │
└─────────────────────────────────────────────────────┘

       ┌─────────────────┐         ┌─────────────────┐
       │ Analysis Filter │         │ Synthesis Filter│
       └─────────────────┘         └─────────────────┘

┌─────────────────────────────────────────────────────┐
│     Filtered Signal in Time and Frequency Domain     │
└─────────────────────────────────────────────────────┘
```
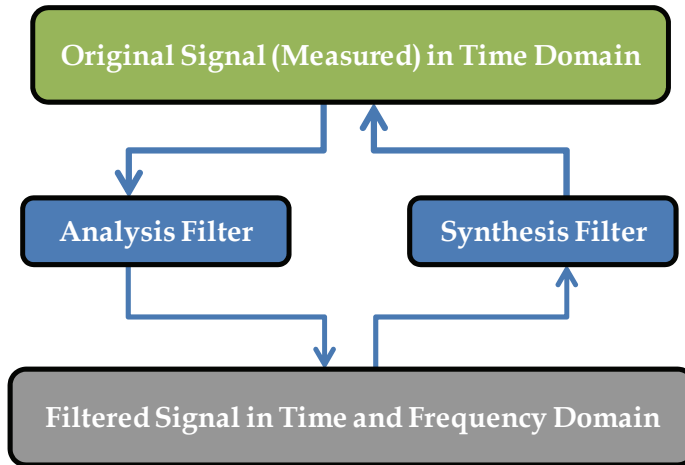
Fig. 2. Bank of filters used by wavelet transform

These filters are applied to the signal through the temporal convolution of its coefficients with the signal coefficients.

It is important to mention that there are a lot of filter families, but these filters can only be characterized as a Wavelet Transform if the synthesis and analysis filters are orthogonal to each other (Daubechies, 1992).

Another important factor to be taken into account is that the response of WT is better if the filters have more coefficients. However, this amount of coefficients must respect the size of the original signal, because of delays and processing time.

2.2 Shannon entropy

In the analysis of signals, the entropy is defined as a measure of knowledge lack about the information in the signal. Therefore, less noisy signals also have lower entropy (Shannon, 1948). The calculation of the Shannon entropy can be done according to equation (1):

$$S = \sum_{i=1}^{N} p_i \cdot \log(p_i) \tag{1}$$

where, N corresponds to the $i\text{-}th$ window of the signal and p represents the normalized energy of the window.

2.3 Signal energy

The signal energy is calculated to achieve the full potential of a signal (Hu, Zhu & Zhang, 2007). However, some signals have negative sides and therefore a quadratic sum of the sampled points must be calculated as shown in the equation (2):

$$E = \sum_{i=1}^{N} \sum_{j=1}^{M} \text{signal}_{i,j}^2 \tag{2}$$

where, N corresponds to the i-th window and M represents the j-th point of the window.

2.4 Fractal dimension

The fractal dimension has been calculated by using the DWT at the maximum level of the signal. The maximum level of a window or signal can be obtained by the following equation:

$$level_{\max} = \frac{\log(n)}{\log(2)} \tag{3}$$

where n is the number of points of each considered window/signal.

It is important to emphasize that, for a better response of the fractal dimension, the mother-wavelet used by DWT must normally have a lot of support coefficients (over 15), because this ensures a more symmetrical response to the impulse (Al-Akaidi, 2004).

After the DWT is applied, two vectors, $x[.]$ and $y[.]$ were generated, containing the details length of each wavelet sub band and the energy of each of these sub bands respectively. The procedure for the creation of vectors $x[.]$ and $y[.]$ can be seen in Figure 3. In this figure the calculation of fractal dimension about a 32-point-window was considered. Once the vectors are determined, the fractal dimension can be calculated according to equation (4):

$$D = 2 - \left| \frac{\beta - 1}{2} \right| \tag{4}$$

where, β is the angle of the average line that sets the points given by the vectors $x[.]$ (length of each leaf) and $y[.]$ (energy of each leaf), by means of the least squares method. The calculation of least squares can be done according to the following equation:

$$\beta = \frac{j \sum_k \log_2(x_k) \cdot \log_2(y_k) - \sum_k \log_2(y_k) \cdot \sum_k \log_2(x_k)}{j \sum_k \log_2(x_k)^2 - \left(\sum_k \log_2(x_k)^2 \right)} \tag{5}$$

where, j is the signal length, x_k corresponds to the vector $x[.]$ at its k-th position and y_k corresponds to the vector $y[.]$ at its k-th position.

The DWT employed in this study was configured using a Symmlet mother-wavelet with 16 support coefficients.
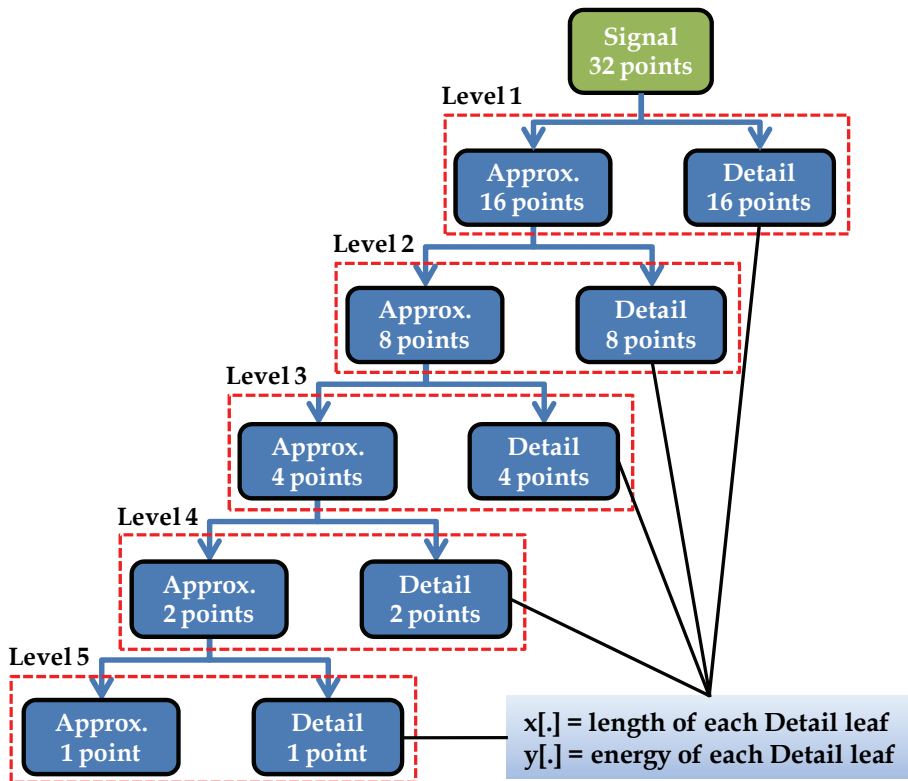
Fig. 3. Calculation of fractal dimension using DWT

3. Intelligent systems

Since the 1990s, intelligent systems have been widely used in researches related to electrical engineering, where the Artificial Neural Networks and Fuzzy Systems are highlighted. However, in recent years the development of hybrid intelligent tools, that combine neural networks and fuzzy systems together with evolutionary algorithms (genetic algorithms and particle swarm optimization), has been increasing. Following the outlined context, this section aims to present the foundations of intelligent systems, namely, artificial neural networks, adaptive neural-fuzzy inference systems and neural-genetic.

3.1 Artificial Neural Networks

Artificial Neural Networks are computational models inspired in human brain, which may acquire and maintain the knowledge. In this chapter, only ANN with MLP architecture will be presented. This architecture is generally applied in pattern recognition, functional approximation, identification and control (Haykin, 1999). Hence, considering the pattern recognition task, this architecture might be applied to disturbances classification. The MLP architecture previously commented is shown in Figure 4.
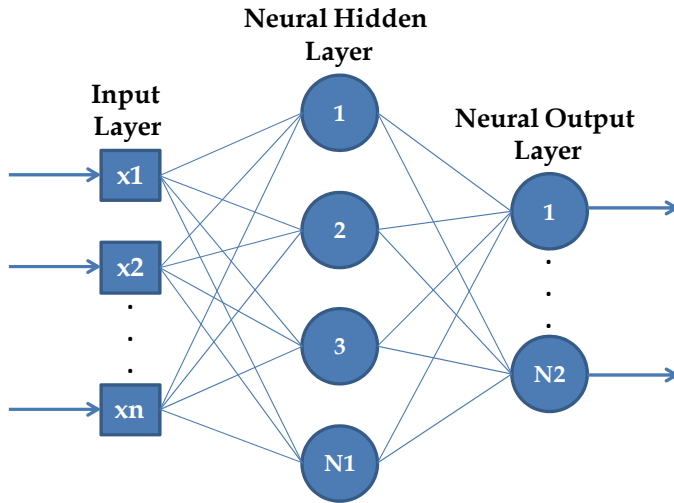
Fig. 4. Architeture of MLP neural networks

The MLP neural networks commonly use as training algorithm the Backpropagation (BP), however, other algorithms such as Levenberg-Marquardt (LM) and Resilient Backpropagation (RPROP) should be employed. In this chapter, these algorithms will be used and will have its performance evaluated.

Backpropagation training algorithm was employed because it is commonly used to train MLP neural networks. The Levenberg-Marquardt training algorithm was employed due to its capacity of accelerating the convergence process. This training algorithm consists in one approximation of the Newton method to non-linear systems (Hagan & Menhaj, 1994). On the other hand, the Resilient Backpropagation was employed due to its capacity of eliminating the harmful effect. This effect is caused by the partial derivatives in the training process. Thus, only the signal of partial derivatives is used to update the synaptic weights (Riedmiller & Braun, 1993).

3.2 Adaptive Neural-Fuzzy Inference Systems (ANFIS)

Fuzzy inference systems are capable of dealing with highly complex processes, which are represented by inaccurate, uncertain and qualitative information. Normally, fuzzy inference systems are based on linguistic rules of type "if ... then", in which the fuzzy set theory (Zadeh, 1965) and fuzzy logic (Zadeh, 1996) provide the necessary mathematical basis to deal with inaccurate information and with the linguistic rules.

In general, fuzzy inference systems are often based on three steps: fuzzification, inference procedures and defuzzification. Normally, in fuzzy inference systems, non-fuzzy inputs (crisp) are considered; resulting from observations or measurements, that is the case of most practical applications. As a result, it is necessary to make a mapping of these data to the fuzzy sets (input). The fuzzification is a mapping from the input variable domain to the fuzzy domain, representing the assignment of linguistic values (primary terms), defined by membership functions, to the input variables. The fuzzy inference procedure is responsible for evaluating the primary terms of the input variables, by applying production rules

(stored on fuzzy rule base) in order to obtain the fuzzy output value of inference system. Once the fuzzy output set is obtained, in the stage of defuzzification, an interpretation of this information is performed. This step is necessary because, in practical applications, accurate outputs are normally required. The defuzzification is typically used to assign a numerical value to the fuzzy output set. Thus, defuzzification can be considered a kind of synthesis of the final fuzzy output set by means of a numerical value. In the Figure 5, a block diagram representing the components of fuzzy inference systems commented above can be visualized.
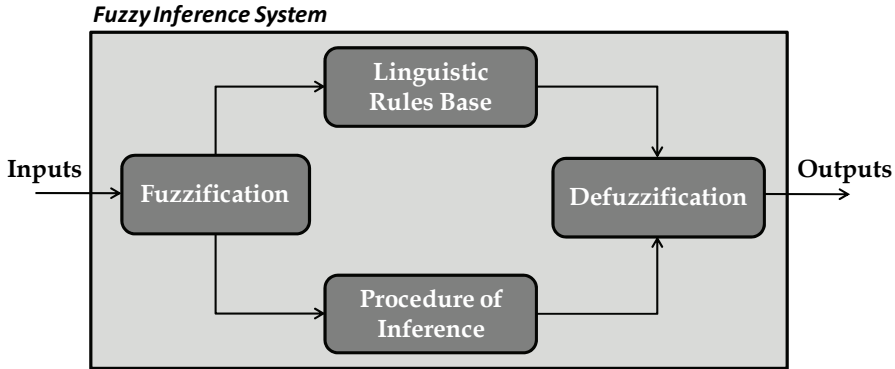
Fig. 5. Structure of a fuzzy inference system

However, this subsection is intended to neural-fuzzy inference systems that differ from a conventional fuzzy system for obtaining and tuning/adjustment of the linguistic rules base. When using a neural-fuzzy inference system, rules and fuzzy sets are adjusted and tuned by information contained in the data set. It is worth commenting also that the adaptive neural-fuzzy inference system is based on the Takagi-Sugeno inference model (Takagi & Sugeno, 1985), where a linguistic rule is given as follows:

$$R_i : \text{If } \mu_1 \text{ is } A_1 \text{ and } \mu_2 \text{ is } A_2 \text{ Then } y_i = B_i$$

and, the final result is obtained by the weighted average of all results found in each activated rule (R_i), i.e.:

$$y = \frac{\sum_{i=1}^{N} \mu_i \cdot y_i}{\sum_{i=1}^{N} \mu_i} \tag{6}$$

where, y is the output of the system, N denotes the total number of rules activated and μ_i is the membership degree to each activated rule.

3.3 Neural-genetic
The neural-genetic system presented in this subsection has been fully based on the architecture of an MLP neural network as well as that presented in Figure 4. However, the

neural network training step is performed by a genetic algorithm instead of the methods normally used for this type of network (Backpropagation, Levenberg-Marquardt, Resilient Backpropagation). Thus, the genetic algorithm becomes responsible for estimating the best matrix of synaptic weights, i.e., a good solution inside the search space.

Genetic Algorithms (GA) are methods applied to search and optimization, which are based on the principles of natural selection and survival of the best individuals as defined by Charles Darwin in 1859. In addition, the functioning of genetic algorithms depends on the adjustment of the genetic operators (selection, crossover and mutation). Thus, the Figure 6 illustrates a flowchart representing the operation of a basic genetic algorithm.
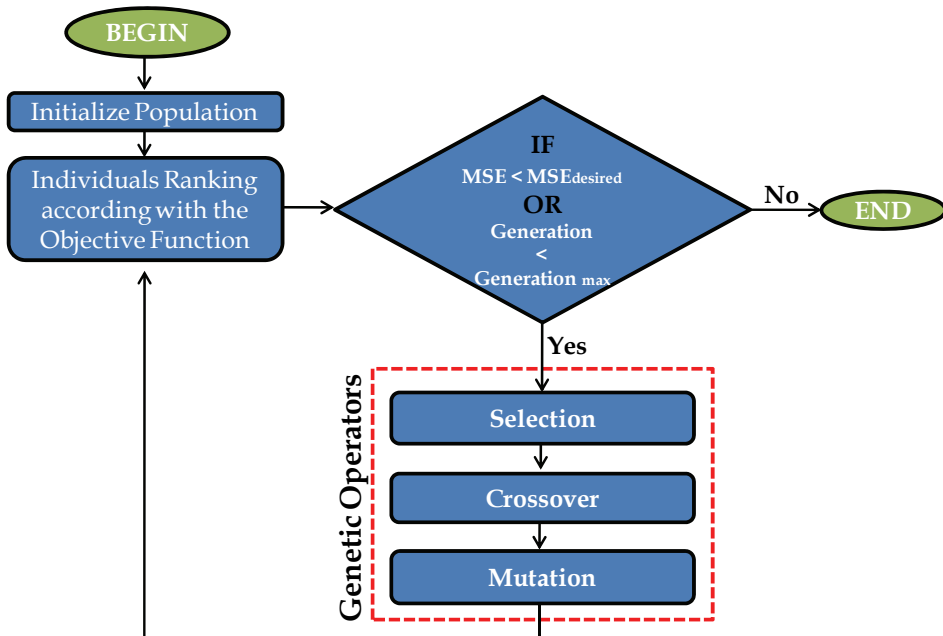
Fig. 6. Flowchart of a basic genetic algorithm

Through the Figure 6, firstly the population of individuals or chromosomes is initialized by means of a uniform distribution. Each individual represents a solution to the problem that is subsequently evaluated by the objective function, which becomes, in this case, the calculation of the Mean Square Error (MSE). Thus, it can be noted that the individual must be better if the MSE is minor. It is important to mention that the GA does not stop its execution until a stopping criterion is satisfied. In this case, two variables are normally employed as stopping criterion: the maximum number of generations and the expected value of MSE. In this chapter, the GA used was parameterized in order to have an elitist selection (De Jong, 1975), i.e., only the best individual was maintained for the next generation. In addition, a BLX-α crossover and a Gaussian mutation were used. So, the individuals of the next generation were obtained by using the following equation:

$$m = p_1 + \alpha(p_2 - p_1) \tag{7}$$

where, p_1 is the actual individual, p_2 is the best individual of the current generation, α is a free parameter that must belong to the search space and m represents the new individual. After the new individuals are obtained, a portion of these individuals has to go through the Gaussian mutation. This mutation replaces a gene of the individual by a random number provided by a Gaussian distribution. Thus, given an individual p with its *n*-th gene selected, an individual m will be obtained as follows:

$$m = \begin{cases} D(p_i, \sigma), \text{ if } i = n \\ \quad p_i \end{cases} \tag{8}$$

where, $D(p_i, \sigma)$ is a Gaussian distribution with its mean in p_i and a standard deviation of σ that is a free parameter. However, the mutation operator is usually dynamic, so it checks whether the best individual is improving or not during a certain number of generations. If the best individual is kept during this pre-defined number of generations, a greater number of individuals will be mutated. This strategy is adopted as an attempt to avoid local minima points (Goldberg, 1989). The parameters of GA used are shown by means of Table 1.

Selection Method	Elitism
Crossover Method	BLX-α
Mutation Method	Gaussian
α parameter (crossover)	0.3
Standard deviation (mutation)	0.5
Minimum MSE (stopping criterion)	e-9
Maximum of Generations (stopping criterion)	1000

Table 1. Parameters of the genetic algorithm

4. Distribution power system simulated

The computer simulation has been developed using the ATP (Alternative Transients Program) software, which is properly used for modeling a real distribution system. It should be emphasized that the system has been designed by using data provided by a local utility. The ATP software enables the configuration of all parameters needed to construct the model and the variables to extract the disturbances data. Then, it can be stated that it was modeled to have great similarity with those found in the field. For all simulated situations, the sampling rate of 7680Hz has been considered. The power system modeled through ATP can be seen in Figure 7.

With respect to Figure 7, the substation transformer (138 Δ/13.8 Y kV, 25MVA), the distribution transformers T3 and T13 (45kVA) and the particular transformer TP4 (45kVA) has been modeled according to their real saturation curves. The other transformers have been modeled without considering their saturation curves. It should be noticed that both the distribution transformers and the particular ones have $\Delta - Y$ connections with the grounding resistance of zero ohm.
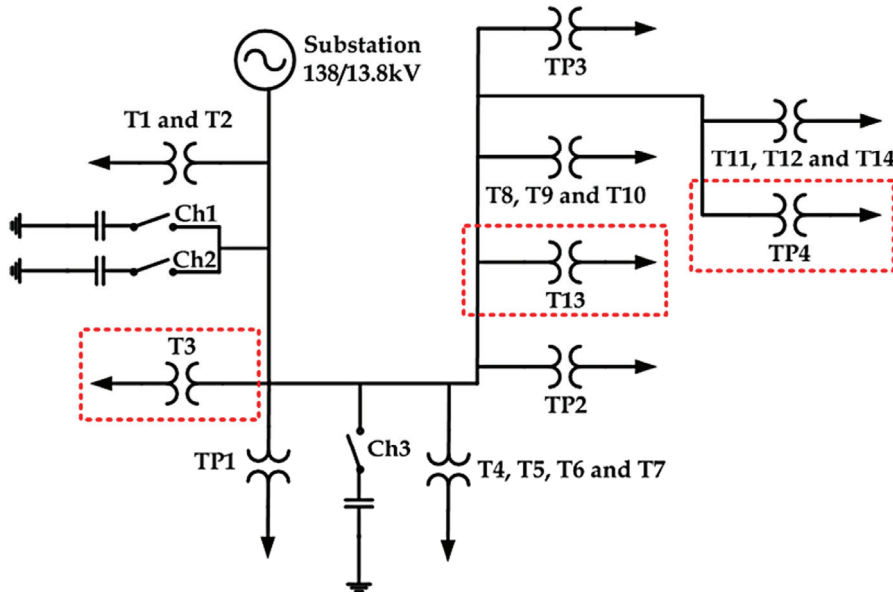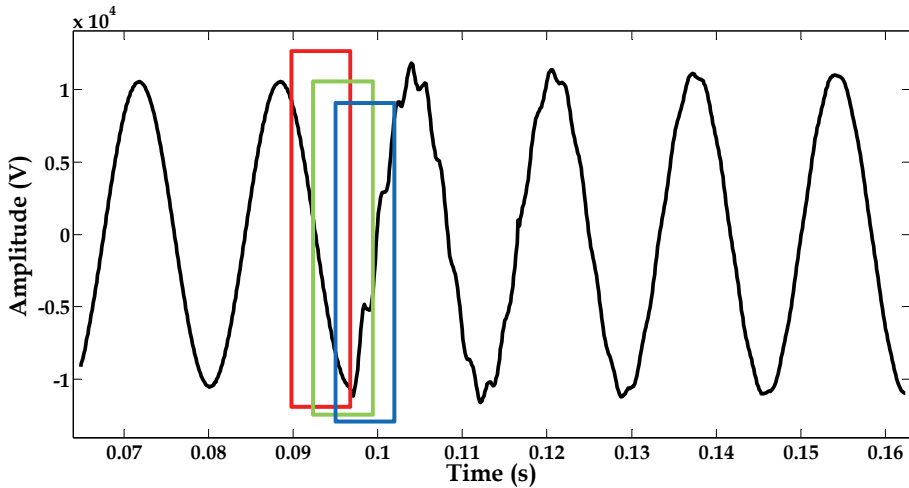
Fig. 7. Distribution Power System Simulated

Fig. 8. Moving window process

The loads connected to these transformers represent a similar approach to that found in practice.

It can also be verified that, in the distribution system previously mentioned, there are three banks of capacitors, two of them been modeled for 600kVAr and the other for 1,200kVAr.

The cabling of the main feeder consists of a CA-477 MCM bare cable in a conventional overhead structure represented by coupled RL elements.

As the analyzed power system has been simulated, the extraction of data is given by the ATP software at a sampling rate of 7680 Hz.

In order to test the proposed technique, 89 cases have been generated to form a representative database, which was divided in:

- 34 cases of voltage sags;
- 28 cases of voltage swells;
- 15 cases of oscillatory transients; and
- 12 cases of interruptions.

Considering these events, windowing of data signal has been necessary to create a homogeneous database, and to better prepare the data to the pre-processing stage. Thus, a window containing 32 samples/points, which corresponds to a quarter of the cycle of the analyzed voltage signal has been used. It is worth mentioning that the window of data moves in a step of 8 samples. An example of this window is showed in Figure 8.

5. Data pre-processing and disturbances analysis

In this section, the disturbances detection will be presented by means of fractal dimension calculation, which is based on WT. It is worth mentioning that the method can be applied to both entire signal and window of signal. In the sequence, four examples of fractal dimension calculation applied to disturbances detection are shown by Figures 9 to 13. As the fractal dimension uses a Wavelet Transform, this one was configured using a Symmlet mother-wavelet with 16 support coefficients. The windowing of the signal was done using a 32-points window, which corresponds to a quarter of the cycle of original measured signal.
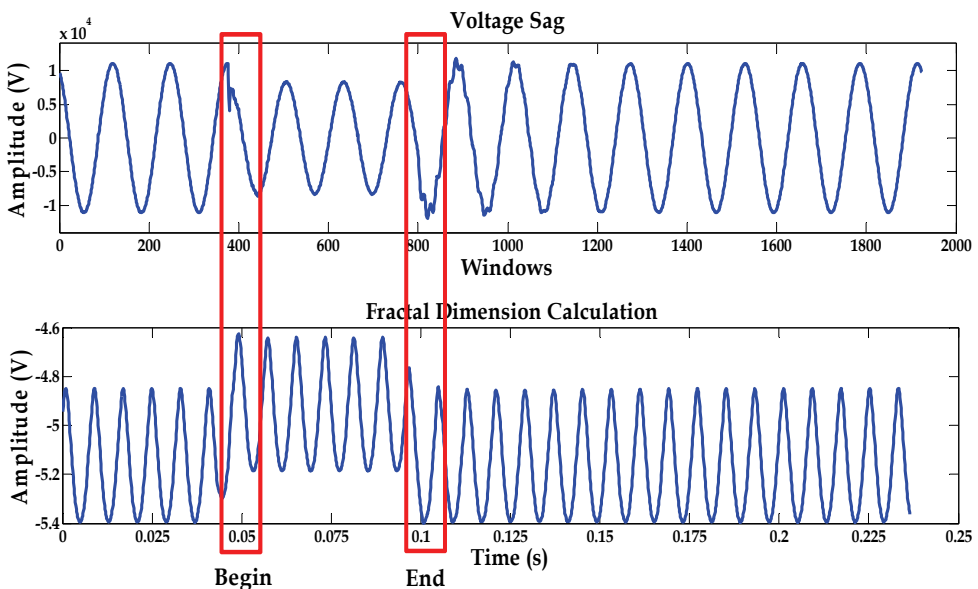
Fig. 9. Fractal dimension calculation applied to a voltage signal containing sag
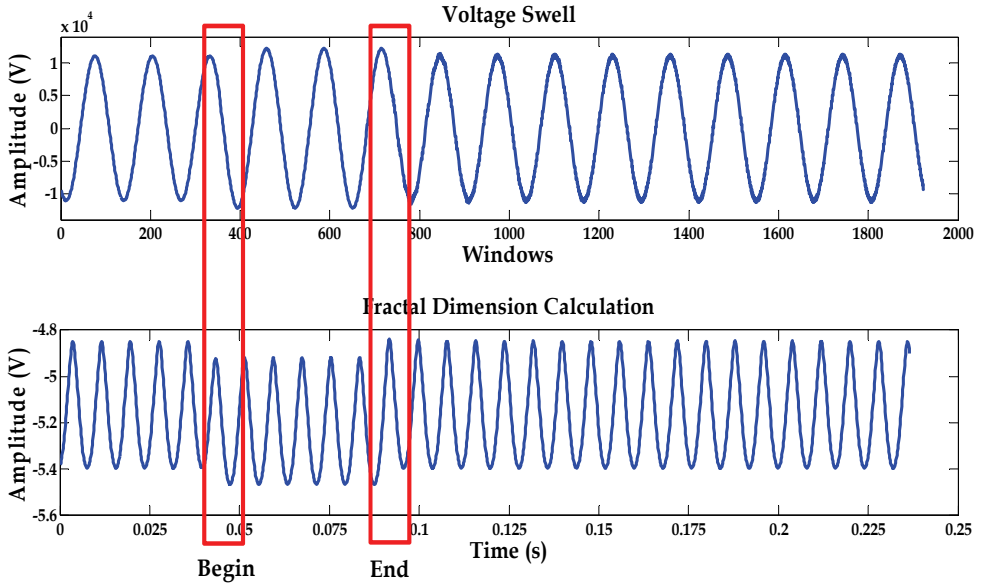
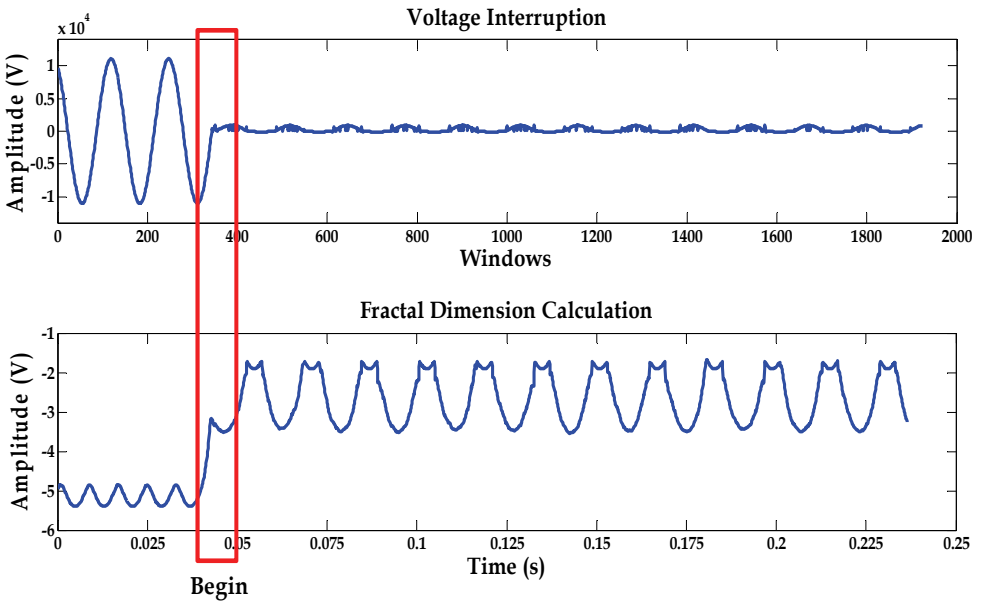Fig. 10. Fractal dimension calculation applied to a voltage signal containing swell

Fig. 11. Fractal dimension calculation applied to a voltage signal containing interruption
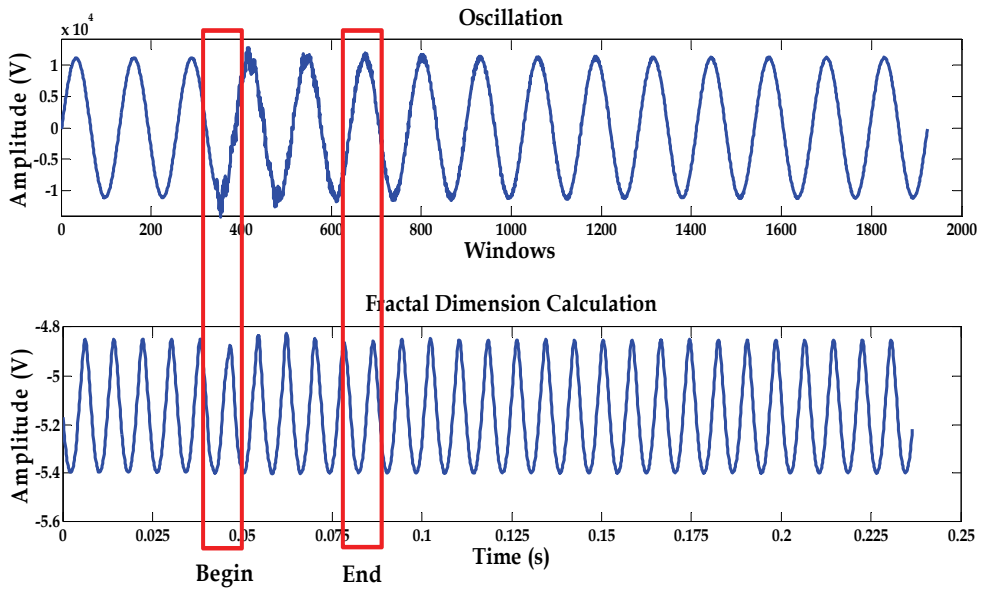
Fig. 12. Fractal dimension calculation applied to a voltage signal containing oscillation
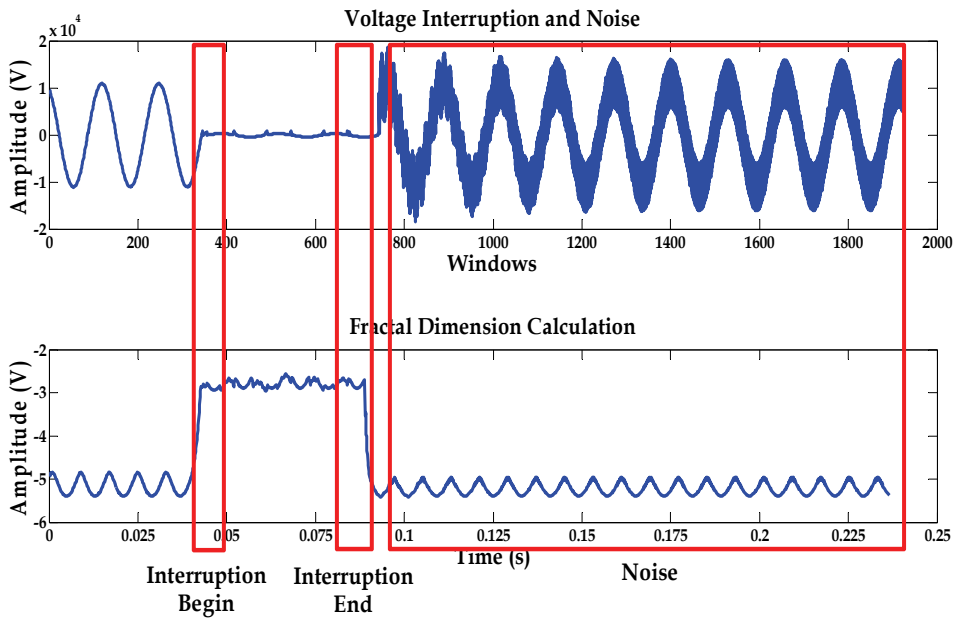

Fig. 13. Fractal dimension calculation applied to a voltage signal containing interruption and noise

The figures above show an easy characterization of the disturbances, as well as its temporal positions.

It is noteworthy that after the detection of disturbances, there is still a need to classify them. Following this premise, classifiers were implemented based on intelligent systems, which were previously mentioned in Section 3. The disturbances classification was first accomplished by providing a 32-points window of signal directly to the inputs of intelligent systems. This test was done in order to show that the pre-processing is an extremely important step for classification of power quality disturbances. The results obtained by this classification are shown in Table 2.

	Accuracy of MLP Neural Networks (%)			Accuracy of Hybrid Intelligent Systems (%)	
Disturbances	BP	LM	RPROP	ANFIS	Neural-Genetic
Sags	75.9	98.1	98.3	-	59.0
Swells	95.9	96.4	98.1	-	67.1
Interruptions	96.6	100	100	-	85.9
Oscillations	84.4	99.0	96.8	-	83.3
Mean (%)	88.2	98.4	98.3	-	73.7

Table 2. Performance of intelligent systems without pre-processing stage

Some disturbances presented by Table 2 reach good results, but the mean percentage, mainly for neural-genetic and MLP with Backpropagation training algorithm were low. Besides of this, ANFIS is not capable to run because of the huge number of input signals. In this way, a new test was performed, where a pre-processing stage was used based on fractal dimension, Shannon entropy and energy. The results for this new test can be verified in Table 3.

	MLP Neural Networks			Hybrid Intelligent Systems	
Disturbances	BP	LM	RPROP	ANFIS	Neural-Genetic
Sags	94.2	100	99.5	94.0	85.8
Swells	92.2	100	99.8	94.8	88.8
Interruptions	99.9	100	100	100	83.2
Oscillations	89.9	100	99.6	88.8	98.5
Mean	94.1	100	99.7	94.4	89.1

Table 3. Performance of intelligent systems with pre-processing stage

Comparing Table 3 with Table 2, it is evident that the pre-processing stage is essential for the proper classification of the disturbances that affect the power quality. It is necessary to comment that the neural networks (with BP, LM and RPROP training algorithms), as well

as, the neural-genetic hybrid system use a MLP architecture with 15 neurons in the first hidden layer, 20 neurons in the second hidden layer and 1 neuron in the output layer. All hidden layers use a hyperbolic tangent as activation function and the output layer uses a linear activation function.

6. Conclusions

This chapter consisted in developing an alternative technique for signals pre-processing based on calculations of the fractal dimension, Shannon entropy and signal energy that enables the classification of disturbances occurring in electrical power distribution systems.

It is possible to highlight that the proposed methodology for pre-processing has provided a good data preparation for the disturbances classification stage, improving the convergence of the intelligent systems, which has consequently supplied satisfactory results for identifying disturbances associated with power quality.

It is important to say that this methodology has been developed carrying out certain data window of the signals that characterize the simulated events, where, for each window, the dimension of fractal, the Shannon entropy and the energy have been calculated. After this data pre-processing stage, intelligent systems are parameterized and the variables calculated in the pre-processing stage are provided as inputs.

The results show that the intelligent systems present better results with pre-processing stage. Therefore, the contribution of pre-processing tools for disturbances classification is evidenced here.

Thus, for future works the application of the methodology used in data pre-processing in different tasks of classification of disturbances should be used, such as to detect the saturation of the transformers, and other problems related to electrical power distributions systems.

7. References

Addison, P. S. (2002). *The Illustrated Wavelet Transform Handbook – Introductory Theory and Applications in Science, Engineering, Medicine and Finance* (1st Ed.), Institute of Physics Publishing, ISBN: 0750306920, Philadelphia.

Al-Akaidi, M. (2004). *Fractal Speech Processing* (1st Ed.), Cambridge University Press, ISBN: 0521814588, New York.

Behera, H. S.; Dash, P. K. & Biswal, B. (2010). Power Quality Time Series Data Mining Using S-Transform and Fuzzy Expert System. *Applied Soft Computing*; Vol. 10, Oct. 2010, pp. 945-955, ISSN: 1568-4946.

Daubechies, I. (1992). Ten Lectures on Wavelets. *CBMS-NSF Regional Conference Series in Applied Mathematics,* ISBN: 0898712742, Philadelphia.

De Jong, K. A. (1975). An Analysis of the Behavior of a Class of Genetic Adaptative Systems. Ph.D. Thesis, University of Michigan, 1975.

Dugan, R. C.; McGranaghan, M. F.; Santoso, S. & Beaty, H. W. (2003). *Electrical Power Systems Quality* (2nd Ed.), McGraw Hill, ISBN: 9780071386227, New York.

EEUG (1987). Alternative Transients Program Rule Book. LEC.

Goldberg, D. E. (1989). *Genetic Algorithms in Search, Optimization and Machine Learning*, Addison-Wesley Longman Publishing Co., Inc. Boston, MA, USA.

Hagan, M. T. & Menhaj, M. B. (1994). Training Feedforward Networks with the Marquardt Algorithm. *IEEE Transactions on Neural Networks*; Vol. 5, No. 6, Nov. 1994, pp. 989-993, ISSN: 1045-9227.

Haykin, S. (1999). *Neural Networks – A Comprehensive Foundation* (2nd ed.), Prentice Hall, ISBN: 0132733501, Ontario.

Hooshmand, R. & Enshaee, A. (2010). Detection and Classification of Single and Combined Power Quality Disturbances Using Fuzzy Systems Oriented by Particle Swarm Optimization Algorithm. *Electric Power Systems Research*; Vol. 80, Dec. 2010, pp. 1552-1561, ISSN: 0378-7796.

Hu, G.; Zhu, F. & Zhang, Y. (2007). Power Quality Faint Disturbance Using Wavelet Packet Energy Entropy and Weighted Support Vector Machine. *3rd International Conference on Natural Computation (ICNC)*, ISBN: 0769528759, Haikou, Aug. 2007.

Janik, P. & Lobos, T. (2006). Automated Classification of Power-Quality Disturbances Using SVM and RBF Networks. *IEEE Transactions on Power Delivery*; Vol. 21, No. 3, July. 2006, pp. 1663-1669, ISSN: 0885-8977.

Jayasree, T.; Devaraj, D. & Sukanesh, R. (2010). Power Quality Disturbance Classification Using Hilbert Transform and RBF Networks. *Neurocomputing*; Vol. 73, Mar. 2010, pp. 1451-1456, ISSN: 0925-2312.

Meher, S. K. & Pradhan, A. K. (2010). Fuzzy Classifiers for Power Quality Events Analysis. *Electric Power Systems Research*; Vol. 80, Jan. 2010, pp. 71-76, ISSN: 0378-7796.

Moravej, Z.; Pazoki, M. & Abdoos, A. A. (2011). Wavelet Transform and Multi-Class Relevance Vector Machines Based Recognition and Classification of Power Quality Disturbances. *European Transactions on Electrical Power*; Vol. 21, Jan. 2011, pp. 212-222, ISSN: 1546-3109.

Oleskovicz, M.; Coury, D. V.; Delmont Filho, O.; Usida, W. F.; Carneiro, A. A. F. M. & Pires, L. R. S. (2009). Power Quality Analysis Applying a Hybrid Methodology with Wavelet Transform and Neural Networks. *Electrical Power and Energy Systems*; Vol. 31, Jun. 2009, pp. 206-212, ISSN: 0142-0615.

Riedmiller, M. & Braun, H. (1993). A Direct Adaptive Method for Faster Backpropagation Learning: The RPROP Algorithm. *Proc. of the IEEE International Conference on Neural Networks*, ISBN: 0780309995, San Francisco, Mar. 1993.

Shannon, C. E. (1948). Mathematical Theory of Communication. *Bell System Technical Journal*; Vol. 27, Jun. and Oct. 1948, pp. 379-423 and pp. 623-656.

Takagi, T. & Sugeno, M. (1985). Fuzzy Identification of Systems and Its Applications to Modeling and Control. *IEEE Transactions on System, Man, and Cybernetics*; Vol. 15, No. 1, Feb. 1985, pp. 116-132, ISSN: 00189472.

Uyar, M.; Yildirim, S. & Gencoglu, M. T. (2008). An Effective Wavelet-Based Feature Extraction Method for Classification of Power Quality Disturbance Signals. *Electrical Power Systems Research*; Vol. 78, No. 10, Oct. 2008, pp. 1747-1755, ISSN: 0378-7796.

Walker, J. S. (1999). *A Primer on Wavelets and Theis Scientific Applications*, Chapman & Hall (CRC), ISBN: 0849382769, Whashington.

Zadeh, L. A. (1965). Fuzzy Sets. *Information and Control*; Vol. 8, No. 3, Jun. 1965, pp. 338-353, ISSN: 0019-9958.

Zadeh, L. A. (1996). Fuzzy Logic = Computing with Words; *IEEE Transactions on Fuzzy Systems*, Vol. 4, No. 2, May 1996, pp. 103-111, ISSN: 1063-6706.

Zhang, M.; Li, K. & Hu, Y. (2011). A Real-Time Classification Method of Power Quality Disturbances. *Electric Power Systems Research*; Vol. 81, Feb. 2011, pp. 660-666, ISSN: 0378-7796.

Zhu, T. X.; Tso, S. K. & Lo, L. K. (2004). Wavelet-Based Fuzzy Reasoning Approach to Power-Quality Disturbance Recognition. *IEEE Transactions on Power Delivery*; Vol. 19, No. 4, Oct. 2004, pp. 1928-1935, ISSN: 0885-8977.

Selection of Voltage Referential from the Power Quality and Apparent Power Points of View

Helmo K. Morales Paredes[1], Sigmar M. Deckmann[1],
Luis C. Pereira da Silva[1] and Fernando P. Marafão[2]
[1]School of Electrical and Computer Engineering, University of Campinas,
[2]Group of Automation and Integrated Systems, Unesp – Univ Estadual Paulista
Brazil

1. Introduction

When one tries to go further into the discussions and concepts related to Power Quality, one comes across basic questions about the voltage and current measurements. Such issues do not emerge only because of the evolution of sensors and digital techniques, but mainly because of the need to better understand the phenomena related with three-phase circuits under asymmetrical and/or distorted waveform conditions.

These issues are fundamental, both for establishing disturbance indicators as well as for power components formulation under non sinusoidal and/or asymmetrical waveforms. This can be verified by the various conferences that have been dedicated to this topic and the growing number of articles published about this subject (Depenbrock, 1993; Akagi et al, 1993; Ferrero, 1998; Emanuel, 2004; Czarneck, 2008; IEEE Std 1459, 2010; Tenti et al., 2010; Marafao et al., 2010).

Several discussions have shown that the choice of the voltage reference point can influence the definitions and calculation of different power terms and power factor (Emmanuel, 2003; Willems & Ghijselen, 2003; Willems, 2004; Willems et al., 2005). Consequently, it may influence applications such as revenue metering, power conditioning and power systems design. Taking into account two of the most relevant approaches (Depenbrock, 1993; IEEE Std 1459, 2010), regarding to, e.g., the power factor calculation, it can be seen that quantitative differences are practically irrelevant under normal operating conditions, as discussed and demonstrated in (Moreira et al., 2006). However, under severe voltage and current deterioration, particularly in case of power circuits with a return conductor, the differences may result significant.

Nevertheless, the matter of voltage referential is much more extensive than the definitions or calculations of power terms and it can have a direct effect on many other power system's applications, such as: power quality instrumentation and analysis, protection, power conditioning, etc.

Thus, this chapter deals with the selection of the very basic voltage referential and its influence of the quantification of some power quality indicators, as well as, in terms the apparent power definition.

The analysis of some power quality indices will illustrate how the selection of the voltages referential may influence the evaluation of, e.g., the total harmonic distortion, unbalance

factors and voltage sags and swells, especially in case of three-phase four-wire circuits. Such case deserves special attention, both, from instrumentation and regulation points of view.

Finally, based on the classical Blakesley's Theorem, a possible methodology will be presented in order to allow the association of the most common voltage measurement approaches, in such a way that the power quality (PQ) and power components definitions would not be improperly influenced.

2. Choosing the voltage referential in three phase power systems

It is not possible to discuss the choice of a circuit voltage referential, without first recalling Blondel's classic definition (Blondel, 1893), which demonstrates that in a polyphase system with "m" wires between source and load, only "m-1" wattmeters were needed to measure the total power transferred from source to load. In this case, one of the wires should be taken as the referential, be it either a phase or a return (neutral) conductor (Fig. 1).
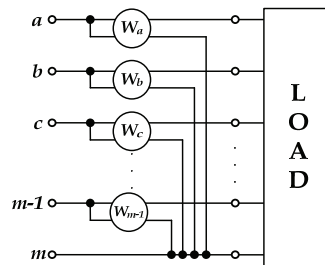
Fig. 1. Illustration of the measuring method according to Blondel

This hypothesis was extended to various other power system applications and it is also currently used, as can be seen, for example, in (IEEE Std 1459, 2010). However, other proposals have also been discussed, such as the utilization of a referential external to the power circuit (Depenbrock, 1993; Willems & Ghijselen, 2003; Blondel, 1893; Marafão, 2004).

2.1 External voltage referential

In this case, all wires, including the neutral (return), should be measured to a common point outside the circuit (floating), as shown in Fig. 2. This common point was designated by Depenbrock as a *virtual reference or a virtual star point (*)*. In the same way as Blondel's work, the author originally dealt with the problem of choosing the voltage referential from the point of view of power transfer.

In practice, this method requires that an external point (*) be used as the voltage referential. This point can be obtained connecting "m" equal resistances (or sensor's impedances) among each wire on which the voltage should be measured. Voltage drops over these resistors correspond to the voltages that characterize the electromagnetic forces involved. Depenbrock has demonstrated that such measured voltages always sum up to zero, according to Kirchhoff's Voltage Law (Depenbrock, 1998).

Therefore this method is applicable to any number of wires, independently of the type of connection (Y-n, Y ou Δ). It must be emphasized that measured voltages in relation to the virtual point can be interpreted as virtual phase voltages, although they do not necessarily equal the voltages over each branch of a load connected in Y-n, Y or Δ, especially when they

are unbalanced. Thus, the use of voltages in relation to the virtual point needs to be treated in a special way so as to arrive at phase or line quantities, as will be shown further on.
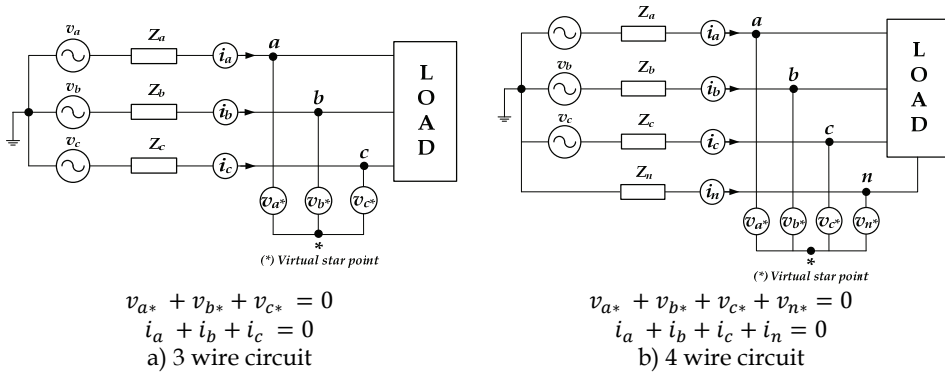

$$v_{a*} + v_{b*} + v_{c*} = 0$$
$$i_a + i_b + i_c = 0$$
a) 3 wire circuit

$$v_{a*} + v_{b*} + v_{c*} + v_{n*} = 0$$
$$i_a + i_b + i_c + i_n = 0$$
b) 4 wire circuit

Fig. 2. Voltages measurement considering a virtual star point (*)

2.2 Internal voltage referential

Based on Blondel's proposals, recent discussions and recommendations made by Standard 1459 (IEEE Std 1459, 2010) suggest that voltage should be measured in relation to one of the system's wires, resulting in phase to phase voltages (line voltage) or phase to neutral voltages, according to the topology of the system used. In this approach, the number of voltage sensors is smaller than in the case of measurements in relation to a virtual point. Fig. 3 shows a measuring proposal considering one of the system's conductor as the reference.

$$v_{ab} + v_{bc} = -v_{ca}$$
$$i_a + i_c = -i_b$$
a) 3 wire circuit

$$v_{an} + v_{bn} + v_{cn} = 3v^0$$
$$i_a + i_b + i_c = 3i^0 = -i_n$$
b) 4 wire circuit
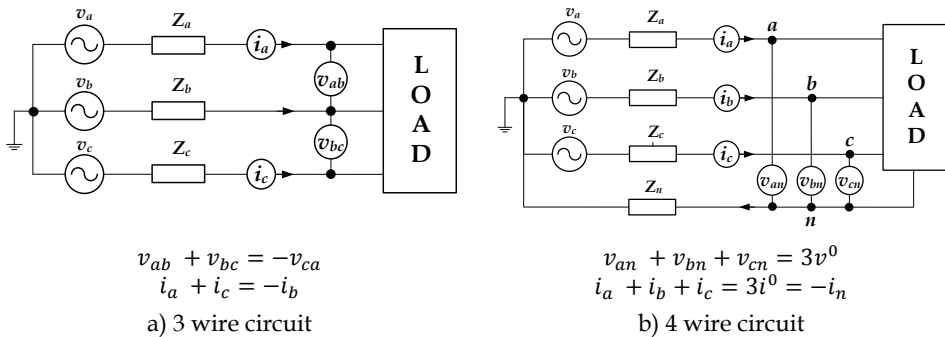
Fig. 3. Voltage measurement considering an internal referential

Note that, in case of 4 wire the phase voltages and currents may not sum zero. Where v^0 and i^0 are the zero sequence voltage and current components.

3. Considerations on three phase power system without return conductor

In this circuit topology, the lack of a return conductor allows either the selection of a virtual reference point (Fig. 2a) or a phase conductor reference (Fig. 3a). Apart from the fact that there is no zero-sequence current circulation, in the three-phase three-wire connection

(system without a return wire), the zero-sequence voltage is also eliminated from the quantities measured between the phases. This is a direct consequence of Kirchhoff's laws.

Thus, considering three-wire systems and taking into account different applications, both measuring methods can have advantages and disadvantages. For example:

- With regard to low voltage applications one can conclude that the measurement of line quantities (Fig. 3a) results in the reduction of costs associated to voltage transducers;
- Assuming a common external point (Fig. 2a), the measurements need to be manipulated (adjusted) to obtain line voltages;
- However if we take into account high and medium voltage applications, measurements based on the scheme shown in Fig. 3a may not be the most adequate. Usually at these levels of voltage two methods are employed: the first requires the use of Voltage Transformers (VTs), which have a high cost, since they handle high line voltages. The second strategy, which is cheaper, is to employ capacitive dividers, which, in general, use the physical grounding of the electric system as a measuring reference. The problem is that this type of grounding is the natural circulation path for transient currents, leakage currents, atmospheric discharges, etc. resulting in a system with low protection levels for the measuring equipment;
- Therefore, when considering the previous case (high and medium voltage), the use of a virtual reference point may be a good strategy, since it would guarantee that the equipment is not subjected to disturbances associated to the grounding system. However, this connection with a floating reference point could cause safety problems to the instrument operator, since during transients the voltage of the common point could fluctuate and reach high values in relation to the real earth (operator).

4. Considerations on three phase power system with return conductor

The presence of the return conductor allows the existence of zero-sequence fundamental or harmonic components (homopolars: v^0 and i^0), and in this case, it is extremely important that these components are taken into account during the power quality analyses or even in the calculation of related power terms.

According to Fig. 3b, the reference in the return wire allows the detection of zero-sequence voltage (v^0) by adding up the phase voltages. According to Fig. 2b, the detection of possible homopolar components would be done directly through the fourth transducer to the virtual point (v_{n*}), which represents a common floating point, of which the absolute potential is irrelevant, since only voltage differences are imposed on the three-phase system. In the same way as for three-wire systems, there are some points that should to be discussed in case of four-wire systems:

- Considering the costs associated to transducers, it is clear that the topology suggested in Fig. 3b would be more adequate because of the reduction of one voltage sensor.
- On the other hand, many references propose the measurement of phase voltage (a,b,c,) and also of the neutral (n). The problem in this case is that it is not always clear which is the voltage reference and which is the information contained in such neutral voltage measurements. Usually phase voltages are considered in relation to the neutral wire and neutral voltage is measured in relation to earth or a common floating point (*). This cannot provide the same results. In order to attend the Kirchhoff's Law, the sum of the measured voltages must be zero, which can only happen when voltages are measured in relation to the same potential.

- Comparing the equations related to Figs. 2b and 3b, we would still ask: what is the relationship between v_{n*} e $3v^0$, since the voltages measured in relation to the virtual point are different from those measured in relation to the neutral conductor? Therefore, taking into account these two topologies, it is essential the discussion about the impact of the voltage's referential on the assessment of homopolar components (zero-sequence), as well as on the RMS value calculation or during short-duration voltage variations. As will be shown, the measured voltages in relation to an external point has its homopolar components (fundamental or harmonic) attenuated by a factor of **1/m** (m = number of wires), which has direct impact on the several power quality indicators.

5. Apparent power definitions using different voltage referential

To analyze the influence of the voltage referential for apparent power and power factor calculations, two different apparent power proposals have been considered: the FBD Theory and the IEEE Std 1459. The following sections bring a briefly overview of such proposals.

5.1 Fryze-Buchholz-Depenbrock power theory (FBD-Theory)

The FBD-Theory collects the contribution of three authors (Fryze, 1932; Buchholz, 1950, Depenbrock, 1993) and it was proposed by Prof. Depenbrock (Depenbrock, 1962, 1979), who extended the Fryze's concepts of active and non active power and current terms to polyphase systems. At the same time, Depenbrock exploited some of the definitions of apparent power and collective quantities which were originally elaborated by Buchholz.

The FBD-Theory can be applied in any multiphase power circuit, which can be represented by an uniform circuit on which none of the conductors is treated as an especial conductor. In this uniform circuit, the voltages in the m-terminals are referred to a virtual star point "*". The single requirement is that Kirchhoff's laws must be valid for the voltages and currents at the terminals (Depenbrock, 1998).

Considering the three-phase four-wire systems (Fig. 2b), the collective instantaneous voltage and current have been defined as:

$$v_\Sigma(t) = \sqrt{v_{a*}^2 + v_{b*}^2 + v_{c*}^2 + v_{n*}^2}$$
$$i_\Sigma(t) = \sqrt{i_a^2 + i_b^2 + i_c^2 + i_n^2}$$

(1)

Thus leading straight to the collective RMS voltage and current

$$V_\Sigma = \sqrt{V_{a*}^2 + V_{b*}^2 + V_{c*}^2 + V_{n*}^2}$$

$$I_\Sigma = \sqrt{I_a^2 + I_b^2 + I_c^2 + I_n^2}$$

(2)

Differently from conventional definitions of apparent power, the Collective Apparent Power has been defined as:

$$S_\Sigma = V_\Sigma I_\Sigma = \sqrt{V_{a*}^2 + V_{b*}^2 + V_{c*}^2 + V_{n*}^2}\sqrt{I_a^2 + I_b^2 + I_c^2 + I_n^2}$$

(3)

Considering the existing asymmetries in real three-phase systems and the high current level which can circulate through the return conductor (when it is available), this definition also takes into account the losses in this path, which is not common in many other definitions of apparent power. According to various authors, this definition is the most rigorously presented up to that time, since it takes into account all the power phenomena which take place in relation to currents and voltages in the electric system (losses, energy transfer, oscillations, etc.).

The (collective) active power was given by:

$$P_\Sigma = \frac{1}{T}\int_0^T (v_{a*}i_a + v_{b*}i_b + v_{c*}i_c + v_{n*}i_n)dt \tag{4}$$

For three-wire systems (Fig. 2a) $I_n = 0$ and $V_{n*} = 0$ the expressions (3) and (4) become:

$$S_\Sigma = V_\Sigma I_\Sigma = \sqrt{V_{a*}^2 + V_{b*}^2 + V_{c*}^2}\sqrt{I_a^2 + I_b^2 + I_c^2} \tag{5}$$

and

$$P_\Sigma = \frac{1}{T}\int_0^T (v_{a*}i_a + v_{b*}i_b + v_{c*}i_c)dt \tag{6}$$

The collective active power has the same meaning and becomes identical to the conventional active (average) power (P), for both three- or four-wire systems, as indicated in (4) and (6). Finally the collective power factor has been defined as:

$$\lambda_\Sigma = \frac{P_\Sigma}{S_\Sigma} \tag{7}$$

And it represents the overall behavior (or efficiency) of the polyphase power circuit.

5.2 IEEE Standard 1459

One of the main contributions of STD 1459 is the recommendation of the use of "equivalent" voltage and current for three-phase three- and four-wire systems (Emanuel, 2004; IEEE Std 1459, 2010). These values are based on a model of a balanced equivalent electric system, which should have exactly the same losses and/or use of power as the real unbalanced system (Emanuel, 2004; IEEE Std 1459, 2010).

Considering a three-phase four-wire system, the STD 1459 recommends using the values of the equivalent or effective voltage and current as:

$$V_e = \sqrt{\frac{3(V_{an}^2 + V_{bn}^2 + V_{cn}^2) + V_{ab}^2 + V_{bc}^2 + V_{ca}^2}{18}}$$

$$\tag{8}$$

$$I_e = \sqrt{\frac{I_a^2 + I_b^2 + I_c^2 + I_n^2}{3}}$$

The voltage and current equivalent variables were initially defined by Buchholz and Goodhue (Emmanuel, 1998) in a similar formula and as an alternative way by Depenbrock

(2). Note that the effective current depends on all line and return currents and the effective voltage represents an equivalent phase voltage, which is based on all phase-to-neutral and line voltages.

Thus, the Effective Apparent Power has been defined as:

$$S_e = 3V_eI_e = 3\sqrt{\frac{3(V_{an}^2 + V_{bn}^2 + V_{cn}^2) + V_{ab}^2 + V_{bc}^2 + V_{ca}^2}{18}}\sqrt{\frac{I_a^2 + I_b^2 + I_c^2 + I_n^2}{3}} \tag{9}$$

This effective apparent power represents the maximum active power which can be transmitted through the three-phase system, for a balanced three-phase load, supplied by an effective voltage (V_e), keeping the losses constant in the line.

And the active power is:

$$P = \frac{1}{T}\int_0^T (v_{an}i_a + v_{bn}i_b + v_{cn}i_c)dt \tag{10}$$

For three-wire systems $I_n = 0$. Then, considering only the line voltages the STD 1459 suggests using the following equation for the effective apparent power:

$$S_e = 3V_eI_e = 3\sqrt{\frac{V_{ab}^2 + V_{bc}^2 + V_{ca}^2}{9}}\sqrt{\frac{I_a^2 + I_b^2 + I_c^2}{3}} \tag{11}$$

and

$$P = \frac{1}{T}\int_0^T (v_{ab}i_a + v_{cb}i_c)dt \tag{12}$$

Consequently, the Effective Power Factor has been defined as:

$$PF_e = \frac{P}{S_e} \tag{13}$$

Equation (13) represents the relationship between the real power to a maximum power which could be transmitted whilst keeping constant the power losses in the line. In the same way as in (7), the effective power factor indicates the efficiency of the overall polyphase power circuit.

5.3 Comparison between the FBD and IEEE STD 1459 power concepts

Accordingly to the previous equations and based on the Blondel theorem (Blondel, 1893), it is possible to conclude that the active power definitions from FBD or STD do not depend on the voltage referential, which could be arbitrary at this point. It means that:

$$P_\Sigma = \frac{1}{T}\int_0^T (v_{a*}i_a + v_{b*}i_b + v_{c*}i_c + v_{n*}i_n)dt = \frac{1}{T}\int_0^T (v_{an}i_a + v_{bn}i_b + v_{cn}i_c)dt = P \tag{14}$$

Considering the analyses of the collective and effective currents and voltages by means of symmetrical components, the following relations could be extracted from (Willems et al. 2005):

$$I_\Sigma = \sqrt{3} I_e = \sqrt{(I^+)^2 + (I^-)^2 + 4(I^0)^2} \tag{15}$$

where the positive sequence, negative sequence and zero-sequence components are indicated by the subscripts + , - and 0, respectively.

Moreover, in case of unbalanced three phase sinusoidal situation, the collective RMS values of the voltage (FBD) can also be expressed by means of the sequence components, such as:

$$V_\Sigma = \sqrt{(V^+)^2 + (V^-)^2 + \frac{1}{4}(V^0)^2} \tag{16}$$

Now, assuming the equivalent voltage from the STD:

$$V_e = \sqrt{(V^+)^2 + (V^-)^2 + \frac{1}{2}(V^0)^2} \tag{17}$$

It is possible to observe that the equivalent and collective currents match for both proposals, except for the factor $\sqrt{3}$, which indicates the difference between the single and three-phase equivalent models of the STD and FBD, respectively. However, from (16) and (17) one can notice that the equivalent voltages differ for these two proposals.

Consequently, the choice of the voltage referential affects the zero-sequence components calculation and therefore, it affects the effective and collective voltages definitions, as well as the apparent power and power factor calculations in both analyzed proposals.

Next sections will illustrate the influence of the voltage referential in terms of several power quality indicators.

6. The influence of the voltage referential on power quality analyses

In this section, several simulations will be presented and discussed considering three-phase three- and four-wire systems. The main goal is to focus on the effect of different voltage referentials (return conductor or virtual star point) on the analyses of some Power Quality (PQ) Indicators. The resulting voltage measurements and PQ indicators using both voltage referentials will be also compared to the voltages at the load terminals. The main disturbances considered in the analysis are: harmonic distortions, voltage unbalances and voltage sag.

The analyses of such disturbance can be exploited in terms of the following indicators:

- RMS value:

$$V = \sqrt{\frac{1}{T} \int_0^T v^2(t) \, dt} \tag{18}$$

- Total Harmonic Distortion (THD$_V$):

$$THD_V = \sqrt{\frac{\sum_{k=2}^{\infty} V_k^2}{V_1^2}} \tag{19}$$

- Voltage Unbalance Factors:

$$K^- = \frac{V^-}{V^+}$$
$$K^0 = \frac{V^0}{V^+}$$
(20)

In the first case, events in the voltage source are generated to quantify the impact of the voltage reference on the occurrence of voltage sags. In the second case, distortions are generated in the voltage source by injecting odd harmonics up to the fifth order with amplitudes of 50% of the fundamental. In the third case, imbalances are imposed through the voltage source, generating negative- and zero-sequence components.

6.1 Three phase power system without return conductor

Considering the line quantities estimation (load in delta configuration) and assuming the voltage measurements referred to a virtual point, an adaptation of the algorithm is necessary since these voltages are virtual phase voltages, and the line voltages can be expressed as:

$$v_{a*} - v_{b*} = v_{ab}$$

$$v_{b*} - v_{c*} = v_{bc}$$
(21)

$$v_{c*} - v_{a*} = v_{ca}$$

and the RMS values are:

$$V_{ab} = \frac{1}{T}\int_0^T (v_{a*} - v_{b*})dt$$

$$V_{bc} = \frac{1}{T}\int_0^T (v_{b*} - v_{c*})dt$$
(22)

$$V_{ca} = \frac{1}{T}\int_0^T (v_{c*} - v_{a*})dt$$

In the case of an under-voltage event, Fig. 4 shows that both measuring methods adequately represent the impact effectively experienced by load (superimposed curves), either in terms of their magnitude or duration of the voltage sag. On the other hand, Fig. 5 shows that both measuring topologies being discussed are equivalent with regard to the measuring of harmonic components, thus representing their impact on the loads (superimposed spectra).

To assess the performance of both methodologies with regard to the unbalance factors, the three-phase source was defined with amplitude and phase angle as indicated in Table 1.

b) Reference at phase *b*   b) Reference at the virtual point
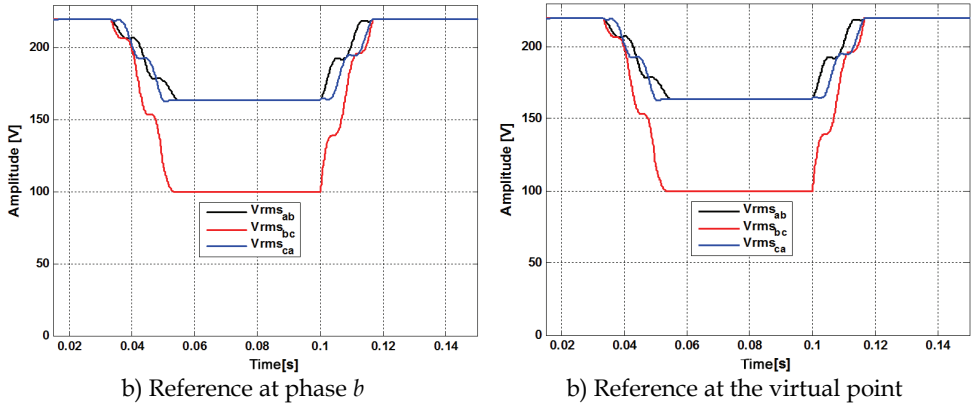
Fig. 4. Evolution RMS values during voltage sag between phases *b* and *c* from 220V to 100V (4 cycles).

b) Reference at phase *b*   b) Reference at the virtual point
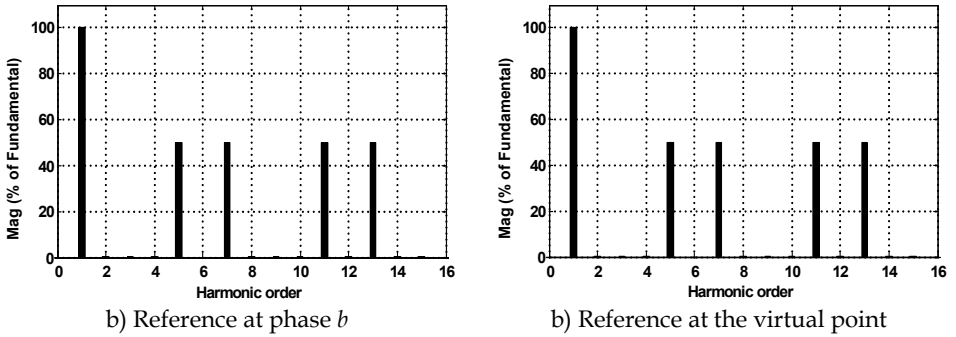
Fig. 5. Spectral analysis with each measuring topology (3 wires)

	Test 1		Test 2	
Source Voltage	Amplitude	Angle	Amplitude	Angle
v_a	179.61 V	0°	179.61 V	0°
v_b	159.81 V	-104.4°	159.81 V	-104.4°
v_c	208.59 V	132.1°	208.59 V	144°
	Test 3		Test 4	
	Amplitude	Angle	Amplitude	Angle
v_a	197.57 V	0°	197.57 V	0°
v_b	171.34 V	-125.21°	171.34 V	-114.79°
v_c	171.34 V	125.21°	171.34 V	114.79°

Table 1. Voltages and phase angles programmed at the power source

In this case the negative-sequence unbalance factor (K⁻) is identical for both measuring methodologies (vide table 2), which also coincides with the theoretical value and the

measurements at the load terminals. As it was expected, the zero-sequence unbalance factor (K^0) is nil due to the lack of a return conductor.

Test	Theoretical Value		Reference at phase b		Reference at the virtual Point		Measurement at load terminals	
	$K^-(\%)$	$K^0(\%)$	$K^-(\%)$	$K^0(\%)$	$K^-(\%)$	$K^0(\%)$	$K^-(\%)$	$K^0(\%)$
1	15.92	0.00	15.92	0.00	15.92	0.00	15.92	0.00
2	19.49	0.00	19.49	0.00	19.49	0.00	19.49	0.00
3	10.00	0.00	10.00	0.00	10.00	0.00	10.00	0.00
4	0.00	0.00	0.00	0.00	0.00	0.00	0.00	0.00

Table 2. Unbalance factor calculated according to each measurement method

6.2 Three phase power system with return conductor

Fig. 6a shows that the voltage measurement using the return wire as the reference, correctly detects the presence of odd harmonics, with 50% amplitudes. Therefore, it is in this scenery that the real impact on the load Fig. 6 is being quantified. Note that when the virtual point is used as voltage reference (Fig. 6b) the harmonics multiples of 3 are not correctly detected. These homopolar components are attenuated by a factor of ¼ in relation to the expected voltage spectrum on the load. The other harmonic components do not suffer attenuation, because they either are of positive- or negative-sequence.

a) Reference at neutral conductor   b) Reference at the virtual point
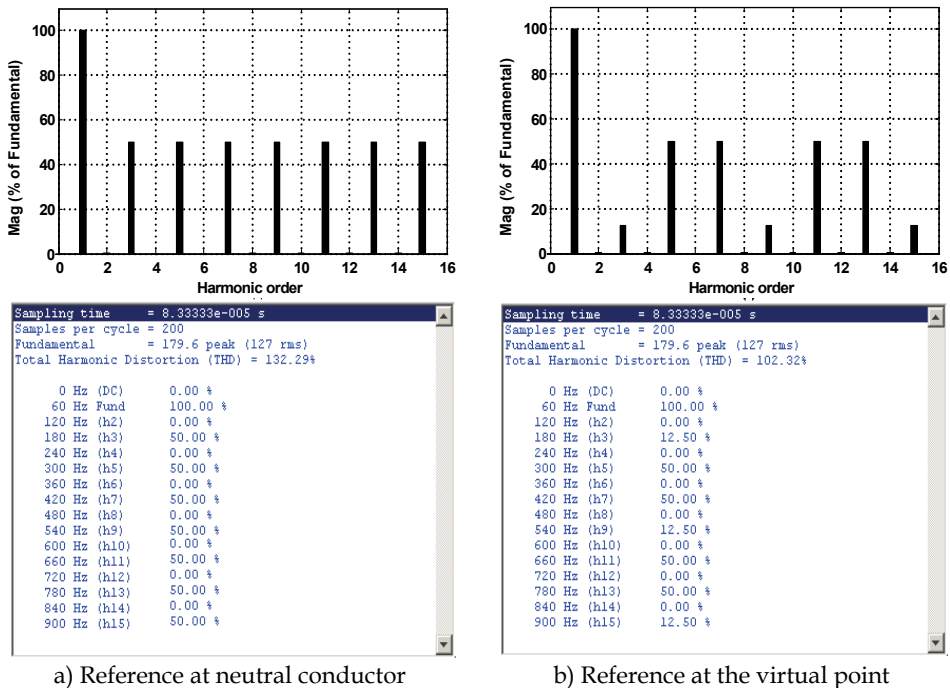
Fig. 6. Spectrum analysis with each measuring topology (4 wires)

a) Reference at neutral conductor   b) Reference at the virtual point
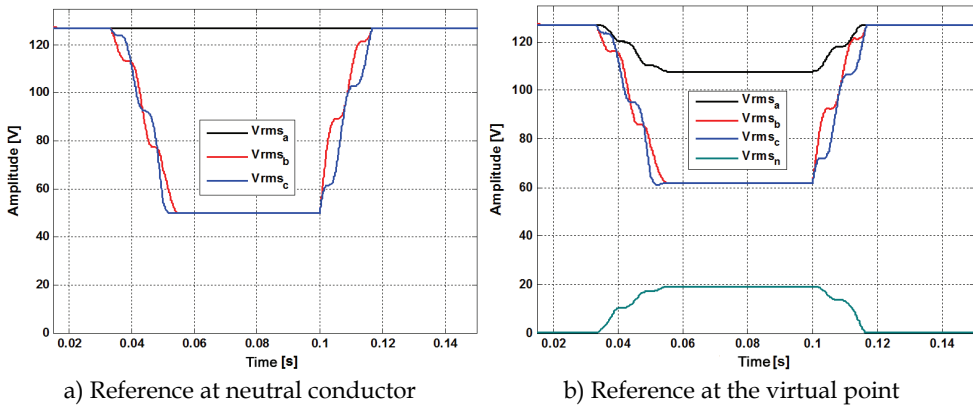
Fig. 7. Evolution of RMS values during a voltage sag between phases *b* and *c* from 127V to 50V (4 cycles)

Fig. 7a shows when the reference is set in the return conductor the event is correctly detected and quantified (amplitude and duration) in all phases, thus representing the exact impact on the load. However with the use of a virtual point as the voltage reference the event is detected, but it does not show how it is generated or how it could affect the load (Fig. 7b). Thus, this measuring method affects the assessment of the impact during voltage sag.

According to Table 3 both the voltage reference on the return wire and on the virtual point detected equal imbalances for the negative component (K-). However, the zero-sequence indicator (K^0), calculated by means of the virtual reference point voltages is different from expected. It is attenuated by a factor of ¼ (1/m).

Test	Theoretical Value		Reference at the neutral conductor		Reference at the virtual point		Measurement at load terminals	
	$K^-(\%)$	$K^0(\%)$	$K^-(\%)$	$K^0(\%)$	$K^-(\%)$	$K^0(\%)$	$K^-(\%)$	$K^0(\%)$
1	15.92	0.00	15.92	0.00	15.92	0.00	15.92	0.00
2	19.49	8.02	19.49	8.02	19.49	2.01	19.49	8.02
3	10.00	0.00	10.00	0.00	10.00	0.00	10.00	0.00
4	0.00	10.00	0.00	10.00	0.00	2.50	0.00	10.00

Table 3. Unbalance factor calculated according to each type of measurement

7. Attenuation and recovery of the zero-sequence component

From the previous results it can be concluded that in case of three-phase four wire circuits and in the presence of zero-sequence components (fundamental or harmonic), there is a clear difference between the two voltage referential methods. Therefore, it is important to provide a careful analysis of the two methodologies and the differences found between them.

Consider a set of three-phase and periodic voltage sources v_a, v_b e v_c, connected as in Fig. 8. In terms of symmetric components these voltages can be expressed as:

$$v_a = v_a^+ + v_a^- + v^0$$

$$v_b = v_b^+ + v_b^- + v^0 \qquad (23)$$

$$v_c = v_c^+ + v_c^- + v^0$$
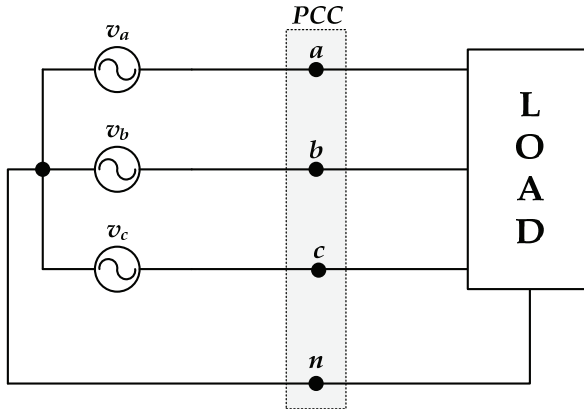
Fig. 8. Three-phase four-wire system

Considering the measurements with voltage reference at the neutral, Fig. 9 shows a circuit on which the neutral is utilized as the voltage reference, where R is the resistance of the voltage meter.
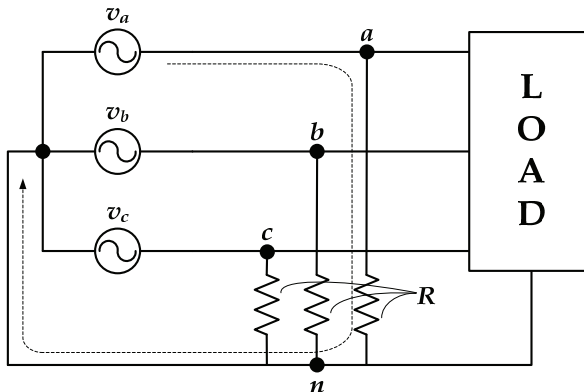

Fig. 9. Measurement topology considering the reference on the return conductor

Assuming that the value of R is much greater than the values of the load impedances, we can take into account only the links formed by the voltage sources and the measuring instruments, and substitute the voltages of the sources by their respective sequence components. Thus, the circuit of Figure 9 can be represented as in Fig. 10.
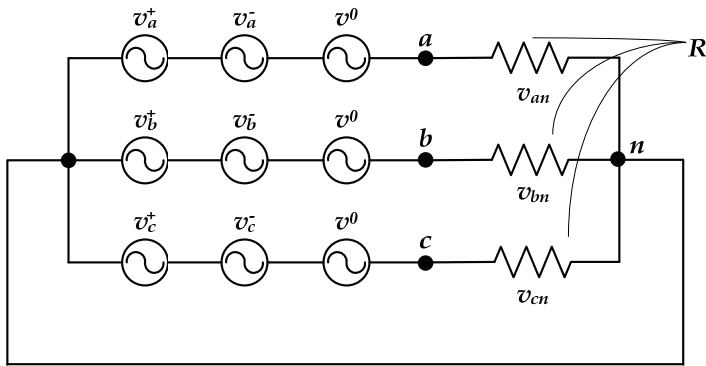
Fig. 10. Equivalent circuit for measuring to the neutral conductor

Since v_{an}, v_{bn} e v_{cn} are the voltage drops over each instrument's resistances, it follows that:

$$v_{an} = v_a^+ + v_a^- + v^0$$
$$v_{bn} = v_b^+ + v_b^- + v^0 \qquad (24)$$
$$v_{cn} = v_c^+ + v_c^- + v^0$$

In this way, it can be seen that the measured voltages in relation to the neutral correspond to the imposed voltages by the source, containing all sequence components (positive, negative and zero), as it has been shown earlier in the sag, harmonics and unbalance tests.

On the other hand, Fig. 11 shows a circuit on which the virtual point is used as the voltage referential. As in the circuit of Fig. 10, we can represent the circuit shown in Fig. 11 through its sequence components (Fig. 12).
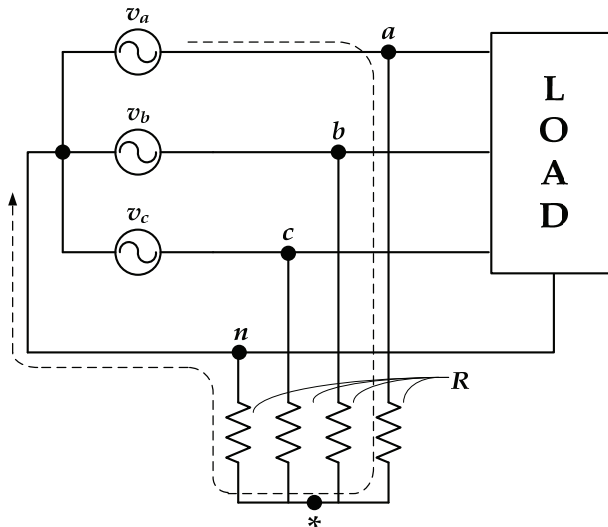
Fig. 11. Measurement topology considering the reference on the virtual point
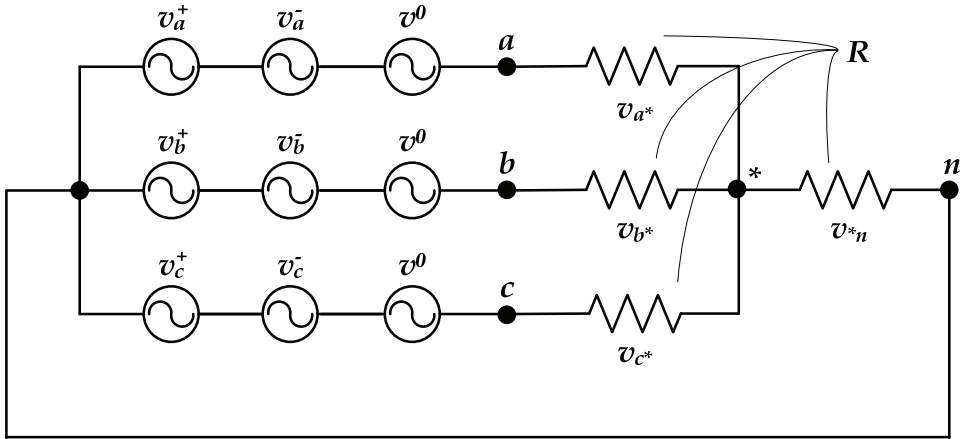
Fig. 12. Equivalent circuit for measuring to the virtual point

As it is known, the negative- and zero-sequence components are indicators of abnormal conditions (imbalances and/or harmonics) of an electric circuit. If we consider that the negative-sequence components "see" practically the same circuit as the positive-sequence components, the return (neutral) wire therefore is not necessary, as opposed to the zero-sequence current that only occurs in the presence of a return wire.

In this way, if we consider the superposition theorem, we can decompose the circuit in Fig. 12 into a circuit containing positive- and negative- components (Fig. 13) and another circuit containing only zero-sequence components (Fig.14).
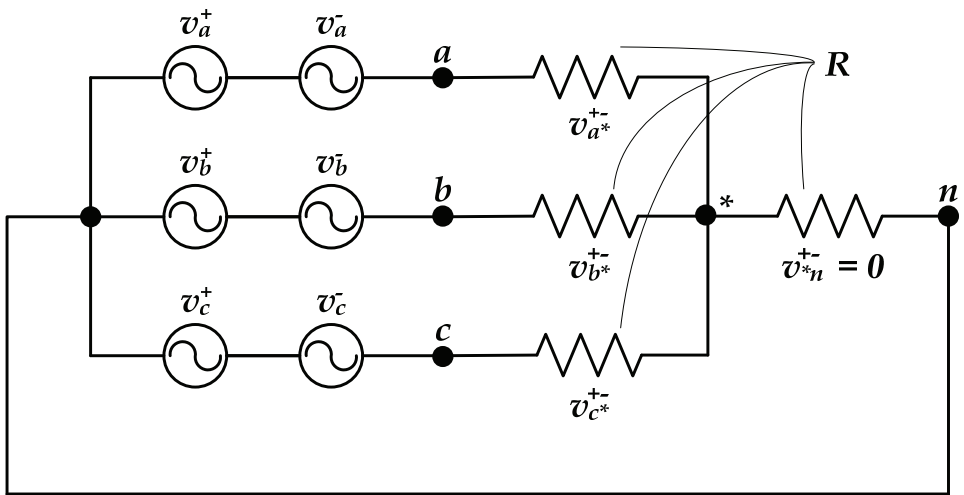
Fig. 13. Decomposition: positive- and negative-sequence circuit by superposition theorem
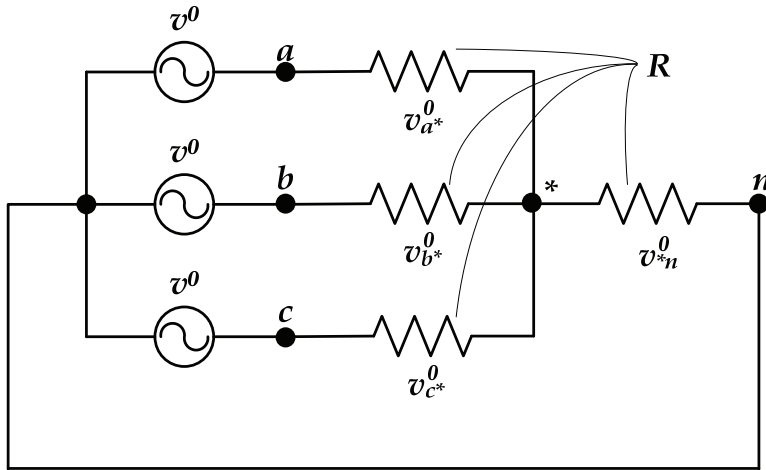
Fig. 14. Decomposition: zero-sequence circuit by superposition theorem

From the circuit in Fig. 13 we have the following:

$$v_{a*}^{\pm} = v_a^+ + v_a^-$$

$$v_{b*}^{\pm} = v_b^+ + v_b^- \tag{25}$$

$$v_{c*}^{\pm} = v_c^+ + v_c^-$$

According to the superposition theorem (Fig.13 and 14), the measured voltages to a virtual point can be written as:

$$v_{a*} = v_{a*}^{\pm} + v_{a*}^0$$

$$v_{b*} = v_{b*}^{\pm} + v_{b*}^0 \tag{26}$$

$$v_{c*} = v_{c*}^{\pm} + v_{c*}^0$$

On the other hand, Fig. 14 can also be represented by the circuit shown in Fig. 15, based on Blakesley transform (Blakesley, 1894).
Thus, for the circuit in Fig. 15 we can apply the voltage divider rule:

$$v_{a*}^0 = v_{b*}^0 = v_{c*}^0 = \frac{R_{Eq}}{R_T} v^0 = \frac{1}{4} v^0$$

$$\tag{27}$$

$$v_{n*} = \frac{R}{R_T} v^0 = -v_{*n} = -\frac{3}{4} v^0$$
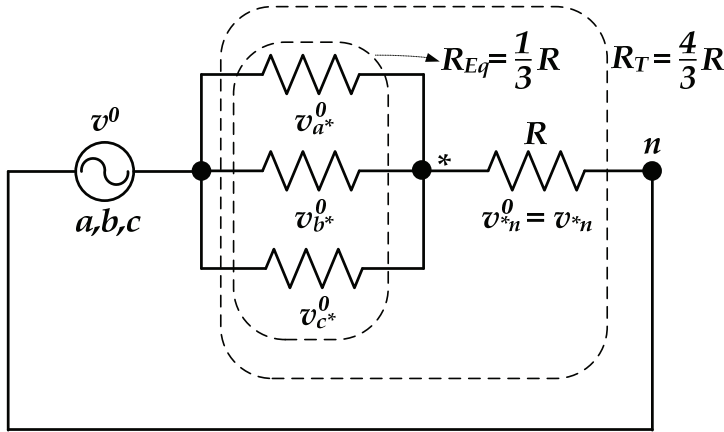
Fig. 15. Transformed Zero-sequence Circuits (Blakesley's theorem)

Equation (27) indicates the zero-sequence components of phase and neutral voltages regarding to the virtual point. In this way, the total voltages (measured to the virtual point), taking into account positive-, negative- and zero-sequence components, can be obtained by substituting (27) in (26):

$$v_{a*} = v_a^+ + v_a^- + \frac{1}{4}v^0$$

$$v_{b*} = v_b^+ + v_b^- + \frac{1}{4}v^0 \tag{28}$$

$$v_{c*} = v_c^+ + v_c^- + \frac{1}{4}v^0$$

Note that the zero sequence component is attenuated by a factor of ¼ of its real value, which means that for applications where its quantification is necessary, the measured value must be corrected. This can be done by adding (¾ v^0) on both sides of the equation (29):

$$v_{a*} + \frac{3}{4}v^0 = v_a^+ + v_a^- + v^0$$

$$v_{b*} + \frac{3}{4}v^0 = v_b^+ + v_b^- + v^0 \tag{29}$$

$$v_{c*} + \frac{3}{4}v^0 = v_c^+ + v_c^- + v^0$$

From (31) we have:

$$\frac{3}{4}v^0 = -v_{n*} \tag{30}$$

Equation (30) finally provides the relationship between the measured voltage between the neutral and the virtual point and the zero-sequence component (homopolar). This equation allows us, to compare both measuring methodologies, as well as to provide algorithms for the measuring and monitoring equipments, which are correct, independently of the type of connection chosen by the end user.

Due to the differences in the apparent power, as indicated by (16) and (17), inclusion of equation (30) may be necessary in order to avoid miscalculation of the power terms and possible costumer's penalization.

8. Conclusions

It has been shown that in case of three-phase three-wire systems (without a return wire), both voltage references (neutral or virtual point) provide identical measurements due to the lack of homopolar components (zero-sequence), which are filtered by the topology of the system itself. However for return-wire systems, there is a need to take certain aspects into consideration, as for example, the attenuation of homopolar components (zero-sequence) if measuring the voltages to a virtual star point.

In this way, to measure voltage in modern installations with the presence of distortions and imbalances, the choice of a reference point must be made very carefully and its implications must be taken into account in applications such as pricing, measurement, power quality monitoring, compensation, protection, etc.

Despite of the demonstration of how to recover the homopolar components, attenuated by the virtual point measurements, the connection referenced to the neutral continues to be the best option, especially for low voltage applications, due to the fact that it needs less one measuring channel. However, considering applications in high-voltage systems (3 wires), the use of an external virtual point may be an interesting option, from the point of view of the protection of the measuring equipments.

Finally, it is worth pointing out that the proposed methodology to associate two methods for measuring voltages, by using Blakesley Theorem, can also be used in order to find a convergence point between the different power theories.

9. Acknowledgment

10. References

Akagi, H. and Nabae A. (1993). The p-q Theory in Three-Phase Systems Under Non-Sinusoidal Conditions. *ETEP European Transaction on Electrical Power Engineering*. Vol. 3, No. 1, (January/February 1993), pp. 27-31.

Blakesley T. H. (1894). A New Electrical Theorem. *Proceedings of the Physical Society of London*, Vol.13, pp. 65-67.

Blondel A. (1893). Measurement of Energy of Polyphase currents. *Proceeding of. International Electrical Congress Chicago III*, pp. 112-117.

Buchholtz, F. (1950). Das Bergiffsystem Rechtleistung, Wirkleistung, totale Blindleistung. Selbstverlag München, 1950.

Czarnecki, L .S. (2008). Currents' Physical Components (CPC) Concept: A Fundamental of Power Theory. *Przegląd Elektrotechniczny (Electrical Review).* Vol. 84, No. 6, pp. 28-37.

Depenbrock, M. (1962). Untersuchungen über die Spannungs- und Leistungsverhältnisse bei Umrichtern ohne Energiespeicher. PhD Thesis, Technical University of Hannover, Germany.

Depenbrock, M. (1979). Wirk- und Blindleistungen Periodischer Ströme in Ein- u. Mehrphasensystemen mit Periodischen Spannungen beliebiger Kurvenform. *ETG Fachberichte* No. 6, pp. 17-59.

Depenbrock, M. (1993). The FBD-Method, a Generally Applicable Tool for Analyzing Power Relations. *IEEE Transaction on Power Systems.* Vol.8, No.2, (May 1993), pp. 381-387, ISSN 0885-8950.

Depenbrock, M. (1998). Quantities of a MultiTerminal Circuit Determined on the Basis of Kirchhof's Laws, *ETEP European Transactions on Electrical Power*, Vol. 8, No. 4, pp. 249–257.

Emanuel, A. E. (1998). The Buchholz-Goodhue Apparent Power Definition: The Practical Approach For Nonsinusoidal and Unbalanced Systems. *IEEE Transaction on Power Delivery*, Vol. 3, pp. 344-350, ISSN: 0885-8977.

Emanuel, A. E. (2003). Reflections on the Effective Voltage Concept. *Proceedings of Sixth International Workshop on Power Definitions and Measurements under Non-sinusoidal Conditions*, pp. 1-8, Milano, Italy, October 13-25.

Emanuel, A. E. (2004). Summary of IEEE Standard 1459: Definitions for the Measurement of Electric Power Quantities under Sinusoidal, Nonsinusoidal, Balanced or Unbalanced Conditions. *IEEE Transactions on Industry applications*. Vol. 40, No. 3, (May/June 2004), pp. 869-876, ISSN: 0093-9994.

Ferrero, A. (1998). Definitions of Electrical Quantities Commonly Used in Nonsinusoidal Conditions. *ETEP European Transaction on Electrical Power Engineering*, Vol. 8, No. 4, (July/August 1998), pp. 235-240.

Fryze, S. (1933). Wirk-, Blind- und Scheinleistung in Elektrischen Stromkreisen mit Nichtsinusförmigem Verlauf von Strom und Spannung" Elektrotechnische Zeitschrift. Vol. 53, No. 25, pp.596-599, 625-627, 700-702.

IEEE Standard 1459 (2010). *IEE Standard Definitions for the Measurement of Electric Power Quantities under Sinusoidal, Non-sinusoidal, Balanced or Unbalanced Conditions*. ISSN 978-0-7381-6058-0, New York USA.

Marafão F. P. (2004). Análise e Controle da Energia Elétrica Através de Técnicas de Processamento Digital de Sinais. PhD. Thesis, Universidade de Campinas (UNICAMP), Campinas, Brazil.

Marafao, F. P. Liberado, E. V. Morales Paredes, H. K. and Pereira da Silva, L. C. (2010). Three-Phase Four-Wire Circuits Interpretation by means of Different Power Theories. *Proceedings of IEEE International School on Nonsinusoidal Currents and Compensation*, pp. 104-109, ISBN: 978-1-4244-5436-5, Poland, June, 2010.

Moreira, A. C. Marafão, F. P. Deckmann, S. M. and Morales Paredes, H. K. (2006). Análise Comparativa das Técnicas de Medição de Potência Baseadas na Recomendação IEEE 1459-2000 e no Método FBD. *Proceedings of IEEE Industry Applications Conference.*

Tenti, P. Mattavelli, P. and Morales Paredes, H. K. (2010). Conservative Power Theory, Sequence Components and Accounting in Smart Grids. *Przegląd Elektrotechniczny (Electrical Review)*. Vol. 86, No. 6, pp. 30-37, ISSN PL 0033-2097.

Willems J. L. and Ghijselen J. A. (2003). The Choice of the Voltage Reference and the Generalization of the Apparent Power. *Proceedings of Sixth International Workshop on Power Definitions and Measurements under Non-sinusoidal Conditions*, pp. 9-18. Milano, Italy, October 13-25.

Willems J. L. Ghijselen J. A. Emanuel A. E. (2005). The Apparent Power Concept and the IEEE Standard 1459-2000. *IEEE Transaction on Power Delivery*, Vol.20, No.2, pp. 876-884, ISSN 0885-8977.

Willems, J. L. (2004). Reflections on Apparent Power and Power Factor in Non-sinusoidal and Poly-phase Situations. *IEEE Transaction on Power Delivery*. Vol 19, No.2, pp. 835-840, ISSN 0885-8977.

Single-Point Methods for Location of Distortion, Unbalance, Voltage Fluctuation and Dips Sources in a Power System

Zbigniew Hanzelka, Piotr Słupski, Krzysztof Piątek,
Jurij Warecki and Maciej Zieliński
AGH-University of Science & Technology, Krakow
Poland

1. Introduction

The old model in which the problem of power quality (PQ) involved two partners – the electricity supplier and the customer – is replaced by a new configuration where at least four, mutually dependent parties participate: the customer, supplier of electric power, manufacturer of equipment and electrical installation contractor. The supplier often insists that sources of disturbances are located at the customer's side, whereas the latter complains about causes located in the supply network. It happens that their discussion leads to the conclusion, shared by both parties, that the equipment is not properly installed or adequately designed, to be operated in the given electromagnetic environment.

Often, in the case of a significant level of a disturbance in electrical power system, at the customer's supply terminals, there is a need for locating the source of harmonics (e.g. [7-9,14,21,27,32-35,38,40-43]), voltage fluctuations (e.g. [10-13,36,]), voltage dips (e.g. [17,19,22,25,26,29-31,37,39]), occasionally also asymmetry. With the deregulation of power industry, utilities have become increasingly interested in quantifying the responsibilities for power quality problems. This issue gains particular meaning when formulating contracts for electric power supply and enforcing, by means of tariff rates, extra charges for worsening the power quality.
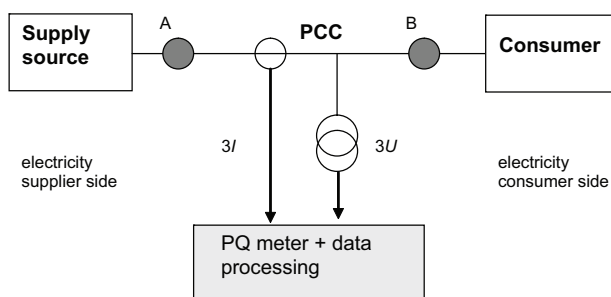

Fig. 1. Problem of locating the voltage disturbance sources

There are two, sometimes separate problems which can be stated as follows (Fig. 1). First details concerning the location of disturbance source. A power quality monitor captures disturbance-containing voltage and current waveforms at the point of common coupling (PCC). It is required to determine if the disturbance comes from the upstream or the downstream. As a result, both the supply utility and customer can obtain a list of disturbances, their severity and directions. Such information will greatly facilitate the resolution of disputes between the two parties if a disturbance results in financial losses to either party.

The second is to assess the emission level of the particular considered load or supplier in order to quantitative evaluation of the both parts contribution to the total disturbance level measured at the point of power delivery. The goal is to check the fulfilment of standard or contract requirements.

Solution for both problems posed above is not a trivial task. Works focused on this subject have been carried out for many years. Numerous methods have been proposed and published, only a part of them having practical significance. They differ in the probability of inference correctness (e.g. locating a disturbance source), the value of error made (e.g. determining an individual customer's share in the total disturbance level), the time required to carry out measurements, the number and complexity of equipment needed, etc.

This chapter deal with the first of the two problems specified above - location of the disturbance source based on measurements made at a single point of a network (PCC), and does not concern an assessment of individual emission. Selected methods are presented for high harmonics, voltage fluctuations, voltage dips and unbalance, that allow determining location of the disturbance source: at the supplier side (upstream) or at the customer side (downstream), as viewed from PCC.

2. Voltage harmonics

The most commonly practical method for locating harmonic sources is based on determining the direction of active power flow for given harmonics, though many authors indicate its limitations e.g. [7,34,42,43]. Many other techniques are based on investigation of the "critical impedance" [21], the so-called voltage index value [32-34,41], interharmonic injection [42], determining voltage and current relative values [38], etc. Some methods determine the dominant harmonics source together with their quantitative contribution.

In most cases these methods, aside from their technical complexity, require precise information on values of equivalent parameters of the analysed system, which are difficultly accessible, or can only be obtained in result of costly measurements. As the examples some selected methods are more detail described below. They are presented employing the equivalent Thevenin circuit for the considered harmonic analysis (Fig. 2).
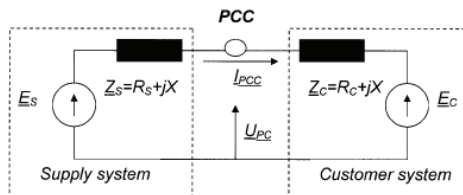

Fig. 2. Equivalent circuit for disturbance analysis $\underline{U}_{PCC}, \underline{I}_{PCC}$ - voltage and current values measured at PCC; $\underline{Z}_S$, $\underline{Z}_C$ – equivalent impedances of the supplier and customer sides; $\underline{E}_S$, $\underline{E}_C$ – harmonic voltages at the supplier and customer sides

2.1 The criterion of active power flow direction

The dominant source of the considered harmonic (h-th order) can be located analysing this harmonic active power (P_h) flow at PCC. Analysing the sign of this power at the measurement point we can conclude that:

- the positive sign of active power at PCC ($P_h>0$) means the dominant source of the considered harmonic is the supplier,
- the negative sign of active power at PCC ($P_h<0$) means the dominant source of the considered harmonic is the consumer.

A non-zero value of active power is the result of mutual interaction of the same frequency voltage and current, and is determined by the formula:

$$P_h = U_h I_h \cos\left(\Phi_{U_h} - \Phi_{I_h}\right) = U_h I_h \cos\varphi_h \tag{1}$$

where: U_h and I_h – rms voltage and current values of the h-th harmonic
         Φ_{U_h} and Φ_{I_h} - the h-th harmonic current and voltage phase angles.

The method is equivalent to examining of the phase shift angle φ_h between the considered harmonic voltage and current. If this angle is contained within the interval $-\pi/2 \langle \varphi \langle \pi/2$ then, according to this criterion, the dominant disturbance source is located at the supplier side. If the condition $\pi/2 \langle \varphi \langle 3\pi/2$ is fulfilled, the customer is the dominant source of the considered harmonic. For $\varphi = \pm\pi/2$ there is no decision about the dominant source of harmonic.
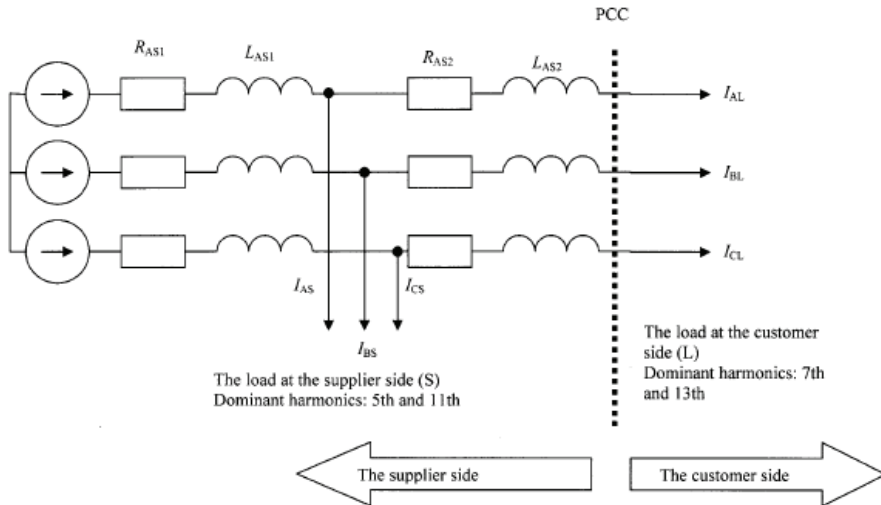

Fig. 3. Model of the electric power network chosen for simulations illustrating the active power flow method

Fig. 3 shows a simplified model of electric power network employed in the investigation, the supplier and customer sides are indicated. For the purpose of illustration let us assume the supplier is the dominant source of 5th and 11th harmonics and the customer is the dominant source of 7th and 13th harmonics. The above assumption is valid for both the

balanced and unbalanced system (Table 1). Balanced *RL* loads are connected in parallel with non-linear loads represented by currents I_{iS}, I_{iL} for i = A, B, C.

Fig. 4 summarizes the simulation results for selected cases. It is evident that in the case of balance for the considered harmonic the method correctly locates the dominant source of disturbance: at the supplier or customer side, also in the case where non-linear loads are connected at both sides of PCC

In the latter case a change in the phase shift angle between the current harmonics generated at the supplier and customer side may, in a certain interval of values, affect correctness of the inference about the disturbance source location. Fig. 6 shows the fifth harmonic active power variation at PCC for the case when the customer and supplier fifth harmonic relations were (a) 1:1.2 and (b) 1:1.8, and the phase shift angle between the 5th harmonic currents was varying within the interval 0-360⁰. The larger the difference between the values of customer and supplier harmonic currents, the wider is the angle interval in which the inference is correct.

| h	Phase A				Phase B				Phase C			
	Supplier		Customer		Supplier		Customer		Supplier		Customer	
	$I_{\mathrm{m}}[A]$	$\varphi_{Ih}[^o]$	$I_{\mathrm{m}}[A]$	$\varphi_{Ih}[^o]$	$I_{\mathrm{m}}[A]$	$\varphi_{Ih}[^o]$	$I_{\mathrm{m}}[A]$	$\varphi_{Ih}[^o]$	$I_{\mathrm{m}}[A]$	$\varphi_{Ih}[^o]$	$I_{\mathrm{m}}[A]$	$\varphi_{Ih}[^o]$
5	2.75/2.7	41/41	1.5/1.5	26/26	2.75/2.5	161/74	1.5/1.3	146/33	2.75/5	281/-123	1.5/2.7	266/-150.7
7	1/1	-25/-25	2.3/2.3	-15/-15	1/1.2	-145/-15	2.3/1.6	-135/-22	1/2.2	-265/-160	2.3/3.9	-255/167
11	1.6/1.6	100/100	0.9/0.9	79/79	1.6/1.35	220/199	0.9/1.1	199/96	1.6/1.9	340/-36	0.9/2	319/-91.6
13	0.2/0.2	-75/-75	0.65/0.65	-56/56	0.2/0.3	-195/30	0.65/0.7	-176/-77	0.2/0.3	-315/172	0.6/1.4	-296/112.7

Table 1. The supplier and customer harmonics – balanced/unbalanced system

Fig. 5 shows analogical simulations but for an unbalanced system. In the case of harmonic source located only at one side of PCC the calculated powers of harmonics in particular phases have different values but in the analysed case maintain the same sign and correctly indicate the source of disturbance.

In the case harmonic sources are located at both the supplier and customer side, the inference based on this method can not be correct. Comparison of simulation results in Fig. 5 with data contained in Table 1 indicates that the party responsible for 13th harmonic distortion was wrongly identified. The dominant party, responsible for the 13th harmonic presence in all phases is the customer, whereas the result of identification indicates the supplier in phases B and C. Thus the method fails also in the case of the considered circuit unbalance.
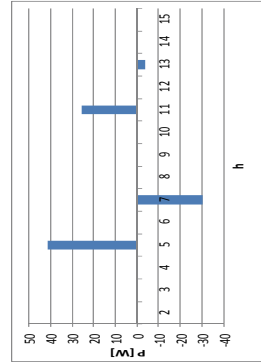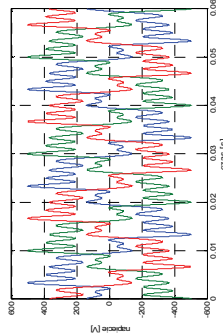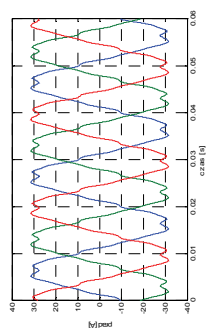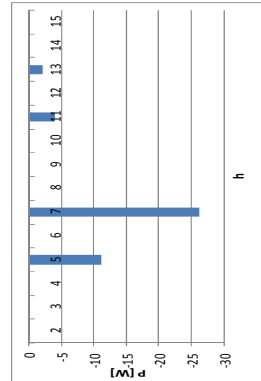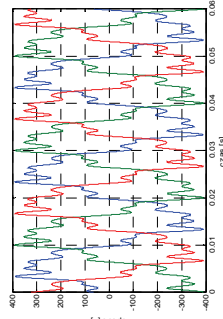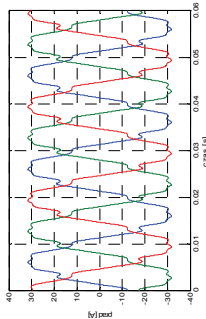
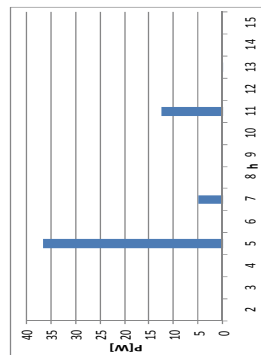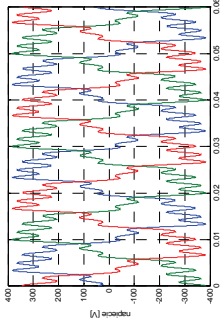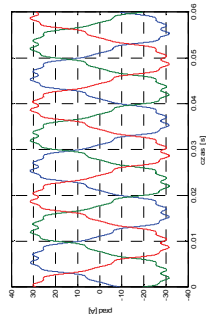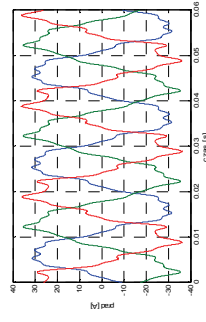Fig. 4. The active power direction criterion for particular harmonics – example simulation results for a balanced system (Fig. 3)
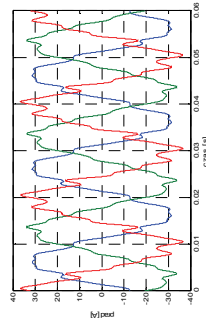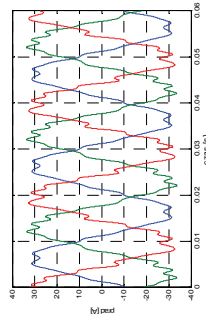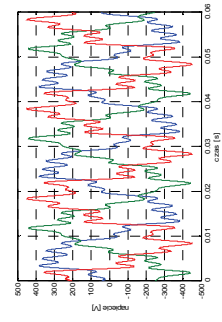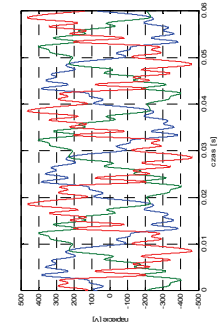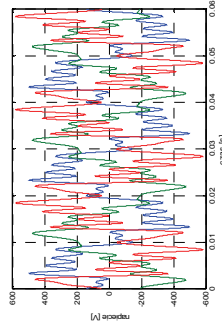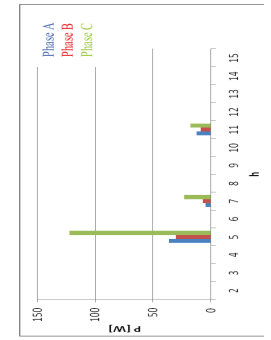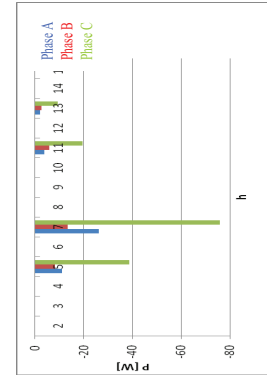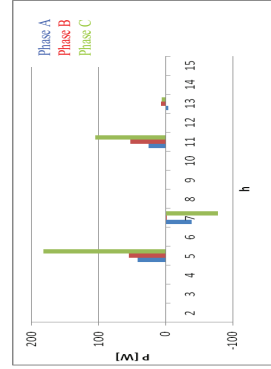
Fig. 5. The active power direction criterion for particular harmonics – example simulation results for an unbalanced system (Fig. 3)
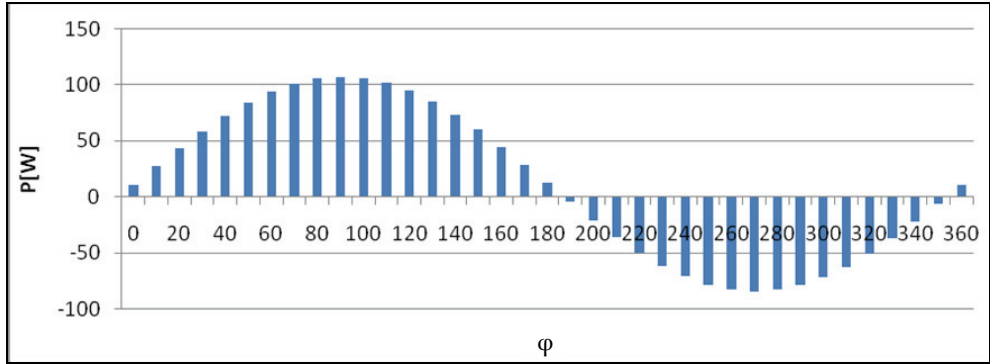
a)
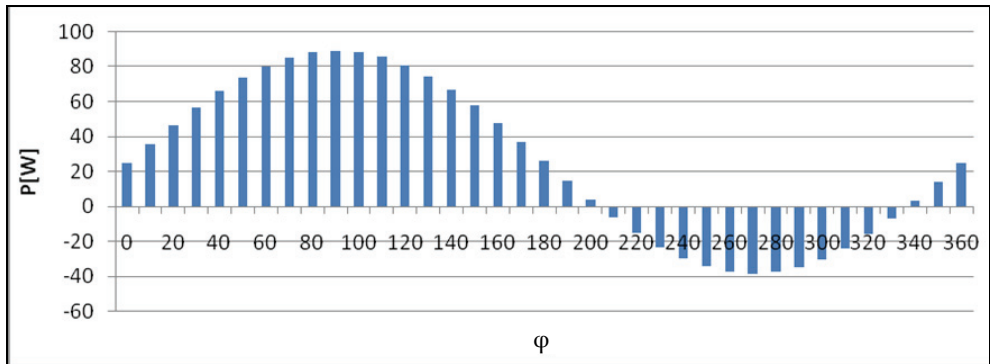
b)

Fig. 6. Variation of the 5th harmonic active power at PCC for different values of the phase shift angle φ between the customer and supplier current and various relations between their rms values: (a) 1:1.2; (b) 1:1.8
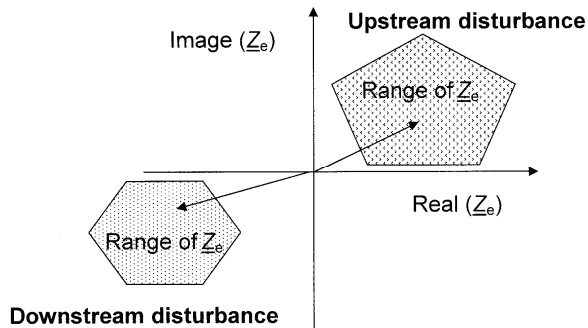
Fig. 7. Impedance plane illustration for result interpretation (criterion of the real part of the equivalent impedance at PCC – Chapter 2.2)

2.2 Criterion of the real part of the equivalent impedance at PCC [37]

The balance system of Fig. 1 can be represented by an equivalent one-phase circuit shown in Fig. 2. This is a h. harmonic circuit, $\underline{Z}_S$ and $\underline{E}_S$ are equivalent impedance and internal voltage source of the left side (supply system, upstream). $\underline{Z}_C$ and $\underline{E}_C$ are the similar parameters for the customer system on the right side.

Assume a disturbance occurs on the customer-side and leads to a voltage change at PCC (for considered harmonic), the measurements satisfy this equation before the occurrence of the event:

$$\underline{U}_{PCC} = \underline{E}_S - \underline{I}_{PCC}\underline{Z}_S \tag{2}$$

When a disturbance occurs, the voltage and current are changed to $\underline{U}_{PCC} + \Delta\underline{U}_{PCC}$ and $\underline{I}_{PCC} + \Delta\underline{I}_{PCC}$, where $\Delta\underline{U}_{PCC}$ and $\Delta\underline{I}_{PCC}$ are the voltage and current changes due to the customer-side event. If we assume that the parameters on the supply-side ($\underline{Z}_S$ and $\underline{E}_S$) remain unchanged during the disturbance period, a similar equation can be written as:

$$\underline{U}_{PCC} + \Delta\underline{U}_{PCC} = \underline{E}_S - \left(\underline{I}_{PCC} + \Delta\underline{I}_{PCC}\right)\underline{Z}_S \tag{3}$$

Since the probability that a disturbance occur on both sides simultaneously is practically zero, the above assumption that the parameters on the no disturbance side are constant is justifiable. Subtracting (2) from (3), we can find: the impedance of the no disturbance (supply) side as:

the impedance of the no disturbance (supply) side $\qquad \underline{Z}_S = -\dfrac{\Delta\underline{U}_{PCC}}{\Delta\underline{I}_{PCC}}$

the customer-side impedance if a disturbance occurs on the supply-side $\qquad \underline{Z}_C = \dfrac{\Delta\underline{U}_{PCC}}{\Delta\underline{I}_{PCC}}$

It can be seen that the quantity $\underline{Z}_e = \Delta\underline{U}_{PCC} / \Delta\underline{I}_{PCC}$ gives different signs depending on the origin of the disturbance. The basic idea is, therefore, to estimate $\underline{Z}_e$. In fact, $\underline{Z}_e$ has a physical meaning. It is the equivalent impedance of the no disturbance side. If the disturbance occurs on the supply-side, $\underline{Z}_e$ is the customer impedance. If the disturbance occurs on the customer-side, $\underline{Z}_e$ is the supply impedance multiplied by (-1). Since the resistance should always be positive, it is possible to determine the direction of harmonic source by checking the sign of the real part of the impedance $\underline{Z}_e$. This forms the basis of the method: calculate the equivalent impedance once a voltage disturbance is detected at monitoring point:

$$\underline{Z}_e = \frac{\Delta\underline{U}_{PCC}}{\Delta\underline{I}_{PCC}} = \frac{\underline{U}_{before} - \underline{U}_{after}}{\underline{I}_{before} - \underline{I}_{after}} \tag{4}$$

where ($\underline{U}_{before}, \underline{I}_{before}$) and ($\underline{U}_{after}, \underline{I}_{after}$) are pairs of pre-variation and after variation h. voltage and current harmonic, respectively. This gives rise to conclusions:

If $Real\left(\underline{Z}_e\right) > 0$ the source of h. harmonic is on supply-side

If $Real\left(\underline{Z}_e\right) < 0$ the source of h. harmonic is on customer-side

(a)

(b)
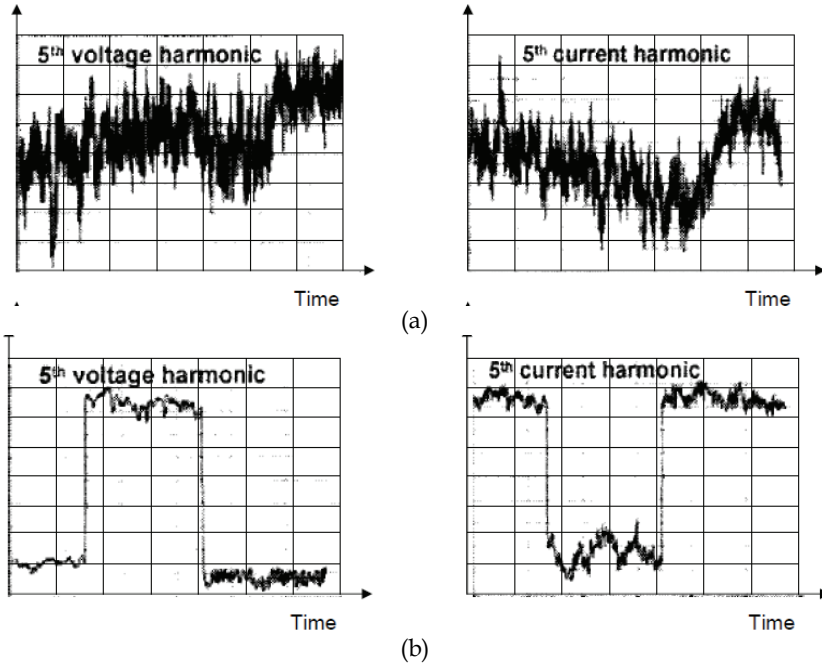
Fig. 8. (a) Unfavourable case: the 5 harmonic voltage and its variation are too small; (b) favourable case: the 5 harmonic variation is very significant [39]

The above method can be graphically illustrated on the impedance plane as shown in Fig. 7. If the calculated impedance $\underline{Z}_e$ lies in either the first or fourth quadrant ($R_e > 0$), the harmonic source is on the supply-side. And if the impedance lies in either the second or third quadrant ($R_e < 0$), the harmonic source is on the customer-side.

Because this method is based on harmonic variation, if the harmonic variation is too weak, it is very difficult to determine harmonic impedance with enough accuracy (Fig. 8).

The method drawbacks are: (a) high requirements for voltage and current harmonics measurement, especially with respect to their arguments; (b) time interval between measurements should be short (of the order of 1 - 3s) thus a large number of calculations is required; (c) accuracy of calculations can be solely achieved where the dominant harmonic source is at one side (either the supplier or the customer).

2.3 The "source" criterion [8,34]

The basis for the analysis is the equivalent circuit shown in Fig. 2, whose implication is the relation:

$$\underline{I}_{PCC} = \frac{\underline{E}_S - \underline{E}_C}{\underline{Z}_S + \underline{Z}_C} \quad \text{where: } \underline{E}_C = E_C \exp(j\varphi_C) \quad \underline{E}_S = E_S \exp(j\varphi_S) \tag{5}$$

The current at PCC can be represented by two components (Fig. 9):

$$\underline{I}_{PCC} = \underline{I}_{C-PCC} - \underline{I}_{S-PCC} \tag{6}$$

where $\underline{I}_{C-PCC}$, $\underline{I}_{S-PCC}$ are components associated with the customer and supplier side, respectively. The component $\underline{I}_{C-PCC}$ results from the *h*-th order harmonic source presence at the customer side, whereas the component $\underline{I}_{S-PCC}$ results from the *h*-th order harmonic source presence at the supplier side. The influence of a source located at the customer side on the current $\underline{I}_{PCC}$ is characterized by the projection of the current $\underline{I}_{C-PCC}$ vector onto the current $\underline{I}_{PCC}$ vector, whereas the influence of a source located at the supplier side – by the projection of the current $\underline{I}_{S-PCC}$ vector (Fig. 9).
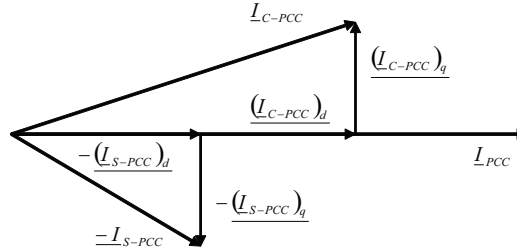
Fig. 9. Components of the current $\underline{I}_{PCC}$ at PCC [34]

As follows from Fig. 9:

$$\underline{I}_{C-PCC} = \sqrt{\left(I_{C-PCC}\right)_d^2 + \left(I_{C-PCC}\right)_q^2} \quad \underline{I}_{S-PCC} = \sqrt{\left(I_{S-PCC}\right)_d^2 + \left(I_{S-PCC}\right)_q^2} \tag{7}$$

and

$$\left(I_{C-PCC}\right)_q = \left(I_{S-PCC}\right)_q \tag{8}$$

The quotient of component modules $\underline{I}_{C-PCC}$, $\underline{I}_{S-PCC}$ is given by the formula:

$$\frac{I_{C-PCC}}{I_{S-PCC}} = \frac{\sqrt{\left(I_{C-PCC}\right)_d^2 + \left(I_{C-PCC}\right)_q^2}}{\sqrt{\left(I_{S-PCC}\right)_d^2 + \left(I_{S-PCC}\right)_q^2}} \tag{9}$$

Taking into consideration the relation 8 it can be concluded that the relationship between the component modules $\underline{I}_{C-PCC}$ and $\underline{I}_{S-PCC}$ is the same as the relationship between their projections onto the current $\underline{I}_{PCC}$ vector. It can be, therefore, concluded that if the projection of the current $\underline{I}_{C-PCC}$ vector onto the current $\underline{I}_{PCC}$ vector is greater than the projection of the current $\underline{I}_{S-PCC}$, i.e. the harmonic source at the customer side has a stronger influence on current $\underline{I}_{PCC}$ than the source at the supplier side, the condition:

$$\underline{I}_{C-PCC} \rangle \underline{I}_{S-PCC} \tag{10}$$

is fulfilled. Conversely: components $\underline{I}_{C-PCC}$, $\underline{I}_{S-PCC}$ can be determined using the relation:

$$\underline{I}_{C-PCC} = -\frac{E_C}{\underline{Z}_S + \underline{Z}_C} \quad \underline{I}_{S-PCC} = \frac{E_S}{\underline{Z}_S + \underline{Z}_C} \tag{11}$$

Thus the following relations are true:

If $\underline{I}_{C-PCC} \rangle \underline{I}_{S-PCC}$ then $E_C \rangle E_S$ the dominant disturbance source is
                                                 located at the customer side
If $E_C = E_S$ there is no decision about the dominant   (12)
                                                 source of harmonic
If $\underline{I}_{C-PCC} \langle \underline{I}_{S-PCC}$ then $E_C \langle E_S$ the dominant disturbance source is
                                                 located at the supplier side

According to the considered criterion the inference is based on source voltages $\underline{E}_C$ and $\underline{E}_S$, that are unknown. They can be determined from voltages and currents measured at PCC and the knowledge of equivalent impedances $\underline{Z}_C$ and $\underline{Z}_S$:

$$\underline{U}_{PCC} = \underline{E}_S - \underline{I}_{PCC}\underline{Z}_S = \underline{E}_C + \underline{I}_{PCC}\underline{Z}_C \tag{13}$$

However, the internal impedances of equivalent harmonic sources, representing the supplier and customer sides, are also unknown and their determination is not an easy task, it is significant disadvantage of this method.

2.4 The "critical impedance" criterion

The authors of publication [21] observed in a power system shown in Fig. 2 a strong association between the sign of reactive power and the relation between source voltages modules $\underline{E}_S$ and $\underline{E}_C$. This is explained by the formula determining the source E_S active and reactive power values in the case where the circuit equivalent resistance is negligibly small:

$$P = E_S I_{PCC} \cos\Theta = \frac{E_S E_C}{X}\sin\delta \tag{14}$$

$$Q = E_S I_{PCC} \sin\Theta = \frac{E_S}{X}(E_C \cos\delta - E_S) \tag{15}$$

where: $R = \mathrm{Re}(\underline{Z})$, $X = \mathrm{Im}(\underline{Z})$, $\underline{Z} = \underline{Z}_S + \underline{Z}_C$, $\underline{Z}_C = R_C + jX_C$, $\underline{Z}_S = R_S + jX_S$

$\Theta = \arg\underline{E}_S - \arg\underline{I}_{PCC}$, $\delta = \arg\underline{E}_C - \arg\underline{E}_S$

According to (14), the direction of active power flow (i.e. its sign) is exclusively determined by phase angles of voltages at both: the supply and load end of a line, and does not depend on the relation between modules of voltages E_C and E_S. This relation, however, determines the sign of reactive power. It is noticeable from relations (15) that if $Q>0$, then $E_C > E_S$, i.e. the dominant source of the considered current harmonic at PCC is a source at the customer side. Because of the presence of $\cos\delta$ in the formula (15) it cannot be concluded that if $Q<0$ then $E_C < E_S$, i.e. the supplier is the dominant source of the considered current harmonic. Publication [21] gives theoretical basis for the decision making process utilizing the examination of reactive power also if $Q<0$ introducing the concept of the so-called critical impedance.

The base of this method is finding the answer to the question: how far the reactive power generated by the source E_S can "flow" along the impedance jX, assuming this impedance is distributed evenly between the sources E_S and E_C. In order to find the answer has been defined the voltage value at an arbitrary point m between sources E_S and E_C (Fig. 2):

$$\underline{U}_m = \frac{X_1}{X_1 + X_2}\underline{E}_S + \frac{X_2}{X_1 + X_2}\underline{E}_C \tag{16}$$

where: $X = X_1 + X_2$, and X_2 is the part of X at the source E_S side. The point of the least voltage U_m value can be determined from the condition $\frac{\partial U_m}{\partial X_2} = 0$:

$$x = \frac{E_S^2 - E_S E_C \cos\delta}{E_S^2 + E_C^2 - 2E_S E_C \cos\delta} X \tag{17}$$

where x is the reactance of the source E_S for the point of the least voltage value. It is noticeable that:

$$I_{PCC}^2 = \frac{E_S^2 + E_C^2 - 2E_S E_C \cos\delta}{X} \tag{18}$$

Regarding (15) and (18), we have:

$$x = \frac{-Q}{I_{PCC}^2} = -\frac{E_S}{I_{PCC}}\sin\Theta \tag{19}$$

As inferred from the formula (19) x is the most distant point to which the reactive power generated by the source E_S can "flow". If the point x is closer to the customer side ($x > X/2$) then the dominant source of the considered harmonic is located at the supplier side. If $x < X/2$ then E_C is the dominant source.

The so-called critical impedance CI, which is the basis for inferring in this method, is defined in [21]:

$$CI = 2\frac{Q}{I_{PCC}^2} \tag{20}$$

Taking into account the circuit equivalent resistance ($R \neq 0$), [21] gave this concept a practical value. Thus the relations (14) and (15) take the form:

$$P = \frac{E_S E_C}{X}\sin(\delta + \beta) - \frac{E_S^2}{Z}\sin\beta \qquad Q = \frac{E_S E_C}{X}\left(\cos(\delta + \beta) = \frac{E_S^2}{Z}\cos\beta\right) \tag{21}$$

where: $\beta = arctg\frac{R}{X}$. Using transformation of powers expressed by (22) [34]:

$$\begin{bmatrix} P^* \\ Q^* \end{bmatrix} = T\begin{bmatrix} P \\ Q \end{bmatrix} = \begin{bmatrix} \dfrac{E_S E_C}{Z}\sin\delta \\[2mm] \dfrac{E_S E_C}{Z}\cos\delta - \dfrac{E_S^2}{Z} \end{bmatrix} \quad \text{where} \quad \begin{bmatrix} \cos\beta & -\sin\beta \\ \sin\beta & \cos\beta \end{bmatrix} \tag{22}$$

we obtain the same relations that describe the active and reactive power as for the condition $R=0$ and the basis for inference about location of the dominant harmonic source remains true. Then the index CI is given by relation:

$$CI^* = 2\frac{E_S}{I_{PCC}}\sin(\Theta + \beta) \tag{23}$$

This index is determined from the voltage and current measurements at PCC, which are utilized for the source voltage $\underline{E}_S$ calculation:

$$\underline{E}_S = \underline{U} + \underline{I}_{PCC}\underline{Z}_S \tag{24}$$

The impedance $\underline{Z}_S$, which occurs in (24) is not always exactly known. In consequence, the source voltage $\underline{E}_S$ may not be determined accurately. Another quantity that occurs in the formula for CI (23), which is inaccurately determined when the impedance $\underline{Z}_S$ and, above all, the impedance $\underline{Z}_C$ are not exactly known, is the angle β. The above factors cause that decisions taken according to the criterion (25) may not be correct.

If $\quad CI > 0$ or $CI < 0$ and $|CI| \langle Z_{min}$ $\qquad$ the dominant source of the considered harmonic is located at the customer side

If $\quad Z_{min} \langle |CI| \langle Z_{max}$ $\qquad$ there is no decision about the dominant source of the considered harmonic $\qquad$ (25)

If $\quad CI < 0$ and $|CI| \rangle Z_{max}$ $\qquad$ the dominant source of the considered harmonic is located at the supplier side

where Z_{min}, Z_{max} determine the interval of impedance Z changes.

2.5 The voltage indicator criterion [34]
The method is based on the equivalent circuit diagram presented in Fig. 2, created for the investigated harmonic. By investigating the quotient of source voltages of the supplier's and the consumer's side, known as "voltage indicator"[1]:

$$\Theta_U = \frac{E_C}{E_S} = \frac{|\underline{Z} + \underline{Z}_C|}{|\underline{Z} - \underline{Z}_S|} \quad \text{where } \underline{Z} = \frac{U_{PCC}}{I_{PCC}} \tag{26}$$

it is possible to determine the location of the dominant distortion source in the electrical power network, according to the following criterion:

If $\quad \Theta_U \rangle 1$ $\quad$ the dominant source of the investigated harmonics is located at the consumer's side

If $\quad \Theta_U = 1$ $\quad$ it is impossible to explicitly identify the location of the dominant source of the disturbance $\qquad$ (27)

If $\quad \Theta_U \langle 1$ $\quad$ the dominant source of the investigated harmonics is located at the supplier's side

Impedance values $\underline{Z}_S$ and $\underline{Z}_C$ have been assumed as known. Since this requirement is difficult to meet, the criterion is modified to the form (28), which takes into account approximate knowledge of equivalent impedance values $\underline{Z}_S$ and $\underline{Z}_C$. The ranges are determined which may contain the values of such impedances, evaluated on the basis of the

---

[1]A detailed theoretical justification of the method is to be found in works [32,33,34,41].

analysis of various operating conditions of an investigated electrical power system. Impedance $\underline{Z}_x$ variation range where $x \in (C, S)$ is defined by means of equations: $Z_{x\min} \leq Z_{xn} \leq Z_{x\max}$ and $\alpha_{x\min} \leq \alpha_{xn} \leq \alpha_{x\max}$, where Z_{xn}, α_{xn} are the modulus and the argument, respectively, of the impedance $\underline{Z}_x$. On this basis, indicator extreme values $\Theta_{U\min}$ and $\Theta_{U\max}$, are determined, which are the basis for the following conclusions:

$$
\begin{array}{lll}
\text{If} & \Theta_{U\min} \rangle 1 & \text{the dominant source of the investigated harmonics is} \\
& & \text{located at the consumer's side} \\
\text{If} & \Theta_{U\min} \langle 1 \langle \Theta_{U\max} & \text{it is impossible to explicitly identify the location of the} \qquad (28) \\
& & \text{dominant source of the disturbance} \\
\text{If} & \Theta_{U\max} \langle 1 & \text{the dominant source of the investigated harmonic is} \\
& & \text{located at the supplier's side}
\end{array}
$$

The results of example simulations illustrating this method (according with Fig. 3 and Table 1) are presented in Fig. 10. Fig. 11 shows the results of the identification of the disturbance source by means of the voltage indicator method, depending on the phase shift angle between 5 harmonic current of the supplier and the consumer for two distinct relations between rms values of these currents. The change of phase shift angle value does not affect the correctness of conclusions in the analysed case.
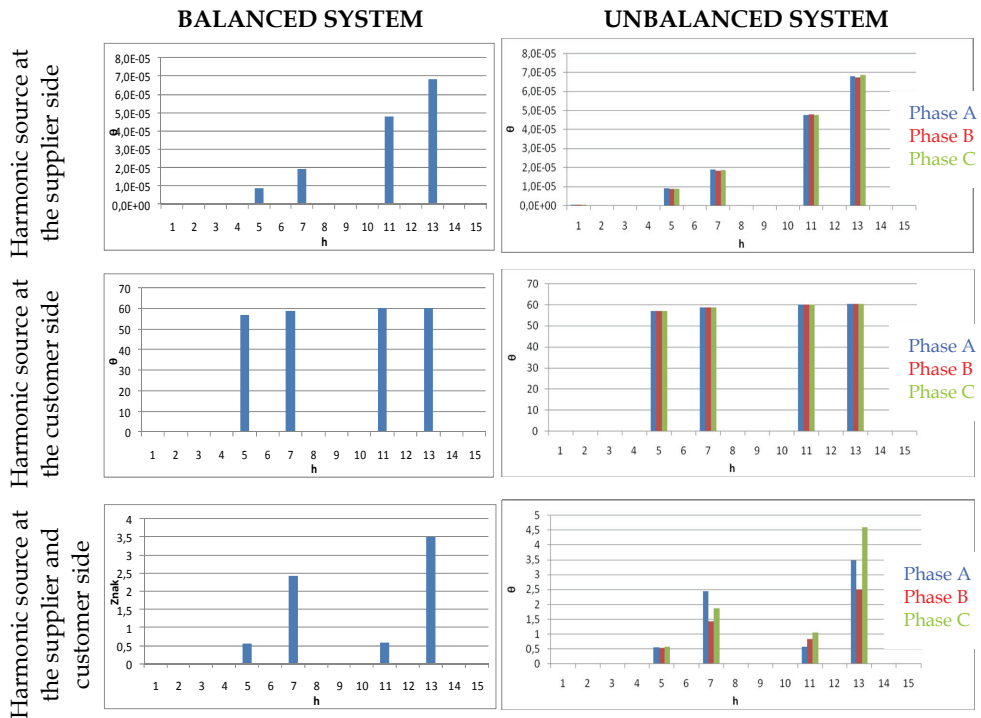

Fig. 10. Criterion of voltage indicator – example results of simulations for a system as that presented in Fig. 3
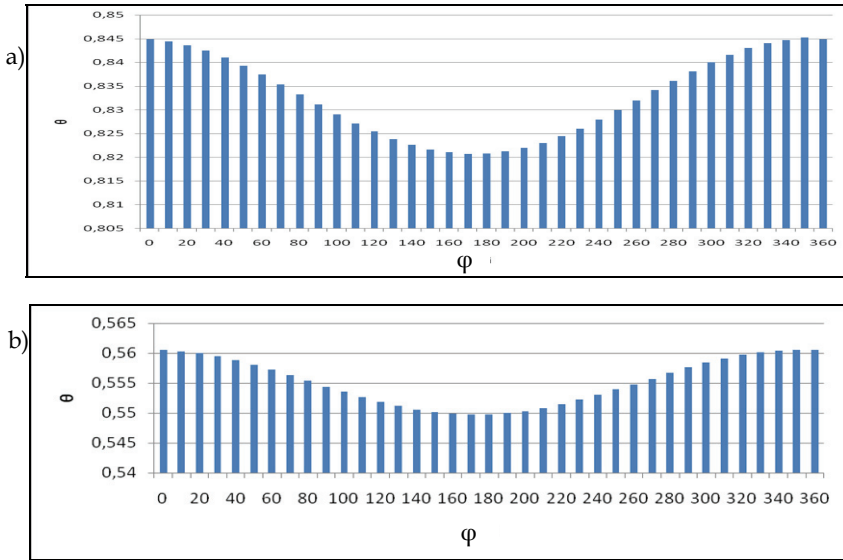
Fig. 11. Variation of 5th harmonic active power value for various values of phase shift angle
φ between the supplier's and the consumer's current harmonic and for various relations
between their rms values: (a) 1:1,2; (b) 1:1,8

2.6 Criterion of the relative values of voltage and current harmonics [38]

This method consists in comparison of relative harmonic values measured with respect to
the fundamental voltage and current values. While analysing the correctness of decisions
made on the basis of this method the equivalent circuit diagram of an electrical power
system, presented in Fig. 2, is used In the case of a single harmonic source, located, for
example, at the energy supplier's side, the following equations are valid:

for the fundamental component – index (1)

$$\underline{U}_{PCC(1)} = \underline{E}_{S(1)} - \underline{I}_{PCC(1)}\underline{Z}_{S(1)} = \underline{I}_{PCC(1)}\underline{Z}_{C(1)}$$

for h. harmonic

$$U_{PCCh} = \underline{E}_{Sh} - \underline{I}_{PCCh}\underline{Z}_{Sh} = \underline{I}_{PCCh}\underline{Z}_{Ch}$$

Therefore, voltage quotient:

$$\frac{U_{PCCh}}{U_{PCC(1)}} = \frac{I_{PCCh}Z_{Ch}}{I_{PCC(1)}Z_{C(1)}} = \frac{I_{PCCh}}{I_{PCC(1)}}\left|\frac{\underline{Z}_{Ch}}{\underline{Z}_{C(1)}}\right| = \frac{I_{PCCh}}{I_{PCC(1)}}K \tag{29}$$

Assuming that: $\quad \underline{Z}_{C(1)} = R_{C(1)} + jX_{C(1)}$ and $\underline{Z}_{Ch} = R_{C(1)} + jhX_{C(1)}$ $\tag{30}$

for $h > 1$ the following inequality is satisfied: $\sqrt{R_{C(1)} + h^2 X_{C(1)}^2} \rangle \sqrt{R_{C(1)} + X_{C(1)}^2}$ which means that

$K > 1$ and, as a result $\dfrac{U_{PCCh}}{U_{PCC(1)}} \rangle \dfrac{I_{PCCh}}{I_{PCC(1)}}$. A similar reasoning may be carried out for the case when

a single harmonic source is located at the consumer's side and for sources located at both sides
of the PCC [34]. In each case the conclusion criterion is based on the relations (for $h = 2,3,4 \ldots$):

$$\frac{U_{PCCh}}{U_{PCC(1)}} \geq \frac{I_{PCCh}}{I_{PCC(1)}}$$ The dominant harmonic source is located at the supplier's side

$$\frac{U_{PCCh}}{U_{PCC(1)}} < \frac{I_{PCCh}}{I_{PCC(1)}}$$ The dominant harmonic source is located at the consumer's side

The above reasoning is correct if equation (30) is approximately valid.

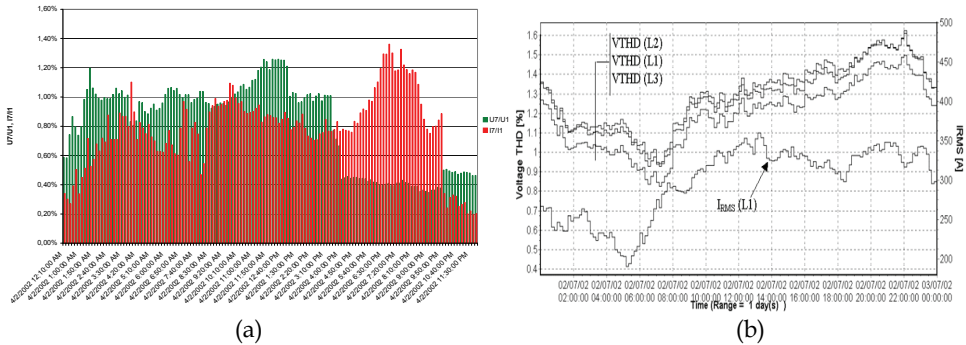(a)   (b)

Fig. 12. (a) Relative values of the 7th voltage and current harmonic in phase L3; (b) the change in the phase-to-neutral voltages distortion factor during an example workday 24 hours (110kV network)

It happens that the influence of some harmonics on the voltage to current ratio is increased due to the resonance, and therefore the above relations are amplified or reduced. For the above reasons it is essential that harmonics should be analysed comprehensively, taking into consideration several lowest, especially odd harmonics from the 3rd to 11th, on which the impedance from the supply side has the lowest influence. An example of the 7th harmonic measurements at the feed point of 110 kV distribution network in large city is shown in Fig. 12a. A dominant influence of the municipal network loads during evening hours is evident and confirmed by the daily THD time characteristic, measured at the same point (Fig. 12b).

2.7 Statistical approach from simultaneous measurement of voltage and current harmonics [13]

Voltage and current harmonics are measured simultaneously at the point of evaluation during longer periods of time - Fig. 13 (10-minutes values, measured during one week).

In Fig. 13a, the experimental points are spread over the area delimited by the two straight lines. This means that the harmonic current and the resulting voltage are actually resulting from the combined influences of the background level and the considered distorting load, without any prevalence of one or the other. In Fig. 13b, however the load acts clearly as a rather dominant emitter at the PCC: the points are mostly grouped along the straight line. This means that the influence of the considered installation is greater than the background harmonic level.

A similar reasoning may be based on the investigation of the correlation between voltage harmonic value and, for instance, current rms value or active power.
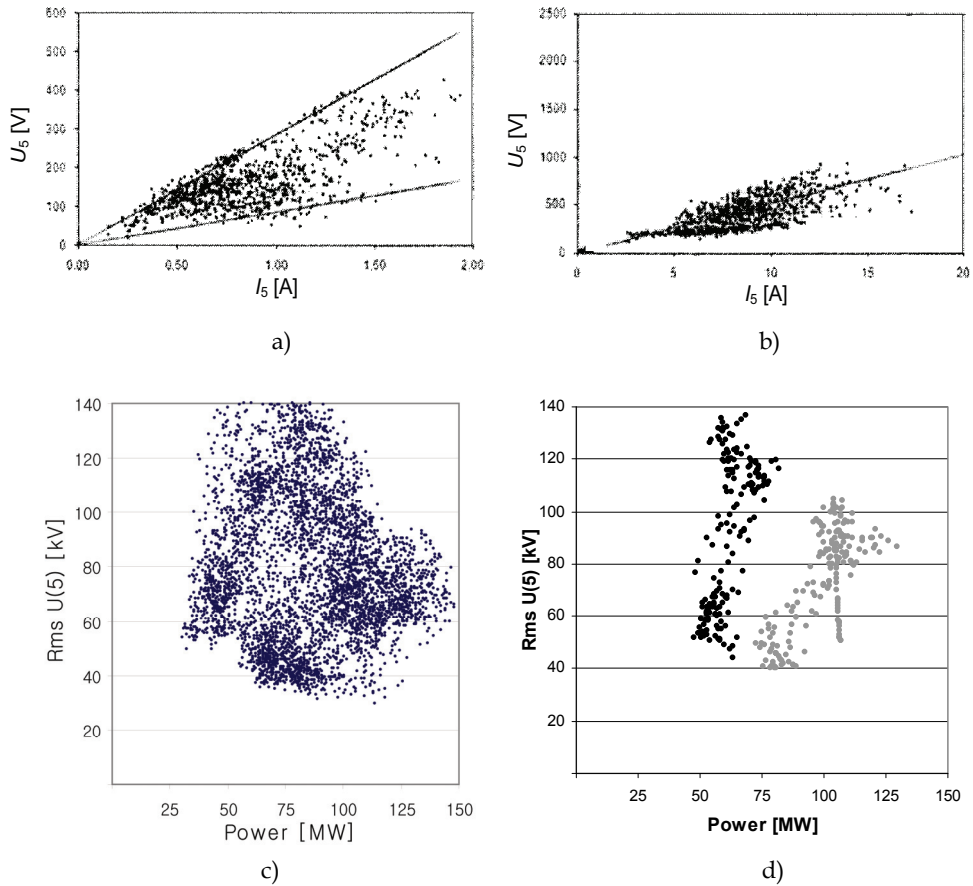
Fig. 13. Examples of: 5th voltage harmonic vs. (a,b) 5th current harmonic and (c,d) active power of a large industrial company fed from 110 kV line - 4 months of measurement (d), selected days of operation that shows a load acting as a dominant emitter (gray dots) and the supply that acts as a dominant emitter (black dots)

3. Voltage dips

The procedure of locating the dip source is usually a two-stage technique. The first part involves inferring whether the dip has occurred upstream or downstream of the measuring point, i.e. at the supplier's or the consumer's side. In the next step the algorithm that precisely computes the voltage dip location is applied. This chapter deals with the first stage. Even though a methodology for the exact locations of voltage dips does not exist yet, several methods for voltage dip source detection have already been reported. They are based mainly on: the analysis of voltage and current waveforms; the analysis of the system operation trajectory during the dip; the analysis of the equivalent electric circuit; the analysis of power and energy during the disturbance; the analysis of voltages; asymmetry factor value and symmetric component phase angle and algorithms for the operation of protection

automatics systems (impedance variation analysis, the analysis of current real part, "distance" protection).
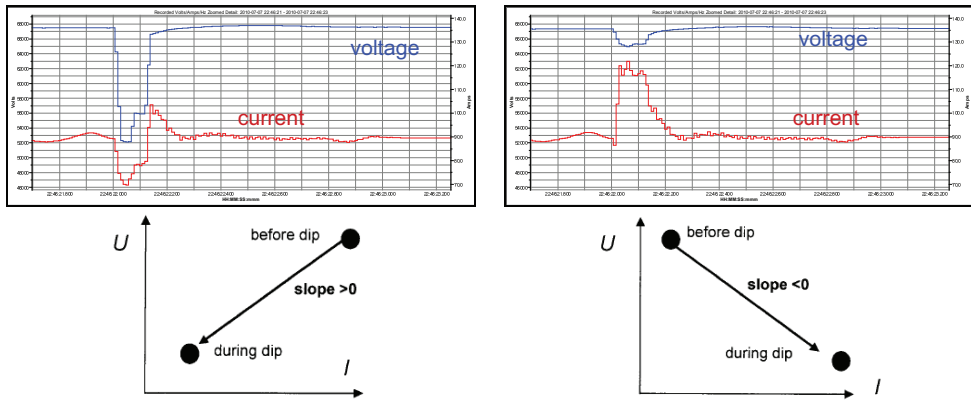

Fig. 14. Slope of the trajectory line of the (U-I) system during the dip for various short circuit locations: a) upstream (point A at Fig. 1), b) downstream (point B at Fig. 1)

3.1 Analysis of the voltage and current waveforms at PCC
The location of the point of connection of the motor whose start causes a disturbance (in general: a voltage dip source) can be sometimes identified with respect to the considered point of a supply network (the measurement point) on the basis of recorded voltages and currents — Fig. 14. A noticeable increase in the current during a voltage dip may indicate that the cause of a disturbance is located downstream the monitoring point (Fig. 14b). That does not always hold true. At reduced voltage the current of induction motor loaded with a constant torque increases, although, as a rule, it is smaller than the increase necessary to cause a voltage dip. Similarly, the increase of current can result from the voltage control at the consumer's side or the response a power electronic interface control.

3.2 The criterion using the system operating conditions trajectory during the dip
The natural consequence of waveform analysis during the disturbance is an empirical method based on the investigation of the trajectory of the supply system operation point before and during the disturbance [22].
In the example used to illustrate this method it has been assumed that there is one source supplying a passive load, while the monitoring device is connected in the PCC point (Fig.1). Two cases of three-phase short circuits have been investigated: in points A and B, which result in a voltage dip. Both short circuits lead to voltage reduction in point PCC; however, current value variation will be different in each case.
During the short circuit in point A the current measured in point PCC will be typically lower in comparison with its value before the disturbance occurred. In the other case (short circuit in point B) the current measured in point PCC will be the sum of short-circuit current and load current during the dip. Its value will be higher than before the disturbance occurrence.

The above statements are also illustrated in Fig. 14. Particular operating conditions of the supply system are presented by means of points representing voltage and current before and after the dip. The sign of derivative of the segment joining these two points makes it possible to identify the short circuit location: a positive derivative suggests the short circuit at the source side (in point A), while a negative derivative suggests the short circuit at the load side (in point B). Although originally the method was intended for a system with a single supply source, it can also be applied, after small modifications, to two-side supply systems, such as that presented in Fig. 15 (also including non-linear elements) [22].

In this case the disturbance source location is determined in relation to the assumed direction of active power flow in the measurement point. If the disturbance source is located on the right side of the measurement point (i.e. in the same direction as that of active power flow) it means it is located at the "lower" side. Disturbances on the left side of the measurement point (the direction is opposite to that of active power flow) indicate that the source is located at the "upper"side.
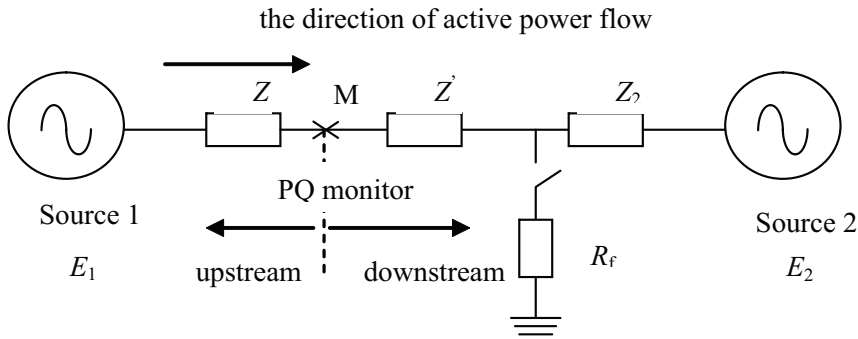
Fig. 15. A two-source system locating the dip source [22]

Fig. 15 shows a short circuit (represented by resistance R_f), which occurs on the right side of the measurement point, while those elements of the equivalent circuit diagram which are on the left side remain unchanged. Voltage in the measurement point (which is not PCC) can be expressed by the equation:

$$\underline{U} = \underline{E}_1 - \underline{I}\,\underline{Z} \tag{31}$$

where $\underline{U}$ and $\underline{I}$ can be measured directly in point M. Multiplying both sides of equation (31) by current conjugate value $\underline{I}^*$, and taking into account only the real part, results in the following equation:

$$UI\cos\theta_2 = E_1 I\cos\theta_1 - I^2 R \tag{32}$$

where θ_2 – phase angle between vectors $\underline{U}$ and $\underline{I}$, θ_1 – phase angle between $\underline{E}_1$ i $\underline{I}$, R represents the real part of complex impedance $\underline{Z}$. Transforming (32) to the form:

$$U\cos\theta_2 = -IR + E_1\cos\theta_1 \tag{33}$$

results in the equation, the form of which is convenient to determine the inclination of the
U-I trajectory. For example, if $\cos\Theta_2 \rangle 0$, the direction of active power flow is such as has
been assumed, i.e. such as has been shown in Fig. 15, while the disturbance source is located
at the lower side and $|U\cos\Theta_2| = U\cos\Theta_2$. Each point representing the system operating
conditions in coordinate system $(I, |U\cos\Theta_2|)$ is placed on the straight line with the
inclination –R, like in Fig. 16a (assuming that $\cos\theta_1$ does not significantly change its
value).

a)   b)
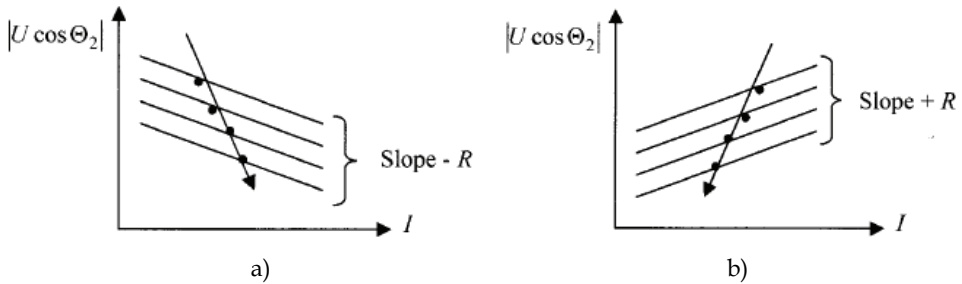
Fig. 16. The slope of system trajectory during the disturbance: the disturbance source is
located (a) downstream, (b) upstream the measurement point [22]

If $\cos\Theta_2 \langle 0$, active power flows from E_2 to E_1, the disturbance is located at the upper side,
and the equation has the following form:

$$U\cos\theta_2 = IR - E_1\cos\theta_1 \tag{34}$$

Every point representing the system operating conditions in coordinate system $(I,$
$|U\cos\Theta_2|)$ is placed on the straight line with the slope +R (Fig. 16b). The line which is
connecting these points during the disturbance has positive inclination then – providing
$\cos\theta_1$ does not significantly change its value during the disturbance.
It can be demonstrated that during the disturbance $|\cos\theta_1|$ usually decreases when current
I increases for the disturbance source at the lower side and decreases for the upper side. This
ensures that in practical cases conclusions are drawn in the correct way.
It has been assumed so far that the direction of active power flow does not change before
and after the disturbance occurrence, which is not always the case. Variations are possible,
however, only in the case of disturbances at the upper side, while for disturbances at the
lower side the direction of active power flow remains unchanged. This fact may be used for
the identification of voltage dip source location: if the direction of active power flow
changes, the event must have occurred at the upper side. This additional hint, together with
the identification of the inclination of the trajectory U-I during the dip may help draw
correct conclusions.
The investigated method has been used in simulation studies, the aim of which was to locate
the voltage dip source using a modified model of *IEEE 37-Node Test Feeder* network [18]. Its
diagram is presented in Fig. 17a. A three-phase short circuit, which occurred in node 703,
has been simulated; the study investigated if the disturbance in nodes 702 and 709 was
located correctly (Fig. 17b).

a)

NODE 702   NODE 709

Phase-to-neutral voltage waveforms

Line current waveforms
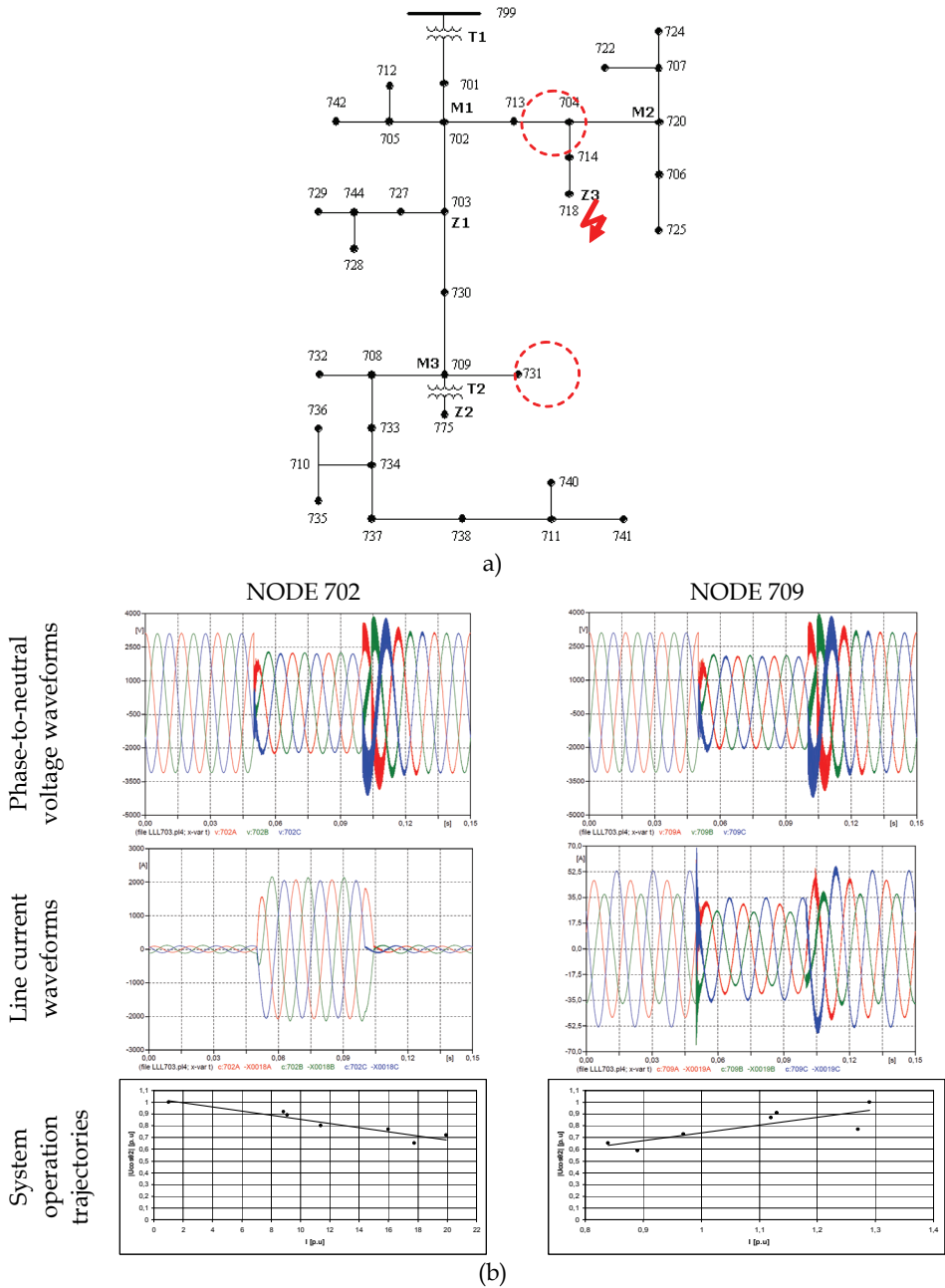
System operation trajectories

(b)

Fig. 17. Example results of a three-phase short circuit simulation in node 703 of 23 network model; waveforms of voltages and currents in nodes 702 and 709 as well as system operation trajectories in these points for phase L1 (analogous waveforms in other phases)

Both this and other simulation studies have confirmed that it is highly probable to draw correct conclusions concerning the dip source location in the case of symmetrical disturbances; incorrect conclusions can be drawn in the case of asymmetrical disturbances, in particular single-phase earth faults.

3.3 The analysis of the equivalent electric circuit

In the investigated point of the supply system, both current and voltages are measured at the same time. The measured current is the basis for calculating the voltage value on the basis of the equivalent circuit diagram of the studied system. Conclusions concerning the disturbance location are drawn on the basis of the relationship between the measured (U_m) and the calculated (U_S) voltage value in PCC (Fig. 18). If the relationship is $U_S \approx U_m$, it means that the disturbance source is located "downstream" the measurement point (at the consumer's side), whereas if $U_S << U_m$, the disturbance source is located at the supplier's side.
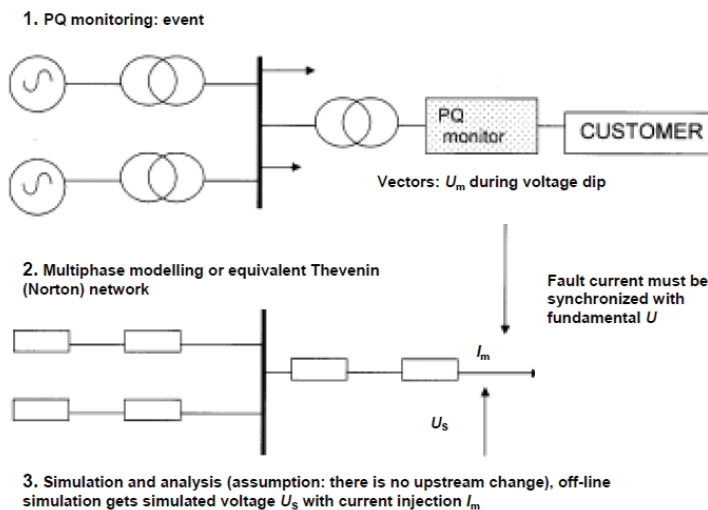
Fig. 18. The method of dip source location on the basis of the comparison between measured and calculated voltage variation value in PCC [39]

3.4 The criterion using power and energy during the disturbance

The circuit of a short-circuit which has occurred at the consumer's side takes power from the supply network. On the other hand, during a short circuit that has occurred at the supplier's side energy in transient state will flow from the consumer's side. The direction of flow of instantaneous power and energy is determined on the basis of registered voltage and current waveforms.

In the steady state, assuming that the network is a symmetrical one, instantaneous power has practically constant value which changes as a result of variations in voltage and current instantaneous waveforms. The difference in power between the steady state and the disturbance state is the so-called "disturbance power" - DP. According to this definition, in the steady state the DP value approximately equals zero (assuming very brief intervals between subsequent measurements), while during short circuit it is different than zero.

As a result of integrating the DP value, disturbance energy – DE – is determined. Information concerning DP and DE variation makes it possible to locate the voltage dip source, because during a short circuit energy flows towards the place of the short circuit occurrence (Fig. 19) – the increase of DE during the disturbance indicates that the disturbance source is located downstream the measurement point. On the other hand, DE decreases if the disturbance source is located upstream the measurement point [33]. The method requires that a threshold value of energy is assumed; since the reliability of results depends on this value, the method works correctly as long as the value has been accurately chosen.
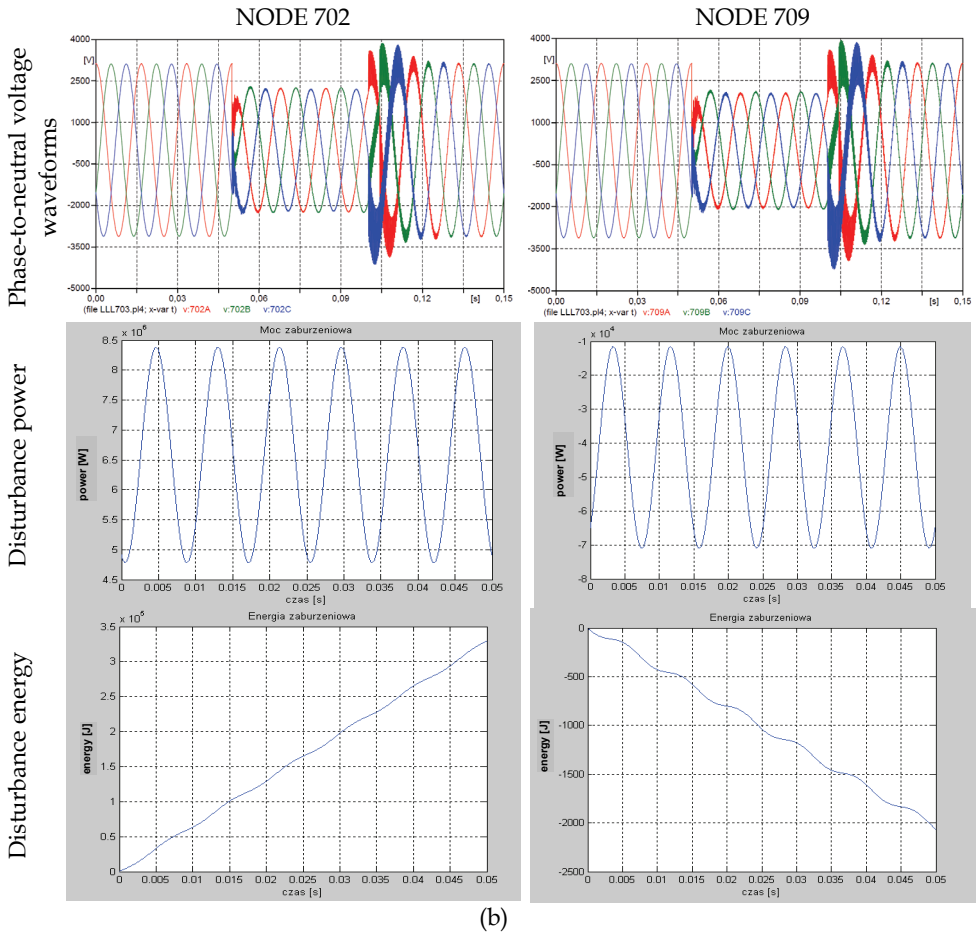
(b)

Fig. 19. The method of dip source location on the basis of the analysis of power and energy during the disturbance – example results of the simulation of a tree-phase short circuit in node 703 of the model network (Fig. 17a) waveforms of voltages and currents in nodes 702 and 709 as well as of disturbance power and energy

Fig. 19 shows the results of simulation studies aimed at locating the voltage dip source using the network model such as that in Fig. 17a. A three-phase short circuit, which occurred in

node 703, has been simulated; the study investigated if the disturbance in nodes 702 and 709 was located correctly. Correct conclusions are guaranteed also in the case of other types of short circuits.

3.5 Voltage criterion

In this method the dip source is located only on the basis of voltage measurement [20]. It consists in comparing the dip depth at the primary and secondary side of the transformer before and after the dip (Fig. 20):

$$U_1^* = \frac{U_{1-dip}}{U_{1-before}} \qquad U_2^* = \frac{U_{2-dip}}{U_{2-before}} \tag{35}$$

where U_{i-dip} is the voltage during the dip, while $U_{i-before}$ is the voltage before the dip occurrence. The value by which voltage decreases on both sides of the transformer is represented by the following equations:

$$\Delta U_1 = Z_1 I_{SC} \qquad \Delta U_2 = (Z_1 + Z_{Tr}) I_{SC} \tag{36}$$

where Z_{Tr} is the transformer impedance, and I_{SC} is the short-circuit current. The value by which voltage decreases is higher at this side where the dip source is located. Therefore, if $\Delta U_2 > \Delta U_1$ ($U_2^* \rangle U_1^*$), the dip source is located at the lower side; otherwise, it is located at the upper side (orientation according to the direction of active power flow).
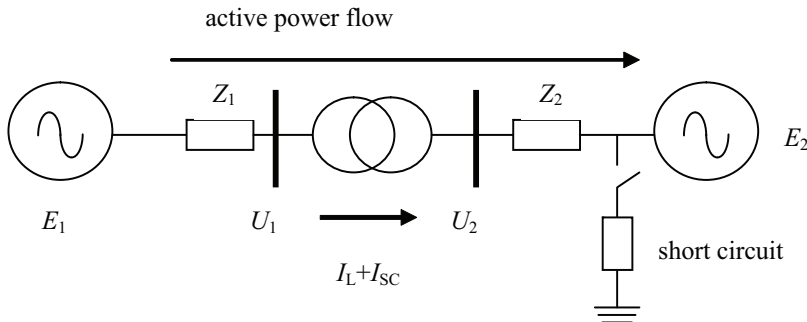
Fig. 20. The circuit showing the method of voltage dip location [20]

If the lower side of the system does not contain any energy sources and the dip source is located at the upper side, U_1 and U_2 have the same value in relative units.

The described method can easily be applied to transformers with connections of Y-Y type, which is a typical connection in the case of transmission grids. On the basis of characteristics of various types of voltage dips according to Bollen's classification [6,20] describes relationships between dip depths at both sides of the transformer with a Δ-Y connection.

The nature of load may affect the correctness of conclusions. The original assumption that only a short circuit at the lower side of the system may lead to the increase of current flowing through the transformer may be wrong in the case of a constant power load and transient response of milliseconds. In such a case, voltage reduction during the dip also leads to the increase of load current.

3.6 The criterion using asymmetry indicators

The method is based on the analysis of the factors of voltage and current asymmetry in PCC (Fig. 21). As far as most industrial loads (such as induction motors, rectifiers) are concerned, the current asymmetry factor is considerably higher than the voltage asymmetry factor in the case of an asymmetrical dip the source of which is located at the supplier's side. For example, induction motor impedance for a negative sequence component is very low; hence, even low voltage asymmetry will cause a high value of current negative sequence component (such a phenomenon will not occur in the case of synchronous machines).
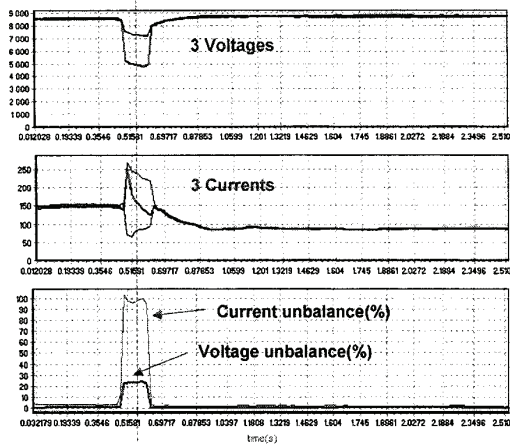

Fig. 21. Registration in PCC of an industrial consumer [39]

The disturbance source can also be located using the variation of phase angle $\Delta\Phi$ of the symmetric positive sequence component of current for the state before and during the short circuit [31]. The rule of the method is as follows: if $\Delta\Phi>0$, the dip is located "upstream" the PCC, otherwise it is located "downstream" the PCC, where the angle $\Delta\Phi$ is in the range (- π) $\div$ π .

Drawing correct conclusions depends on the choice of period for the analysis before and after the short circuit occurrence in order to calculate the vector complex value of current symmetric component for both distinguished states.

3.7 The criterion of protection automatics systems functioning

Since voltage dips are mainly caused by short circuits, it is appropriate to use the knowledge of protection automatics systems in order to locate the dip source.

3.7.1 The criterion based on the analysis of impedance variation

The concept of "increase impedance" applied in protection systems may be used as the basis for the dip source location [37]. It can be demonstrated that impedance calculated on the basis of current and voltage variations before and during the disturbance will be located in various quadrants of the complex plane, depending on the short circuit location. The procedure to follow is analogous to that presented in chapter 2.2, but this time it concerns the fundamental harmonic. The study is focused on the sign of the real part of the

impedance measured in PCC for the fundamental harmonic (according to the relationships presented in chapter 2.2). Since resistance should always have a positive sign, it is possible to locate the disturbance source on the basis of checking the sign of the real part of impedance $\underline{Z}_e$. Thus, the application algorithm of this method is as follows: equivalent impedance should be calculated in the measurement point during the registration of the disturbance in voltage, by means of the following equation:

$$\underline{Z}_e = \frac{\Delta \underline{U}}{\Delta \underline{I}} = \frac{\underline{U}_{dip} - \underline{U}_{before}}{\underline{I}_{dip} - \underline{I}_{before}} \tag{37}$$

where ($\underline{U}_{before}, \underline{I}_{before}$) and ($\underline{U}_{dip}, \underline{I}_{dip}$) are pairs of voltage and current fundamental harmonic values before and during the dip. The above method may be presented graphically on the complex variable plane. Since electrical power network impedance is usually of inductive character for the fundamental frequency, impedance $\underline{Z}_e$ vector will be most often located in the first or third quadrant of the coordinate system, like in Fig. 8. The conclusion algorithm is then as follows:

If $Real(\underline{Z}_e) > 0$ the source dip is located at the supplier's side

If $Real(\underline{Z}_e) < 0$ the source dip is located at the consumer's side

The above condition is true for current flow direction like in Fig. 2. In a practical algorithm it can be assumed that the current direction is compatible with the direction of active power flow.

This method can also be applied to asymmetrical voltage dips, due to the fact that the estimated value of impedance for the positive sequence component does not depend on the disturbance type.

In theory the method works correctly; there are, however, two basic difficulties in its application in practice.

The results (equivalent impedance values) are different for various voltage and current periods accepted for analysis before and during the dip. Accepting only one period as the basis for the analysis during the dip may give incorrect results. In order to improve the quality of conclusions drawn on the basis of this method the authors of [37] suggest a multi-period analysis and the method of least squares to estimate impedance or the choice of voltage period number on the basis of an additional analysis of power during the disturbance.

The **second** factor which may reduce the method reliability is the assumption concerning the linearity of the system. In fact, there are very often non-linear elements, i.e. regulated electric drives or induction motors at the consumer's side. Both types of the loads can operate with constant power. Their reaction during a voltage dip may be fundamentally different than that of linear loads. In order to reduce the influence of this factor some modifications of the investigated method are suggested [37].

Another impedance based methods is proposed in [30], which is based on the assumption that the estimated impedance during the voltage dip changes both in magnitude $|\underline{Z}|$ and in phase $\angle\underline{Z}$. Thus, new criterion is introduced, where the results obtained before and during the dip are compared, i.e.:

If $\left|\underline{Z}_{dip}\right|\langle\left|\underline{Z}_{before}\right|$ and $\angle\underline{Z} > 0$ the source dip is located at the supplier's side

Else   the source dip is located at the consumer's side

3.7.2 The criterion using real current component

In order to locate the voltage dip source in relation to the measurement point the current active component measured in the measurement point is analysed; on the basis of its sign in the dip initial phase the disturbance source is located [16].

For a two-source system, the equivalent circuit diagram of which is presented in Fig. 22, the current flowing from source E_1 to E_2 is described by the following equation:

$$\underline{I} = \frac{\underline{E}_1 - \underline{E}_2}{\underline{Z}} \tag{38}$$
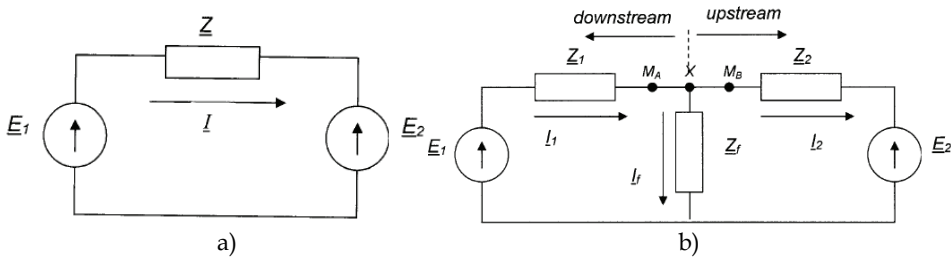

Fig. 22. A two-source system: (a) before a short circuit; (b) during a short circuit [16]

Upon the short circuit in point X with short-circuit impedance $\underline{Z}_f$, like in Fig. 22b, in point X voltage becomes reduced practically to 0. There are three currents in the circuit: $\underline{I}_1$ – flowing from the source E_1, $\underline{I}_2$ – flowing from the source E_2 and $\underline{I}_f$ – flowing through the impedance Z_f. The direction of current $\underline{I}_1$ is the same as the direction of the current flowing before the short circuit occurred. If impedance Z_2 is much higher than impedance Z_f, current I_2 approximately equals zero, and the current of the source E_1 will be almost the only current flowing in the circuit. If the above condition is not satisfied, current I is seen as the current flowing from the source E_2. This idea of the directions of currents during the short circuit is used for the voltage dip source location.

For a short circuit in point X voltage in point M_A is:

$$\underline{U} = \underline{E}_1 - \underline{I}\underline{Z}_1 \tag{39}$$

where $\underline{U}$ and $\underline{I}$ are voltage and current measured in point M_A. Multiplying both sides of equation (39) by $\underline{I}^*$ results in the following equation:

$$\underline{U}\underline{I}^* = \underline{E}_1\underline{I}^* - I^2\underline{Z}_1 \tag{40}$$

The real part of equation (40):

$$UI\cos(\theta - \alpha) = E_1 I\cos(\phi_1 - \alpha) - I^2 R \tag{41}$$

where θ and a are phase angles of, respectively, voltage and current in the measurement point M_A, while $\cos(\theta-a)$ is the power factor in point M_A.

On the basis of equation (41), in the measurement point M_A the current flows from E_1 to X, and $I\cos(\theta-a)>0$. In such case it is concluded that the short circuit leading to the dip is located downstream the point M_A. In the case of the point M_B the current $I\cos(\theta-a)<0$ is seen as the current flowing from E_2 to X, while the voltage dip source is located upstream the point M_B. The described method can also be applied to a single-source system.

If impedance $Z_f<<Z_2$, the current from the source E_2 will not flow. However, in the initial phase of a voltage dip, the current resulting from a sudden change of circuit configuration can be considerably higher than the steady state current. Therefore, even if short-circuit impedance is very low, at the beginning of the short circuit a sudden change of the current direction can be observed. Consequently, the direction of current at the very beginning of the short circuit is a more appropriate indicator of the dip source location. So, the final procedure to follow in order to locate the dip source consists of the following steps: (i) measuring values and phase angles of voltage and current in the measurement point before and during the dip; (ii) determining the value of the component $I\cos(\theta-a)$ for a few periods before and during the dip; (iii) graphical representation of $I\cos(\theta-a)$ in the function of time and (iv) checking the sign of the component $I\cos(\theta-a)$ at the very beginning of the dip. If the sign is positive, the dip source is located at the lower side. On the other hand, if the sign is negative, the dip source is located at the upper side.

3.7.3 Criterion employing distance protection

Distance relays provide basic protection of HV electric power lines against all types of faults. The basis of their operation is measuring the impedance as "seen" from their terminals. Connection of all phase voltages and currents of the protected line to the relay analogue inputs, required for the correct impedance measurement, allows also determining fault location. This property of distance relays and their widespread application enable their use for voltage dips location [30].
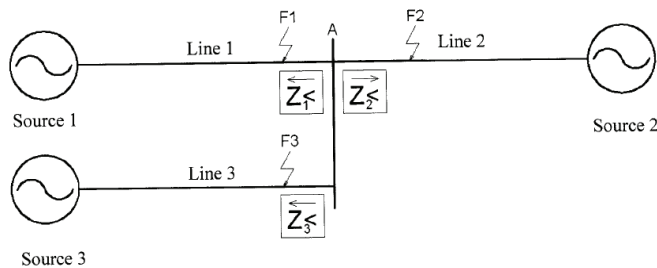
Fig. 23. A fragment of a power system

Fig. 23 shows busbars of substation A being a node of a power system. Each line bay at the substation is equipped with a distance relay "directed toward the line". It should be determined whether a voltage dip occurs "upstream" or "downstream" a specified point; it is assumed that this point is the bay of line 2. This information could be crucial for determining quality indices of power transmitted to or received from the second source. The subject of analysis are changes in the impedance($Z_2<$) seen by the distance protection of line 2 during faults F_1, F_2, F_3, that obviously will give rise to voltage dips at the above specified

measurement point. Upon the occurrence of fault F_2 a disturbance current will flow in the line 2 from the substation A busbars to the fault location. Thus the impedance seen by the distance protection $Z_2<$ decreases, and its phasor is situated in the first quadrant of complex plane. The occurrence of the faults at points F_1 or F_3 will cause in the line 2 a disturbance current flow towards busbars of the substation A. Therefore the impedance seen by the distance protection $Z_2<$ will also decrease, but its phasor will be situated in the third quadrant of a complex plane. The distance protection will select voltages and currents in proper phases in order to correctly determine the fault current loop impedance. Thus, the condition for a voltage dip occurrence upstream the protection, can be expressed as:

$$\left|Z_{dip}\right| < \left|Z_{before}\right| \ and \ \angle Z_{dip} > 0 \tag{42}$$

where:

Z_{before} - the impedance seen by the distance protection prior to the fault occurrence,

Z_{dip} – the impedance seen by the distance protection after the fault occurrence,

$\angle Z_{dip}$ – argument of the impedance as seen after the fault occurrence.

If the above condition is not fulfilled, but $\left|Z_{dip}\right| < \left|Z_{before}\right|$ then a fault, and consequently a voltage dip, is localized downstream the protection. It is also possible that the line 2 is disconnected due to a failure, maintenance or repair. In this case the occurrence of a fault at points F_1 or F_3 does not change the impedance seen by the protection at the measurement point. Thus this method does not prove itself for open networks and this is major disadvantage. A possible solution could be to combine the described algorithm with observation of the voltage at the measurement point. All newly installed distance relays are based on microprocessor technique and their structure contains under/over voltage protections. If the voltage at busbars decreases and a flow of short-circuit power from/toward busbars does not occur (the impedance seen by the directional protection does not change) we can infer that voltage dip occurs downstream the protection. Where the busbars voltage decreases, and the impedance seen by the directional protection changes, the algorithm described by relation (42) is employed.

Fig. 24 shows typical impedance characteristics of presently used directional protections. Most of protection zones are set in "forward" direction, usually only one zone is set in "reverse" direction. This results in a limited reach of correct location of voltage dips occurring downstream the protection since the reverse zone is set to a small distance. Another limitation for the use of distance relays is the method of their operation. They measure the impedance as seen from their terminals but the information about a change in the impedance is exclusively acquired by comparison with a threshold value. In other words, if the impedance does change but the change is not sufficient to exceed the threshold value, the protection will not detect it. A voltage dip caused by e.g. overloading the line 2 (Fig. 23) may cause a voltage reduction below the limit value but, because of insufficient sensitivity, the distance protection will not "recognize" the impedance change, leading thereby to erroneous location of the voltage dip. Also voltage dips of very short durations – below *20 ms*, may not be detected since the distance protection requires over *30 ms* for its proper operation. The above limitations result from the fact that distance protections are intended and designed for faults detection and clearing, and not for voltage dips detection.

Possible settings that would determine the information about a change in the impedance should be selected for the specific site at which this method is applied to voltage dips location.
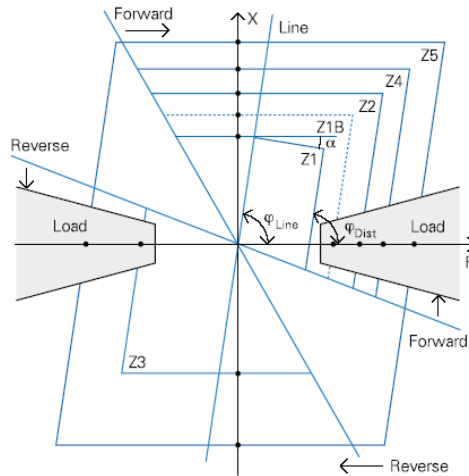
Fig. 24. Impedance characteristics of presently used directional relays

The advantage of the presented solution is its simplicity. The only procedure that should be carried out is a modification of the distance relay configuration, since all necessary electrical connections are already made during its installation.

In order to prove the above method and to illustrate its drawbacks were carried out simulation tests of the power system configuration shown in Fig. 23. The network voltage was assumed 110kV and lines lengths are as follows: line 1: 50 km; line 2: 10 km; line 3: 15 km.

The simulation was carried out for voltage dips caused by phase-to-earth and three-phase faults with transient resistance of the order of 1 Ω. The transient resistance values seen by distance protections, obtained for different locations of three-phase faults, are tabulated in tables 2-5. Results for phase-to-earth faults are not included because the obtained impedance values were, as expected, almost identical with those obtained for three-phase faults. Differences occurred solely in their real parts because of different values of phase-to-earth and three-phase fault currents and a non-zero transient resistance. Thus, without loosing generality of conclusions, the results for phase-to-earth faults can be disregarded.

Considering solely the protection $Z2<$ it is evident from data in Table 2 that this protection identifies correctly voltage dips at busbars of substation A caused by faults in line 2 - the impedance module decreases and its phasor is situated in the first quadrant of complex plane. Such situation occurs even after disconnection of line 2 at its end. But if the line 2 is disconnected and a fault occurs at the point F_3, the impedance seen by $Z2<$ does not change (Table 3). In this case the direction of a voltage dip can be inferred from the reduced busbars voltage and additional information that the line 2 is disconnected (the line current is zero).

Tables 3 and 4 show the impedance seen by the distance protections in the event of faults at the origin of lines 1 and 3. In both cases a decrease in the impedance $Z2<$ is evident and its phasor is situated in the third quadrant of complex plane. Although the conditions of the method algorithm are fulfilled, a voltage dip at busbars of the substation A will be not correctly located. This is because the reverse zone pick up value shall be no greater than the impedance seen by this protection during a fault a the origin of line 3 (faults in lines 1 and 3 are located by the protection Z2< in its reverse zone). Thus voltage dips at the measurement point, caused by faults in line 1, will be correctly located exclusively in the case of faults near

to the substation A busbars. This results from significant differences in the lines lengths and may occur in real systems.

No. of the distance protection	Impedance under normal operating conditions		Impedance under disturbance conditions	
	module [Ω]	argument [deg]	module [Ω]	argument [deg]
Z1	262.1	298.0	12.7	210.2
Z2	57.5	27.8	2.9	22.1
Z3	53.4	194.5	3.8	200.4

Table 2. Fault in the middle of line (F2)

No. of the distance protection	Impedance under normal operating conditions		Impedance under disturbance conditions	
	module [Ω]	argument [deg]	module [Ω]	argument [deg]
Z1	183.7	347.1	48.2	192.6
Z2	∞	-	∞	-
Z3	183.5	167.4	48.2	12.9

Table 3. Fault at the origin of line 3 (F3) – line 2 disconnected

No. of the distance protection	Impedance under normal operating conditions		Impedance under disturbance conditions	
	module [Ω]	argument [deg]	module [Ω]	argument [deg]
Z1	262.1	298.0	13.8	48.5
Z2	57.5	27.8	37.0	246.9
Z3	53.4	194.5	22.0	214.7

Table 4. Fault at the origin of line 1 (F1)

No. of the distance protection	Impedance under normal operating conditions		Impedance under disturbance conditions	
	module [Ω]	argument [deg]	module [Ω]	argument [deg]
Z1	262.1	298.0	87	209.7
Z2	57.5	27.8	25.3	184.1
Z3	53.4	194.5	19.9	9.8

Table 5. Fault at the origin of line 3 (F3)

The method correctness depends to a large extent on the system configuration and this dependence results from the method of operation of the distance protection.

3.8 Vector-space approach [28]

The testing of all these methods show that in cases of asymmetrical voltage dips, they are rather ineffective. Furthermore, al the discussed methods, except the energy based one, require computation of voltage and current phasors for the fundamental-frequency component.

Because voltage dips are transient disturbance events, all phasor-based methods might produce questionable results due to inherent averaging in the harmonic analysis of the input signals [28].
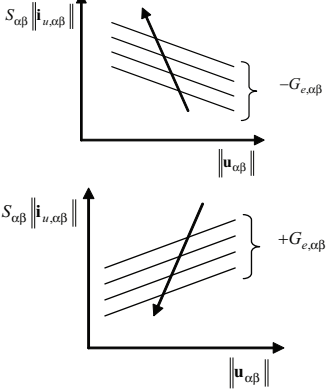
Type of methods	Criterion		Notes
Voltage-current method	Slope $\left(\left\| \mathbf{u}_{\alpha\beta}(t) \right\|, S_{\alpha\beta} \left\| \mathbf{i}_{u,\alpha\beta}(t) \right\| \right)$	$>0 \to$ upstream $<0 \to$ downstream	

where:

$u_{\alpha\beta}$ and $i_{\alpha\beta}$ - voltage and current vectors defined in the orthogonal coordinate system $\alpha\beta$

$\left\| u_{\alpha\beta}(t) \right\|$ - norm of the voltage vector $u_{\alpha\beta}$

$u_\alpha, u_\beta \left(i_\alpha, i_\beta \right)$ - components of vector $u_{\alpha\beta}$ ($i_{\alpha\beta}$) in the orthogonal coordinate system $\alpha\beta$

$p_{\alpha\beta}(t) = u_\alpha i_\alpha + u_\beta i_\beta$ - instantaneous real power [1]

$i_{\alpha\beta}(t) = G_{e,\alpha\beta} u_{\alpha\beta}(t)$

$$G_{e,\alpha\beta}(t) = \frac{p_{\alpha\beta}(t)}{\left\| u_{\alpha\beta}(t) \right\|^2} \qquad S_{\alpha\beta} = sign\left(G_{e,\alpha\beta}(t) \right) \qquad S_{\alpha\beta} \left\| i_{u,\alpha\beta}(t) \right\| = \frac{p_{\alpha\beta}(t)}{\left\| u_{\alpha\beta}(t) \right\|}$$

Type of methods	Criterion		Notes
Active current based methods	If first peak of $S_{\alpha\beta} = sign\left(G_{e,\alpha\beta}(t) \right)$	$<0 \to$ upstream $>0 \to$ downstream	Time response of $S_{\alpha\beta} = sign\left(G_{e,\alpha\beta}(t) \right)$ is calculated for a few cycles before and during voltage dips
Impedance based methods	If $\dfrac{sign\left(first\,peak\left(\Delta \left\| \mathbf{u}_{\alpha\beta}(t) \right\| \right) \right)}{sign\left(first\,peak\left(\Delta \left(S_{\alpha\beta} \left\| i_{\alpha\beta}(t) \right\| \right) \right) \right)}$	$>0 \to$ upstream $<0 \to$ downstream	$\Delta \left\| u_{\alpha\beta}(t) \right\| = \left\| u_{\alpha\beta}(t) \right\|_{dip} - \left\| u_{\alpha\beta}(t) \right\|_{befor\,dip}$ $\Delta \left(S_{\alpha\beta} \left\| i_{u,\alpha\beta}(t) \right\| \right) = \left(S_{\alpha\beta} \left\| i_{u,\alpha\beta}(t) \right\| \right)_{dip} -$ $\qquad - \left(S_{\alpha\beta} \left\| i_{u,\alpha\beta}(t) \right\| \right)_{before\,dip}$
Energy based method	If $\Delta w_{\alpha\beta}(t) = \int\limits_0^t \Delta p_{\alpha\beta}(\tau)d\tau$	$<0 \to$ upstream $>0 \to$ downstream	$\Delta p_{\alpha\beta}(t) = p_{\alpha\beta}(t)_{dip} - p_{\alpha\beta}(t)_{before\,dip}$

Table 6. Voltage dip source detecting using vector space approach [28]

In order to overcome these difficulties vector-space approach is proposed for voltage dip detection. These methods are based on instantaneous voltage and current vectors and their transformation into α,β,0 Clarke's components. In this way other methods used for voltage dip source detection like the system operating conditions trajectory during the dip (chapter 3.2), the active current based method (chapter 3.7.2), impedance based methods (chapter 3.7.1) and energy based method (chapter 3.4) can be presented in general form.

In Table 6 are presented the generalized methods using a vector space approach.

4. Voltage flictuations

Voltage fluctuations are a series of rms voltage changes or a variation of the voltage envelope. Where only one dominant source of disturbance occurs its identification is usually a simple task. In extensive networks or in the case of several loads interaction, the location of a dominant disturbance source is a more complex process. Where large voltage fluctuations occur in several branch lines it may happen that measurements of flicker severity indices carried out at a power system node, do not indicate disturbing loads downstream the measurement point. The reason is a mutual compensation of voltage fluctuations from various sources.
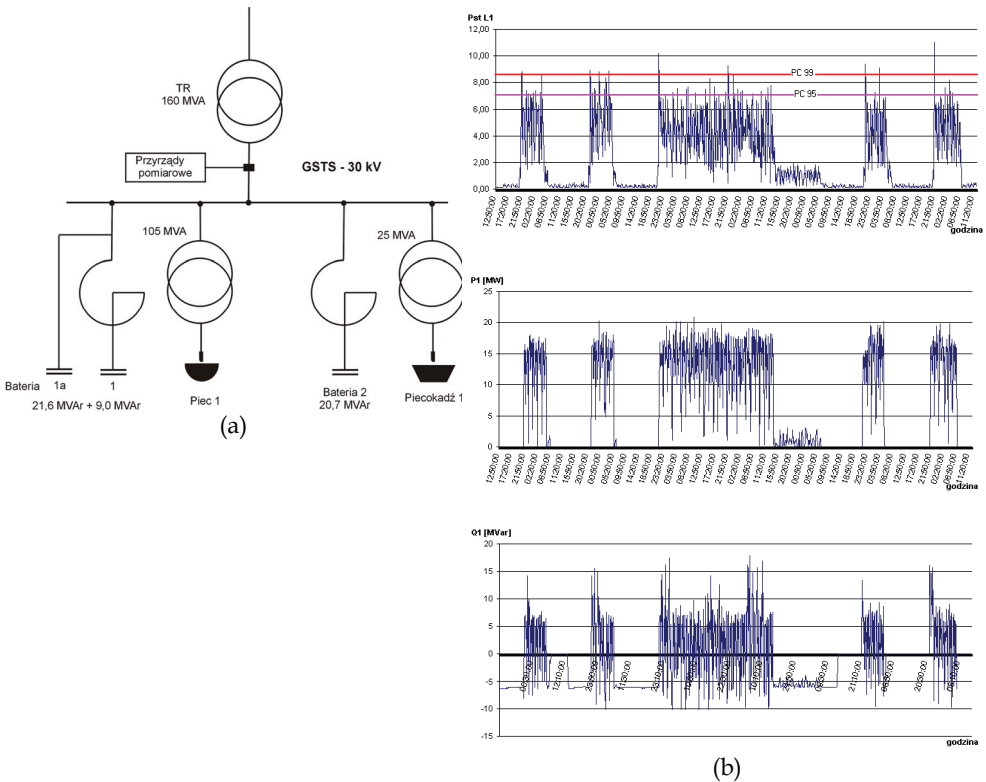

Fig. 25. An example of changes in the flicker severity and the active and reactive power — phase L1 (diagram in (a))

4.1 Criterion of voltage fluctuations during a fluctuating load operation and after turning it off

The recorded quantities are: the flicker severity P_{st} and changes in the reactive power Q (also the active power P, if needed) at PCC. The measurements are carried out during the load operation and, where technically possible, after it is turned off. An example records from a steelwork during the arc furnace operation is shown in Fig. 25. Figure shows the results of one week's measurement of the flicker severity P_{st}, active power P and reactive power Q (phase L1). The dependence of flicker severity values on changes in power, caused by the arc furnace operation, is evident. During the periods the furnace is turned off the reactive power at the measurement point is capacitive due to the presence of fixed capacitor banks. In case several loads are analyzed the measurements have to be carried out during the operation of each load separately.

4.2 Correlation of changes in the flicker severity P_{st} and/or changes in the active and reactive power

The method consists in the analysis of mutual correlation between changes in the reactive power Q (and also the active power P, particularly for low-voltage networks) and the flicker severity value P_{st}. It allows define the dominant source of disturbance and assess the influence of a change in the load power on the voltage fluctuation in the measurement point. This method can also be applied for assessing the influence of disturbances in individual branches of the network on the total P_{st} at PCC.

(a)   (b)
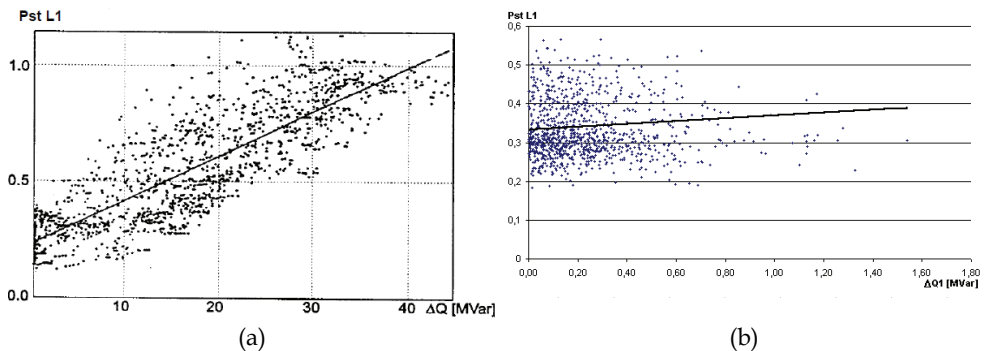
Fig. 26. An example of correlation characteristics of flicker severity P_{st} and reactive power changes

Fig. 26 shows correlation characteristics of flicker severity P_{st} and reactive power changes. Characteristic (a) exhibits a strong correlation; it means that a load supplied from the monitored line is the dominant source of voltage fluctuation. In the case (b) the examined load cannot be regarded to be the dominant source.

4.3 Examination of the *U-I* characteristic slope [23]

Consider two sources of flicker which cause voltage fluctuation at the measurement location PCC: case 1 involves a flicker generating branch at point A and case 2 a similar at point B (Fig. 1). As a result of this flicker caused in the system, the voltage measured at PCC will fluctuate – the current at PCC will show different behaviour for these two cases, similar to criterion used for voltage dip localization.

For case 1, the measured current will be the load current at the lower voltage – the current measured at PCC will decrease as the voltage decreases during the flicker occurrence, and increase as the voltage increases (Fig. 27a).

For case 2, the measured current will be the sum of the load current and the flicker-caused load current at the lower voltage – therefore, the current measured at PCC will increase as the voltage decreases during the flicker occurrence, and decrease as the voltage increases (Fig. 27b).

These observations are presented graphically in Fig. 27. Each event is characterized by straight line, which represents the correlation between measured rms voltage and current. It can be seen that the slopes of the lines are different for the two cases. A positive slope shows that the flicker is from upstream and a negative slope shows that it is from downstream.

Although the idea was conceived for a one-source system, it has been found that it is also valid for two-source system as in Fig. 15 [23].
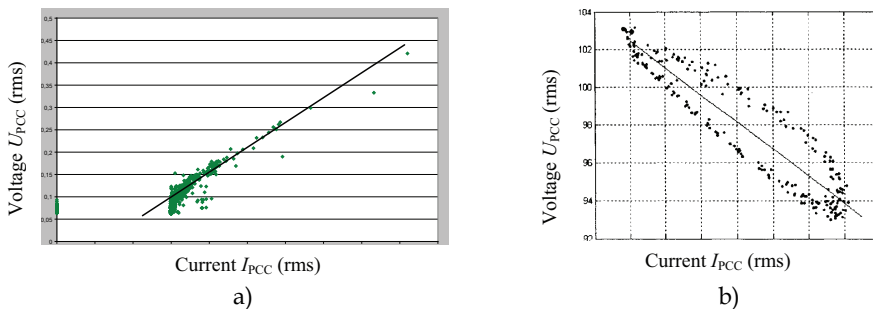

Fig. 27. Slope characteristics for the *U-I* correlations

4.4 Identification of interharmonic power direction [24]

The method utilises two common observations:

- interharmonics cause flicker – the fundamental and an interharmonic component of a voltage waveform are not in synchronous, therefore the voltage can be represented as the one of with modulated magnitude, which causes flicker.
- flicker cause interharmonics – voltage variations can be treated as amplitude modulation of the voltage, therefore by means of Fourier analysis the voltage can be decomposed on harmonic and interharmonic components.

Thus, the problem of locating flicker source can be solved by locating interharmonic source. If the customer appears as a source of interharmonics i.e. the active interharmonic power is negative, the customer is also a flicker source. If the customer appears as an interharmonic load i.e. the active interharmonic power is positive, the customer is not a flicker source.

The method is applied as follows:

- a power quality monitor is installed at the branch related to the suspected consumer, and records voltage and current waveforms as flicker occurs.
- Fourier based algorithm is used to investigate main interharmonics i.e. the components that have the maximum magnitude.
- for each of the interharmonic active power is calculated.
- if the consumer produces interharmonic power, he can be identified as interharmonic source and consequently the flicker source.

The frequency of an interharmonic signal depends on operation of the customer's equipment, so it is almost impossible that two devices produce the same interharmonics at the same time. Consequently it is relatively easy to locate the source of interharmonics. This method is fund not to be effective for random flicker source detection.

4.5 Examination of the "voltage fluctuation power"

A conception similar to the method of examining the direction of dominant interharmonics active power flow is presented in [1,3,4]. Similarly to the definition of active power in the time domain there could be introduced so called "flicker power". Lets define supply voltage and line current in PCC as sinusoidal waveforms with modulated amplitudes as follows

$$u_{PCC}(t) = (U_1 + m_U(t))\cos(\omega_1 t) \qquad i_{PCC}(t) = (I_1 + m_I(t))\cos(\omega_1 t + \varphi_I) \qquad (43)$$

where $u_{PCC}(t)$, $i_{PCC}(t)$ are voltage and current waveforms respectively, U_1, I_1 are magnitudes of the fundamental components, $m_I(t)$, $m_U(t)$ are amplitude modulation function of current and voltage respectively, φ_I is phase shift of the current with respect to the voltage, ω_1 is the angular frequency of the fundamental component.

The human sensitivity to flicker is a function of both modulating frequency and degree of modulation. That means the frequency signals $m_U(t)$ and $m_I(t)$ must be filtered according to how the human responds to flicker. This is achieved by using the sensitivity filter described in the IEC 61000-4-15. The out signals $m_{UF}(t)$ and $m_{IF}(t)$ indicate how an average human responds to flicker. By multiplying and integrating $m_{UF}(t)$ and $m_{IF}(t)$ a new quantity "flicker power" FP is achieved:

$$FP = \frac{1}{T}\int_0^T m_{UF}(t)m_{IF}(t)dt \qquad (44)$$

where T is integration time. The flicker power provides two important pieces of information:
- the sign of FP provides information whether flicker source is placed upstream or downstream with respect to the monitoring point.
- when several consumers are investigated, magnitude of FP provides information which outgoing line contributes most to the actual flicker level.

Positive sign of flicker power means the same flow direction as the fundamental power flow. It means that voltage modulation $m_U(t)$ is correlated with current modulation $m_I(t)$ i.e. decreasing in supply voltage amplitude results in decreasing the load current. Consequently the flicker source is placed upstream with respect to the measuring point. Negative sign of flicker power means the opposite flow direction to the fundamental power flow, and consequently the voltage modulation is negative correlated with current modulation i.e. increasing the current load results in voltage drop. Therefore the flicker source is placed downstream with respect to the measuring point meaning that the load is responsible for voltage variation.

There could be noted, that the method is valid in a specific area of the load reactive power variation.

The method gives correct results under inductive load (the current lags the voltage), and limited capacitive power load (the current waveform leads the voltage waveform). There is also possibility of misinterpretation when a load of constant power demand is considered.

In such a case a voltage drop results in increased current flow. When the reaction is considerable it could be misinterpreted as having the flicker source downstream. The described situations, however, seldom arises in most practical situations.

5. Voltage asymmetry

A three-phase power system is called balanced or symmetrical if the three-phase voltages and currents have the same amplitudes and their phases are shifted by 120° with respect to each other. If either or both of these conditions are not fulfilled, the system is called unbalanced or asymmetrical.

The generator terminal voltages provided to the power system are almost perfectly sinusoidal in shape with equal magnitudes in the three phases and shifted by 120°. If the impedances of the system components are linear and equal for three phases, and if all loads are three-phase balanced, the voltages at any system bus will remain balanced. However, many loads are single-phase and some large unbalanced loads may be connected at higher voltage levels (e.g. traction systems, furnaces). The combined influence of such diverse loads, drawing different currents in each phase, may give rise to the 3-phase supply voltage unbalance. The supply voltage unbalance will then affect other customers connected to the same power network.

To quantify an unbalance in voltage or current of a three-phase system the symmetrical components (Fortescue components) can be used. The three-phase system is thus decomposed into a system of three symmetrical components: direct or positive-sequence, inverse or negative-sequence and homopolar or zero-sequence, indicated by subscripts 1, 2, 0. These transformations are energy-invariant, so for any power quantity computed from either the original or transformed values the same result is obtained. Thus, for active power of a three-phase system we obtain the equation:

$$P = P_s \tag{45}$$

where: $\quad P = P_A + P_B + P_C = U_A I_A \cos\varphi_A + U_B I_B \cos\varphi_B + U_B I_B \cos\varphi_C$

and $\quad P_s = 3(P_0 + P_1 + P_2) = 3(U_0 I_0 \cos\varphi_0 + U_1 I_1 \cos\varphi_1 + U_2 I_2 \cos\varphi_2)$

The subscripts A, B, C denote the different phases. It should be, however, noted that phase active powers have positive direction (from a source to load). Active powers of the symmetrical components P_0, P_1, P_2 have no physical meaning and their values depend on the character of the system asymmetry. It can be demonstrated that active power of the direct component has the same direction as the total system active power, but direction of active power of the inverse component depends on the system asymmetry nature. Direction of the inverse component may be used for identifying location of asymmetry source in the system.
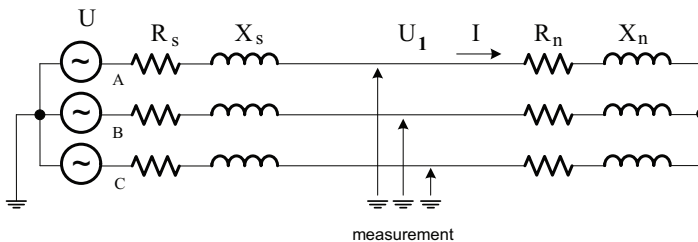
Fig. 28. Circuit diagram for asymmetry source location identification

Fig. 28 shows the circuit diagram for illustration the method, where equivalent parameters U, R_s, X_s represent a power system side and R_n, X_n – load side.

Circuit conditions	Active power components		Source voltage	Measured voltage	Measured current
	Load active power	Active powers of symmetrical components			
Symmetrical	$P_{ABC} = 1060.5$	$P_1 = 353.5$ $P_2 = 0$ $P_s = 3(P_{1s}+P_{2s}) =$ 1060.5			
Unbalanced load side parameters (balanced system side parameters and phase voltages)	$P_{ABC} = 969.6$	$P_1 = 352.2$ $P_2 = -29.0$ $P_s = 3(P_{1s}+P_{2s}) = 969.6$			

Unbalanced system side parameters (balanced load side parameters and phase voltages)

$P_{ABC} = 1280.4$

$P_1 = 397.8$

$P_2 = 29.0$

$P_s = 3(P_{1s}+P_{2s}) = 1280.4$

Unbalanced system phase voltages (balanced system side parameters and load side parameters)

$P_{ABC} = 765.9$

$P_1 = 245.5$

$P_2 = 9.8$

$P_s = 3(P_{1s}+P_{2s}) = 765.9$

Table 7. Comparative asymmetry analysis in the point of measurement

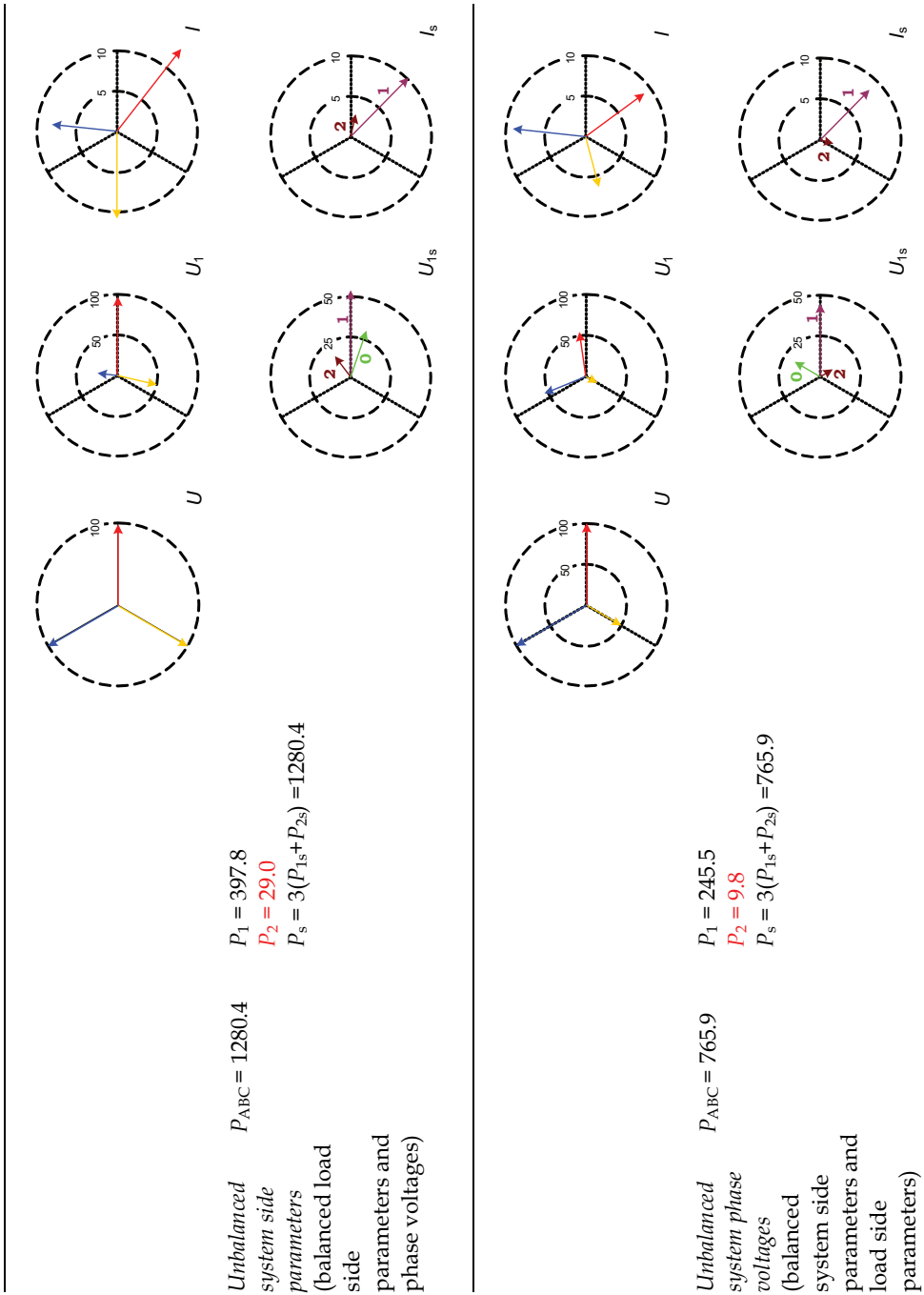In order to examine the method of asymmetry source locating in the analysed diagram the following parameters are taken (in per unit values): $U = 100$; $R_s = R_n = R = 3.536$ and $X_s = X_n = X = 3.536$. Thus, for symmetrical conditions we obtain: $I = 10$ and $U_1 = 50$.

The following sources of asymmetry in the circuit in Fig. 25 are considered:

-   unbalanced load side parameters: $R_{nA} = 0.1R$, $R_{nB} = R$, $R_{nC} = 2R$,
                                                $X_{nA} = 0.1X$, $X_{nB} = X$, $X_{nC} = 2X$
-   unbalanced system side parameters: $R_{sA} = 0.1R$, $R_{sB} = R$, $R_{sC} = 2R$,
                                                $X_{sA} = 0.1X$, $X_{sB} = X$, $X_{sC} = 2X$
-   unbalanced system phase voltages: $\underline{U}_A = Ue^{j0^0}$, $\underline{U}_B = 0,5Ue^{-j120^0}$, $\underline{U}_C = Ue^{j120^0}$

Results of the calculation are shown in Table 7. As can be seen, the positive sign of the inverse component active power indicates the system side as the source of asymmetry at the point of measurement (irrespective to voltage or impedance asymmetry), the negative sign of the inverse component active power indicates the load side as the source of asymmetry.

6. Conclusion

In many cases, the quantitative determination of the supplier's and customer's share in the total disturbance level at the point of common coupling (PCC) is also required. Seeking non-expensive, reliable and unambiguous methods for locating disturbances and assessing their emission levels in power system, not employing complex instrumentation, is one of the main research areas which require the prompt solution. As a result, such research has become an important topic recently.

7. References

[1] Akagi H., Kanazawa Y., Nabae A.: Generalized theory of instantaneous reactive power in three-phase circuit, *Proceedings of the International Power Electronics Conference*, Tokyo, Japan, 1983, 1375-1386.

[2] Axelberg P.G.V., Bolen M., Gu L.: A measurement method for determining the direction of propagation of flicker and for tracing a flicker source, *International Conference CIRED'2005*, Turin (Italy), June 2005.

[3] Axelberg P.G.V., Bollen M.,: An algorithm for determining the direction to a flicker source, *IEEE Trans. on Power Delivery*, 21, 2, 755-760, 2006.

[4] Axelberg P.G.V., Bollen M., Gu L.: Trace of flicker sources using the quantity of flicker power, *IEEE Tran. On Power Delivery*, 23, 1, 465-471, 2008.

[5] D'Antona G., Muscas C., Sulis S.: Harmonic source estimation: a new approach for the localization of nonlinear loads, 978- 1-4244- 1 770-4/08, 2008 IEEE.

[6] Bollen M.H.J.: Understanding power quality problems – voltage sags and interruptions. *IEEE Press Series on Power Engineering* 2000.

[7] Chang G. W., Chen C. I, Teng Y. F.: An application of radial basis function neural network for harmonics detection, 978-1-4244-1770-4/08,2008 IEEE.

[8] Chen C., Liu X, Koval D.,, Xu W., Tayjasanant T.: Critical impedance method - a new detecting harmonic sources method in distribution systems, *IEEE Transactions on Power Delivery*, 19, 1, January 2004.

[9] Cristaldi L., Ferrero A.: Harmonic power flow analysis for the measurement of the electric power quality, *IEEE Tran. Instrum. Meas*, 44, 6,1995, pp. 683-685.

[10] Dán A.M.: Identification of flicker sources, *8th ICHQP '98, Athens*, Greece, Oct. 14-16, 1998.

[11] De Jaeger E.: Measurement of flicker transfer coefficient from HV to MV and LV systems. UIEPQ-9630.

[12] De Jaeger E.: Measurement and evaluation of the flicker emission level from a particular fluctuating load, *CIGRE/CIRED Joint Task Force* C4.109, Oct. 2007.

[13] De Jaeger E.: Disturbances emission levels assessment techniques (CIGRE/CIRED Joint Working Group C4-109).

[14] Emanuel A. E.: On the assessment of harmonic pollution, *IEEE Trans. on Power* Delivery, 10, 3, 1995.

[15] *Guide to quality of electrical supply for industrial installations*. Part 5: Flicker, UIEPQ 1999.

[16] Hamzah N., Mohamed A., Hussain A.: A new approach to locate the voltage sag source using real current component, *Electric Power Systems Research*, 2004, vol. 72, pp. 113-23.

[17] IEEE guide for protective relay applications to transmission lines, *IEEE Std.* C37.113, 1999.

[18] IEEE Power Engineering Society, Distribution System Analysis Subcommitee, *IEEE 37 Node Test Feeder*

[19] Khosrayi A., Melendez J., Colomer J.: A hybrid method for sag source location in power network, *9th International Conference, Electrical Power Quality and Utilization*, Barcelona, 9-lI, October 2007.

[20] Leborgne R.C., Olguin G., Bollen M.: The Influence of PQ-Monitor Connection on Voltage Dip Measurements, *In Proc. 4th Mediterranean IEEE Conference on Power Generation, Transmission, Distribution and Energy Conversion*, Cyprus, 2004.

[21] Li C., Xu W., Tayjasanant T.: A critical impedance based method for identifying harmonic sources, *IEEE Transaction on Power Delivery*, 19, 1, April 2004.

[22] Li, C., Tayjasanant, T., Xu W., Liu X.: A method for voltage sag source detection by investigating slope of the system trajectory, *IEEE Proceedings on Generation, Transmission & Distribution*, 150, 3, 2003 pp.367-372.

[23] Nassif A., Nino E., Xu W.: A V-I slope based method for flicker source detection, *Annual North American Power Symposium*, Edmonton (Canada), October 2005, 0-7803-9255-8/2005 IEEE.

[24] Nasif A., Zhang D., Xu W.: Flicker source identification by interharmonic power direction, *IEEE CCECE/CCGEI'2005 International Conference*, Saskatoon (Canada), May 2005, 0-7803-8886-0/2005 IEEE.

[25] Nunez V.B., Moliner X.B., Frigola J.M., Jaramillo S.H., Sanchez J., Castro M.: Two methods for voltage sag source location. *13th ICHQP 2008*, Australia.

[26] Parsons A. C., Grady W.M., Powers E.J., Soward J.C.: A direction finder for power quality disturbances based upon disturbance power and energy, *IEEE Trans. Power Delivery*, 2000, 15, 3, pp. 1081-1086.

[27] Pfajfar T., Blaźić B., Papić I.: Methods for estimating customer voltage harmonic emission levels, 978-1-4244-1 770-4/08 IEEE.

[28] Polajzer B., Stumberger G., Seme S., Dolinar D.: Generalization of methods for voltage sag-sag source detection using vector-space approach, *IEEE Trans. on IA*, 6,45,2009.

[29] Prakash K. S., Malik O. P., Hope G. S. Amplitude comparator based algorithm for directional comparison protection of transmission lines, *IEEE Trans. on Power Delivery*, 4, 4, 1989, pp. 2032-2041.

[30] Pradhan A.K. , Routray A.: Applying distance relay for voltage sag source detection, *IEEE Trans. on Power Delivery*, 20, 2005, pp. 529-31.

[31] Pradhan A.K, Routray A., Madhan S.: Fault direction estimation in radial distribution system using phase change in sequence current, *IEEE Tran. on Power Delivery*, 22, 2007, pp. 2065-2071.

[32] Pyzalski T., Wilkosz K.: Critical analysis of approaches to localization of harmonic generation, *Electrical Power Quality and Utilisation*, Cracow, Sep. 17-19, 2003.

[33] Pyzalski T., Wilkosz K.: New approach to localization of harmonic sources in a power system, *Electrical Power Quality and Utilisation*, Cracow, Sep. 17-19, 2003.

[34] Pyzalski T.: Localization of harmonic sources in a power system, Ph.D. dissertation, Wroclaw University of Technology, 2006.

[35] Review of methods for measurement and evaluation of the harmonic emission level from an individual distorting load, *CIGRE 36.05/CIRED 2 Joint WG* CCO2, 1998.

[36] Stade D. etc.: Simultaneous measurements for analysing the flicker dissipation in meshed HV power systems, *8th ICHQP*, Athens, Greece, Oct. 14-16, 1998.

[37] Tayjasanant, T., Li C., Xu W.: A resistance sign-based method for voltage sag source detection. *IEEE Tran. on Power Delivery* 20, 4, 2005, pp. 2554-2551.

[38] Technical specification, 1133A Power Sentinel™, Arbiter Systems.

[39] *The 12th ICHQP Tutorial*, Portugal, October 1, 2006.

[40] Tsukamoto M., Kouda I., Natsuda Y., Minowa Y., Nishimura S.: Advanced method to identify harmonics characteristic between utility grid and harmonic current sources, *8th ICHQP*, Athens, Greece, Oct. 14-16, 1998.

[41] Wilkosz K.: A generalized approach to localization of sources of harmonics in a power system, *13th ICHQP*, Australia, 2008.

[42] Xu W., Liu Y.: A method for determining customer and utility harmonic contributions at the point of common coupling, *IEEE Trans. on Power Delivery*, 15, 2, 2000.

[43] Xu W., Liu X., Liu Y.: An investigation on the validity of power direction method for harmonic source determination, *IEEE Trans. Power Delivery*, 18, 1, 2003, pp. 214-219

S-Transform Based Novel Indices for Power Quality Disturbances

Zhengyou He and Yong Jia
Southwest Jiaotong University
China

1. Introduction

Power quality (PQ) has recently become an increasing concern for electric utilities and their customers due to the ever-growing proliferation of power electronic devices and nonlinear loads in electrical power networks. The opening of power markets, and the deregulation and restructuring throughout the world are further changing the framework in which power quality is addressed (Beaulieu et al., 2002). Therefore, the techniques for power quality study and power disturbance mitigation are capturing increasing attention, and consequently, manufacturers are integrating power quality monitoring functions in their products such as power meters, digital relays and event recorders (Ward, 2001). One of the most important aspects in power quality analysis is to evaluate the extent of power disturbances and their negative impacts on power systems. Power quality indices, as a powerful tool for quantifying power quality disturbances, are the concise numerical representations characterizing the nature based on the time and frequency information of the disturbance waveform (Lin & Domijan, 2005). They also serve as the basis for illustrating the negative impacts of electrical disturbances and for assessing compliance with the required standards or recommendations within a given regulatory framework.

A power quality disturbance usually involves a variation in the electric voltage or current and can be classified based on the waveform time-statistical characteristics into two groups: steady disturbances (harmonic distortion, unbalance, flicker etc.) and transient disturbances (voltage sags, voltage swells, impulses, oscillatory transient etc.). Several power quality indices identified and utilized in the past were accepted and worked well for single and three-phase balanced systems and with periodic stationary waveforms, however, pitfalls of these indices in common use are discussed in (Heydt, 1998, 2000). With the severe changes in the waveforms of the current and voltage signals in the power network, the traditional definitions of the previous indices are no longer valid. As transient disturbances are characterized by spectral components that are significantly time varying in amplitude and/or in frequency; it is important to accommodate the time information in the indices calculation so that they can provide more sensitive interpretation of the disturbances.

Recently, one of the most interesting applications is the assessment of power quality by redefining new indices for transient disturbances using signal processing techniques. New power quality indices have been suggested based on the short time Fourier transform (STFT) (Jaramillo et al., 2000), time frequency distribution(TFD)(Shin et al., 2006) and stationary wavelet transform(SWT)(Morsi & Hawary, 2008). The integrating of the time

information into the calculation of several power quality indices using STFT is addressed in (Jaramillo et al., 2000); however, although the STFT technique offered a partial solution for the time information, it has limitations due to its fixed window length, which has to be chosen prior to the analysis. This drawback is reflected in the achievable frequency resolution when analyzing non-stationary signals with both low and high-frequency components (Gargoom et al., 2005). Wavelet transform (WT) presents a signal in the time-frequency plane using adaptive windows and Mallat fast algorithm. However, WT is not suitable for analyzing low frequency disturbance, in addition, some importance frequency components of the disturbance are not extracted precisely due to the non-adjustable central frequency and frequency bands once the sampling frequency is determined (Lin & Domijan, 2005). The various types of time frequency distributions namely "Cohen' class" synthetically, are a bilinear transformation providing simultaneous time and frequency information on the energy content of the signal. As the disturbances in power systems are characterized by the presence of multiple frequency components over a short duration, interference is also problematic.

Recently, to overcome the limitations of the previous techniques, the previous works (Stockwell et al., 1996, Mishra et a., 2008, Zhan et al. 2005, Chilukuri & Dash, 2004) introduce the S-transform (ST) as a new power quality analysis technique. This chapter is concerned with investigating the power quality indices obtained in the S-transform domain for transient disturbances assessment. The chapter is organized as follows. Section X.2 discusses the theoretical background of STFT, WT and S-transform. The indices that are most frequently used in international standards and recommendations are introduced in section X.3. Section X.3 will also define four new power quality indices for transient disturbances based on S-transform. Then, section IV discusses the performance of these indices on simulated power quality signals. Finally, conclusions are given in Section V.

2. Theoretical background

Signal processing techniques have been widely used for automatic power quality (PQ) disturbance detection and recognition (Bollen & Gu, 2006). As for power quality assessment, these high-performance signal-analysis techniques are potential to calculate PQ indices based on the knowledge of what spectral components are present in the signal and where they are located in time (time frequency representations). In this section, the background theories of the STFT, WT and S-transform are presented.

2.1 Short-time Fourier Transform

As is well-known, the Fourier Transform is the main tool for signal spectral decomposition. The Fourier transform (FT) of a s signal $x(t)$ with $t \in (-\infty, +\infty)$ is defined by Equation(1) below:

$$FT(f) = \int_{-\infty}^{+\infty} x(t) e^{j2\pi ft} \, dt \qquad (1)$$

In the discrete time domain, the Fourier transform of a discrete sampled waveform $x(n)$ is defined as follows:

$$FT(f) = \sum_{n=-\infty}^{\infty} x(n) e^{j2\pi fnT} \qquad (2)$$

In practical applications, time domain waveforms are finite sequences of samples. If a finite sequence of L samples of the waveform $x(n)$, n = 0, 1,…, L-1, is considered, its L-point DFT is given by:

$$\mathrm{DFT}(k) = \sum_{n=0}^{L-1} x(n)\mathrm{e}^{j2\pi kn/L} \quad k = 0,1,...,L-1 \tag{3}$$

To improve the analysis of signals whose spectrum changes with time we introduce the widely used and well-defined short-time Fourier transform. The STFT is a simple extension of the FT of a general signal $x(t)$, where the FT is evaluated repeatedly for a windowed version of the time domain signal. In practice, each FT gives a frequency domain 'slice' associated with the time value at the centre of the window. With such an approach, the waveform can be represented in a three-dimensional plot so it is possible to know what spectral components are present in the signal and where they are located in time (time frequency representation). In the continuous time domain, STFT is defined by:

$$\mathrm{STFT}(f,\tau) = \int_{-\infty}^{+\infty} x(t)w(t-\tau)\mathrm{e}^{j2\pi ft}\,dt \tag{4}$$

where w is the sliding time window of length T_w, and τ is the time to which the spectrum refers. In the discrete time domain, Equation (4) becomes:

$$\mathrm{STDFT}(k) = \sum_{n=0}^{L-1} x(n)w(n-m)\mathrm{e}^{j2\pi kn/L} \quad k = 0,1,...,L-1 \tag{5}$$

where $x(n)$ and $w(n)$ are the sampled versions of the signal and of the sliding time window, respectively, L is the number of samples and m is related to the discrete time to which the spectrum refers.

The shape of the sliding time window can influence the spectral component values. The choice of the window (e.g. rectangular, Gaussian, Hanning) is therefore an important issue, and this topic has been discussed extensively in the literature when power quality disturbances are dealt with (Gallo, et al., 2002, 2004). In practice, the rectangular window is used frequently when the issue of power quality indices is considered. The STFT has been used as a basis for the development of a short term harmonic distortion (STHD) index in (Jaramillo et al., 2000). Similar extensions for other waveform distortion indices, such as the K-factor and the crest factor, have been considered.

2.2 Wavelet transform

The wavelet transform (WT) has been proposed more and more for processing power quality disturbances. It, like the STFT, is a form of time frequency technique since it allows the simultaneous analysis of waveforms in both time and frequency domains. The main advantage of WT over the STFT is the possibility of conducting multi-resolution time frequency analyses, which allows different resolutions of an analyzed spectrum to be obtained at different frequencies.

The continuous wavelet transform (CWT) of a given signal $x(t)$ with respect to the mother wavelet $\psi_{a,b}(t)$ is the following dot product:

$$\mathrm{CWT}(a,b) = \langle x,\psi_{a,b}\rangle = \int_{-\infty}^{+\infty} x(t)\frac{1}{\sqrt{a}}\psi^*(\frac{t-b}{a})dt \tag{6}$$

$$\psi_{a,b}(t) = \frac{1}{\sqrt{a}}\psi(\frac{t-b}{a}) \tag{7}$$

where * means the complex conjugate. $\psi_{a,b}(t)$ is called the mother wavelet with $a \in$ R+ and b $\in$ R. The wavelet $\psi_{a,b}(t)$ can be dilated (stretched) and translated (shifted in time) by adjusting the two parameters that characterize it.

For an assigned pair of parameters a and b, the coefficient obtained by Equation (6) represents how well the signal $x(t)$ and the scaled and translated mother wavelet match. By varying the values of a and b, we can obtain the wavelet representation of the waveform $x(t)$ in time (corresponding to the b coefficient) and frequency (corresponding to the a coefficient) domains with respect to the chosen mother wavelet.

In order to obtain discrete scale and time parameters, the wavelet function can choose discrete scaling and translation parameters such as $a = a_0^j$ and $b = kb_0 a_0^j$ where k and j are integers and $a_0 > 1$, $b_0 > 0$ are fixed. The result is:

$$\psi_{j,k}(t) = \frac{1}{\sqrt{a_0^j}}\psi(\frac{t - kb_0 a_0^j}{a_0^j}) \tag{8}$$

The wavelet transform of a continuous signal $x(t)$ using discrete scale and time parameters of wavelets leads to the following wavelet coefficients:

$$\text{CWT}(j,k) = \langle x, \psi_{j,k} \rangle = \frac{1}{\sqrt{a_0^j}} \int_{-\infty}^{+\infty} x(t) \; \psi^*(\frac{t - kb_0 a_0^j}{a_0^j}) \; dt \tag{9}$$

The most delicate steps in WT analysis are the choice of the mother wavelet and the choice of the number of expansion levels. With reference to the choice of the mother wavelet, only knowledge of the phenomena to be analyzed and experience can help to make the best choice and often several trials are necessary to obtain the best choice. Just as when making the choice of an appropriate mother wavelet, knowledge of the phenomena to be analyzed and experience are necessary in order to make the best choice of the number of decomposition levels.

2.3 S-transform

S-transform is an extension of the ideas of the continuous wavelet transform (CWT) based on a moving and scalable localizing Gaussian window, so it can be considered as generation of the combination of CWT and STFT. The S-Transform $S(\tau, f)$ of a function is $x(t)$ defined as follows.

$$S(\tau, f) = \int_{-\infty}^{\infty} x(t) w_f(\tau - t) e^{-i2\pi ft} dt \tag{10}$$

$$w_f(\tau - t) = \frac{|f|}{\sqrt{2\pi}} e^{-\frac{f^2(\tau - t)^2}{2}} \tag{11}$$

Where, $w_f(\tau - t)$ is the Gaussian window function. τ is the shift parameter which can adjust the position of the Gaussian window in the time axis. f is the scale parameter.

Define $X(f)$ as the Fourier transient result of $x(t)$. Then the relationship between S-transform and Fourier transient can be described as follows.

$$X(f) = \int_{-\infty}^{\infty} S(\tau, f) d\tau \qquad (12)$$

The equation above shows that the time average of the local spectral representation should result identically in the complex-valued global Fourier Spectrum. S-transform can also be written as function of $X(f)$ as

$$S(\tau, f) = \int_{-\infty}^{\infty} X(v + f) e^{-2\pi^2 v^2 / f^2} e^{j\pi v\tau} dv \qquad (13)$$

The discrete version of the S-transform is calculated by taking the advantage of the efficiency of the fast Fourier transform (FFT) and the convolution theorem. The discrete S-Transform of $x[kT]$ is obtained by making f equal to n/NT and τ equal to kT:

$$S[kT, \frac{n}{NT}] = \sum_{m=0}^{N-1} X[\frac{m+n}{NT}] e^{-\frac{2\pi^2 m^2}{n^2}} e^{j\frac{2\pi n}{N}k} \qquad (14)$$

where N is the length of the analyzed signal, the index k, m and n are equal to 0,1…N –1. T is the time interval between two consecutive samples. The above equation represents a two dimensional matrix called the S-matrix in which the row is corresponding with frequency and the column is corresponding with time. Each column, thus, represents the local spectrum at one point of time and each element of the S-matrix is complex valued corresponding with the amplitude.

The S-transform produces a time-frequency representation of a time series. It uniquely combines a frequency-dependent resolution that simultaneously localizes the real and imaginary spectra. Compared with STFT, the advantage of S-transform is that the width and the height of the time-frequency window vary with the frequency. Like wavelet transform, S-transform is suitable for analyzing non-stationary signals because of its excellent performance of local time-frequency analysis, which means that it has higher frequency resolution in low frequency bands and lower time resolution in high frequency bands. Because of the combination of absolutely referenced phase information and frequency invariant amplitude of the S-transform, one can directly extract the fundamental and harmonic components of the signal from the S-matrix. In the next section, several novel power quality indices will be introduced based on the good time-frequency localization properties of S-transform.

3. Power quality indices

Power quality indices are a few representative numbers that are the result of characterizing, reducing, or extracting from a large volume of power quality measurement data. As much as feasible, the number of quality indices should be kept at their minimum, they should also be easy to assess and be representative of the actual impact of the disturbances they characterize. From the above considerations, it can see that there is a need for common power quality indices in order, for different system operators, to measure and report power quality disturbances quality in a consistent and harmonized manner, either to their clients or to the regulators. In this section, an overview of several traditional indices is provided firstly and shortcomings of these indices are discussed, then four new indices are defined for transient disturbance assessment.

3.1 Traditional power quality indices

The most frequently encountered power disturbances, which are low frequency and high frequency phenomena, are classified into several categories in (IEEE Std. 1159). The existing indices for each disturbance are as follows.

A. Waveform distortions

Waveform distortions (voltage or current) are mainly characterized by the total harmonic distortion factor (THD), which is defined as the RMS of the harmonic content divided by the RMS value of the fundamental component, usually multiplied by 100. Harmonic index is based on the spectrum of voltage or current over a given window of time. Various methods for obtaining the spectrum are being discussed in the technical literature, but the method almost exclusively used in power quality monitoring is the Fourier transform. A number of international standard documents define the measurement process, including (EN 50160, IEC 61000-3-6, IEC 61000-4-7, IEC 61000-4-30).

B. Slow voltage variations

Slow voltage variations are usually quantified by calculation of the RMS value of the supply voltage. In assessing RMS supply voltage, measurement has to take place over a relatively long period of time to avoid the instantaneous effect on the measurement caused by individual load switching (e.g. motor starting, inrush current) and faults. (IEC 61000-4-30) defines the procedure for the RMS voltage measurements and, as in (EN 50160, 2000), assigns the 10-min RMS value of the supply voltage (short interval value) to quantify slow voltage variations and considers a week as the minimum measurement period.

C. Unbalances

The severity of voltage unbalances is often quantified by means of the voltage unbalance factor, which is defined as the ratio between the negative-sequence voltage component and the positive-sequence voltage component, usually expressed as a percentage. All the standards and guidelines usually consider a week to be the minimum measurement period. The whole measurement and evaluation procedure for the short and long interval values of the negative-sequence voltage unbalance factor is defined in detail in (IEC 61000-4-30).

D. Voltage fluctuations

Voltage fluctuations can cause light intensity fluctuations that can be perceived by our brains. This effect, popularly known as flicker, can cause significant physiological discomfort. More precisely, flicker is the impression of unsteadiness of visual sensation induced by a light stimulus whose luminance or spectral distribution properly fluctuates with time. The most common reference for flicker measurement is (IEC 61000-4-15), and the minimum measurement period is one week.

E. Voltage sags

A single voltage dip can be characterized according to (IEC 61000-4-30) by a pair of data (residual voltage or depth and duration) or by a single index obtained by properly handling the aforementioned pair of data (the voltage sag aggressiveness index, voltage tolerance curve-based indices, the voltage dip energy index or the voltage sag severity index) (IEEE Std. 1564).

F. Transient overvoltage

A transient overvoltage can be classified as oscillatory or impulsive. An oscillatory transient event is described by its voltage peak, predominant frequency and decay time (duration).

An impulsive transient event is described by rise time, decay time and peak value. The characterization of transient events is, in most cases, only based on peak value and duration. The peak value of transient overvoltage is the highest absolute value of the voltage waveform; the duration is the amount of time during which the voltage is above a threshold. The choice of the threshold level will affect the value of the duration. The higher the threshold level, the lower the resulting value for the duration. A suitable choice for the threshold used to calculate the duration would be the same as that used to detect the transient. Obviously, the conventional PQ indices such as the total harmonic distortion (THD), flicker factor, imbalance factor, etc., characterize specific types of power disturbances rather than their overall effects, and these indices are based on measurements made within an observation window, therefore they are not able to reveal the time varying characteristic of even a specific type of power disturbance. In additional, under practical circumstances, a PQ event usually consists of a combination of the power disturbances and most power disturbances are non-stationary. In consequence, the conventional PQ indices cannot completely satisfy practical applications. Therefore, desirable PQ indices need to characterize the overall effects of these power disturbances rather than a specific type and address the overall negative impact of the distorted waveform. At the same time, desirable PQ indices should be able to reflect the time varying characteristics of power disturbances as well as the distorted waveform caused by these disturbances.

3.2 Novel power quality indices

The transient disturbances occurring in power system can be considered as non-stationary and containing multiple frequency components. Therefore, new power quality indices should be able to reflect the time varying characteristics of transient disturbances as well as the distorted waveform caused by these disturbances. By not translating the oscillatory exponential kernel, S-transform localizes the real and the imaginary components of the spectrum independently, localizing the phase spectrum as well as the amplitude spectrum. Thus based on the good time-frequency localization properties of S-transform, four new power quality indices are introduced in this section to evaluate the transient disturbances.

A. Instantaneous RMS (IRMS)

The IRMS is defined as

$$\text{IRMS} = \sqrt{0.5 \times \left(\sum_n \left(A_1 \left[kT, nf_1 \right] \right)^2 \right)} \tag{15}$$

where A_1 is the amplitude spectrum calculated from the S-matrix of the disturbance signal. IRMS can be considered as a transient version of RMS accommodating the time information and contain all fundamental and harmonic components in the disturbance signal. As an instantaneous value, IRMS represents the RMS varying over time.

B. Instantaneous Harmonic Distortion Ratio (IHDR)

The IHDR is defined as

$$\text{IHDR} = \frac{\sqrt{\sum_{n \neq 1} \left(A_d \left[kT, nf_1 \right] \right)^2}}{A_0 \left[kT, f_1 \right]} \times 100\% \tag{16}$$

where $A_d=A_1-A_0$ and A_1, A_0 are the amplitude spectrum of the disturbance signal and pure sinusoid signal respectively. Both the signals are normalized in unit before the S-transform processing. THD is a very common power quality index which estimates the overall deviation of distorted signal for its fundamental. The definition of the IHDR in the S domain is interpreted as the harmonic component in the disturbance signal divided by the fundamental component of the pure sinusoid signal. Thus IHDR represents the time-varying nature of the harmonic component relative to the sinusoid fundamental and correspondingly, does not subject to the impact of fundamental frequency RMS of the low frequency disturbances.

C. Instantaneous Waveform Distortion Ratio (IWDR)

The IWDR is defined as

$$\text{IWDR} = \sqrt{\frac{\sum_n \left(A_d\left[kT, nf_1\right]\right)^2}{\sum_n \left(A_0\left[kT, nf_1\right]\right)^2}} \times 100\% \tag{17}$$

where A_d, A_0 denote the same definition in (16). IWDR is a global index which represents the degree of disturbance waveform distortion from the pure sinusoid with unit amplitude. Different form the IHDR defined in equation (16), the molecule contains the fundamental component distortion of the transient disturbances. So IHDR can represent the waveform distortion caused by a low frequency disturbance such as interruption, sag or swell.

D. Instantaneous Average Frequency (IAF)

The IAF is defined as

$$\text{IAF} = \frac{\sum_n \left(nf_1 \times A_1\left[kT, nf_1\right]\right)^2}{\sum_n \left(A_1\left[kT, nf_1\right]\right)^2} \tag{18}$$

where A_1 denote the same definition in equation (16). Frequency is a very common physical quantity to describe the signal, but for the non-stationary signal with time-varying frequency, another frequency concept, instantaneous frequency should be introduced. Taking into account the disturbance signal containing the multiple frequency components, the IAF is calculated from the S-matrix using a first-order moment (Shin et al., 2006). Consequently, typical power system waveforms are characterized by a fundamental component that is the main component at a rated frequency and in the presence of a disturbance, larger frequency content will result in higher value of IAF than lower frequency content. In practice, IAF provides the deviation of the frequency from the fundamental frequency due to the presence of harmonic components.

4. Application examples

The performance of the four new power quality indices is evaluated using mathematical and PSCAD/EMTDC simulated disturbance signals. Firstly, in order to investigate the accuracy of S-transform based indices in power quality evaluation, transient disturbance signal

represented mathematically with known parameters are tested. Then two PSCAD/EMTDC simulated disturbance signals due to ground fault and capacitor switching are analyzed using four power quality indices. The sampling frequency for all the transient disturbances is 5 kHz.

4.1 Mathematical transient disturbances

Case1 is low frequency disturbance as voltage sag, swell and interruption that can be expressed mathematically as

$$s(t) = \left(1 + \alpha(u(t_2) - u(t_1))\right)\sin(2\pi f_0 t) \tag{19}$$

where f_0 is 50Hz, t_1 and t_2 are the disturbance starting and ending time respectively, α is amplitude change factor: $a=-0.1\sim-0.9$ corresponding to voltage sag, $a=0.1\sim0.8$ corresponding to swell and $-1\leq a\leq-0.9$ corresponding to interruption.

There 30% voltage sag, 50% swell and interruption are constructed using (10) by set $a=-0.3$, 0.5, -0.9 respectively. The disturbances start at $t_1=0.1$s and end at $t_2=0.28$s. The low frequency disturbance waveforms and S-transform based time frequency distributions are shown is Fig.1. It is can seen that not only fundamental component vary during disturbances occur, but also high frequency component exist at disturbance start and end time.

Fig. 2 shows the four power quality indices of three low frequency disturbances. The IRMS of voltage sag, swell, and interruption in Fig.2(a) is 0.495, 1.061, and 0.0707 respectively during the disturbance occurred, but 0.707 at other time. In Fig.2(b), the IHDR shows two local maximum values corresponding to the start and end time of the three disturbances. The peak values of IHDR for voltage sag, swell, and interruption are 4.63%, 7.93%, 14.6% located exactly at 0.1s and 3.77%, 6.6%, 12.2% at 0.28s. The IWDR of sag, swell and interruption in Fig.2(c) represents the distortion with the value 30%, 50% and 90% from the pure sinusoid, which are consistent with the initial amplitude parameters respectively. With the same local maximum values similar to IHDR, the IAF in Fig.2(d) represents the time-varying instantaneous average frequency for the three disturbances and respective peak values are 51.8Hz, 52.3Hz, 85Hz and 50.5Hz, 50.7Hz, 60Hz.

It can be concluded that these indices effectively represent the transient characteristics of low frequency disturbances. The value of sag amplitude is 0.7 and the corresponding RMS is 0.7 divided by 1.414, which is equal to 0.495. The right results are also represented for voltage swell and interruption; therefore, IRMS accurately represents the RMS varying over time. Compared Fig.2(c) with Fig.2(b), the greater IWDR corresponds with a larger IHDR, this is because there is a larger amplitude change at the start/end time. The IAF shows the similar quantitative relationship corresponding to IWDR and IAF is less deviation from 50 Hz as few high frequency components contained in low frequency disturbances, especially when the disturbances start or end at the zero-crossing point.

In Case2, transient oscillation signal which is a simulation of a capacitor switching event is expressed as

$$s(t) = \sin(2\pi f_0 t) + \beta e^{-(t-t_1)/\tau}\sin(2\pi f_1 t)(u(t_2) - u(t_1)) \tag{20}$$

where, f_0 and f_1 is the fundamental and transient frequency respectively, t_1 and t_2 are the oscillation starting and ending time, β is the amplitude of exponential function, τ is the decay time coefficient.
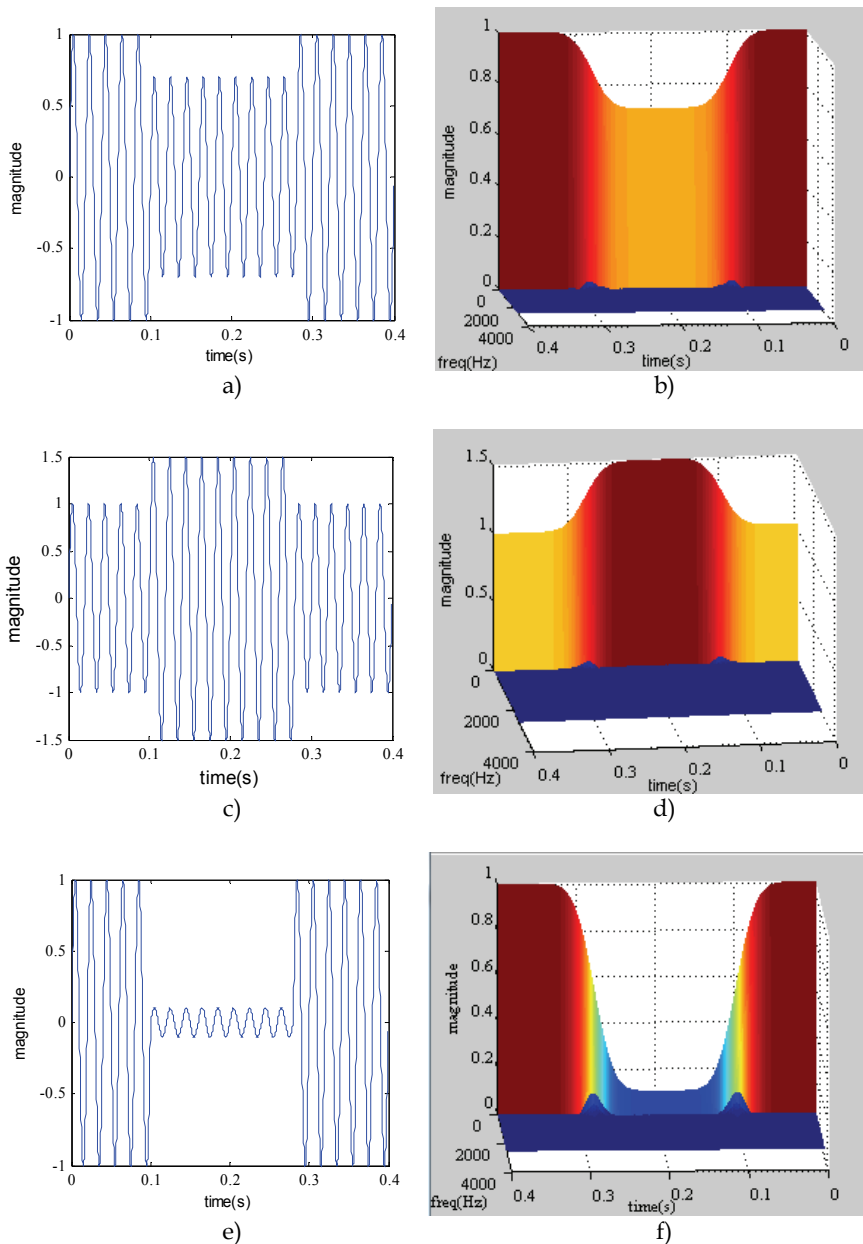
Fig. 1. Low frequency disturbances and S-transient based time-frequency distributions: (a) Voltage sag waveform. (b) Time frequency distribution of voltage sag. (c) Voltage swell waveform. (d) Time frequency distribution of voltage swell. (e) Voltage interruption waveform. (d) Time frequency distribution of voltage interruption
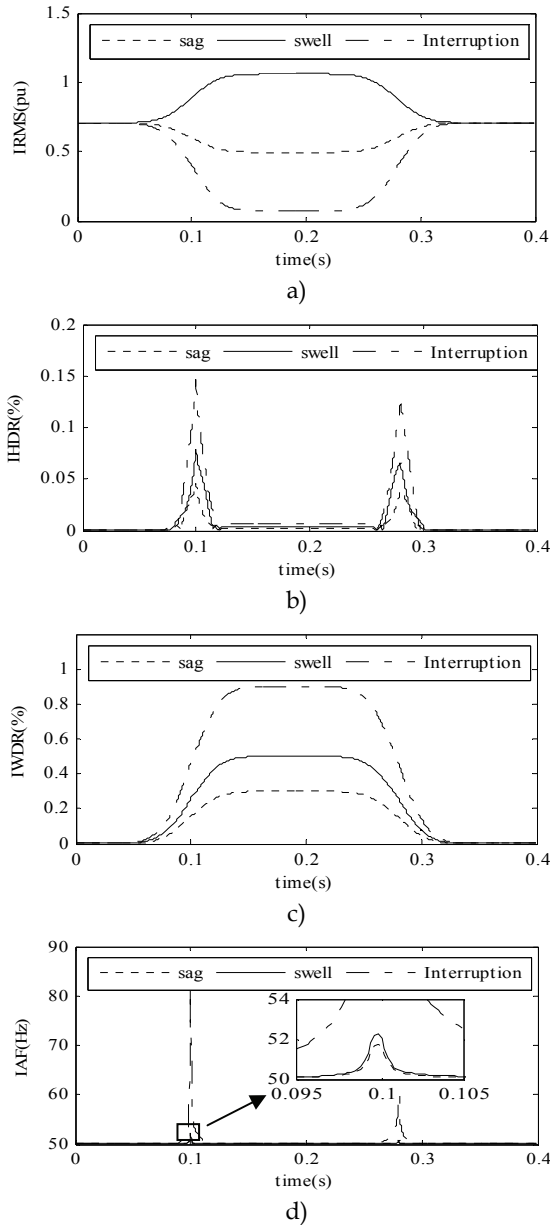
Fig. 2. S-transform based power quality indices of voltage sag, swell and interruption: (a) Instantaneous RMS (IRMS). (b) Instantaneous Harmonic Distortion Ratio (IHDR) (c) Instantaneous Waveform Distortion Ratio (IWDR). (d) Instantaneous Average Frequency (IAF)

a)

b)
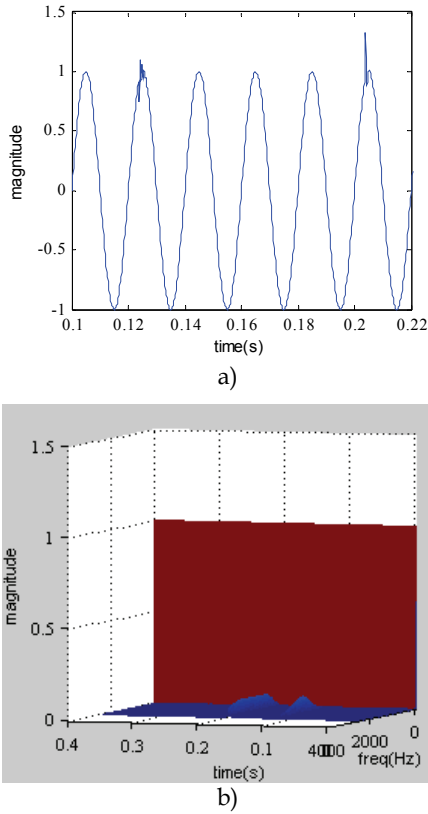
Fig. 3. Transient oscillations and S-transient based time-frequency distribution: (a) Transient oscillation waveform. (b) Time frequency distribution of Transient oscillations

In Fig. 3(a), transient oscillation signal contains two oscillations superposed on the pure sinusoid. The first disturbance is fast oscillation started at t=0.124s (f_1 is 1500Hz, β is0.2 and τ is 2.5) and the second disturbance is slow oscillation started at t=0.204s (f_1 is 600Hz, β is0.4 and τ is 5). The time-frequency distribution based on S-transform is shown in Fig. 3(b). The IRMS in Fig.4(a) shows two local maximum values 0.754 at 0.124s and 0.795 at 0.204s corresponding to the fast and slow oscillation respectively, which corresponds to the initial amplitude parameter β=0.2 and β=0.4. Moreover, the IRMS of the signal in steady-state time is 0.707 exactly. As there is almost no distortion in fundamental component of the transient oscillation compared with pure sinusoid, that is different from the low frequency disturbance in case 1, the IHDR in Fig.4(b) and the IWDR in Fig.4(c) represent a very similar result with peak value 37.1% and 50.8% at the time oscillations occurred. The IAF represents the deviation of average frequency from f0 and shows peak values 235Hz and 339Hz in Fig.4(d) for the fast and slow oscillation. Though the fast oscillation has a higher frequency component, the slow oscillation induces a greater IAF value than the fast oscillation due to its larger oscillation amplitude and accordingly greater spectral content of high frequency.
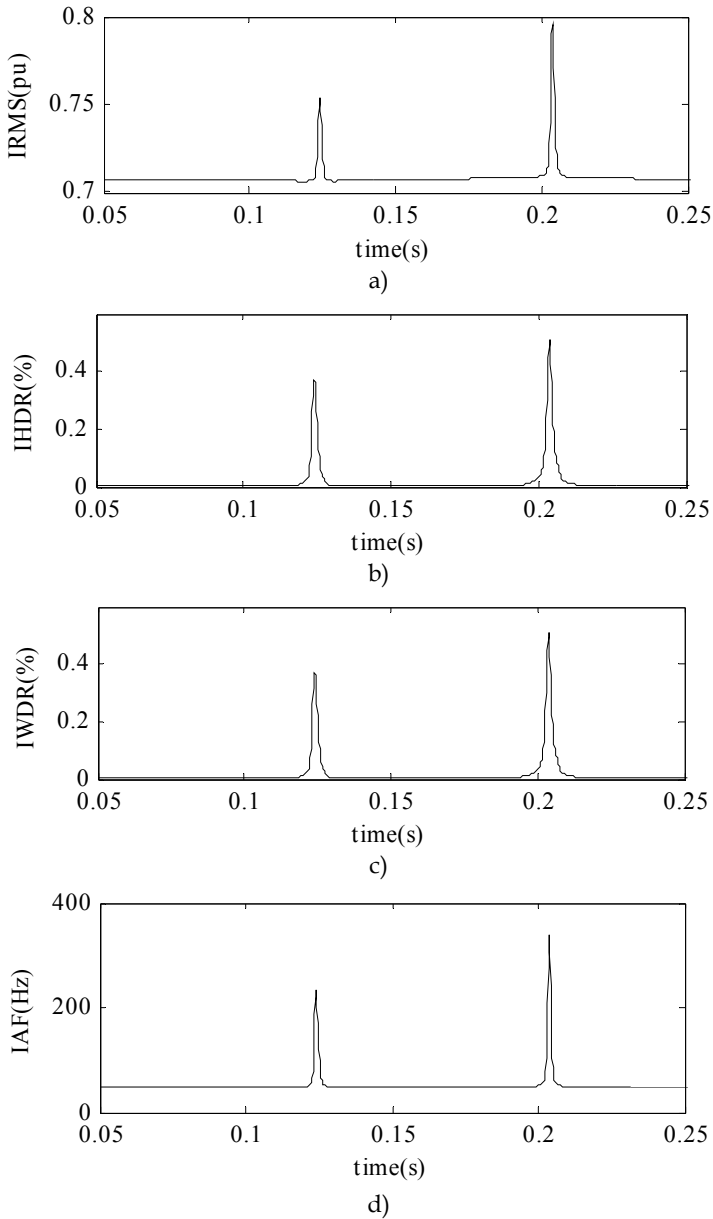
Fig. 4. S-transform based power quality indices of transient oscillations: (a) Instantaneous RMS (IRMS). (b) Instantaneous Harmonic Distortion Ratio (IHDR) (c) Instantaneous Waveform Distortion Ratio (IWDR). (d) Instantaneous Average Frequency (IAF)

Concluded from the low frequency disturbances and transient oscillations with known parameters analyzed in the case1 and case2, the results show that the four power quality

indices accurately represent the transient characters of the transient disturbances. IRMS can accurately represent the RMS accommodating the time information. IHDR mainly represents the harmonic component relative to the pure sinusoid fundamental. However, IWDR focuses on the fundamental component distortion of the transient disturbances and also the harmonic distortion. Therefore there is the similar result between IHDR and IWDR when the transient oscillation is analyzed, that is very different from the results of low frequency disturbances. IAF represents the instantaneous average frequency of the transient disturbances and denotes the rated frequency when there is no disturbance occurred.

4.2 PSCAD/EMTDC simulated disturbances

A simple distribution model is built in PSCAD/EMTDC and two transient disturbances: voltage sag and capacitor switching which are two most common disturbances are obtained to illustrate the performance of four power quality indices.
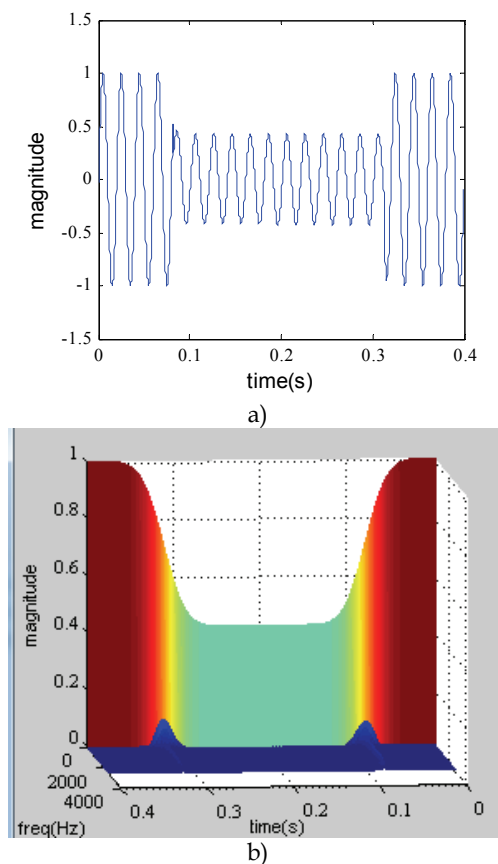

a)

b)

Fig. 5. Voltage sag due to A phase grounded fault: (a) Voltage sag waveform. (b) S-transform based time frequency distribution of voltage sag

A voltage sag caused by A phase grounded fault is simulated and the waveform of A phase voltage is shown in Fig. 5(a). Fig. 5(b) shows the time frequency distribution based on S-transform. The disturbance occurs at 0.082s and ends at 0.313s. The four power quality indices: RMS, IHDR, IWDR and IAF are calculated and a summary of these indices is show in Tab. 1. Similar to the results of the voltage sag in case1, the IRMS is 0.3 and the IWDR is 57.6% during the disturbance occurred. The steady values of IRMS and IWDR are 0.707 and 0. There are also two peaks in the IHDR and IAF corresponding to the start and end time, which are 28.2% and 190Hz at 0.082s and 22.3% and 109Hz at 0.313s respectively. Compared with the voltage sag in case1, this disturbance is not start/end at the zero-crossing point; moreover, there is a larger amplitude change with the IWDR value 57.6%. Consequently, more harmonic content is contained in the disturbance signal, leading to a higher IHDR and a higher IAF.

| indices		transient	steady
IRMS (pu)		0.3	0.707
IWDR (%)		57.6	0
indices		start	end
IHDR	t (s)	0.082	0.313
	peak (%)	28.2	22.3
IAF	t (s)	0.082	0.313
	peak(Hz)	190	109

Table 1. S-transform based four indices of voltage sag

Another disturbance as transient oscillation due to capacitor switching is showed in Fig.6 and the 0.3MVAR capacitor is put into operation at 0.153s. Tab.2. provides the transient peak values and steady values of the four indices. The peak value of IRMS is 0.722 at 0.153s and the peak value of IWDR is 20.1% at the same time that is almost equivalent to the IHDR. The IAF also has a peak value 98Hz when transient oscillation occurred and maintain at 50Hz once the oscillation ended. As the IRMS is a little deviation from the rated value, there is less harmonic content in the disturbance. Accordingly, the value of IHDR, IWDR and IWDR is smaller relative to the disturbance in case2.

Obviously, the two transient disturbances as voltage sag and capacitor switching are characterized well by the four power quality indices. Therefore one can accurately represent the transient information over the time based on the good time-frequency localization properties of S-transform.

indices	Transient (peak)	steady
IRMS (pu)	0.722	0.707
IHDR (%)	20.1	0
IWDR (%)	20.1	0
IAF (Hz)	98	50

Table 2. S-transform based four indices of capacitor switching
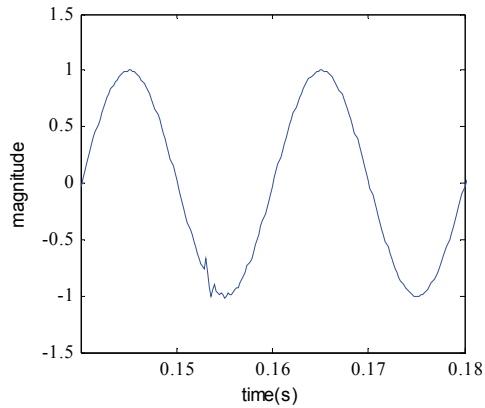
a)
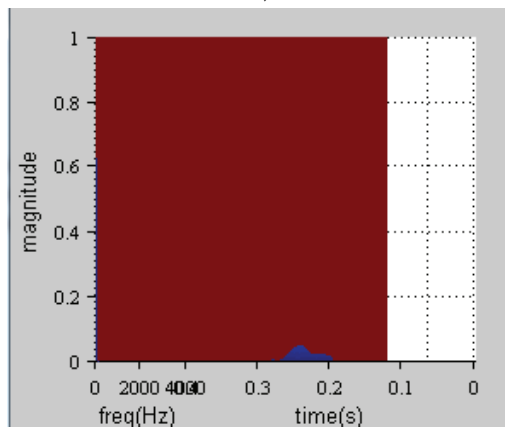
b)

Fig. 6. Transient oscillation due to capacitor switching: (a) capacitor switching waveform. (b) S-transform based time frequency distribution of transient oscillation

5. Conclusion

In this chapter, power quality assessment for transient disturbance signals has been carefully treated based on S-transform. The limitations of the traditional Fourier series coefficient based power quality indices, which inherently require periodicity of the disturbance signal, have been resolved by use of time-frequency analysis. In order to overcome the limitations of the traditional power quality indices in analyzing transient disturbances which are non-stationary waveforms with time-varying spectral component, four instantaneous power quality indices based on S-transform are presented. S-transform is shown to be a new time frequency analysis tool producing instantaneous time frequency representation with frequency dependent resolution. In the S-transform domain, new power quality indices: IRMS, IHDR, IWDR and IAF are defined and discussed. The effectiveness of these indices was tested using a set of disturbances represented mathematically and

simulated in PSCAD/EMTDC respectively. The results show that the instantaneous property of transient disturbance can be characterized accurately.

The transient power-quality indices provide useful information about the time varying signature of the transient disturbance for assessment purposes. However, if the time-varying signature can be quantified as a single number, it would be more informative and convenient for an assessment and comparison of transient power quality. The power quality indices proposed in this chapter can be extended to general indices assessment, which should collapse to the standard definition for the periodic case and also be calculable by a standard algorithm that yields consistent results. It is a subject of future research.

6. References

Beaulieu, G.; Bollen, M. H. J.; Malgarotti, S. & Ball, R.(2002). Power quality indices and objectives: Ongoing activates in CIGREWG36-07, *Proc. 2002 IEEE Power Engineering Soc. Summer Meeting*, pp. 789-794.

Bollen, M. and Yu Hua Gu, I. (2006). Signal Processing of Power Quality Disturbances, *Wiley IEEE Press, New Jersey*.

CENELEC EN 50160, Voltage characteristics of electricity supplied by public distribution systems.

Chilukuri, M.V. & Dash, P.K.(2004). Multiresolution S-transform-based fuzzy recognition system for power quality events, *IEEE Trans. Power Delivery*, vol. 19, no. 1, pp.323-330.

Domijan, A.; Hari, A. & Lin, T. (2004). On the selection of appropriate wavelet filter bank for power quality monitoring, Int. J. Power Energy Syst., Vol. 24, pp.46-50.

Gallo, D., Langella, R. & Testa, A. (2002). A Self Tuning Harmonics and Interharmonics Processing Technique, *European Transactions on Electrical Power*, 12(1), 25-31.

Gallo, D., Langella, R. & Testa, A. (2004). On the Processing of Harmonics and Interharmonics: UsingHanning Windowin Standard Framework, *IEEE Transactions on Power Delivery*, 19(1), 28-34.

Gargoom, A.M., Ertugrul, N. and Soong, W.L. (2005) A comparative study on effective signal processing tools for power quality monitoring, The 11th European Conference on Power Electronics and Applications (EPE), pp.11-4 .

Heydt G. T. & Jewell W. T.(1998). Pitfalls of electric power quality indices, *IEEE Trans. Power Delivery*, vol. 13, no. 2, pp. 570-578.

Heydt, G. T.(2000). Problematic power quality indices, *IEEE Power Eng. Soc. Winter Meeting*, vol. 4, pp. 2838-2842.

IEEE Recommended Practice for Monitoring Electric Power Quality. (1995). IEEE Std. 1159-1995.

IEC 61000-3-6, Assessment of emission limits for distorting loads in MV and HV power systems.

IEC 61000-4-7, General guide on harmonics and interharmonics measurements and instrumentation for power supply systems and equipment connected thereto.

IEC 61000-4-15, Flickermeter, functional design and specifications.

IEC 61000-4-30, Power quality measurement methods.

Jaramillo, S.H.; Heydt, G.T. & O'Neill-Carrillo, E. (2000) 'Power quality indices for a periodic voltages and currents', IEEE Transactions on Power Delivery, April, Vol. 15, No. 2, pp.784–790.

Lin, T. & Domijan, A.(2005). On power quality Indices and real time measurement, *IEEE Trans. Power Delivery*, vol. 20, no. 4, pp.2552-2562.

Mishra, S.; Bhende, C.N. & Panigrahi. B.K. (2008) Detection and classification of power quality disturbances using S-transform and probabilistic neural network, *IEEE Trans. Power Delivery*, vol. 23, no. 1, pp. 280-287.

Morsi, W. G. & EI-Hawary, M. E. (2008). A new perspective for the IEEE standard 1459-2000 via stationary wavelet transform in the presence of non-stationary power quality disturbance, *IEEE Trans. Power Delivery*, vol. 23, no. 4, pp. 2356-2365.

Shin, Y. J.; Powers, E. J.; Grady, M. & Arapostathis, A.(2006) Power quality indices for transient disturbances, *IEEE Trans. on Power Delivery*, vol. 21, no. 1, pp.253-261.

Stockwell, R. G.; Mansinha, L. & R. P. Lowe (1996). Localization of the complex spectrum: The S-transform, IEEE Trans. Signal Processing, vol.144, pp. 998–1001.

Ward, D.J. (2001). Power quality and the security of electricity supply, *Proceedings of the IEEE,* pp.1830-1836.

Voltage sag indices draft 2, working document for IEEE P1564, December 2001.

Zhan, Y.; Cheng, H. Z. & Ding, Y. F.(2005) S-transform-based classification of power quality disturbance signals by support vector machines, *Proceedings of the CSEE*, vol. 25, no. 4, pp. 51-56.

Part 2

Power Quality Enhancement and Reactive Power Compensation and Voltage Sag Mitigation of Disturbances

Active Load Balancing in a Three-Phase Network by Reactive Power Compensation

Adrian Pană

"Politehnica" University of Timisoara
Romania

1. Introduction

1.1 Brief overview of the causes, effects and methods to reduce voltage unbalances in three-phase networks

During normal operating condition, a first cause of voltage unbalance in three-phase networks comes from the asymmetrical structure of network elements (electrical lines, transformers etc.). Best known example is the asymmetrical structure of an overhead line, as a result of asymmetrical spatial positioning of the conductors. Also the total length of the conductors on the phases of a network may be different. This asymmetry of the network element is reflected in the asymmetry of the phase equivalent impedances (self and mutual, longitudinal and transversal). The impedance asymmetry causes then different voltage drop on the phases and therefore the voltage unbalance in the network nodes. As an example of correction method for this asymmetry is the well-known method of transposition of conductors for an overhead electrical line, which allows reducing the voltage unbalance under the admissible level, of course, with the condition of a balanced load transfer on the phases.

But the main reason of the voltage unbalance is the loads supply, many of which are unbalanced, single-phase - connected between two phases or between one phase and neutral. Many unbalanced loads, having small power values (a few tens of watts up to 5-10 kW), are connected to low voltage networks. But the most important unbalance is produced by high power single-phase industrial loads, with the order MW power unit, that are connected to high or medium voltage electrical networks, such as welding equipment, induction furnaces, electric rail traction etc. Current and voltage unbalances caused by these loads are most often accompanied by other forms of disturbance: harmonics, voltage sags, voltage fluctuations etc. (Czarnecki, 1995).

Current unbalance, which can be associated with negative and zero sequence components flow, lead to increased longitudinal losses of active power and energy in electrical networks, and therefore lower efficiency.

Voltage unbalance causes first negative effects on the rotating electrical machines. It is associated with increased heating additional losses in the windings, whose size depends on amount of negative sequence voltage component. It also produces parasitic couples, which is manifested by harmful vibrations. Both effects can reduce the useful life of electrical machines and therefore significant material damage.

Transformers, capacitor banks, some protection systems (e.g. distance protection), three-phase converters (three-phase rectifiers, AC-DC converters) etc. are also affected by a three-phase unbalanced system supply voltages.

Regarding limiting voltage unbalances, as they primarily due to unbalanced loads, the main methods and means used are aimed at preventing respectively limiting the load unbalances. From the measures intended to prevent load unbalances, are those who realize a natural balance. It may mention here two main methods:

- balanced repartition of single-phase loads between the phases of the three-phase network. This is particularly the case of single-phase loads supplied at low voltage;
- connecting unbalanced loads to a higher voltage level, which generally corresponds to the solution of short-circuit power level increasing at their terminals. Is the case of industrial loads, high power (several MVA or tens of MVA) to which power is supplied by its own transformer, other than those of other loads supplied at the same node. Under these conditions the voltage unbalance factor will decrease proportionally with increasing the short-circuit power level.

From the category of measures to limit unbalanced conditions are:

- balancing circuits with single-phase transformers (Scott and V circuit) (UIE, 1998);
- balancing circuits through reactive power compensation (Steinmetz circuit), single and three phase, which may be applied in the form of dynamic compensators type SVC (Static Var Compensator) (Gyugyi et al., 1980; Gueth et al., 1987; San et al., 1993; Czarnecki et al., 1994; Mayordomo et al., 2002; Grünbaum et al., 2003; Said et al., 2009).
- high performance power systems controllers - based on self-commutated converters technology (e.g. type STATCOM - Static Compensator) (Dixon, 2005).

This chapter is basically a theoretical development of the mathematical model associated to the circuit proposed by Charles Proteus Steinmetz, which is founded now in major industrial applications.

2. Load balancing mechanism in the Steinmetz circuit

As is known, Steinmetz showed that the voltage unbalance caused by unbalanced currents produced in a three-phase network by connecting a resistive load (with the equivalent conductance G) between two phases, can be eliminated by installing two reactive loads, an inductance (a coil, having equivalent susceptance $B_L = G / \sqrt{3}$) and a capacitance (a capacitor with equivalent susceptance $B_C = -G / \sqrt{3}$). The ensemble of the three receivers, forming a delta connection (Δ), can be equalized to a perfectly balanced three-phase loads, in star connection (Y), having on each branch an equivalent admittance purely resistive (conductance) with the value G (Fig. 1).
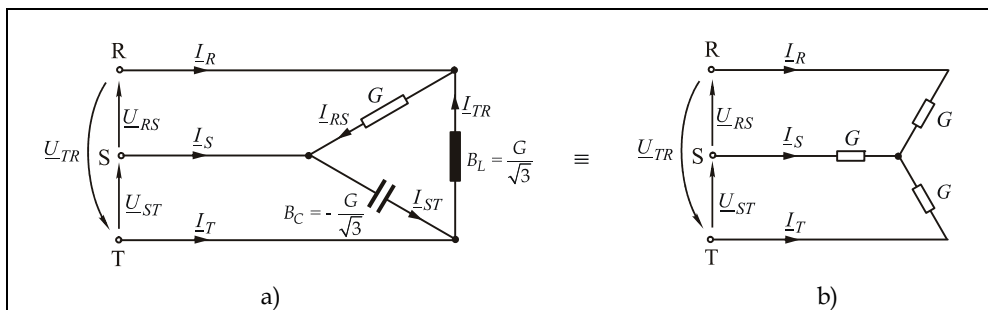

Fig. 1. Steinmetz montage and its equivalence with a load balanced, purely resistive

To explain how to achieve balancing by reactive power compensation of a three-phase network supplying a resistive load, it will consider successively the three receivers, supplied individually. For each receiver will determine the phase currents, which are then decomposed by reference to the corresponding phase to neutral voltages, to find active and reactive components of currents, which are used then to determine the active and reactive powers flow on the phases of the network. It is assumed that the phase-to-neutral voltages and phase-to-phase voltages at source forms perfectly symmetrical three-phase sets. Also conductor's impedances are neglected.

Therefore, for the case of supplying the resistive load having equivalent conductance G between R and S phases (Fig. 2.), a current in phase with the applied voltage is formed on the R phase conductor:
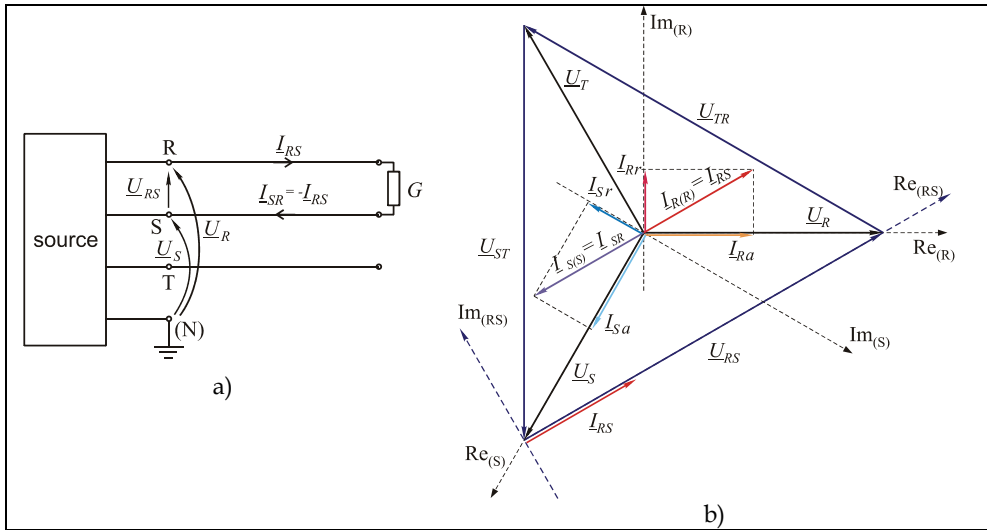

Fig. 2. Resistive load supplied between R and S phases

$$\underline{I}_{RS} = \underline{U}_{RS} \cdot G \tag{1}$$

The equation to calculate the rms value is:

$$I_{RS} = \sqrt{3} \cdot U \cdot G \ , \tag{2}$$

where U is the rms value of phase-to-neutral voltage, considered the same on the three phases.

On the S phase conductor, an equal but opposite current like the one on the R phase is formed:

$$\underline{I}_{SR} = -\underline{I}_{RS} \tag{3}$$

The two currents are now reported each to the corresponding phase-to-neutral voltage, in order to find the active respectively reactive components of each other. For this, the complex plane is associated to the phase-to-neutral voltage; its phasor is positioned in the real axis,

positive direction. It is noted that the current phasor on the phase R, $\underline{I}_{R(R)} = \underline{I}_{RS}$, is leading the corresponding phase-to-neutral voltage phasor, $\underline{U}_R$, with an phase-shift equal to $\pi/6$ rad, which means that the reactive component has capacitive character:

$$\underline{I}_{R(R)} = I_{R1(R)a} + jI_{R1(R)r} = I_{R1(R)} \cdot \cos\frac{\pi}{6} + jI_{R1(R)} \cdot \sin\frac{\pi}{6} = \frac{3}{2} \cdot U \cdot G + j\frac{\sqrt{3}}{2} \cdot U \cdot G \tag{4}$$

It can now deduce the equations for the active and reactive power flow on R phase:

$$\underline{S}_{R1} = P_{R1} + jQ_{R1} = U_R \cdot \underline{I}_{R1(R)}^* = \frac{3}{2} \cdot U^2 \cdot G - j\frac{\sqrt{3}}{2} \cdot U^2 \cdot G \tag{5}$$

On the S phase, the current phasor is lagging the voltage $\underline{U}_S$ with a phase-shift equal to $\pi/6$ rad, which means that the reactive component has inductive character. By a similar calculation with the above, active and reactive powers flow on the S phase are obtained:

$$\underline{S}_{S1} = P_{S1} + jQ_{S1} = U_S \cdot \underline{I}_{S1(S)}^* = \frac{3}{2} \cdot U^2 \cdot G + j\frac{\sqrt{3}}{2} \cdot U^2 \cdot G \tag{6}$$

It may be noted that the resistive load supplied between two phases, absorbs active power equal on the two phases. But it occurs also on the reactive power flow on the network phases, absorbing reactive power on the S phase, but returning it to the source on the R phase, without modifying the reactive power flow on all three phases.
On this ensemble, result:

$$P_1 = P_{R1} + P_{S1} = 3 \cdot U^2 \cdot G = (\sqrt{3} \cdot U)^2 \cdot G \quad \text{și} \quad Q_1 = Q_{R1} + Q_{S1} = 0 \tag{7}$$

A similar demonstration can be done for supplying the capacitive load having the equivalent susceptance $B_C = -G/\sqrt{3}$, between phases S and T (Fig. 3).
The current formed on the S phase conductor is leading the voltage with a phase-shift equal to $\pi/2$ rad (the complex plane associated to the phase-to-phase voltage $\underline{U}_{ST}$):

$$\underline{I}_{ST} = j \cdot U_{ST} \cdot |B_C| \tag{8}$$

The rms value can be determined by the equation:

$$I_{ST} = \sqrt{3} \cdot U \cdot |B_C| = U \cdot G \tag{9}$$

The current formed on the T phase, have the same rms value and is opposite to that on the S phase:

$$\underline{I}_{TS} = -\underline{I}_{ST} \tag{10}$$

Now reporting the two currents to the corresponding phase-to-neutral voltages, it can be determined the active and reactive components of this, and then the active and reactive powers on the two phases:

$$\underline{S}_{S2} = P_{S2} + jQ_{S2} = U_S \cdot \underline{I}_{S2(S)}^* = -\frac{1}{2} \cdot U^2 \cdot G - j\frac{\sqrt{3}}{2} \cdot U^2 \cdot G \tag{11}$$

$$\underline{S}_{T2} = P_{T2} + jQ_{T2} = U_T \cdot \underline{I}_{T2(S)}^* = \frac{1}{2} \cdot U^2 \cdot G - j\frac{\sqrt{3}}{2} \cdot U^2 \cdot G \qquad (12)$$

It is noted that the capacitive load absorbs the same reactive power on the two phases at which it is connected. It occurs also on the active powers flow, absorbs active power on phase T, but returns it to the source on the phase S. On all three phases of the network, results:

$$P_2 = P_{S2} + P_{T2} = 0 \quad \text{şi} \quad Q_2 = Q_{S2} + Q_{T2} = -(\sqrt{3} \cdot U)^2 \cdot |B_C| = -\sqrt{3} \cdot U^2 \cdot G \qquad (13)$$
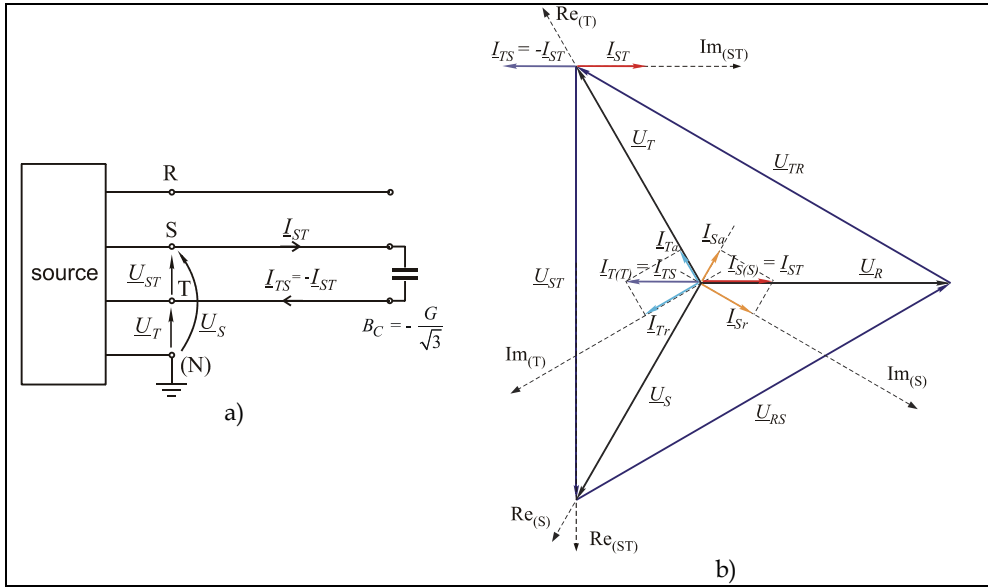

Fig. 3. The capacitive load supplied between phases S and T

The same method applies now to the case of inductive load, having equivalent susceptance $B_L = G / \sqrt{3}$ supplied between T and R phases (Fig. 4).
The current formed on the T phase conductor is lagging the supplying voltage with an phase-shift equal to $\pi / 2$ rad:

$$\underline{I}_{TR} = -j \cdot \underline{U}_{TR} \cdot B_L \qquad (14)$$

The rms value can be determined using the equation:

$$I_{TR} = \sqrt{3} \cdot U \cdot B_L = U \cdot G \qquad (15)$$

The current formed on the R phase, have the same rms value and is opposite to that on the T phase:

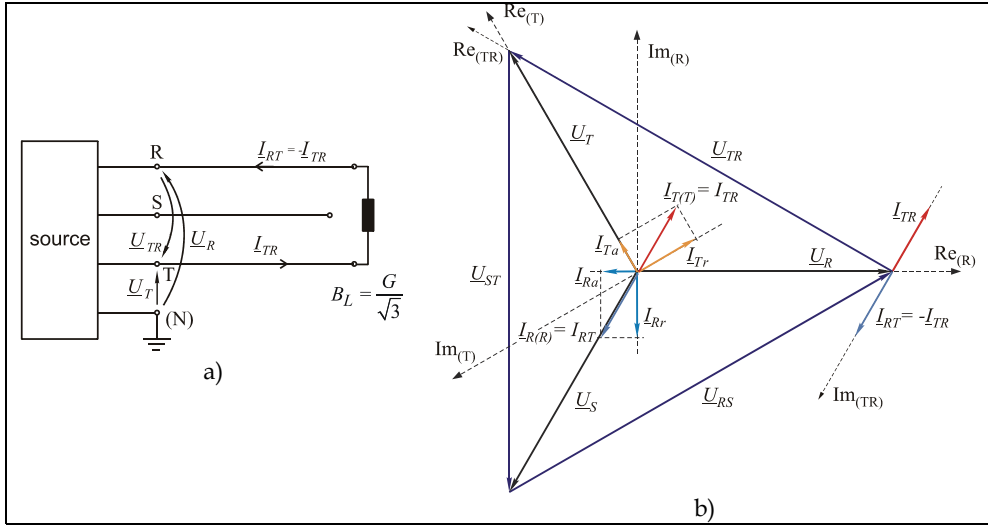$$\underline{I}_{RT} = -\underline{I}_{TR} \qquad (16)$$

Fig. 4. Inductive load supplied between T and R phases

Now reporting the two currents to the corresponding phase-to-neutral voltages, it can be determined the active and reactive components of this, and then the active and reactive powers on the two phases:

$$\underline{S}_{T3} = P_{T3} + jQ_{T3} = U_T \cdot \underline{I}_{T3(T)}^* = \frac{1}{2} \cdot U^2 \cdot G + j\frac{\sqrt{3}}{2} \cdot U^2 \cdot G \tag{17}$$

$$\underline{S}_{S3} = P_{S3} + jQ_{S3} = U_T \cdot \underline{I}_{R3(R)}^* = -\frac{1}{2} \cdot U^2 \cdot G + j\frac{\sqrt{3}}{2} \cdot U^2 \cdot G \tag{18}$$

It is noted that the inductive load absorbs the same reactive power on the two phases at which it is connected. It occurs also on the active powers flow, absorbs active power on phase T, but returns it to the source on the phase R. On all three phases of the network, results:

$$P_3 = P_{T3} + P_{R3} = 0 \quad \text{and} \quad Q_3 = Q_{T3} + Q_{R3} = (\sqrt{3} \cdot U)^2 \cdot B_L = \sqrt{3} \cdot U^2 \cdot G \tag{19}$$

To deduce the power flow on the network phases that supply simultaneously the three loads previously considered, we can apply the superposition theorem (Fig. 5). Active and reactive powers flow run on the network phases that supply the ensemble of all three loads are obtained by algebraic addition of active and reactive power previously deducted for the individual supplying circuits. It obtains:

$$P_R = P_{R1} + P_{R3} = U^2 \cdot G, \quad Q_R = Q_{R1} + Q_{R3} = 0 \tag{20}$$

$$P_S = P_{S1} + P_{S2} = U^2 \cdot G \qquad Q_S = Q_{S1} + Q_{S2} = 0 \tag{21}$$

$$P_T = P_{T2} + P_{T3} = U^2 \cdot G \qquad Q_T = Q_{T2} + Q_{T3} = 0 \tag{22}$$

$$P = P_R + P_S + P_T = 3 \cdot U^2 \cdot G \quad Q = Q_R + Q_S + Q_T = 0 \tag{23}$$
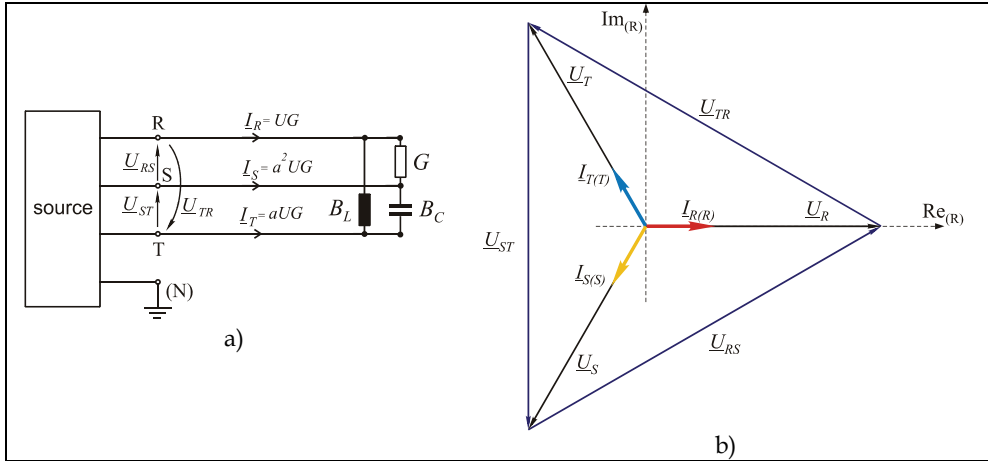

Fig. 5. The ensemble of the three loads

It notes that after the compensation, in the supplying network of the ensemble of the three receivers, only active power flows, the same on the three phases. The compensation conduces to maximize the power factor ($Q = 0$) and to active load balancing on the three phases:

$$P = 3 \cdot P_{phase} = 3 \cdot U^2 \cdot G \tag{24}$$

The ensemble of the three loads, in Δ connection can be equated with three equal active loads, single-phase, each having equivalent conductance with value G, in Y connection (Fig. 1). The three currents have the same phase-shift with the corresponding phase-to-neutral voltages and have the same rms value (Fig. 5):

$$I_R = I_S = I_T = U \cdot G \tag{25}$$

3. Most common applications of Steinmetz circuit

Steinmetz circuit is usually applied to balance large loads, with values of order MW of power, whose contribution to the voltage unbalance in the connecting node is very high.

Figure 6.a presents simplified supply circuit diagram of a three-phase network, of a single-phase induction furnace. Furnace coil is connected secondary of the single-phase transformer T. Its primary is connected between two phases of a medium voltage network. Capacitance C_1 connected in parallel with the load, is to compensate its reactive component and therefore to improve the power factor. Capacitance C_2 and inductance L_2 are sized to achieve load balancing active component, as shown above. But the active power of the load is variable, depending on the specific technological process. To ensure adaptive single-phase load balancing, capacitor banks having the capacitances C_1 and C_2 and inductance L_2 have to allow the control of these values according to load variation.
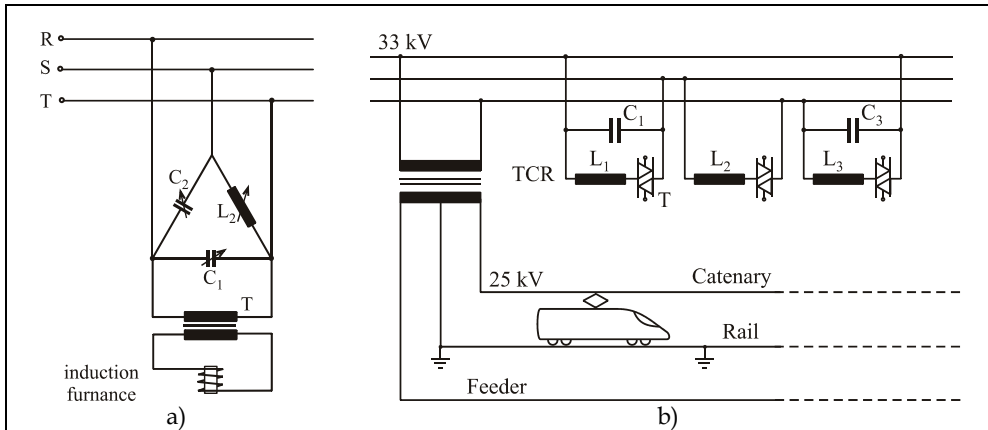
Fig. 6. Simplified circuit of Steinmetz installation for load-balancing applications in the case:
a) induction furnace; b) railway electric traction

Another important application of the Steinmetz circuit is load balancing in three-phase
networks which supplies electric traction railway, equivalent to a single-phase load. Figure
6.b shows the simplified circuit diagram of a substation supply of section from an electric
railway line. Since the load is changing rapidly and within large limits, the compensator
elements must satisfy the same requirements. Is needed a dynamic load balancing
(Grünbaum et al., 2003). The solution applied use a SVC (Static Var Compensator) realized
by a TCR (Thyristor Controlled Reactor). Controlling the thyristors (connected back-to-back)
which are in series with the inductances L_1, L_2 and L_3 allow a dynamic control of inductive
and capacitive currents on the branches of the compensator. Thus is performed a dynamic
compensation of reactive load (increasing the power factor) and dynamic balancing of active
load in the supply network.

Application of the Steinmetz circuit is a simple solution, relatively inexpensive and efficient,
which can be applied to any voltage level at any value of load power, a perfect load balancing
on the three phases is obtained. However, it presents the following inconveniences:

- the frequency of 50 Hz, the ensemble load - compensator can be equated with
  impedance perfectly balanced, but on other frequencies, namely the higher harmonics
  that can be generated by the same load or close loads, it causes a strong unbalance;
- dimensioning the compensator should be made taking into account the restriction to
  avoid parallel resonance between the equivalent capacitance of the compensator and
  the network equivalent inductance seen at the point of connection to the network, for
  harmonic frequencies present in the steady operation conditions, the capacitors will be
  included in passive filters for harmonic currents.

4. The generalized Steinmetz circuit

The circuit available for a single phase active load connected between two phases can be
extended to a certain unbalanced three-phase load with active and reactive components
(inductive and / or capacitive). The mathematical model for sizing the compensator
elements and determining the currents flow and powers flow for the purpose of
understanding the compensation mechanism and for conception of control algorithms

depend on the presence or not of neutral conductor and so of the presence or not of zero sequence components of currents. In the following, the two situations are analyzed.

4.1 The generalized Steinmetz circuit for three-phase three-wire networks

A certain three-phase electric load is considered, connected to a three-wire network supplied by a balanced phase to phase voltages set.

In such situations usually can only know the values of the phase currents and phase to phase voltages, network neutral don't exist or is not accessible.

The set of phase to phase voltages is considered symmetrical (Fig. 7b), and the equivalent circuit of the load is taken in Δ connection, whose elements, for practical reasons, are considered like admittances (Fig. 7a).
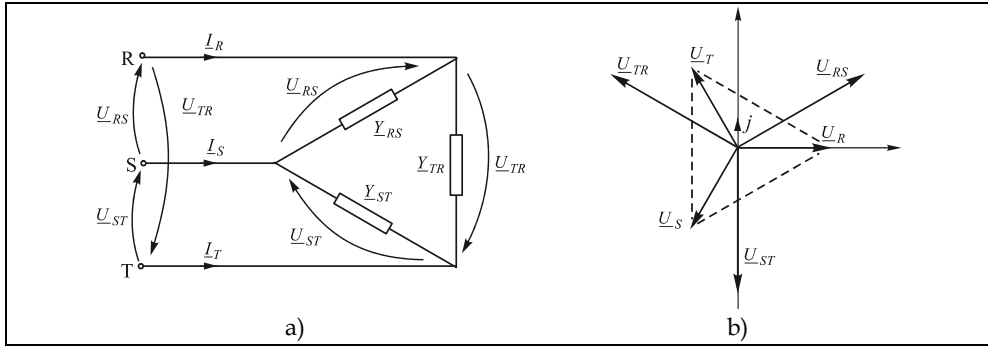

Fig. 7. The equivalent Δ connection with admittances for a certain three-phase load:
a) - definition of electrical quantities, b) - phasor diagram of voltages

For the network in figure 7 we therefore have the following sets of equations:

$$\underline{Y}_{RS} = G_{RS} - jB_{RS} \qquad \underline{Y}_{ST} = G_{ST} - jB_{ST} \qquad \underline{Y}_{TR} = G_{TR} - jB_{TR} \tag{26}$$

$$\underline{I}_{RS} = \underline{U}_{RS} \cdot \underline{Y}_{RS} \qquad \underline{I}_{TR} = \underline{U}_{TR} \cdot \underline{Y}_{TR} \qquad \underline{I}_{ST} = \underline{U}_{ST} \cdot \underline{Y}_{ST} \tag{27}$$

$$\underline{U}_R = U \qquad \underline{U}_S = \mathrm{a}^2 \cdot \underline{U}_R = \mathrm{a}^2 \cdot U \qquad \underline{U}_T = \mathrm{a} \cdot \underline{U}_R = \mathrm{a} \cdot U \tag{28}$$

$$\underline{U}_{RS} = \underline{U}_R - \underline{U}_S = U \cdot (1 - \mathrm{a}^2) \qquad \underline{U}_{ST} = \underline{U}_S - \underline{U}_T = U \cdot (\mathrm{a}^2 - \mathrm{a}) \qquad \underline{U}_{TR} = \underline{U}_T - \underline{U}_R = U \cdot (\mathrm{a} - 1) \tag{29}$$

$$\underline{I}_R = \underline{I}_{RS} - \underline{I}_{TR} \qquad \underline{I}_S = \underline{I}_{ST} - \underline{I}_{RS} \qquad \underline{I}_T = \underline{I}_{TR} - \underline{I}_{ST} \tag{30}$$

Using the equations (26) ÷ (30) it obtains:

$$
\begin{aligned}
\underline{I}_R &= U\left[\left(\frac{3}{2}G_{RS} + \frac{\sqrt{3}}{2}B_{RS} + \frac{3}{2}G_{TR} - \frac{\sqrt{3}}{2}B_{TR} \right) + j\left(\frac{\sqrt{3}}{2}G_{RS} - \frac{3}{2}B_{RS} - \frac{\sqrt{3}}{2}G_{TR} - \frac{3}{2}B_{TR} \right) \right] \\
\underline{I}_S &= U \cdot \left[\left(-\frac{3}{2} \cdot G_{RS} - \frac{\sqrt{3}}{2} \cdot B_{RS} - \sqrt{3} \cdot B_{ST} \right) + j\left(-\frac{\sqrt{3}}{2} \cdot G_{RS} + \frac{3}{2} \cdot B_{RS} - \sqrt{3} \cdot G_{ST} \right) \right] \\
\underline{I}_T &= U \cdot \left[\left(\sqrt{3} \cdot B_{ST} - \frac{3}{2} \cdot G_{TR} + \frac{\sqrt{3}}{2} \cdot B_{TR} \right) + j\left(\sqrt{3} \cdot G_{RS} + \frac{\sqrt{3}}{2} \cdot G_{TR} + \frac{3}{2} B_{TR} \right) \right]
\end{aligned}
\tag{31}
$$

Necessary and sufficient condition for the three phase currents to form a balanced set is the cancellation of the negative sequence current component:

$$\underline{I}_i = \frac{1}{3} \cdot \left(\underline{I}_R + a^2 \cdot \underline{I}_S + a \cdot \underline{I}_T \right) = 0 \tag{32}$$

Putting the cancellation conditions for the real and imaginary parts of $\underline{I}_i$ obtained by substituting equations (31) in (32) we obtain the conditions:

$$\begin{cases} -G_{RS} + 2 \cdot G_{ST} - G_{TR} + \sqrt{3} \cdot \left(B_{TR} - B_{RS} \right) = 0 \\ \sqrt{3} \cdot \left(G_{TR} - G_{RS} \right) + B_{RS} - 2 \cdot B_{ST} + B_{TR} = 0 \end{cases} \tag{33}$$

This system of equations define the relationship that should exist between the six elements of the equivalent Δ connection of a load, so that, from the point of view of the network it appear as a perfectly balanced load ($\underline{I}_i = 0$).

These conditions can be obtained by changing (compensating) the equivalent parameters using a parallel compensation circuit, also in Δ connection, so that equations (33) (Gyugyi et al., 1980) to be satisfied for the ensemble load - compensator (Fig. 8).
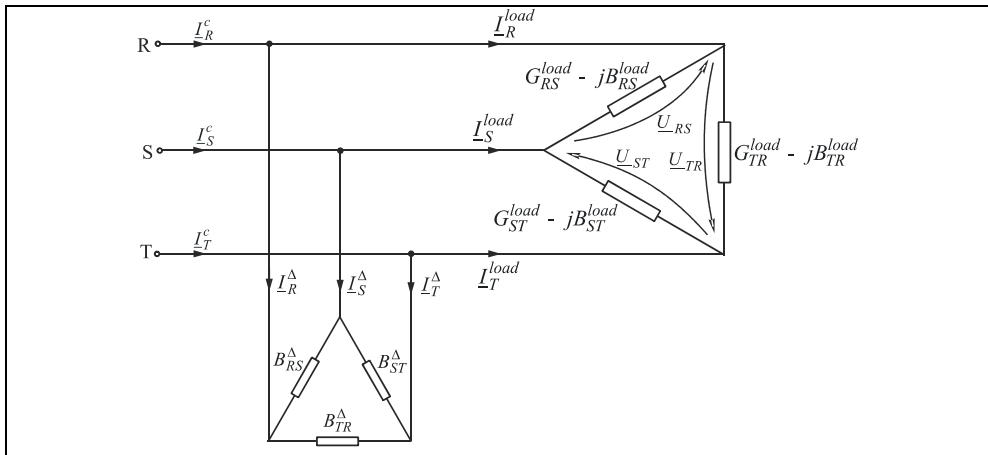

Fig. 8. The ensemble unbalanced load - shunt compensator

The problem lies in determining the elements of the compensator, so that, knowing the elements of the equivalent circuit of the load, to obtain an ensemble which is perfectly balanced from the point of view of the network, as it means that after the compensation, the currents on the phases satisfy the condition:

$$\underline{I}_R^c = a \cdot \underline{I}_S^c = a^2 \cdot \underline{I}_T^c \tag{34}$$

The compensator will not produce changes in the total active power absorbed from the network (which would mean further losses) and hence will contain only reactive elements ($G_{RS}^\Delta = G_{ST}^\Delta = G_{TR}^\Delta = 0$).

In equations (33) will be replaced so:

$$G_{RS} = G_{RS}^{load} \qquad\qquad G_{ST} = G_{ST}^{load} \;;\qquad\qquad G_{TR} = G_{TR}^{load}$$
$$B_{RS} = \left(B_{RS}^{load} + B_{RS}^{\Delta}\right);\qquad B_{ST} = \left(B_{ST}^{load} + B_{ST}^{\Delta}\right);\qquad B_{TR} = \left(B_{TR}^{load} + B_{TR}^{\Delta}\right) \tag{35}$$

From the equations (33) resulting the equation system:

$$\begin{cases} B_{RS}^{\Delta} - B_{TR}^{\Delta} = A \\ B_{RS}^{\Delta} - 2\cdot B_{ST}^{\Delta} + B_{TR}^{\Delta} = B \end{cases} \tag{36}$$

Where:

$$A = -\frac{1}{\sqrt{3}}\cdot G_{RS}^{load} - B_{RS}^{load} + \frac{2}{\sqrt{3}}\cdot G_{ST}^{load} - \frac{1}{\sqrt{3}}\cdot G_{TR}^{load} + B_{TR}^{load}$$
$$B = \sqrt{3}\cdot G_{RS}^{load} - B_{RS}^{load} + 2\cdot B_{ST}^{load} - \sqrt{3}\cdot G_{TR}^{load} - B_{TR}^{load} \tag{37}$$

Unknowns are therefore: B_{RS}^{Δ} , B_{ST}^{Δ} and B_{TR}^{Δ} .

With two equations and three unknowns, we are dealing with indeterminacy. A third equation, independent of the first two, which expresses a relationship between the three unknowns, will result by imposing any of the following conditions:

a.   full compensation of reactive power demand from network;
b.   partial compensation of reactive power demand (up to a required level of power factor);
c.   voltage control on the load bus bars trough the control of reactive power demand;
d.   install a minimum reactive power for the compensator;
e.   minimize active power losses in the supply network of the load.

In this chapter we will consider only the operation of the compensator sized according to the **a** criterion, other criteria can be treated similarly.

4.1.1 Sizing the compensator elements based on the criterion of total compensation of reactive power demand from the network

According to **a** criterion, in addition to load balancing, compensation should also lead to cancellation of the reactive power absorbed from the network on the positive sequence ($\cos\varphi^{+} = 1$). This is equivalent to the additional condition:

$$\mathrm{Im}\left(\underline{I}_{c}^{+}\right) = 0 \tag{38}$$

$\underline{I}_{c}^{+}$ is the positive sequence component corresponding to the load current of the ensemble load - compensator. But for this it can write the condition:

$$\underline{I}_{c}^{+} = \frac{1}{3}\cdot\left(\underline{I}_{R}^{c} + a\cdot\underline{I}_{S}^{c} + a^{2}\cdot\underline{I}_{T}^{c}\right) = \underline{I}_{R}^{c} \;, \tag{39}$$

because $\underline{I}_{R}^{c} = a\cdot\underline{I}_{S}^{c} = a^{2}\cdot\underline{I}_{T}^{c}$, where $\underline{I}_{R}^{c}$, $\underline{I}_{S}^{c}$ and $\underline{I}_{T}^{c}$ are the currents absorbed by the network after the compensation. As the supplementary condition will be:

$$\mathrm{Im}\left(\underline{I}_{R}^{c}\right) = 0 \tag{40}$$

mean:

$$G_{RS} - G_{TR} - \sqrt{3}\left(B_{RS} + B_{TR}\right) = 0 \tag{41}$$

Associating now the equations (33) and (41), where the equations (35) are replaced, the system of three equations with three unknowns is obtained:

$$\begin{bmatrix} 1 & 0 & -1 \\ 1 & -2 & 1 \\ 1 & 0 & 1 \end{bmatrix} \cdot \begin{bmatrix} B_{RS}^{\Delta} \\ B_{ST}^{\Delta} \\ B_{TR}^{\Delta} \end{bmatrix} = \begin{bmatrix} A \\ B \\ C \end{bmatrix} \tag{42}$$

where:

$$C = \frac{1}{\sqrt{3}} \cdot \left(G_{RS}^{\,load} - \sqrt{3} \cdot B_{RS}^{\,load} - G_{TR}^{\,load} - \sqrt{3} \cdot B_{TR}^{\,load} \right) \tag{43}$$

Solving the system (42) leads to the following solutions:

$$B_{RS}^{\Delta} = \frac{1}{2} \cdot (A + C)$$

$$B_{ST}^{\Delta} = \frac{1}{2} \cdot (B + C) \tag{44}$$

$$B_{TR}^{\Delta} = \frac{1}{2} \cdot (-A + C)$$

mean:

$$\begin{cases} B_{RS}^{\Delta} = -B_{RS}^{load} + \dfrac{1}{\sqrt{3}} \left(G_{ST}^{load} - G_{TR}^{load} \right) \\[2mm] B_{ST}^{\Delta} = -B_{ST}^{load} + \dfrac{1}{\sqrt{3}} \left(G_{TR}^{load} - G_{RS}^{load} \right) \\[2mm] B_{TR}^{\Delta} = -B_{TR}^{load} + \dfrac{1}{\sqrt{3}} \left(G_{RS}^{load} - G_{ST}^{load} \right) \end{cases} \tag{45}$$

Using now the equations of transformation of a delta connection circuit in a equivalent Y connection circuit, is achieved:

$$G_R = G_S = G_T = G_{RS}^{load} + G_{ST}^{load} + G_{TR}^{load} = G \tag{46}$$
$$B_R = B_S = B_T = 0$$

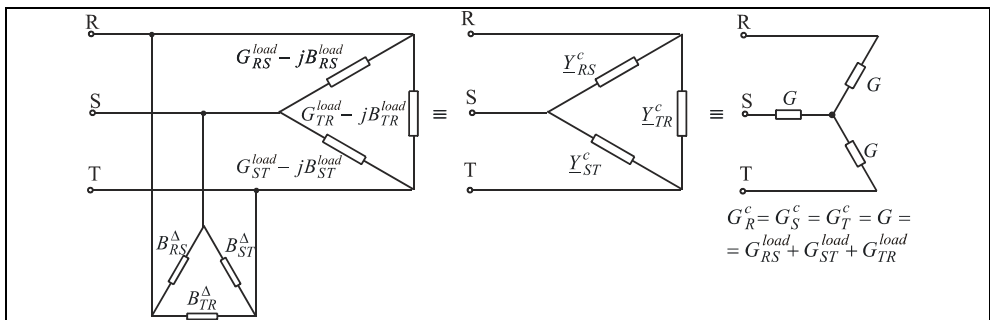These equivalences are illustrated in Figure 9.

Fig. 9. Equivalence of the ensemble load – compensator with a balanced active load

4.1.2 The compensation circuit elements expressed by using the sequence components of the load currents

Expressing the compensation circuit elements by using the sequence components of the load currents will allow a full interpretation of the mechanism of compensation.

For this, lets' consider again the general three-phase unbalanced load, supplied from a balanced three-phase source, without neutral, represented by the equivalent Δ circuit as shown in Fig. 7. The three absorbed load currents will be:

$$
\begin{aligned}
\underline{I}_R^{load} &= U \cdot \left[\underline{Y}_{RS}^{load} \cdot (1 - a^2) - \underline{Y}_{TR}^{load} \cdot (a - 1) \right] \\
\underline{I}_S^{load} &= U \cdot \left[\underline{Y}_{ST}^{load} \cdot (a^2 - a) - \underline{Y}_{RS}^{load} \cdot (1 - a^2) \right] \\
\underline{I}_T^{load} &= U \cdot \left[\underline{Y}_{TR}^{load} \cdot (a - 1) - \underline{Y}_{ST}^{load} \cdot (a^2 - a) \right]
\end{aligned}
\tag{47}
$$

We apply the known equations for the sequence components:

$$
\begin{aligned}
\underline{I}_{load}^+ &= \frac{1}{3} \cdot (\underline{I}_R^{load} + a \cdot \underline{I}_S^{load} + a^2 \cdot \underline{I}_T^{load}) \\
\underline{I}_{load}^- &= \frac{1}{3} \cdot (\underline{I}_R^{load} + a^2 \cdot \underline{I}_S^{load} + a \cdot \underline{I}_T^{load}) \\
\underline{I}_{load}^0 &= \frac{1}{3} \cdot (\underline{I}_R^{load} + \underline{I}_S^{load} + \underline{I}_T^{load})
\end{aligned}
\tag{48}
$$

where $\underline{I}_{load}^+$, $\underline{I}_{load}^-$ and $\underline{I}_{load}^0$ are the positive, negative and zero sequence components (corresponding to the reference phase, R). Replacing the equations (47) in equations (48) the symmetrical components depending on the load admittances are obtained:

$$
\begin{aligned}
\underline{I}_{load}^+ &= U \cdot (\underline{Y}_{RS}^{load} + \underline{Y}_{ST}^{load} + \underline{Y}_{TR}^{load}) \\
\underline{I}_{load}^- &= -U \cdot (a^2 \cdot \underline{Y}_{RS}^{load} + \underline{Y}_{ST}^{load} + a \cdot \underline{Y}_{TR}^{load}) \\
\underline{I}_{load}^0 &= 0
\end{aligned}
\tag{49}
$$

Symmetrical components of currents on the compensator phases are obtained by the same way:

$$
\begin{aligned}
\underline{I}_\Delta^+ &= -j \left(B_{RS}^\Delta + B_{ST}^\Delta + \underline{B}_{TR}^\Delta \right) \cdot U \\
\underline{I}_\Delta^- &= j \left(a^2 \cdot B_{RS}^\Delta + B_{ST}^\Delta + a \cdot B_{TR}^\Delta \right) \cdot U = U \cdot \frac{\sqrt{3}}{2} \cdot \left(B_{TR}^\Delta - B_{RS}^\Delta \right) + j \cdot U \cdot \frac{1}{2} \cdot \left(B_{RS}^\Delta - 2 \cdot B_{ST}^\Delta + B_{TR}^\Delta \right) \\
\underline{I}_\Delta^0 &= 0
\end{aligned}
\tag{50}
$$

Writing symmetrical components of the phase currents absorbed from the network by the ensemble load - compensator:

$$
\begin{aligned}
\underline{I}_c^+ &= \underline{I}_{load}^+ + \underline{I}_\Delta^+ \\
\underline{I}_c^- &= \underline{I}_{load}^- + \underline{I}_\Delta^- \\
\underline{I}_c^0 &= 0
\end{aligned}
\tag{51}
$$

The sizing conditions receive the form:

$$\begin{cases} \mathrm{Im}(\underline{I}_c^+) = 0 \\ \mathrm{Re}(\underline{I}_c^-) = 0 \\ \mathrm{Im}(\underline{I}_c^-) = 0 \end{cases} \Rightarrow \begin{cases} \mathrm{Im}(\underline{I}_{load}^+) - U \cdot \left(B_{RS}^\Delta + B_{ST}^\Delta + B_{TR}^\Delta \right) = 0 \\ \mathrm{Re}(\underline{I}_{load}^-) - U \cdot \dfrac{\sqrt{3}}{2} \left(B_{TR}^\Delta - B_{RS}^\Delta \right) = 0 \\ \mathrm{Im}(\underline{I}_{load}^-) - U \cdot \dfrac{1}{2} \left(B_{RS}^\Delta - 2 B_{ST}^\Delta + B_{TR}^\Delta \right) = 0 \end{cases} \tag{52}$$

Solving this system of equations give the following solutions:

$$B_{RS}^\Delta = -\frac{1}{\sqrt{3} \cdot U} \cdot \left[-\frac{1}{\sqrt{3}} \cdot \mathrm{Im}(\underline{I}_{load}^+) + \mathrm{Re}(\underline{I}_{load}^-) - \frac{1}{\sqrt{3}} \cdot \mathrm{Im}(\underline{I}_{load}^-) \right]$$

$$B_{ST}^\Delta = -\frac{1}{\sqrt{3} \cdot U} \cdot \left[-\frac{1}{\sqrt{3}} \cdot \mathrm{Im}(\underline{I}_{load}^+) + \frac{2}{\sqrt{3}} \cdot \mathrm{Re}(\underline{I}_{load}^-) \right] \tag{53}$$

$$B_{TR}^\Delta = -\frac{1}{\sqrt{3} \cdot U} \cdot \left[-\frac{1}{\sqrt{3}} \cdot \mathrm{Im}(\underline{I}_{load}^+) - \mathrm{Re}(\underline{I}_{load}^-) - \frac{1}{\sqrt{3}} \cdot \mathrm{Im}(\underline{I}_{load}^-) \right]$$

Since the positive sequence and negative sequence currents flow can be considered independent, Δ compensator also can be decomposed into two independent Δ compensators, fictitious or real. Therefore one compensator will be symmetrical (Δ+) and produce compensation (cancellation) of the reactive component of the positive sequence load currents and the other will be unbalanced (Δ-), and will compensate the negative sequence load current. The mechanism of the compensation of the sequence load currents components is illustrated in Figure 10.
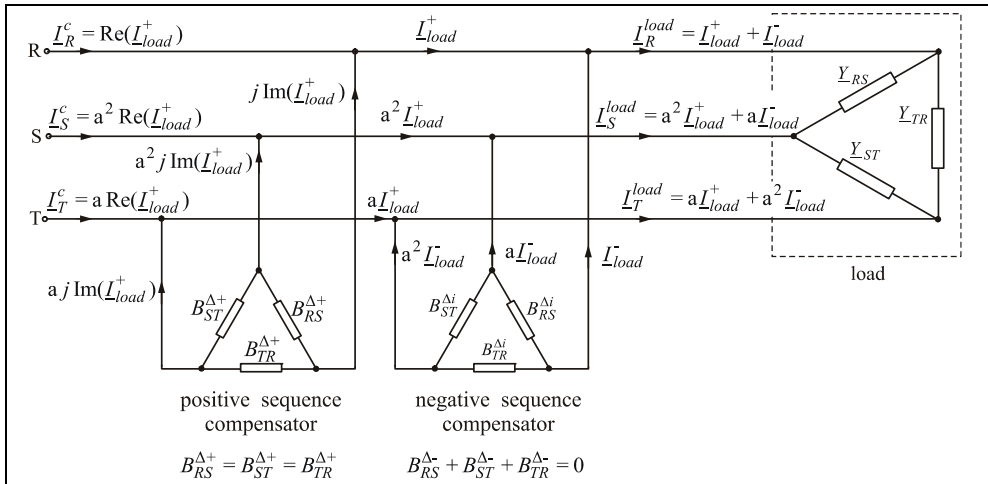

Fig. 10. Compensator representation by two independent compensators: one for the positive sequence compensation and other for the negative sequence compensation of the load current

The elements of the two compensators will be:

$$B_{RS}^{\Delta+} = B_{ST}^{\Delta+} = B_{TR}^{\Delta+} = \frac{1}{3 \cdot U} \cdot \text{Im}(\underline{I}_{load}^+)$$

$$B_{RS}^{\Delta-} = -\frac{1}{\sqrt{3} \cdot U} \cdot \text{Re}(\underline{I}_{load}^-) + \frac{1}{3 \cdot U} \cdot \text{Im}(\underline{I}_{load}^-)$$

$$B_{ST}^{\Delta-} = -\frac{2}{3 \cdot U} \cdot \text{Im}(\underline{I}_{load}^-)$$ \hfill (54)

$$B_{TR}^{\Delta-} = \frac{1}{\sqrt{3} \cdot U} \cdot \text{Re}(\underline{I}_{load}^-) + \frac{1}{3 \cdot U} \cdot \text{Im}(\underline{I}_{load}^-)$$

Expressing then real and imaginary parts of symmetrical components depending on the elements of the equivalent circuit of the load, i.e.:

$$\text{Im}(\underline{I}_{load}^+) = -\left(B_{RS}^{load} + B_{ST}^{load} + B_{TR}^{load} \right) \cdot U$$

$$\text{Re}(\underline{I}_{load}^-) = \left(\frac{1}{2} \cdot G_{RS}^{load} + \frac{\sqrt{3}}{2} B_{RS}^{load} - G_{ST}^{load} + \frac{1}{2} \cdot G_{TR}^{load} - \frac{\sqrt{3}}{2} \cdot B_{TR}^{load} \right) \cdot U$$ \hfill (55)

$$\text{Im}(\underline{I}_{load}^-) = \left(\frac{\sqrt{3}}{2} \cdot G_{RS}^{load} - \frac{1}{2} B_{RS}^{load} + B_{ST}^{load} - \frac{\sqrt{3}}{2} \cdot G_{TR}^{load} - \frac{1}{2} \cdot B_{TR}^{load} \right) \cdot U,$$

it obtain:

$$B_{RS}^{\Delta+} = B_{ST}^{\Delta+} = B_{TR}^{\Delta+} = -\frac{1}{3} \cdot (B_{RS}^{load} + B_{ST}^{load} + B_{TR}^{load})$$

$$B_{RS}^{\Delta-} = \frac{2}{3} \cdot B_{RS}^{load} - \frac{1}{3} \cdot B_{ST}^{load} - \frac{1}{3} \cdot B_{TR}^{load} + \frac{1}{\sqrt{3}} \cdot (G_{TR}^{load} - G_{ST}^{load})$$

$$B_{ST}^{\Delta-} = -\frac{1}{3} \cdot B_{RS}^{load} + \frac{2}{3} \cdot B_{ST}^{load} - \frac{1}{3} \cdot B_{TR}^{load} + \frac{1}{\sqrt{3}} \cdot (G_{RS}^{load} - G_{TR}^{load})$$ \hfill (56)

$$B_{TR}^{\Delta-} = -\frac{1}{3} \cdot B_{RS}^{load} - \frac{1}{3} \cdot B_{ST}^{load} + \frac{2}{3} \cdot B_{TR}^{load} + \frac{1}{\sqrt{3}} \cdot (G_{ST}^{load} - G_{RS}^{load})$$

It is noted that the sum of Δ- compensator elements values is zero.

$$B_{RS}^{\Delta-} + B_{ST}^{\Delta-} + B_{TR}^{\Delta-} = 0$$ \hfill (57)

Instead, the sum of the Δ+ compensator elements will be equal and opposite to the sum of the reactive elements of the load.

4.1.3 Currents flow in the ensemble load - compensator expressed by symmetrical components

On the basis of equations (53), the currents on the branches of the two Δ+ and Δ- fictitious compensators can be determined, using real and imaginary parts of the sequence currents of load:

$$I_{RS}^{\Delta+} = I_{ST}^{\Delta+} = I_{TR}^{\Delta+} = \frac{1}{\sqrt{3}} \cdot \mathrm{Im}\left(\underline{I}_{load}^{+}\right)$$

$$I_{RS}^{\Delta-} = -\mathrm{Re}\left(\underline{I}_{load}^{-}\right) + \frac{1}{\sqrt{3}} \cdot \mathrm{Im}\left(\underline{I}_{load}^{-}\right)$$

$$I_{ST}^{\Delta-} = -\frac{2}{\sqrt{3}} \cdot \mathrm{Im}\left(\underline{I}_{load}^{-}\right)$$ (58)

$$I_{TR}^{\Delta-} = \mathrm{Re}\left(\underline{I}_{load}^{-}\right) + \frac{1}{\sqrt{3}} \cdot \mathrm{Im}\left(\underline{I}_{load}^{-}\right)$$

With these equations we can determine the currents on the phases of both fictitious compensators, and then the currents flow in symmetrical components, into the ensemble load - compensator.

$$\underline{I}_{R}^{\Delta+,-} = \frac{1}{2} \cdot \left(\underline{I}_{RS}^{\Delta+,-} - \underline{I}_{TR}^{\Delta+,-}\right) + j\left(-\frac{\sqrt{3}}{2} \cdot \underline{I}_{RS}^{\Delta+,-} - \frac{\sqrt{3}}{2} \cdot \underline{I}_{TR}^{\Delta+,-}\right)$$

$$\underline{I}_{S}^{\Delta+,-} = -\frac{1}{2} \cdot \left(\underline{I}_{RS}^{\Delta+,-} + 2 \cdot \underline{I}_{ST}^{\Delta+,-}\right) + j\frac{\sqrt{3}}{2} \cdot \underline{I}_{RS}^{\Delta+,-}$$ (59)

$$\underline{I}_{T}^{\Delta+,-} = \frac{1}{2} \cdot \left(\underline{I}_{TR}^{\Delta+,-} + 2 \cdot \underline{I}_{ST}^{\Delta+,-}\right) + j\frac{\sqrt{3}}{2} \cdot \underline{I}_{TR}^{\Delta+,-}$$

Δ+ compensator produces a three-phase set of positive sequence currents, which compensate the reactive component of the positive sequence load current on each phase, and Δ- compensator produces a three-phase set of negative sequence currents, which compensate the negative sequence load current on each phase (both active and reactive component):

$$\underline{I}_{R}^{\Delta+} = -j\,\mathrm{Im}\left(\underline{I}_{load}^{+}\right) \quad \underline{I}_{S}^{\Delta+} = a^2 \cdot \left[-j\,\mathrm{Im}\left(\underline{I}_{load}^{+}\right)\right] \quad \underline{I}_{T}^{\Delta+} = a \cdot \left[-j\,\mathrm{Im}\left(\underline{I}_{load}^{+}\right)\right]$$ (60)

$$\underline{I}_{R}^{\Delta-} = -\underline{I}_{load}^{-} \quad \underline{I}_{S}^{\Delta-} = a \cdot \left(-\underline{I}_{load}^{-}\right) \quad \underline{I}_{T}^{\Delta-} = a^2 \cdot \left(-\underline{I}_{load}^{-}\right)$$ (61)

The currents on the three phases, after compensation, represent a balanced set, positive sequence and contain only the active component (they have zero phase-shift relative to the corresponding phase-to-neutral voltage), equal to the active component of positive sequence load current:

$$\underline{I}_{R}^{c} = \underline{I}_{R}^{load} + \underline{I}_{R}^{\Delta+} + \underline{I}_{R}^{\Delta-} = \mathrm{Re}\left(\underline{I}_{load}^{+}\right)$$

$$\underline{I}_{S}^{c} = \underline{I}_{S}^{load} + \underline{I}_{S}^{\Delta+} + \underline{I}_{S}^{\Delta-} = a^2 \cdot \mathrm{Re}\left(\underline{I}_{load}^{+}\right)$$ (62)

$$\underline{I}_{T}^{c} = \underline{I}_{T}^{load} + \underline{I}_{T}^{\Delta+} + \underline{I}_{T}^{\Delta-} = a \cdot \mathrm{Re}\left(\underline{I}_{load}^{+}\right)$$

Figure 11 shows the compensation mechanism of load currents symmetrical components using phasor diagram.
Starting from the three phasors of unbalanced load currents, considered arbitrary, but check the condition $\underline{I}_R + \underline{I}_S + \underline{I}_T = 0$ (which means they have a common origin in the center of gravity of the triangle formed by the peaks of the phasors), were determined the reference

symmetrical components phasors (corresponding to phase R, Figure 11.a). They will allow for the determination of the phasors $\underline{I}_R^{\Delta+}$ and $\underline{I}_R^{\Delta-}$ because:

$$\underline{I}_R^{\Delta+} = -\mathrm{Im}(\underline{I}_{load}^+)$$
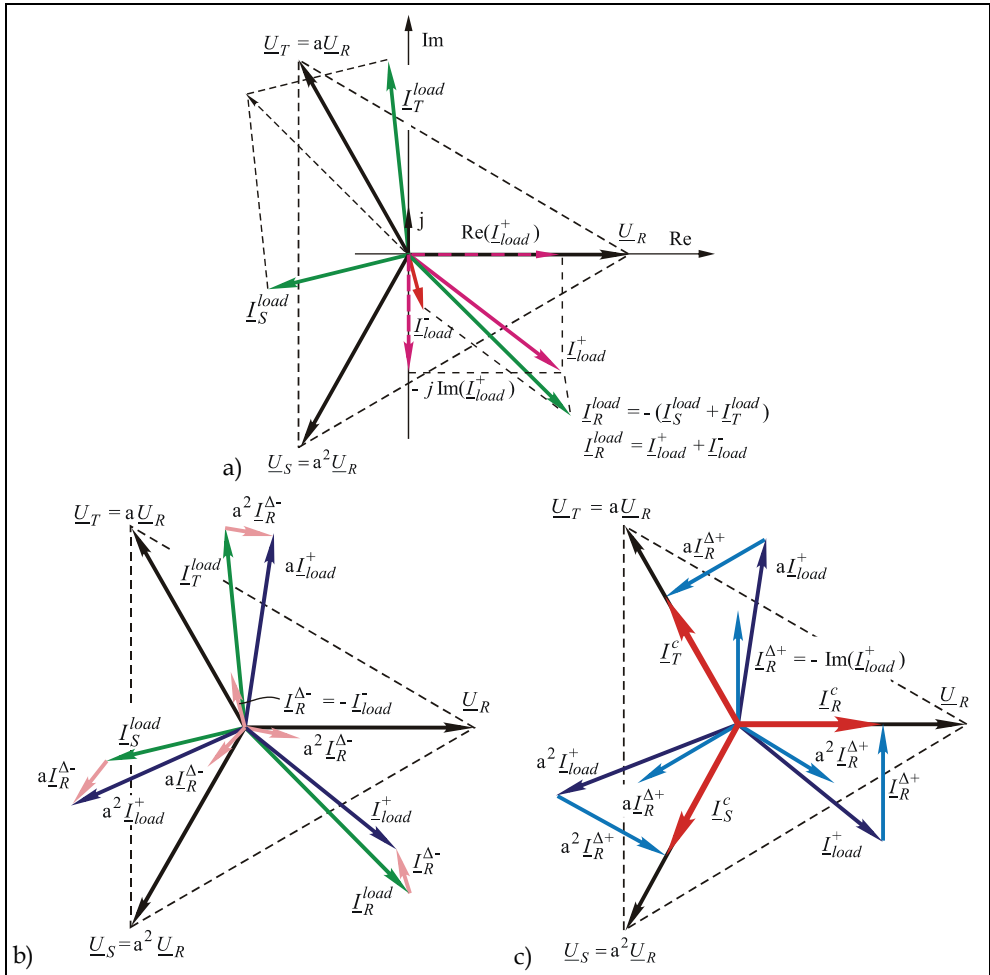$$\underline{I}_R^{\Delta-} = -\underline{I}_{load}^-$$

(63)

Fig. 11. Phasor diagram illustrating the compensation mechanism of the load current symmetrical components: a) - determination of symmetrical components of reference (phase R), b) - compensation of the negative sequence component, c) - compensation of the imaginary part of the positive sequence component

Currents on the phases of the ensemble load - compensator are then obtained, first by compensating the negative sequence (Figure 11.b) and then by compensating the positive sequence (Figure 11.c) realized on the basis of equations:

$$\underline{I}_R^c = \underline{I}_R^s + \underline{I}_R^{\Delta d} + \underline{I}_R^{\Delta i}$$

$$\underline{I}_S^c = \underline{I}_S^s + a^2 \cdot \underline{I}_R^{\Delta d} + a \cdot \underline{I}_R^{\Delta i} \qquad (64)$$

$$\underline{I}_T^c = \underline{I}_T^s + a \cdot \underline{I}_R^{\Delta d} + a^2 \cdot \underline{I}_R^{\Delta i}$$

Obviously that in practical applications is not economically to use two compensators. A single compensator, having variables susceptances will be sufficient to produce both positive sequence compensation (increasing power factor) and the negative sequence load currents compensation (load balancing).

4.1.4 Currents and compensation circuit elements expressed by load currents

Using the currents equations on the load phases with active and reactive components and supposing their inductive character, mean:

$$\underline{I}_R^{load} = I_{Ra} - jI_{Rr}$$

$$\underline{I}_S^{load} = a^2 \cdot (I_{Sa} - jI_{Sr}) \qquad (65)$$

$$\underline{I}_T^{load} = a \cdot (I_{Ta} - jI_{Tr}),$$

and replacing into the sequence currents equations (48) results:

$$\underline{I}_{load}^+ = \frac{1}{3} \cdot (I_{Ra} + I_{Sa} + I_{Ta}) - j\frac{1}{3} \cdot (I_{Rr} + I_{Sr} + I_{Tr})$$

$$\underline{I}_{load}^- = \frac{1}{3} \left(I_{Ra} - \frac{1}{2} \cdot I_{Sa} + \frac{\sqrt{3}}{2} \cdot I_{Sr} - \frac{1}{2} \cdot I_{Ta} - \frac{\sqrt{3}}{2} \cdot I_{Tr} \right) + j\frac{1}{3} \left(-I_{Rr} + \frac{1}{2} \cdot I_{Sr} + \frac{\sqrt{3}}{2} \cdot I_{Sa} + \frac{1}{2} \cdot I_{Tr} - \frac{\sqrt{3}}{2} \cdot I_{Ta} \right) \qquad (66)$$

By developing the equations (58), we obtain relations between currents respectively susceptances on the compensator branches respectively active and reactive components of currents on the load phases:

$$\underline{I}_{RS}^{\Delta} = \frac{1}{3} \cdot (I_{Sa} - I_{Ra}) - \frac{1}{3\sqrt{3}} \cdot (2 \cdot I_{Rr} + 2 \cdot I_{Sr} - I_{Tr})$$

$$\underline{I}_{ST}^{\Delta} = \frac{1}{3} \cdot (I_{Ta} - I_{Sa}) - \frac{1}{3\sqrt{3}} \cdot (-I_{Rr} + 2 \cdot I_{Sr} + 2 \cdot I_{Tr}) \qquad (67)$$

$$\underline{I}_{TR}^{\Delta} = \frac{1}{3} \cdot (I_{Ra} - I_{Ta}) - \frac{1}{3\sqrt{3}} \cdot (2 \cdot I_{Rr} - I_{Sr} + 2 \cdot I_{Tr})$$

$$B_{RS}^{\Delta} = \frac{1}{3\sqrt{3} \cdot U} \cdot \left[(I_{Sa} - I_{Ra}) + \frac{1}{\sqrt{3}} \cdot (I_{Tr} - 2 \cdot I_{Rr} - 2 \cdot I_{Sr}) \right]$$

$$B_{ST}^{\Delta} = \frac{1}{3\sqrt{3} \cdot U} \cdot \left[(I_{Ta} - I_{Sa}) + \frac{1}{\sqrt{3}} \cdot (I_{Rr} - 2 \cdot I_{Sr} - 2 \cdot I_{Tr}) \right] \qquad (68)$$

$$B_{TR}^{\Delta} = \frac{1}{3\sqrt{3} \cdot U} \cdot \left[(I_{Ra} - I_{Ta}) + \frac{1}{\sqrt{3}} \cdot (I_{Sr} - 2 \cdot I_{Rr} - 2 \cdot I_{Tr}) \right]$$

And for the fictitious Δ+ and Δ- compensators, taking into account the equations (58), are obtained:

$$I_{RS}^{\Delta+} = I_{ST}^{\Delta+} = I_{TR}^{\Delta+} = -\frac{1}{3\sqrt{3}} \cdot (I_{Rr} + I_{Sr} + I_{Tr})$$

$$I_{RS}^{\Delta-} = \frac{1}{3} \cdot (-I_{Ra} + I_{Sa}) + \frac{1}{3\sqrt{3}} \cdot (-I_{Rr} - I_{Sr} + 2 \cdot I_{Tr})$$

$$I_{ST}^{\Delta-} = \frac{1}{3} \cdot (-I_{Sa} + I_{Ta}) + \frac{1}{3\sqrt{3}} \cdot (2 \cdot I_{Rr} - I_{Sr} - I_{Tr})$$ (69)

$$I_{TR}^{\Delta-} = \frac{1}{3} \cdot (-I_{Ta} + I_{Ra}) + \frac{1}{3\sqrt{3}} \cdot (-I_{Rr} + 2 \cdot I_{Sr} - I_{Tr})$$

$$B_{RS}^{\Delta+} = B_{ST}^{\Delta+} = B_{TR}^{\Delta+} = -\frac{1}{9 \cdot U} \cdot (I_{Rr} + I_{Sr} + I_{Tr})$$

$$B_{RS}^{\Delta-} = \frac{1}{3\sqrt{3}U}\left[-I_{Ra} + I_{Sa} + \frac{1}{\sqrt{3}}(-I_{Rr} - I_{Sr} + 2I_{Tr}) \right]$$

$$B_{ST}^{\Delta-} = \frac{1}{3\sqrt{3}U}\left[-I_{Sa} + I_{Ta} + \frac{1}{\sqrt{3}}(2I_{Rr} - I_{Sr} - I_{Tr}) \right]$$ (70)

$$B_{TR}^{\Delta-} = \frac{1}{3\sqrt{3}U}\left[-I_{Ta} + I_{Ra} + \frac{1}{\sqrt{3}}(-I_{Rr} + 2I_{Sr} - I_{Tr}) \right]$$

4.1.5 The currents and powers flow into the ensemble load-compensator expressed in phase components

Analytical determination of the currents and powers flow into the ensemble load - compensator is useful for performing calculations for sizing or for checking the accuracy of compensation in real installations.

Using equations (59), written to the complex plane associated with phase R, is determined the current equations $\underline{I}_S^{\Delta+,-}$, respectively $\underline{I}_T^{\Delta+,-}$ written in complex plans associated to corresponding phase-to-neutral voltages (noted $\underline{I}_S^{\Delta+,-*}$ respectively $\underline{I}_T^{\Delta+,-*}$), making the operations:

$$\underline{I}_S^{\Delta+,-*} = a \cdot \underline{I}_S^{\Delta+,-} \qquad \underline{I}_T^{\Delta+,-*} = a^2 \cdot \underline{I}_T^{\Delta+,-}$$ (71)

Result:

$$\underline{I}_R^{\Delta+,-*} = \frac{1}{2} \cdot (I_{RS}^{\Delta+,-} - I_{TR}^{\Delta+,-}) - j\frac{\sqrt{3}}{2} \cdot (I_{RS}^{\Delta+,-} + I_{TR}^{\Delta+,-})$$

$$\underline{I}_S^{\Delta+,-*} = \frac{1}{2} \cdot (I_{ST}^{\Delta+,-} - I_{RS}^{\Delta+,-}) - j\frac{\sqrt{3}}{2} \cdot (I_{RS}^{\Delta+,-} + I_{ST}^{\Delta+,-})$$ (72)

$$\underline{I}_T^{\Delta+,-*} = \frac{1}{2} \cdot (I_{TR}^{\Delta+,-} - I_{ST}^{\Delta+,-}) - j\frac{\sqrt{3}}{2} \cdot (I_{TR}^{\Delta+,-} + I_{ST}^{+,-})$$

Combining now the equations (69) with (72) the equations for the currents on the Δ+ and Δ- phases, relatively to the corresponding phase-to-neutral voltages are obtained:

$$\underline{I}_R^{\Delta+*} = \underline{I}_S^{\Delta+*} = \underline{I}_T^{\Delta+*} = j\frac{1}{3}\cdot(I_{Rr}+I_{Sr}+I_{Tr})$$

$$\underline{I}_R^{\Delta-*} = \frac{1}{3}\cdot\left[-2\cdot I_{Ra}+I_{Sa}+I_{Ta}+j(2\cdot I_{Rr}-I_{Sr}-I_{Tr})\right]$$

$$\underline{I}_S^{\Delta-*} = \frac{1}{3}\cdot\left[-2\cdot I_{Sa}+I_{Ta}+I_{Ra}+j(2\cdot I_{Sr}-I_{Tr}-I_{Rr})\right] \tag{73}$$

$$\underline{I}_T^{\Delta-*} = \frac{1}{3}\cdot\left[-2\cdot I_{Ta}+I_{Ra}+I_{Sa}+j(2\cdot I_{Tr}-I_{Rr}-I_{Sr})\right]$$

Using now the equations (69), (72), and (73), for the currents on the compensator phases are obtained the equations:

$$\underline{I}_R^{\Delta*} = \underline{I}_R^{\Delta+*}+\underline{I}_R^{\Delta-*} = \frac{1}{3}\cdot(-2\cdot I_{Ra}+I_{Sa}+I_{Ta})+jI_{Rr}$$

$$\underline{I}_S^{\Delta*} = \underline{I}_S^{\Delta+*}+\underline{I}_S^{\Delta-*} = \frac{1}{3}\cdot(I_{Ra}-2\cdot I_{Sa}+I_{Ta})+jI_{Sr} \tag{74}$$

$$\underline{I}_T^{\Delta*} = \underline{I}_T^{\Delta+*}+\underline{I}_T^{\Delta-*} = \frac{1}{3}\cdot(I_{Ra}+I_{Sa}-2\cdot I_{Ta})+jI_{Tr}$$

It can be seen clear that the compensator provides on each phase a reactive current component which is equal and opposite to the reactive component of load current.
As the active components of the compensating currents, it is positive or negative, being equal to the difference between the active component of positive sequence current (which is the network load on each phase after compensation) and the active component of load each current.
Can be now calculated the currents absorbed on each phase by the ensemble load - compensator:

$$\underline{I}_R^{c*} = \underline{I}_R^{load*}+\underline{I}_R^{\Delta+*}+\underline{I}_R^{\Delta-*}$$

$$\underline{I}_S^{c*} = \underline{I}_S^{load*}+\underline{I}_S^{\Delta+*}+\underline{I}_S^{\Delta-*} \tag{75}$$

$$\underline{I}_T^{c*} = \underline{I}_T^{load*}+\underline{I}_T^{\Delta+*}+\underline{I}_T^{\Delta-*}$$

It's obtained:

$$\underline{I}_R^{c*} = \underline{I}_S^{c*} = \underline{I}_T^{c*} = \frac{1}{3}\cdot(I_{Ra}+I_{Sa}+I_{Ta}) = \mathrm{Re}\left(\underline{I}_{load}^+\right) \tag{76}$$

The active and reactive powers on the three phases of the compensator can now be easily calculated:

$$P_R^\Delta = U_R\cdot I_{Ra}^{\Delta*} = U\cdot\frac{1}{6}\cdot\left[-2\cdot I_{Ra}+I_{Sa}+I_{Ta}+\sqrt{3}\cdot(I_{Tr}-I_{Sr})\right] = U\cdot\frac{1}{3}\cdot(-2\cdot I_{Ra}+I_{Sa}+I_{Ta})$$

$$P_S^\Delta = U_S\cdot I_{Sa}^{\Delta*} = U\cdot\frac{1}{6}\cdot\left[I_{Ra}-2\cdot I_{Sa}+I_{Ta}+\sqrt{3}\cdot(I_{Rr}-I_{Tr})\right] = U\cdot\frac{1}{3}\cdot(I_{Ra}-2I_{Sa}+I_{Ta}) \tag{77}$$

$$P_T^\Delta = U_T\cdot I_{Ta}^{\Delta*} = U\cdot\frac{1}{6}\cdot\left[I_{Ra}+I_{Sa}-2\cdot I_{Ta}+\sqrt{3}\cdot(I_{Sr}-I_{Rr})\right] = U\cdot\frac{1}{3}\cdot(I_{Ra}+I_{Sa}-2I_{Ta})$$

$$P_R^{\Delta+} = P_S^{\Delta+} = P_T^{\Delta+} = 0$$
$$P_R^{\Delta-} = P_R^{\Delta}, \quad P_S^{\Delta-} = P_S^{\Delta}, \quad P_T^{\Delta-} = P_T^{\Delta} \tag{78}$$

So, the positive sequence compensator intervenes only on the reactive power flow, and the negative sequence compensator, although it change the active power on each phase of the compensated network, on the ensemble of the three phases don't change the active power balance because:

$$P_R^{\Delta-} + P_S^{\Delta-} + P_T^{\Delta-} = 0 \tag{79}$$

This means that on some phase(s) the Δ- compensator absorbs active power, and on the other(s) debits active power as otherwise noted above. He thus produces a redistribution of active power between the phases, balancing them. It can be said that it made active power compensation. After compensation:

$$P_R^c = P_S^c = P_T^c = U \cdot \frac{1}{3} \cdot (I_{Ra} + I_{Sa} + I_{Ta}) \tag{80}$$

and so:

$$\sum_{ph=R,S,T} P_{ph}^c = \sum_{ph=R,S,T} P_{ph}^{load} = U \cdot (I_{Ra} + I_{Sa} + I_{Ta}) \tag{81}$$

For the reactive powers are obtained the equations:

$$Q_R^{\Delta} = U \cdot \frac{1}{6} \cdot \left[-4 \cdot I_{Rr} - I_{Sr} - I_{Tr} + \sqrt{3} \cdot (I_{Sa} - I_{Ta}) \right]$$
$$Q_S^{\Delta} = U \cdot \frac{1}{6} \cdot \left[-I_{Rr} - 4 \cdot I_{Sr} - I_{Tr} + \sqrt{3} \cdot (I_{Ta} - I_{Ra}) \right] \tag{82}$$
$$Q_T^{\Delta} = U \cdot \frac{1}{6} \cdot \left[-I_{Rr} - I_{Sr} - 4 \cdot I_{Tr} + \sqrt{3} \cdot (I_{Ra} - I_{Sa})) \right]$$

$$Q_R^{\Delta+} = Q_S^{\Delta+} = Q_T^{\Delta-} = -U \cdot \frac{1}{3} \cdot (I_{Rr} + I_{Sr} + I_{Tr}) \tag{83}$$

$$Q_R^{\Delta-} = U_R \cdot I_{Rr}^{\Delta-} = U \cdot \frac{1}{3} \cdot (-2I_{Rr} + I_{Sr} + I_{Tr})$$
$$Q_S^{\Delta-} = U_S \cdot I_{Sr}^{\Delta-} = U \cdot \frac{1}{3} \cdot (I_{Rr} - 2I_{Sr} + I_{Tr}) \tag{84}$$
$$Q_T^{\Delta-} = U_T \cdot I_{Tr}^{\Delta-} = U \cdot \frac{1}{3} \cdot (I_{Rr} + I_{Sr} - 2I_{Tr})$$

For the ensemble load-compensator:

$$Q_R^c = Q_R^{load} + Q_R^{\Delta+} + Q_R^{\Delta-} = 0$$
$$Q_S^c = Q_S^{load} + Q_S^{\Delta+} + Q_S^{\Delta-} = 0 \tag{85}$$
$$Q_T^c = Q_T^{load} + Q_T^{\Delta+} + Q_T^{\Delta-} = 0$$

On each phase the Δ+ compensator compensates the reactive power corresponding to the positive sequence component of load currents and Δ- compensator the reactive power corresponding to the negative sequence component of load currents.

On each phase the compensator produces a reactive current equal and opposite sign to the load reactive current.

The Δ+ compensator is symmetrical and makes the total compensation for the reactive power of the load.

$$\sum_{ph=R,S,T} Q_{ph}^{\Delta} = - \sum_{ph=R,S,T} Q_{ph}^{load} \tag{86}$$

The Δ- compensator is unbalanced, the unbalance depends on the load unbalance.

On each phase Δ- intervenes with different reactive powers absorbed or debited, but on the ensemble of the three phases it don't affects the reactive power flow because:

$$\sum_{ph=R,S,T} Q_{ph}^{\Delta-} = 0 \tag{87}$$

It can be said therefore that the Δ-compensator performs a redistribution of reactive power between phases of the compensated network.

4.2 Steinmetz generalized circuit for three-phase four-wire networks

For the case of three-phase four-wire network, displaying the mathematical model will be brief, mathematical development method is the same as in the previous case.

Consider an unbalanced load, which may be an individual receiver or an equivalent load reduced at the interest section of the network (e.g. bars of a low voltage transformer), supplied from a three-phase four-wire network. The neutral conductor indicates the presence of single-phase receivers, typical sources of current unbalance. Equivalent circuit of such a load will always be Y_n connection.

Artificial load balancing on the network phases that supply such a load can be done, as in the case of three-wire networks, by static reactive power sources, which makes shunt compensation. But this time will be used simultaneously two such three-phase compensators, containing only reactive circuit elements, which need will be justified during the exposure of the mathematical model: one with Δ connection and another with Y_n connection.

Figure 12 shows the simplified electrical circuit for an unbalanced load, using the two compensators mentioned, where were specified in some of the notations used in the mathematical model.

The mathematical model used the following hypotheses:
-   was considered only steady operating conditions;
-   three - phase sets of phase-to-phase and phase-to-neutral voltages in the interest section are perfectly balanced;
-   do not consider non-sinusoidal regime: supplying voltages waves are perfectly sinusoidal and the load elements and the network are considered linear.
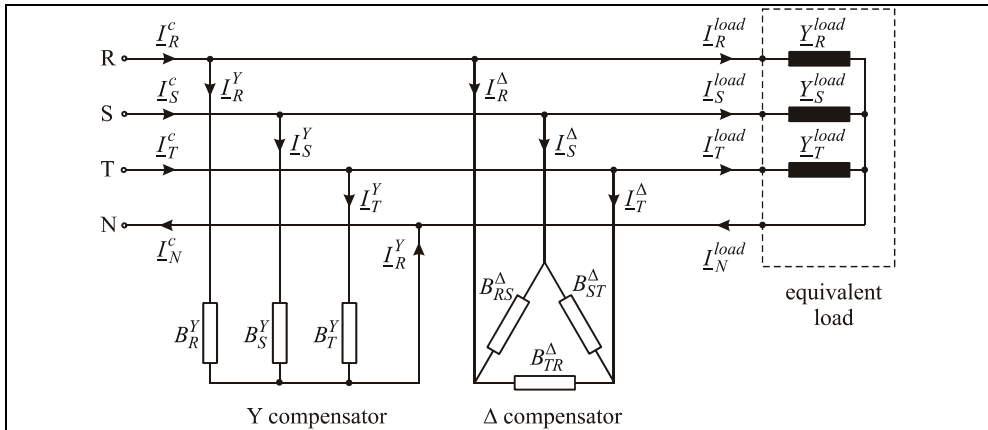
Fig. 12. Reactive power shunt compensators installed to balance a load supplied from a three-phase four-wire network - equivalent electrical circuit

4.2.1 Criteria for sizing of the compensators elements

Setting values of the two compensators susceptances will be done on the basis of some criterions regarding both unbalanced regime and power factor improvement, interdependent actions for unbalanced power distribution networks. Moreover, a simultaneous approach of those two questions must be made necessarily because, as has been noted in the previous case, they are always interrelated.

To compensate will use a single compensator or both, as the aim is only load balancing, only power factor improvement or a simultaneous action. But the reactive power flow change produced by the compensators requires intervention to check the voltage level in the network buses, which is an element of restriction. On the other hand, reactive power flow control can be a method of voltage control. We cannot forget the techno-economic efficiency of the compensation, which can be maximized by minimization the investment costs for facilities that maximize the benefits offset by increasing power quality and efficiency of electricity use.

Therefore, to sizing the elements of the two compensators can be applied one of the following criteria, or sub-criteria:

a.   power factor improvement without taking into account the unbalanced regime;
    a1.   power factor improvement in the supply network by the full compensation of the reactive current component of positive sequence, using a symmetrical compensation;
    a2.   minimize total active power losses in the supply network;
b.   load balancing without taking into account the improvement of power factor;
c.   power factor improvement and unbalance decreasing;
    c1.   minimize load unbalance by cancellation the zero sequence current by compensation and power factor increase by full compensation of positive sequence reactive power;
    c2.   reduce the load unbalance by full compensation of the negative sequence current and power factor increase by full compensation of the positive sequence reactive power;

    c3. full balancing and power factor maximization;
        c3-1.   intervention of Δ compensator only for the negative sequence current flow;
        c3-2.   minimization of the active power losses on the compensators;
        c3-3.   minimization of the installed reactive power for the compensators;
    c4. load balancing and reactive power compensation to a required power factor;
d.   Minimization of the total active power losses in the supply network.

As in the case of the three-wire network are interest the components of the compensator and the currents and powers flow on the ensemble load-compensator. These objectives are necessary to both sizing the compensation equipment and process control, when the compensation is subject of dynamic control.

For the present study was chosen to present the case of dimensioning the two compensators elements by applying the criterion C3 (full load balancing and power factor maximization). This criterion corresponds to a regime that can be considered the most advantageous from the technical point of view of network operating conditions.

As before, the symmetrical components method is applied, based on symmetrical components of currents equations corresponding on the load phases and on the two compensators, based on the phase components:

$$\underline{I}_{load}^{+} = \frac{1}{3}\left(I_{Ra} + I_{Sa} + I_{Ta}\right) - j\frac{1}{3}\left(I_{Rr} + I_{Sr} + I_{Tr}\right)$$

$$\underline{I}_{load}^{-} = \frac{1}{3}\left[I_{Ra} - \frac{1}{2}\left(I_{Sa} + I_{Ta}\right) + \frac{\sqrt{3}}{2}\left(I_{Sr} - I_{Tr}\right)\right] + j\frac{1}{3}\left[\frac{\sqrt{3}}{2}\left(I_{Sa} - I_{Ta}\right) - I_{Rr} + \frac{1}{2}\left(I_{Sr} + I_{Tr}\right)\right] \qquad (88)$$

$$\underline{I}_{load}^{0} = \frac{1}{3}\left[I_{Ra} - \frac{1}{2}\left(I_{Sa} + I_{Ta}\right) - \frac{\sqrt{3}}{2}\left(I_{Sr} - I_{Tr}\right)\right] + j\frac{1}{3}\left[-\frac{\sqrt{3}}{2}\left(I_{Sa} - I_{Ta}\right) - I_{Rr} + \frac{1}{2}\left(I_{Sr} + I_{Tr}\right)\right]$$

$$\underline{I}_{Y}^{+} = -j\frac{1}{3}\left(I_{R}^{Y} + I_{S}^{Y} + I_{T}^{Y}\right)$$

$$\underline{I}_{Y}^{-} = \frac{1}{6}\left[\sqrt{3}\left(I_{S}^{Y} - I_{T}^{Y}\right) + j\left(-2\cdot I_{R}^{Y} + I_{S}^{Y} + I_{T}^{Y}\right)\right] \qquad (89)$$

$$\underline{I}_{Y}^{0} = \frac{1}{6}\left[\sqrt{3}\left(I_{T}^{Y} - I_{S}^{Y}\right) + j\left(-2\cdot I_{R}^{Y} + I_{S}^{Y} + I_{T}^{Y}\right)\right]$$

$$\underline{I}_{\Delta}^{+} = -j\frac{1}{\sqrt{3}}\left(I_{RS}^{\Delta} + I_{ST}^{\Delta} + I_{TR}^{\Delta}\right)$$

$$\underline{I}_{\Delta}^{-} = \frac{1}{2}\left(I_{RS}^{\Delta} - I_{TR}^{\Delta}\right) + j\frac{1}{2\sqrt{3}}\left(2I_{ST}^{\Delta} - I_{RS}^{\Delta} - I_{TR}^{\Delta}\right) \qquad (90)$$

$$\underline{I}_{\Delta}^{0} = 0$$

The meaning of the notations in the above equations is no longer needed to be explained.

4.2.2 Determination of compensation currents and susceptances

Maximizing the power factor requires the full compensation of positive sequence reactive power, so the cancellation of the imaginary component of positive sequence current. Total load balancing requires, as in the case of three-wire network, the negative sequence current

cancellation of load currents, by the cancellation of its real and imaginary parts. But this time, in the network is also present the zero sequence component of load current; on the neutral conductor of the load flow a current three times greater than this. The reactive shunt compensation produced by the two compensators will have to cancel that component, also by the cancellation of its real and imaginary parts. From the analytical point of view results, for the sequence components of currents on the phases of the ensemble load - compensator, the following five conditions:

$$\mathrm{Im}\left(\underline{I}_c^+\right)=0, \qquad \mathrm{Re}\left(\underline{I}_c^+\right)=0, \qquad \mathrm{Im}\left(\underline{I}_c^-\right)=0, \qquad \mathrm{Re}\left(\underline{I}_c^0\right)=0, \qquad \mathrm{Im}\left(\underline{I}_c^0\right)=0 \tag{91}$$

where:

$$\begin{aligned}
\underline{I}_c^+ &= \underline{I}_{load}^+ + \underline{I}_Y^+ + \underline{I}_\Delta^+ \\
\underline{I}_c^- &= \underline{I}_{load}^- + \underline{I}_Y^- + \underline{I}_\Delta^- \\
\underline{I}_c^0 &= \underline{I}_{load}^0 + \underline{I}_Y^0 + \underline{I}_\Delta^0
\end{aligned} \tag{92}$$

To determine the six currents on the branches of the two compensators, a sixth condition is needed. In this paper we consider the condition **c3-1**, as shown above, results from the condition:

$$I_{RS}^\Delta + I_{ST}^\Delta + I_{TR}^\Delta = 0 \tag{93}$$

Equation (93) refers to the reactive components of currents on the branches of the Δ compensator.
Applying equations (88) (89) (90) in (92) and by joining the conditions (91) and (93) form a system of six equations with six unknowns, which, expressed in matrix, has the form:

$$\begin{bmatrix} -1 & -1 & -1 & -\sqrt{3} & -\sqrt{3} & -\sqrt{3} \\ 0 & 1 & -1 & \sqrt{3} & 0 & -\sqrt{3} \\ -2 & 1 & 1 & -\sqrt{3} & 2\sqrt{3} & -\sqrt{3} \\ 0 & -1 & 1 & 0 & 0 & 0 \\ -2 & 1 & 1 & 0 & 0 & 0 \\ 0 & 0 & 0 & 1 & 1 & 1 \end{bmatrix} \cdot \begin{bmatrix} I_R^Y \\ I_S^Y \\ I_T^Y \\ I_{RS}^\Delta \\ I_{ST}^\Delta \\ I_{TR}^\Delta \end{bmatrix} = \begin{bmatrix} A \\ B \\ C \\ D \\ E \\ 0 \end{bmatrix} \tag{94}$$

In (94), A, B, C, D, E are known quantities, with expressions that can be written depending on active and reactive components of currents on the load phases, respectively on the sequence components of these:

$$\begin{aligned}
A &= -\left(I_{Rr} + I_{Sr} + I_{Tr}\right) = 3\,\mathrm{Im}\left(\underline{I}_{load}^+\right) \\
B &= \frac{1}{\sqrt{3}}\left(-2I_{Ra} + I_{Sa} + I_{Ta}\right) - I_{Sr} + I_{Tr} = -2\sqrt{3}\,\mathrm{Re}\left(\underline{I}_{load}^-\right) \\
C &= \sqrt{3}\left(-I_{Sa} + I_{Ta}\right) + 2I_{Rr} - I_{Sr} - I_{Tr} = -6\,\mathrm{Im}\left(\underline{I}_{load}^-\right) \\
D &= \frac{1}{\sqrt{3}}\left(-2I_{Ra} + I_{Sa} + I_{Ta}\right) + I_{Sr} - I_{Tr} = -2\sqrt{3}\,\mathrm{Re}\left(\underline{I}_{load}^0\right) \\
E &= \sqrt{3}\left(I_{Sa} - I_{Ta}\right) + 2I_{Rr} - I_{Sr} - I_{Tr} = -6\,\mathrm{Im}\left(\underline{I}_{load}^0\right)
\end{aligned} \tag{95}$$

Solving the system of equations (94), we obtain the currents equations on the branches of two compensators:

$$I_R^Y = \frac{A+E}{3}, \qquad I_S^Y = \frac{2A+3D-E}{3}, \qquad I_T^Y = \frac{2A-3D-E}{3}$$
$$I_{RS}^\Delta = \frac{-3B+C-3D-E}{6\sqrt{3}}, \qquad I_{ST}^\Delta = \frac{-C+E}{3\sqrt{3}}, \qquad I_{RS}^\Delta = \frac{3B+C+3D+E}{6\sqrt{3}}$$

(96)

$$I_R^Y = \tfrac{1}{\sqrt{3}}(I_{Ta}-I_{Sa}) - I_{Rr} \qquad I_{RS}^\Delta = \tfrac{2}{3}(I_{Sa}-I_{Ra})$$
$$I_S^Y = \tfrac{1}{\sqrt{3}}(I_{Ra}-I_{Ta}) - I_{Sr} \qquad I_{ST}^\Delta = \tfrac{2}{3}(I_{Ta}-I_{Sa})$$
$$I_T^Y = \tfrac{1}{\sqrt{3}}(I_{Sa}-I_{Ra}) - I_{Tr} \qquad I_{TR}^\Delta = \tfrac{2}{3}(I_{Ra}-I_{Ta})$$

(97)

Immediately results the equations for the six susceptances:

$$B_R^Y = \tfrac{1}{U}\left[\tfrac{1}{\sqrt{3}}(I_{Ta}-I_{Sa}) - I_{Rr}\right] \qquad B_{RS}^\Delta = \tfrac{2}{3\sqrt{3}U}(I_{Sa}-I_{Ra})$$
$$B_S^Y = \tfrac{1}{U}\left[\tfrac{1}{\sqrt{3}}(I_{Ra}-I_{Ta}) - I_{Sr}\right] \qquad B_{ST}^\Delta = \tfrac{2}{3\sqrt{3}U}(I_{Ta}-I_{Sa})$$
$$B_R^Y = \tfrac{1}{U}\left[\tfrac{1}{\sqrt{3}}(I_{Sa}-I_{Ra}) - I_{Tr}\right] \qquad B_{TR}^\Delta = \tfrac{2}{3\sqrt{3}U}(I_{Ra}-I_{Ta})$$

(98)

$$B_R^Y = \tfrac{1}{\sqrt{3}}(G_T^s - G_S^s) - B_R^s \qquad B_{RS}^\Delta = \tfrac{2}{3\sqrt{3}}(G_S^s - G_R^s)$$
$$B_S^Y = \tfrac{1}{\sqrt{3}}(G_R^s - G_T^s) - B_S^s \qquad B_{ST}^\Delta = \tfrac{2}{3\sqrt{3}}(G_T^s - G_S^s)$$
$$B_R^Y = \tfrac{1}{\sqrt{3}}(G_S^s - G_R^s) - B_T^s \qquad B_{TR}^\Delta = \tfrac{2}{3\sqrt{3}}(G_R^s - G_T^s)$$

(99)

4.2.3 The current flow on the ensemble load - compensator, in phase components

The currents equations on the phases of Δ compensator respectively Y, written for the complex plans reported to phase-to-neutral voltages involved (notation "*"), are:

$$\underline{I}_R^{\Delta*} = \tfrac{1}{2}(I_{RS}^\Delta - I_{TR}^\Delta) - j\tfrac{\sqrt{3}}{2}(I_{RS}^\Delta + I_{TR}^\Delta)$$
$$\underline{I}_S^{\Delta*} = \tfrac{1}{2}(I_{ST}^\Delta - I_{RS}^\Delta) - j\tfrac{\sqrt{3}}{2}(I_{RS}^\Delta + I_{ST}^\Delta)$$
$$\underline{I}_R^{\Delta*} = \tfrac{1}{2}(I_{TR}^\Delta - I_{ST}^\Delta) - j\tfrac{\sqrt{3}}{2}(I_{TR}^\Delta + I_{ST}^\Delta)$$

(100)

$$\underline{I}_R^{Y*} = -j \cdot I_R^Y$$
$$\underline{I}_S^{Y*} = -j \cdot I_S^Y$$
$$\underline{I}_T^{Y*} = -j \cdot I_T^Y$$

(101)

Using equations for calculating the six compensation currents resulted from the criterion C3-1 (97) currents on the phases of two compensators can be deduced:

$$\underline{I}_R^{\Delta*} = \tfrac{1}{3}(-2I_{Ra}+I_{Sa}+I_{Ta}) + j\tfrac{1}{\sqrt{3}}(I_{Ta}-I_{Sa})$$
$$\underline{I}_S^{\Delta*} = \tfrac{1}{3}(I_{Ra}-2I_{Sa}+I_{Ta}) + j\tfrac{1}{\sqrt{3}}(I_{Ra}-I_{Ta})$$
$$\underline{I}_T^{\Delta*} = \tfrac{1}{3}(I_{Ra}+I_{Sa}-2I_{Ta}) + j\tfrac{1}{\sqrt{3}}(I_{Sa}-I_{Ra})$$

(102)

$$\underline{I}_R^{Y*} = j\left[\tfrac{1}{\sqrt{3}}\left(I_{Sa} - I_{Ta}\right) + I_{Rr}\right]$$

$$\underline{I}_S^{Y*} = j\left[\tfrac{1}{\sqrt{3}}\left(I_{Ta} - I_{Ra}\right) + I_{Sr}\right] \tag{103}$$

$$\underline{I}_R^{Y*} = j\left[\tfrac{1}{\sqrt{3}}\left(I_{Ra} - I_{Sa}\right) + I_{Tr}\right]$$

As a useful observation, the rms values of the three phase currents on the phases of Δ compensator are equal, as expected, the three currents forming a symmetrical and balanced set, of negative sequence:

$$I_R^{\Delta*} = I_R^{\Delta*} = I_R^{\Delta*} = \tfrac{2}{3}\left(I_{Ra}^2 + I_{Sa}^2 + I_{Ta}^2 - I_{Ra}I_{Sa} - I_{Sa}I_{Ta} - I_{Ta}I_{Ra}\right)^{1/2} \tag{104}$$

Calculating now the currents absorbed on the phases of the ensemble load - compensator, with the equations:

$$\underline{I}_R^{c*} = \underline{I}_R^{load*} + \underline{I}_R^{\Delta*} + \underline{I}_R^{Y*}$$

$$\underline{I}_S^{c*} = \underline{I}_S^{load*} + \underline{I}_S^{\Delta*} + \underline{I}_S^{Y*} \tag{105}$$

$$\underline{I}_T^{c*} = \underline{I}_T^{load*} + \underline{I}_T^{\Delta*} + \underline{I}_T^{Y*}$$

It obtains:

$$I_{ph\,r}^{\Delta*} + I_{ph\,r}^{Y*} + I_{ph\,r}^{load} = 0, \quad I_{ph\,r}^{\Delta*} + I_{ph\,r}^{Y*} = -I_{ph\,r}^{load} \quad (ph = phase = R, S, T) \tag{106}$$

$$\underline{I}_R^{c*} = \underline{I}_S^{c*} = \underline{I}_T^{c*} = \tfrac{1}{3}\left(I_{Ra} + I_{Sa} + I_{Ta}\right) = \mathrm{Re}\left(\underline{I}_c^+\right) = \mathrm{Re}\left(\underline{I}_{load}^+\right) \tag{107}$$

It finds that the sizing conditions (91) are satisfied: the negative and zero sequence currents, and the reactive component of the positive sequence current were canceled by compensation. In other words, load balancing and full compensation are obtained ($\cos\varphi^c = \cos\varphi^+ = 1$). After the compensation the phase currents become purely active, balanced with the rms value equal to the arithmetic average of the three active currents of the load.

But let's not forget the currents flow on neutral conductors. To determine the current equation on the load neutral conductor, using the formula:

$$\underline{I}_N^{load} = \underline{I}_R^{load} + \underline{I}_S^{load} + \underline{I}_T^{load} \tag{108}$$

Using the currents equations written for the complex plane associated with phase R:

$$\underline{I}_R^{load} = I_{Ra} - j \cdot I_{Rr}$$

$$\underline{I}_S^{load} = a^2 \cdot \left(I_{Sa} - j \cdot I_{Sr}\right) = -\tfrac{1}{2}I_{Sa} - \tfrac{\sqrt{3}}{2}I_{Sr} + j \cdot \left(\tfrac{1}{2}I_{Sr} - \tfrac{\sqrt{3}}{2}I_{Sa}\right) \tag{109}$$

$$\underline{I}_T^{load} = a \cdot \left(I_{Ta} - j \cdot I_{Tr}\right) = -\tfrac{1}{2}I_{Ta} + \tfrac{\sqrt{3}}{2}I_{Tr} + j \cdot \left(\tfrac{1}{2}I_{Tr} + \tfrac{\sqrt{3}}{2}I_{Ta}\right)$$

result:

$$\underline{I}_N^{load} = \tfrac{1}{2}\left(2I_{Ra} - I_{Sa} - I_{Ta}\right) + \tfrac{\sqrt{3}}{2}\left(I_{Tr} - I_{Sr}\right) + j \cdot \left[\tfrac{1}{2}\left(-2I_{Rr} + I_{Sr} + I_{Tr}\right) + \tfrac{\sqrt{3}}{2}\left(I_{Ta} - I_{Sa}\right)\right] \tag{110}$$

The current on the neutral conductor of Y compensator:

$$\underline{I}_N^Y = \underline{I}_R^Y + \underline{I}_S^Y + \underline{I}_T^Y \,, \tag{111}$$

where:

$$
\begin{aligned}
\underline{I}_R^Y &= -j \cdot I_R^Y \\
\underline{I}_S^Y &= a^2 \cdot \left(-j \cdot I_S^Y\right) = -\tfrac{\sqrt{3}}{2} I_S^Y + j \cdot \tfrac{1}{2} I_S^Y \\
\underline{I}_S^Y &= a \cdot \left(-j \cdot I_T^Y\right) = \tfrac{\sqrt{3}}{2} I_T^Y + j \cdot \tfrac{1}{2} I_T^Y
\end{aligned}
\tag{112}
$$

Using equations (97) for the currents on the phases of Y compensator, for the current $\underline{I}_N^Y$ results:

$$\underline{I}_N^Y = -\underline{I}_N^{load} \,, \tag{113}$$

so that:

$$\underline{I}_N^c = \underline{I}_N^Y + \underline{I}_N^{load} = 0 \tag{114}$$

It can be concluded that:

$$\underline{I}_c^0 = \frac{1}{3} \cdot \underline{I}_N^c = 0 \tag{115}$$

So the compensator Y inject on the neutral conductor a current equal and opposite to that on the neutral conductor of the load, canceling it.

4.2.4 The powers flow into the ensemble load - compensator
The active powers equations on the load phases are:

$$
\begin{aligned}
P_R^{load} &= U_R \cdot I_{Ra} = U \cdot I_{Ra} \\
P_S^{load} &= U_S \cdot I_{Sa} = U \cdot I_{Sa} \\
P_T^{load} &= U_T \cdot I_{Ta} = U \cdot I_{Ta}
\end{aligned}
\tag{116}
$$

The active powers on the phases of the Δ compensator are:

$$
\begin{aligned}
P_R^\Delta &= U_R \cdot I_{Ra}^{\Delta^*} = U\tfrac{1}{3}\left(-2I_{Ra} + I_{Sa} + I_{Ta}\right) \\
P_S^\Delta &= U_S \cdot I_{Sa}^{\Delta^*} = U\tfrac{1}{3}\left(I_{Ra} - 2I_{Sa} + I_{Ta}\right) \\
P_T^\Delta &= U_T \cdot I_{Ta}^{\Delta^*} = U\tfrac{1}{3}\left(I_{Ra} + I_{Sa} - 2I_{Ta}\right)
\end{aligned}
\tag{117}
$$

It may be noted that the Δ compensator modifies on each phase the active power flow: on some phase debits while on the others absorbs active power. But on the ensemble of the three phases, the active power flow is not affected because:

$$\sum_{ph=R,S,T} P_{ph}^\Delta = 0 \tag{118}$$

Instead, the Y compensator does not intervene at all on the active power flow:

$$P_R^Y = P_S^Y = P_T^Y = 0 \tag{119}$$

After compensation:

$$
\begin{aligned}
P_R^c &= U_R \cdot I_{Ra}^c = U \tfrac{1}{3}\left(I_{Ra} + I_{Sa} + I_{Ta}\right) \\
P_S^c &= U_S \cdot I_{Sa}^c = U \tfrac{1}{3}\left(I_{Ra} + I_{Sa} + I_{Ta}\right) \\
P_T^c &= U_T \cdot I_{Ta}^c = U \tfrac{1}{3}\left(I_{Ra} + I_{Sa} + I_{Ta}\right)
\end{aligned}
\tag{120}
$$

It is noted once again that the presence of the compensator does not affect the active power absorbed from the network (the same value before and after compensation).

$$\sum_{ph=R,S,T} P_{ph}^{load} = \sum_{ph=R,S,T} P_{ph}^c = U \cdot \left(I_{Ra} + I_{Sa} + I_{Ta}\right) \tag{121}$$

For the reactive powers on the three phases into the ensemble load - compensator it obtains:

$$
\begin{aligned}
Q_R^{load} &= U_R \cdot I_{Rr} \\
Q_S^{load} &= U_S \cdot I_{Sr} \\
Q_T^{load} &= U_T \cdot I_{Tr}
\end{aligned}
\tag{122}
$$

$$
\begin{aligned}
Q_R^\Delta &= U_R \cdot I_{Rr}^{\Delta*} = U \cdot \tfrac{1}{\sqrt{3}}\left(I_{Sa} - I_{Ta}\right) \\
Q_S^\Delta &= U_S \cdot I_{Sr}^{\Delta*} = U \cdot \tfrac{1}{\sqrt{3}}\left(I_{Ta} - I_{Ra}\right) \\
Q_T^\Delta &= U_T \cdot I_{Tr}^{\Delta*} = U \cdot \tfrac{1}{\sqrt{3}}\left(I_{Ra} - I_{Sa}\right)
\end{aligned}
\tag{123}
$$

$$
\begin{aligned}
Q_R^Y &= U_R \cdot I_{Rr}^{Y*} = U \cdot \left[\tfrac{1}{\sqrt{3}}\left(I_{Ta} - I_{Sa}\right) - I_{Rr}\right] \\
Q_S^Y &= U_S \cdot I_{Sr}^{Y*} = U \cdot \left[\tfrac{1}{\sqrt{3}}\left(I_{Ra} - I_{Ta}\right) - I_{Sr}\right] \\
Q_T^Y &= U_T \cdot I_{Tr}^{Y*} = U \cdot \left[\tfrac{1}{\sqrt{3}}\left(I_{Sa} - I_{Ra}\right) - I_{Tr}\right]
\end{aligned}
\tag{124}
$$

It is noted once again the full compensation of reactive power. The two compensators determine together on the each phase a reactive current flow, equal and opposite to the load reactive current. It can be observed that:

$$\sum_{ph=R,S,T} Q_{ph}^\Delta = 0 \tag{125}$$

So, the Δ compensator absorbs reactive power on some phase and debits reactive power on the others, but it does not affect the reactive power flow on the ensemble of the three phases. Therefore it can be said that the compensator realizes a redistribution of reactive power between the three phases.
It can be observed also:

$$\sum_{ph=R,S,T} Q_{ph}^Y = -\sum_{ph=R,S,T} Q_{ph}^{load} \tag{126}$$

In fact, the Y compensator is that one which effectively realizes the reactive power compensation of the load.

4.2.5 The currents flow into the ensemble load - compensator expressed by symmetrical components of load currents

Expressing the compensation current depending on symmetrical components of the load currents allows a complete interpretation of the mechanism of the reactive power compensation and load balancing.

Considering the same sizing criterion (c3-1), the sizing conditions (91) will be written as:

$$
\begin{cases}
\mathrm{Im}\left(\underline{I}_{load}^{+}\right) = -\mathrm{Im}\left(\underline{I}_{\Delta}^{+}\right) - \mathrm{Im}\left(\underline{I}_{Y}^{+}\right) \\
\mathrm{Re}\left(\underline{I}_{load}^{-}\right) = -\mathrm{Re}\left(\underline{I}_{\Delta}^{-}\right) - \mathrm{Re}\left(\underline{I}_{Y}^{-}\right) \\
\mathrm{Im}\left(\underline{I}_{load}^{-}\right) = -\mathrm{Im}\left(\underline{I}_{\Delta}^{-}\right) - \mathrm{Im}\left(\underline{I}_{Y}^{-}\right) \\
\mathrm{Re}\left(\underline{I}_{load}^{0}\right) = -\mathrm{Re}\left(\underline{I}_{\Delta}^{0}\right) - \mathrm{Re}\left(\underline{I}_{Y}^{0}\right) \\
\mathrm{Im}\left(\underline{I}_{load}^{0}\right) = -\mathrm{Im}\left(\underline{I}_{\Delta}^{0}\right) - \mathrm{Im}\left(\underline{I}_{Y}^{0}\right)
\end{cases}
\tag{127}
$$

Expressing the sequence components of the currents on the phases of the two compensators expressed by the compensation currents, it's obtained the equation system:

$$
\begin{cases}
\mathrm{Im}\left(\underline{I}_{load}^{+}\right) = \frac{1}{\sqrt{3}}\left(I_{RS}^{\Delta} + I_{ST}^{\Delta} + I_{TR}^{\Delta}\right) + \frac{1}{3}\left(I_{R}^{Y} + I_{S}^{Y} + I_{T}^{Y}\right) \\
\mathrm{Re}\left(\underline{I}_{load}^{-}\right) = \frac{1}{2}\left(I_{TR}^{\Delta} - I_{RS}^{\Delta}\right) + \frac{1}{2\sqrt{3}}\left(I_{T}^{Y} - I_{S}^{Y}\right) \\
\mathrm{Im}\left(\underline{I}_{load}^{-}\right) = \frac{1}{2\sqrt{3}}\left(I_{RS}^{\Delta} - 2I_{ST}^{\Delta} + I_{TR}^{\Delta}\right) + \frac{1}{6}\left(2I_{R}^{Y} - I_{S}^{Y} - I_{T}^{Y}\right) \\
\mathrm{Re}\left(\underline{I}_{load}^{0}\right) = \frac{1}{2\sqrt{3}}\left(I_{S}^{Y} - I_{T}^{Y}\right) \\
\mathrm{Im}\left(\underline{I}_{load}^{0}\right) = \frac{1}{6}\left(2I_{R}^{Y} - I_{S}^{Y} - I_{T}^{Y}\right)
\end{cases}
\tag{128}
$$

Adding the additional condition (93), results the matrix form:

$$
\begin{bmatrix}
\frac{1}{3} & \frac{1}{3} & \frac{1}{3} & \frac{1}{\sqrt{3}} & \frac{1}{\sqrt{3}} & \frac{1}{\sqrt{3}} \\[2mm]
0 & -\frac{1}{2\sqrt{3}} & \frac{1}{2\sqrt{3}} & -\frac{1}{2} & 0 & \frac{1}{2} \\[2mm]
\frac{1}{3} & -\frac{1}{6} & -\frac{1}{6} & \frac{1}{2\sqrt{3}} & -\frac{1}{\sqrt{3}} & \frac{1}{\sqrt{3}} \\[2mm]
0 & \frac{1}{2\sqrt{3}} & -\frac{1}{2\sqrt{3}} & 0 & 0 & 0 \\[2mm]
\frac{1}{3} & -\frac{1}{6} & -\frac{1}{6} & 0 & 0 & 0 \\[2mm]
0 & 0 & 0 & 1 & 1 & 1
\end{bmatrix}
\cdot
\begin{bmatrix}
I_{R}^{Y} \\ I_{s}^{Y} \\ I_{T}^{Y} \\ I_{RS}^{\Delta} \\ I_{ST}^{\Delta} \\ I_{TR}^{\Delta}
\end{bmatrix}
=
\begin{bmatrix}
\mathrm{Im}(I_{load}^{+}) \\ \mathrm{Re}(I_{load}^{-}) \\ \mathrm{Im}(I_{load}^{-}) \\ \mathrm{Re}(I_{load}^{0}) \\ \mathrm{Im}(I_{load}^{0}) \\ 0
\end{bmatrix}
\tag{129}
$$

The solutions have the equations:

$$I_{RS}^{\Delta} = -\text{Re}\left(\underline{I}_{load}^{-}\right) + \tfrac{1}{\sqrt{3}}\text{Im}\left(\underline{I}_{load}^{-}\right) - \text{Re}\left(\underline{I}_{load}^{0}\right) - \tfrac{1}{\sqrt{3}}\text{Im}\left(\underline{I}_{load}^{0}\right)$$

$$I_{ST}^{\Delta} = -\tfrac{2}{\sqrt{3}}\text{Im}\left(\underline{I}_{load}^{-}\right) + \tfrac{2}{\sqrt{3}}\text{Im}\left(\underline{I}_{load}^{0}\right) \tag{130}$$

$$I_{TR}^{\Delta} = \text{Re}\left(\underline{I}_{load}^{-}\right) + \tfrac{1}{\sqrt{3}}\text{Im}\left(\underline{I}_{load}^{-}\right) + \text{Re}\left(\underline{I}_{load}^{0}\right) - \tfrac{1}{\sqrt{3}}\text{Im}\left(\underline{I}_{load}^{0}\right)$$

$$I_{R}^{Y} = \text{Im}\left(\underline{I}_{load}^{+}\right) + 2\,\text{Im}\left(\underline{I}_{load}^{0}\right)$$

$$I_{S}^{Y} = \text{Im}\left(\underline{I}_{load}^{+}\right) + \sqrt{3}\,\text{Re}\left(\underline{I}_{load}^{0}\right) - \text{Im}\left(\underline{I}_{load}^{0}\right) \tag{131}$$

$$I_{T}^{Y} = \text{Im}\left(\underline{I}_{load}^{+}\right) - \sqrt{3}\,\text{Re}\left(\underline{I}_{load}^{0}\right) - \text{Im}\left(\underline{I}_{load}^{0}\right)$$

Now it can deduce the equations for the currents on the phases of the: Δ compensator, Y compensator, load and the ensemble of these, expressed with symmetrical components of currents on the load phases:

$$\underline{I}_{R}^{\Delta} = \tfrac{1}{2}\left(I_{RS}^{\Delta} - I_{TR}^{\Delta}\right) + j\tfrac{\sqrt{3}}{2}\left(-I_{RS}^{\Delta} - I_{TR}^{\Delta}\right) = -\underline{I}_{load}^{-} + \underline{I}_{load}^{0} - 2\,\text{Re}\left(\underline{I}_{load}^{0}\right)$$

$$\underline{I}_{S}^{\Delta} = -\tfrac{1}{2}\left(I_{RS}^{\Delta} + 2I_{ST}^{\Delta}\right) + j\tfrac{\sqrt{3}}{2}I_{RS}^{\Delta} = -\text{a}\cdot\underline{I}_{load}^{-} + \text{a}\cdot\underline{I}_{load}^{0} - 2\text{a}\cdot\text{Re}\left(\underline{I}_{load}^{0}\right) \tag{132}$$

$$\underline{I}_{T}^{\Delta} = \tfrac{1}{2}\left(I_{TR}^{\Delta} + 2I_{ST}^{\Delta}\right) + j\tfrac{\sqrt{3}}{2}I_{TR}^{\Delta} = -\text{a}^{2}\cdot\underline{I}_{load}^{-} + \text{a}^{2}\cdot\underline{I}_{load}^{0} - 2\text{a}^{2}\cdot\text{Re}\left(\underline{I}_{load}^{0}\right)$$

$$\underline{I}_{R}^{Y} = -j\cdot I_{R}^{Y} = -j\,\text{Im}\left(\underline{I}_{load}^{+}\right) - 2\underline{I}_{load}^{0} + 2\,\text{Re}\left(\underline{I}_{load}^{0}\right)$$

$$\underline{I}_{S}^{Y} = \text{a}^{2}\cdot\left(-j\cdot I_{S}^{Y}\right) = -\text{a}^{2}\cdot j\,\text{Im}\left(\underline{I}_{load}^{+}\right) + \text{a}^{2}\cdot\underline{I}_{load}^{0} + 2\text{a}\cdot\text{Re}\left(\underline{I}_{load}^{0}\right) \tag{133}$$

$$\underline{I}_{T}^{Y} = \text{a}\cdot\left(-j\cdot I_{T}^{Y}\right) = -\text{a}\cdot j\,\text{Im}\left(\underline{I}_{load}^{+}\right) + \text{a}\cdot\underline{I}_{load}^{0} + 2\text{a}^{2}\cdot\text{Re}\left(\underline{I}_{load}^{0}\right)$$

$$\underline{I}_{R}^{load} = \underline{I}_{loadh}^{0} + \underline{I}_{load}^{+} + \underline{I}_{load}^{-}$$

$$\underline{I}_{S}^{load} = \underline{I}_{load}^{0} + \text{a}^{2}\cdot\underline{I}_{load}^{+} + \text{a}\cdot\underline{I}_{load}^{-} \tag{134}$$

$$\underline{I}_{T}^{load} = \underline{I}_{load}^{0} + \text{a}\cdot\underline{I}_{load}^{+} + \text{a}^{2}\cdot\underline{I}_{load}^{-}$$

$$\underline{I}_{R}^{c} = \underline{I}_{R}^{load} + \underline{I}_{R}^{\Delta} + \underline{I}_{R}^{Y} = \text{Re}\left(\underline{I}_{load}^{+}\right)$$

$$\underline{I}_{S}^{c} = \underline{I}_{S}^{load} + \underline{I}_{S}^{\Delta} + \underline{I}_{S}^{Y} = \text{a}^{2}\cdot\text{Re}\left(\underline{I}_{load}^{+}\right) \tag{135}$$

$$\underline{I}_{T}^{c} = \underline{I}_{T}^{load} + \underline{I}_{T}^{\Delta} + \underline{I}_{T}^{Y} = \text{a}\cdot\text{Re}\left(\underline{I}_{load}^{+}\right)$$

It can be observed that on the phases of the ensemble load-compensator a three phase positive sequence current it's formed, corresponding to the active components of the positive sequence load currents.

To explain the compensation mechanism, the equations of the currents on the phases of the two compensators are written so as to highlight the components of positive, negative and zero sequence sets:

$$\underline{I}_R^\Delta = \quad \left(-\underline{I}_{load}^-\right) + \quad j\,\mathrm{Im}\left(\underline{I}_{load}^0\right) - \mathrm{Re}\left(\underline{I}_{load}^0\right)$$

$$\underline{I}_S^\Delta = \mathrm{a}\cdot\left(-\underline{I}_{load}^-\right) + \mathrm{a}\cdot\left[\,j\,\mathrm{Im}\left(\underline{I}_{load}^0\right) - \mathrm{Re}\left(\underline{I}_{load}^0\right)\right] \tag{136}$$

$$\underline{I}_R^\Delta = \underbrace{\mathrm{a}^2\left(-\underline{I}_{load}^-\right)}_{\Delta_1^-} + \underbrace{a^2\left[\,j\,\mathrm{Im}\left(\underline{I}_{load}^0\right) - \mathrm{Re}\left(\underline{I}_{load}^0\right)\right]}_{\Delta_2^-}$$

$$\underline{I}_R^Y = \quad -j\,\mathrm{Im}\left(\underline{I}_{load}^+\right) \quad -j\,\mathrm{Im}\left(\underline{I}_{load}^0\right) + \mathrm{Re}\left(\underline{I}_{load}^0\right) \quad -\mathrm{Re}\left(\underline{I}_{load}^0\right) - j\,\mathrm{Im}\left(\underline{I}_{load}^0\right)$$

$$\underline{I}_S^Y = -\mathrm{a}^2 j\,\mathrm{Im}\left(\underline{I}_{load}^+\right) \quad -\mathrm{a}\cdot\left[\,j\,\mathrm{Im}\left(\underline{I}_{load}^0\right) - \mathrm{Re}\left(\underline{I}_{load}^0\right)\right] - \mathrm{Re}\left(\underline{I}_{load}^0\right) - j\,\mathrm{Im}\left(\underline{I}_{load}^0\right) \tag{137}$$

$$\underline{I}_T^Y = \underbrace{-\mathrm{a}\cdot j\,\mathrm{Im}\left(\underline{I}_{load}^+\right)}_{Y^+} \quad \underbrace{-\mathrm{a}^2\left[\,j\,\mathrm{Im}\left(\underline{I}_{load}^0\right) - \mathrm{Re}\left(\underline{I}_{load}^0\right)\right]}_{Y^-} \underbrace{- \mathrm{Re}\left(\underline{I}_{load}^0\right) - j\,\mathrm{Im}\left(\underline{I}_{load}^0\right)}_{Y^0}$$

It's found that the currents on the phases of Δ compensator can be decomposed in two three-phase sets, both of negative sequence:

- one equal and opposite two the negative sequence of the currents on the load phases (noted Δ_1^-), which cancels,
- one which depends on the active and reactive components of the zero sequence current on the load phases (Δ_2^-).

The currents on the phases of the Y compensator can be decomposed in three three-phase sets:

- one of positive sequence (Y^+), equal and opposite to the set formed by the reactive components of positive sequence currents of the load, which cancels,
- one of negative sequence (Y^-), equal and opposite to the set of the currents on the phases of the compensator (Δ_2^-), the two sets canceling each other,
- the third one, of zero sequence (Y^0), equal and opposite to the zero sequence set of currents on the load phases, which cancels.

It also observes that the current on the neutral conductor of the Y compensator compensates the current on the load neutral conductor, because:

$$\underline{I}_R^Y + \underline{I}_S^Y + \underline{I}_T^Y = \underline{I}_N^Y = -3\underline{I}_{load}^0 \tag{138}$$

4.2.6 The compensation susceptances expressed depending on the sequence components of the load current

Based on the equations (130) and (131), can be established equations for the calculation of the sixths compensation susceptances expressed depending on the active and reactive components of the sequence currents (available for the criterion c3-1):

$$B_{RS}^\Delta = \frac{1}{\sqrt{3}U}\left[-\mathrm{Re}\left(\underline{I}_{load}^-\right) + \tfrac{1}{\sqrt{3}}\mathrm{Im}\left(\underline{I}_{load}^-\right) - \mathrm{Re}\left(\underline{I}_{load}^0\right) - \tfrac{1}{\sqrt{3}}\mathrm{Im}\left(\underline{I}_{load}^0\right)\right]$$

$$B_{ST}^\Delta = \frac{1}{\sqrt{3}U}\left[-\tfrac{2}{\sqrt{3}}\mathrm{Im}\left(\underline{I}_{load}^-\right) + \tfrac{2}{\sqrt{3}}\mathrm{Im}\left(\underline{I}_{load}^0\right)\right] \tag{139}$$

$$B_{TR}^\Delta = \frac{1}{\sqrt{3}U}\left[\mathrm{Re}\left(\underline{I}_{load}^-\right) + \tfrac{1}{\sqrt{3}}\mathrm{Im}\left(\underline{I}_{load}^-\right) + \mathrm{Re}\left(\underline{I}_{load}^0\right) - \tfrac{1}{\sqrt{3}}\mathrm{Im}\left(\underline{I}_{load}^0\right)\right]$$

$$B_R^Y = \frac{1}{U}\left[\operatorname{Im}\left(\underline{I}_{load}^+\right) + 2\operatorname{Im}\left(\underline{I}_{load}^0\right)\right]$$

$$B_S^Y = \frac{1}{U}\left[\operatorname{Im}\left(\underline{I}_{load}^+\right) + \sqrt{3}\operatorname{Re}\left(\underline{I}_{load}^0\right) - \operatorname{Im}\left(\underline{I}_{load}^0\right)\right] \tag{140}$$

$$B_T^Y = \frac{1}{U}\left[\operatorname{Im}\left(\underline{I}_{load}^+\right) - \sqrt{3}\operatorname{Re}\left(\underline{I}_{load}^0\right) - \operatorname{Im}\left(\underline{I}_{load}^0\right)\right]$$

Since the currents flow on the three symmetrical sequences are independent, these susceptances can be decomposed to form five fictitious compensators:

$$B_{RS}^\Delta = B_{RS}^{\Delta_1^-} + B_{RS}^{\Delta_2^-}, \qquad B_{ST}^\Delta = B_{ST}^{\Delta_1^-} + B_{ST}^{\Delta_2^-}, \qquad B_{TR}^\Delta = B_{TR}^{\Delta_1^-} + B_{TR}^{\Delta_2^-}$$
$$B_R^Y = B_R^{Y^+} + B_R^{Y^-} + B_R^{Y^0}, \quad B_S^Y = B_S^{Y^+} + B_S^{Y^-} + B_S^{Y^0}, \quad B_T^Y = B_T^{Y^+} + B_T^{Y^-} + B_T^{Y^0} \tag{141}$$

in which:

$$B_{RS}^{\Delta_1^-} = \frac{1}{\sqrt{3}U}\left[-\operatorname{Re}\left(\underline{I}_{load}^-\right) + \tfrac{1}{\sqrt{3}}\operatorname{Im}\left(\underline{I}_{load}^-\right)\right]$$

$$B_{ST}^{\Delta_1^-} = \frac{1}{\sqrt{3}U}\left[-\tfrac{2}{\sqrt{3}}\operatorname{Im}\left(\underline{I}_{load}^-\right)\right] \tag{142}$$

$$B_{TR}^{\Delta_1^-} = \frac{1}{\sqrt{3}U}\left[\operatorname{Re}\left(\underline{I}_{load}^-\right) + \tfrac{1}{\sqrt{3}}\operatorname{Im}\left(\underline{I}_{load}^-\right)\right]$$

$$B_{RS}^{\Delta_2^-} = \frac{1}{\sqrt{3}U}\left[-\operatorname{Re}\left(\underline{I}_{load}^0\right) - \tfrac{1}{\sqrt{3}}\operatorname{Im}\left(\underline{I}_{load}^0\right)\right]$$

$$B_{ST}^{\Delta_2^-} = \frac{1}{\sqrt{3}U}\left[\tfrac{2}{\sqrt{3}}\operatorname{Im}\left(\underline{I}_{load}^0\right)\right] \tag{143}$$

$$B_{TR}^{\Delta_2^-} = \frac{1}{\sqrt{3}U}\left[\operatorname{Re}\left(\underline{I}_{load}^0\right) - \tfrac{1}{\sqrt{3}}\operatorname{Im}\left(\underline{I}_{load}^0\right)\right]$$

$$B_R^{Y^+} = B_S^{Y^+} = B_T^{Y^+} = \frac{1}{U}\operatorname{Im}\left(\underline{I}_{load}^+\right) \tag{144}$$

$$B_R^{Y^-} + B_R^{Y^0} = \frac{2}{U}\operatorname{Im}\left(\underline{I}_{load}^0\right)$$

$$B_S^{Y^-} + B_S^{Y^0} = \frac{1}{U}\left[\sqrt{3}\operatorname{Re}\left(\underline{I}_{load}^0\right) - \operatorname{Im}\left(\underline{I}_{load}^0\right)\right] \tag{145}$$

$$B_S^{Y^-} + B_S^{Y^0} = \frac{1}{U}\left[-\sqrt{3}\operatorname{Re}\left(\underline{I}_{load}^0\right) - \operatorname{Im}\left(\underline{I}_{load}^0\right)\right]$$

It can observe that the susceptances constituted in Δ_1^- can be determined with the same equations as in the case of the three-wire network (equations 54). To compensate the imaginary parts of the positive sequence currents, this time it's used a symmetrical compensator in star connection (Y^+), which is not necessary the connection with the neutral conductor of the network.

The zero sequence components of the load currents are compensated by a mix compensator $\Delta_2^- + Y^- + Y^0$. The Y^- and Y^0 compensators can be grouped into a single receiver Y connection ($Y^{-,0}$), which must allowed the closure of zero sequence compensation currents, which is possible only in an Y_n connection.
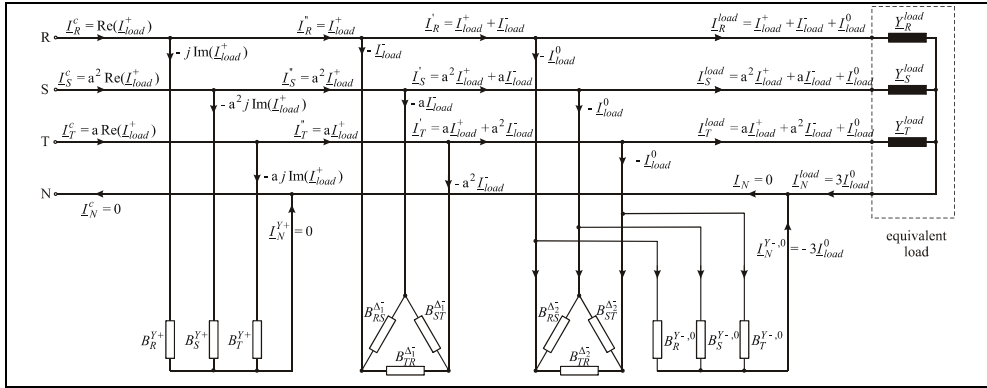
Fig. 13. The decomposition of the compensators in three fictitious compensators (Y^+, Δ_1^-, $\Delta_2^- + Y^{-,0}$) and the compensation mechanism illustrated by symmetrical components
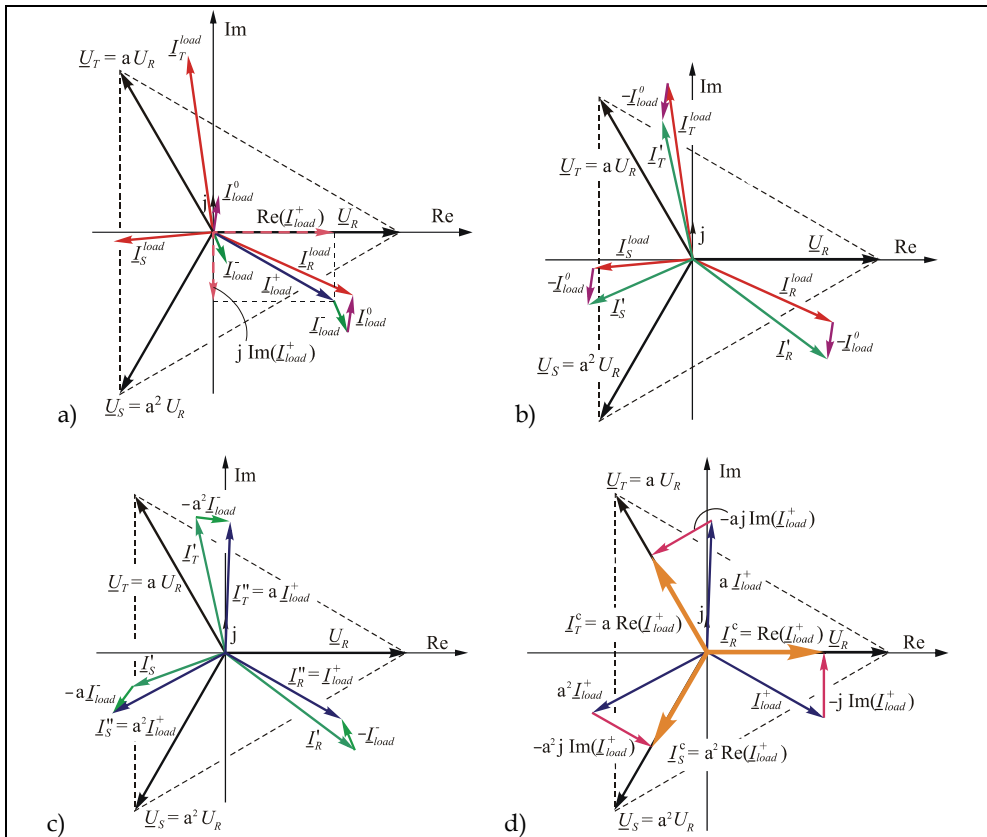

Fig. 14. The phasor diagrams illustrate the compensation mechanism for unbalanced load in three-phase four-wire network

The five compensators can be reduced to three, each one realizing the compensation on one of the sequences. Figure 13 presents the three fictitious compensators and the sequence currents flow into the ensemble load - compensator and Figure 14 presents the phasor diagram and the compensation mechanism.

In the last one is first illustrated the three phases currents of the load constituted in a three-phase unbalanced set, by which were determined the reference sequence currents (fig. 14.a). It can be observed the successive intervention of the fictitious compensators which cancels the zero sequence components (fig. 14.b), the negative sequence component (fig. 14.c) and the reactive component of the positive sequence current (fig. 14.d). After the compensation remains a three-phase currents set perfectly balanced and purely active (in phase with corresponding simple voltages).

5. Conclusions

Unbalance of phase equivalent impedance and/or load unbalance on a three-phase electrical network, determine unequal voltage drops on the three phases and hence the voltage unbalance. The main negative effects of current and voltage unbalances in an electrical network consist of yields reduction of processes and dysfunctions at a wide range of equipment, effects which can be equated with damages caused by additional energy losses, deterioration of quality of processes and life shortening of the equipments.

One of the most popular means of mitigating the load unbalance in three-phase networks is the Steinmetz circuit. It may be used to convert a purely active load, connected between two phases, in an equivalent three-phase active load, perfectly balanced, using the shunt reactive compensation. Active load balancing method in a three-phase network by shunt reactive compensation can be generalized to any three-phase loads, supplied by three or four wire networks.

This chapter presents the developed mathematical model for this method, including the sizing of reactive compensation elements, the currents flow into the compensator, respectively the currents and powers flow into the load-compensator ensemble.

For this, it has been used as tools both the symmetrical components method and the phase components method.

Analytical relations for power flow into the load-compensator ensemble established in the mathematical model, helps to explain the mechanism of load balancing by reactive compensation, showing how the compensators determine the active and reactive power redistribution between the phases of the network, thus achieving both reactive power compensation on positive sequence (for increase the power factor to the required level or for network voltage control) and load balancing (cancellation of currents on negative and zero sequence).

Shunt reactive compensation achieved with passive reactive elements (reactors and capacitors), is an efficient solution for optimization the operating conditions of networks, by increasing the power factor, voltage control and load balancing. Balancing compensators remain efficient due to relatively low cost compared to equipment type STATCOM, for the case of large loads having relatively slow variation. They will contains reactors and capacitors fixed sized so that it can compensate the higher voltage unbalances. The control of compensation currents depending on the load currents will be made by static switching equipment, with an individual command on the branches of the compensator. Such equipment is therefore SVC type and it will have like control elements reactors or capacitors

controlled by thyristors (TCRs – Thyristor - Controlled Reactors respectively TCCs – Thyristor - Controlled Capacitors). One of the disadvantages of such a compensator is given by the high value of reactive power that must be installed in passive reactive elements, which must be at least equal to the reactive load. Another disadvantage is given by the need to adopt efficient measures to mitigate the non-sinusoidal regime resulted from the operation of the SVC and to avoid the parallel resonances that may be produce between compensator and network and which can amplify the non-sinusoidal conditions.

6. References

Czarnecki, L., S. & Hsu, S., M. (1994). Thyristor controlled susceptances for balancing compensators operated under nonsinusoidal conditions, *IEE Proceedings on Electric Power Applications*, Vol. 141, No. 4, 1994, pp. 177-185

Czarnecki, L., S. (1995). Power related phenomena in three-phase unbalanced systems. *IEEE Transactions on Power Delivery*, Vol. 10, No. 3, 1995, pp. 1168-1176

Dixon, J., Morán, L., Rodríguez, J., Domke, R. (2005). Reactive Power Compensation Technologies, State of-the-Art Review, *Proceedings of the IEEE*, Vol. 93, No. 12, December 2005, pp. 2144-2164

Grünbaum, L., Petersson, A., Thorvaldsson, B. (2003). FACTS improving the performance of electrical grids, *ABB Review* (Special Report on Power Technologies), Year 2003, pp. 13-18

Gueth, G., Enstedt, P., Rey, A., Menzies, R., W. (1987). Individual phase control of a static compensator for load compensation and voltage balancing, *IEEE Transactions on Power Systems*, Vol. 2, 1987, pp. 898-904

Gyugyi, L., Otto, R., Putman, T. (1980), Principles and Applications of Static Thyristor - Controlled Shunt Compensators, *IEEE Transactions on PAS*, Vol. PAS-97, October 1980, No. 5, pp. 1935-1945

Mayordomo, J., G., Izzeddine, M., Asensi, R. (2002). Load and Voltage Balancing in Harmonic Power Flows by Means of Static VAr Compensators, *IEEE Transactions on Power Delivery*, Vol. 17, No. 3, July 2002, pp. 761-769

Said, I., K. & Pirouti, M. (2009). Neural network-based Load Balancing and Reactive Power Control by Static VAR Compensator, *International Journal of Computer and Electrical Engineering*, Vol. 1, No. 1, April 2009, pp. 25-31.

San, Y., L. & Chi, J., W. (1993). On-line reactive power compensation schemes for unbalanced three phase four wire distribution feeders, *IEEE Transaction on Power Delivery*, Vol. 8, No. 4, 1993, pp. 1958-1965

UIE [International Union for Electroheat] (1998). *Power Quality* Working group WG2, Guide to quality of electrical supply for industrial installations, Part 4: Voltage unbalance, January 1998

Compensation of Reactive Power and Sag Voltage Using Superconducting Magnetic Energy Storage System

Mohammad Reza Alizadeh Pahlavani

Malek-Ashtar University of Technology (MUT), Shabanlo St., Lavizan, Tehran
Iran

1. Introduction

Technological developments such as Flexible AC Transmission Systems (FACTS) can improve the power quality of the power system and can respond to the ever-increasing demand for electrical energy. Superconducting magnetic energy storage (SMES) is a FACTS device that has been used for several years at utility and industrial sites throughout the United States, Japan, Europe, and South Africa to provide both transmission voltage support and power quality to customers who are vulnerable to fluctuating power quality [1]-[3]. SMES systems are classified into two groups: voltage source inverter (VSI) and current source inverter (CSI) SMES. The VSI SMES has many advantages when compared with the CSI SMES; for example, in the VSI SMES, the power rating of power electronic devices that are used in the inverter is much less than that of the CSI SMES, resulting in fewer switching and power losses. Also, the VSI SMES can be used as a Static synchronous Compensator (STATCOM) when its chopper is out of service. Moreover, for the same condition, the VSI SMES can store more energy than the CSI SMES; these advantages encouraged the authors to study VSI SMES.

This type of SMES is composed of a magnetic energy storage coil with various structures and power conditioning systems that are also composed of different parts, such as AC-DC filters, a multi-level chopper, a capacitor bank, and a multi-level converter (i.e. an inverter or rectifier). These power conditioning systems are also used in many different sustainable energy systems, such as bio fuels, solar power, wind power, wave power, geothermal power, and tidal power.

The converter is an interface between the power network and the capacitor bank and controls the electrical energy exchange between the two. Likewise, the chopper is also an interface between the magnetic energy storage coil and the capacitor bank, and controls electrical energy exchange between them. To store the electrical energy in the capacitor bank and the magnetic energy storage coil in the range of mega joules, it is necessary to employ high power-rating converters; to overcome the limitations of the current and voltage range of the semiconductors, multi-level converters are used. The advantages of using such converters include reducing voltage on the switches, harmonic order correction, decreasing or eliminating lateral equipment, decreasing switching frequency, decreasing total harmonic distortion (THD), decreasing switching losses, and decreasing the output current ripple.

Multi-level converters, on the other hand, have some disadvantages associated with their use, such as the complexity of the control systems, increasing the number of power electronic devices, and increasing the asymmetry of the capacitor voltages during charge and discharge [4]-[8]. However, the trend toward increasing the speed of electronic processors and the steady decrease in the cost of power electronic devices, coupled with the ability to implement advanced modulation methods such as the SVPWM, encourage engineers to ignore the disadvantages of multi-level converters. There are three different multi-level voltage source converters: diode-clamped, flying capacitor, and cascade H-bridge. For the same voltage level, there are fewer capacitors in a diode-clamped multi-level converter than in the other multi-level converters, making it much more cost-effective than other two converters. When there are three voltage levels, a three-level diode-clamped converter is referred to as a neutral point clamped (NPC). With respect to the fact that an appropriate choice of switching strategy for SVPWM effectively reduces the low order harmonics, a novel and optimized switching strategy for SVPWM has been proposed for the first work in this chapter in order to mitigate some low order harmonics in the NPC voltage source inverter [9]-[13].

Depending on its application, a SMES device is controlled in two ways: first, the transmitted active and reactive power to the network is controlled using a NPC voltage source inverter and the capacitor voltage is stabilized using a chopper. In the second approach, the NPC voltage source inverter controls the transmitted reactive power to the network while stabilizing the capacitors voltage and the chopper controls the transmitted active power to the network. It should be noted that if the capacitors voltage is stabilized during all switching operations, low-capacity capacitors can be used in the SMES system, resulting in a lower cost of configuration. The voltage variation in low-capacity capacitors is faster during the course of supplying the power network by the SMES; consequently, a controller with a differential part, i.e. PID, will make the capacitor's voltage unstable and will transmit any noise to the power electronic devices of the chopper. Thus, PI controllers are used in this study to stabilize the capacitors voltage of the SMES by generating the real-time duty cycles of the three-level chopper in different operation modes. Stabilization of capacitors voltage will correct any imbalance due to asymmetry within the SMES circuit and its operation.

Superconducting Magnetic Energy Storage System (SMES)
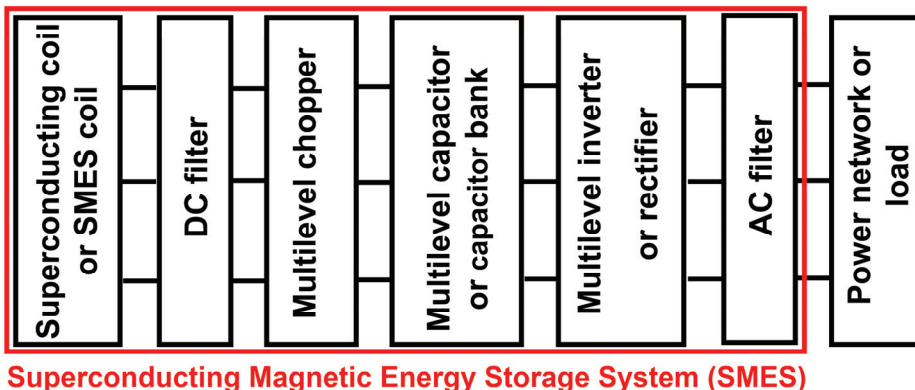
Fig. 1. The VSI SMES

Power quality is involved with a wide range of electromagnetic phenomena such as transient state, short- and long-term variations, voltage imbalance and variations, wave distortion, and frequency oscillations in power systems. In fact, the magnitude of variations in voltage, current, and frequency within power systems determines the power quality. In recent years, the voltage quality has been hailed as the most important index of power quality. Among voltage quality indicators, voltage sag has been shown to be especially important; voltage sag is defined as a temporary voltage drop that lasts between 0.5 and 30 cycles, and has a typical magnitude of 0.1 to 0.9 per unit range [14], [15].

A voltage sag can cause the same amount of downtime as a complete loss of power, especially if, for example, machines need to be rebooted or production processes need to be restarted. This issue poses a major challenge when estimating the economic cost of power interruptions and power-quality events. One way to compensate for voltage sag is to use VSI SMES, which is studied as a second work in this chapter by proposing a novel compensation algorithm. So this chapter presents a novel and optimized switching strategy and control approach for a three-level two-quadrant chopper in a three-level Neutral point clamped (NPC) voltage source inverter (VSI) superconducting magnetic energy storage (SMES). Using the proposed switching strategy, the voltage of the inverter capacitors in SMES can be independently controlled; also, the minimum power and switching losses - as well as the proper convection - can be achieved using this same strategy. The simulation results indicate that when combined with a proportional-integral (PI) control approach the proposed switching strategy can be easily implemented in the power networks and can balance and stabilize the multi-level inverters' capacitor voltage level. The voltage variation of the capacitors in the steady state condition is less than (0.062%) which is 15 times better than the IEEE standard requirement (1%). To investigate the effectiveness and reliability of the proposed approach in stabilizing capacitor voltage, SMES performance using the presented approach is compared with that of SMES when the capacitors of the three-level inverter are replaced with equal and ideal voltage sources. This comparison is carried out from the power quality point of view and it is shown that the proposed switching strategy with a PI controller is highly reliable [16]- [17]. Considering that the Space Vector Pulse Width Modulation (SVPWM) is highly effective in decreasing low order harmonics, this article utilizes this type of modulation when it is combined with the most optimized switching strategy.

In addition, this chapter proposes a new algorithm for SMES to compensate the voltage sag in the power networks. Simulation results show that the VSI SMES, when combined with the proposed algorithm, is able to compensate the voltage sag and phase voltage in less than one cycle, which is 5 times better than other voltage sag compensators.

2. Switching strategies of the three-level NPC inverter

Fig. 2 shows a case study in which a three-level NPC inverter supplies the three phase power network. A filter is used between the inverter and the power network to eliminate the high order harmonics; it is noted that parts of the low order harmonics are mitigated by applying SVPWM. Different switching states of the three-level NPC inverter are shown in Table 1: 1 and 0 indicate the on/off states of the switches, respectively. As seen in this table, in order to prevent a capacitor leg short-circuit, all switches in a leg are never turned on simultaneously.
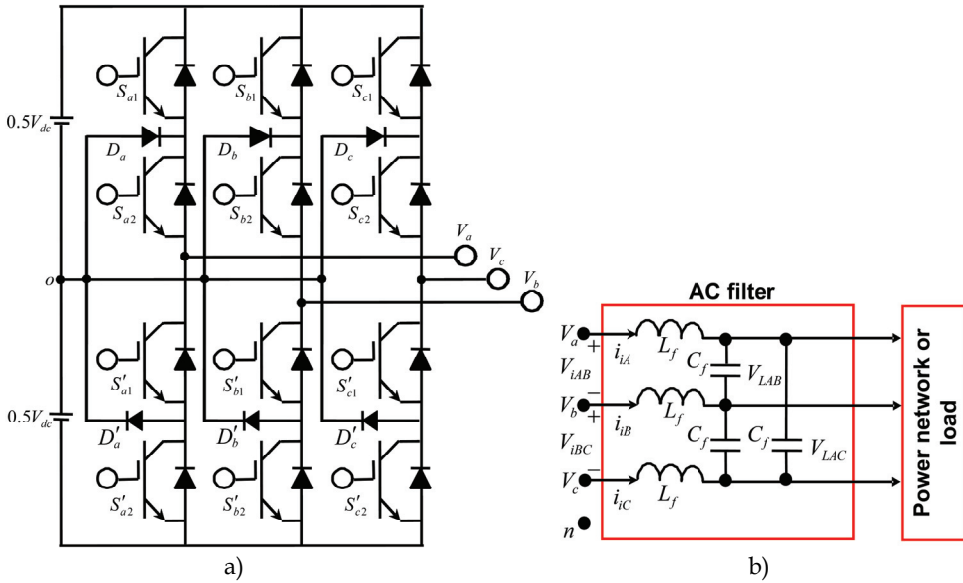
Fig. 2. a) The three-level three-phase Inverter, b) The power network (Load) and the LC Filter

C_i	S_{i1}	S_{i2}	S'_{i2}	S'_{i1}
1	1	1	0	0
0	0	1	1	0
-1	0	0	1	1

Table 1. Different switching states of the three-level inverter

From Fig. 2 and Table 1:

$$V_{io} = C_i V_{dc} / 2 \quad i = a,b,c \tag{1}$$

Assuming that the inverter output voltage is balanced and symmetrical:

$$V_{in} = V_{io} - V_{no} \tag{2}$$

$$V_{an} + V_{bn} + V_{cn} = 0 \tag{3}$$

Replacing (2) in (3) results in:

$$V_{no} = \left(V_{ao} + V_{bo} + V_{co}\right) / 3 \tag{4}$$

Also, substituting (1) and (4) in (2) gives:

$$\begin{bmatrix} V_{an} \\ V_{bn} \\ V_{cn} \end{bmatrix} = \begin{bmatrix} 2/3 & -1/3 & -1/3 \\ -1/3 & 2/3 & -1/3 \\ -1/3 & -1/3 & 2/3 \end{bmatrix} \begin{bmatrix} V_{ao} \\ V_{bo} \\ V_{co} \end{bmatrix} \tag{5}$$

If $(wt = 0)$, Park's transformation gives :

$$\vec{V}_{ref} = V_d + jV_q = \sqrt{\frac{2}{3}}\left(V_{an} + aV_{bn} + a^2V_{cn}\right), a = e^{j2\pi/3}$$

(6)

$$\vec{V}_{ref} = \frac{V_{dc}}{\sqrt{6}}\left(C_a + aC_b + a^2C_c\right)$$

(7)

Using (7) and the values of (C_a, C_b, C_c) that are given in Table 1, 27 space vectors are obtained; the corresponding space vector plan is shown in Fig. 3 and shows that the vectors $V_{14}, V_7,$ and V_0 will short-circuit the load. In fact, these vectors are zero voltage vectors in the space vector plan; the other space vectors are active vectors. The active vectors V_{21} to V_{26} that have a magnitude of $2V_{dc}/\sqrt{6}$ form a large hexagon; the active vectors V_{15} to V_{20} that have a magnitude of $V_{dc}/\sqrt{2}$ form a medium hexagon, while the active vectors that have a magnitude of $V_{dc}/\sqrt{6}$ draw a small hexagon in the space vector plan. As seen in Fig. 3, each hexagon is divided into six sectors; moreover, each sector in the large hexagon is divided into four triangles. So there are 24 triangles in the large hexagon. At any instant, the vector $\vec{V}_{ref}$ is located inside one of the 24 triangles. The average value of the output voltage $(\vec{V}_{ref})$ is computed from the linear composition of the vectors of the triangle in which $\vec{V}_{ref}$ is located, as is shown in Fig. 4.
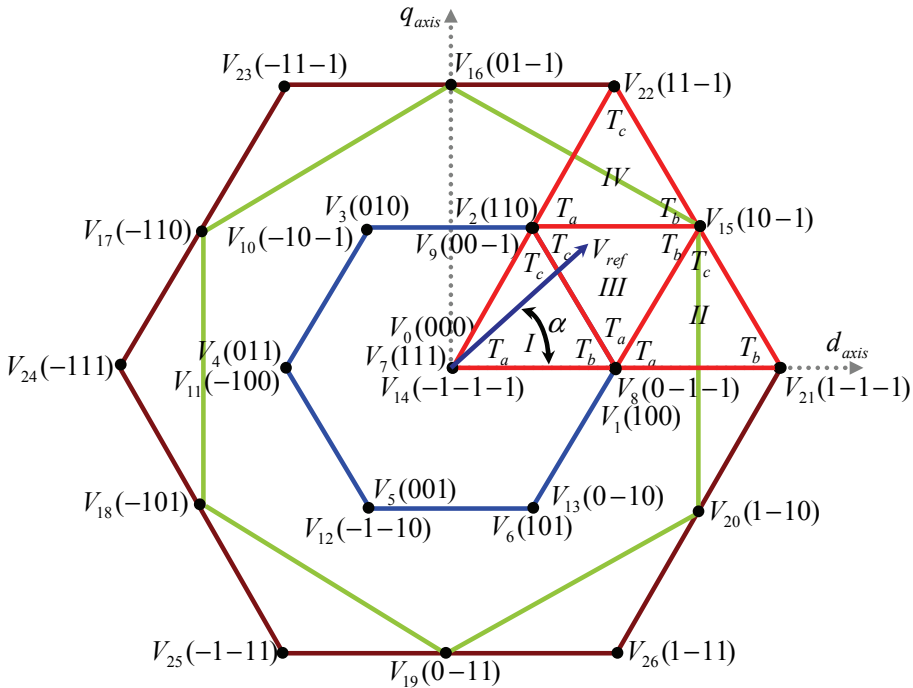
Fig. 3. The space vector plan
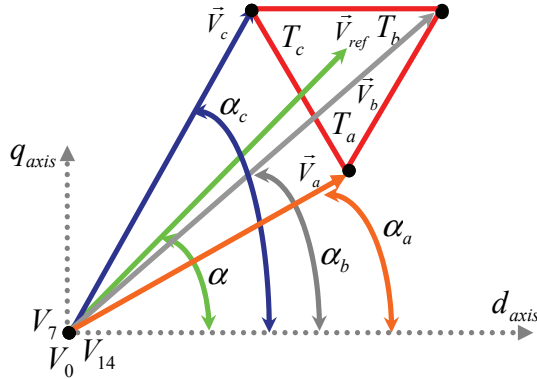
Fig. 4. Operation time calculation of each triangle vector

$$\int_0^{T_S} \vec{V}_{ref}\,dt = \int_0^{T_a} \vec{V}_a\,dt + \int_{T_a}^{T_a+T_b} \vec{V}_b\,dt + \int_{T_a+T_b}^{T_S} \vec{V}_c\,dt \tag{8}$$

$$T_S\vec{V}_{ref} = T_a\vec{V}_a + T_b\vec{V}_b + T_c\vec{V}_c \tag{9}$$

The projection of the vectors in (9) on the d-q axis and composing the obtained vectors results in:

$$T_s\left|\vec{V}_{ref}\right|\cos\alpha = T_a\left|\vec{V}_a\right|\cos\alpha_a + T_b\left|\vec{V}_b\right|\cos\alpha_b + T_c\left|\vec{V}_c\right|\cos\alpha_c \tag{10}$$

$$T_s\left|\vec{V}_{ref}\right|\sin\alpha = T_a\left|\vec{V}_a\right|\sin\alpha_a + T_b\left|\vec{V}_b\right|\sin\alpha_b + T_c\left|\vec{V}_c\right|\sin\alpha_c \tag{11}$$

$$m_a = \left|\vec{V}_{ref}\right|\bigg/\left(\frac{2}{\sqrt{6}}V_{dc}\right),$$
$$T_a + T_b + T_c = T_S, \tag{12}$$
$$\omega t + \varphi_{inv} = 2\pi f t = \alpha$$

where m_a is the modulation index, T_S is the switching period [the inverse of the switching frequency (f_S)], φ_{inv} is the inverter phase, and f is the frequency of the inverter output voltage. Assuming that the switching period, the phase, and the magnitude of the vectors $\left|\vec{V}_{ref}\right|, \left|\vec{V}_a\right|, \left|\vec{V}_b\right|,$ and $\left|\vec{V}_c\right|$ are known, solving equations (10), (11), and (12) gives $T_a, T_b,$ and T_c. These, shown in each triangle in Fig. 3, determine the operation time of the triangle vectors. Note that by knowing the value of $\omega t + \varphi_{inv}$ at any time, the number of the space sector in which $\vec{V}_{ref}$ is located can be determined. The above equations can be extended to all sectors of the large hexagon by changing α to $\alpha - ((n-1)\pi/3)$ where $n = 1, \dots, 6$ is the sector number. Table 2 gives the operation times of the vectors of the 4 triangles created in the nth sector.

triangles' number	$T_i \quad i = a, b, c$
I	$T_a = T_s - T_b - T_c$
	$T_b = 2\sqrt{2}\left\|V_{ref}\right\|T_S \sin(-\alpha + n\pi / 3) / V_{dc}$
	$T_c = 2\sqrt{2}\left\|V_{ref}\right\|T_S \sin(\alpha - (n-1)\pi / 3) / V_{dc}$
II	$T_a = T_s - T_b - T_c$
	$T_b = 2\sqrt{2}\left\|V_{ref}\right\|T_S \sin(-\alpha + n\pi / 3) / V_{dc}$
	$T_c = 2\sqrt{2}\left\|V_{ref}\right\|T_S \sin\alpha / V_{dc}$
III	$T_a = T_s - T_b - T_c$
	$T_b = -T_s + 2\sqrt{2}\left\|V_{ref}\right\|T_S \cos(\alpha + (1-2n)\pi / 6) / V_{dc}$
	$T_c = T_s - 2\sqrt{2}\left\|V_{ref}\right\|T_S \sin(-\alpha + n\pi / 3) / V_{dc}$
IV	$T_a = T_s - T_b - T_c$
	$T_b = 2\sqrt{2}\left\|V_{ref}\right\|T_S \sin(-\alpha + n\pi / 3) / V_{dc}$
	$T_c = -T_s + 2\sqrt{2}\left\|V_{ref}\right\|T_S \sin(\alpha - (n-1)\pi / 3) / V_{dc}$

Table 2. The operation times of the vectors of 4 triangles of the nth sector

Depending on the number of space vectors in each sector and the operation time of each space vector in generating $\vec{V}_{ref}$, many different switching strategies can be presented. The authors of the present work demonstrated that, in order to minimize THD in the inverter output voltage, the zero vectors should be distributed at the beginning, middle, and end of the switching periods in each sector whenever possible, [23]-[24]. Also, to minimize the switching losses, this distribution should be performed so that the minimum number of displacements in the switching states in each switching period of each sector occurs. The switching strategy of the space vector pulse width modulation is shown in Table 3; this strategy is based on the 24 triangles that were generated in the large hexagon as previously indicated. This switching strategy is implemented such that both the minimum THD and the minimum switching losses are realized. Note that C_{aij} in this table indicates the switching states in the inverter leg-a at sector *i* in triangle *j*. It should also be noted that the operation time of the vectors of each triangle in this switching strategy is determined by the times indicated in each triangle shown in Fig. 3. The switching strategy shown in Table 3 is the most appropriate strategy among the other switching strategies of the SVPWM [23] because it:
- Minimizes the THD in the line voltage
- Has the minimum THD in the phase voltage in 60% of the modulation index interval
- Creates the minimum number of the harmonic orders in both the line and the phase voltage, resulting in the minimum distortion power losses
- Has the minimum ratio of harmonic orders to the fundamental order
- Has the minimum switching losses to switching frequency ratio

- Has a low dependency of the THD on the high harmonic orders in the high modulation index.
- Reduces the size of the filter inductance (L_f). This is because the order of the low order harmonic (LOH) increases
- Creates the minimum power and switching losses in the 50% and 100% modulation index interval, respectively
- Produces the maximum number of levels in the line or phase voltage
- Provides rapid damping of the distortion factor (DF) of the line and the phase voltage versus the switching frequency. Because of this rapid damping, DF is independent of the switching frequency
- Reduces the transient time for one cycle period to obtain a sinusoidal voltage and load current
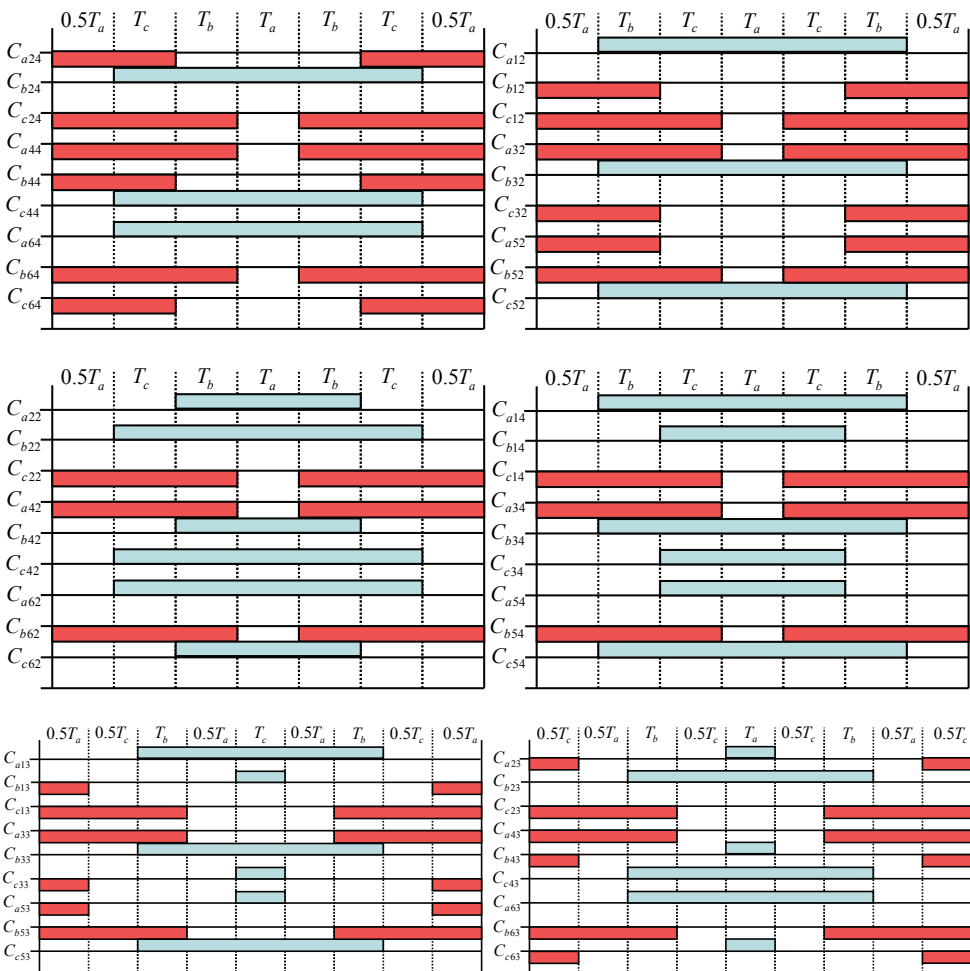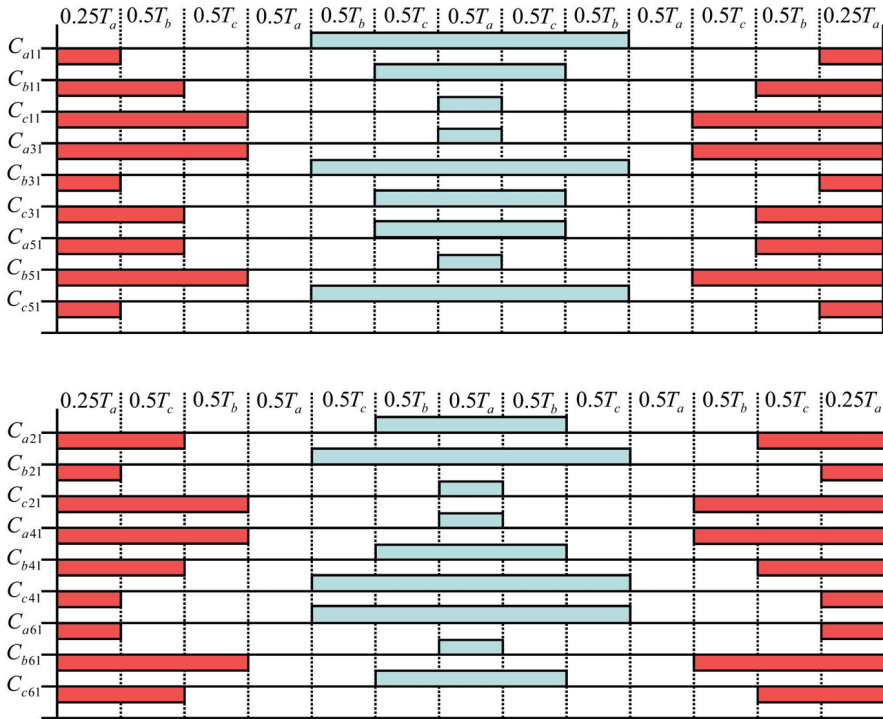
Table 3. The implemented switching strategy in the three-level NPC inverter with Space Vector Pulse Width Modulation

3. A novel switching strategy for the two-quadrant three-level chopper

As was previously discussed, the SMES control methods for stabilizing capacitors voltage depends upon the power networks. In the first control approach, the transmitted active and reactive power to the network is controlled by a NPC voltage source inverter, while the capacitors voltage is stabilized using a chopper. This approach is used to investigate the interaction between the SMES and the power networks. This control approach is easily implemented if an optimized and appropriate switching strategy for the chopper is defined; 5 shows a two-quadrant three-level chopper that was studied in this work.

In Table 4, all possible switching states in the three-level chopper as well as the SMES coil current path are provided. One of the main requirements for the switching strategy of the multi-level choppers is to minimize both the switching losses and the frequency in order to eliminate the need for high frequency electronic switches. Moreover, minimization of the power loss is obtained by minimizing the number of on-switches with the minimum on-time in each switching period. Therefore, the switching states in which each chopper switching period creates the minimum number of displacements in the switching states are selected as the best states for the SMES coil charge and discharge modes. The optimum switching states are highlighted in Table 4; other switching states that do not satisfy the aforementioned conditions were not used [28].

Mode	V_{load}	$(S_{d1},S_{d2},S'_{d1},S'_{d2})$	Current path
FCM	$V_{C1}+V_{C2}$	(1111)	$S'_{d1},S'_{d2},S_{d1},S_{d2}$
CM	V_{C2}	(0111)	$S'_{d1},S'_{d2},D_d,S_{d2}$
	0	(0110)	S'_{d1},D'_d,D_d,S_{d2}
	V_{C1}	(1110)	$S'_{d1},D'_d,S_{d1},S_{d2}$
FDM	$-V_{C1}-V_{C2}$	(0000)	D_e,D'_e
DM	$-V_{C2}$	(0010)	S'_{d1},D'_d,D'_e
	0	(0110)	S'_{d1},D'_d,D_d,S_{d2}
	$-V_{C1}$	(0100)	D_e,D_d,S_{d2}
Unusable	0	(1100)	D_e,S_{d1},S_{d2}
	0	(1101)	D_e,S_{d1},S_{d2}
	0	(1011)	S'_{d1},S'_{d2},D'_e
	0	(0011)	S'_{d1},S'_{d2},D'_e
	$-V_{C1}$	(0101)	D_e,D_d,S_{d2}
	$-V_{C1}-V_{C2}$	(1010)	D_e,D'_e
	$-V_{C1}-V_{C2}$	(1001)	D_e,D'_e
	$-V_{C1}-V_{C2}$	(1000)	D_e,D'_e
	$-V_{C1}-V_{C2}$	(0001)	D_e,D'_e

Table 4. Switching states in a two-quadrant three-level chopper

Another requirement in the switching strategy of the multi-level choppers is the independent action of the capacitors voltage controllers. The switching strategy that satisfies the two cited requirements is outlined in Table 5. The charge and discharge modes (CM and DM) in Table 5 are obtained from the proper states in Table 4, assuming that the chopper switching period is $2T_{ch}$.

Note that T_o and T_u are, respectively, the operation times that the voltage of the upper and lower capacitors are connected to the positive and the negative polarities of the load during the charge and the discharge modes. Also, T_z is the chopper operation time when the load is short circuit; this occurs at both the charge and discharge modes. Hence, the duty cycles of the chopper can be defined as follows:

$$d_o = T_o/2T_{ch}, d_u = T_u/2T_{ch}, T_o + T_u + T_z = 2T_{ch} \tag{13}$$

From this equation, it can be seen that d_o, d_u, and d_z vary within the range [0, 1]. Also, Table 5 shows that in the charge and the discharge modes, $d_o + d_u$ is always less than one, which means that the required time for compensating the capacitor voltage to the reference voltage is less than a single switching period of the chopper. In other words, if $d_o + d_u$ is more than one, the required time for the compensation of the capacitors voltage to the reference voltage will be more than a single switching period of the chopper.

In this case, the compensation of the capacitors voltage to the reference voltage should be performed simultaneously. The fast charge and discharge (FCM and FDM) modes have

been considered for this case; note that in changing from the fast charge mode to the charge mode, or from the fast discharge mode to the discharge mode and vice versa, the minimum number of switch displacements of each chopper switching period occurs, resulting in a minimum of switching losses presenting an advantage of the proposed switching strategy.
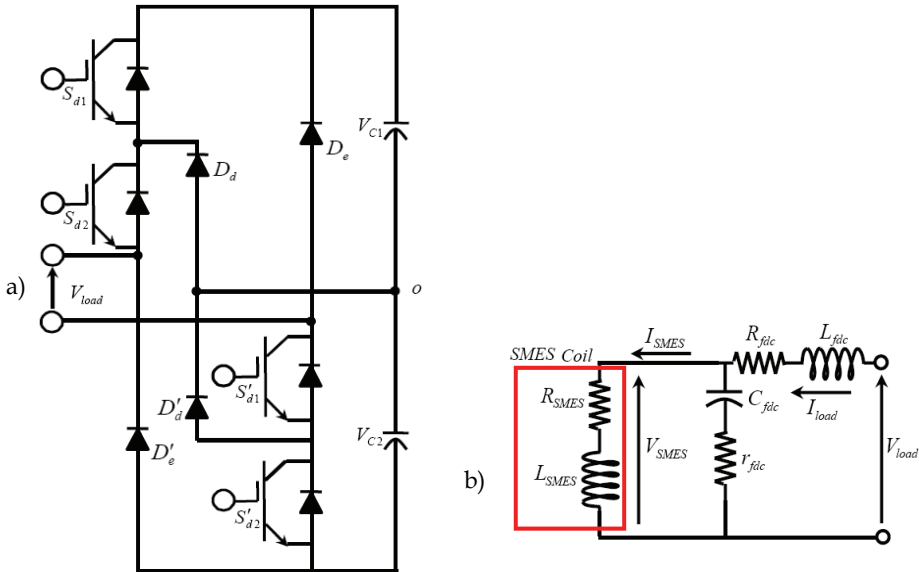
Fig. 5. a) The two-quadrant three-level chopper, b) The load (DC filter and SMES coil)
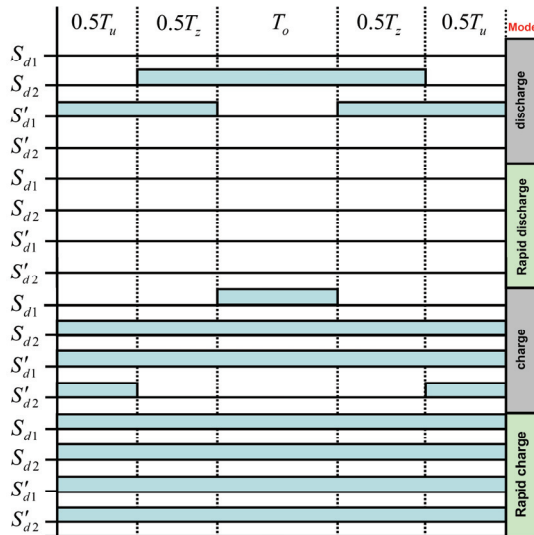
Table 5. The implemented switching strategy in the two-quadrant three-level chopper

4. Chopper duty cycle controller design

In this section, a block diagram for generating the duty cycle of CM and FCM is presented (Fig. 6). To enhance the system dynamic response when balancing the capacitors voltage, it is necessary to ensure that the capacitors voltages are equal prior to connecting the inverter to the power network. To achieve this, the voltages of the upper and the lower capacitors are compared with the reference voltage, which is assumed to be $0.5V_{dc}$, as seen in Fig. 6. Subsequently, the difference in the voltages is passed through the limiters with [0 0.5] interval. These limiters work so that each capacitor is charged for only 50% of the switching period; in fact, the outputs of these limiters can only produce the charge mode (CM). After connecting the inverter to the power network, the PI controllers begin operating and the voltage errors are fed to these controllers. Using the signal holders, the outputs of the PI controllers are sampled every $2T_{ch}$ period. The signal holders with a $2T_{ch}$ sampling time are used to avoid abrupt variations in the duty cycles. If the duty cycles vary abruptly, the turn on/off times should be zero, but this is practically impossible. The signal holder outputs are passed through the limiters with [0 1] interval; these limiters can produce both the charge and the fast charge modes (CM, FCM).
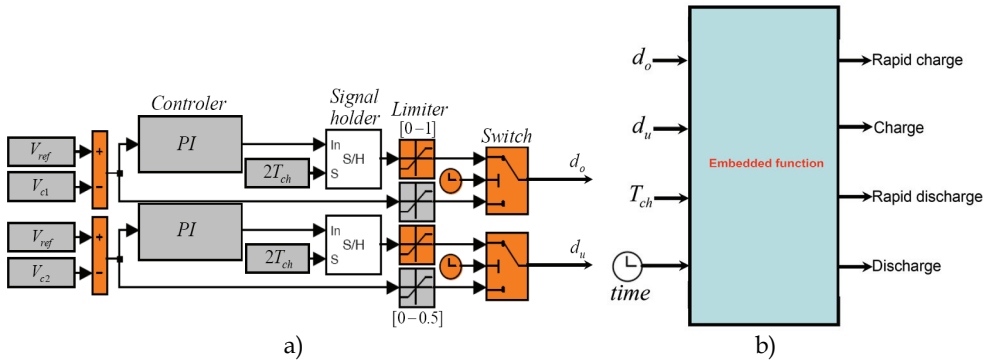
Fig. 6. The chopper duty cycle controller

With the availability of d_o, d_u, T_{ch}, and by using the Embedded MATLAB Functions shown in Fig. 6, the various modes of the chopper (CM, FCM, DM, and FDM) can be determined. Finally using these modes, the corresponding switching strategies are applied to the chopper switches based on Table 5.

5. Simulation results of the switching strategy of the three-level chopper

In this section, the strategies presented in sections 2 through 4 are simulated using MATLAB® software. The power network to which the SMES is connected is shown in Fig. 7 and was modeled using the M-file in MATLAB®. The power network and the SMES parameters are given in Appendix I.

In Fig. 8, the SMES performance using the developed approaches is compared with that of the SMES when the capacitors of the three-level NPC inverter are replaced with equal and ideal voltage sources (SMES with ideal VSI). These comparisons are from the perspective of the THD and the DF of the inverter output line voltage. As seen in this figure, the

performance of the SMES using the chopper duty cycle controller is the same as that of the SMES with an ideal VSI.
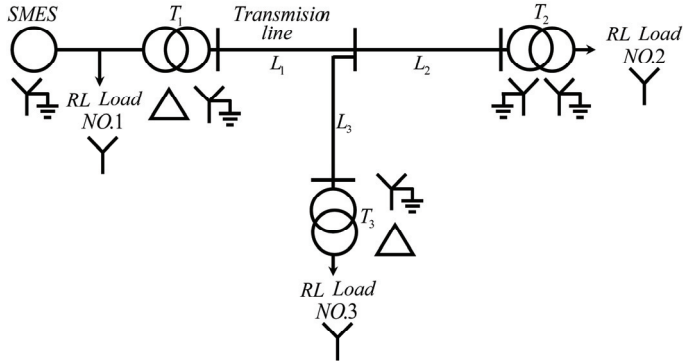
Fig. 7. The power network
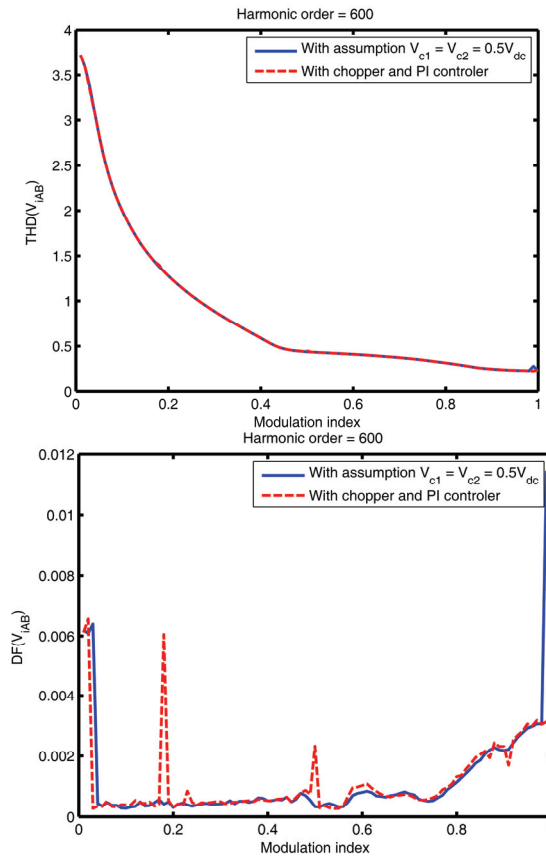
Fig. 8. THD and DF variation of the inverter output line voltage

Fig. 9 shows the voltage variation of the capacitors versus the modulation index; this figure indicates that the proposed schemes are capable of stabilizing the capacitors voltage to the reference voltage (with less than 0.5% error in the worst case scenario). The smallest voltage variation (with 0.0625% error) is obtained when the modulation index is 0.65, as shown in Figure 9. This is because PI controllers have been regulated for this modulation index; in short, the variation of the capacitor voltage depends on both the modulation index and the parameters of the PI controllers. Therefore, in order to obtain the best results, it is recommended that the parameters of the PI controllers be deregulated for each modulation index.
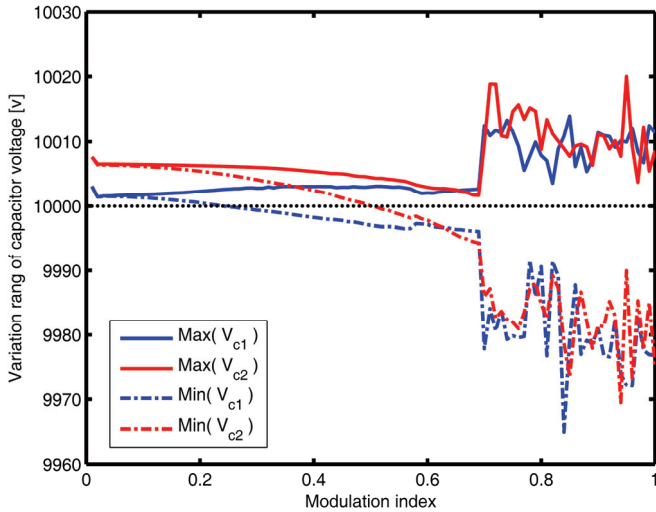
Fig. 9. The capacitors voltage variation versus index modulation
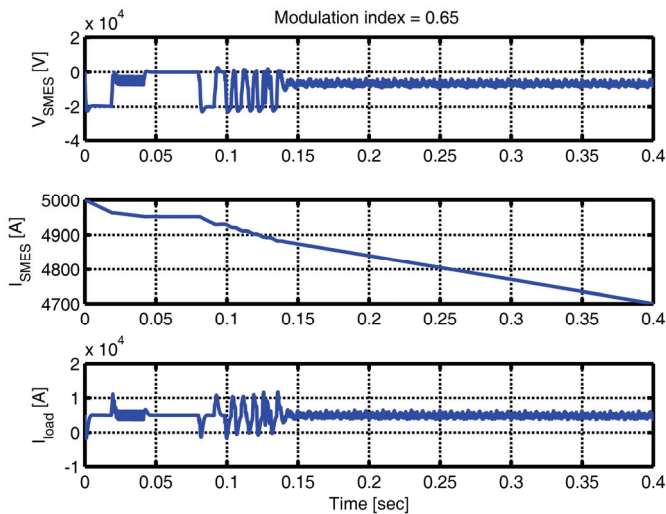
Fig. 10. The current and the voltage of the SMES coil and the current of the load

Fig. 10 shows the voltage and current of the SMES coil and the current of the load. From this figure, it can be seen that the current of the SMES coil is decreasing, or rather, that the stored energy in the coil is discharging. The discharged energy is transmitted to the chopper in the active power form because in this transmission, the current of the load and the voltage of the SMES coil remain constant.
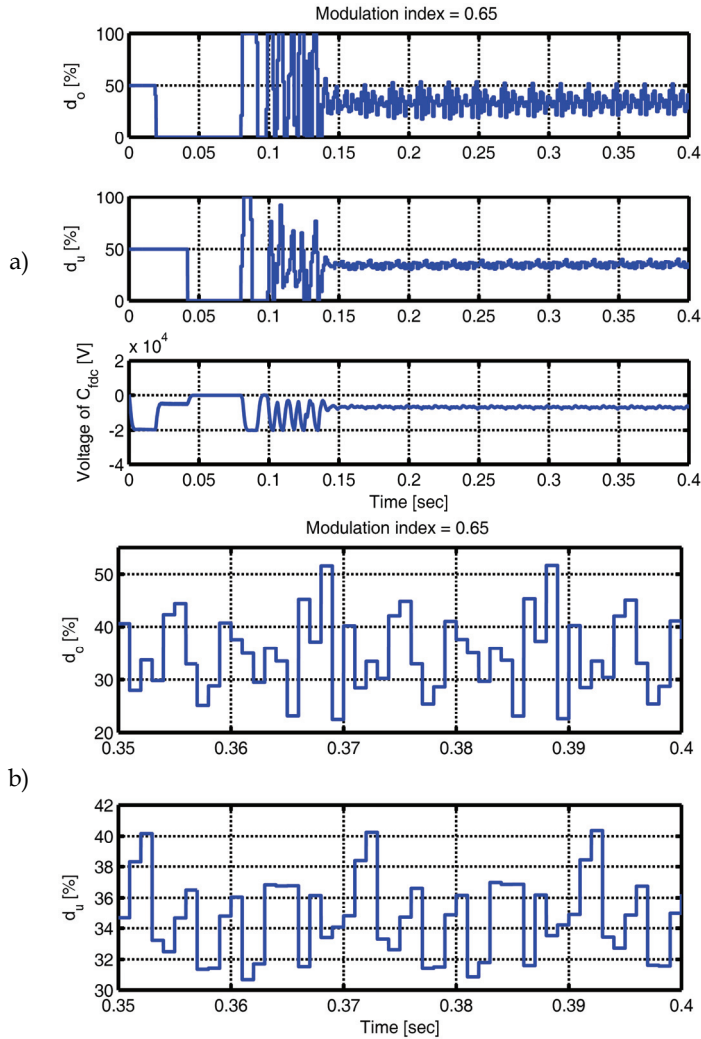
Fig. 11. a) The voltage of the capacitor C_{fdc} and the chopper duty cycle percent,
b) Steady state duty cycle percent

Fig. 11 depicts the variation of the chopper duty cycle and the voltage of the DC filter capacitor. In this figure, the inverter is connected to the power network at $t = 0.08\,[\text{sec}]$. It is concluded from this figure that before $t = 0.08\,[\text{sec}]$, the CM mode has been selected by the

Embedded MATLAB function, and after this time, both the CM and the FCM modes have been selected as well. Also, as observed in Fig. 11a, the voltage of the C_{fdc} is important in stabilizing the voltage of the SMES coil; Fig. 11b shows that in steady state condition, only the CM mode occurs for this power network.

Fig. 12 shows the voltage variation of the capacitors; the initial voltages of the capacitors C_1 and C_2 were $9800\,[V]$ and $9500\,[V]$, respectively. As noticed in Fig. 12, the proposed switching strategy properly stabilizes the capacitors voltage before and after connecting the inverter to the power net-work. In Fig. 12, the voltage variations of the capacitors in the steady state condition, as can be verified in Fig. 9, is less than $6.25\,[V]$ (0.062%) Compared with the values defined in the IEEE standard specifications and obtained in [27] (i.e. 1%), this value has been reduced approximately 15 times.
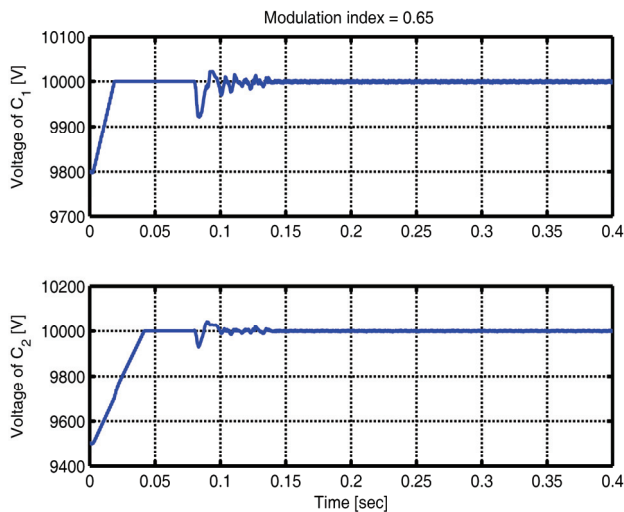
Fig. 12. Variation of the voltage of the capacitors C_1 and C_2

The parameters of the PI controllers, as seen in Appendix I, should be independently tuned for the upper and lower capacitors. This is because when using the SVPWM, the upper and the lower capacitors are not discharged at the same rate; consequently, the number of the PI controllers should be equal to that of the level of the inverters, and the parameters of each PI controller should be independently tuned. In fact, using this approach, the voltage of the inverter capacitors can be stabilized even when the power network is asymmetric and unbalanced. To verify the simulation results obtained by the proposed switching strategy given in Tables 3 and 4, part of the implemented switching strategy in the inverter and the three-level chopper are shown in Figs. 13 and 14, respectively. These figures show that the carrier waves of the chopper and the inverter are triangular, that the period of these carrier waves for the inverter and the chopper are $2T_S = 0.001\,[\mathrm{sec}]$ and $2T_{ch} = 0.001\,[\mathrm{sec}]$, and that their magnitudes are T_S and T_{ch}, respectively.

In Fig. 15, the steady state line voltage and the current of loads 2 and 3 are shown. Fig. 16 shows the steady state line voltage and the current of the inverter prior to filtering.

Comparisons of Figs. 15 and 16 show that the AC passive filter successfully filters out the current and the voltage harmonics that are produced by the inverter at the load terminals.
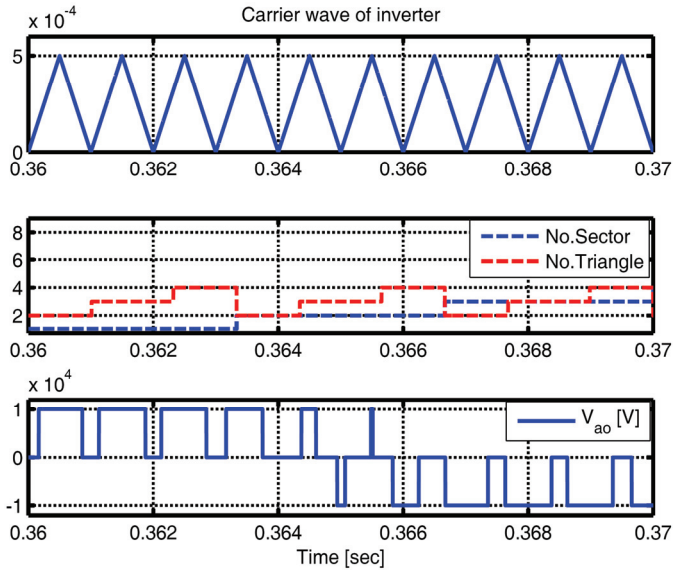
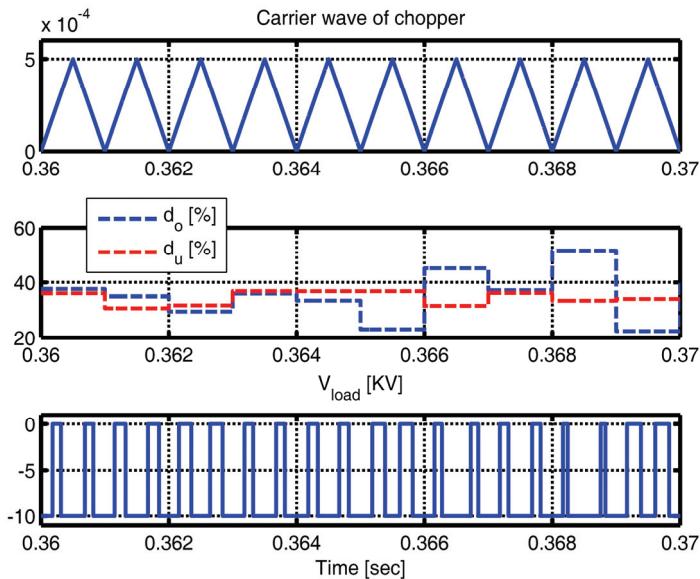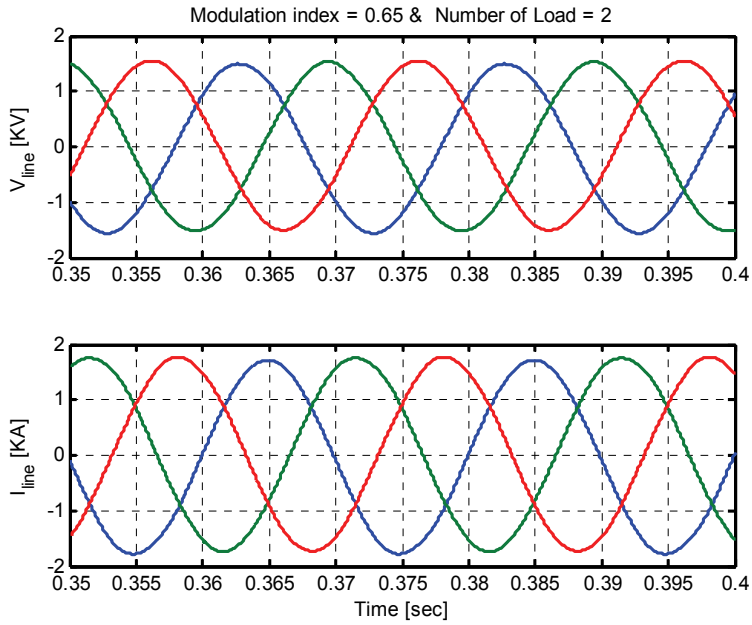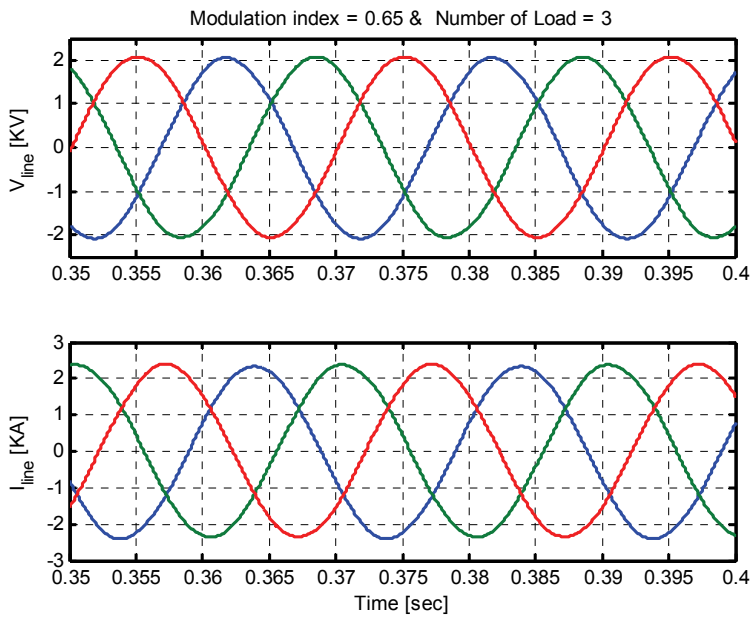Fig. 13. Part of the proposed switching strategy for the inverter using the SVPWM

Fig. 14. Part of the proposed switching strategy for the three-level chopper

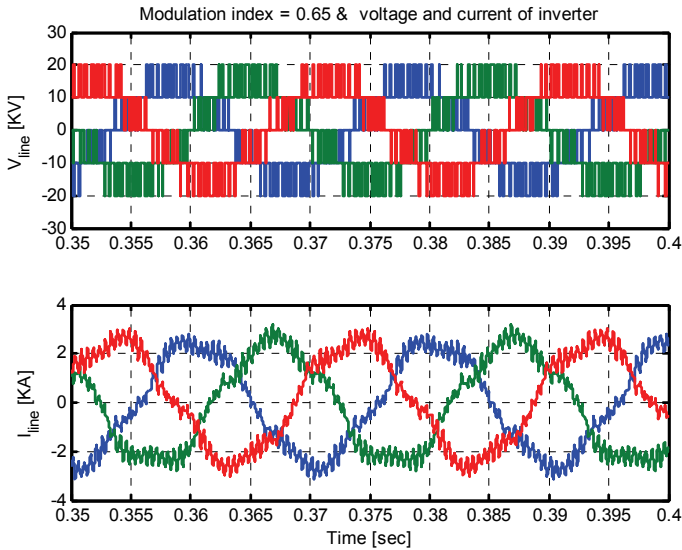Fig. 15. Steady state line voltage and the current of the loads: a) No.2, b) No.3.

Fig. 16. The steady state output voltage and the current of the inverter

6. Voltage sag compensation algorithm

Here, a new algorithm is presented to compensate the sag voltage in an R-L load using SMES. Fig. 17 shows the configuration of the studied power network, the R-L loads, and the SMES.
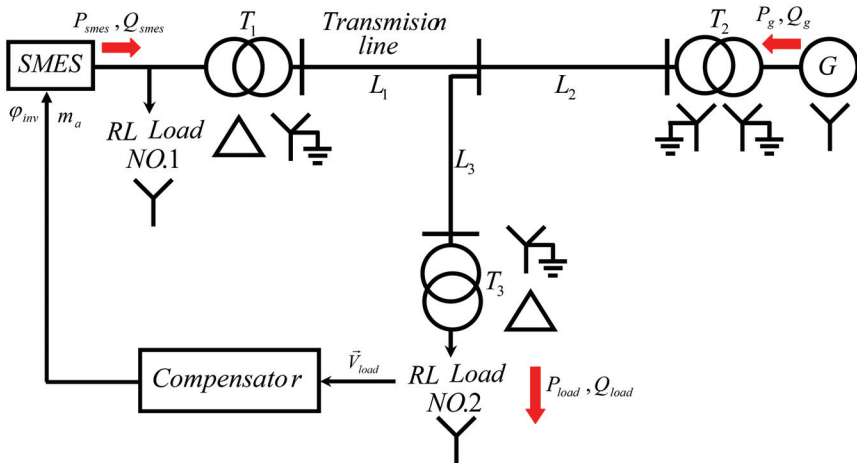
Fig. 17. Configuration of the R-L load, the SMES, and the power network

To compensate the voltage sag using SMES, it is necessary that the proper values of m_a and φ_{inv} be calculated and applied to the inverter. If the phasor voltage of the R-L load 2

(resulting only from the generator) before and after the voltage sag is shown by $\vec{v}_p$ and $\vec{v}_n$, respectively, and the phasor voltage of this R-L load (resulting only from connecting the SMES to the power network) after the voltage sag is shown by $\vec{v}_{smes}$, then the phasor diagram of the R-L load voltage can be shown as given in Fig. 18, using which, the following equations can be obtained:

$$\varphi_{smes} = \tan g^{-1}\left(\frac{v_p \sin \varphi_p - v_n \sin \varphi_n}{v_p \cos \varphi_p - v_n \cos \varphi_n}\right) \qquad (14)$$

$$v_{smes} = \left(v_p \cos \varphi_p - v_n \cos \varphi_n\right)\big/\cos \varphi_{smes} \qquad (15)$$

By calculating φ_{smes} and v_{smes} from (14) and (15), and by using the power flow that considers only the effect of the SMES system, the values of the m_a and φ_{inv} for applying to the three-level NPC inverter can be calculated.
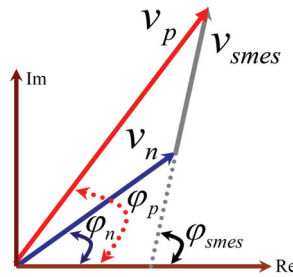
Fig. 18. The phasor diagram of the voltage sag compensation in the R-L load

7. Simulation rsults and dscussion

The power network shown in Fig. 17 was simulated using MATLAB software; the parameters used in this figure are the same as those defined in Fig. 7, and the parameters for the generators are provided in Appendix I; in addition, the sag compensation of the voltage for load 2 using the SMES is shown in Fig. 19. In this study, the voltage of the generator drops to 0.5 [$p.u.$]; in Fig. 19a, the voltage immediately decreases at $t = 0.5$ [sec] from its full value to the sag value in essentially zero time, while in Fig. 19b, the same observation occurs during one cycle in ramp rate. In Figs. 19a and b, the *Compensator* begins sampling the magnitude and phase of the voltage of load 2 after one cycle and again after three cycles of voltage sag, respectively. As can be seen in this figure, the SMES successfully uses the proposed algorithm and compensates the load voltage in less than one cycle. Performance comparison shows that the dynamic response time of the SMES using the proposed algorithm when compensating for the voltage sag is 5 times faster than that which is presented in [32], and is equal to the responses obtained by the current source inverter (CSI) SMES presented in [33]-[36].

To study the active and reactive powers at steady state, in all other figures that are presented in this section, the *Compensator* is regulated to begin measuring and compensating after three cycles of the voltage sag. Fig. 20 shows the compensation of the phase and the

magnitude of the voltage of load 2. As seen in this figure, the SMES uses the presented algorithm to successfully compensate both the magnitude and the phase of the load voltage and return them to their initial values. In Fig. 20, the voltage variation of the load in steady state condition is approximately $1.1559\,[V]\,(0.0365\%)$, which is 136 times less than the IEEE-519 standard (5%).
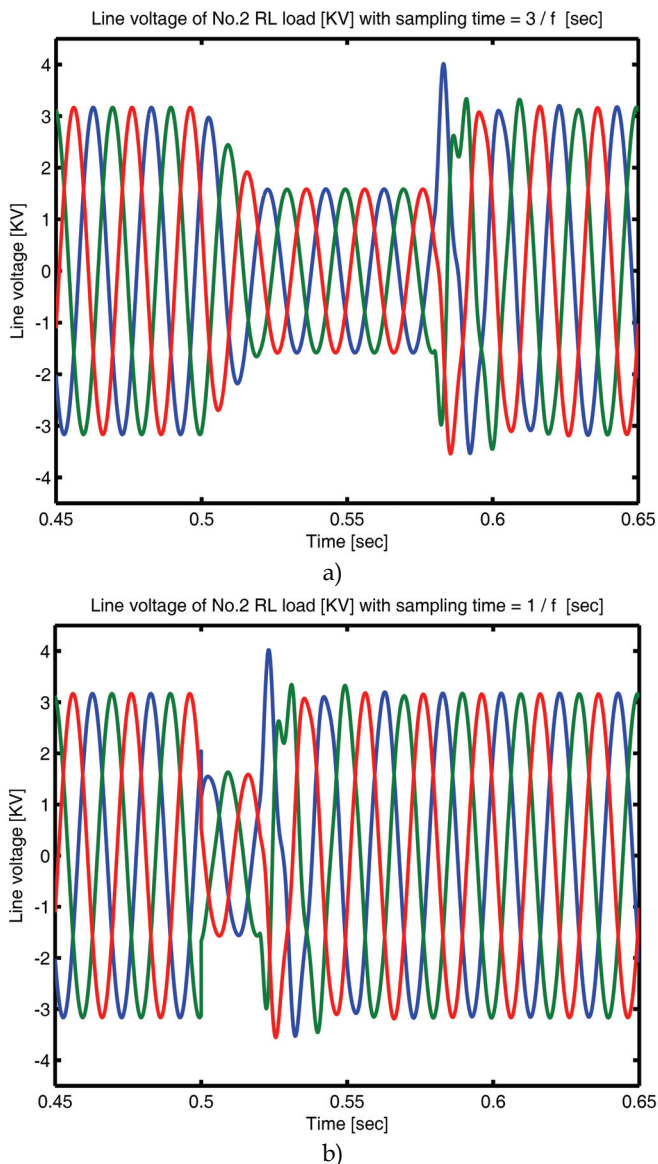
Line voltage of No.2 RL load [KV] with sampling time = 3 / f [sec]

a)

Line voltage of No.2 RL load [KV] with sampling time = 1 / f [sec]

b)

Fig. 19. The voltage sag compensation of the load No. 2
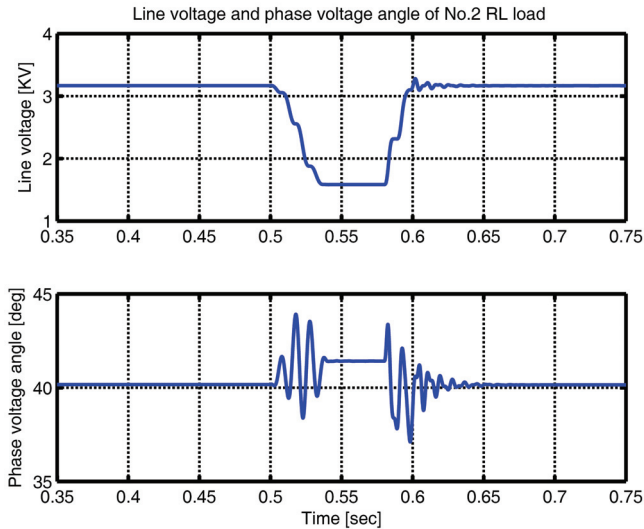
Fig. 20. Compensation of the phase and magnitude of the voltage of the load No. 2.

8. Conclusion

In this study an appropriate switching strategy for the NPC VSI with several advantages for the SMES regarding its ability to improve the performance of this device was presented. Some advantages of using this strategy for the NPC VSI presented in this chapter include:

- Optimizing power quality by implementing a proper switching strategy in SVPWM for VSI SMES
- Better stabilization of the capacitors voltage of the VSI SMES than that of the IEEE standard
- Implementing the rapid charge and discharge modes as opposed to the charge and discharge modes in order to increase the dynamic response time when stabilizing the capacitors voltage of the VSI SMES
- Independent control of the capacitors voltage in the VSI SMES for compensating asymmetric and unbalanced loads
- Minimizing the switching and power losses, resulting in easy and reliable convection from multi-level converter's switches
- Using the proposed switching strategies, resulting in the power quality becoming equal with the case in which the capacitors of the inverter are replaced with an ideal and equivalent voltage source (SMES with ideal VSI)
- Effective and highly reliable performance of the presented strategy when used with a PI control approach
- Compensating capacitors voltage of the VSI SMES prior to connecting the SMES to the power network (stand-by mode)
- Furthermore, an algorithm was presented for the VSI SMES in order to compensate the voltage sag. Some advantages of the proposed algorithm include:
- Compensating the voltage sag and the voltage phase of the load in less than one cycle

- Compensating the active and the reactive power in less than four cycles
- Load voltage stabilizing in good agreement with the IEEE-519 standard

9. Appendix I

The parameters of the PI controllers:

$$KP_O = 0.1, KI_O = 0.1, KP_U = 0.04, KI_U = 0.03$$

Specifications of the transmission line:

$$X_{L_1} = 15\,[\Omega], R_{L_1} = 1.5\,[\Omega], X_{L_2} = 15\,[\Omega],$$
$$R_{L_2} = 1.5\,[\Omega], X_{L_3} = 30\,[\Omega], R_{L_3} = 3\,[\Omega]$$

Specifications of the synchronous generator:

$$X_G = 0.15\,[p.u.], R_G = 0.015\,[p.u.],$$
$$V_G = 20\,[KV], S_G = 50\,[MVA]$$

Specifications of the transformers:

$$X_{T_1} = 0.1\,[p.u.], R_{T_1} = 0.01\,[p.u.], S_{T_1} = 30\,[MVA],$$
$$V_{T_1} = 20\,/\,132\,[KV], X_{T_2} = 0.1\,[p.u.], R_{T_2} = 0.01\,[p.u.],$$
$$S_{T_2} = 30\,[MVA], V_{T_1} = 132\,/\,20\,[KV], X_{T_3} = 0.1\,[p.u.],$$
$$R_{T_3} = 0.01\,[p.u.], S_{T_3} = 50\,[MVA], V_{T_3} = 132\,/\,13.2\,[KV]$$

Specifications of the R-L loads:

$$L_{RL_1} = 2\,[mH], R_{RL_1} = 5\,[\Omega], S_{RL_1} = 30\,[MVA],$$
$$V_{RL_1} = 18\,[KV], L_{RL_2} = 0.2\,[mH], R_{RL_2} = 0.5\,[\Omega],$$
$$S_{RL_2} = 30\,[MVA], V_{RL_2} = 18\,[KV], L_{RL_3} = 0.2\,[mH],$$
$$R_{RL_3} = 0.5\,[\Omega], S_{RL_3} = 50\,[MVA], V_{RL_1} = 13.2\,[KV]$$

Assumed specifications of the NPC VSI and the SMES:

$$IGBT : SEMIKRONSKM, R_{IGBT} = 0.75\,[m\Omega], V_{FO} = 1.1\,[V],$$
$$P_S = 0.05\,[W], V_{dc} = 20\,[KV], f_{ch} = 2\,[KHz], C_f = 400\,[\mu F]$$
$$L_f = 800\,[\mu H], L_{fdc} = 1\,[mH], R_{fdc} = 20\,[m\Omega], M = 0.65,$$
$$f = 50\,[Hz], L_{SMES} = 10\,[H], R_{SMES} = 2\,[\mu\Omega], C_2 = 200\,[mF]$$
$$C_{fdc} = 700\,[\mu F], r_{fdc} = 2\,[\Omega], f_s = 2\,[KHz], C_1 = 200\,[mF]$$

10. References

[1] S. Massoud Amin, Clark W. Gellings, The North American power delivery system: Balancing market restructuring and environmental economics with infrastructure security, *Energy*, Volume 31, Issues 6-7, May-June 2006, Pages 967-999.

[2] Z. Xiaoxin, Y. Jun, S. Ruihua, Y. Xiaoyu, L. Yan, T. Haiyan, An overview of power transmission systems in China, *Energy*, In Press, Corrected Proof, Available online 12 June 2009.

[3] H. Chao, Global electricity transformation The critical need for integrated market design and risk management research, *Energy*, Volume 31, Issues 6-7, May-June 2006, Pages 923-939.

[4] A. A. Bayod-Rújula, Future development of the electricity systems with distributed generation, *Energy*, Volume 34, Issue 3, March 2009, Pages 377-383.

[5] M. R. Qader, Optimal location of advanced static VAR compensator (ASVC) applied to non-linear load model, *Energy*, Volume 31, Issue 12, September 2006, Pages 1761-1768.

[6] A. B. Cambel, F.A. Koomanoff, High-temperature superconductors and CO_2 emissions, *Energy*, Volume 14, Issue 6, June 1989, Pages 309-322.

[7] P. Varghese, K. Tam, Structures for superconductive magnetic energy storage, *Energy*, Volume 15, Issue 10, October 1990, Pages 873-884.

[8] V. D. Linden, Septimus, Bulk energy storage potential in the USA, current developments and future prospects, *Energy* Volume 31, Issue 15, December 2006, Pages 3446-3457.

[9] H. Li, T. L. Baldwin, C. A. Luongo, and D. Zhang, A Multilevel Power Conditioning System for Superconductive Magnetic Energy Storage, *IEEE Trans, Applied Superconductivity*, vol. 15, no. 2, Jun. 2005.

[10] J. Shi, Y. Tang, L. Ren, J. Li, and S. Cheng, Discretization-Based Decoupled State-Feedback Control for Current Source Power Conditioning System of SMES, *IEEE Trans. Power Del*, vol. 23, no. 4, Oct. 2008.

[11] H. Zhang, J. Ren, Y. Zhong, J. Chen, Design and Test of Controller in Power Conditioning System for Superconducting Magnetic Energy Storage, *In Proc. The 7th International Conference on Power Electronics* Oct. 22-26, 2007 / Exco, Daegu, Korea.

[12] D. H. Leea, Power conditioning system for superconductive magnetic energy storage based on multilevel voltage source converter, *Blacksburg, Virginia,* July 6, 1999.

[13] S. Nomura, N. Watanabe, C. Suzuki, H. Ajikawa, M. Uyama, S. Kajita, Y. Ohata, H. Tsutsui, S. Tsuji, R. Shimada, Advanced configuration of superconducting magnetic energy storage, *Energy*, Volume 30, Issues 11-12, August-September 2005, Pages 2115-2127.

[14] P. H. Rebut, Perspectives on nuclear fusion, *Energy,* Volume 18, Issue 10, October 1993, Pages 1023-1031.

[15] G. Boukettaya, L. Krichen, A. Ouali, A comparative study of three different sensor less vector control strategies for a Flywheel Energy Storage System, *Energy*, Volume 35, Issue 1, January 2010, Pages 132-139.

[16] M. Saxe, A. Folkesson, P. Alvfors, Energy system analysis of the fuel cell buses operated in the project: Clean Urban Transport for Europe, *Energy,* Volume 33, Issue 5, May 2008, Pages 689-711.

[17] P. Purkait and R. S. Sriramakavacham, A New Generalized Space Vector Modulation Algorithm for Neutral point clamped Multi-level Converters, *Progress in Electromagnetic Research Symposium*, Cambridge, USA, pp. 26-29, Mar. 2006.

[18] L. G. Franquelo, Simple and Advanced Three dimensional Space Vector Modulation Algorithm for Four-Leg Multi-level Converters Topology,*In 30th Annual Conference of the IEEE Industrial Electronics Society*, Busan, Korea, pp. 2 – 6, Nov. 2004.

[19] K. Zhou and D. Wang, Relationship between Space Vector Modulation and Three-Phase Carrier-Based PWM A Comprehensive Analysis, *IEEE Trans, Industrial Electronics*, vol. 49, no. 1, Feb. 2002.

[20] M. Delos, A. M. Prats, New Space Vector Modulation Algorithms, *HAIT Journal of Science and Engineering B*, vol. 2, Issues 5-6, pp. 690-714, 2005.

[21] A. Kwasinski, Time Domain Comparison of Pulse-Width Modulation Schemes, *IEEE Power Electronics Letters*, vol. 1, no. 3, Sep. 2003.

[22] T. Bernet, S. Recent, Development of High Power Converters for Industry and Traction Application, *IEEE Trans. on Power Electronics*, Vol. 15, Nov. 2000.

[23] M. R. Alizadeh Pahlavani, A. Shoulaie, Comparison of Space Vector Pulse Width Modulation Switching Patterns in Three Level Inverter to Approach Power Quality Factors, *in Proc. 23rd International Power System Conf*, Tehran, Iran, Nov. 2008, Persian.

[24] M. R. Alizadeh Pahlavani, A. Shoulaie, Switching Pattern Optimization of Space Vector Pulse Width Modulation In Two Level Inverters With Different Objective Functions, *in Proc. 22nd International Power System Conf*, Tehran, Iran, October. 2007, Persian.

[25] A. K. Gupta, A. M. Khambadkone, A Space Vector PWM Scheme for Multilevel Inverters Based on Two-Level Space Vector PWM, *IEEE Trans, Industrial Electronics*, vol. 53, no. 5, Oct. 2006.

[26] A. K. Gupta, A. M. Khambadkone, A Simple Space Vector PWM Scheme to Operate a Three-Level NPC Inverter at High Modulation Index Including Overmodulation Region, With Neutral Point Balancing,*IEEE Trans, Industrial Applications*, vol 43, no. 3, May/June 2007.

[27] H. Mao, D. Boroyevich and F. C. Lee, Multi-level 2-quadrant boost choppers for superconducting magnetic energy storage, *Conference of the IEEE*.1996.

[28] M. R. Alizadeh Pahlavani, H. A. Mohammadpour, A. Shoulaie, A Novel Scheme for Chopper Switching to Control Three Level Inverter Capacitor Voltage, *17th Iranian Conference on Electrical Engineering (ICEE),* Tehran, Iran, IUST, 2009, Persian.

[29] M. H. J. Bollen, Understanding power quality problems-voltage sags and interruptions, *IEEE Pres*, 2000.

[30] Recommended practice for the establishment of voltage sag indices, Draft 6, *IEEE P1564*, Jan. 2004.

[31] K. H. LaCommare, J. H. Eto, Cost of power interruptions to electricity consumers in the United States (US), Energy, Volume 31, Issue 12, September 2006, Pages 1845-1855

[32] A. Bra, P. Hofinann, R. Mauro, C. J. Melhorn, An Evaluation of Energy Storage Techniques for Improving Ride-Through Capability for Sensitive Customers on Underground Networks, *in Proc. 1996 IEEE*.

[33] X. Jiang, X. Liu, X. Zhu, Y. He, Z. Cheng, X. Ren, Z. Chen, L. Gou, and X. Huang, A 0.3 MJ SMES Magnet of a Voltage Sag Compensation System, *IEEE Trans, Applied Superconductivity*, vol. 14, no. 2, Jun. 2004.

[34] X. Jiang, X. Zhu, Z. Cheng, X. Ren, and Y. He, A 150 kVA/0.3 MJ SMES Voltage Sag Compensation System, *IEEE Trans, Applied Superconductivity*, vol. 15, no. 2, Jun. 2005.

[35] A. Rong Kim, G. Kim, J. H. Kim, M. Hasan Ali, M. Park, I. Yu, H. Kim, S.H. Kim, and K. Seong, Operational Characteristic of the High Quality Power Conditioner with SMES, *IEEE Trans, Applied Superconductivity*, vol. 18, no. 2, Jun. 2008.

[36] M. R. Alizadeh Pahlavani, H. A. Mohammadpour, A. Shoulaie, Voltage Stabilization of VSI SMES Capacitors and Voltage Sag Compensation by SMES Using Novel and Optimized Switching Strategies, *in Proc. 24th Int. International Power System Conf, Tehran, Iran*, no. 98-F-PQA-0110 , Nov. 2009.

Optimal Location and Control of Flexible Three Phase Shunt FACTS to Enhance Power Quality in Unbalanced Electrical Network

Belkacem Mahdad
Department of Electrical Engineering, Biskra University
Algeria

1. Introduction

The problem of voltage or current unbalance is gaining more attention recently with the increasing awareness on power quality. Excessive unbalance among the phase voltages or currents of a three phase power system has always been a concern to expert power engineers. An unbalanced voltage supply can cause power electronic converters to generate more harmonic distortions. It may result in the malfunction of sensitive three-phase electronic equipment. In fact, the voltage and current unbalance has been regarded as one of the basic power quality attributes (Birt et al., 1976).

The asymmetry in transmission lines and loads produces a certain degree of unbalance in real power systems. Under these conditions, low quantities of negative and zero sequence voltages can be observed in power networks. These magnitudes are considered to be a disturbance whose level must be controlled by power quality standards to maintain the electromagnetic compatibility of the system (Mamdouh Abdel-Akher et.al, 2005).

In order to cope with these kind of problems and increase usable power transmission capacity, Flexible AC transmission systems (FACTS), where developed and introduced to the market. FACTS philosophy was first introduced by Hingorani (Hingorani, N.G, 1988) from the Electric power research institute (EPRI). The objective of FACTS devices is to bring a system under control and to transmit power as ordered by the control centers, it also allows increasing the usable transmission capacity to its thermal limits. With FACTS devices we can control the phase angle, the voltage magnitude at chosen buses and/or line impedances (Mahdad.b et al., 2006)

In practical installation of FACTS in power system, there are six common requirements as follows (Mahdad.b et al., 2007) :

1. What Kinds of FACTS devices should be installed?
2. Where in the system should be placed?
3. How much capacity should it have?
4. How to coordinate dynamically the interaction between multiple FACTS and the network to better exploit FACTS devices?
5. How to estimate economically the optimal size and number of FACTS to be installed in a practical network?
6. How to adjust dynamically the three phase recative power in unbalanced network?

Recent developments and research indicate clearly that artificial intelligence techniques like fuzzy logic (Tmsovic, 1992), (Su, C. T. et al., 1996), Artificial Neural Network (Scala et al., 1996), and expert system (Bansilal et al., 1997) may be useful for assisting experienced planning engineers in energy centre dispatch. In recent years many interesting applications of fuzzy systems to reactive power planning and voltage control have been developed and applied in practical power system distribution. (Udupa et al., 1999) presented approach based in fuzzy set theory for reactive power control with purpose to improve voltage stability of power system. (Su et al., 1996) presented a knowledge-based system for supervision and control of regional voltage profile and security using fuzzy logic.

In the literature, many applications for optimal placement and control of FACTS devices are developed using the positive-sequence power systems. The application of these methods for unbalanced power systems may be unrealistic and could not be able to characterize accurately the real behaviour of the unbalanced distribution system.

One of the main tasks of a planning engineers in electricity distribution system is to ensure that network parameters, such as bus voltages, and line load, are maintained within predefined limits (desired value). This chapter tries to give answers to the following important questions:

- How an experienced planning engineers can choose effeciently locations and coordination of multiple shunt FACTS devices (SVC, STATCOM) in unbalanced practical network which are probably high suitable?
- How they can exploit efficiently the performance of these devices without violating the constraints limits?

Static Var Compensator (SVC) is one of the key elements in power system that provides the opportunity to improve power quality. This chapter presents a methodology that coordinate the expertise of power system engineer formulated in flexible fuzzy rules to adjust dynamically the reactive power compensation based three phase model shunt FACTS controller installed at critical buses. The main taget of this proposed tecnique is to reduce the asymmetrical voltage and to enhance the system loadability with consideration of unbalanced electrical network. The proposed approach has been tested on a variety of electrical network 5-Bus, IEEE 30-Bus. Testing results indicate clearly that the proposed approach based in asymmetrical compensation reduces the effect of asymmetrical voltage in distribution power system and improve the indices of power quality.

2. Flexible AC Transmission Systems (FACTS) technology

The objective of FACTS technology is to bring a system under control and to transmit power as ordered by the control centre, it also allows increasing the usable transmission capacity to its maximum thermal limits.

The central technology of FACTS involves high power electronics, a variety of thyristor devices, microelectronics, communications and advanced control centres. Power flow through an ac line is a function of phase angle, line end voltages and line impedance, and there is little or no control over any of these variables. The consequences of this lack of fast, reliable control and stability problems, power flowing through other than the intended lines, the inability to fully utilize the transmission resources, undesirable Var flows, higher losses, high or low voltages, cascade tripping and long restoration time. With FACTS devices we can control the phase angle, the voltage magnitude at chosen buses and/or line impedances. Power flow is electronically controlled and it flows as ordered by the control centre (Mahdad. B, 2010).

2.1 Basic types of FACTS controllers

In general, FACTS Controllers can be divided into three categories (Hingorani et al., 1999):

- Series Controllers
- Shunt Controllers
- Combined series-series Controllers

2.2 Role of FACTS controllers

The following points summarize the objectives of FACTS devices in power system control and operation:

- Control of power flow as ordered
- Increase the loading capability of lines to their thermal capabilities
- Increase the reliability and system security through raising the transient stability limit, limiting short-circuit currents and overloads, managing cascading blackouts
- Provide greater flexibility in sitting new generation
- Reduce reactive power flows, thus allowing the lines to carry more active power
- Reduce loop flows.
- Enhance the economic dispatch of generating units.

2.3 Three phase static var compensator modelling

Model presented by (Acha et.al, 2004), is based on the concept of a variable susceptance B_k^{pq}, which adjust itself in order to constrain the nodal voltage magnitude. This changing susceptance represents the total equivalent susceptance of all modules making up the SVC, independently of their operating mode and electric characteristics. Based on Fig. 1, the SVC transfer admittance equation expressed as follows:
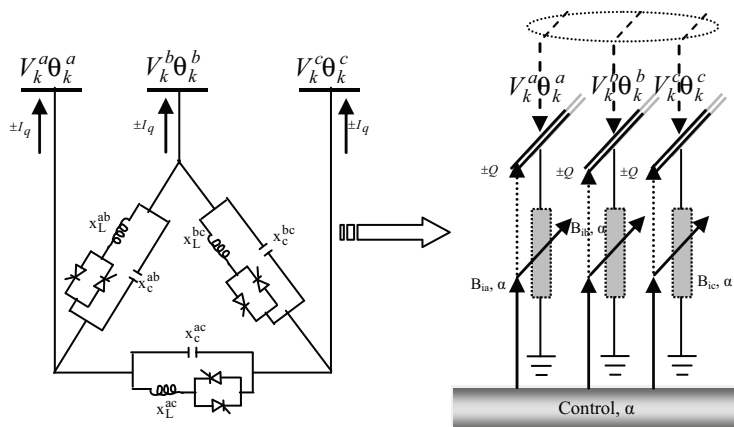
Fig. 1. SVC based on FC-TCR modules in delta-connected arrangement

$$\begin{bmatrix} I_k^a \\ I_k^b \\ I_k^c \end{bmatrix} = j \begin{bmatrix} B_k^{ab} + B_k^{ca} & -B_k^{ab} & B_k^{ca} \\ -B_k^{ab} & B_k^{ab} + B_k^{bc} & -B_k^{bc} \\ -B_k^{ca} & -B_k^{bc} & B_k^{bc} - B_k^{ca} \end{bmatrix} \begin{bmatrix} V_k^a \\ V_k^b \\ V_k^c \end{bmatrix}. \tag{1}$$

A three-phase SVC model presented by (Acha, et al. 2004) is implemented and adapted within the proposed algorithm to regulate and control the reactive power injected or absorbed in the unbalanced three phase power systems. As shown in Fig. 1, every branch has a fixed capacitor and a thyristor-controlled capacitor reactor. Equation (2) is the equivalent susceptance or admittance of each branch by controlling the firing delays angles (α) of thyristor.
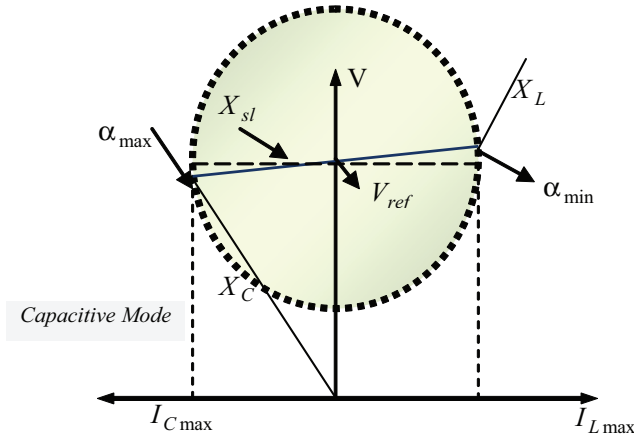
Fig. 2. Typical steady state V-I Characteristics of SVC

$$B_{TCR}^{pq} = \frac{2\left(\pi - \alpha_{TCR}^{pq}\right) - \sin 2\alpha_{TCR}^{pq}}{\pi \omega L_{TCR}^{pq}} \tag{2}$$

The superscripts p, q correspond to phases a, b and c.
The steady-state control law for the SVC is the typical current-voltage characteristic, illustrated in Fig. 2.

2.4 Three-phase power flow equation

The network branch modelling in unbalanced multi-wire distribution systems is typically done and simplified using the Carson's equations to self and the mutual impedances, and by applying the kron reduction to determine the reduced impedance matrix Zabc of each branch, referred to the phases a, b and c.
The power-flow equations at buses k and m based on Fig. 3 may be given by:

$$P_k^p = V_k^p \left\{ \sum_{i=k,m} \sum_{j=a,b,c} V_i^j \left[G_{ki}^{pj} \cos\left(\theta_k^p - \theta_i^j\right) + B_{ki}^{pj} \sin\left(\theta_k^p - \theta_i^j\right) \right] \right\}, \tag{3}$$

$$Q_k^p = V_k^p \left\{ \sum_{i=k,m} \sum_{j=a,b,c} V_i^j \left[G_{ki}^{pj} \sin\left(\theta_k^p - \theta_i^j\right) - B_{ki}^{pj} \sin\left(\theta_k^p - \theta_i^j\right) \right] \right\}, \tag{4}$$

Where the subscript k, m represent the bus number while the subscript p represent the phase a, b and c.
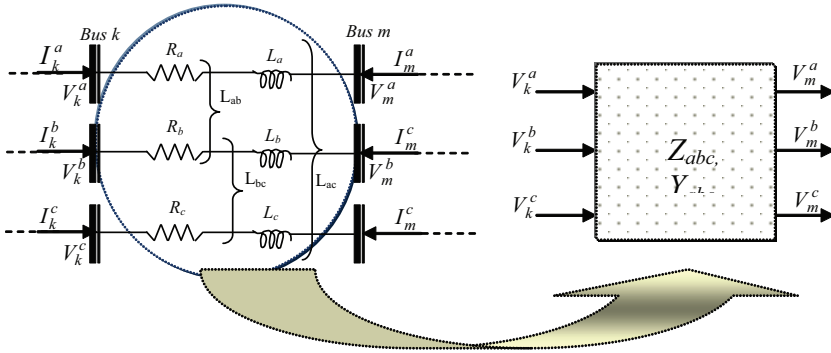
Fig. 3. Representation of a branch reduced to the three-phase branch impedance matrix

The power mismatch equations at buses may be given by:

$$\Delta P_k^p = -Pd_k^p + P_k^p = 0 \tag{5}$$

$$\Delta Q_k^p = -Qd_k^p + Q_k^p = 0 \tag{6}$$

Where Pd_m^p and Qd_m^p are the active and reactive load powers of phase p at bus m, respectively. P_k^p and Q_k^p, which are given by (3) and (4), are the sum of the active and reactive power flows of phase p at bus m, respectively.
In the following, the three-phase Newton power flow algorithm in polar coordinates, which is similar to that proposed in (Acha, et al. 2004), will be described. the non-linear equations can be combined and expressed in compact form.

$$f(x) = 0 \tag{7}$$

Where, $f(x) = 0$ represents the whole set of power-flow mismatch and machine terminal constraint equations, x is the state variable vector and given by

$$x = \left[\theta^a, V^a, \theta^b, V^b, \theta^c, V^c, \delta^a, E^a\right]^t . \tag{8}$$

The Newton equation is given by

$$J(x)\Delta x = -f(x) \tag{9}$$

Where , $J(x) = \partial f(x) / \partial x$ is the system Jacobian matrix.
The resulting linearised equation, suitable for iterative solutions, becomes:

$$\begin{bmatrix} \Delta P_l^p \\ \Delta Q_l^p \end{bmatrix}^i = \begin{bmatrix} \dfrac{\partial P_l^p}{\partial \theta_j^p} & \dfrac{\partial P_l^p}{\partial V_j^p} V_j^p \\[2ex] \dfrac{\partial Q_l^p}{\partial \theta_j^p} & \dfrac{\partial Q_l^p}{\partial V_j^p} V_j^p \end{bmatrix}^i \begin{bmatrix} \Delta \theta_j^p \\[2ex] \dfrac{\Delta V_j^p}{V^p} \end{bmatrix}^i \tag{10}$$

Where l=k, m, j=k, m and (i) is the iteration number.

3. Dynamic strategy for asymetric control of multiple shunt compensator

One of the principal tasks of the operator of an electricity distribution system is to ensure that network parameters, such as bus voltages and line load, are maintained within predefined limits. The problem of system imbalance has considerable effects on power systems. The effects of zero sequence current on protection relays and negative sequence current on motors are well known by power engineers (Mahdad.b et al., 2006). However, others effects such as increasing system loss, decreasing system capacity, and increasing the inductive coupling between parallel lines or feeders are often overlooked.
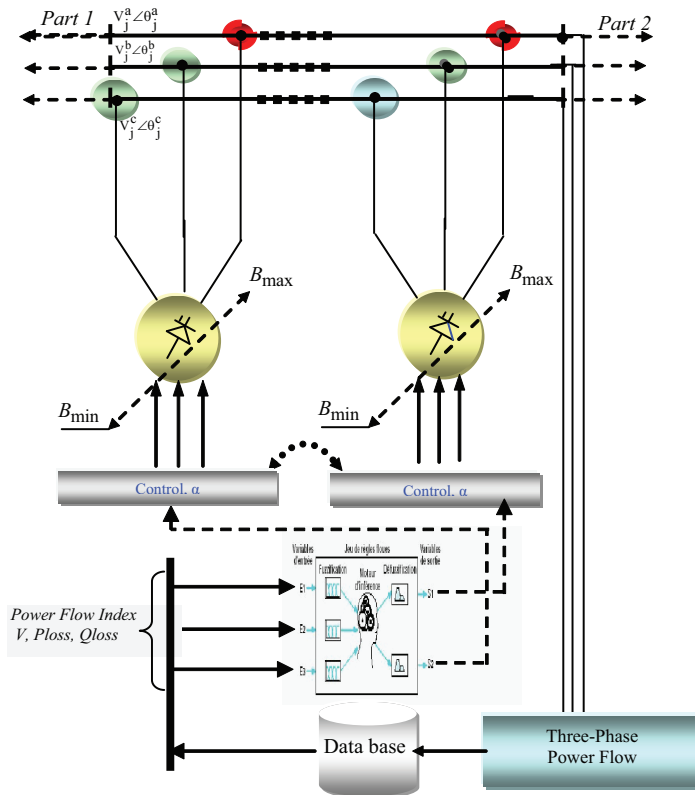
Fig. 4. A global block control strategy

The intensive use of FACTS devices in the emerging electricity market environment demands more robust and online FACTS control methodologies.
The main objective of this section is to formulate the basic idea behind the proposed approach.

3.1 Practical experience rules and fuzzy logic

A review of the literature on reactive power compensation in distribution feeders indicates that the problem of capacitors Allocation has been extensively researched over the past

several decades (Mahdad.b et al., 2007). The solution techniques for the reactive power planning problem can be classified into three categories:

- Analytical,
- numerical programming, heuristics,
- and artificial intelligence based.

The choice of which method to use depends on: the problem to be solved, the complexity of the problem, the accuracy of desired results. Once these criteria are determined, the appropriate capacitor Allocation techniques can be chosen.

The use of fuzzy logic has received increased attention in recent years because of it's usefulness in reducing the need for complex mathematical models in problem solving (Mahdad.b, 2010).

Fuzzy logic employs linguistic terms, which deal with the causal relationship between input and output variables. For this reason the approach makes it easier to manipulate and solve problems.

So why using fuzzy logic in Reactive Power Planning and coordination of multiple shunt FACTS devices?

- Fuzzy logic is based on natural language.
- Fuzzy logic is conceptually easy to understand.
- Fuzzy logic is flexible.
- Fuzzy logic can model nonlinear functions of arbitrary complexity.
- Fuzzy logic can be blended with conventional control techniques.
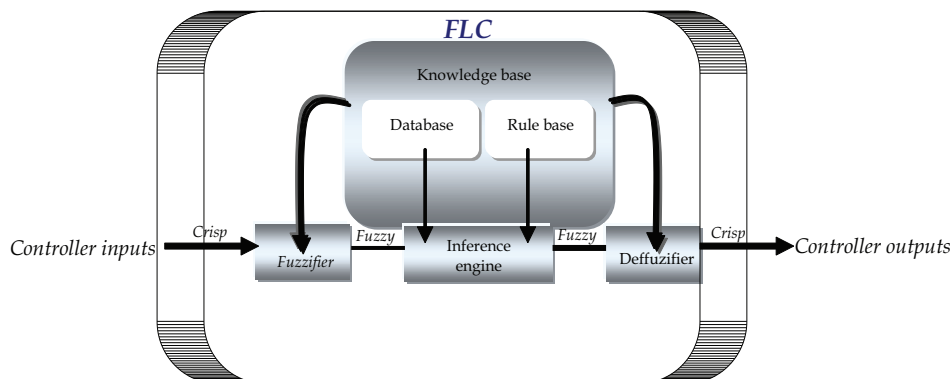
Fig. 5. Schematic diagram of the FLC building blocks

It is intuitive that a section in a distribution system with high losses and low voltage is ideal for installation of facts devices, whereas a low loss section with good voltage is not. Note that the terms, high and low are linguistic.

3.2 Membership function

A membership function use a continuous function in the range [0-1]. It is usually decided from humain expertise and observations made and it can be either linear or non-linear. The basic mechanism search of fuzzy logic controller is illustrated in Fig. 5.

It choice is critical for the performance of the fuzzy logic system since it determines all the information contained in a fuzzy set. Engineers experience is an efficient tool to achieve a

design of an optimal membership function, if the expert operator is not satisfied with the concepetion of fuzzy logic model, he can adjust the parmaters used to the design of the membership functions to adapt them with new database introduced to the practical power system. Fig. 6 shows the general bloc diagram of the proposed coordinated fuzzy approach applied to enhance the system loadability in an Unbalanced distribution power system.
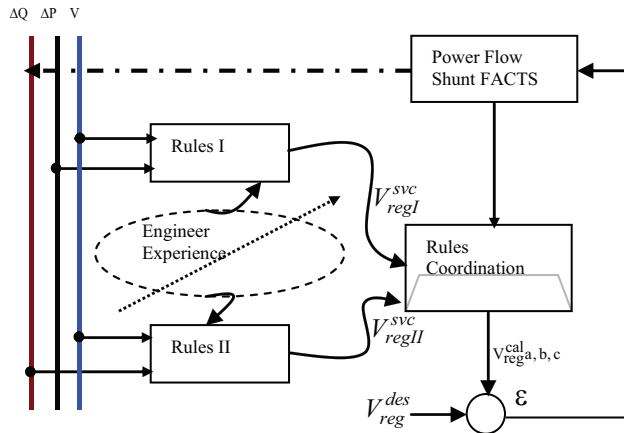

Fig. 6. General schematic diagram of the proposed coordinated fuzzy approach

Phase a			
VL	L	M	H
VL	L	M	H

$Q_{svc}^{(a)}$ (left of second data row of Phase a)

Phase b			
VL	L	M	H
VL	L	M	H

$Q_{svc}^{(b)}$

Phase c			
VL	L	M	H
VL	L	M	H

$Q_{svc}^{(c)}$

$$Q_{svc}^{\rho} = \begin{bmatrix} Q_{svc}^{a} \\ Q_{svc}^{b} \\ Q_{svc}^{c} \end{bmatrix}^{Step1}$$

Where; Q_{svc}^{ρ}, reactive power for three phase.

The solution algorithm steps for the fuzzy control methodology are as follows:

1. Perform the initial operational three phase power flow to generate the initial database $\left(V_{i}^{\rho}, \Delta P_{i}^{\rho}, \Delta Q_{i}^{\rho} \right)$.

2. Identify the candidate bus using continuation load flow.

3. Identify the candidate phase for all bus $\left(\min V_{i}^{\rho} \right)$.

4. Install the specified shunt compensator to the best bus chosen, and generate the reactive power using three phase power flow based in fuzzy expert approach:

a.   Combination Active and Reactive Power Rules. Fig. 7.
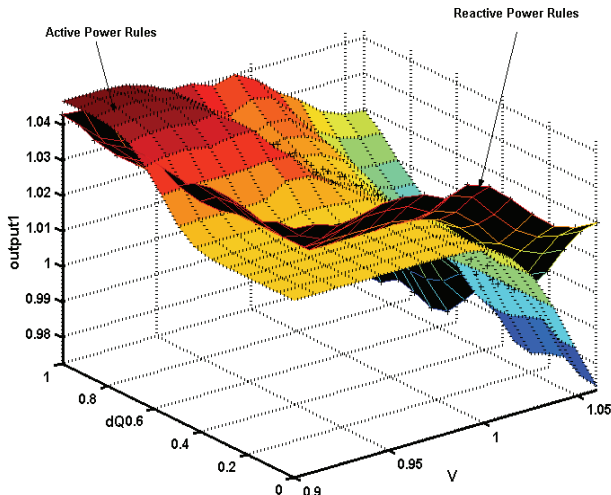
Fig. 7. Combination voltage, active and reactive power rules

b.   Heuristic Strategy Coordination
-   If $\tau_a = \tau_b = \tau_c$ which correspond to the balanced case,
    where τ_a , τ_b , τ_c the degree of unbalance for each phase compared to the balanced case.
    In this case, $\left(Q_{svc}^a = Q_{svc}^b = Q_{svc}^c \right)$.

-   If $\tau_c > \tau_b > \tau_a$ then increment Q_{svc}^c , while keeping Q_{svc}^b , Q_{svc}^a fixed. Select the corrected
    value of Q_{svc}^c which verify the following conditions:

$$\tau_{tot} \leq \tau_{des}$$

    and $\Delta P_{asy} \leq \Delta P_{bal}$

    where τ_{tot} represent the maximum degree of unbalance.

    τ_{des} the desired degree of unbalance.

    ΔP_{asy} power loss for the unbalanced case.

    ΔP_{bal} power loss for the balanced case.
5.   If the maximum degree of unbalance is not acceptable within tolerance (desired value
     based in utility practice). Go to step 4.
6.   Perform the three phase load flow and output results.

3.3 Minimum reactive power exchanged
The minimum reactive power exchanged with the network is defined as the least amount of
reactive power needed from network system, to maintain the same degree of system
security margin. One might think that the larger the SVC or STATCOM, the greater increase
in the maximum load, based in experience there is a maximum increase on load margin with
respect to the compensation level (Mahdad.b et al., 2007).

In order to better, evaluate the optimal utilization of SVC and STATCOM we introduce a supplementary rating level, this technical ratio shows the effect of the shunt dynamic compensator Mvar rating in the maximum system load, therefore, a maximum value of this factor yields the optimal SVC and STATCOM rating, as this point correspond to the maximum load increase at the minimum Mvar level.

This index is defined as:

$$RIS^{(\rho)} = \frac{LoadFactor(KLd)}{\sum_{i=1}^{N_{sht}} Q_{Shunt}{}^{(\rho)}} . \tag{11}$$

where: N_{sht} is the number of shunt compensator

Kld: Loading Factor.

$Q_{Shunt}{}^{(\rho)}$: Reactive power exchanged (absorbed or injected) with the network at phase ρ (a, b, c).

ρ Index of phase, a, b, c.

Fig. 8. Schematic diagram of reactive power index sensitivity

Fig. 8 shows the principle of the proposed reactive index sensitivity to improve the economical size of shunt compensators installed in practical network. In this figure, the curve represents the evolution of minimum reactive exchanged based in system loadability, the curve has two regions, the feasible region which contains the feasible solution of reactive power. At point 'A', if the SVC outputs less reactive power than the optimal value such as at point 'B', it has a negative impact on system security since the voltage margin is less than the desired margin, but the performances of SVC Compensator not violated. On the other hand, if the SVC produces more reactive power than the minimum value (Q_{min}), such as point 'C', it contributes to improving the security system with a reduced margin of system loadability, this reactive power delivered accelerates the saturation of the SVC Controllers.

4. Numerical results

In this section, numerical results are carried out on simple network, 5-bus system and IEEE 30-bus system. The solution was achieved in 4 iterations to a power mismatch tolerance of 1e-4.

4.1 Case studies on the 5-bus system
The following cases on the 5-bus network have been studied:

Case1: Balanced network and the whole system with balanced load.

> The results given in Table. 1 are identical with those obtained from single-phase power flow programs. The low voltage is at bus 5 with 0.9717 p.u, the power system losses are 6.0747 MW. Neither negative nor zero sequence voltages exist.

Bus	Phase A (p.u)		Phase B (p.u)		Phase C (p.u)	
1	1.06	0	1.06	240	1.06	120
2	1	-2.0610	1	237.9390	1	117.9390
3	0.9873	-4.6364	0.9873	235.3636	0.9873	115.3636
4	0.9841	-4.9567	0.9841	235.0433	0.9841	115.0433
5	0.9717	-5.7644	0.9717	234.2356	0.9717	114.2356
Total Power Losses 6.0747 (MW)						

Table 1. Three-phase bus voltages for the balanced case. 1

Case2: Balanced network and the whole system with unbalanced load.

4.1.1 Optimal placement of shunt FACTS based voltage stability
Before the insertion of SVC devices, the system was pushed to its collapsing point by increasing both active and reactive load discretely using three phase continuation load flow (Mahdad.b et al., 2006). In this test system according to results obtained from the continuation load flow, we can find that based in Figs. 9, 10, 11 that bus 5 is the best location point.
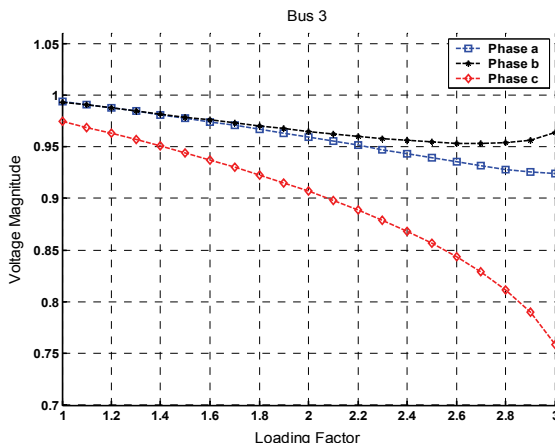
Fig. 9. Three phase voltage solution at bus 3 with load Incrementation
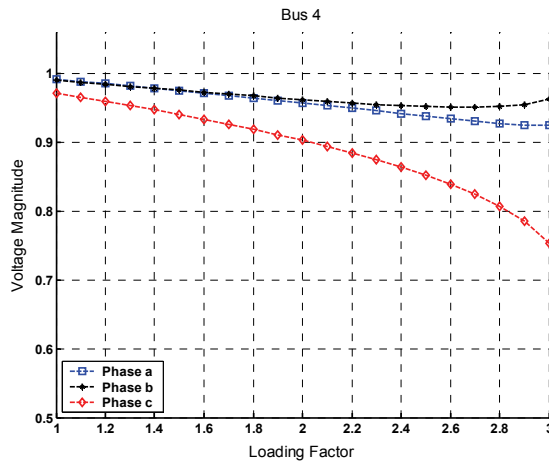
Fig. 10. Three phase voltage solution in bus 4 with load Incrementation
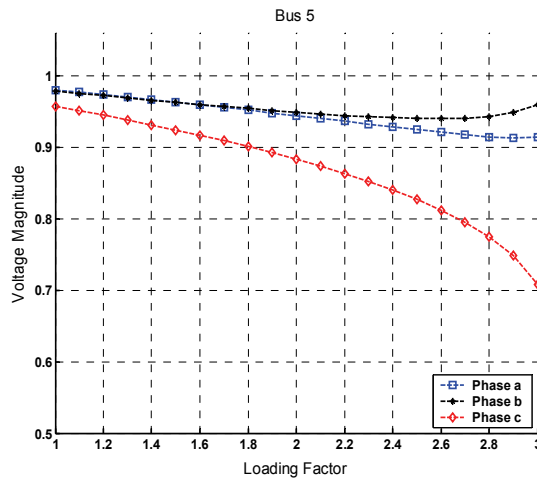
Fig. 11. Three phase voltage solution in bus 5 with load Incrementation

To affirm these results we suppose the SVC with technical values indicated in Table. 2 installed on a different bus. Figs. 9-10-11, show the three phase voltage solution at different buses with load Incrementation. Fig. 12 shows the variation of negative sequence voltage in bus 3, 4, 5 with load incrementation.

	Bmin (p.u)	Bmax (p.u)	Binit (p.u)
Susceptance Model One SVC	-0.35	0.35	0.025
Susceptance Model Multi-SVC	-0.25	0.25	0.020

Table 2. SVCs data

Optimal Location and Control of Flexible Three Phase Shunt FACTS
to Enhance Power Quality in Unbalanced Electrical Network
293
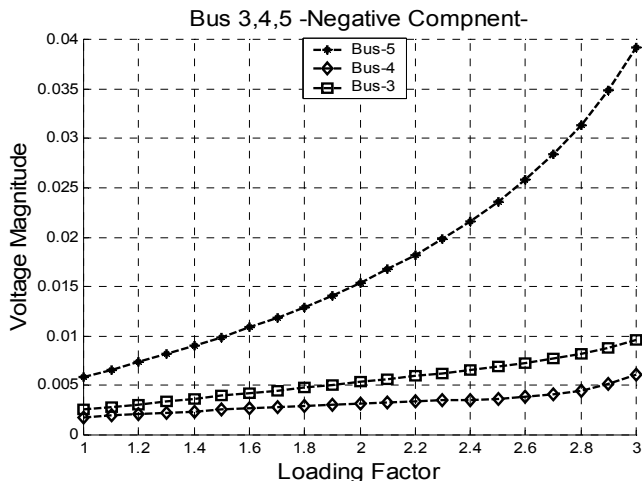
Fig. 12. Negative sequence voltage in bus 3-4-5 with load incrementation

Case2: Unbalanced Load Without Compensation

Table. 3 shows the three phase voltage solution for unbalanced load, the impact of unbalanced load on system performance can be appreciated by comparing the results given in Table. 3 -4 and Table.1, where small amounts of negative and zero sequence voltages appeared. In this case the low voltage appeared in bus 5 with 0.9599 p.u at phase 'c' which is lower than the balanced case, the system power losses are incremented to 6.0755 MW with respect to the balanced case. Table. 4 shows the results of power flow for the unbalanced power system, it can be seen from results that all three phases are unbalanced.

Bus	Phase A	Phase B	Phase C	V-
1	1.06	1.06	1.06	/
2	1	1	1	/
3	0.9820	0.9881	0.9908	0.0026
4	0.9811	0.9831	0.9872	0.0018
5	0.9789	0.9755	0.9599	0.0059
Total Power Loss 6.0755 (MW)				

Table 3. Three-phase bus voltages for the unbalanced case.2

Bus	Phase A	Phase B	Phase C	V-
1	1.06	1.06	1.06	/
2	1	1	1	/
3	1.0013	0.9995	0.9608	0.0132
4	0.9991	0.9963	0.9569	0.0136
5	0.9887	0.9848	0.9419	0.0150
Total Power Loss (MW) 6.0795				

Table 4. Three phase bus voltages for the unbalanced case.2: other degree of unbalance

Case 3: Unbalanced Load With Shunt Compensation based Fuzzy Rules

Figs 13, 14, 15, show the results of the application of the heuristic startegy coordinated with standard fuzzy rules to find the minimum efficient value of reactive power exchanged between shunt compensator (SVC) and the network needed to assure efficient degree of security. In Fig. 13, for one SVC installed at bus 5 and at the step control '10', the reactive power for the three phase Q_{svc}^ρ =[0.0468 0.0702 0.1170] represent the minimum reactive power needed to assure the degree of system security margin. The low voltage appeared in bus 5 with 0.9720 p.u at phase 'c' which is higher than the case without compensation. Tables. 5-6-7-8, show the results of the three phase power flow solution for the unbalanced newtwork.
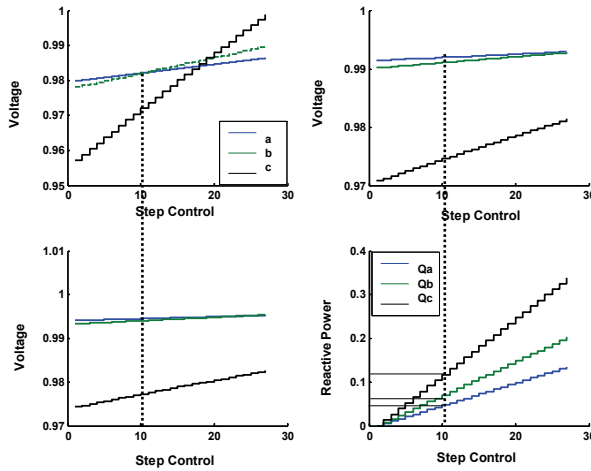
Fig. 13. Minimum reactive power exchanged with SVC installed at bus 5
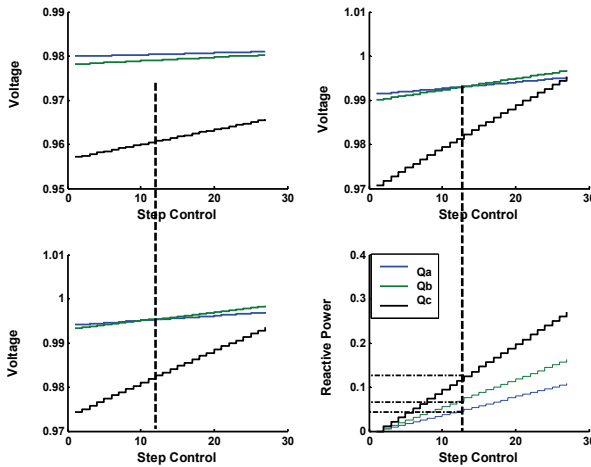
Fig. 14. Minimum reactive power exchanged with SVC installed at bus 4
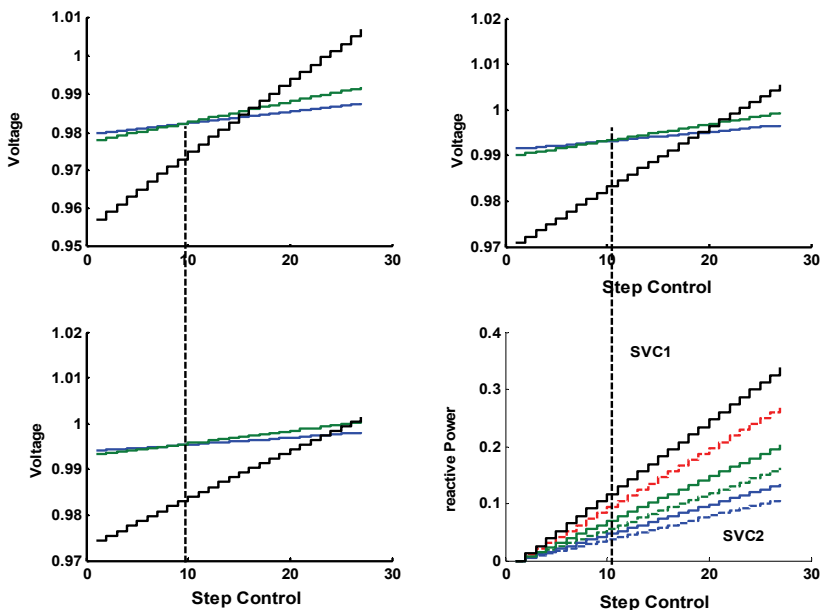
Fig. 15. Minimum reactive power exchanged with SVC installed at bus 4, 5

Bus	Phase A (p.u)	Phase B (p.u)	Phase C (p.u)	
3	0.9954	0.9956	0.9833	
4	0.9833	0.9932	0.9823	
5	0.9805	0.9791	0.9611	
Q_{svc}^{ρ} (p.u)	0.0499	0.0749	0.1248	
RIS^{ρ} (p.u)	7.0126	4.6729	2.8043	**14.4898**

Table 5. SVC installed at bus 4 (ka=1, kb=0.9, kc=1.1, loading factor =1)

Bus	Phase A (p.u)	Phase B (p.u)	Phase C (p.u)	
3	0.9945	0.9940	0.9772	
4	0.9920	0.9911	0.9746	
5	0.9822	0.9822	0.9720	
Q_{svc}^{ρ} (p.u)	0.0468	0.0702	0.1170	
RIS^{ρ} (p.u)	7.4794	4.9850	2.9913	**15.4557**

Table 6. SVC installed at bus 5, step control '10' (ka=1, kb=0.9, kc=1.1, loading factor=1)

Bus	Phase A (p.u)	Phase B (p.u)	Phase C (p.u)	
3	0.9948	0.9946	0.9798	
4	0.9924	0.9919	0.9778	
5	0.9842	0.9858	0.9848	
Q^{ρ}_{svc} (p.u)	0.0884	0.1326	0.2210	
RIS^{ρ} (p.u)	3.9588	2.6392	1.5838	**8.1818**

Table 7. SVC at bus 5, step control'18' (ka=1, kb=0.9, kc=1.1, loading factor=1)

Bus	Phase A (p.u)	Phase B (p.u)	Phase C (p.u)	
3	0.9953	0.9955	0.9829	
4	0.9930	0.9930	0.9818	
5	0.9823	0.9824	0.9730	
Q^{ρ}_{svc4} (p.u)	0.0416	0.0624	0.1040	
Q^{ρ}_{svc5} (p.u)	0.0374	0.0562	0.0936	
RIS^{ρ}_4 (p.u)	6.0096	4.0064	2.4038	**12.4198**
RIS^{ρ}_5 (p.u)	6.6845	4.4484	2.6709	**13.8038**

Table 8. SVC at bus 4 and bus 4, 5 (ka=1, kb=0.9, kc=1.1, loading factor=1)
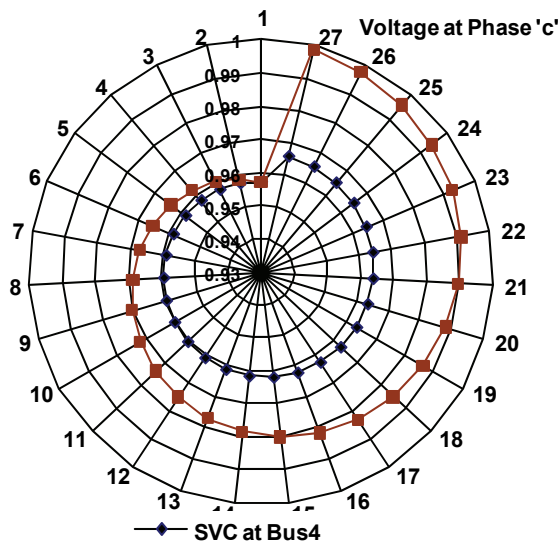
Fig. 16. Voltage profiles for the phase 'c' at different SVC installation bus 5, and bus 4
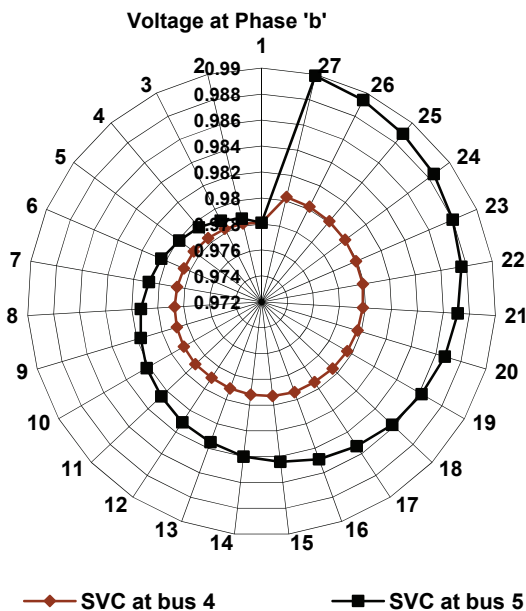
Fig. 17. Voltage profile for the phase 'b' at different SVC installation bus 5, and bus 4
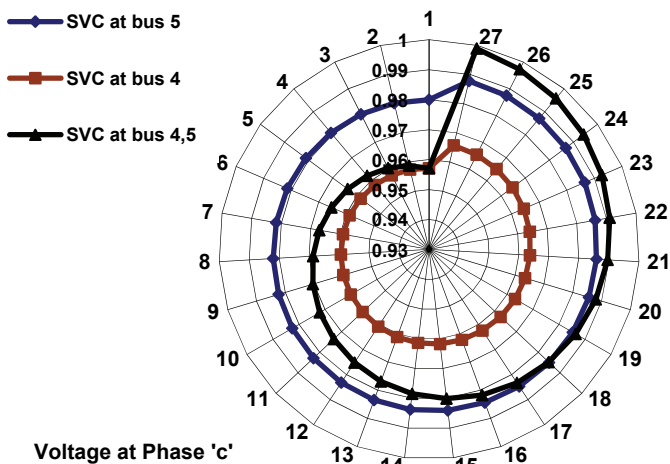
Fig. 18. Voltage profiles for phase 'c': One SVC installed at bus 5, bus 4, and two SVC installed at buses: 4, 5

4.2 Case studies on the IEEE 30-Bus system
4.2.1 Optimal location based negative sequence component
In order to investigate the impact of the efficient location of FACTS devices using complementary information given by negative sequence voltage and to realize a flexible control of reactive power injected by SVC in a network with unbalanced load the following cases were carried out.

Case 1: unbalanced load at Bus 30 with ka=1, kb=0.9, kc=1.1, where ka, kb, kc represent the degree of unbalance.
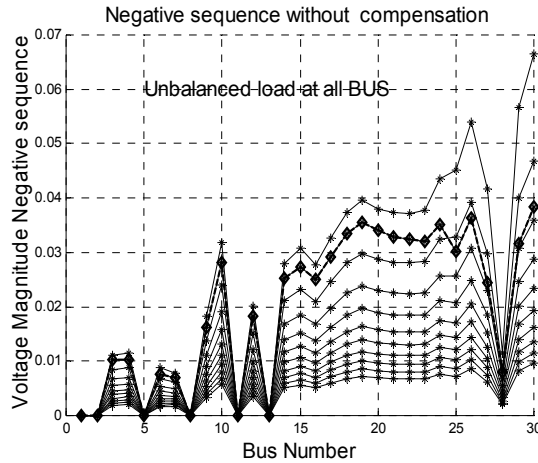
Fig. 19. Negative sequence voltage in all buses with load incrementation- without compensation-unbalance at all Bus
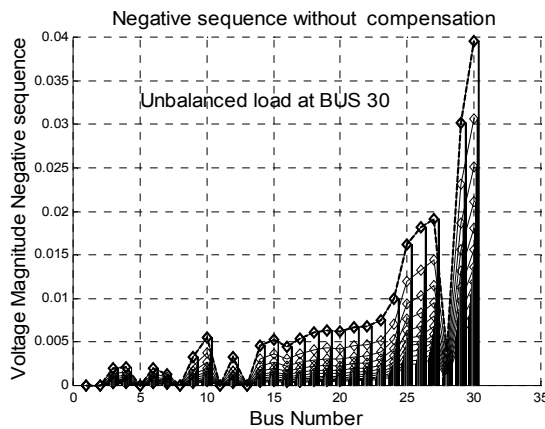
Fig. 20. Negative sequence voltage at all buses without compensation-unbalance-Bus 30

The lowest voltage magnitude is a necessary information and a good index to analyse the voltage stability and to estimate the efficient location of shunt compensator, but not

sufficient, complementary information based in the variation of negative sequence is presented and tested in a network with unbalanced load. Figs. (6-7) give results of the voltage magnitude of an unbalanced three-phase power systems in normal condition with load incrementation, we can seen from Fig. 7 that the lower voltage is at phase 'c'. Figs. (8-9) show the variation of the negative sequence voltage in all buses with load incrementation, without compensation with unbalance at all Bus and unbalance at bus-30. Figs. (10-11) show the variation of the negative sequence voltage in all buses with load incrementation, with balanced and unbalanced compensation and unbalance at bus-30. The amount of negative sequence voltage is reduced greatly in the unbalanced case to 0.0135 p.u compared to the balanced compensation case with 0.0310 p.u.
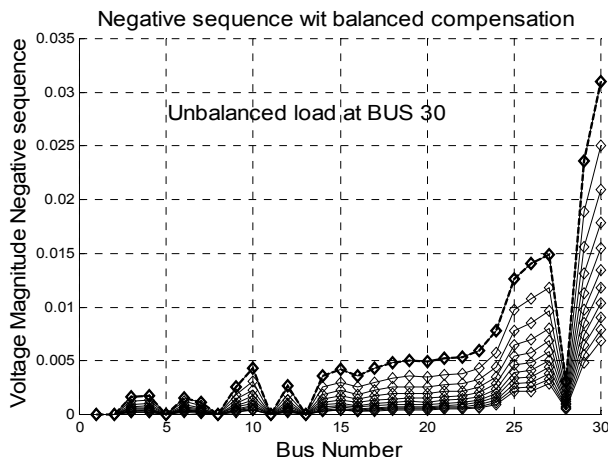
Fig. 21. Negative sequence voltage in all buses with *balanced compensation*. Unbalance at bus 30
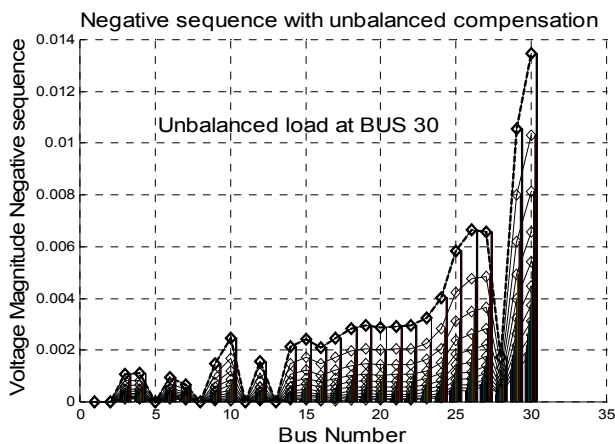
Fig. 22. Negative sequence voltage in all buses with *unbalanced compensation*–unbalance at bus 30
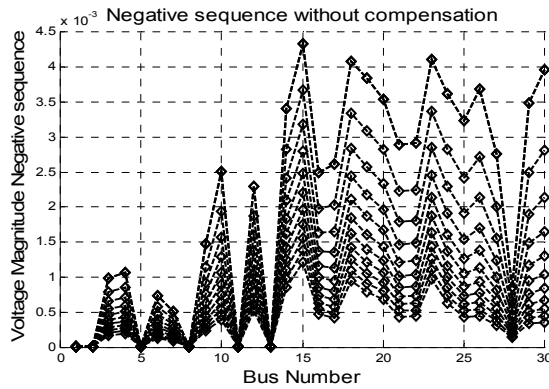
Fig. 23. Negative sequence voltage in all buses with load incrementation – *without compensation* Unbalance at Bus 26
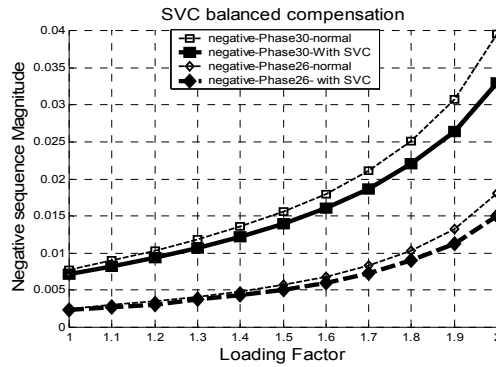
Fig. 24. Impact of SVC Controllers based balanced compensation on negative voltage component: SVC installed at buse 26, and bus 30

Fig. 25. Impact of SVC Controllers based unbalanced compensation on negative voltage component: SVC installed at bus 26, and bus 30
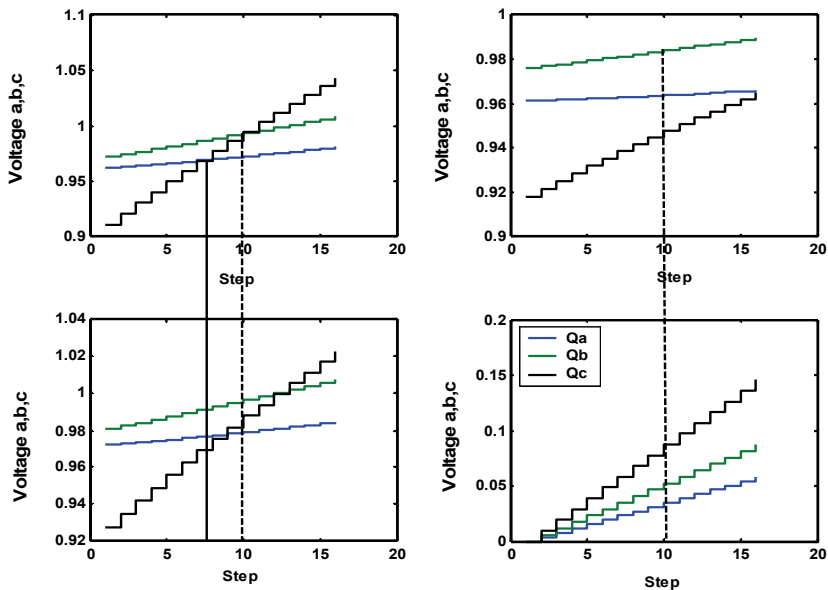
Fig. 26. Minimum reactive power exchanged with SVC installed at bus 30

Bus	Phase A (p.u)	Phase B (p.u)	Phase C (p.u)	
	Without Compensation (p.u)			
30	0.9620	0.9721	0.9102	
29	0.9722	0.9808	0.9273	
26	0.9613	0.9759	0.9180	
	With one SVC at bus 30			
30	0.9726	0.9935	0.9946	
29	0.9792	0.9967	0.9879	
26	0.9638	0.9841	0.9477	
Q^{ρ}_{svc} (p.u)	0.0349	0.0524	0.0873	
RIS^{ρ} (p.u)	10.0301	6.6800	4.0096	**20.7197**

Table 10. SVC at bus 29, step control'10' (ka=1, kb=0.9, kc=1.1, loading factor=1)

In this case an unbalanced load at all buses is applied with ka=1, kb=0.9, kc=1.1, where ka, kb, kc represent the degree of unbalance. In Fig. 26, for one SVC installed at bus 30 and at the step control '10', the reactive power for the three phase $\left[Q^{\rho}_{svc}, RIS^{\rho} \right] = [0.0349\ 0.0524\ 0.0873\ 20.7197]$ represent the minimum reactive power needed to assure the degree of system security margin. Fig. 27 shows the impact of the unbalanced compensation to the voltage magnitude in normal condition.
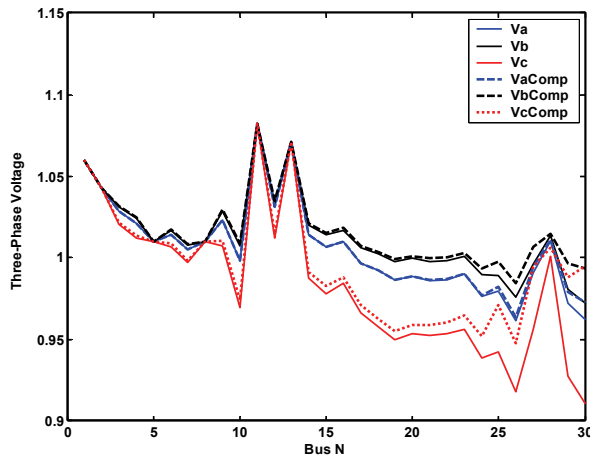
Fig. 27. Three-phase voltage profile improvement with SVC installed at bus 30

5. General results interpretation

1. In our presented approach the real power loss membership function is combined with reactive power loss membership function with the same form to enhance the final decision.
2. The combination of active and reactive fuzzy expert rules with the function coordination that is based on the heuristic strategy leads to better results.
3. In addition it has found that based on the complementary information given by the reactive index sensitivity, the expert engineer can choose economically the size of the shunt compensator to be installed in a practical network. A maximum value of this factor yields the optimal size of SVC and STATCOM rating, this point correspond to the suitable security margin at the minimum Mvar level.
4. Optimal location and sizing of shunt controllers results in lower power loss, better voltage profiles and improvement power quality. Figs 16-17-18 show the voltage profiles of phase 'b', and phase 'c'. It is clear that the location of SVC controllers contribute to the improvement of voltage deviation
5. Our analysis has shown that unbalanced compensation based shunt FACTS devices is an alternative solution to enhance the power quality.
6. In addition to the important points discussed, we can also draw some recommendations for futur research:
-   Further research is needed into this issue (power system operation and control), related to the integration of multi type of FACTS Controllers in unbalanced distribution systems.
-   Optimal location and control of three phase FACTS Controllers with the standard power flow using artificial intelligence techniques is an important research area.
-   The control in real time of FACTS devices requires flexible and robust three-phase models combined with efficient dynamic fuzzy rules to enhance the indices of power quality.

6. Conclusion

Reactive power control based shunt FACTS devices is one of the important issues in power system planning and control. The problem of finding out which locations are the most

effective and how many Flexible AC Transmission System (FACTS) devices have to be installed and controlled in a deregulated and unbalanced practical power systems is a question of great significance for the expert engineers to deliver power to the consumers within the desired power quality required.This chapter has recalled the fundamentals and some specfic details related to the improvment of power quality in unbalanced power systems. The proposed technique, demonstrates that an efficient coordination between expertise engineers formulated in practical fuzzy rules with asymetric dynamic compensation based shunt FACTS devices is able to improve the power system quality in unbalanced power systems. The main objective of the proposed strategy is to find the optimal reactive power compensation between multi shunt FACTS devices (SVC Controllers) in unbalanced power systems based on three-phase power program, the method is applicable to many types of unbalanced network configuration.

Today, the prices of SVCs compensator are not much higher than the traditional system compensation; this will make the applications of shunt FACTS devices especially SVCs economically justified in unbalanced distribution network. Based on results presented in this chapter, we can conclude that integration of FACTS devices models in unbalanced practical distribution power system requires an efficient three-phase power flow program.

7. References

Acha E., Fuerte-Esquivel C, Ambiz-Perez (2004), FACTS Modelling and Simulation in Power Networks. *John Wiley & Sons*.

Bansilal, D. Thukaram, K. parthasarathy, An expert system for alleviation of network overloads, *Electric Power System Research*, vol. 40, pp. 143-153, 1997.

Bhasaputra, P., Bhasaputra and W. Ongsakul, Optimal placement of multi–type FACTS devices by hybrid TS/SA approach, 2003 *IEEE*.

Birt K. A., Graff J. J., McDonald J.D., and El-Abiad A. H., Three phase load flow program, *IEEE Trans. Power App.Syst*, vol. 95, no. 1, pp. 59-65, Jan/Feb. 1976.

Chen, B. K., M. S. Chen, R.R. Shoults, C.C. Liang, Hybrid three phase load flow, *Proc-Gener. Transm. Distrib*. vol. 137, No. 3, May 1990.

El-Keib, A. A., X. Ma, Application of artificial neural networks in voltage stability asssesment, *IEEE Trans. Power Systems*, vol. 10, no. 4, pp. 1654-1890, 1995.

Fuerte CR, Acha E, Tan SG , Rico JJ, Efficient object oriented power systems software for the analysis of large-scale networks containing FACTS controlled branches, *IEEE Trans. Power Systems*, vol. 13, no. 2, pp. 464-472, May 1998.

Hingorani, N.G, High Power Electronics and Flexible AC Transmission System, *IEEE Power Engineering review,* july 1988.

Hingorani, NG., Gyugyi L, Understanding FACTS: Concepts and Technology of Flexible A Transmission Systems. *IEEE Computer Society Press*, 1999.

Mahdad Belkacem, Tarek Bouktir, Kamel Srairi , Dynamic Compensation of the Reactive Energy using a Fuzzy Controller, *Leonardo Electronic Journal of Practices and Technologies*, Issue 7, July-December 2005, pp 1-16, ISSN 1583-1078, Academic

Mahdad, B., Optimal Power Flow with Consideration of FACTS devices Using Genetic Algorithm: Application to the Algerian Network, Doctorat Thesis, Biskra University Algeria, 2010

Mahdad, B., T. Bouktir, K. Srairi, A three-phase power plow modelization: a tool for optimal location and control of FACTS devices in unbalanced power systems, *The 32nd Annual*

Conference of the IEEE Industrial Electronics Society, Conservatoire National des Arts & Metiers Paris, FRANCE , November 7-10, 2006 Page(s): 2238 - 2243, 1-4244-0136-4/06.

Mahdad, B., T. Bouktir, K. Srairi, Flexible methodology based in fuzzy logic rules for reactive power planning of multiple shunt FACTS devices to enhance system loadability, *Power Engineering Society General Meeting,*. IEEE, 24-28 June 2007 Page(s):1 – 6, Digital Object Identifier 10.1109/PES.2007.385750.

Mahdad, B., T. Bouktir, K. Srairi, Methodology Based in Practical Fuzzy Rules Coordinated with Asymmetric Dynamic Compensation Applied to the Unbalanced Distribution Network, *International Review of Electrical Engineering (IREE),* vol. 3, no. 2, pp. 145-153 (2007), ISSN 1827- 6660, Praise Worthy Prize, Italy.

Mahdad, Belkacem; Bouktir, T.; Srairi, K. A Three-Phase Power Flow Modelization: A Tool for Optimal Location and Control of FACTS Devices in Unbalanced Power Systems, *IEEE Industrial Electronics, IECON -32nd Annual Conference on*, 6-10 Nov. 2006 Page(s):2238–2243.

Mamdouh Abdel-Akher, Khalid Mohamed Nor, and Abdul Halim Abdul Rachid, Improved three-phase power-flow methods using sequence components, *IEEE Trans. Power Systems*, vol. 20, no. 3, pp. 1389-1397, August 2005.

Marques B., and N. Toranto, A knoledge based system for supervision and control of regional voltage profile and securuty, *IEEE Trans. Power Systems*, vol. 20, no. 4, pp. 400-407, 2005.

Mayordomo, J.G, M. Izzeddine, S. Martinez, R. Asensi, A. Gomez Exposito and W. Xu, Compact and flexible three-phase power flow based on a full Newton formulation, *IEE Proc-Gener. Trans. Distrib*. Vol. 149, No. 2, March 2002.

San-Yi Lee, Wei-Nan Chang, and Chi-Jui Wu, A compact algorithm for three-phase three-wire system reactive power compensation and load balancing, *IEEE Catalogue No. 95TH 8130*, pp. 358-363, IEEE 1995.

Scala, M. L., M. Trovato, F. Torelli, A neural network based method for voltage security monitoring, *IEEE Trans. Power Systems*, vol. 11, no. 3, pp. 1332-1341, 1996.

Su, C. T., C. T. Lu, A new fuzzy control approach to voltage profile enhancement for power systems, *IEEE Trans. Power Systems*, vol. 11, no. 3, pp. 1654-1659, 1996.

Tmsovic, K. , A fuzzy linear programming approach to the reactive power/voltage control problem, *IEEE Trans. Power Systems*, vol. 7, no. 1, pp. 287-293, 1992.

Trujillo, T.V, C.R. Fuerte-Esquivel and J.H. Tovar Hernandez, Advanced three-phase static VAR compensator models for power flow analysis, *IEE Proc-Gener. Transm. Distrib*. Vol. 150, No. 1, January 2003.

Udupa, A. N., D. Thukaram, and K. Parthasaranthy, An expert fuzzy control approach to voltage stability enhancement, *International Journal of Electrical Power and Energy Systems*, vol. 21, pp. 279-287, 1999.

William D. Rosehart, Claudio A, Canizares, and Victor H. Quintana. Effect of detailed power system models in traditional and voltage-stability-constrained optimal power-flow problems, *IEEE Trans. Power Systems*, vol. 18, no. 1, February 2003.

Wilsun Xu, Hermann W. Dommel, Jose R. Marti, A generalised three-phase power flow method for initialisation of EMTP simulations, pp. 875-879, *IEEE* 1998.

Xiao-Ping Zhang, Ping Ju and Edmund Handshin, Continuation three-phase power flow: A tools for voltage stability analysis of unbalanced three-phase power systems, *IEEE Trans. Power Systems*, vol. 20, no. 3, pp. 1320-1329, August 2005.

Zhang, X. P., H. Chen, Asymetrical three-phase load-flow study based on symetrical component theory, *IEE Proc-Gener. Transm. Distrib*. Vol. 141, No. 3, May 1994.

Performance of Modification of a Three Phase Dynamic Voltage Restorer (DVR) for Voltage Quality Improvement in Electrical Distribution System

R. Omar[1], N.A. Rahim[2] and Marizan Sulaiman[3]
[1] Faculty of Electrical, Universiti Teknikal Malaysia Melaka, Durian Tunggal, Melaka,
[2]Centre of Research for Power Electronics, Drives, Automation and Control
University of Malaya, Kuala Lumpur,
[3]Faculty of Electrical, Universiti Teknikal Malaysia Melaka, Durian Tunggal, Melaka,
Malaysia

1. Introduction

There is growing concern over power quality of ac supply systems. Power quality can be defined as the ability of utilities to provide electric power without interruption. Various power quality problems can be categorized as voltage sags, swells, harmonics, transients and unbalance are considered are the most common power quality problems in electrical distribution systems (Elandy etl., 2006). These types of disturbances can cause fails in the equipments, raising the possibility of an energy interruption.Voltage swells can be defined as a short duration increase in rms of main source with an increase in voltage ranging from 1.1 p.u up to 1.8 p.u. of nominal voltage source. There are various solutions to these problems. One of the most effective solutions is the installation of a Dynamic Voltage Restorer (DVR) (Alves etl., 1999), (Boonchiam etl., 2006), (Ezoji etl', 2009), (Banaei etl., 2006). Traditional DVR (Vilathgamuwa etl., 2002) functions by injecting three single phase AC voltages in series with three-phase incoming voltage during disturbances, compensating for the difference between faulty and nominal voltages. Figure1. where the DVR consists of essentially a series connected injection transformer, a voltage source inverter (VSI), inverter output filter and an energy storage device connected to the dc-link. The power system upstream to DVR is represented by an equivalent voltage source and source impedance. The disturbances correction capability of the restorer depends on the maximum voltage injection capability of the device. In (Elnady etl., 2007) an analysis of the energy requirement of the DVR is presented and a control scheme is proposed.

A voltage sag can be defined as a decrease between 0.1 and 0.9 p.u. in the voltage root mean square value at the power frequency for durations from 0.5 cycles to 1 minute (Lam etl., 2008). The widespread use of equipment sensitive to voltage variation, has made industrial applications more susceptible to supply voltage sags. Voltage sags are normally caused by single and three phase fault in the distribution system and by the startup of induction motors of large rating (Wang etl., 2006), (Sanchez etl., 2009). Voltage sags/swells can occurs more frequently than other power quality phenomenon. These sags/swells are the most

important power quality problems in the power distribution system. IEEE 519-1992 and IEEE 1159-1995 describe the voltage sags/swells as shown in Figure 2 (IEEE Standards 1995), (Sabin etl., 1996), (Bollen etl., 1999), (Vilathgamuwa etl., 2002).
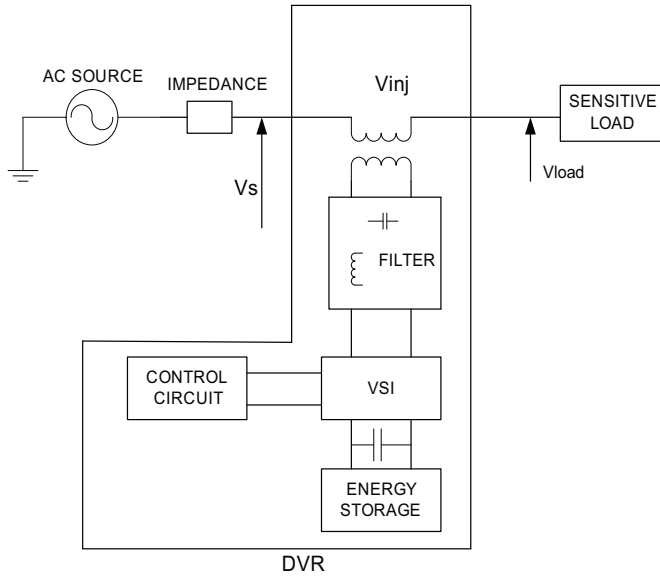

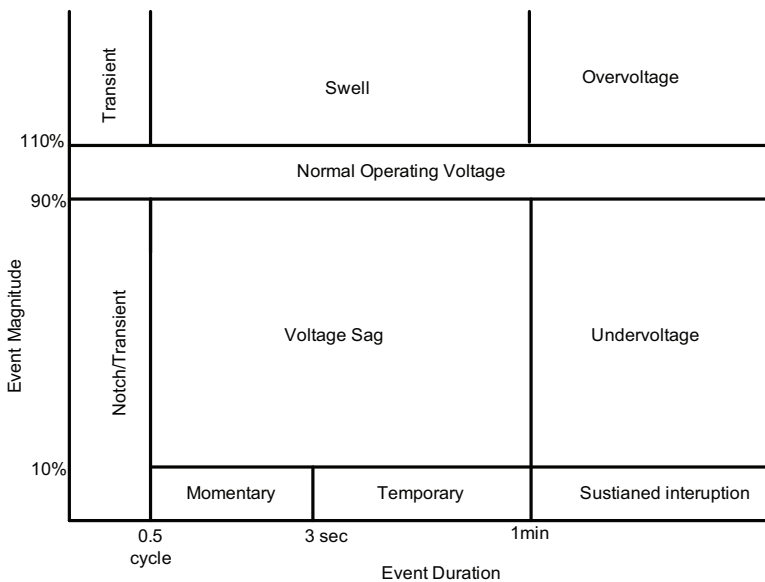Fig. 1. Conventional DVR Circuit Topology (Nielsen etl., 2005)

Fig. 2. Voltage Reduction Standard of IEEE Std 1159-1995

2. Materials and methods

2.1 DVR concept in distribution system

Figure. 1 shows a DVR is connected in series between sensitive loads in order to mitigate unbalanced loads or faults in feeder. The possibility of compensation of voltage disturbances can be limited by a number of factors including finite DVR, power rating, different load conditions, background power quality problems and different types of disturbances in the distribution system. There are several types of energy storage been used in the DVR such as battery, superconducting coil, and flywheels. These types of energy storages are very important in order to supply active and reactive power to DVR. The controller is an important part of the DVR for switching purposes. The switching inverter is responsible to do conversion process from DC to AC. The inverter ensures that only the swells or sags voltage is injected to the injection transformer. (Kim etl., 2004),(Sasitharan etl., 2010).

In this chapter, a new topology of the DVR is proposed by using a three phase four wire, three phase inverter with six Insulated Gate Bipolar Transistor (IGBTs), DVR with split capacitors (C_{dc1} and C_{dc2}) and new installation of the capacitors filtering scheme. With these new topologies the proposed DVR offers the following advantages over the traditional DVRs:

- A Three phase four wire DVR is used, the beneficial of this configuration is that to control the zero sequence voltage during the unbalanced faults period.
- A three phase DVR with three single phase full bridge inverter has been proposed in the previous DVR. Typically, only one capacitor is used at the dc side of the inverter. In these configuration three control systems and many IGBTs switches are needed, so it's very costly.
- The placement of the capacitors filter at the high voltage side causes the harmonics for the voltage at the connected load is reduced.
- The DVR with split capacitors (C_{dc1} and C_{dc2}) causes zero sequence current to circulate through the DC –link; therefore unbalanced voltage sags with zero sequence can be compensated effectively.

2.2 The circuit of the proposed topology

Four different system topologies for DVRs has been analyzed and tested in (Nielsen etl., 2005). Figure 3 illustrates a new configuration model of the proposed DVR system, and the system consists of a DC voltage source (V_{dc}), three single phase injection transformer, a three phase voltage source PWM inverter, L-C output filter and sensitive loads. In this proposed designed of DVR, special attention must be paid on three types of configuration as follows;

- Filtering schemes configuration
- Isolation or distribution transformer and
- Injection transformer winding.

 Filtering configuration for DVR is very important as it related with the system dynamic response. The filtering system of the DVR can be placed either on the high voltage or the low-voltage side of the injection transformer and are referred to as line side filter and inverter-side filter respectively. (Kim etl., 2004), (Sasitharan etl., 2010). In the proposed filtering system as shown in Figure 3, the filtering scheme is installed for both on the low and high voltages. The filter inductor, capacitor and resistor (L_{fa},L_{fb},L_{fc} ,C_{fa},C_{fb},C_{fc} and R_a,R_b,R_c) are installed on low voltage side between the series inverter and the transformer

and the high voltage side(C_1,C_2 and C_3), when it is placed in low voltage side, high order harmonics from the three phase voltage source PWM inverter is by pass by the filtering scheme and its impact on the injection current rating can be ignored. The type of this filtering configuration can also eliminate switching ripples produced by the inverter.

In Figure.3 also highlighted that the three phase isolation or distribution transformer has a Delta connected primary winding and a Wye connected secondary winding. The input and output rated line to line voltage of 415 V_{rms}. The values of the load resistors R_a, R_b and R_c are chosen to be 47 ohm, therefore the current through each load resistor are as follows;

$$I_{Load\ resistor} = \frac{|V_{phase}|}{Load\ Resistor} = \frac{240 V_{rms}}{47 \Omega} = 5.10 A_{rms}$$

The minimum apparent power with an additional 25 % safety factor can be calculated as follow;

$$S_{transformer,1\varphi} \, (\min) = 1.25 \left[\sqrt{3} \, (V_{L-L})(I_L) \right]$$
$$= 1.25 \left[\sqrt{3} \, (415)(5.1) \right]$$
$$= 4.6 \, KVA$$

Based on the value of $S_{transformer}$, the minimum ratings of a 5KVA isolation transformer was chosen. In this research a Delta-Wye step-down transformer with the neutral grounded is used. The advantages of its configuration, zero sequence current will not propagate through the transformer when unbalanced faults occur on the high voltage level. Also third harmonic voltages are eliminated by the circulation of the harmonic current trapped in the primary Delta winding. However, a Wye-Wye step down distribution transformer with the neutral grounded will not solve these problems in unbalanced fault situation.
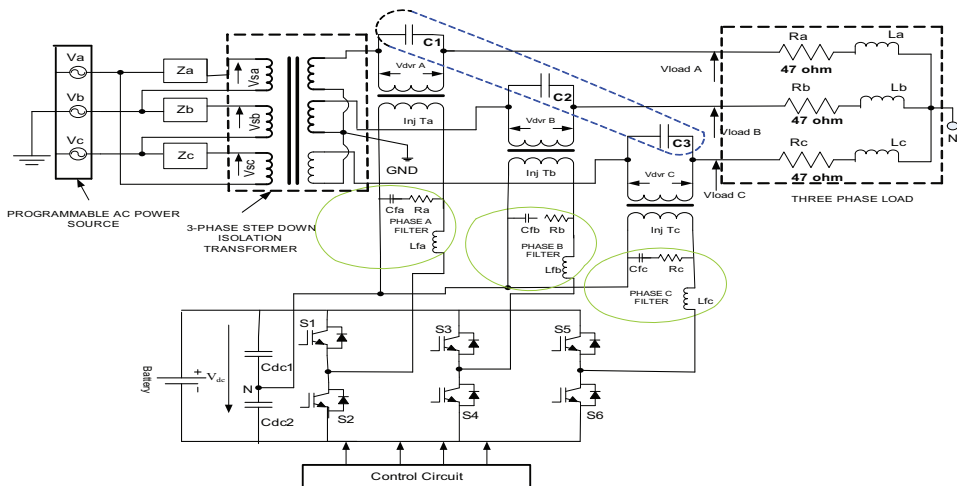
Fig. 3. New configuration of the proposed DVR

Performance of Modification of a Three Phase Dynamic Voltage Restorer (DVR)
for Voltage Quality Improvement in Electrical Distribution System
309

A three phase DVR with three single phase full bridge inverter has been proposed in (Zhou etl., 2006). Typically, only one capacitor is used at the dc side of the inverter. In these configuration three control systems and many IGBTs switches are needed, so it's very costly. In this research a three phase four wire DVR with three phase inverter is proposed to control the zero sequence voltage during unbalanced faults.

The new types of DVR systems employ the d-q-0 transformation or Park's transformation for balanced and unbalance voltage detection. The proposed d-q-0 operated DVR system is implemented using DSP board. The main aspects of the control system are shown in Figure 4 and include the following blocks:
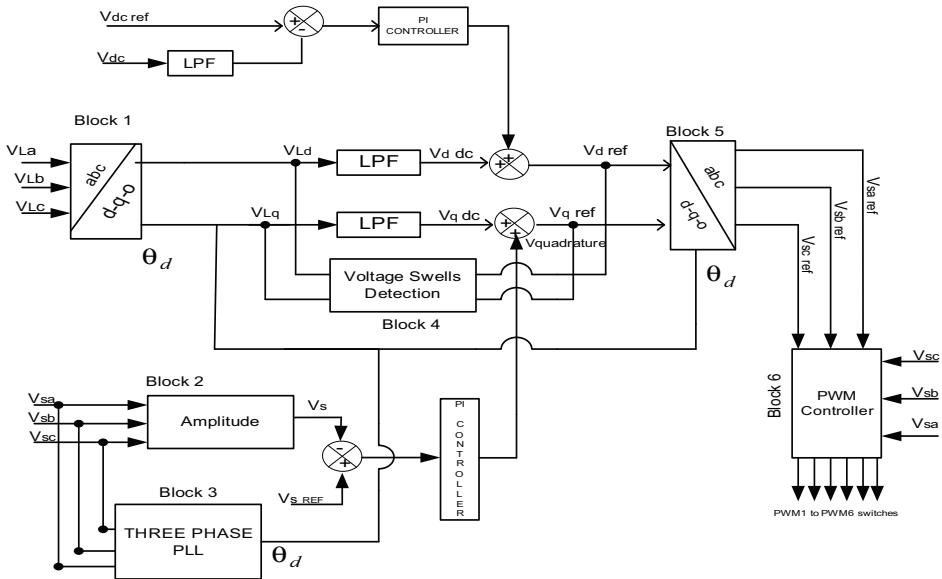
Fig. 4. Block Diagram Control of the proposed Scheme of DVR for Voltage Swells Detection

- Block 1 is used to convert the three phase load voltages (V_{La}, V_{Lb}, V_{Lc}) into the α-β-0 coordinates as in equation (1)

$$\begin{bmatrix} V_\alpha \\ V_\beta \\ V_o \end{bmatrix} = Q \begin{bmatrix} V_{La} \\ V_{Lb} \\ V_{Lc} \end{bmatrix} \tag{1}$$

Where $Q = \dfrac{2}{3} \begin{bmatrix} 1 & \dfrac{-1}{2} & \dfrac{-1}{2} \\ 0 & \dfrac{\sqrt{3}}{2} & \dfrac{-\sqrt{3}}{2} \\ \dfrac{1}{2} & \dfrac{1}{2} & \dfrac{1}{2} \end{bmatrix}$

- Block 1 is also used to convert the three phase load voltages (V_{La}, V_{Lb}, V_{Lc}) into the α-β-o coordinates as in equation (1), the three phase load voltages reference components $V_{\alpha\text{-ref}}$, $V_{\alpha\text{-ref}}$ and Vo_{ref} can be converted to $V_{d\,ref}$ and $V_{q\,ref}$ as shown in equation (2).

$$\begin{bmatrix} V_d \\ V_q \end{bmatrix} = \frac{2}{3} \begin{bmatrix} \cos\theta & \sin\theta \\ -\sin\theta & \cos\theta \end{bmatrix} \begin{bmatrix} V_\alpha \\ V_\beta \end{bmatrix} \tag{2}$$

Transformation to dqo to abc

$$\begin{bmatrix} V_\alpha \\ V_\beta \end{bmatrix} = \frac{2}{3} \begin{bmatrix} \cos\theta & -\sin\theta \\ \sin\theta & \cos\theta \end{bmatrix} \begin{bmatrix} V_d \\ V_q \end{bmatrix} \tag{3}$$

$$\begin{bmatrix} V_a \\ V_b \\ V_c \end{bmatrix} = \begin{bmatrix} 1 & 0 & 1 \\ -0.5 & \dfrac{\sqrt{3}}{2} & 1 \\ -0.5 & \dfrac{\sqrt{3}}{2} & 1 \end{bmatrix} \begin{bmatrix} V_\alpha \\ V_\beta \\ V_o \end{bmatrix} \tag{4}$$

- Block 2 is considered as a source voltages (V_{sa}, V_{sb}, V_{sc}). The amplitude of AC voltage at the sources (V_{source}) can be calculated as shown in equation (5);

$$V_{source} = \frac{2}{3}\left(\sqrt{\left(V_{sa}\right)^2 + \left(V_{sb}\right)^2 + \left(V_{sc}\right)^2} \right) \tag{5}$$

Block 3 is a three phase PLL (Phase-locked loop). PLL comprises a Phase Detection (PD) scheme, a Loop Filter (LF), and a Voltage Controlled Oscillator (VCO). The phase difference between the input and the output signals is measured using a phase detection scheme and passed through a loop filter to generate an error signal driving a voltage-controlled oscillator (VCO) which generates the output signal. The PLL block is implemented in d-q-0 synchronous reference frame as shown in Figure 5. The PLL block allows to detect the amplitude and phase (V_s and θ) of fundamental positive sequence components of the source voltages. A PI regulator is used to control this variable and the output of this regulator is the source frequency, the source voltage angle can be obtained through the integration of the source frequency. The PLL output (θ_d) is an estimation of the source angle to the fundamental frequency. Let us detail the PLL block as shown in Fig.5(a). Let the measured network voltages at the Point Common Coupling (PCC) are given by V_{PCC} (a,b,c) could be converted to the d-q-0 dynamic reference frame V_{PCC} (d,q,0) using the Park Transformation as follow:

$$V_{PCC}\left(d,q,0\right) = S \bullet V_{PCC}\left(a,b,c\right) \tag{6}$$

where $S =$ can be defined as:

$$S = \sqrt{\frac{2}{3}} \begin{pmatrix} \dfrac{1}{\sqrt{2}} & \dfrac{1}{\sqrt{2}} & \dfrac{1}{\sqrt{2}} \\ \cos\theta & \cos\left(\theta - \dfrac{2\pi}{3}\right) & \cos\left(\theta + \dfrac{2\pi}{3}\right) \\ -\sin\theta & -\sin\left(\theta - \dfrac{2\pi}{3}\right) & -\sin\left(\theta + \dfrac{2\pi}{3}\right) \end{pmatrix} \tag{7}$$

The input voltage is considered sinusoidal with amplitude V, then:

$$V_{PCC}(a,b,c) = \begin{pmatrix} V_{PCC,\,a} \\ V_{PCC,\,b} \\ V_{PCC,\,c} \end{pmatrix} = \begin{pmatrix} V\sin\left(\omega_s t + \phi\right) \\ V\sin\left(\omega_s t + \phi - \dfrac{2\pi}{3}\right) \\ V\sin\left(\omega_s t + \phi + \dfrac{2\pi}{3}\right) \end{pmatrix} \tag{8}$$

The value of $\omega_s t + \phi$ in (8) can be replaced by θ_s, equations (8) and (6) could be substituted in equation (7), the below expression is obtained after rejecting the homopolar component since it not be used[18],

$$V_{PCC}(d,q) = \begin{pmatrix} V_{PCC,\,d} \\ V_{PCC,\,q} \end{pmatrix} = \sqrt{\frac{3}{2}}\, V \begin{pmatrix} \sin\left(\theta_s - \theta_d\right) \\ -\cos\left(\theta_s - \theta_d\right) \end{pmatrix} \tag{9}$$

$$V_{PCC}(d,q) = \begin{pmatrix} V_{PCC,\,d} \\ V_{PCC,\,q} \end{pmatrix} = \sqrt{\frac{3}{2}}\, V \begin{pmatrix} \sin\left(\Delta\theta\right) \\ -\cos\left(\Delta\theta\right) \end{pmatrix} \tag{10}$$

Where $\Delta\theta = \left(\theta_s - \theta_d\right)$

The supply voltages will be locked by the PLL if there is an error between the phase of the supply voltage and the output of the PLL system is equal zero, in the case of $\Delta\theta = 0$

Block 4 is the detection scheme for the voltage Unbalanced compensator. From Figure 5 shows that, the synchronous frame variables, V_d and V_q are used as inputs for low pass filters to generate voltage references in the synchronous frame. Block 5 receive the components of the load voltage vectors V_d ref and V_q ref and transforms them to three phase coordinates using equation (3) and (4) the generation voltages are used as the voltage reference. The DC link error in Figure 4 is used to get optimized controller output signal because the energy on the DC link will be changed during the unbalance voltage. Block 6 is the PWM block, this block provides the firing for the Inverter switches (PWM1 to PWM6). The injection voltage is generated according to the difference between the reference load voltage and the supply voltage and is applied to the voltage source Inverter (VSI).
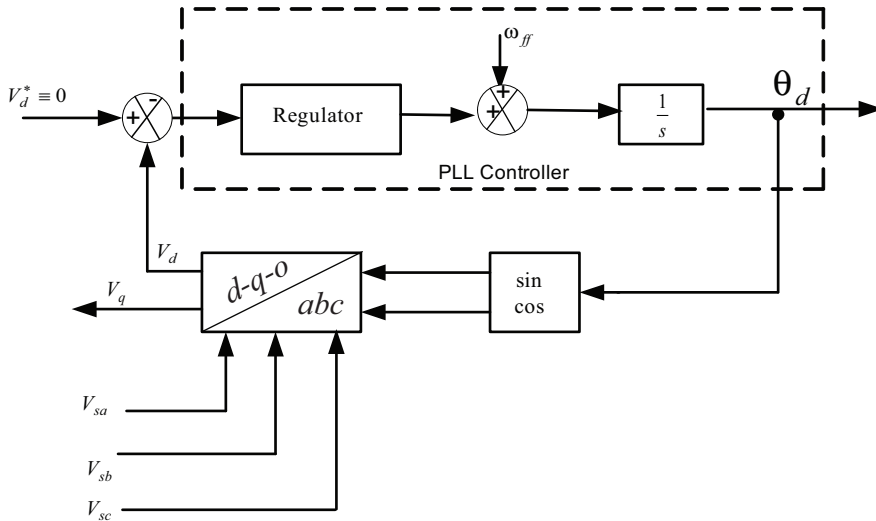
Fig. 5. The Diagram of the three phase dq PLL

In this research a Delta-Wye isolation or distribution transformer with the neutral grounded is used. The advantages of its configuration, zero sequence current will not propagate through the transformer when unbalanced faults occur on the high voltage level. The DVR with split capacitors (C_{dc1} and C_{dc2}) causes zero sequence current to circulate through the DC –link; therefore unbalanced voltage sags with zero sequence can be compensated effectively. A Three phase four wire DVR is used, the beneficial of this configuration is that to control the zero sequence voltage during the unbalanced faults period the placement of the capacitors filter at the high voltage side causes the harmonics for the voltage at the connected load is reduced. The used PLL algorithm is based on a fictitious electrical power (three phase dq PLL), the selected structure has a simple digital implementation and therefore low computational burden. An improvement of the proposed controller uses the d-q-0 rotating reference frame as it accuracy is high as compared to stationary frame-based techniques. The proposed controller is able to detect the voltage disturbances and control the inverter to inject appropriate voltages in order restore the load voltage. This control strategy uses the d-q-0 rotating reference frame because it offers higher accuracy than stationary frame-based techniques.

2.3 DSP implementation

The DSP modeled eZdsp™ F2812 based on the Texas Instruments TMS320F2812 DSP produced by Spectrum Digital Incorporated was used to verify control algorithms proposed for the proposed DVR. The TMS320F2812 was selected as it has a 32-bit CPU performing at 150 MHz [*Data Manual*, Texas Instruments, 2006]. Among its interesting features, useful in this work, were a 12-bit A/D module handling 16 channels, and two on- chip event manager peripherals, providing a broad range of functions particularly useful in applications of control. The architecture of the TMS320F2812 DSP from Texas Instruments are summarized in the diagram from Figure 6.

TMS320F2812 DSP BLOCK DIAGRAM

Code Security

| 128 Kwords Sectored Flash | 18K Words RAM | 4K Words Boot ROM |

XINTF — **Memory Bus**

Interrupt Management

150-MPS C2812 32-Bit DSP

32x32-Bit Multiplier | R-M-W Atomic ALU

32-Bit Timers (3) | 32-Bit Register File

Real-Time JTAG

Event Manager A

Event Manager B

12-Bit ADC

Watchdog

MeBSP

CAN 2.0B

SCI-A

SCI-B

SPI

GPIO
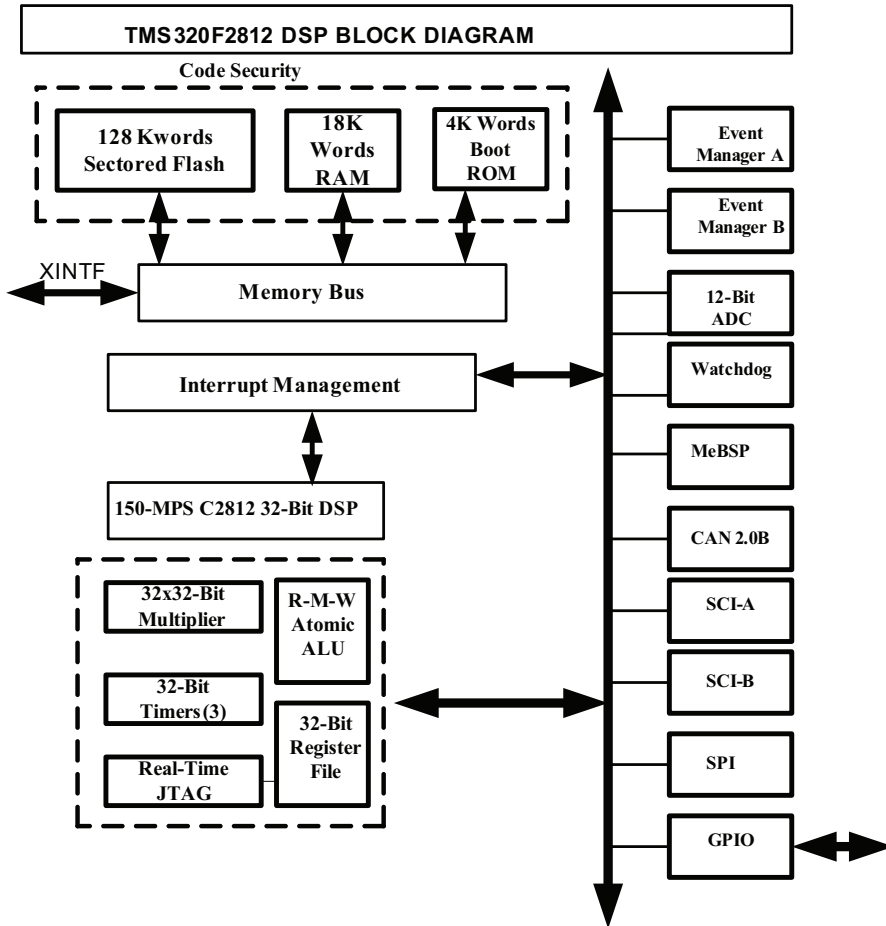
Fig. 6. TMS320F2812 Architecture

Texas Instruments facilitates development of software for TI DSPs by offering Code Composer Studio (CCS). Used in combination with Embedded Target for TI C2000 DSP and Real-Time Workshop, CCS provides an integrated environment. Executing code generated from Real-Time Workshop on "TMS320F2812 DSP", requires that Real-Time Workshop to generate target code that is tailored to the specific hardware target. Target-specific code include I/O device drivers and interrupt service routines (ISRs). Generated source code must be compiled and linked using CCS so that it can be loaded and excuted on DSP. The voltage and current sources were sent to the analog digital converter of the DSP. The sampling times are governed by the DSP timer called a CpuTimer0 which generates periodic interrupt at each sampling times Ts. The Interrupt Service Routine (ISR) will read the sampling value of the voltage and current source from the analog digital converter (ADC) The DSP controller offers a display function, which monitor the disturbances in the real

time. The control algorithm which is proposed in section 4 is tested with a control using DSP TMS 320F 2812. The controller has its own ADC converters and PWM pulse outputs. The inputs of a 3-leg Voltage Source Inverter (VSI) are the PWM pulses which are generated by the digital controller.
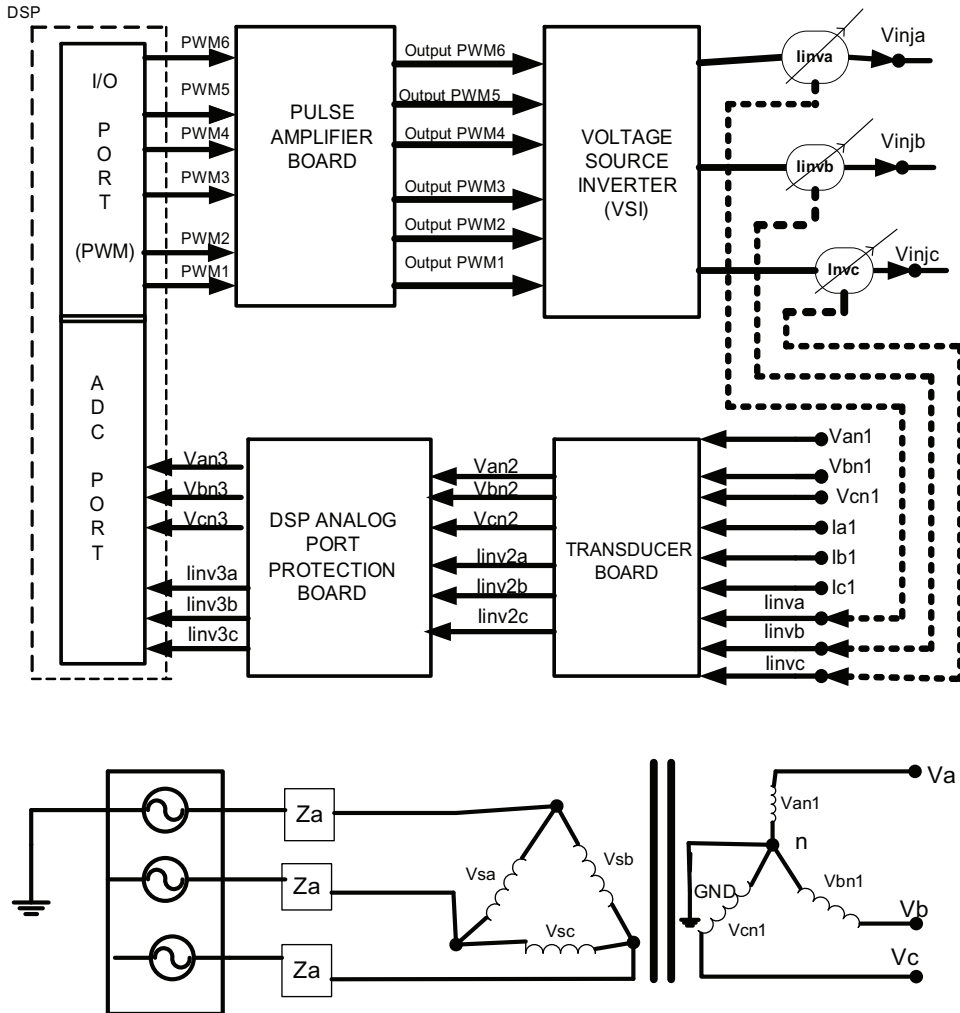
Fig. 7. A schematic diagram for overall control of DSP

Figure 8 shows the signal flow of the input and output of the DVR prototype. The designed transducer board consists of the three LV25-P voltage transducer and the three LA55-P current transducers. The inputs of the ADC of the DSP controller (TMS320F2812) chosen for this application are limited to 0 to 3V. Therefore the power signals have to be scaled accordingly in order to generate signal of magnitude variation between 0 to 3V. In this

application the voltage and current transducers are used to scale down and convert the signals to a ground referenced signal suitable for the DSP. A power supply of a 5V is required to power both the voltage and current transducers for their operation. The three source side terminal voltages between the line and neutral V_{an1}, V_{bn1} and V_{cn1} from the transformer in Figure 8 are measured by three of the voltage transducers LV25-P. The inverter output currents I_{inva}, I_{invb}, I_{invc} from the Voltage Source Inverter (VSI) are also detected by the three of current transducers LA55-P. The inverter currents are used to boost up the voltage response of the DVR. The three source voltages and the inverter output currents are entered to DSP through the DSP Analog Port Protection Board. The output signals of the transducer board as shown in Figure 8 must be fed into the DSP Analog Port Protection Board before connecting them to the ADC port of the DSP. This is to ensure that the DSP board is protected from any over voltage that may occur during signal acquisition. The line currents I_{a1}, I_{b1} and I_{c1} control independently of the three phase voltage signals V_{an1}, V_{bn1} and V_{cn1} to ensure the VSI can operate properly and avoid it from damage. The whole control system was coded by C language and compiled into DSP board. The ADC port of the DSP board receives all these signals from the DSP Analog Port Protection Board and it will process the sampled voltage and current signals. Six digital PWM pulses are produced via I/O Port (PWM) and the output signals of the I/O Port (PWM) are passed through to a Pulse Amplifier Board. The Pulse Amplified Board is needed to up the PWM digital signals to the voltage level required by the VSI. The VSI will produce the three phase output voltages required for voltage disturbances mitigation.

3. Results and discussion

The system modeled in Figure 3 has been simulated using Matlab/Simulink. The performance of the system has been considered with the load is represented by a series equivalent rated at $415V_{rms}$, 5KVA at 0.95 load power factor. Simulation and experimental parameters are given in Table 1. The performance of the DVR for different supply disturbances is tested under various operating conditions. Several simulation of the DVR with proposed controller scheme and new configuration of it have been made.

As for the filtering scheme is placed in the high voltage side in this case, high order harmonic currents will penetrates through the injection transformer and it will carry the harmonic voltages. Fast Fourier Transform (FFT) analyses for the output voltage at the connected load has been done without or with capacitors filter (C_1, C_2 and C_3) at the high voltage level side of the transformer as shown in Figure 8. Figure.8 (a) shows that FFT analysis when the transformer at the high voltage level is not installed with the capacitors filter. The Total Harmonics Distortion (THD) for the voltage is about 33.29% ,when the capacitors filter are placed at the high level side, THD value decreases to 2.34% as shown in Figure. 8(b). Thus the harmonics are reduced from 33.29 % to 2.34%. The THD value of 2.34 % when capacitors filter are placed at the high voltage transformer side is satisfying the IEEE-519 standard harmonic voltage limit.

Investigation on the DVR performance can be observed through testing under various disturbances condition on the source voltage. The proposed control algorithm was tested for balanced and unbalanced voltages swells in the low voltage distribution system. In case of balance voltage swell, the source voltage has increased about 20-25% of its nominal value. The simulation results of the balance voltage swells as shown in Figure 9(a). The swells

voltages occur at the time duration of 0.06s and after 0.12 s the voltage will restore back to its normal value. The function of the DVR will injects the missing voltage in order to regulate the load voltage from any disturbance due to immediate distort of source voltage. The restore voltage at the load side can be seen in Figure 9(b). The Figure shows the effectiveness of the controller response to detect voltage swells quickly and inject an appropriate voltage. In case of unbalance voltage swells, this phenomenon caused   due to single phase to ground fault. One of the phases of voltage swells have increased around 20-25% with duration time of swells is 0.06 s. The swells voltage will stop after 0.12 s. At this stage the DVR will injects the missing voltage in order to compensate it and the voltage at the load will be protected from voltage swells problem.

Main Supply Voltage per phase	415 V_{rms}
Line Impedance	Ls =0.5mH Rs = 0.1 Ω
Series transformer turns ratio	1:1
DC Bus Voltage	100V
Filter Inductance	2mH
Filter capacitance	1uF
Load resistance	47 Ω
Load inductance	60mH
Line Frequency	50Hz
Switching Frequency	5kHz

Table 1. Simulated And Experimental System Parameters

The third simulation study is to show the performance of proposed configuration DVR for one single phase to ground fault. As shown in Figure 10 the proposed topology injects the desired voltage to the grid in order to mitigate voltage swells in the distribution system. From the results, the swells load terminal voltage is restored and help to maintain a balanced and constant to its nominal voltage.
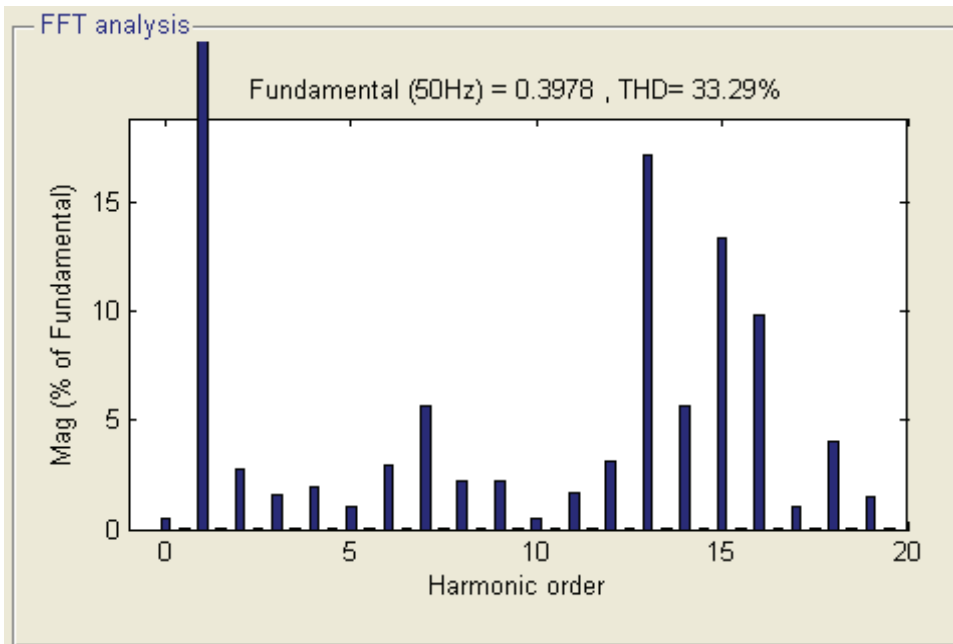
a)
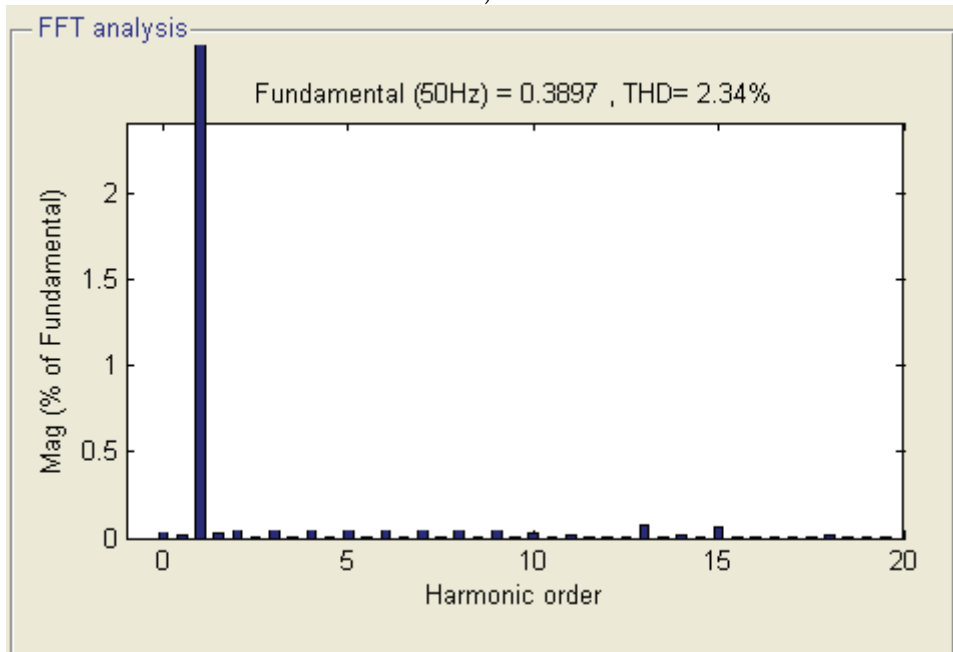
b)

Fig. 8. FFT Analysis for Voltage a) without or b) with Capacitors Filter
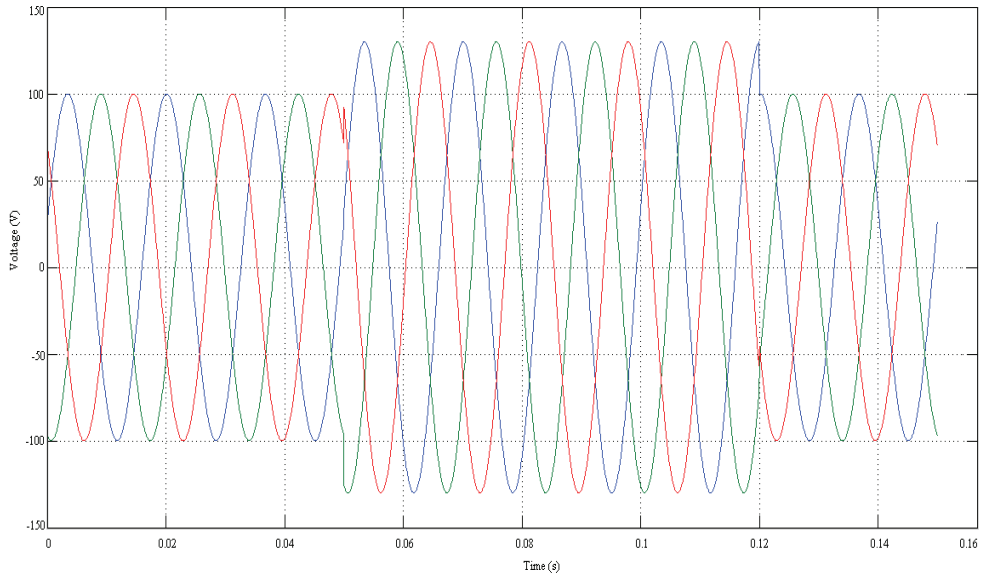
a)
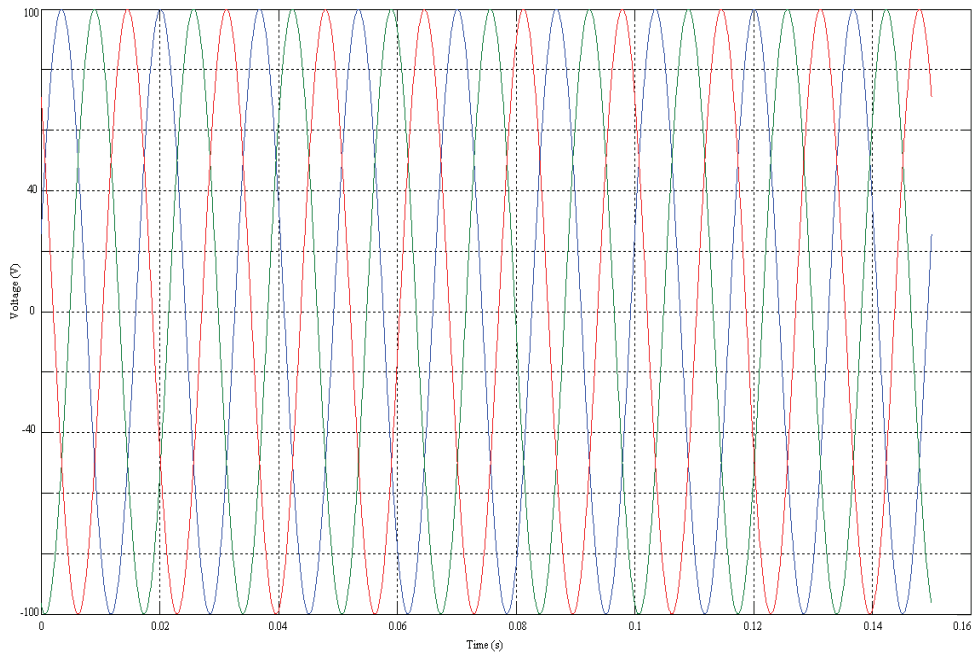
b)

Fig. 9. a) Balanced Voltages Swells, and b) Load Voltages Compensation
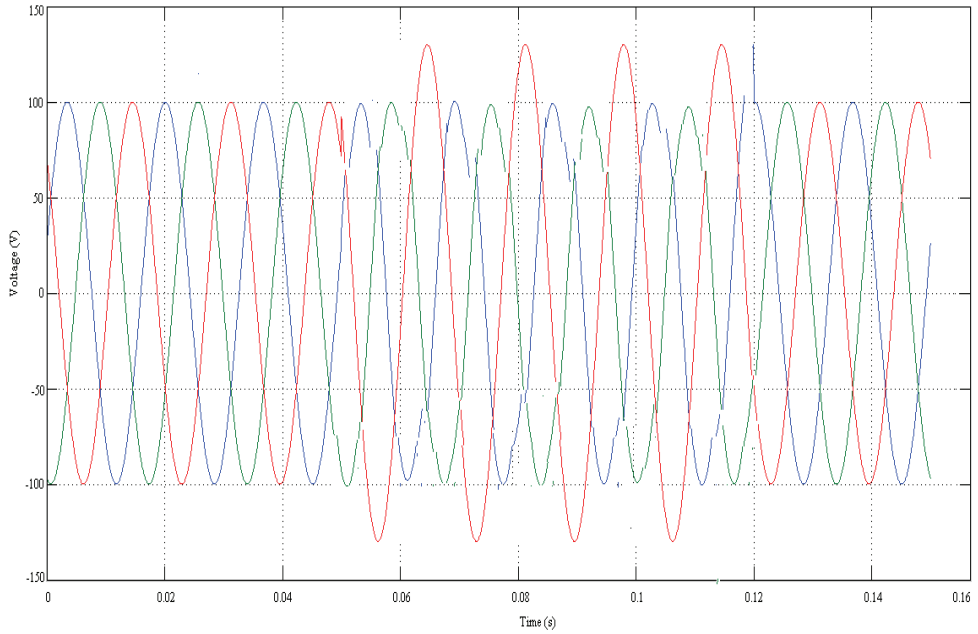
a)
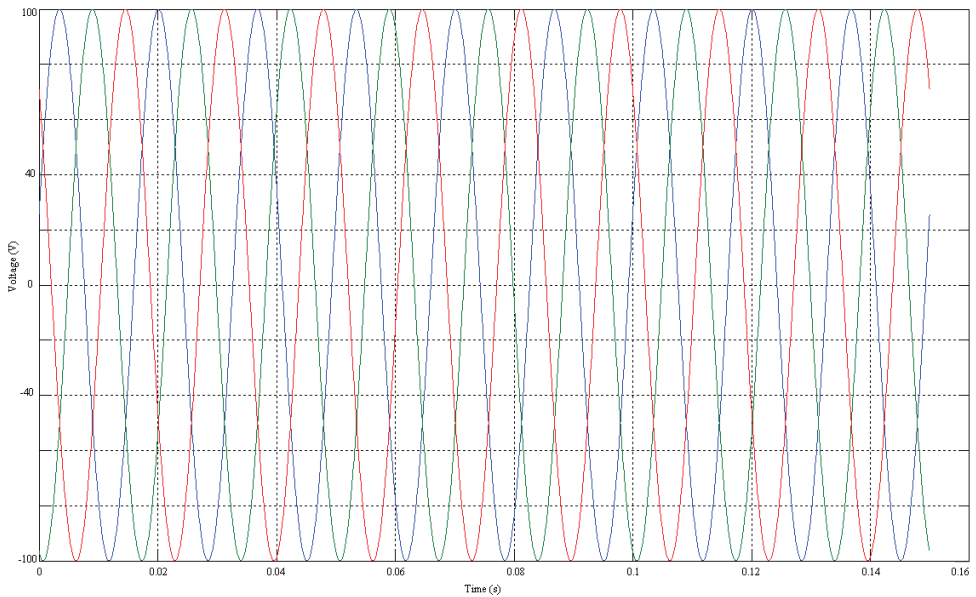
b)

Fig. 10. a) One Phase Voltage Swells, and b) Voltage Swells after Compensation
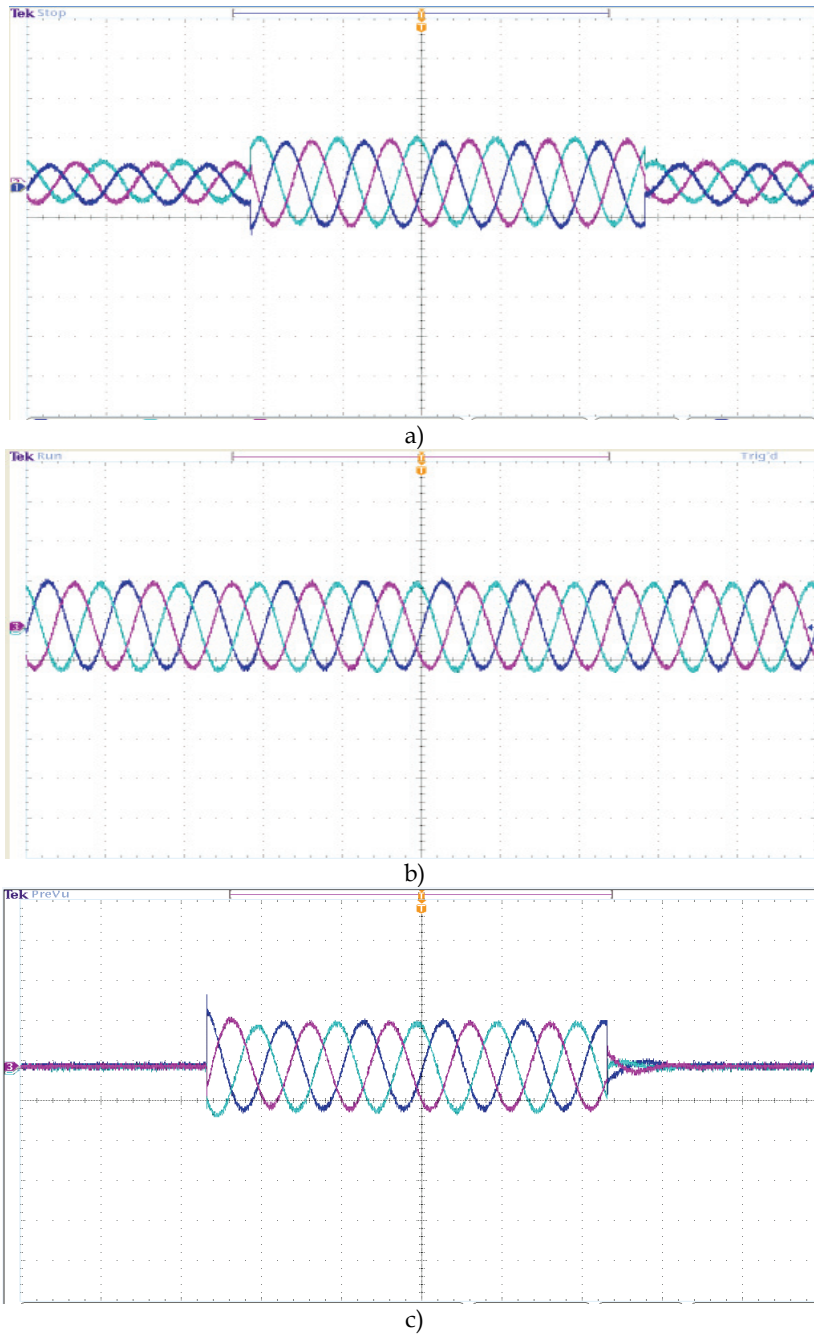
Fig. 11. a) Balanced Voltages Swells (50V/div), b) Compensation of balanced Voltages Swells (50V/div), and c) injection Voltages (50V/div)
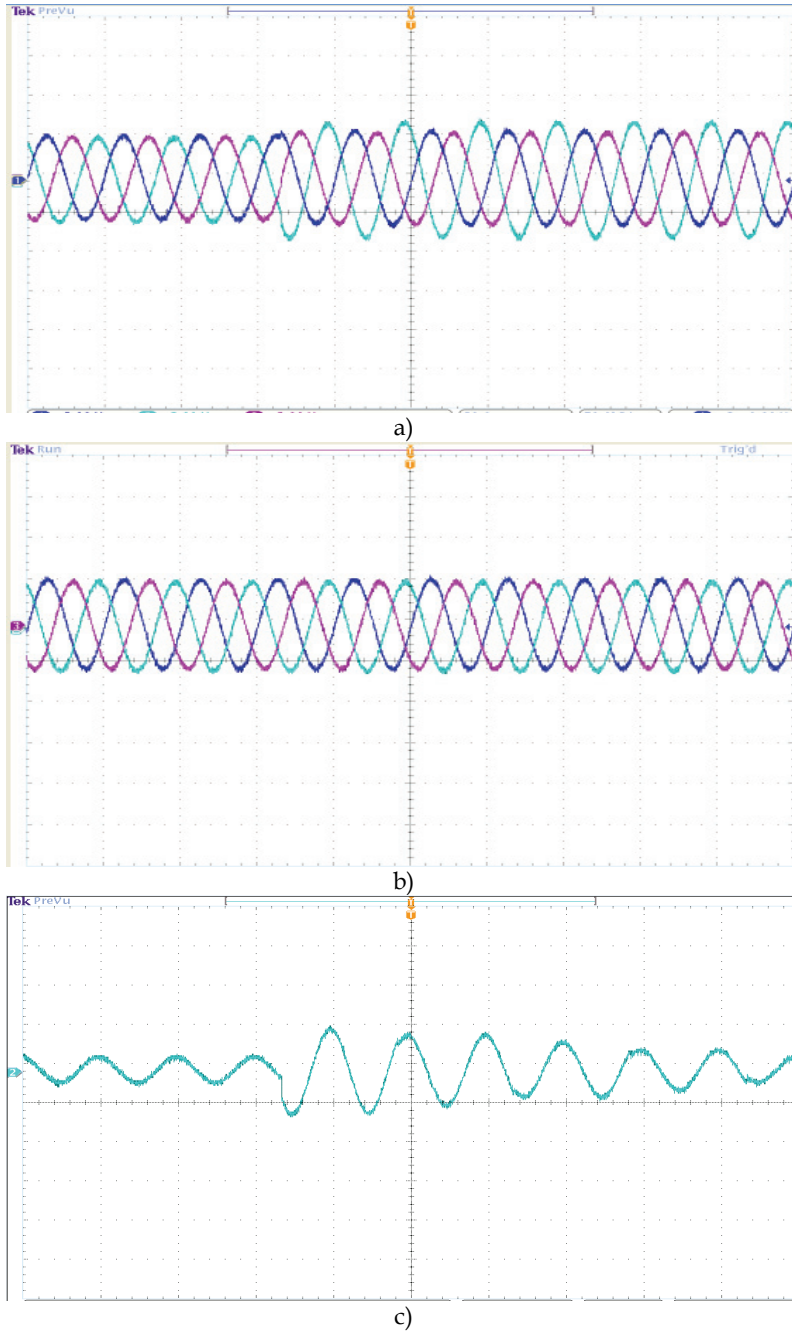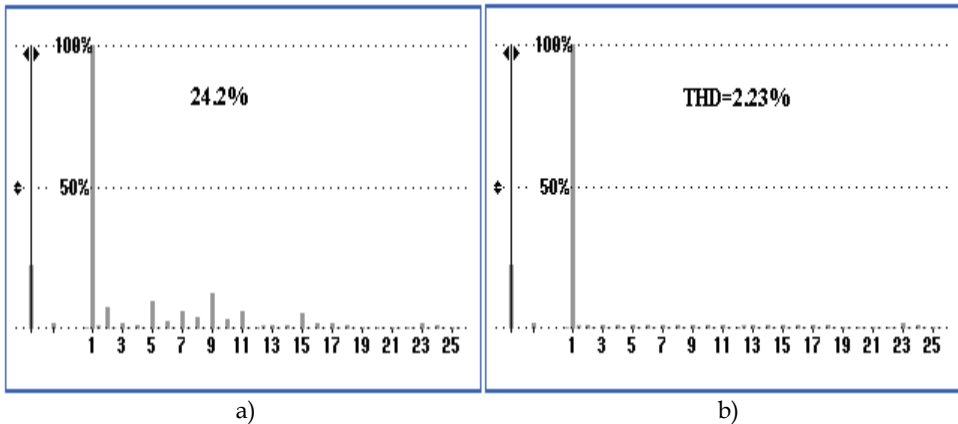
a)

b)

c)

Fig. 12. a) Unbalanced Voltages Swells (50V/div), (b) Compensation of unbalanced Voltages
Swells (50V/div), and c) an injection Voltages of unbalanced voltage swells (50V/div)

Fig. 13. a) Total Harmonic Distortion Current (THD$_I$) under unstable dc-link, b) Total Harmonic Distortion Current (THD$_I$) under stable dc-link
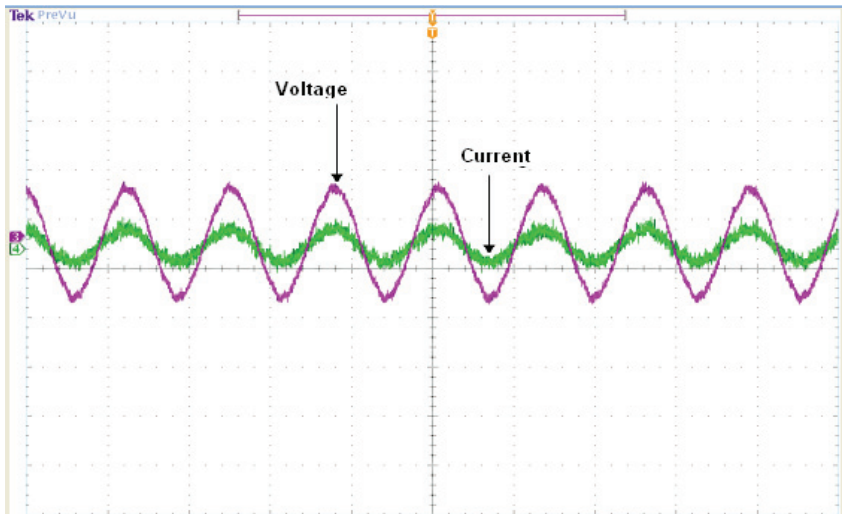
Fig. 14. Phase voltage (50V/div) and current (10 A/div) at the connected load

In the experiment, a 25% three phase and single phase swells are generated from their nominal voltage. The experimental results obtained for both conditions are shown in Figures 11 and 12 respectively. Figure 11(a) shows the waveform of utility voltage when the tested system suffered a disturbance of 25% voltage swells. Balanced voltage swells are created immediately after a fault. The DVR injects fundamental voltage in series with the supply voltage. Figure 11(b) shows the load terminal voltages which are restored through the compensation by DVR. An injection voltages in order to recovery balanced voltage swells can be shown in Figure 11(c). The capabilities of the DVR in mitigating one single phase to ground fault is also investigated. Figure 12 (a) shows the series of voltages components for unbalanced conditions for one phase to ground fault. The DVR load

voltages are shown in Figure 12 (b). As can be seen the swells load terminal voltage is compensated and help to maintain a balanced and constant load voltage and the control method that can generate the required voltages from significantly disturbance source voltages. Figure 12(c) shows the injection voltage of a single phase swells. As shown in Figure 3 there are two DC-link capacitors were used, it acts as an energy storage element of the DVR. The rating of the IGBT is totally depending on the DC link of the DVR prototype. Harmonic current is depending on the DC link voltage. The function of the DC link is to absorb the ripple, therefore the values of the DC side capacitors (Cdc1 and Cdc2) should be large enough without the distorting the dc bus voltage much. If there is distortion in the dc voltage the inverter output will get distorted with third harmonic content. With the stability of the DC bus and the Total Harmonic Distortion for current (THD_I) for third harmonics current is reduced 24.2 % to 2.23% as shown in Figure. 13(a) and 13(b). Phase voltage and current at the load are the sinusoidal waveform without any distortion due to design of the good capacitor filter and use of the suggested controller, this can be seen in Figure 14.
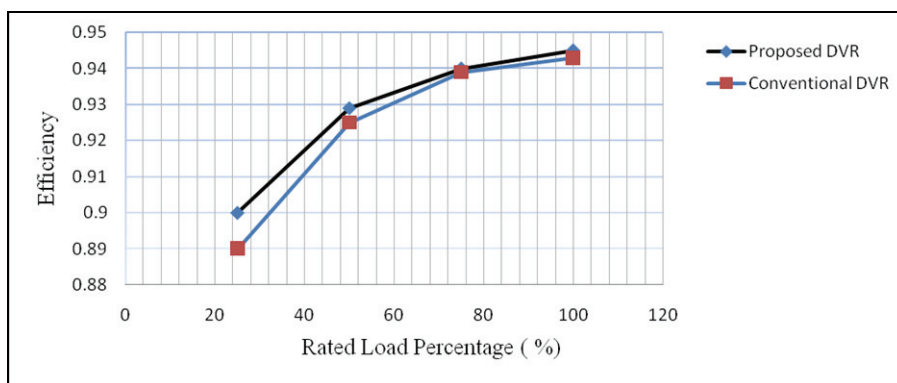
Fig. 15. Efficiency for Proposed and Conventional DVRs

The efficiencies between the proposed DVR with capacitors filter scheme as shown in Figure 3 and the conventional DVR without capacitors filter have been compared and it is observed that the proposed DVR is more efficient than the conventional one as shown in Figure 15.

4. Conclusions

The proposed topologies to be a promising solution to voltage quality improvement in distribution network. Sensitive equipment can be protected from potential voltage swells using modification of a three phase DVR . The performance of the proposed topologies and an improvement of suggested controller can be observed through simulation and experimental results. These results validate the proposed method for the detection and control of the DVR from voltage swells problem in low voltage distribution system.

5. References

Alves M.F., Ribeiro T.N., Voltage Sag an Overview of IEC and IEEE Standards and Application Criteria, *Proceedings of IEEE Conference on Transmission and Distribution*, 1999,Vol 2. pp. 585-589.

Banaei M.R., Hosseini S.H., Khanmohamadi S. and Gharehpetian G.B.,Verification of a New Energy Control Strategy for Dynamic Voltage Restorer by simulation, *ELSEVIER Simulation Modeling Practice and Theory*, 14(2006),pp. 113-125.

Boonchiam P., and Mithulananthan N., Dynamic Control Strategy in Medium Voltage DVR for Mitigating Voltage Sags/Swells *International Conference on Power System Technology*, 2006, pp. 1-5.

Elnady A. and Salama M.M. A., Mitigation of Voltage disturbances using adaptive perception –based control algorithm, *IEEE Trans. Power Delivery.*, vol. 20, no.1, pp,309-318, Jan.2005.

Elnady, A., and Salama, M.M. A: Mitigation of Voltage Disturbances Using Adaptive Perceptron-Based Control Algorithm, *IEEE , Transactions on Power Delivery*, 2005, 20, (1),pp, 309-318.

Ezoji, A. Sheikholeslami, Tabasi M. and Saeednia M.M., Simulation Of Dynamic Voltage Restorer Using Hysteresis Voltage Control, *European Journal of Scientific Research* (EJSR), 27(1) (2009), pp. 152-166.

IEEE Standards Board (1995), *IEEE Std.* 1159-1995, IEEE Recommended Practice for Monitoring Electric Power Quality. IEEE Inc. New York.

Kim H, Kim J H and Sul S K, A Design Consideration of Output Filters for dynamic Voltage Restorer. 35th *Annual IEEE Power Electronic Specialist Conference* 2004.

Lam C.S., Wong M.C., and Han Y.D., Voltage swell and over-voltage compensation with unidirectional power flow controlled dynamic voltage restorer, *IEEE Trans. Power Delivery.*, vol.23, no.4, pp. 2513-2521, Oct. 2008.

MS320F2812 Digital Signal Processors, *Data Manual*, Texas Instruments, 2006.

Nielsen J.G. and Blaabjerg F., A Detailed Comparison of system J Topologies for Dynamic Voltage Restorer, *IEEE Transaction on Industrial Applications*, vol.41, no.5, Sept/Oct.2005, pp.1272-1280.

Sabin D., An assessment of distribution system power quality, Elect.Power Res. Inst., Palo Alto, CA, EPRI Final Rep. TR-106294-V2, vol. 2, Statistical Summary Report, May 1996.

Sanchez P.R., Acha E., Calderon J.E.O., Feliu V., and Cerada A.G., A versatile control scheme for a dynamic voltage restorer for a dynamic voltage restorer for power quality improvement, *IEEE Trans. Power Delivery.*, vol. 24, no.1, pp. 277-284 Jan. 2009.

Sasitharan S., Mahesh K. Mishra, B. Kalyan Kumar, V. Jayashankar, Rating and design issues of DVR injection transformer. *International Journal of Power Electronics* 2010 - Vol. 2, No.2 pp. 143 – 163.

Vilathgamuwa M., Ranjith Pcrcra A. A. D. and Choi *S.* S., Performance improvcmcnt of the dynamic voltage restorer with closed-loop load voltage and current-mode control, *IEEE Transactions on PowerElectronics,* vol. 17, no. *5,* Sept. 2002, pp. 824-834.

Wang B., Venkataramanan G., and IIIindala M., Operation and control of a dynamic voltage restorer using transformer coupled H-bridge converter, *IEEE Trans. Power Electron.*,vol.21, no.4, pp. 1053-1061 Jul. 2006.

Zhou G., Shi X, Fu C. and Wang Y., Operation of a Three phase Soft Phase Locked Loop Under Distorted Voltage Conditions Using Intelligent PI Controller, in *Proc. 2006 IEEE Region 10 Conf.* (TENCON 2006), pp 315-320.

Voltage Sag Mitigation
by Network Reconfiguration

Nesrallh Salman, Azah Mohamed and Hussain Shareef
Universiti Kebangsaan Malaysia
Malaysia

1. Introduction

The electric power distribution system must be designed to operate and supply acceptable level of electrical energy to customers. Power utilities must ensure that the power supply to customers is with voltage magnitude within standard levels. Other features like minimal interruptions and minimal system power loss also must be considered. Hence, the quality and reliability of supply must be maintained in an acceptable level even during contingencies.

Voltage magnitude is one of the parameters that determine the quality of power supply. A decrease in voltage magnitude may result in voltage sag which is currently considered as one of the main power quality problems. Voltage sag is defined as a decrease in magnitude between 0.1 and 0.9 pu in rms voltage at a power frequency of duration from 0.5 cycle to 1 min (IEEE Std 1159, 1995). Voltage sag may cause sensitive equipment to malfunction and process interruption and therefore are highly undesirable for some sensitive loads, especially in high-tech industries. However, loads at distribution level are usually subjected to frequent voltage sags due to various reasons.

Voltage sag can be treated as a compatibility problem between equipment and power supply. When installing a new piece of equipment, a customer needs to compare the equipment sensitivity with the performance of the supply. There are various engineering solutions available to eliminate, correct or reduce the effects of power quality problems (Kusko &Thomson, 2007). Currently, a lot of research works are under way to solve the problem of voltage sag in distribution systems. Most of these research works focus on installing voltage sag mitigation devices (Sensarma et al., 2000). Other researchers focus on improving the immunity level of customer equipment by installing custom power devices to improve the voltage sag ride through capability (Shareef et al., 2010). Some other research works focus on utility efforts in finding feasible solutions to mitigate voltage sag problem. Since system faults are considered as main causes of voltage sags, utilities try to prevent faults and modify the available fault clearing practice in power systems. Normally, voltage sag assessment at a particular site in the network consists of determining the frequency of sags of specified sag magnitude and duration over a period of interest (Conrad & Bollen, 1997). It is also dependent on the utility fault performances, the way the fault affects propagation of disturbance in the system, and the customer's service quality requirements (Shen et al., 2007). For voltage sag assessment, voltage sag characteristics has to be

accurately reproduced by means of a time-domain simulation tool, and using a stochastic prediction to incorporate the random nature of voltage sag in the mitigation process (Qader et al., 1999, Heine & Lehtonen, 2003, Aung & Milanovic´, 2006 & Martinez et al., 2006).

A method of minimising cost of losses due to voltage sag by employing network reconfiguration was introduced by (Sanjay et al., 2007). (Chen et al., 2003) introduced a voltage sag mitigation method by means of implementing a series of utility strategies for a period of 10 years. Network reconfiguration was proposed as a voltage sag mitigation method by using feeder transfer switches in power distribution systems. Switches at sectionalizing points of a distribution network are used to find the weak points during voltage sags and to transfer the customers at the weak points to other sources (Sang et al., 2000). The graph theory was employed as a tool in finding suitable solution to alter system switches to reconfigure distribution networks (Sabri et al., 2007 & Assadian et al., 2007). The power distribution network can be reinforced against voltage sag propagation, where the graph theory is selected as an efficient tool to find the shortest path between the main power source and every fault location (Salman et al., 2009). Based on the electrical distance towards the fault current, network reconfiguration is employed for voltage sag mitigation where the exposed weak area in distribution network is initially identified. Then the size of the exposed weak area of specified voltage sag is reduced by network reconfiguration. Based on the new technique of switching action, the weak areas in distribution systems can be identified and placed as far away as possible from the main source considering distribution system operation.

This chapter focuses on the utility efforts towards voltage sag mitigation in particular employing the network reconfiguration strategy. The theoretical background of the proposed method is first introduced and then the analysis and simulation tests on a practical system are described to highlight the suitability of network reconfiguration as a method for voltage sag mitigation. The analysis of simulation results suggest some significant findings that may assist utility engineers to take the right decision in network reconfiguration.

2. Overview of utility efforts in voltage sag mitigation

The utility engineers considered faults as the main source of voltage sags. Reducing the number of faults is a considerable way of mitigating voltage sags. The duration of voltage sag can be reduced by the reduction of fault clearing time of power protection equipment. The change in the distribution system design and structure may affect the voltage sag performance and propagation. An overview about the utility efforts on voltage sag mitigation was introduced by (Sannino et al., 2000). Brief overview on utility efforts in voltage sag mitigation are explained in the following sections 2.1, 2.2 and 2.3.

2.1 Reducing the number of faults

Limiting the number of faults is an effective way to reduce not only the number of voltage sags, but also the frequencies of short and long interruptions. Fault prevention actions may include the institution of tree trimming policies, the addition of lightning arresters, insulator washing and the addition of animal guards. A considerable reduction in the number of faults per year can otherwise be achieved by replacing overhead lines by underground cables, which are less affected by adverse weather.

2.2 Reducing the fault-clearing time

Reducing the fault-clearing time leads to less severe voltage sags. This method does not affect the number of events, but their durations. The modern static circuit breakers are able to clear the fault well within a half cycle at the power frequency, thus ensuring that no voltage sag can last longer. Moving from the load to the source, the tripping delay increases from 300 to 500 ms. If faster fault clearing is needed, then the whole system has to be redesigned and all the protective devices have to be replaced with faster ones. This would greatly reduce the grading margin between the breakers, thus leading to a significant reduction in fault-clearing time.

2.3 System design and configuration

Many actions in distribution system design can be employed for mitigating voltage sag. A certain improvement can be achieved by installing current-limiting reactors or fuses in all the other feeders originating from the same bus as the sensitive load. These actions increase the "electrical distance" between the fault and the common bus, thus decreasing the depth of the sag for the sensitive load. The increase in the electrical distance can also be achieved by change in system configuration.

3. Network reconfiguration in power distribution systems

Network reconfiguration is a process of altering the topological structures of distribution feeders by changing the open/closed status of the sectionalizing and tie switches. A whole feeder, or part of a feeder, may be served from another feeder by closing a tie switch linking the two while an appropriate sectionalizing switch must be opened to maintain radial structures (Civanlar, et al., 1988). In other words, network reconfiguration is a switching action which may be applied to change the network configuration for improving operation performance.

The network reconfiguration process is generally used for loss reduction, load balancing and voltage profile improvement in distribution systems. It may be used to reinforce the network against voltage sags propagation by increasing the line impedance towards fault current during short circuit events (Salman et al., 2009). A brief overview of network reconfiguration to reinforce against voltage sag propagation is presented below. The idea is based on the principles of circuit theory. To understand this idea, consider a typical distribution system shown in Fig. 1. If the substation is treated as a point of common coupling (PCC) between the power source and fault location, V_{source} is main source voltage, Z_s is he Thevenin's impedance behind the source, Z_f is fault impedance and Z_i is a line impedance of the feeder i. Then the substation bus voltage V_{pcc} during a fault event at bus i can be derived as:

$$V_{pcc} = \frac{Z_i + Z_f}{Z_i + Z_f + Z_s} V_{source} \qquad (1)$$

From (1), it can be understood that V_{pcc} can be improved by finding another higher impedance route between substation and bus i. For example, if $Z_n > Z_i$, the bus i can be supplied through feeder, n by closing the tie switch, SW_n and opening sectionalizing switch, S_i as shown in Fig. 1. This change in configuration will increase the substation bus voltage magnitude. After reconfiguration, if $Z_f = 0$, the new substation voltage magnitude can be written as:

$$V_{pcc1} = \frac{Z_n}{Z_n + Z_s} V_{source} \tag{2}$$

where V_{pcc1} is the voltage magnitude of substation which is taken as the point of common coupling after reconfiguration.
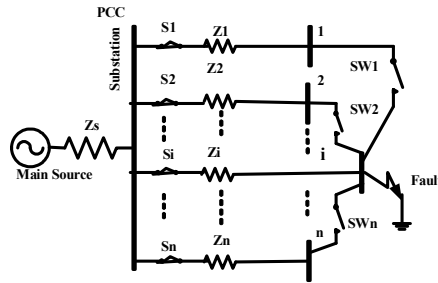

Fig. 1. Typical distribution system

The feasible reconfiguration must be valid according to the operation constraints of the distribution network. The operation constraints are summarized as:
i.   The network must be of radial structure.
ii. All the network nodes and loads must be connected,
iii. The nominal bus voltages must be within standard limits, $V_{min} \leq V_i \leq V_{max}$ where V_{min} is the lower limit of nominal voltage magnitude; V_i is the voltage magnitude of bus i and V_{max} is the upper limit of nominal voltage magnitude.
iv. The current flows must be within the thermal limits of the lines, $I_i \leq I_{imax}$. where I_i is the current of line i and I_{imax} is the thermal limit of the line i.
v.   System line loss (F_{loss}) must be within acceptable limits. F_{loss} can be formulated as:

$$F_{loss} = \sum_{1}^{n} R_i \frac{P_i^2 + Q_i^2}{V_i^2} \tag{3}$$

where R_i : branch resistance;
       n   : number of branches;
       P_i : branch i active power flow;
       Q_i : branch i reactive power flow;
       V_i : voltage magnitude at the end bus of line i.
Although, this change in network configuration improves the voltage magnitude during the fault event, sometimes it may cause unacceptable voltage drop in the lines and hence inadequate nominal voltage at various buses during steady state operation. It means that the network reconfiguration must be done in such a way that it does not violate the limits of system voltage profile at steady state condition.
Network reconfiguration can be employed as a siutable tool for voltage sag mitigation as well as for line loss reduction in distribution systems. Based on the right decision of reconfiguring a distribution network, a suitable objective function of network reconfiguration can be formulated. If the decision to be taken is for reducing the financial losses, voltage sag can be mitigated by a very cheap and feasible method, that is by only switching action.

In network reconfiguration, the switching action must be done in the manner of improving voltage magnitudes for a considerable number of system buses. It is important to determine the weak area in the system before implementing the switching action for network reconfiguration. Weak area is defined as a bus or group of buses that can be considered as effective in voltage sag propagation throughout the same distribution system. It means that the system buses that experience voltage sag during the occurrence of short circuit event are considered as buses in the weak area. By implementing appropriate switching actions, the distribution network can be reconfigured. Thus, the aim of network reconfiguration is to place the weak area as far away as possible from the main power source.

4. Distribution system reinforcement by network reconfiguration

This section illustrates the proposed method of distribution system reinforcement by network reconfiguration. The procedure includes system modelling, power flow and short circuit analysis, application of graph theory and network reconfiguration. The graph theory technique is utilized to find the shortest path between the main power source and the defined weak buses. Based on the graph theory, a feasible solution can be obtained for solving the distribution network reconfiguration problem considering voltage sag mitigation. Mitigating of voltage sag can be achieved by increasing the number of buses reaching the healthy condition due to network reconfiguration. In this case a bus is said to be healthy when its voltage magnitude lies between 0.9 pu and 1.06 pu. Based on the selection of a suitable path by the graph theory, the objective of increasing the number of healthy buses (N_{hlth}) can be carried out by changing the status of predefined switches (i.e. the tie and sectionalizing switches) in the distribution system. The principle behind the graph theory is described as follows:

A graph G = (V,E) consists of a set of vertices (or nodes) V = {A, B, C & S} and edges E = {1, 2, 3, 4, 5 & 6}. Generally, every edge connects two vertices. Fig. 2(a) shows an undirected graph consisting of four vertices connected with six edges. For example vertex A has three incident edges: 1, 3 & 4 while Vertex B has three incident edges: 2, 3 & 5 and etc. In the graph theory, a path π in a graph is a sequence of vertices such that from each of its vertices there is an edge to the next vertex in the sequence. The first vertex is called the start vertex and the last vertex is called the end vertex. A path is the m-th path starting from any start vertex and ending at a specified vertex. The set of m alternative paths ending at vertex, i can be described as:

$$\Pi_m^i = \left\{ \Pi_1^i, \Pi_2^i, \ldots\ldots, \Pi_m^i \right\} \tag{4}$$

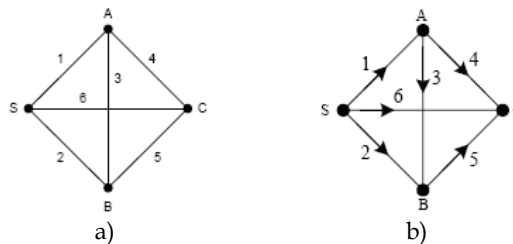a)   b)

Fig. 2. Example of graph with 4 nodes in a) undirected b) directed type

For example, all alternative paths from the start vertex, S to the end vertex, A can be searched in both graphs as depicted in Fig. 2. In the undirected graph, it is realized that five alternative paths can be obtained as:

$$\Pi_1^A = 1, \Pi_2^A = 2-3, \Pi_3^A = 6-4, \Pi_4^A = 2-5-4, \Pi_5^A = 6-5-3 \qquad (5)$$

Meanwhile, in the directed graph, only the end node with one path can be achieved: $\Pi_1^A = 1$. Graph theory is employed to determine the shortest path between the main source and fault location after every switching action. The shortest path is considered as the fault current route during fault events. The impedance of the fault current route is considered as significant element of fault current reduction. To understand the employment of graph theory in finding suitable impedance for the fault current path, the 16-bus distribution system shown in Fig. 3a is selected. If a fault location at bus 12 is appointed, the graph representation of the system is shown in Fig. 3b. The shortest path between the main source and fault location can be presented as:

$$\Pi_i^{12} = 1.2 - 2.8 - 8.9 - 9.12 \qquad (6)$$

where i=1, 2, 3, . . . , maximum number of configurations. 1.2 indicates the branch joining between the buses 1 and 2, 2.8 is the branch joining between 2 and 8 and etc.
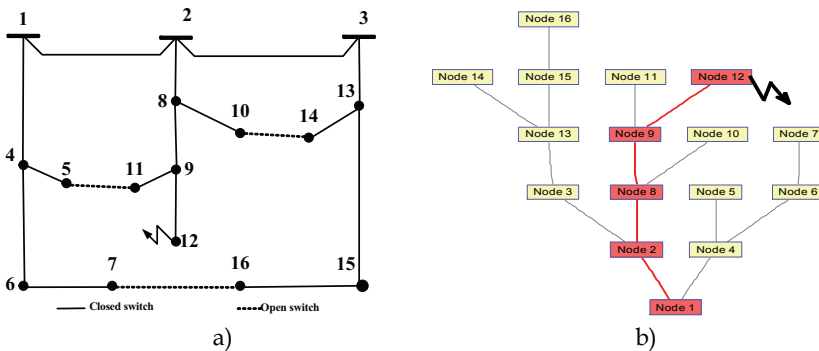
Fig. 3. 16-bus distribution system before reconfiguration a) one line diagram, b) graph representation

The total impedance of the path Π_i (Z_{Π}) can be calculated as:

$$Z_{\Pi_i} = Z_{1.2} + Z_{2.8} + Z_{8.9} + Z_{9.12} \qquad (7)$$

where $Z_{1.2}, Z_{2.8}, Z_{8.9},$ and $Z_{9.12}$ are the series impedances of the branches 1.2, 2.8, 8.9 and 9.12 respectively.

If some switching action is done by opening the branch 1.2 and closing the branch 5.11, the 16-bus system is reconfigured as shown in Fig.4a. The 16-bus system can be presented by applying graph theory to find the new shortest path between the main source (bus 1) and fault location (bus 12) as shown in Fig. 4b. The shortest path can be presented as:

$$\Pi_{i+1}^{12} = 1.4 - 4.5 - 5.11 - 11.9 - 9.12 \qquad (8)$$

where Π_{i+1} is the next path after reconfiguration, comprising of the corresponding branches and the total impedance of the path Π_{i+1}. $Z_{\pi i+1}$ can be calculated as:

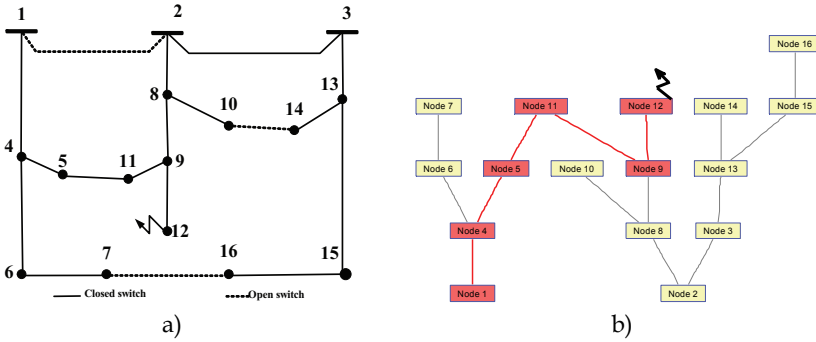$$Z_{\Pi_{i+1}} = Z_{1.4} + Z_{4.5} + Z_{5.11} + Z_{11.9} + Z_{9.12} \tag{9}$$

a)   b)

Fig. 4. 16-bus distribution system after reconfiguration a) one line diagram b) graph representation

The increase in the impedance of fault current path results an increase in the electrical distance between the main source and the fault location. Based on the increase of impedance path the exposed area of the fault location is reduced. The reduction of the exposed area means mitigating the voltage sag propagation. In other words, the system network can be reconfigured to mitigate voltage sag by using the graph theory algorithm as a tool for finding the suitable electrical distance between the main source and the weak bus.

During reconfiguration process, for every change in the system configuration the number of healthy buses (N_{hlth}) and system losses (F_{loss}) must be calculated by the short circuit analysis and steady state load flow. In other words, an algorithm is to be developed to maximize the number of healthy buses ($V \geq 0.9$ pu) due to reconfiguration action. If C_i is the healthy condition (0 or 1) for bus i during voltage sag duration, then it can be formulated as:

$$C_i = \begin{cases} 1 \cdots\cdots 0.9 \leq V_i \leq 1.06 \\ 0 \cdots\cdots else \end{cases} \tag{10}$$

If N_{bus} is the total number of the system buses, the number of healthy buses (N_{hlth}) can be calculated as:

$$N_{hlth} = \sum_{i=1}^{Nbus} C_i \tag{11}$$

Equation (11) is used for calculating the number of healthy buses (N_{hlth}). The calculation must be done before and after each reconfiguration process. The reconfiguration process is subjected to the system operation constraints as mentioned earlier in Section 3.

If $N_{hlth}b$ and $N_{hlth}a$ represent the calculated number of healthy buses before and after reconfiguration, respectively, the calculated improvement of the number of healthy buses due to reconfiguration process (N_{imp}) can be expressed as:

$$N_{imp} = \frac{N_{hlth}a - N_{hlth}b}{N_{hlth}b} \times 100 \tag{12}$$

An acceptable increment of losses of the system (INd) must be defined before the reconfiguration. The value of INd can be defined according to the required improvement of the number of healthy buses for the system reliability level.

If $F_{loss}b$ and $F_{loss}a$ represent the system losses before and after reconfiguration, respectively, the calculated percentage increase of system losses after each reconfiguration process (INc) can be expressed as:

$$INc = \frac{F_{loss}a - F_{loss}b}{F_{loss}b} \times 100 \tag{13}$$

where $F_{loss}b$ and $F_{loss}a$ can be calculated by (3). The reconfiguration process is constrained by computed INc ≤ INd and other system operation constraints as mentioned in Section 3.

4.1 Distribution system modeling

All distribution system components, i.e., lines and cables, loads, transformers, large motors and generators have to be converted into equivalent reactance (X) and resistance (R) on common bases. The main system components models are described below.

i.   Lines and cables: Lumped parameter models are adopted for lines and cables, as they are much simpler to model and still provide results of appropriate accuracy. R is the resistance, X is the reactance and B is the line Susceptance (Martin et al., 2006). The line or cable model is shown in Fig. 5.
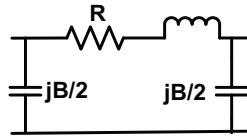
Fig. 5. Equivalent circuit for lines and cables

ii.   Loads: The static loads can be approximated as constant impedance, where each load is converted into equivalent impedance of same values for positive and negative sequence (Martin et al., 2004). The load model is shown in Fig. 6.
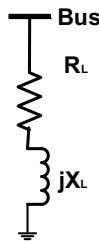
Fig. 6. Equivalent circuit for load

In Fig.6, if the load bus voltage is V_L and the load is $P_L + jQ_L$, the load impedance ($R_L + jX_L$) can be calculated using (13).

$$R_L + jX_L = \frac{V_L^2}{P_L + jQ_L} \tag{13}$$

iii. Generators: There are three values of reactance defined in generator, namely sub-transient reactance (X_d''), transient reactance (X_d') and synchronous reactance (X_d) (J. J. Grainger, 1994) as shown in Fig. 7a, Fig. 7b and Fig. 7c respectively. Because most short-circuit protecting devices, such as circuit breakers and fuses, operate well before steady-state conditions are reached, generator synchronous reactance is excluded in calculating fault currents (K. R. Padiyar, 1995). Generators are modelled in short circuit analysis by resistance and sub-transient reactance in series with a constant driving voltage (K. R. Padiyar, 1995) as shown in Fig. 7a.
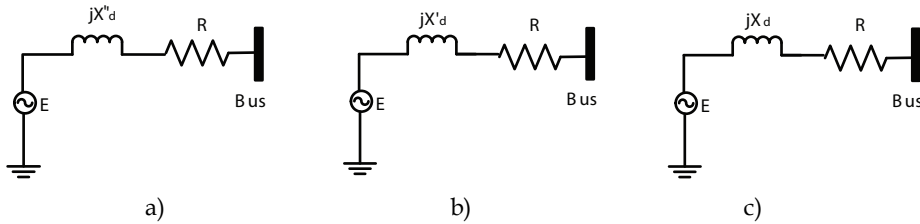
Fig. 7. Equivalent circuit for synchronous generator with internal voltage E and
a) subtransient reactance X''_d b) transient reactance X'_d; c) synchronous reactance X_d

iv. Transformer: Transformer modelling is one of the most important issues in voltage sag simulations. Linear models of transformers are suitable if the sag is caused by short circuit faults. It can be used to obtain accurate voltage sag characteristics (Martin et al., 2006). Voltage sag characteristics is significantly affected by the difference in winding connections, grounding methods, and tap settings, where transformers introduce different sequence representation and different values of voltage and current resulting in quite different fault current flows in fault calculation. The transformer is modelled as series impedance ($Z_T = R_T + jX_T$), where R_T and X_T are transformer resistance and reactance respectively. The parameters R_T and X_T can be determined by short circuit test and they are equal in value for bath positive and negative sequence representation. The connections of the primary and secondary windings of three phase transformer are considered main principles to derive the zero sequence equivalent circuit and to determine the phase shift in the positive and negative sequence circuits. Fig. 8 shows the five commonly used transformer connections and their zero sequence equivalent circuits.

The impedance, Z_0 accounts for the leakage impedance, Z_T and the neutral impedances, Z_N and Z_n where applicable which can be calculated as $Z_0 = Z_T + 3Z_n$. Z_N and Z_n are the neutral impedances of primary and secondary windings of the transformer, respectively (Grainger, 1994). The tap-changing ratio must be taken into account in the transformer impedance calculation. The different types of delta-wye connections of transformer winding result in a phase shift of n×30 (n =1, 5, 11, . . ., etc). The voltage sag propagation is affected by these phase shifts and therefore must be considered in the models (IEEE Std-1346, 1998). The admittance matrix can be built at first using the above models and the impedance system matrix can be determined by using the inversing admittance matrix.
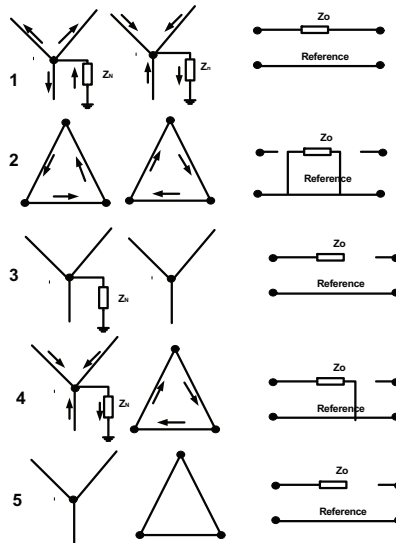
Fig. 8. Zero sequence representation of transformer connections (Grainger, 1994)

4.2 Simulation procedure

The simulation procedure for implementing network reinforcement using the graph theory is described as follows:

i.   Prepare all the required system data for load flow, fault analysis and voltage sag calculation i.e.; lines and cables, buses, transformers, loads and generators.

ii. Define the permitted increase percentage of system losses (INd) and the maximum permitted improvement in the number of healthy buses (N_{hlth}).

iii. Run load flow analysis program to identify the steady state voltage profile and system losses before reconfiguration.

iv. Simulate faults at all buses in the system except system substations to determine the weak area in terms of voltage sag. The fault locations are considered as the main sources of voltage sag propagation and the number of healthy buses due to fault at the weak bus must be calculated by (10) and (11).

v.   Apply the graph theory algorithm to change the network configuration and to find a path in the network with suitable line impedance between the weak area and the main power source by (8) and (9).

vi. Evaluate the new configuration by running load flow analysis to check the limitations of system buses voltage magnitudes (0.9pu ≤ V ≤ 1.06pu) and lines Currents (I ≤ Imax) as well as the checking of the increase in system losses (INc ≤ INd).

vii. Check the improvement in voltage magnitude of all buses and calculate the number of healthy buses (N_{hlth}) by (10) and (11).

viii. Repeat steps v to vii until the number of healthy buses is improved significantly during the fault at weak bus.

ix. Repeat step iv after network reconfiguration to confirm that there is no weak area.

The proposed network reconfiguration method for mitigating voltage sag by improving the number of healthy buses during fault events can be shown in terms of a flowchart as in Fig. 9.
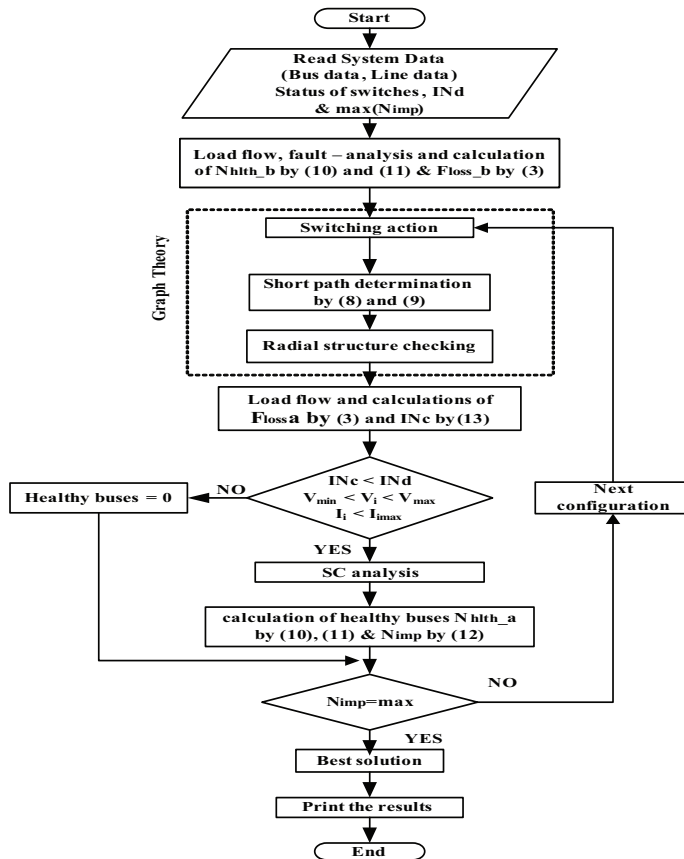
Fig. 9. Proposed distribution system reinforcement using network reconfiguration

5. Results and analysis

A practical distribution system shown in Fig. 10 is selected to validate the proposed method. The system is composed of 47 buses and 42 lines supplied by a 132KV sub transmission system through four substations which are connected to buses 2, 17, 34 and 39. The substations 2 and 17 are fed by 132/11KV, 30MVA, while the substations 34 and 39 are fed by 132/33KV, 45MVA and bus 1 is the swing bus. The seven tie switches (SWs) between buses 25-38, 29-38, 24-29, 20-23, 16-18, 4-19 and 4-14 may be used as alternatives to change the configuration of the system in case of some events or contingencies.

The selected system represents multi voltage levels of 132KV, 33KV, 11KV, 6.6KV, 3.3KV and 0.433KV, where the voltage levels are fed through 15 transformers of difference sizes. The system includes three large induction motors of 2000 KW which are connected to buses of numbers 9 (3.3KV), 10 (0.433KV) and 21 (3.3KV). Capacitor banks of 2 MVAR are also used in the system and are connected to buses 42 (33KV) and 38 (11KV). Two mini hydro power plants of capacities 2000 KVA, 6.6KV and 3000 KVA, 3.3KV are connected to the buses 32 and 8, respectively. These power plants are used as distributed generation units to

control voltage magnitudes of the buses to which they are connected. The system can be represented in terms of a graph by using the graph theory algorithm. Fig. 11 shows the 47-bus distribution system represented in the graphical form, where the shortest path of the fault current between the main source and fault location is shown.
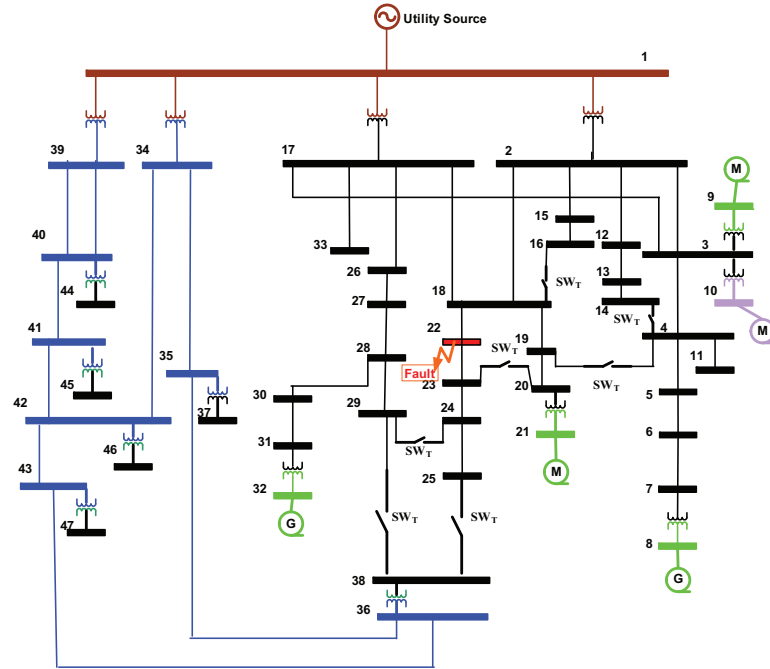

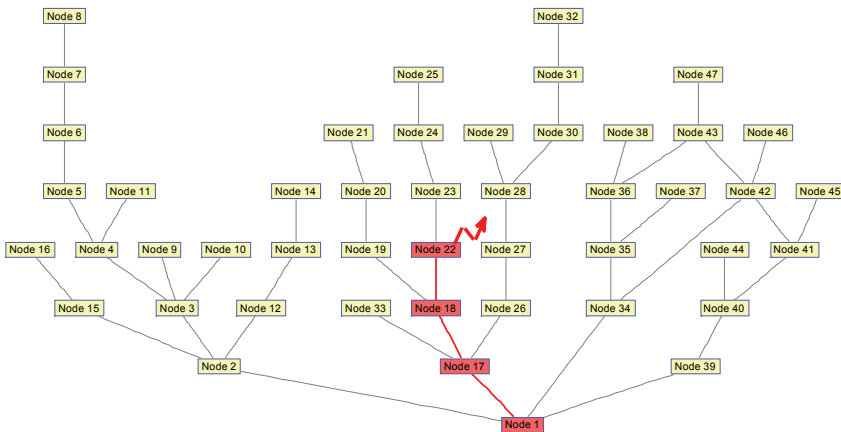Fig. 10. A practical 47-bus test distribution system

Fig. 11. Graph presentation of the practical 47-bus test distribution system

5.1 Determination of weak area

Fault analysis simulations were done for all the buses of voltage level of 11kV and below except the main substations and the buses that are supplied through more than one feeder. The buses 1, 2, 3, 17, 18, 33, 34, 35, 36, 39, 40, 41, 42, and 43 are excluded from simulation, where bus 1 is the main source, buses 2 and 17 are the main substations, buses 3 and 18 are supplied by two feeders, bus 33 is a service bus for local loads and the buses 34, 35, 36, 39, 40, 41, 42 and 43 are at 33KV voltage level. The voltage sag distribution on all system buses for three phase fault and fault resistance (Z_f=0) is shown in Fig. 12.
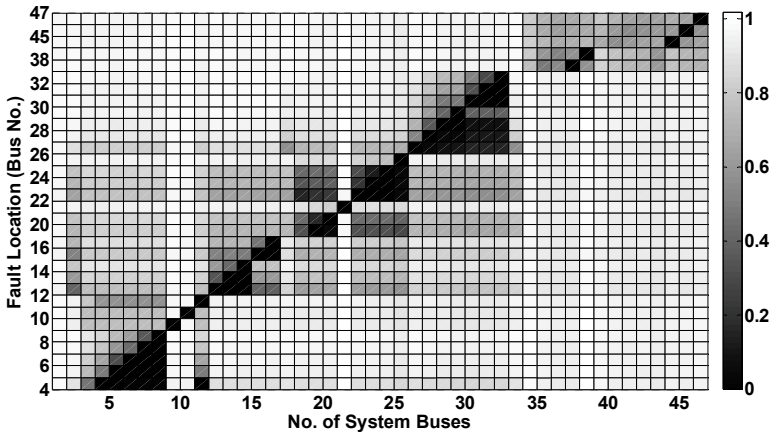
Fig. 12. Voltage sag distribution on system buses due to three phase fault
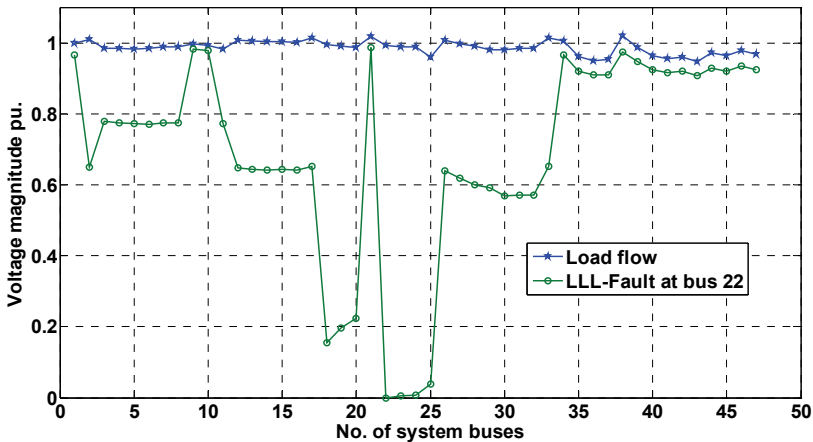
Fig. 13. Voltage magnitudes of system buses after steady state load flow and during three phase fault at bus 22

From Fig. 12, it is obvious from the dark points of voltage sag distribution (Z-axis) that buses 19, 20, 22, 23 and 24 are the most sensitive in propagating voltage sags throughout the system. This group of buses is considered as weak area in the system. In the same manner

bus 22 is considered as the weakest bus in this group and in the system. It is considered as the most sensitive bus in propagating voltage sags, where most system buses are affected due to the fault event at this bus. The voltage distribution due to three phase fault at bus 22 is shown in Fig. 13 along with base case voltage profile of the system. From this figure it is clear that all bus voltage magnitudes are within standard limits during steady state but causes voltage sag at most buses due to a three phase fault at bus 22.

Fig. 14 shows the voltage distribution with varying degree of darkness of phase A at all the system buses due to single line to ground fault at various fault locations. The same fault locations are again noted as the most sensitive buses in propagating sags throughout the whole system. Bus 22 is considered as the weakest bus in the system. The determination of the weak bus is a significant step in voltage sag assessment and mitigation.

Fig. 15 shows the effect of single line to ground fault at bus 22 on voltage distribution of all system buses. It is noted that most of the buses also experience voltage swell at the other two phases.
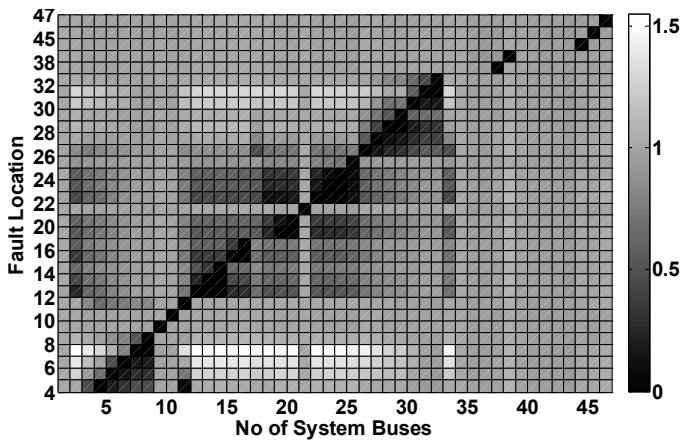

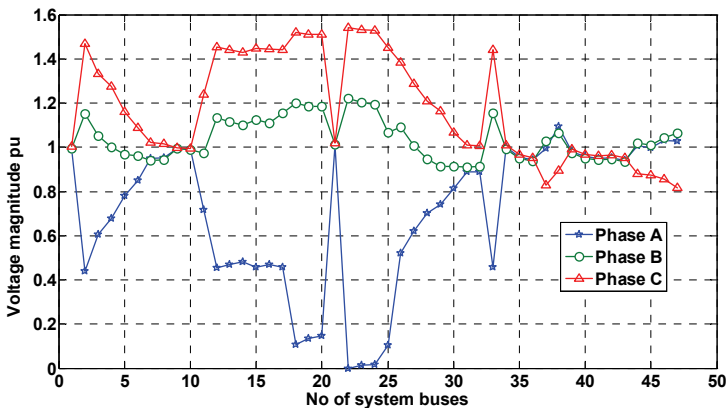Fig. 14. Voltage sag distribution of phase A on system buses due to single line to ground fault

Fig. 15. Voltage magnitudes of system buses during single line to ground fault at bus 22

5.2 Network reconfiguration and reinforcement

Based on the results of the weak area determination (bus 22), network reconfiguration is carried out by performing switching actions. The graph theory algorithm is applied to find a new path of the fault current in terms of the electrical distance between the main power supply and the fault location. Network configuration is carried out according to the proposed algorithm shown in Fig. 9, where the permitted increase of system losses (INd) is defined by a large value (20%) and the maximum improvement of healthy buses (N_{imp}) is also defined by a big value (100%). The one line diagram of the practical system after reconfiguration is shown in Fig. 16, where the change in switches status can be observed. Fig. 17 shows the graphical presentation of the studied system after reconfiguration.
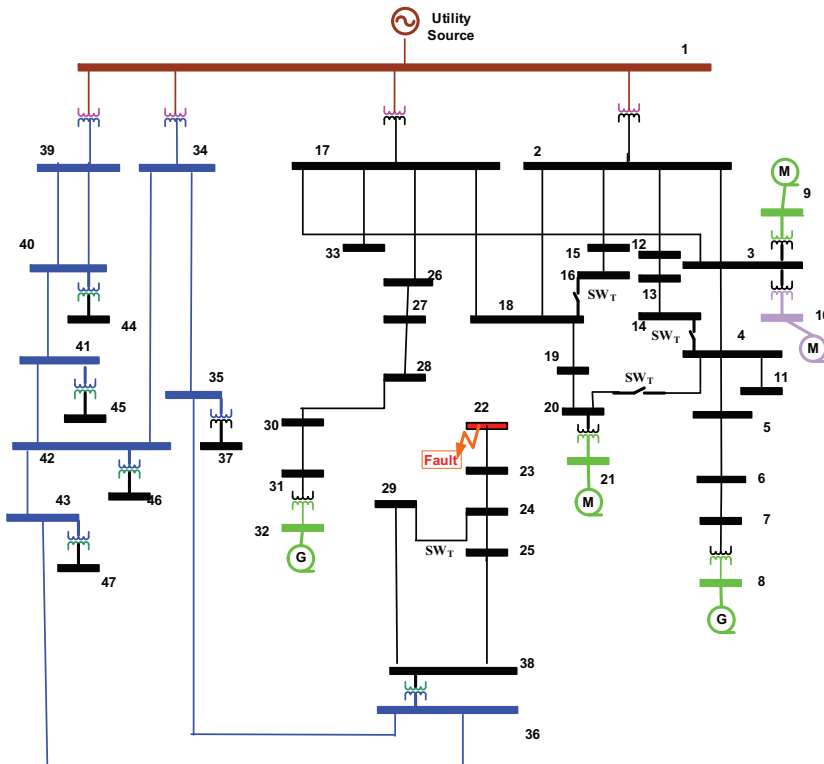

Fig. 16. One line diagram of the practical 47-bus system after reconfiguration

In comparison with Fig. 11, there is a significant increase in the electrical distance of the path of fault current between the main source and the fault location (bus 22). Table 1 shows the system status before and after reconfiguration where the group of open switches is changed and the number of healthy buses is improved in which the bus number is 36 out of 47 compared with the number 18 out of 47 before reconfiguration. It means that the percentage improvement in the number of healthy buses (N_{imp}) is increased up to 100%. The exposed voltage sag area due to a fault event at bus 22 is reduced from 61.7% to 23.4%. But the

improvement of voltage sag performance is accompanied by an increase in system losses, where the percentage increase in system losses becomes 18.24%.
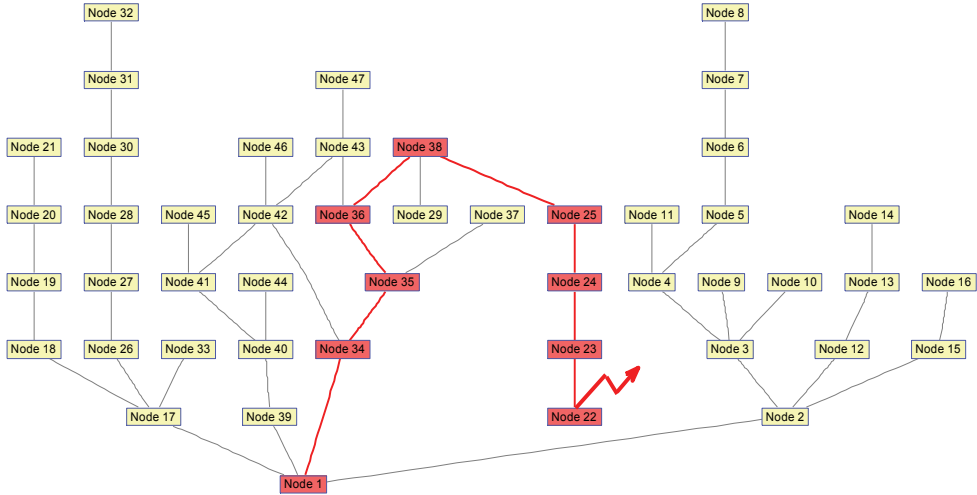

Fig. 17. Graph presentation of the studied practical system after reconfiguration

System status	Open Switches	No. of Healthy Buses	Sag Exposed Area %	System Losses MW
Before Reconfiguration	19-4, 14-4, 16-18, 20-23, 24-29, 25-38, 29 -38	18	61.7	2.119
After Reconfiguration	2-18, 17-3, 19-4, 14-4, 16-18, 20-23, 24-29, 18-22, 28 -29	36	23.4	2.505
The Results		Improvement N_{imp}=100%	Reduction 38.3	INc=18.24

Table. 1. System status before and after network reconfiguration

Fig. 18 shows the voltage distribution on all system buses with varying degree of darkness due to three phase fault at various fault locations, after reconfiguration. In comparison with Fig. 12, there is a significant improvement in voltage sag performance for most number of system buses considering all fault locations and network reconfiguration.
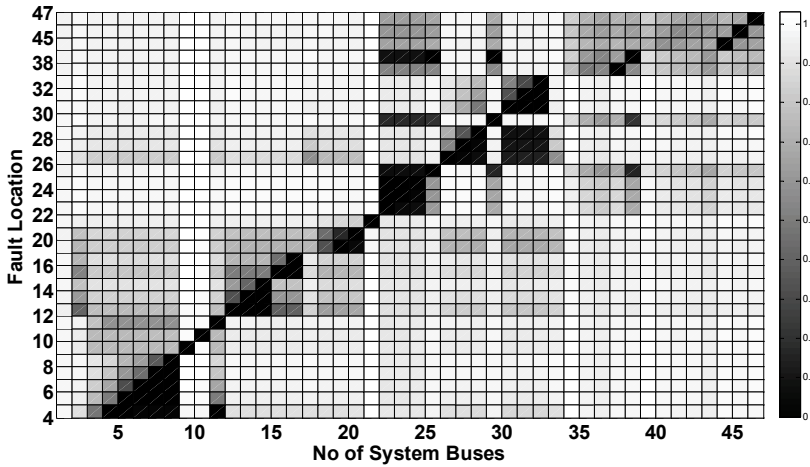
Fig. 18. Voltage sag distribution on system buses due to three phase fault

Simulation results of short circuit analysis after reconfiguration due to a fault at bus 22 is shown in Fig. 19 along with the steady state voltage profile. An improvement in voltage magnitudes at most number of system buses can be observed after reconfiguration as compared with the results of Fig. 13. The improvement in voltage sag performance after reconfiguration can also be observed in case of unbalanced faults. Fault analysis results of the studied system due to single line to ground fault at bus number 22 (weak bus) is shown in Fig. 20. The results of Fig. 20 can be compared with the results of Fig. 15 to prove the effect of network reconfiguration on voltage profile improvement.
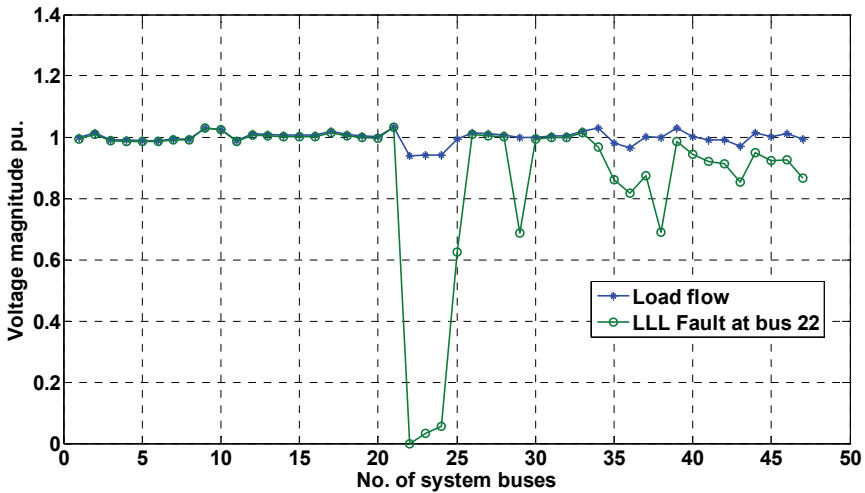

Fig. 19. Voltage magnitudes of system buses at steady state load flow and during three phase fault at bus 22 after reconfiguration
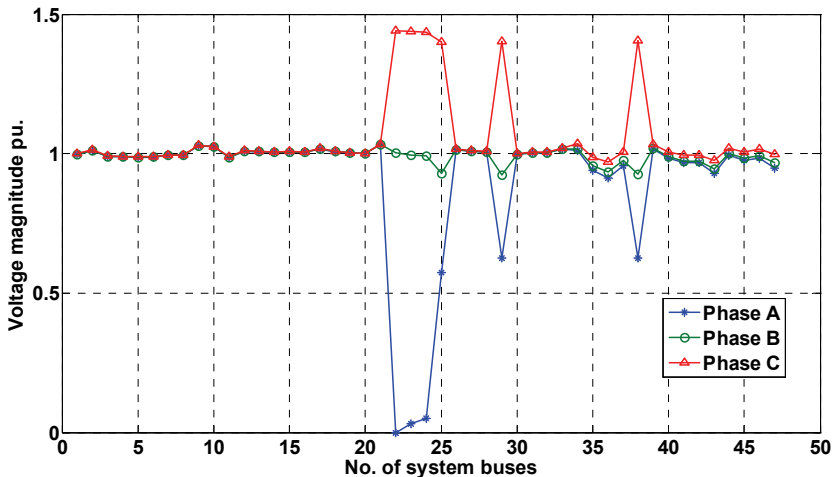
Fig. 20. Voltage magnitudes of system buses during single line to ground fault at bus 22 after reconfiguration

6. Conclusions

The simulation results prove that the proposed network reconfiguration method based on the graph theory algorithm is efficient and feasible for improving the bus voltage profile. The weak area is first determined before performing the appropriate switching action in network reconfiguration. The network reconfiguration solution is achieved by placing the weak area or the voltage sag sources as far as possible away from the main power supply. This method is also efficient for network reinforcement against voltage sag propagation. By applying the proposed method, voltage sag at some buses can be completely mitigated while other buses are partially mitigated. However, the voltage sag problem at the partially mitigated buses can be solved by placing other voltage sag mitigation devices. Although the reconfiguration process involves just a change is switching status, it solves majority of the voltage sag problems.   The proposed method may assist the efforts of utility engineers in taking the right decision for network reconfiguration. The right decision can be taken after evaluating the benefits from line loss reduction and financial loss reduction due to implementation of network reconfiguration.

7. References

Assadian, M.; Farsangi, M.M.(2007). Optimal Reconfiguration of Distribution System by PSO and GA using graph theory. *International Conference on Applications of Electrical Engineering*, pp 83-88, ISBN 978-960-8457-74-4, Turkey, May 27-29, 2007. Istanbul.

Aung, M. T. & Milanović´, J. V. (2006). Stochastic Prediction of Voltage Sags by Considering the Probability of the Failure of the Protection System, *IEEE Trans on Power Delivery*, Vol. 21, No. 1, January 2006, pp 322 – 329, ISSN 0885-8977.

Chen, S.L, Hsu S.C. (2002). Mitigation of voltage sags by network reconfiguration of a utility power system. *Proceedings of the IEEE Power Engineering Society Transmission and*

Distribution Conference, Vol.3,pp. 2067-2072, ISBN 0-7803-7525-4, Asia Pacific. IEEE/PES, 6-10 Oct. 2002.

Civanlar, S.; Grainger, J.J.; Yin, H. & Lee, S.S.H. (1988). Distribution Feeder Reconfiguration For Loss Reduction, *IEEE Trans. Power Delivery,* Vol. 3, No. 3, July 1988, pp. 1217-1223, ISSN 0885-8977.

Conrad, L. E. & Bollen, M. H. J. (1997). Voltage sag coordination for reliable plant operation, *IEEE Trans. Industrial Application*, Vol. 33, Nov.-Dec., pp. 1459–1464, 1997, ISSN 0093–9994.

Grainger, J. J. (1994). *Power system analysis*. McGraw-Hill, ISBIN 0-07-113338-0, Singapore.

Gupta, B.R. (2004). *Power System Analysis and Design* S. Chand & Company, Ltd., ISBN 81-219-2238-0, New Delhi India.

Haque, M.H. (2001). Compensation Of Distribution System Voltage Sag By Dvr And D-STATCOM, *IEEE Porto Power Tech Conference*, pp 1-5, ISBN 0-7803-71 39-9, Porto, Portugal 10 – 13 Sep. 2001.

Heine, P. & Lehtonen, M. (2003). Voltage Sag Distributions Caused By Power System Faults, *IEEE Trans. on Power Systems*, Vol. 18, No. 4, November 2003, pp. 1367-1373, ISSN 0885-8950.

Institute of Electrical and Electronics Engineers Inc. (1993). *Recommended Practice For Electric Power Distribution For Industrial Plants(Std, 141)*. IEEE Press, ISBN 1-55937-333-4, NewYork.

Institute of Electrical and Electronics Engineers Inc. (1995). *Recommended Practice For Monitoring Electric Power Quality(Std,1159),* IEEE Press, ISBN 1-55937-549-3, NewYork.

Institute of Electrical and Electronics Engineers Inc. (1998). *Recommended Practice For Evaluating Electric Power System Compatibility With Electronic Process Equipment(Std,1346)*, IEEE Press, ISBN 0-7381-0184-2, NewYork.

Jianming, Y.; Zhang, F.; Feng, N. & Yuanshe M. (2009). Improved Genetic Algorithm with Infeasible Solution Disposing of Distribution Network Reconfiguration, *IEEE Proceedings of the 2009 WRI Global Congress on Intelligent Systems,* pp 48-52, ISBN 978-0-7695-3571-5, Xiamen, 19-21 May 2009.

Kusko, A.; Thompson, M.T. (2007). *Power Quality in Electrical Systems*, McGraw-Hill ISBN 0-07-147075-1, New York.

Martinez, J.A. & Martin- J. A.(2006). Voltage sag studies in distribution networks -- Part I: System modelling, *IEEE Transactions on Power Delivery*, Vol. 21, July. 2006, pp. 1670-1678, ISSN 0885-8977.

Martinez, J.A. & Martin-Arnedo, J. (2004). Advanced load models for voltage sag studies in distribution networks, *IEEE Power Engineering Society General Meeting*, pp 614 - 619, ISBN 0-7803-8465-2 , 6-10 June 2004.

Martinez, J.A.; & Martin- J. A.(2006), Voltage Sag Studies in Distribution Networks—Part III:Voltage Sag Index Calculation, *IEEE Trans On Power Delivery,* Vol. 21, No. 3, July 2006, pp 1689-1697, ISSN 0885-8977.

Martinez, J.A.; Martin- J. A & Milanovic, J. V. (2003). Load modelling for voltage sag studies, *IEEE Power Engineering Society General Meeting*, pp 2508-2513, ISBN 0-7803-7989-6, 13-17 July 2003.

Nara, K.; Shiose, A.; Kitagawa, M. & Ishihara, T. (1992). Implementation Of Genetic Algorithm For Distribution Systems Loss Minimum Re-Configuration, *IEEE Trans on Power Systems*, Vol. 7, No. 3, August 1992, pp 1044 – 1051. ISSN 0885-8950.

Padiyar, K. R. (1997). *Power system dynamics: stability and control,*: John Wiley, ISBN: 978-0-470-72558-0, New York.

Qader, M. R.; Bollen, M. H. J. & Allan, R. N. (1999). Stochastic Prediction of Voltage Sags in a Large Transmission System, *IEEE Trans. Industrial Application*, Vol. 35, Jan.-Feb. 1999, pp. 152–162, ISSN 0093–9994.

Ravibabu, P.; Ramya, M.V.S.; Sandeep, R.; Karthik, M.V. & Harsha, S. (2010) Implementation of Improved Genetic Algorithm in Distribution System with Feeder Reconfiguration to Minimize Real Power Losses, *2nd IEEE International Conference in computer Engineering and Technology (ICCET),* pp 320-323, ISBN 978-1-4244-6349-7, Chengdu,18-20 April 2010.

Ravibabu, P.; Venkatesh, K. & Kumar, C.S. (2008). Implementation of Genetic Algorithm for Optimal Network Reconfiguration in Distribution Systems for Load Balancing, *IEEE Region 8 International Conference on Computational Technologies in Electrical and Electronics Engineering (SIBIRCON 2008)*, pp 124 – 128, ISBN 978-1-4244-2133-6, Novosibirsk, 21-25 July 2008.

Saadat, H. (2008). *Power System Analysis*, McGraw-Hill ISBN 0-07-123955-3, Singapore.

Sabri, Y.; Sutisna & Hamdani, D. (2007). Reconfiguring Radial-Type Distribution Networks Using Graph-Algorithm, *International Conference on Electrical Engineering and Informatics,* pp 838-841, ISBN 978-979-16338-0-2, Institut Teknologi Bandung, Indonesia, 17-19 June, 2007.

Salman, N; Mohamed, A & Shreef, H. (2009). Reinforcement of Power Distribution Network Against Voltage Sags Using Graph Theory, *Proceedings of 2009 Student Conference on Research and Development (SCOReD 2009),* pp 341-344, ISBN 978-1-4244-5187-6, UPM Serdang, 16-18 Nov. 2009, Malaysia.

Sang, Y. Y & Jang; H. O. (2000). Mitigation of Voltage Sag Using Feeder Transfer in Power Distribution System, *IEEE Power engineering society summer meeting*, Vol. 3 pp 1421 – 1426, ISBN 0-7803-6420-1, Seattle, WA, 16 -20 Jul 2000.

Sannino, A.; Miller, M.G.; Bollen, M.H.J. (2000). Overview of voltage sag mitigation, *Power Engineering Society Winter Meeting, 2000. IEEE* , Vol.4, pp 2872-2878, ISBN 0-7803-5935, 2000.

Sanjay, B.; Milanovic´, J. V.; Zhang, Y.; Gupta, C. P.; & Dragovic, J. (2007). Minimization of Voltage Sags Costs By Optimal Reconfiguration Of Distribution Network Using Genetic Algorithms, *IEEE Transactions on Power Delivery*, Vol. 22, No. 4, (October 2007) pp 2271-2278, ISSN 0885-8977.

Sensarma, P.S.; Padiyar, K.R. & Ramanarayanan, V. (2001). Analysis and Performance Evaluation of A Distribution STATCOM for Compensating Voltage Fluctuations, *IEEE Trans. on Power Delivery* V. 16, No. 2. April 2001, pp 259-264, ISSN 0885-8977.

Shareef, H. ; Mohamed, A. & Mohamed, K. (2010). A Device for Improving the Voltage Sag Ride Through Capability of PCs, *International Review of Electrical Engineering*, Vol. 5, No. 4, July-August 2010, pp. 1413-1417.

Shareef, H.; Mohamed, A. & Marzuki, M. (2009). Analysis of ride through capability of low-wattage fluorescent during voltage sags, *International Review of Electrical Engineering*, Vol. 4, No. 5, September- October 2009, pp. 1093-1101, ISSN 1827-6660.

Shen, C-C. & C-Nan Lu. (2007). A Voltage Sag Index Considering Compatibility Between Equipment and Supply, *IEEE Trans On Power Delivery*, Vol. 22, No. 2, April 2007, pp. 996-1002, ISSN 0885-8977.

Intelligent Techniques and Evolutionary Algorithms for Power Quality Enhancement in Electric Power Distribution Systems

S.Prabhakar Karthikeyan, K.Sathish Kumar, I.Jacob Raglend and D.P.Kothari
Vellore Institute of Technology, Vellore, Tamil Nadu
India

1. Introduction

In the field of power system, equipments like synchronous machine, transformer, transmission line and various types of load occupies prime position in delivering power from the source to the consumer end. By the early 19th century, people were concentrating more on the quantity of power i.e active power which was the main issue and still researchers are working on various sources to meet out the exponentially increasing demand.

But now, the issue of power quality has started ruling the power system kingdom, where the frequency at which the active power is generated / pushed, the voltage profile at which the power is generated, transmitted or consumed and the reactive power which helps in pushing the active power plays a vital role. One main reason in emphasizing power quality is the amount of consumption of active power by the load i.e the efficiency of the system is decided by the quality of power received by the consumer. Any studies related to the above issues can be brought under the power quality domain.

2. Distribution systems

Power system is classified into generation, transmission and distribution based on factors like voltage, power levels and X/R ratio etc.

The well known characteristics of an electric distribution system are:

- Radial or weakly meshed structure
- Multiphase and unbalanced operation
- Unbalanced distributed load
- Extremely large number of branches and nodes
- Wide-ranging resistance and reactance values

2.1 Components of distribution system

In general distribution system consists of feeders, distributors and service mains.

2.1.1 Feeder

A feeder is a conductor which connects to the sub-station or localized generating station to the area where power is to be distributed. Generally no tapings are taken from the feeders so

current in it remains same through out. The main consideration in the design of a feeder is the current carrying capacity.

2.1.2 Distributors
A distributor is a conductor from which tapings are taken for supply to the consumers. The current through the distributors are not constant as tapings are taken at various places along its length. While designing a distributor, voltage drop along the length is the main consideration – limit of voltage variation is +/- 6 Volts at the consumer terminal.

2.1.3 Service mains
A service main is generally a small cable which connects the distributor to the consumer terminals.

2.2 Connection schemes of distribution system
All distribution of electrical energy is done by constant voltage system. The following distribution circuits are generally used.
1.   Radial system
2.   Ring Main system
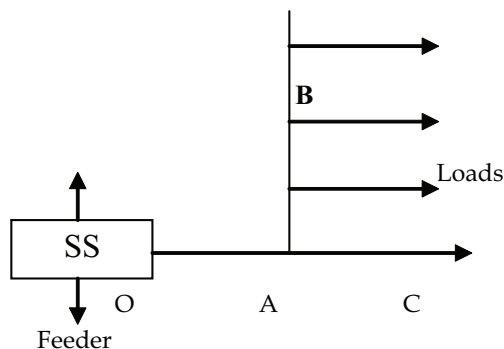3.   Inter connected system

2.2.1 Radial system

Fig. 1. Radial Distribution system

In this system shown in above figure separate feeder radiates from a single substation and feed distributors at one end only. Figure 1 shows the radial system where feeder OC supplies a distributor AB at point A. the radial system is employed only when the power is generated at low voltage and the sub-station is located at the centre of the load.
Advantages: This is the simplest distribution circuit and has a lowest initial cost. The maintenance is very easy and in faulty conditions very efficient to isolate.
Disadvantages:
1.   The end of the distributor nearest to the feeding point will be loaded heavily.
2.   The consumer at the farthest end of the distributor would be subjected to serious voltage fluctuations with the variation of the load.

3. The Consumers are dependent on a single feeder and single distributor. Any fault on the feeder or distributor cut-off the supply to the consumer who is on the side of fault away from the sub-station.

Due to these limitations this system is used for short distance only.

2.2.2 Ring main system

In this system each consumer is supplied via two feeders. The primaries of distribution transformer form a loop. The loop circuit starts from the sub-station busbar, makes a loop through the area to be served and returned to the sub-station.

Advantages:
1. There are less voltage fluctuations at consumer terminals.
2. The system is very reliable as each distributor is fed via two feeders. In the event of fault in any section of the feeder, continuity of the supply is maintained.

2.2.3 Interconnected systems

When the feeder ring is energized by two or more than two generating stations or sub-stations, it is called an interconnected system.

Advantages:
1. It increases the service reliability.
2. Any area fed from one generating station during peak load hours can be fed by other generating stations. This reduces reserve power capacity and increases the efficiency of the system.

2.3 Requirements for a good distribution system
1. The system should be reliable and there should not be any power failure, if at all should be for minimum possible time.
2. Declared consumer voltage should remain with in the prescribed limits i.e. within +/- 6% of the declared voltage.
3. The efficiency of the lines should be maximum (i.e.) about 90%.
4. The transmission lines should not be overloaded.
5. The insulation resistance of the whole system should be high, so that there is no leakage and probable danger to human life.
6. The system is most economical.

2.4 Distribution System Automation (DSA)

Distribution System Automation is carried out all over the world to enhance the reliability of the distribution system and to minimize the huge losses that are occurring in the system. With the fast-paced changing technologies in the Distribution sector, the automation of distribution system is unavoidable. Feeder Reconfiguration (FR) is one of the vital operations to be carried out in successful implementation of the Distribution System Automation. FR can be varied so that the load is supplied at the cost of possible minimal line losses, with **increased system security and enhanced power quality**. Several attempts have been made in the past to obtain an optimal feeder configuration for minimizing losses in distribution systems.

This chapter gives us a clear picture about how intelligent techniques and evolutionary algorithms are used in the sub domains of the distribution systems where quality, quantity, continuous and reliable power can be made available to the consumers

2.5 Distribution feeder reconfiguration
Assessment of distribution system feeder and its reconfiguration using Fuzzy Adaptive Evolutionary computing

The aim of this section is to assess and reconfigure the distribution system using fuzzy adaptive evolutionary computing. Here, the reconfiguration problem can be subdivided into three modules, i.e.

• To detect the system abnormal operation based on S-difference criterion.
• Prioritize the transmission lines to re-route the power flowing through them as per the available transfer capacity.
• Reconfiguration of tie-line and sectionalizing switches using fuzzy adaptation of evolutionary programming.

2.5.1 S-difference criterion

This criterion is based on the apparent-power losses and uses only local data, i.e. voltage and current phasors at every line end in the system be proven that, at the voltage-collapse point, the entire increase in loading of the most critical line is due to increased transmission losses and that the power-loss sensitivities dP_L/dP, dP_L/dQ, dQ_L/dP and dQ_L/dQ go to infinity. Thus, in the vicinity of the voltage collapse, all increase in apparent-power supply at the sending end of the line no longer yields an increase in power at the receiving end

$$\Delta S(k+1)=\Delta U(k+1)*I(k)+\Delta I(k+1)*U\ (k)=0 \tag{1}$$

Equation (1) can be rewritten as follows

$$1+\Delta U_j^{(k+1)}*I_{ji}(k)/\ U_j(k)*\Delta I_{ji}^{(k+1)}\ = 1+ae^{j\Theta}\ = 1+a(\ cos\theta+jsin\theta)=0 \tag{2}$$

The proposed criterion is defined as the real part of the phasor as follows:

$$SDC'= Re(1+ae^{j\Theta}\ ) \tag{3}$$

At the point of the voltage collapse, when $\Delta S = 0$, the criterion equals to zero.

2.5.2 Available Transfer Capability

Available transfer capability (ATC) is a measure of transfer capability remaining in the physical transmission network for future commercial activity over and above already committed uses. Mathematically, ATC is:

$$ATC=TTC-BCF-TRM-CBM \tag{4}$$

Where,
    TTC=total transfer capacity,
    TRM=transient reliability margin.
    CBM= capacity benefit margin.
    BCF=Base case flow.

2.5.3 ATC calculation through Linear Distribution Factor method

In the linear ATC model considered here PTDF and OTDF are not taken into account with line reactance. The linear ATC has been modified from distribution system point of view i.e. PTDF and hence ATC has been calculated by taking real power into account instead of using

line reactance. Some linear distribution factors based on DC model are introduced here to calculate linear ATC.

Power Transfer Distribution Factors (PTDF): In a bilateral transaction ΔTmn between a seller bus m and buyer bus n, further consider a line (let the line be connected between the buses i and j) carrying a part of the transacted power P. For a change in real power transaction between areas, say by ΔTmn, if the change in transmission line quantity is Pij, then the power transfer distribution factor can be defined as:

$$(PTDF)_{ij\text{-}mn} = \Delta P_{ij}/\Delta T_{mn} \tag{5}$$

Line Outage Distribution Factors (LODF): LODF describes the impact of one branch outage on magnitude and direction of the power flow on the other branches. . In case of the outage of another branch 1' (let the line be connected between the buses r, s) having pre-outage real power flow Prs , Let Pij-rs be the post outage flow in a line connected between the buses i, j . The LODF can be defined as the ratio of real power flow change in line I to the real power flow transmitted in the line taken for outage

$$(LODF)_{ij\text{-}rs} = (P_{ij\text{-}rs} - P_{ij}^0)/P_{rs}^0 \tag{6}$$

Outage Transfer Distribution Factor (OTDF): OTDF describes the effect of power interchange between areas on branch power flow on occasion of one branch outage.

$$(OTDF) = PTDF_{ij\text{-}mn} + LODF_{ij\text{-}rs} * PTDF_{rs\text{-}mn} \tag{7}$$

Thermal limits constrained ATC can be expressed as:

$$ATC_{mn\text{-}ij} = (P_{ij}^* - P_{ij}^0)/PTDF_{ij\text{-}mn} \tag{8}$$

Where, p_{ij}^* is the thermal limit of branch L.ATC   calculated based on the combination of PTDF and LODF, can be expressed as:

$$ATC_{mn\text{-}rs} = (P_{ij}^* - P_{ij}^0)/OTDF \tag{9}$$

In conclusion, ATC is defined as:

$$ATC = \min \{ATC_{mn\text{-}ij}, ATC_{mn\text{-}rs}\} \tag{10}$$

Where NL is the total number of branches, and No is the total number of flow gate contingencies.

2.5.4 Reconfiguration using Fuzzy Adaptive Evolutionary computing

For reconfiguration purpose of the assessed system, Fuzzy adaptation of evolutionary programming (FEP) has been considered. The idea behind the adaptation of this particular method is to take into consideration the grey area between the various parameters considered in reconfiguration.

Real power loss minimization: To determine best combination of branches of resulting RDS which incur minimum loss

$$kV_{min} = Vss\sum(Vss\text{-}Vj)Yssj\text{-}\sum PDj \tag{11}$$

where, Vjmin ≤Vj ≤Vjmax   &

Vss= voltage at main station

Yss=admittance b/w main station and bus j

PDj=Real power load at bus j

Improvement of power quality: To quantify the minimum limit violation imposed on voltages at buses voltage deviation index (VDI) is defined

$$VDI=\sqrt{((\sum NVB \ Vli-V_{lilm})^2/N)} \qquad (12)$$

where,

NVB= number of buses violating limit

V_{lilm} = upper limit of the voltage

Fuzzy model of kW loss minimization objective: It defines the objective function that associates the satisfaction level with solution vector Xj

$$\mu_L =(P_{Lmax} – fpl(xj))/(P_{Lmax} –P_{Lmin}) \qquad (13)$$

Where, $P_L$max=maximum loss;

$P_L$min=minimum loss,

fpl(xj)= power loss corresponding to Xj

Fuzzy model of VDI: It defines the objective function that associates the VDI level with solution vector Xj

$$\mu v=(VDmax–fvd(xj))/(VDmax- VDmin) \qquad (14)$$

Where, VDmax=maximum deviation

VDmin=minimum deviation

fvd =VDI corrosponding to Xj

Development of a fuzzy evaluation method of the solution vector: The resultant satisfaction parameter associated with a solution Xj is determined as below.

$$\mu r = \mu L \ X \ \mu v \qquad (15)$$

2.5.5 Case study

Simulation has been performed on the Vellore Bus system (Figure 2). It contains 75 buses and radial in configuration. For simulation purpose the system is assumed to be a balanced network with a generator at bus 1. Simulation has been carried out using MATLAB 6.5.

2.5.6 Simulation & results

SDC & ATC: SDC is calculated on 5th bus of Vellore 75 bus system as shown in Figure 2. From graph(Figure 3a & 3b), the voltage on the 5th bus is decreasing correspondingly the real part of the SDC is also decreasing but since there is no voltage collapse here so real part of SDC is not equal to Zero.

Whereas on bus 45 it can be seen from the graph (Figure 4a & 4b) that at voltage collapse point the real part of SDC is going below zero.

Available Transfer capability (ATC) is calculated on different buses for different loads when line between bus4 - bus5 has tripped to calculate the Line Outage Distribution Factors. . Here the thermal limit is taken as 4.7 MVA.
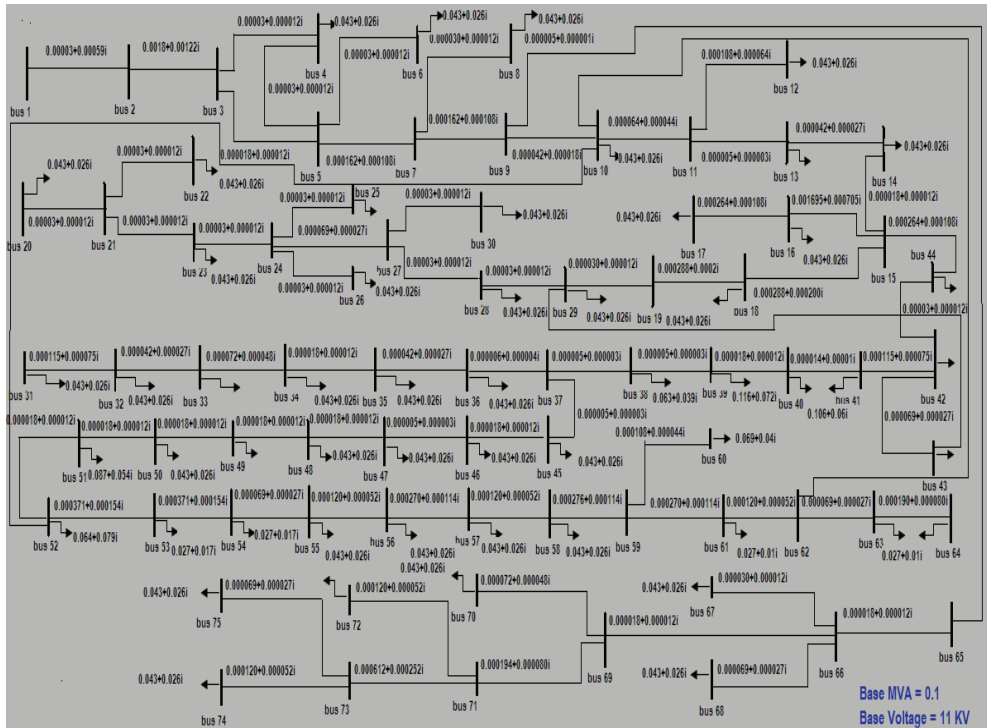
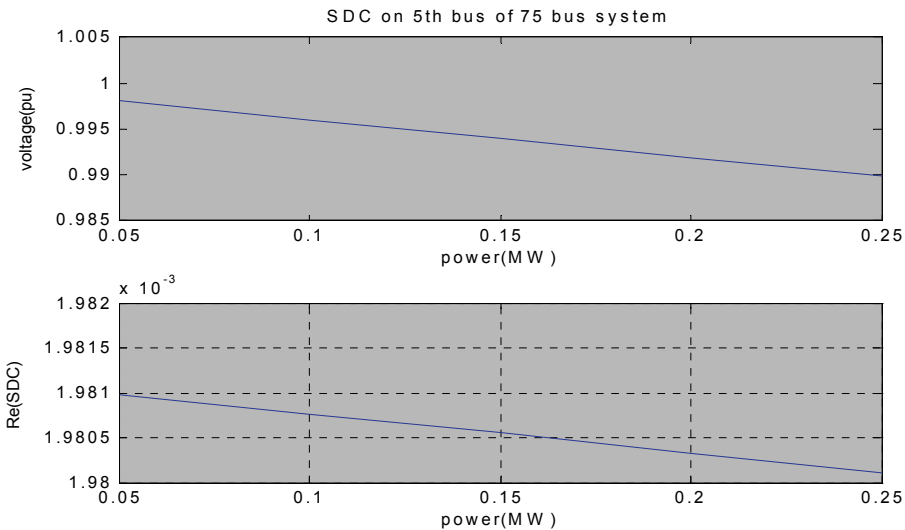Fig. 2. 75 bus Vellore Distribution system

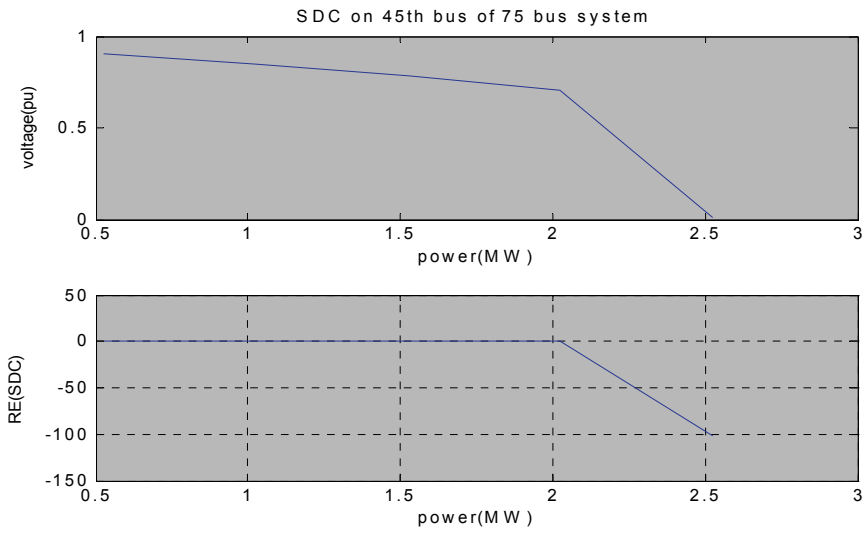Fig. 3. a & b Re (SDC) Vs Increase in real load at 5th bus in 75-bus system

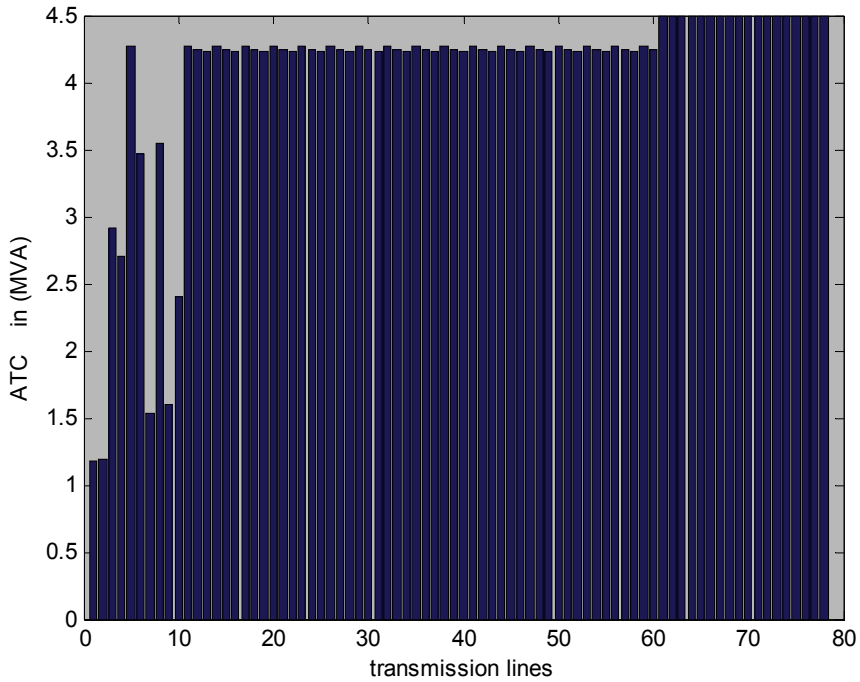Fig. 4. a & b Re (SDC) Vs Increase in real load at 45th bus in 75- bus system

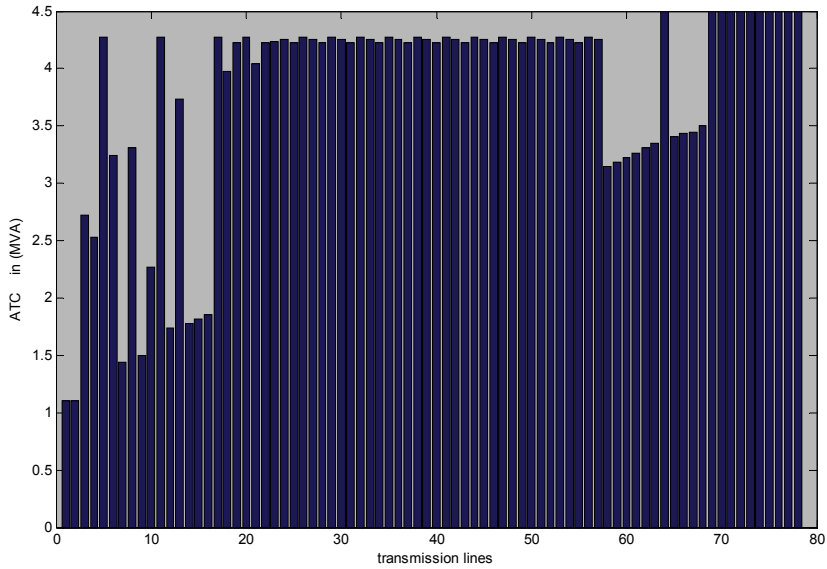Fig. 5. ATC after removing line 4-5 & increasing load on bus 10

Fig. 6. ATC after removing line 4-5 & increasing load by 0.01 MW on bus 64

(B) Reconfiguration using Fuzzy adaptive Evolutionary Computing

From bus	To bus	kW loss	No. buses violating pu voltage limits	VDI
9	65	1.2061e+003	60	0.0570
10	52			
10	62			
29	43			

Table 1. Removing all tie-lines

Removing a tie-line and sectionalizing switches

1st set				2nd set				3rd set				4th set				5th set			
10	46	57	61	12	45	22	61	13	54	22	49	36	56	22	63	25	56	10	59
10	46	56	62	12	46	22	61	13	56	22	48	36	54	22	63	25	56	10	61
10	46	56	60	12	45	22	61	13	56	22	48	36	52	22	63	25	53	10	62
10	47	55	61	12	46	22	62	13	53	22	46	36	52	22	59	25	54	10	60
10	46	53	59	12	49	22	61	13	53	22	47	36	57	22	62	25	55	10	61

Table 2. Various combinations of lines taken from the system

1st set	2nd set	3rd set	4th set	5th set
0.0612	0.0566	0.0613	0.9033	5.8420
0.0623	0.0572	0.0585	1.6155	0.9011
0.0631	0.0566	0.0585	0.9003	1.0099
0.0646	0.0569	0.9086	1.1593	1.0570
0.0662	0.0572	0.9034	0.9072	1.0439

Table 3. VDI corresponding to each set of combination

1st set	2nd set	3rd set	4th set	5th set
1.1636	0.9718	0.9699	1.8091	1.7000
1.1580	0.9713	0.9717	1.7754	1.1775
1.1491	0.9718	0.9717	1.8497	1.6133
1.1486	0.9722	1.6280	1.6822	6.7298
1.1320	0.9723	1.7384	2.1014	1.8348

Table 4. KW loss incurred corresponding to each set of combination

1st set	2nd set	3rd set	4th set	5th set
0.1162	0.0971	0.0969	0.1808	0.1699
0.1157	0.0970	0.0971	0.1774	0.1176
0.1148	0.0971	0.0971	0.1849	0.1612
0.1147	0.0971	0.1527	0.1681	0.6729
0.1131	0.0971	0.1737	0.2100	0.1834

Table 5. Members of fuzzy membership function (μ_L) for min kW loss

1st set	2nd set	3rd set	4th set	5th set
0.8901	0.8901	0.8901	0.8816	0.8322
0.8900	0.8901	0.8901	0.8745	0.8817
0.890	0.8901	0.8901	0.8817	0.8806
0.8900	0.8901	0.8816	0.8791	0.8801
0.8900	0.8901	0.8816	0.8816	0.8802

Table 6. Members of fuzzy membership function (μv) for VDI

1st set	2nd set	3rd set	4th set	5th set
0.1035	0.0864	0.0862	0.1594	0.1414
0.1030	0.0863	0.0864	0.1552	0.1037
0.1022	0.0864	0.0864	0.1630	0.1420
0.1021	0.0864	0.1434	0.1478	0.5922
0.1006	0.0864	0.1532	0.1852	0.1614

Table 7. Corresponding value of μr
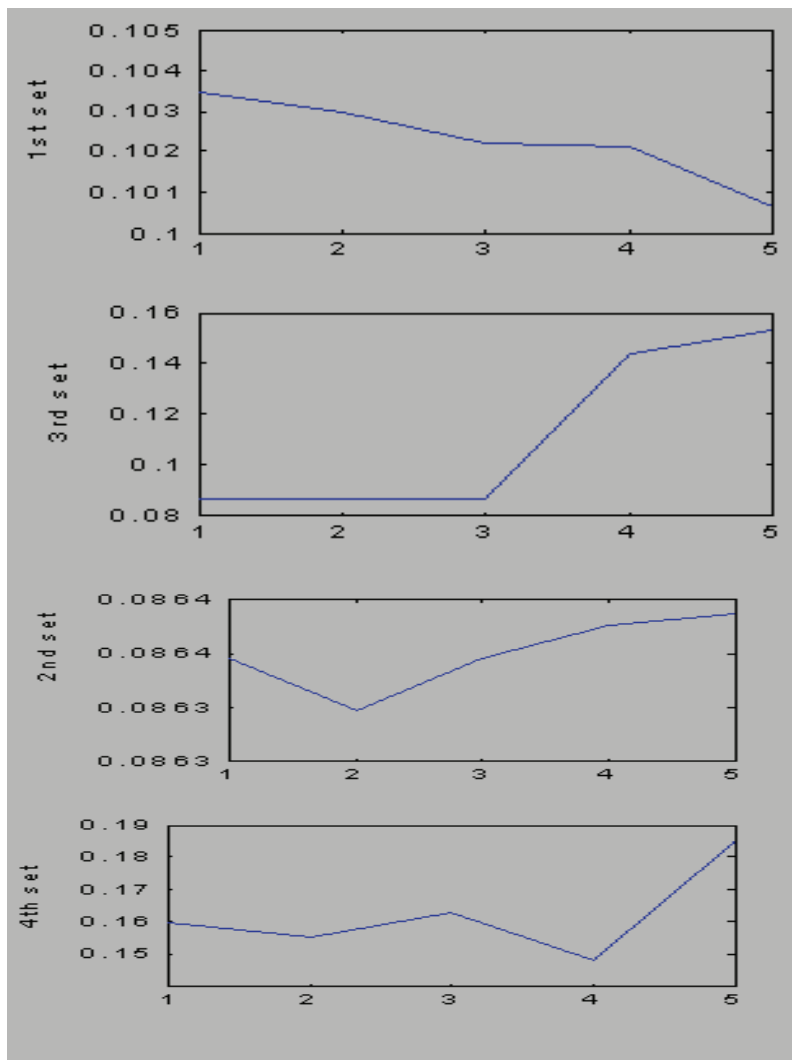
Fig. 6. Graphical representation of membership function of solution vectors

The Vellore 75 bus distribution network has been assessed by detecting the system abnormal operation based on S- difference criterion. It is observed that with increase in load on the system, the observed value of Re (SDC) is reducing with reducing pu voltage on the bus and at voltage collapse point, the criterion is approximately reducing to zero. Similarly linear ATC is reducing for each line with increase in load on buses in step. During the process of reconfiguration on the above test system, it is observed that the optimum performance is obtained by removing following lines [13 54 22 49], i.e.

[(10-62) (18-69) (42-43) (48-49)]

For a configuration having minimum loss is not necessarily to have minimum voltage deviation index, i.e., for a minimum loss configuration power quality may not necessarily be the best. The minimum limit of pu voltage, in a further lowered limit, there is a possibility of a solution having neither of index minimum, yet will give an optimum solution.

2.6 Power system restoration
2.6.1 Introduction
If any electric power supply interruption is caused by a fault, it is important to restore the power system as soon as possible to a target network configuration after the fault.

Various approaches have been presented to solve power system restoration problem. These techniques may very in several major types: automated restoration, Heuristics system, mathematical programming, and computer aided restoration.

2.6.2 Multi-agent technique
Currently, multi-agent technique attracts more and more attention in many fields such as computer science and artificial intelligence. The multi-agent system is a decentralized network to solve problem. All the agents work together to obtain a global goal which may beyond the capability of each individual agent.

Recently, several schemes also have been proposed to utilize multi-agent technique in power system. The implementation areas include stability control, transmission planning, market trading, and substation automation.

A multi-agent system is ideal for control of energy resources to achieve higher reliability, higher power quality, and more efficient (optimum) power generation and consumption. Because multi-agent systems process data locally and only transfer results to an integration center, computation time is largely reduced, and the network bandwidth is very much reduced compared to that of a central control. Multi-agent systems also allow scalability such as when new resources, loads, or interconnections are added to the system and extensibility such as performing new tasks or communicating a new set of data that becomes available.

2.6.3 Navy ship restoration problem

2.6.3.1 System objective and constraints for restoration

It is simple to realize the objective of the power system restoration is to restore the capacity as much as possible to the served loads.

$$\max \sum_{i \in uUS} L_i \tag{16}$$

Where L_i is the load at bus i, and US denotes the set of un-served loads.

And there are several typical constrains for this model:

- There is a limit for the available capacity for system restoration;
- The supply and demand power must be balanced;
- The system must keep radial configuration all the time. This constraint used is mandatory in the real power system operations.

2.6.3.2 Navy ship reference system

The Office of Naval Research (ONR) control challenge reference system is presented in the Figure 7. The complex system includes two finite inertia AC sources and buses, three zonal distribution zones feed by redundant DC power buses, and a variety of dynamic and nonlinear loads. Of course, an actual ship would have a more complex configuration.
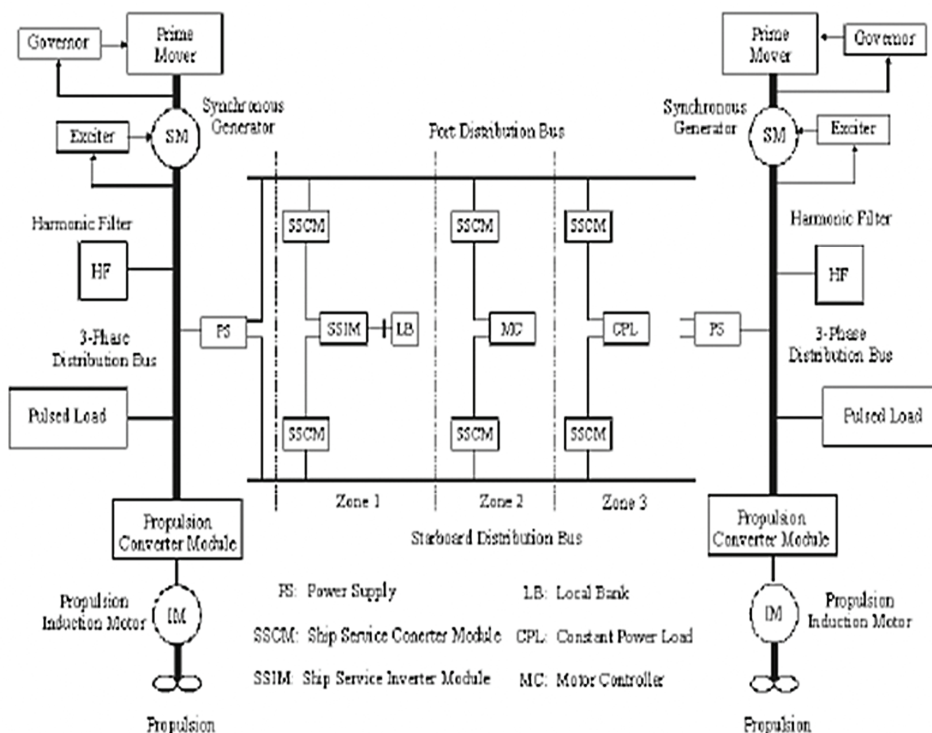
Fig. 7. ONR Control Challenge reference system

2.6.3.3 Multi-agent technique

An agent may be defined as entity with attributes considered useful in a particular domain. In this framework, an agent is an information processor that performs autonomous actions based on information.

A list of common agent attributes is shown below.

- Autonomy: goal-directedness, proactive and self-starting behavior.
- Collaborative behavior: the ability to work with other agents to achieve a common goal.

- "Knowledge-level" communication ability: the ability to communicate with other agents with language more resembling human-like ``speech acts'' than typical symbol-level program-to-program protocols.
- Reactivity: the ability to selectively sense and act.

Temporal continuity: persistence of identity and state over long periods of time.

A multi-agent system is a computational system in which several agents cooperate to achieve some task. The performance of multi-agent systems can be decided by the interactions among various agents. Agents cooperate so that they can achieve more than they would if they act individually.

A list of characteristics of Multi-Agent System is showing as follows:

- each agent has incomplete capabilities to solve a problem
- there is no global system control
- data is decentralized
- computation is asynchronous

Most of these characteristics can be seen in the following sections.

2.6.4 Multi-agent restoration frame work

Since the restoration problem is mainly concentrated on electric demand and supply component, the complex navy ship model has been simplified with only load and source component as in Figure 8. Also, switches and breakers are introduced for the study purpose. At each time, one load can be and only be connected to one power bus.

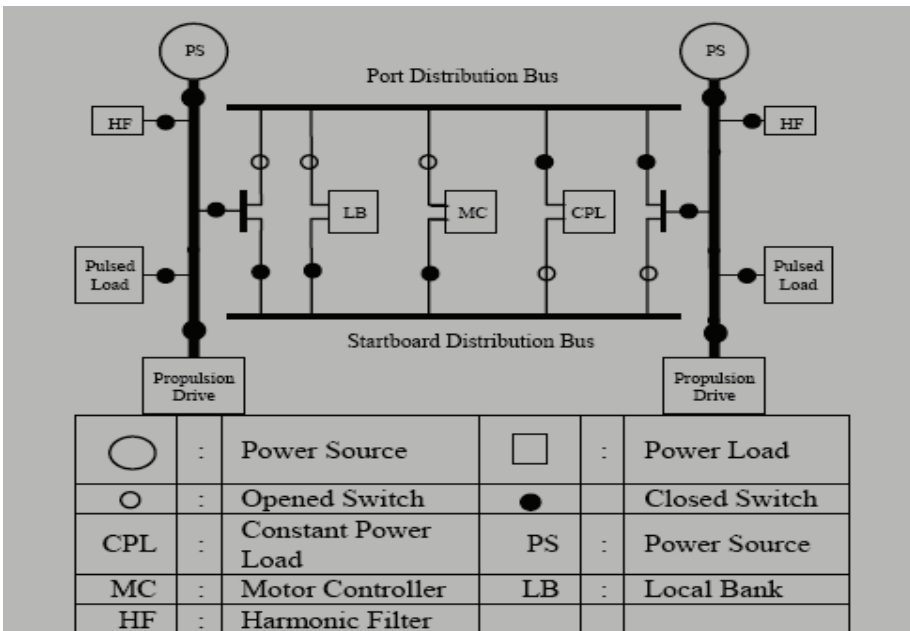| ⬭	:	Power Source	☐	:	Power Load
○	:	Opened Switch	●		Closed Switch
CPL	:	Constant Power Load	PS	:	Power Source
MC	:	Motor Controller	LB	:	Local Bank
HF	:	Harmonic Filter			

Fig. 8. Simplified reference system

The proposed multi-agent architecture for the ship system restoration use object-oriented design technique. To increase the efficiency of whole system, the types and total number of

agents need to be restricted. The proposed restoration system consists of three kinds of agents: a single Negotiating Agent (NA), a number of Load Agents (LA) and a number of Bus Agents (BA). Figure 9. shows the location of each LA and BA of the ship system. There are total 9 LAs and 4 BAs in the system.
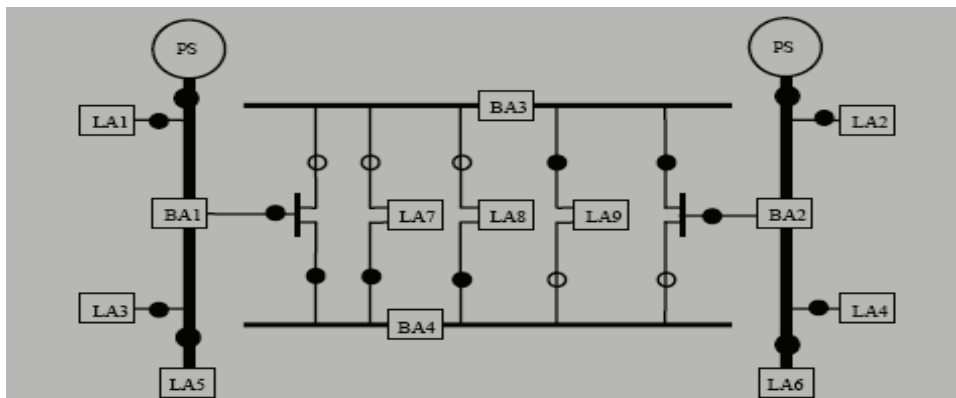

Fig. 9. Agents structure for ship system

Negotiating Agent, Bus Agents and Load Agents are in different levels. The whole system is divided as two subsystems, the communication sub system and operation subsystem.
Figure 10 and Figure 11 illustrate the current and communication paths in system. The dotted line in Figure 10 shows the potential current path.

| LOAD FOR EACH LOAD AGENTS ||
Agent Name	Load
LA1/ LA2	0 –5kW
LA3/ LA4	0 –2kW
LA5/ LA6	0 –37kW
LA7	0 –5kW
LA8	0 –5kW
LA9	0 –5kW

Table 8.

LA is designed to report load status and require for restoration. The active power of each load agent is shown in Table No 8.
The function of Negotiating Agent is to maintain the negotiation process of the whole system. NA receives the restoration request from un-served Load Agent, builds an un-served LA list, and instigates the restoration process by selecting corresponding BA.
BA is designed to decide a suboptimal target configuration after a fault occurs by interaction with other BAs. It is postulated that BA communicates only with its neighboring BAs. BA has the following simple negotiation strategies.

- If the amount of available power for restoration is insufficient, BA tries to restore the bus by negotiating with its neighboring BAs.

- BA always first selects the particular neighboring Bus Agent which connected to it already.
- If the BA succeeds the restoration, it tries to tell the neighboring agents.
- To keep system radial structure, one BA can only receive power from one other BA.
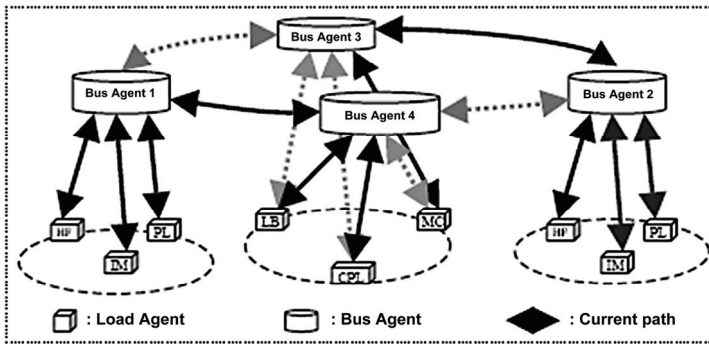

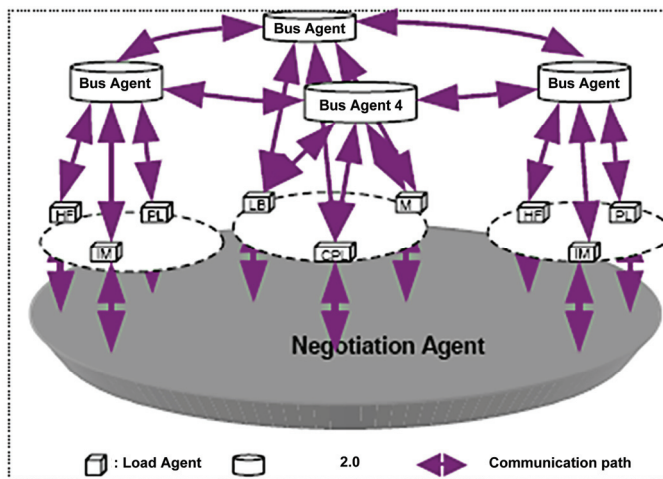Fig. 10. Agents and current path structure for ship system

Fig. 11. Agents and communication paths structure for ship system

When there is a fault, after the fault isolation, the following procedures are proposed for ship system restoration.

Step 1. All the Load Agents report to the Negation Agent.

Step 2. Negotiation Agent creates the set of un-served Load Agents.

Step 3. Negotiation Agent send a "start" message to one and only one Load Agents to begin restoration based on pre-set priority list. When the number of LA in un-served LA list is zero, go to step 11.

Step 4. The selected Load Agent communicates with its connected Bus Agents.

Step 5. The Bus Agent tries to restore the Load Agent with its available capacity.

Step 6. If Bus Agent can finish the restoration by itself, go to step 9. Otherwise go to step 7.

Step 7. BA attempts to make negotiations with neighboring Bus Agents. If the restoration succeeds go to

Step 10. Other wise go to step 8

Step 8. The load Agent begins load shedding. And go to step 5

Step 9. The energized load agent sends a "restored" message to Negotiation Agent.

Step 10. The Negotiation Agent deletes the "restored" load agent from un-served load agent list. Then go to step 3.

Step 11. Terminate the restoration.

2.6.5 Case study

A number of simulations were performed for the proposed strategy. This section will show two typical test cases for total restoration and partial restoration respectively. We assume that the priority list for LAs is LA5>LA6 > LA8> LA9> LA3> LA4> LA7> LA1> LA2.

2.6.5.1 Case 1: Full restoration for fault on bus

We assume a fault on starboard distribution bus, under this particular fault, the shaded area shown in Figure 12 has lost power. Numbers near the LA shows the load, the numbers in the parentheses adjacent to the BAs represent the amount of power flow (left) and the available power capacity (right). The unit is kW.
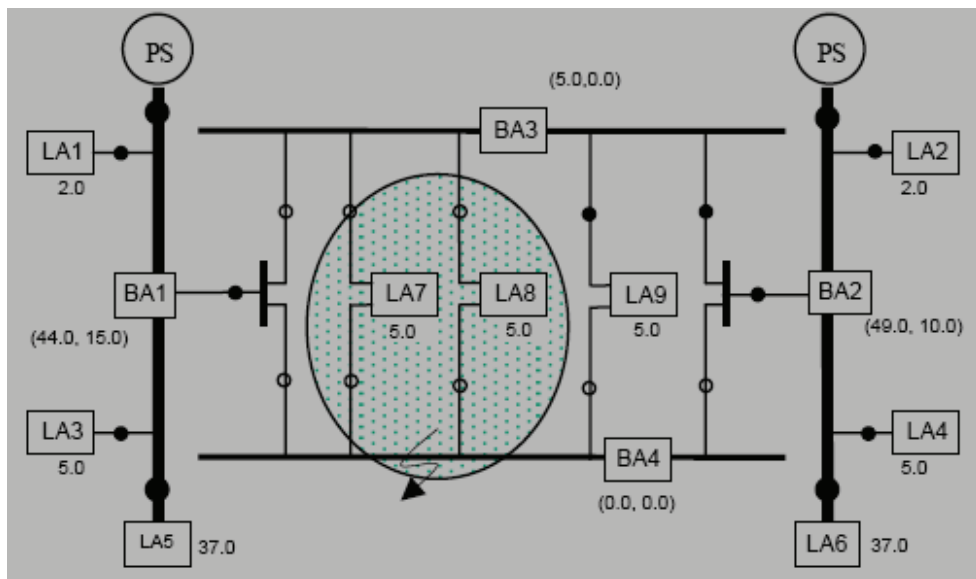

Fig. 12. Post fault network for case 1

In this case, the lines connected to starboard bus are tripped off because of the assumed fault and two loads (LA7, LA8) are to be resupplied by the agent system. For this particular case, BA1, BA2 both have power available for restoration.
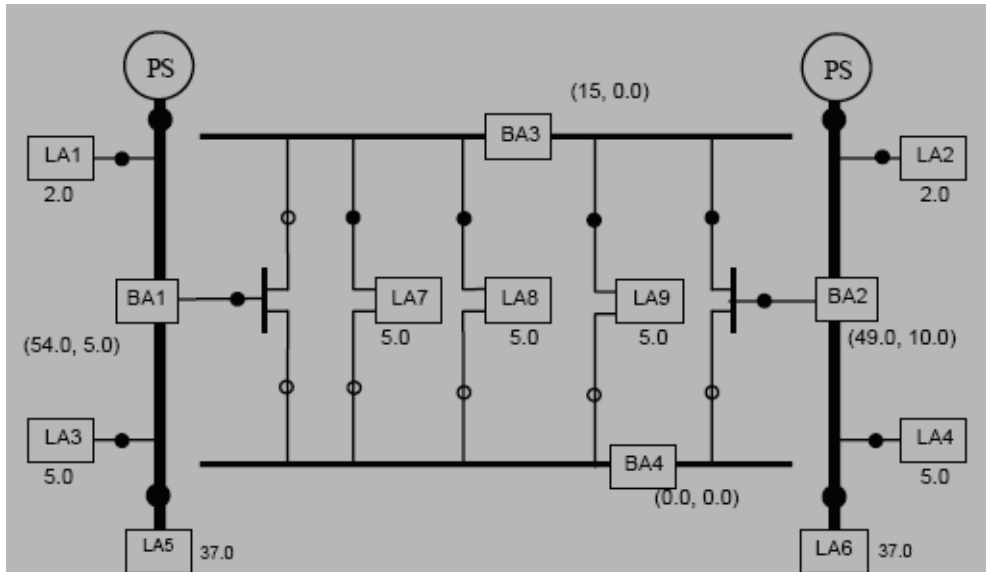
Fig. 13. Network after restoration for case 1

Based on the proposed procedure, negotiation rules, and preset LAs priority list, NA first creates the un-served set (LA7, LA8) and chooses LA8 as first LA to be restored. LA8 then sends restoration request to its Bus Agent BA4. Since the fault is still there, BA4 will send a refuse message to LA8. Thus LA8 tries to restore power from BA3. With 0 available capacities, BA3 first negotiates with its connected neighbor BA2 for more power capacity. Because available capacity of BA2 (10.0) is greater then the request capacity (5.0), BA2 will transfer 5.0 to LA8 through BA3. Once LA8 obtains sufficient power, it will send a message to NA. NA then deletes LA 8 from un-served set. Next, LA7 can also be restored similarly. The communication path is LA7 BA3 BA2. The new network is shown in Figure 13.

2.6.5.2 Case 2: Partial restoration for fault on generator

This case will show partial restoration where the amount of available power falls short of the sum of un-served loads. Now the fault happed in one synchronous generator, the system then lost one of its major power sources. Figure 14 shows the post fault network. Shaded area has lost power.

Like in case 1, the NA first creates un-served set (LA1, LA3, LA5, LA7, LA8). Based on preset priority list, LA5 is selected to be first resorted. Through negotiation path LA5 BA1 BA3 BA2, system can not restore LA5 for insufficient available capacity (10 < 37). Next, LA8 begins the restoration procedure by path LA8 BA4 BA2. After LA8 restoration, LA3 can be restored by path LA3 BA1   BA4 BA2. Later, LA1 and LA7 fail to obtain power.

The amount of available power is only 10. As the total amount of un-served loads is 54, the available power is insufficient to restore all the loads. Although three loads (LA1, LA5, LA7) are unfortunately disconnected as shown in the Figure 15, this is the optimal solution under these conditions.
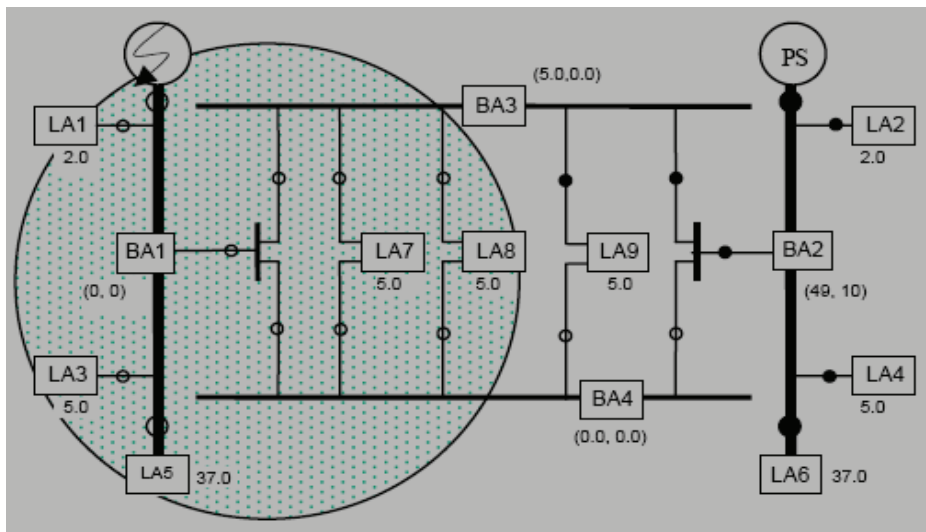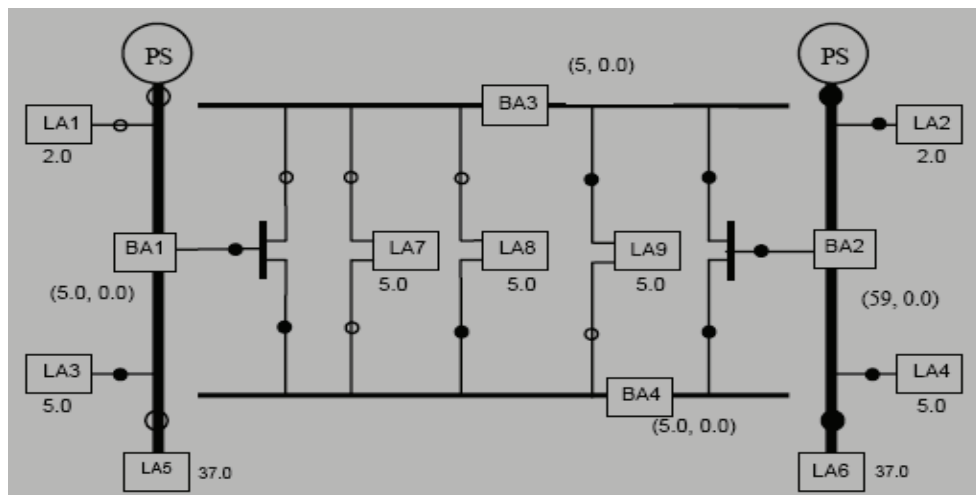
Fig. 14. Post fault network for case 2

Fig. 15. Network after restoration for case 2

This section provides a multi-agent-based approach for navy ship system electric power restoration. The proposed system composed of three different agents. By negotiating among agents, without a control center, the system can perform restoration work by local information. Several test cases have been simulated for the presented method and proved to be successful. Since the whole approach is derived from a simplified ship system structure, the future work of this research will study more complex system structure. Agents control for synchronous generator, propulsion induction motor, and power inverter will be considered.

3. References

Ashish Ahuja, Sanjoy Das, and Anil Pahwa, Fellow, IEEE, 2007, An AIS-ACO Hybrid Approach for Multi-Objective Distribution System Reconfiguration, *IEEE transactions on power systems*, vol. 22, no. 3, pp. 1101-1111.

B. Venkatesh, Rakesh Ranjan, 2000, Optimal radial distribution system reconfiguration using fuzzy adaptation of evolutionary programming, *IEEE transactions on power systems*, vol. 15, no. 3.

D.P. Kothari, I.J.Nagrath. 2007. Power System Engineering, Second Edition. Tata McGraw-Hill Publishing Company Limited. ISBN: 0070647917, 9780070647916, New Delhi.

D.P. Kothari, I.J.Nagrath. 2008. Modern Power System Analysis, Third Edition, McGraw-Hill Publishing Company Limited. ISBN: 0070494894, 9780070494893, New York.

D.P. Kothari, J.S.Dhillon. 2004. Power System Optimisation, Prentice Hall of India Private Limited. ISBN: 8120321979, 9788120321977 , New Delhi.

Dong Zhang, Zhengcai Fu, Liuchun Zhang, 2007, An improved TS algorithm for loss-minimum reconfiguration in large-scale distribution systems, *Electric Power Systems Research*, Volume 77.

Dr. Paramasivam Venkatesh Ramachandran Gnanadass, Dr. Narayana Prasad Padhy, 2004. Available Transfer Capability Determination Using Power Transfer Distribution Factors, The Berkeley Electronic Press.

Elgerd Olle I. 1983. *Electrical energy system theory- An introduction*, Second Edition. Tata McGraw-Hill Publishing Company Limited. ISBN-13: 978-0070992863, New Delhi.

Ghiani E., Member IEEE, Mocci S., Member, IEEE, and Pilo F., Member, IEEE, *Optimal Reconfiguration of Distribution Networks According to the Micro grid Paradigm*.

Momoh James A., Feng Julan, 2009, A Multi-Agent-Based Restoration Approach for Navy Ship Power System, *6th International Conference on Power Systems Operation and Planning*, May 22-26, 2005, Cape Verde, pp.98-102, vol-1.

Mukwanga W. Siti, Dan Valentin Nicolae, Adisa A. Jimoh, Member, IEEE, and Abhisek Ukil, 2007, *Reconfiguration and Load balancing in the LV and MV Distribution Networks for Optimal Performance IEEE transactions on power delivery*, vol. 22, no. 4, pp. 1128-1135.

Nagata T., Sasaki H., and Yokoyama R., 1995, Power system restoration by joint usage of expert system and mathematical programming approach, *IEEE Transactions on Power Systems*, vol. 10, pp. 1473-1479.

Rong-fu Sun, Yue Fan, Yong-hua Song, Senior Member, IEEE, Yuan-zhang Sun, Senior Member, IEEE, 2006, Development and Application of Software for ATC Calculation, *Electric Power Systems Research*, Volume 76.

Salazar Harold, Student Member, Gallego Ramón, and Romero Rubén, Member, IEEE, 2006, Artificial Neural Networks and Clustering Techniques Applied in the Reconfiguration of Distribution Systems, *IEEE transactions on power delivery*, vol. 21, no. 3.

Sivanagaraju, S., Visali, N., Sankar, V., Ramana,T , 2005, Enhancing voltage stability of radial distribution systems by network reconfiguration, *Electric Power Components and Systems* Vol.33 (5) pp. 539-550.

Verbi'c Gregor, Pantoˇs Miloˇs, Gubina Ferdinand, 2006. On voltage collapse and apparent-power losses, *Electric Power Systems Research*, Volume 76.

Wu J. S., Liu C. C., Liou K. L., and Chu R. F., 1997, A petri net algorithm for scheduling of generic restoration actions, *IEEE Transactions on Power Systems*, vol. 12, pp. 69-76.